Structure and Bonding 178
Series Editor: D.M.P. Mingos

Joaquín Pérez Pariente
Manuel Sánchez-Sánchez *Editors*

Structure and Reactivity of Metals in Zeolite Materials

Springer

178
Structure and Bonding

Aims and Scope

Structure and Bonding is a publication which uniquely bridges the journal and book format. Organized into topical volumes, the series publishes in depth and critical reviews on all topics concerning structure and bonding. With over 50 years of history, the series has developed from covering theoretical methods for simple molecules to more complex systems.

Topics addressed in the series now include the design and engineering of molecular solids such as molecular machines, surfaces, two dimensional materials, metal clusters and supramolecular species based either on complementary hydrogen bonding networks or metal coordination centers in metal-organic framework materials (MOFs). Also of interest is the study of reaction coordinates of organometallic transformations and catalytic processes, and the electronic properties of metal ions involved in important biochemical enzymatic reactions.

Volumes on physical and spectroscopic techniques used to provide insights into structural and bonding problems, as well as experimental studies associated with the development of bonding models, reactivity pathways and rates of chemical processes are also relevant for the series.

Structure and Bonding is able to contribute to the challenges of communicating the enormous amount of data now produced in contemporary research by producing volumes which summarize important developments in selected areas of current interest and provide the conceptual framework necessary to use and interpret mega-databases.

We welcome proposals for volumes in the series within the scope mentioned above. Structure and Bonding offers our authors and readers:

- OnlineFirst publication. Each chapter is published online as it is finished, ahead of the print volume
- Wide dissemination. The chapters and the volume will be available on our platform SpringerLink, one of the largest collections of scholarly content in the world. SpringerLink attracts more than 50 million users at 15.000 institutions worldwide.
- Easy manuscript preparation. Authors do not have to spend their valuable time on the layout of their contribution. Springer will take care of all the layout related issues and will provide support throughout the complete process.

More information about this series at http://www.springer.com/series/430

Joaquín Pérez Pariente • Manuel Sánchez-Sánchez
Editors

Structure and Reactivity of Metals in Zeolite Materials

With contributions by

G. Bellussi · G. Berlier · F. Bonino · S. Bordiga · E. Borfecchia · A. Corma · V. Crocellà · T. Jiang · R. F. Lobo · R. Millini · M. Moliner · M. Sánchez-Sánchez · G. Sankar · M. Signorile · I. Sobczak · M. Trejda · A. Wojtaszek-Gurdak · M. Ziolek

Springer

Editors
Joaquín Pérez Pariente
CSIC
Instituto de Catálisis y
Petroleoquímica (ICP)
Madrid, Spain

Manuel Sánchez-Sánchez
CSIC
Instituto de Catálisis y
Petroleoquímica (ICP)
Madrid, Spain

ISSN 0081-5993 ISSN 1616-8550 (electronic)
Structure and Bonding
ISBN 978-3-319-98904-4 ISBN 978-3-319-98905-1 (eBook)
https://doi.org/10.1007/978-3-319-98905-1

Library of Congress Control Number: 2018953018

This Springer imprint is published by the registered company Springer Nature Switzerland AG
The registered company address is: Gewerbestrasse 11, 6330 Cham, Switzerland

Preface

The use of zeolites as adsorbents, ion exchangers, and catalysts benefits from the unique combination of a robust three-dimensional tetrahedral network made of vertex-sharing SiO_4 and AlO_4 tetrahedral units and the intracrystalline porosity of molecular dimensions hosting a variety of charge-compensating cations, which provide chemical functionalities for the interaction with appropriate guest molecules. Replacement of these cations by protons and/or cations with high charge/radius ratio led to reactive acid zeolite materials able to activate a large variety of molecules. The industrial use of zeolites as catalysts was prompted by their excellent performance, if properly prepared, in a plethora of acid-catalyzed reactions involving the transformation of hydrocarbons, such as cracking, hydrocracking, alkylation, and isomerization. They are also active in many organic reactions traditionally catalyzed by homogeneous acids, such as esterification, hydrolysis, and etherification. While the field was initially dominated by low-silica materials used for acid-catalyzed reactions, the scenario changed dramatically in the decade or so between the end of the 1970s and beginning of the 1980s due to two major inventions: first, the preparation of high-silica zeolites by using organic compounds as structure-directing agents, of which ZSM-5 is probably the most widely known representative example, and second, the synthesis of crystalline microporous aluminophosphates, where PO_4 tetrahedra replace SiO_4 tetrahedra in the framework, originating the first families of the so-called zeotypes, the Si-free zeolite-like inorganic microporous materials. In both cases, not only were new topologies and pore architectures available for application in the fields traditionally covered by the low-silica zeolites, but, most importantly, new chemical properties not mirrored by traditional materials rapidly emerged. Among them, the possibility to replace framework Si, Al, or P by metals of appropriate oxidation state and size had a great catalytic impact.

The metals introduced by isomorphous substitution in the framework often exhibited unprecedented chemical reactivity that opened the way to new applications. However, it has also been found that in many cases, during the thermal treatments required to eliminate the structure-directing agent from the pores, part of the metal ions initially present in framework sites are removed to form extra-framework

chemical species which eventually also show remarkable catalytic properties. This volume is devoted to the study of the relationship between structure and catalytic reactivity of metals in zeolite materials. The editors' aim has been to collect in a single volume contributions on the most remarkable aspects of the subject, seeking complementarity in the chapter contents. Therefore, it has been outside the scope to cover every metallic element that has been incorporated in one way or another in zeolite materials. This would have required a multivolume encyclopedia. Each chapter has been conceived to offer the reader not just a digest of the most recent advances but, above all, an in-depth perspective of each topic covered.

The volume opens with a chapter devoted to Ti-containing zeolite materials. The incorporation of Ti into the all-silica MFI framework (TS-1 material) realized in 1983 is a landmark in zeolite science. It not only paved the way to develop new oxidation catalysts, but also demonstrates the scientific and technical relevance of the incorporation of metals in zeolites and stimulates further research in this newborn area. The chapter offers a vivid and thorough discussion of the main factors influencing the performance of TS-1 catalysts, but a section is also devoted to the incorporation of titanium in other zeolite structures. Comparison of both sections highlights how much work is still needed to bring the understanding of the synthesis and catalytic performance of these materials close to the current knowledge on TS-1.

The second chapter introduces a more ample perspective of the reactivity of metals in zeolite materials for catalytic applications, because it covers not only metals in the zeolite lattice, as titanium or tin, but also metals in extra-framework positions, as isolated species, clusters, or even nanoparticles. This contribution allows the reader to get a sense of how fast this field of zeolite chemistry has grown in the last few years concerning the complexity and variety of zeolite-metal systems prepared and serves as a general introduction to some of the topics which will be covered in depth in subsequent chapters.

These two first contributions evidence the crucial role that characterization techniques play in the understanding of structure–reactivity connection in metal-containing zeolites. A full chapter is devoted to this aspect, which focuses on the characterization of metal centers of catalysts for two specific partial oxidation reactions by using a combination of advanced techniques. The first reaction considered is the transformation of methane to methanol by using Cu- and Fe-containing zeolites, which also includes a discussion on operando and in situ methodologies. This study reveals the complex chemistry of metal centers under real working conditions and the necessity of using several techniques to elucidate specific aspects regarding the nuclearity of the chemical environment of the metal sites involved in the process. The second section is devoted to TS-1 catalysts, which provides additional insights that serve to complete the information given on this topic in the introductory chapter.

The versatility of Fe- and Cu-zeolites to activate small molecules is evidenced in the next contribution, where the mechanism of the selective reduction of NO_x with ammonia is discussed. On these grounds, an improved depiction of the reaction

mechanism is presented, which nicely shows the relevance of the basic aspects of the coordination chemistry of copper and iron in this process, offering the readers an original analysis of the complex reaction mechanism from the perspective of inorganic chemistry.

Most of the content of these chapters is devoted basically to three metals, namely, titanium, copper, and iron, which certainly reflects their relevance in current catalytic processes. However, there is certainly life beyond these elements belonging to the first transitions series of the periodic table, as the chapter devoted to the group five elements, V, Nb, and Ta, clearly shows. This is an exhaustive and comprehensive review of the structure–activity relationship in a large variety of different catalytic reactions, including liquid- and gas-phase oxidations, reduction of nitrogen oxides, and acid and bifunctional catalysis. Moreover, emphasis is made on the Lewis acidity and basicity of these metal-containing zeolites.

The information concerning silicon-based frameworks provided in the chapters so far described is completed with that of metal-substituted aluminophosphate microporous materials (MeAPO) in the last chapter. As this is the only contribution devoted exclusively to these materials, it includes sections devoted to a general discussion on their chemistry, as well as relevant aspects of their synthesis in connection with catalysis. Unlike zeolites, $AlPO_4$-based frameworks can easily accommodate divalent metal ions, such as Co^{2+}, Fe^{2+}, and Mn^{2+}, and keep them incorporated after numerous redox catalytic cycles. They are able to catalyze the highly demanding oxidation of the quasi-inert alkanes only with air as an oxidant. In the final section of the chapter, a highly phase-specific structure-directing agent is taken as a driving force to highlight the strong relationship between the preparation of the metal-substituted AlPOs and their catalytic performance.

This volume should not be taken as a complete compilation of all known metal-zeolites, but it covers some of the most significant aspects of these materials, in particular in a catalytic context. Thus, the whole volume addresses an historical perspective of the original metal-doped zeolites (Ti-zeolites), the most successful incorporated metals, current knowledge about the nature of the extra-framework metal species and the environment of the substituted metals into the zeolitic frameworks, the power of advanced characterization for establishing structure–activity relationships, potential and current industrial catalytic applications, both the difficulty and importance of elucidating mechanisms of catalytic reactions, and zeotypes as an alternative to zeolites to incorporate certain catalytically relevant metal ions. Finally, we hope that the critical spirit generally used in the writing of this volume leads readers to face metal-zeolites in a more open, analytical, and comprehensive way.

Madrid, Spain — Joaquín Pérez-Pariente
Madrid, Spain — Manuel Sánchez-Sánchez

Contents

Struct Bond (2018) 178: 1–52
DOI: 10.1007/430_2017_15

Published online: 15 December 2017

Background and Recent Advances in Ti-Containing Zeolite Materials

Giuseppe Bellussi and Roberto Millini

Abstract The incorporation of Ti into the silica framework of zeolites has paved the way for the use of the crystalline microporous solids as shape-selective catalysts for oxidation reactions. This was realized in 1983, when the synthesis of TS-1 and its catalytic properties in the oxidation of several organic substrates with diluted H_2O_2 under mild conditions were claimed. From then on, the TS-1 has been the subject of numerous and in-depth studies aimed at its improvement and understanding of its characteristics, in particular, of the structure of the Ti site. The first part of this chapter is devoted to the synthesis of the TS-1 from its origins to present days, when the focus is on the preparation of materials with hierarchical porosity. A great emphasis is given to the characterization of this material, with particular attention to the structure of the Ti site, to the evaluation of the maximum content of Ti, and to the possible existence of preferential sites for localization of the heteroatom in the framework. The final part of the chapter is devoted to review the synthesis of other Ti-containing zeolites, very promising systems but, with few exceptions (e.g., Ti-beta), still poorly studied.

Keywords Characterization · Synthesis · Ti location · Ti-containing zeolites · Ti-site structure · TS-1

Contents

G. Bellussi (✉) and R. Millini
Research and Technological Innovation Department, Energy Transition Program, Eni S.p.A., San Donato Milanese, Italy
e-mail: giuseppe.bellussi@eni.com

1 Introduction

The isomorphous substitution of Si and/or Al into the zeolite framework by other tri- or tetravalent elements has always been considered as an interesting opportunity for preparing materials with innovative properties. The early examples of isomorphous substitution reported in the 1950s (i.e., Ge into thomsonite [1, 2], Ga and/or Ge in zeolite A, faujasite and harmotome [2]) were considered as scientific curiosities until the end of the 1970s, when it was realized that this approach could lead to the modification of the catalytic properties of zeolites. In this way, boron was incorporated in the framework of several known zeolites producing materials with acid strength weaker than the aluminosilicate parent structures [3]. However, the interest in isomorphous substitution in zeolites strongly increased with the successful incorporation of Ti into the pure silica MFI framework, leading to the discovery of the well-known titanium-silicalite-1 (TS-1) catalyst [4, 5]. Due to the outstanding catalytic properties in oxidation reactions involving H_2O_2 under mild conditions, TS-1 quickly found industrial applications. This increased the interest in this material, which is still widely studied today, and stimulated the researchers to explore the possibility of incorporating Ti in the framework of other zeolites. Before treating the recent advances in the synthesis and characterization of Ti-containing zeolites, it may be worth and interesting for the readers to briefly review the events that have led to the discovery of TS-1.

After the publication of the patent issued to Argauer and Landolt at Mobil Oil Corp. on the synthesis ZSM-5 zeolite [6], several groups started research programs on the synthesis and the applications of this new synthetic zeolite. At the Eni research laboratories, the management of the new research project was entrusted to Prof. Marco Taramasso, one of the leading scientists in gas chromatography in Italy. He was already engaged with the zeolite synthesis and characterization, because of his interest in the application of crystalline microporous materials as stationary phases in the chromatographic columns. The research project leaded by Prof. Taramasso was addressed to study the influence of the organic additives on the synthesis of ZSM-5 and on their effects on the composition of the materials. Very soon, he observed that, unlike the natural zeolites, in ZSM-5 the SiO_2/Al_2O_3 molar ratio can vary in a wide range, until obtaining a pure silica phase. This result raised up great enthusiasm in the research team, which however was quickly dampened when it was found that Edith Flanigen et al. at the Union Carbide had obtained and

patented the same pure silica phase a few months earlier [7, 8]. After passing the consequent discouragement, the attention was focused on the possible uses of this new material, and it was soon realized that the synthesis of a totally siliceous zeolite could be a good starting point for studying the incorporation of elements different from aluminum in the framework.

A huge amount of syntheses were performed in the presence of Si and other elements (hereinafter referred to as *heteroatoms*) such as Cr, Be, Ti, Mn, Fe, Co, Zn, Zr, Rh, Ag, Sn, Sb, and B [9]. All these materials were provided to a group involved in the development of a new catalytic process for the hydroxylation of phenol with hydrogen peroxide. Among the heteroatoms used in the synthesis, Ti showed unexpected and extraordinary results in terms of both activity and selectivity for the mentioned reaction [10]. The knowledge accumulated during this research activity was transferred to a development project aimed to the building of the new and first industrial phenol hydroxylation plant using a zeolite-based catalyst and the H_2O_2 as the oxidant. The related activity included the deep understanding of the physicochemical and catalytic properties of TS-1. Several important achievements were obtained during this period. For instance, the understanding of the negative effect of the alkaline impurities present in the commercial tetrapropylammonium hydroxide (TPAOH) used as a structure-directing agent on the reproducibility of the best TS-1 catalyst has led to the development of a new process for the industrial production of TPAOH [11]. Moreover, the phenol hydroxylation was probably the first process in which a zeolite-based catalyst was used in the liquid phase at low temperature. Under these mild conditions, the diffusion limitations strongly affect the performances of a heterogeneous catalyst. To overcome this drawback, a hierarchical porous catalyst was then developed and produced at industrial scale [12]. In 1985, the first industrial plant for the production of diphenols with a capacity of 12,000 t/y went on stream in the industrial site close to Ravenna, on the Adriatic shore in the northeast of Italy [13, 14]. From then on, other processes such as the ammoximation of cyclohexanone oxime and the oxidation of propylene to propylene oxide were developed, and other industrial plants were built using the same catalyst [15, 16].

This short historical excursus on TS-1 does not highlight the difficulties encountered by researchers not only in the optimization of the synthesis but, above all, in the characterization of this important catalyst. After 34 years from its discovery, efforts are still devoted to improve the characteristics of TS-1 through the application of modern synthesis approaches. Moreover, some important issues concerning the local structure and siting of Ti remain open and are still subject of detailed investigations. Finally, the relative narrow aperture of MFI pores, which imposes strong limitations on the dimensions of the molecules involved in the oxidation reactions, counterbalances the successful results obtained in the industrial applications of TS-1. To solve this problem, the researchers focused on the incorporation of Ti in the frameworks of several other zeolites. These are the topics examined in this chapter, whose aim is to provide the reader the necessary information for better understanding the bright and the dark aspects of TS-1 and in general of Ti-containing zeolites.

2 Synthesis

The synthesis of Ti-containing zeolites proved to be particularly difficult because of the higher tendency of titanium to assume octahedral coordination with oxygen atoms with respect to the tetrahedral one. Therefore, the main issue was to prevent polymerization and precipitation of titanium in the form of hydrated oxides, finding the appropriate conditions for its incorporation into the framework in tetrahedral coordination.

2.1 The Classical Synthesis of TS-1

Two different synthesis procedures, schematized in Fig. 1, were originally proposed by Taramasso et al. [4, 5]:

- The *mixed alkoxides* method based on the controlled hydrolysis of an aqueous solution of tetraethylorthosilicate (TEOS), tetraethylorthotitanate (TEOT), and tetrapropylammonium hydroxide (TPAOH) as structure-directing agent.
- The *dissolved titanium* method based on the addition of H_2O_2 to the titanium-containing solution in order to form stable peroxo-complexes able to release slowly the metal ion during the hydrothermal treatment; colloidal silica is used instead of TEOS.

Between them, the *mixed alkoxides* method is simpler and allows a more accurate control of the synthesis parameters and higher reproducibility of the quality of the products. In the following, we will focus the attention on this method, since the more complex *dissolved titanium* method was rarely applied.

The hydrolysis of the aqueous mixture of TEOS, TEOT, and alkali-free TPAOH is made first at room temperature and successively at 80–90°C for 5 h in order to accelerate the hydrolysis and to remove ethanol; after addition of water, the opalescent homogeneous solution is transferred into an autoclave and heated at 175°C for 10 days. At the end of the hydrothermal treatment, the solid is separated, washed, and calcined at 550°C [4, 5, 17, 18].

In the detailed investigations following the original patent, the most critical parameters affecting the synthesis of TS-1 were identified. First, it was clearly realized that the incorporation of Ti is prevented by the presence of alkali metal ions (mainly, Na^+ and K^+) in the reaction mixture [19–22] usually contained in trace amounts in the commercial TPAOH solutions. Working with high-purity TPAOH, the addition of increasing amounts of NaOH to the reaction mixture produced an increase of the amount of titanium detected in the solid recovered and a decrease of the 960 cm^{-1} IR band, which is considered as a fingerprint of the Ti incorporation in the MFI framework (vide infra). Moreover, at the highest level of sodium, TiO_2 (anatase) was detected by XRD [21]. Based on these evidences, it was concluded that the presence of sodium favors the formation of insoluble titanium-silicate

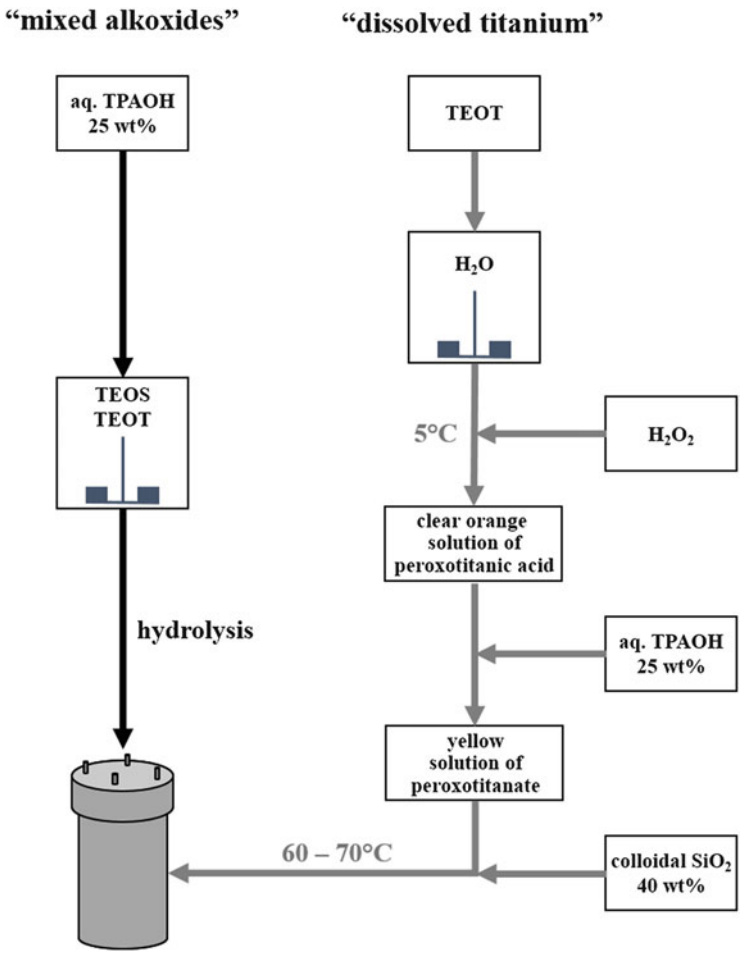

Fig. 1 Original synthesis procedures of TS-1

species, which reduce the amount of heteroatom available for the formation of TS-1 crystals [21]. Later on, it was confirmed that the addition of sodium during the synthesis of TS-1 is detrimental to the catalytic activity in the oxidation of alkanes, alkenes, and phenols at temperatures below 100°C using aqueous H_2O_2 as oxidant [23, 24].

Assessing the detrimental influence of alkali metal ions, Bellussi and Fattore examined the influence of the different parameters on the characteristics of TS-1, identifying the SiO_2/TiO_2 ratio in the reaction mixture and the crystallization temperature as the most critical ones [25]. The influence of the SiO_2/TiO_2 molar ratio in the reagent mixture on the composition of the TS-1 samples is reported in Fig. 2. In the entire compositional range examined, the products systematically show SiO_2/TiO_2 molar ratios higher than the mother solutions. It means that even

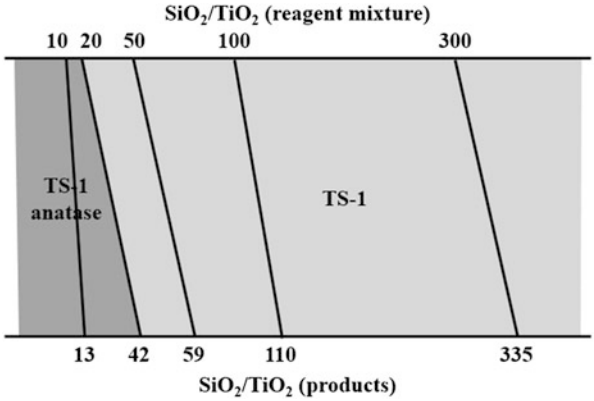

Fig. 2 Influence of the SiO_2/TiO_2 molar ratio in the reagent mixture on the TS-1 composition [25]

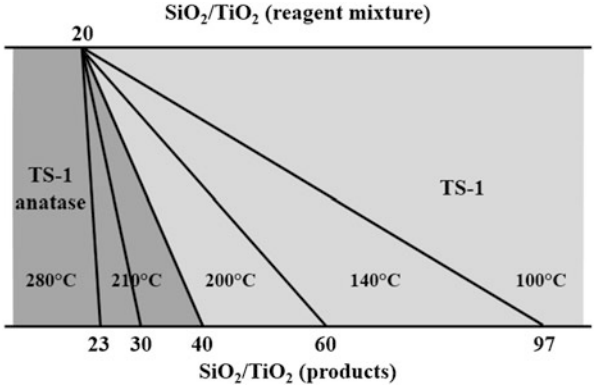

Fig. 3 Influence of the crystallization temperature on the characteristics of TS-1 [25]

for composition well below the upper limit of Ti concentration in the MFI framework ($x = [Ti]/([Ti] + [Si]) = 0.025$ or $SiO_2/TiO_2 = 40$), the incorporation of the heteroatom is not quantitative. Furthermore, it is clear that the SiO_2/TiO_2 molar ratio should not be lower than 20 for obtaining pure and well-crystallized TS-1, since higher concentrations of heteroatom invariably lead to the formation of anatase as a secondary phase.

On the other hand, even the crystallization temperature has a high influence on the composition and phase purity of TS-1 (Fig. 3). Fixing the SiO_2/TiO_2 molar ratio to 20, pure TS-1 can be prepared at $T \leq 200°C$, but the amount of Ti incorporated progressively decreases upon decreasing the temperature. On the other hand, above 200°C, the excess of Ti tends to crystallize in the form of anatase.

As already underlined, the maximum of 2.5 Ti atoms per unit cell (corresponding to $x = [Ti]/([Ti] + [Si]) = 0.025$) has never been overpassed with the original *mixed alkoxides* method, and this seems to be due to kinetic rather than thermodynamic reasons. Therefore, much effort has been made attempting the synthesis of TS-1 with higher Ti content.

In a comprehensive study, van der Pol and van Hooff examined the influence of SiO_2 and TPAOH sources, crystallization time and conditions (static or stirred), OH^-/Si and Si/Ti ratios, and sol concentration on the characteristics of TS-1 [26]. Up to 4 mol% of Ti (i.e., ~4 Ti atoms/unit cell) were incorporated in the framework, as demonstrated by XRD and IR analyses, while it was confirmed that the best results are obtained with TPAOH sources containing small amounts of alkali metal ions. The best conditions for obtaining small crystallites were high SiO_2 concentration and low OH^- and H_2O concentrations. TPAOH should be added very slowly, under vigorous stirring and at low temperature to the TEOS and TEOT in order to avoid the formation of insoluble amorphous TiO_2 species [26]. In other words, it is necessary to have comparable rates of hydrolysis of TEOT and TEOS so as to have sufficient silanol groups for condensing the monomeric hydrolyzed titanium species [27].

The much faster hydrolysis rate of TEOT with respect to TEOS was considered the reason for the limit of $x = 0.025$ of Ti incorporation with the original recipe. As a matter of fact, Thangaraj et al. reported that TS-1 incorporating up to ~9 mol% Ti (i.e., ~9 Ti atoms/unit cell) can be synthesized by using tetrabutylorthotitanate (TBOT) instead of TEOT [28–30]. TBOT is dissolved in dry *i*-PrOH prior to addition to the TEOS/TPAOH solution, in order to prevent its immediate hydrolysis; the hydrolysis is then completed in an open vessel and the gel crystallized under autogenous conditions. However, this exceptionally high extent of Ti incorporation could not be reproduced by other authors, who concluded that the framework composition of TS-1 prepared by this recipe is similar to that achievable with the original recipe, the excess of Ti being segregated in extraframework TiO_2 species [31, 32].

As discussed in the section on characterization, these results have been debated in the scientific community because they are not supported by convincing physicochemical evidences. Tuel and Ben Taârit systematically studied the influence of the nature of Si and Ti alkoxides on the synthesis of TS-1, reaching the conclusion that the extent of Ti incorporation depends on both the silica and titania sources used, the higher concentration ($x = 0.05$) being obtained using tetramethylorthosilicate and tetrapropyl- or tetrabutylorthotitanate [33]. In order to avoid the precipitation of hydrated TiO_2 species during the addition of the alkoxide, the use of aqueous $TiCl_3$ solution was proposed. The sample obtained shows catalytic activity similar to that displayed by conventional TS-1, but no information is reported about the maximum extent of Ti incorporation achievable by this method [34].

What emerged from the early studies is that the synthesis of the TS-1 is very complex and expensive, being strongly influenced by the procedure for the preparation of the synthesis gel as well as by the nature and purity of the reagents. In order to simplify and make less expensive the synthesis of TS-1, numerous attempts were conducted using different sources of Si and Ti, by replacing (at least in part) the expensive alkali-free TPAOH with other SDAs and/or by adding mineralizing agents of various nature (Fig. 4).

With the aim of improving the characteristics of TS-1 and reducing the costs related to the use of expensive reactants (Si and Ti alkoxides, alkali-free TPAOH), alternative reagents and eventually synthesis routes have been proposed. Figure 4

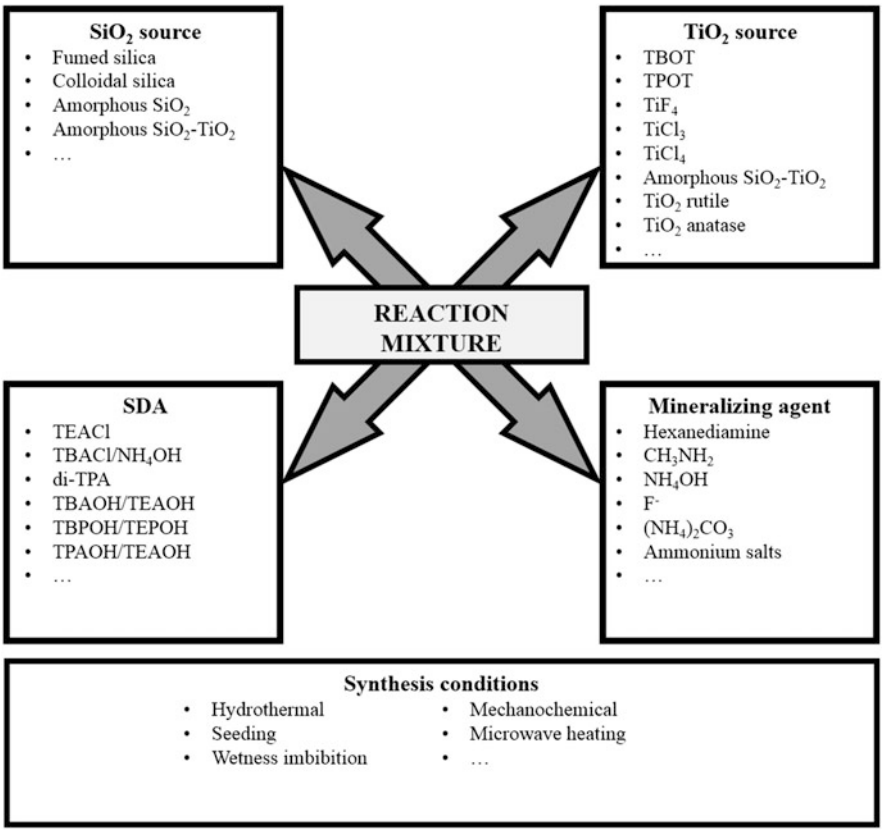

Fig. 4 Some examples of reagents and conditions employed in the syntheses of TS-1. *TBOT* tetrabutylorthotitanate, *TPOT* tetrapropylorthotitanate, *TPA* tetrapropylammonium, *di-TPA* hexapropyl-1,6-hexanediammonium, *TEA* tetraethylammonium, *TBA* tetrabutylammonium, *TBP* tetrabutylphosphonium, *TEP* tetraethylphosphonium

reports a non-exhaustive list of Si and Ti sources, SDAs, mineralizing agents, and synthesis conditions applied.

The replacement of the expensive alkali-free TPAOH by other SDAs, even in combination with mineralizing agents of different nature, did not give interesting results. When mixtures of TPABr and methylamine [35], tetraethylammonium chloride, tetrabutylammonium chloride and ammonium hydroxide [36], or hexanediamine [37] were used, the evidences reported were insufficient for determining the extent of Ti incorporation, while the catalytic activity was very poorly described or not reported at all. The use of di-TPA was more successful, which gave TS-1 samples composed of small crystallites (roughly of the same dimensions of the original TS-1 [18]) showing activities and selectivities similar to those of a standard TS-1 in the hydroxylation of phenol with H_2O_2. On the other hand, only 1.9 Ti/unit cell was incorporated in the framework, significantly lower than the limit of 2.5 achievable with the standard recipe [38].

Tuel et al. examined the use of mixtures of tetrabutylammonium hydroxide (TBAOH) and tetraethylammonium hydroxide (TEAOH). Pure TS-1 was obtained when more than 20% of TBAOH was replaced by TEAOH, while at lower levels of replacement, the crystallization of TS-2 (the MFI/MEL intergrowth structure) was achieved. TS-2 proved to have similar catalytic properties as a standard TS-1 in the hydroxylation of phenol [39]. Similar results were obtained by using mixtures of tetrabutylphosphonium hydroxide (TBPOH) and tetraethylphosphonium hydroxide (TEPOH), even if the maximum Ti incorporation was lower (~1 Ti/unit cell) [40].

The improvement of the characteristics of TS-1 was attempted by varying the nature of the mineralizing agent. Besides the already cited ammonium hydroxide and organic amines, which did not give any positive result, the addition of F^- ions attracted a certain attention. Early attempts were made by Guth et al. [41, 42] and Qiu et al. [43], who started from gels containing F^- ions at nearly neutral conditions (pH = 6.5–7.5). However, no evidence was reported about the effective Ti incorporation in the framework. Anatase impurities were systematically observed in TS-1 samples prepared by this synthesis route [44], while the formation of octahedral extraframework Ti species was confirmed by EXAFS experiments [45]. Carati et al. compared TS-1 samples prepared with the classical method and with the addition of alkali-free TEAOH with those crystallized in the presence of, respectively, NH_4F and HF [46]. They found that the structural and morphological properties of TS-1 are strongly influenced by the addition of fluoride ions; the partial substitution of TPAOH by TEAOH or the addition of NH_4F causes a decrease of the order of the Ti sites and/or of the zeolite framework around them and reduces the stability under H_2O_2 treatment. On the other hand, the addition of HF causes the segregation of Ti as anatase [46].

Grieneisen et al. lightly modified the *mixed alkoxides* method by the addition of HF after the hydrolysis of TEOS and TEOT and the addition of TPAOH. The neutral gel was then heated at 170°C for 5 days. This approach leads to the incorporation of 1.8 Ti atoms/unit cell in large crystals (>10 μm). However, the addition of 2 wt% of silicalite-1 seeds reduced the average dimensions of the crystals down to ~1 μm. The catalytic activity in the hydroxylation of phenol was roughly the same as that prepared by mixed alkoxides method [47].

The group of T. Tatsumi has developed new routes to the synthesis of TS-1 using $(NH_4)_2CO_3$ as a crystallization-mediating agent by modifying the original *dissolved titanium* method [48]. They conclude that the Si/Ti ratio in the framework can be decreased to 34 in contrast to 58 achieved by the original method. The structural and spectroscopic data reported in support, however, suffer of some uncertainties, and overall, the maximum amount of Ti incorporated does not differ so much with respect to that claimed by Taramasso et al. [4].

Later on, the same group systematically investigated the effect of the addition of several ammonium salts as crystallization-mediating agents in the synthesis of TS-1, showing that the fine structure and crystal morphology of the synthesized materials depend on the type of anion [49]. The ammonium salts were added in large amounts ($(NH_4)_nM/SiO_2 = 0.1–0.5$), and with the exception of NH_4F, this led to a significant decrease of the crystallization rate due to the reduction of the pH

value of the reaction gel. The ammonium salts have also a strong influence on the catalytic performance of TS-1, which depends on the substrate molecules. In this way, TS-1 prepared with $(NH_4)_2SO_4$ gave the highest conversion in the epoxidation of 1-hexene, whereas that synthesized with $(NH_4)_2CO_3$ showed the best performance in the hydroxylation of phenol [49].

More recently, Zhu et al. reported that the addition of CO_2 as an alkalinity regulator increases the Ti incorporation from 1.7 Ti/u.c. achieved in the conventional *dissolved titanium*-type synthesis to 2.3 Ti/u.c. Upon increasing the CO_2 pressure, the TS-1 morphology evolved from regular spheroidal particles (400–800 nm) to regular double interpenetrated hexagonal prisms with a twinning angle close to 90° with approximate dimensions of 1 × 0.3 × 2 μm. No dramatic changes of the catalytic activity in the hydroxylation of phenol were observed [50].

The possibility of using Ti and Si sources different from the alkoxides has been extensively explored, and depending on the nature of these sources, this has often imposed the development of new synthesis routes (Fig. 4).

In order to avoid the precipitation of oxidic phases of Ti during the preparation of the gel, some authors proposed the use of Ti halides. Gao et al. reported the synthesis of TS-1 using $TiCl_3$, which was added to the solution of TEOS and TPAOH before the hydrothermal treatment. From the few data reported, the advantages of using $TiCl_3$ with respect to the alkoxides are, however, not clear [34]. TS-1 was recently synthesized from silica sol, $TiCl_3$, NH_3, and TPABr. The addition of ethanolamine altered the distribution of the framework and extra-framework Ti species and favored the formation of large voids in the TS-1 crystals. This hierarchical porous structure reduced the diffusion limitations in such a way that, when tested in continuous ammoximation of cyclohexanone, a high conversion of cyclohexanone (98%) and oxime selectivity (100%) was maintained up to 410 h [51].

Shibata et al. used $TiCl_4$ in rapid syntheses of TS-1 using the so-called in situ seeding method, which involves the pre-heating of the silicate gel with the consequent in situ formation of silicalite-1 seeds before the addition of the Ti source. The crystallization of TS-1, in methylamine medium, is dramatically accelerated, favoring the incorporation of Ti in the framework [52]. Syntheses were also reported by using TiF_3 [44] and TiF_4 [53]. In the first case, the syntheses, carried out in fluoride medium under non-alkaline conditions, led to the formation of very large TS-1 crystals (35–50 μm), not suitable for being used as catalysts in oxidation reactions [44]. On the other hand, Jorda et al. demonstrated that $TiCl_4$ is a suitable Ti source for preparing TS-1 with up to 2 Ti/u.c. in form of small crystals (0.3 μm). Only trace amounts of F^- ions were detected in the products [53].

A number of Si sources have been proposed as an alternative to the expensive tetraalkyl orthosilicates, including fumed [52, 54–56] and colloidal silica [4, 56–58]. None of these sources, however, have produced results that make them more convenient than, e.g., TEOS.

An interesting and simple method for the preparation of TS-1 is based on the use of preformed amorphous SiO_2-TiO_2 solids. This method was originally proposed by Padovan et al., who prepared TS-1 by wetness impregnating with aqueous TPAOH

commercial SiO_2-TiO_2 coprecipitates and then subjecting them to crystallization under autogenous pressure for 10 days [59]. A successive modification of this method involved the dry impregnation of preformed porous SiO_2 microspheres with a solution containing TPAOH and Ti alkoxide, followed by crystallization at 175°C in sealed silica tubes. Pure and well-crystallized TS-1 was obtained after only 10 h, while longer crystallization times induced the formation of extra-framework Ti species [60]. This method was successively improved by the group of D. P. Serrano, who used SiO_2-TiO_2 xerogels prepared by an acid-base two-step process. The xerogels were wetness impregnated with aqueous TPAOH, followed by crystallization at 170°C for 24 h [61–64]. The Ti content in the product is controlled by the xerogel composition, while the upper Ti concentration limit, x, in TS-1 was found to be 0.023 (as determined by the linear increase of the intensity of the 960 cm^{-1} IR band relative to the 800 cm^{-1} band [62]). Interestingly, this method proved to be suitable for the preparation of TS-2 [65], Al-TS-1 [66, 67], and Ti-Al-beta [68].

The interesting, though poorly explored, mechanochemical route was recently proposed. The original recipe involved the use of anatase-type titania powder and fumed silica as Ti and Si sources, respectively. The mixture of these solids (with Si/Ti = 50) was allowed to react mechanochemically through the long (36 h) milling in a silicon nitride planetary ball mill. Aqueous TPAOH was successively added to the resulting silica-titania composite and the resulting mixture heated at 170°C for 3 days. The crystallization of TS-1, in the form of coffin-like crystal with average dimensions of ~2 μm, is reported to be highly reproducible [69, 70]. The same route was employed for preparing Ti-beta and Ti-MCM-41 materials [70]. More recently, the method was improved with the use of low-grade fume silica, TPABr, and *n*-butylamine as low-cost reagents. The cost of TS-1 synthesized by this method, composed of large (5–10 μm) coffin-like crystals, was estimated to be ~5% of that prepared by the conventional route [71].

Several reports deal with the use of microwave (MW)-assisted heating, which has the advantage to get homogeneous nucleation and substantial reduction in the crystallization time with respect to the conventional heating. The early attempts were carried out by Uguina et al. who obtained well-crystallized TS-1 samples having Si/Ti molar ratios up to 53.2 after 30 min of MW heating of conventional gels [72]. Later on, Ramakrishna Prasad et al. employed MW heating to crystallize Ti-rich TS-1 samples starting from TEOS, TBOT, and TPAOH with Si/Ti in the range 10–33.8. They claim to obtain pure and well-crystallized TS-1 samples free from extraframework Ti. In reality, the inspection of the XRD patterns reveals the presence of anatase (weak reflection at $2\theta = 25.4°$) in some of the samples [73]. Cundy et al. employed the conventional and MW heating for preparing colloidal TS-1 [74, 75] and TS-2 [75] from gels containing TEOS, TBOT, TPAOH, and TBAOH, respectively. These detailed investigations revealed that, with respect to the synthesis of silicalite-1, the presence of Ti influences both the nucleation (reduction of number of crystals nucleated) and growth rate (linear growth rate at 175°C with ~2.5 Ti/u.c. $\leq$80 nm h^{-1}, three to eight times lower than that of silicalite-1) [74]. Moreover, the Ti incorporation increases upon

increasing the temperature, the maximum of ~2.5 Ti/u.c. being achieved at 175°C; in the case of TS-2, the maximum Ti content reaches ~3.5 Ti/u.c [75].

MW heating was applied also in the syntheses involving solid SiO_2-TiO_2 precursors. Ahn et al. crystallized TS-1 within 30 min with >90% yield, starting from SiO_2-TiO_2 xerogels dry-impregnated with TPAOH solution [76]. In a more detailed study, the same group investigated the effect of the amorphous Ti-containing solid precursors on the characteristics of the crystalline products. SiO_2-TiO_2 xerogel, sub-μm-sized SiO_2-TiO_2 prepared by thermal plasma process, and Ti-containing mesoporous silica, Ti-HMS, were used as solid substrates; after impregnation with aqueous TPAOH, the mixtures were heated with MW at 170°C for 2 h. The results showed that well-crystallized TS-1 was obtained with SiO_2-TiO_2 xerogel only, while the other substrates led to partially crystallized solids. The 1-hexene epoxidation tests showed that only TS-1 obtained with SiO_2-TiO_2 xerogel showed catalytic performances comparable with those of the conventional and commercial catalysts [77].

3 Characterization of TS-1

As outlined in previous sections, the heteroatom concentration in Ti-zeolites is generally very low, and this makes their characterization rather complex. Nevertheless, their accurate physicochemical characterization is highly important in view of the dramatic differences of the catalytic performances between a well-synthesized sample and one containing extraframework titanium species. This was observed especially in the case of the TS-1, by far the most studied material among the Ti-containing zeolites. In particular, the issues that the structural and spectroscopic investigations shall face concern:

- The assessment of the true framework incorporation of Ti
- The determination of the higher level of Ti incorporation in the framework
- The coordination of Ti in the framework
- The existence of any preferential sites for Ti incorporation

An impressive amount of data is available today and will be hereinafter briefly examined, bearing in mind that, although mainly referred to TS-1, the experimental evidences are valid for all the other Ti-containing zeolites.

The need to address these issues by integrating evidence gathered by different techniques is related to the impossibility of determining the site geometry by direct structural methods, due to the low concentration of Ti in zeolites. This limitation has appeared clear already in the first article on TS-1 in which the authors have combined the experimental evidence from different structural (XRD) and spectroscopic (FT-IR, SEM-EDS) techniques and applied models for the interpretation of the experimental data to support the effective incorporation of Ti in the framework [17]. Once confirmed with reasonable certainty the effective incorporation of Ti, other analytical techniques were used to examine in more details the structural

Table 1 Structural and spectroscopic techniques used for the characterization of Ti-containing zeolites

Technique	Results
XRD, NPD	Phase purity, quantification of framework and extraframework Ti species (crystalline phases only)
TEM	Detection and identification of extraframework Ti species
FT-IR	Detection, quantification, and coordination of framework Ti
Raman	Detection of extraframework Ti species
DRS UV-Vis	Coordination of framework Ti, quantification of extraframework Ti species
XAFS	Coordination of framework Ti, detection of extraframework Ti species
EPR	Coordination of framework Ti, qualitative estimation of framework and extraframework Ti species

features of TS-1, with particular regard to the coordination of the heteroatom, an information considered of fundamental importance to understand the peculiar catalytic properties of this material (Table 1).

3.1 Structural Characterization of TS-1

In the calcined form, TS-1 is characterized by the complex XRD patterns of the MFI-type zeolites: at low Ti content ($x < 0.01$, corresponding to ~1 Ti atom/unit cell), it displays the monoclinic $P2_{1/n}$ symmetry, while at higher Ti content, the transition to the orthorhombic P*nma* symmetry is observed. This behavior is in line with that of the Al (ZSM-5 [78]) and B (H-BOR-C [79]) parent structures. Regardless of the lattice symmetry, a linear dependence of the unit cell parameters and volume on the Ti content was observed. Lattice parameters were originally determined by the least-squares fit to the interplanar spacings of a few selected reflections [17] and later confirmed by the more accurate full-profile fitting (Rietveld method) of laboratory [31] and synchrotron powder diffraction data [80]. The equations relating the unit cell parameter and volume with the Ti content are reported in Table 2. Among them, it is particularly interesting to examine the unit cell volume, whose linear variation (Fig. 5) indicates that TS-1 follows a Vegard-type law, the expansion being attributed to the longer Ti–O bond length (d_{Ti-O}) with respect to the Si–O one (d_{Si-O}). In analogy with B-containing MFI (H-BOR-C [79]), the unit cell volume (V_x) of a TS-1 sample containing a molar fraction (x) of Ti can be related to the unit cell volume of the pure silica parent structure, silicalite-1 (V_{Si}), through the equation:

$$V_x = V_{Si} - V_{Si}\left[1 - (d_{Ti-O}/d_{Si-O})^3\right]x \quad (1)$$

Table 2 Linear regression analysis of the lattice parameters of calcined TS-1[a]

	Millini et al. [31][b]			Lamberti et al. [80][c]		
	u	*v*	*r*	*u*	*v*	*r*
a	1.429	20.098	0.9868	2.410	20.069	0.99945
b	2.975	19.882	0.9924	2.661	19.880	0.9977
c	2.281	13.363	0.9957	1.896	13.372	0.9986
V	2,110.4	5,339.4	0.9993	2,093.0	5,335.8	0.99994

[a]According to the equation, $y = ux + v$; r is the correlation coefficient
[b]TS-1 samples treated with ammonium acetate solution and further calcined at 550°C
[c]TS-1 samples not treated with ammonium acetate solution

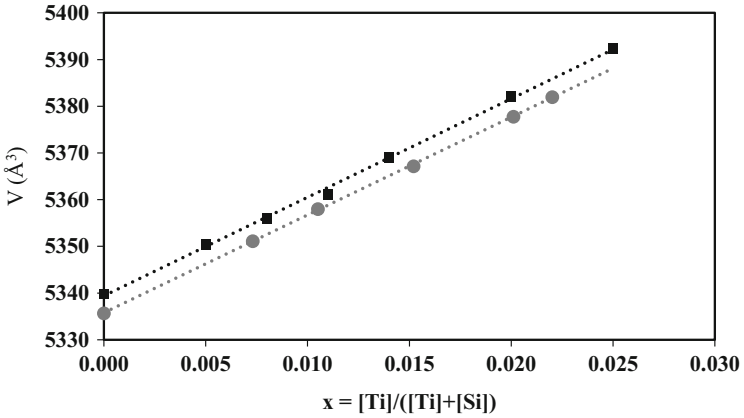

Fig. 5 Unit cell volume variation as a function of the Ti content in TS-1 determined by Rietveld refinement of the laboratory (square [31]) and synchrotron (circle [80]) powder diffraction data

By applying Eq. (1) to the results of Fig. 5 and by attributing to $d_{Si–O}$, the value typically observed in zeolites, 1.61 Å, a $d_{Ti–O}$ of 1.80 Å, was obtained [31]. In this regard, it is interesting to compare the unit cell volume variation determined from the XRD data collected on a conventional laboratory diffractometer on TS-1 samples previously treated with ammonium acetate solution and further calcined at 550°C [31] with those collected with synchrotron radiation under vacuum on untreated samples [80]. The latter systematically display slightly smaller (~5 $Å^3$) unit cell volumes, but the slopes of the two regression lines are practically the same (Fig. 5). As a matter of fact, a $d_{Ti–O}$ of 1.80 Å is computed by applying Eq. (1). This value of $d_{Ti–O}$ was considered a compelling evidence of the incorporation of Ti in the TS-1 framework in tetrahedral coordination. Furthermore, the equation that correlates the unit cell volume with the Ti content is particularly important since it can be used for determining the true framework composition and, by comparing it with the analytical Ti content, the amount of extraframework Ti species, if any, can be estimated [31]. This was confirmed by Lamberti et al. who also highlighted the improvements achievable by the use of synchrotron powder diffraction data collected under vacuum on untreated TS-1 samples [80].

Interestingly, the linear lattice expansion was verified also on the as-synthesized TS-1 samples [81]. In this case, however, the presence of TPA^+ ions in the pores induces an expansion of the unit cell already in the pure silica end-member, and this compensates in part the contribution of Ti; in fact, the slope of the regression curve was much lower than in the case of the calcined samples (Table 3).

The linear variation of the unit cell volume was reported by other authors for supporting the incorporation of Ti in larger amounts with respect to the limit of $x = 0.025$ claimed by Perego et al. [17]. Table 3 compares the equations of the regression lines of the data reported by different authors, together with the maximum Ti concentration as well as the $d_{Ti–O}$ bond length computed from Eq. (1). Attempts to increase the content of Ti in the framework of the TS-1 to values exceeding the limit $x = 0.025$ are justified by the need to improve the catalytic performances of the material. In this way, Thangaraj et al. reported the possibility to prepare TS-1 with a Ti molar fraction up to 0.091 [28], while other authors claimed intermediate values (Table 3). However, upon inspecting the crystallographic data reported, it emerges that the expansion of the unit cell volume reaches a maximum close to that reported by Millini et al. [31]. On the other hand, the slope of the regression line decreases upon increasing the maximum Ti content, and consequently the Ti–O bond length computed from Eq. (1) decreases to 1.67–1.74 Å (Table 3). This could be due to two different reasons: (1) the contraction of the T-O-T angles upon Ti incorporation and (2) Ti atoms form sites different from the tetrahedral ones. The former hypothesis is unlikely because of the low Ti concentration in the MFI framework. On the other hand, different authors invoked the formation of Ti sites with a structure different from the expected tetrahedral one even if not supported by other experimental data. This issue will be discussed later.

Finally, the results reported by Fan et al. [48] deserve attention because they show a systematic and significant decrease of the unit cell volume compared to the other published values (Table 3). The justifications reported by the authors (i.e., measurement of the samples under different conditions, the different lattice sites for the inclusion of Ti, the increase in the particle size, the decrease in the defect sites with increasing framework Ti content, and/or the use of a different refinement program) are not convincing. Examining the data listed in Table 3, excluding those reported in [48], it is clear that the maximum volume of the unit cell lies in a very

Table 3 Linear regression analysis of the unit cell volume of calcined TS-1[a]

u	v	V_{max}	x_{max}	$d_{Ti–O}$	Reference
2,110.4	5,339.4	5,392.3	0.025	1.80	[31]
1,294.1	5,355.8	5,385.6	0.0223	1.73	[81]
2,093.0	5,335.8	5,382.0	0.022	1.80	[80]
606.4	5,340.2	5,396.5	0.091	1.67	[28]
1,362.7	5,339.0	5,389.4	0.039	1.74	[26]
875.0	5,340.0	5,389[b]	0.056	1.69	[33]
4,400.8	5,176.9	5,305[b]	0.028	1.98	[48]

[a]According to the equation, $y = ux + v$; r is the correlation coefficient

[b]Extrapolated from the plots

narrow range (5,389–5,396.5 Å^3) irrespective of the maximum Ti content. This is in agreement with the fact that up to ~2.5 Ti/u.c. ($x = 0.025$) can be accommodated in the MFI framework [31]. What is the reason for this limit? To give an answer to this question, it is necessary to unequivocally determine the nature of the Ti sites in the framework of TS-1.

3.2 Spectroscopic Characterization of TS-1

The vibrational (FTIR and Raman) and electronic (DRS UV-Vis) spectroscopies revealed some important and peculiar features of TS-1. First, a characteristic absorption at 960–970 cm^{-1} is observed in the FTIR spectrum of this phase. This band was soon considered as the "fingerprint" of TS-1 and, in general, of Ti-containing zeolites since it is not observed in pure silica and aluminosilicate zeolites. The intensity of this absorption band is proportional to the Ti content, x [17, 82]; usually, the increase of the ratio between the 960 and 550 cm^{-1} or 800 cm^{-1} band intensities (the latter being characteristic of the MFI structure) with the Ti molar fraction of TS-1 is reported [26, 38, 83, 84]. However, the frequency and intensity of this band are influenced by the degree of hydration [82] and, in some extent, by the crystal size [85]. This hampers the precise determination of the framework composition of TS-1 by FTIR.

Even Raman spectroscopy was extensively used for characterizing Ti in TS-1. Originally, this technique was used for evaluating the presence of extraframework Ti in the form of anatase with a detection limit of 0.5 wt% [86]. More detailed investigations revealed that the incorporation of Ti causes the appearance of new Raman-active modes at 960 and 1,127 cm^{-1}, the latter being IR inactive [87]. By combining these evidences, it was possible to verify the state of Ti in TS-1 [88, 89] as well as in Ti-ZSM-48 and Ti-beta [88]. Li et al. applied UV resonance Raman spectroscopy for identifying Ti in TS-1 [90]. Excitation with a 244 nm laser evidenced the presence of three strong bands at 490, 530, and 1,125 cm^{-1} absent in the spectrum of silicalite-1 and therefore assigned to the presence of Ti. These bands were not observed with excitation wavelengths of 325 and 488 nm, suggesting that these bands are due to the 244 nm UV excitation, which is close to the center of the electronic absorption band of TS-1. Even the band at 960 cm^{-1} was present, but its intensity was unaffected by the excitation wavelength [90]. The group of A. Zecchina in Turin successively confirmed these results [91]. They also explained the different behaviors of the two Raman bands: through ab initio quantum mechanical calculations, they assigned the 1,125 cm^{-1} band to the totally symmetric stretching mode of [Ti(SiO)$_4$] units and the 960 cm^{-1} band to a combination of three asymmetric stretching modes of the same units [92–94].

UV-Vis diffuse reflectance spectroscopy (DRS UV-Vis) also provides useful information on the valence and coordination of Ti in zeolites [60, 82, 95]. In particular, TS-1 samples free from extraframework Ti species display a strong absorption with a maximum in the range 50,000–47,000 cm^{-1} (200–212 nm), assigned to the charge transfer (CT) from the O to an unoccupied orbital of Ti in

[TiO_4] tetrahedra. When relatively large TiO_2 (anatase) particles are present, the DRS UV-Vis spectrum contains a second absorption with a maximum at 32,000–30,000 cm^{-1} (312–328 nm). It is worth noting that the position of this band progressively shifts to lower wavenumber as the size of the segregated TiO_2 particles decreases [96].

Based on these spectroscopic evidences, different hypotheses on the nature of the Ti site were proposed, Fig. 6 [82]. The possible assignment to silanol groups (**I**), which absorb at ~985 cm^{-1} in amorphous silica [97], was soon discarded because it is insensitive to deuterium exchange [85]. On the other hand, the existence of titanyl (Ti = O) moieties (**II**), initially considered, was also considered inconsistent with the features of the DRS UV-Vis spectrum of TS-1. In fact, the presence of Ti = O bonds would imply a CT transition occurring at 25,000–35,000 cm^{-1} (285–400 nm) not observed in TS-1 samples free from extraframework Ti.

Boccuti et al. assigned the band to the Si–O stretching of the polarized $Si–O^{\delta-}–Ti^{\delta+}$ bond (**III**), with Ti in tetrahedral coordination [82]. This assignment accounts well for the sensitivity of the frequency of this band to the treatment with ^{17}O- and ^{18}O-labeled water (Fig. 7), consequent to the variation of the reduced mass of the Si–O–Ti harmonic oscillator, after substitution of ^{16}O with heavier isotopes [83]. Zecchina et al. gave a more detailed interpretation of the 960 cm^{-1} band, depicting two different situations [86]. The first one is based on the hypothesis that the force constants of the Si–O and Ti–O bonds are equivalent; therefore, the replacement of Si with Ti induces a shift of the B mode of vibration of the [TO_4] tetrahedra from 1,120 (T = Si) to 960 cm^{-1} (T = Ti), simply due to mass effects. When the force constants of the two bonds are nonequivalent, a higher polarity is considered for the Ti–O bond so that the 960 cm^{-1} absorption is assigned to the local mode of a [SiO_4] tetrahedron or to the stretching mode of [$Ti(OSiO_3)_4$] cluster, if the difference in polarity between the two bonds is large or small, respectively.

X-ray absorption spectroscopy (XANES/EXAFS) was extensively applied for characterizing the state of Ti in TS-1. At this regard, it should be pointed out that the quality of the TS-1 samples strongly affected the interpretation of the experimental results. As a matter of fact, upon comparing the XANES spectra of dehydrated TS-1 with those of several model compounds, Behrens et al. concluded that Ti is present mainly in octahedral coordination (75%) and in lesser extent in square pyramidal (15%) and tetrahedral (10%) coordination [98, 99], arguing that at ambient conditions all Ti atoms might assume the octahedral coordination [98]. However, the samples used probably contained the majority of Ti in extraframework position,

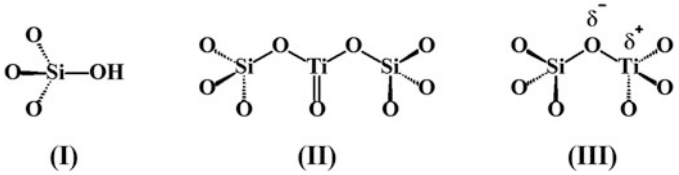

Fig. 6 Proposed assignments for the 960–970 cm^{-1} IR absorption band of TS-1 [82]

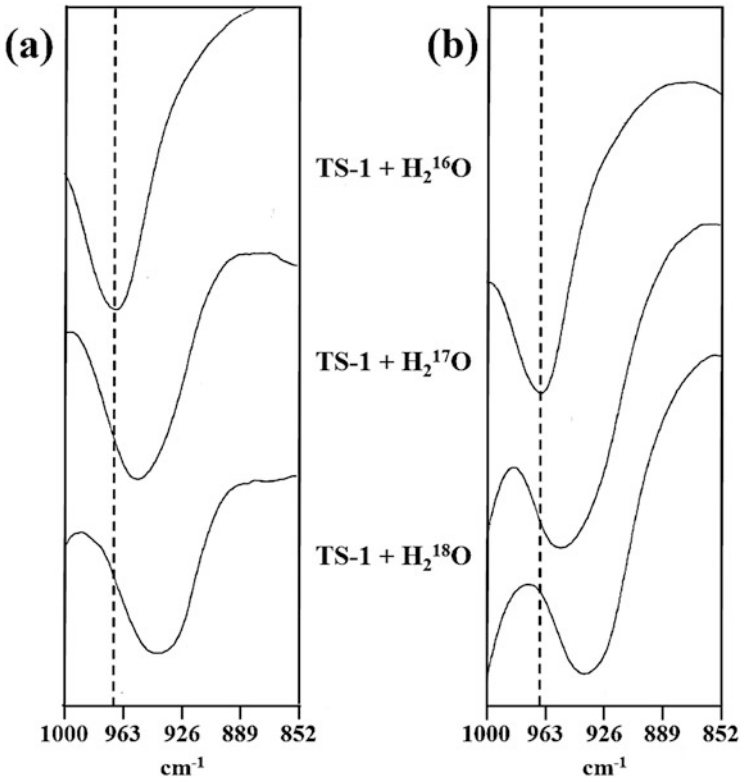

Fig. 7 Frequency variation of the fingerprint band of small (**a**) and large (**b**) crystals of TS-1 upon treatment with ^{17}O- and ^{18}O-labeled water (Unpublished results from Eni laboratories)

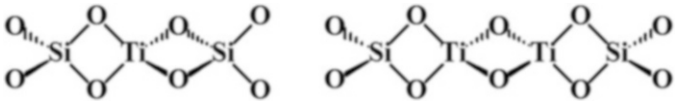

Fig. 8 Ti-site structures proposed by Trong On et al. [84, 101]

since the reported value of the unit cell volume was smaller than that of silicalite-1 [98, 99]. Even the TS-1 samples employed by Shultz et al. likely suffered of the same problem, since only the Ti–O bond length (1.85 Å) was determined but not the coordination number [100].

The interpretation of the EXAFS spectra of TS-2 led to hypothesize the existence of novel Ti-site structures, consisting of $[TiO_4]$ unit edge-sharing with $[SiO_4]$ tetrahedra (Fig. 8) and forming bridges across the channels [84, 101]. These structures should be considered as structural defects rather than a real isomorphous substitution, and following the authors, they would impose less strain to the framework justifying the lower lattice expansion observed for TS-1 samples

containing up to 9 Ti/u.c. [28, 33], with respect to that measured on samples prepared by the original recipe.

However, the existence of these Ti-site structures was soon ruled out both theoretically [102] and experimentally [103–105]. In particular, Pei et al. demonstrated that the structures reported in Fig. 8 were based on the erroneous interpretation of the Fourier-transform peak at 2.1 Å. Their detailed interpretation of the EXAFS spectra led to conclude that Ti is four-coordinated with Ti–O bond distance of 1.80 Å, with no evidence for the presence of five- and six-coordinated Ti species [103]. More recently, a combined EXAFS and photoluminescence study performed in vacuum conditions on TS-1 samples prepared with the original recipe (therefore free from extraframework Ti species) confirmed that Ti is coordinated with O atoms with Ti–O bond distance of 1.79–1.80 Å but with a coordination number of 4.44 ± 0.25. This was interpreted with the existence of two different structural situations for Ti: a $[Ti(OSiO_3)_4]$ "closed site," corresponding to Ti in tetrahedral coordination in the framework, and a defective $[(OH)Ti(HOSiO_3)(OSiO_3)_3]$ "open site" in which Ti is five-coordinated [106].

In summary, the EXAFS/XANES studies corroborate the conclusion that, in well-manufactured TS-1 samples, Ti is incorporated in the MFI framework with a Ti–O bond length in the range 1.79–1.80 Å, in very nice agreement with the XRD analysis [31, 80].

3.3 Interaction of Ti Sites with Polar Molecules

The data reported above mostly refer to samples in dehydrated form. The low coordination of Ti renders it available for the adsorption of polar molecules such as H_2O, NH_3, CH_3OH, and H_2O_2 just for considering those involved in important reactions catalyzed by TS-1.

Boccuti et al. reported that the adsorption of polar molecules modifies in a fully reversible way both the FTIR and the DRS UV-Vis spectra of TS-1 [82]. In particular, the 960 cm^{-1} IR band was shifted upward to 975 cm^{-1} upon adsorption of H_2O (0.5 KPa), to 975–980 cm^{-1} of NH_3 (26 KPa), and to 980 cm^{-1} with CH_3OH (13 KPa); in all cases, the adsorption gave rise to a pronounced broadening and weakening of the band. In the DRS UV-Vis spectrum, the adsorption of H_2O progressively eroded the 208 nm (48,000 cm^{-1}) band with the formation of a new absorption at 238 nm (42,000 cm^{-1}) [82]. Similar results were reported for NH_3 whose adsorption causes the appearance of a new band in the DRS UV-Vis spectrum at 263 nm (38,000 cm^{-1}) [106]. The adsorption of H_2O and NH_3 was successively studied in detail by DRS UV-Vis [94, 104–107] often combined with EXAFS/XANES spectroscopies [92, 94, 104, 105, 107–109], evidencing the increase of the coordination of Ti up to ~6. Microcalorimetry was also employed: since the silica framework also adsorbs these molecules, the Ti coordination number was evaluated by subtracting the calorimetric contribution of a silicalite-1 sample from that measured on TS-1. This renders at least questionable the results since the

heat of absorption may depend on several factors, including the presence and the extent of defective sites within the two samples [109, 110]. More recently, Gallo et al. investigated the interaction of TS-1 with H_2O and NH_3 by valence-to-core X-ray emission spectroscopy (vtc-XES) modeling the data using density functional theory (DFT) calculations. The authors concluded that, contrary to the widely accepted view, Ti sites of TS-1 coordinate only one polar molecule [111].

Apart from H_2O and NH_3, the adsorption of H_2O_2 deserves particular attention since it is the privileged oxidant in the important reactions catalyzed by TS-1. Upon interaction with H_2O_2, the 960 cm^{-1} IR band disappears and is replaced by a weak shoulder in the 900–1,000 cm^{-1} region [22, 112]. The pale yellow adduct displays a new band in the DRS UV-Vis spectrum with a maximum at 385 nm (26,000 cm^{-1}), while the intensity of the original LMCT band at 208 nm (48,000 cm^{-1}) strongly decreases [22, 95]. The same band was observed for $(NH_4)_2[Ti(O_2)F_5]$ adsorbed on silicalite-1, and this was considered as a proof of formation of hydroperoxo-species bonded to framework Ti [95]. The stability of the pale yellow to white TS-1/H_2O_2 adduct at room temperature is low, and it undergoes decomposition within few minutes. For stabilizing it is necessary to cool the sample at −40–50°C or to perform the treatment with H_2O_2 in basic media (NaOH [112] or NH_4OH [113]); in this way, the stable adduct is recovered consisting of an anionic peroxo-derivative stabilized by the alkali metal or ammonium ions. This material did not display any oxidation property, unless the pH of the suspension is brought to neutrality [112].

Once the formation of the adduct was established, it was important to define its structure since it is related to the active intermediate in the oxidation reactions. Two different structures were considered: the "side-on" peroxo-species [Ti = (O_2)] and the "end-on" hydroperoxo-species [Ti–OOH]. Tozzola et al. carried out a vibrational (Raman) and theoretical study on TS-1/H_2O_2 adducts prepared in basic conditions and, on the basis of the O–O stretching frequency, concluded that the "side-on" poroxo-species is more stable than the "end-on" hydroperoxo one [113]. Later on, this conclusion was confirmed by an accurate resonance Raman spectroscopy study performed on TS-1/H_2O_2 adducts prepared in neutral conditions [114]. The formation of a "side-on" peroxo-species was evidenced also on a model compound obtained by complexation of $TiCl_4$ with the hexadentate ligand *trans*-cyclohexanediaminetetraacetic acid [115]. In this case, however, the proposed reaction mechanism involves the formation of a titanyl group, whose presence in TS-1 was ruled out by the spectroscopic evidences.

3.4 The Maximum Level of Ti Incorporation in MFI Framework

From the data reported above, it emerges that the maximum Ti content in TS-1 amounts to ~2.5 Ti/u.c. On the other hand, the reasons of such a limit as well as the

maximum extent of Ti that the MFI framework can incorporate are still unclear and, at the best of our knowledge, not yet examined in the literature. However, starting from some NMR studies performed on as-synthesized zeolites, it is possible to draw some interesting hypotheses that are offered here as a contribution toward the better understanding of these important aspects of TS-1.

Detailed NMR studies performed by the group of R. Lobo evidenced that the positive charge of an SDA molecule, trapped within the high-silica zeolite pores (e.g., TPA^+ in MFI), is compensated by a siloxy groups [Si–O^-] stabilized by three hydrogen bonds with vicinal silanol groups ((**I**) Fig. 9), responsible for the resonance at 10.2 ppm in the ^1H MAS NMR spectra [117, 118]. The NMR analyses performed on all-silica MFI and MTW samples prepared in the presence of per-deuterated SDAs (TPA-d_{28} [117] and benzyltrimethylammonium-d_{16} [118]) corroborated this assignment. The number of siloxy groups decreases upon increasing the trivalent metal ion (e.g., Al^{3+}) content in the framework, while it was very low in the all-silica zeolites prepared in fluoride medium or with neutral amines as SDAs. Several zeolites were investigated in purely siliceous and in aluminosilicate forms, while microporous phases isomorphously substituted with tetravalent elements, such as Ti, were studied some years later by Parker and Millini [116].

The ^1H MAS NMR spectra of as-synthesized TS-1 samples with increasing amount of Ti in the framework evidenced a behavior similar to that of Al- and B-substituted MFI, i.e., a linear decrease of the intensity of the 10.2 ppm resonance (hence of the number of silanol protons H-bonded to siloxy oxygen [Si–$O^-\cdots$H–O–Si] ((**I**) Fig. 9) [116]. Therefore, to account for this unexpected behavior, it was necessary to admit that the Ti sites are negatively charged, e.g., through the coordination of a hydroxy anion ((**II**), Fig. 9), acting as counterions of the TPA^+ cations trapped in the pores. Since the synthesis of TS-1 is performed in the absence of alkali metal ions, which favor the segregation of Ti in extraframework species, it is possible to hypothesize that the MFI framework can incorporate up to 4 Ti/u.c. (Si/Ti = 23), equivalent to the number of TPA^+ ions in the unit cell. Experimentally, however, TS-1 is synthesized with a maximum of 2.5 Ti/u.c., the excess of Ti being segregated in extraframework oxidic species. The data presented in Parker and Millini [116] do not explain the reasons for this limit, but it is plausible that it is the result of an equilibrium between the rates of formation of the structures (**I**)

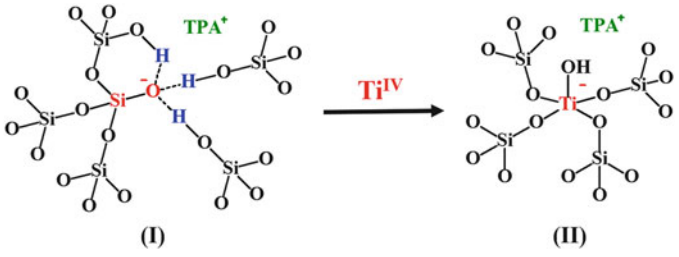

Fig. 9 (**I**) Model of the defect sites in as-synthesized high-silica zeolite highlighting the siloxy oxygen H-bonded to three vicinal silanol groups. (**II**) Model of the Ti sites in as-synthesized TS-1 [116]

and (**II**). As experimentally determined by Shantz and Lobo, the strong electrostatic forces between the SDA and the defect site prevail over the host-guest non-bonding (van der Waals) interactions stabilizing the structure [119]. Moreover, the strong electrostatic forces fix the position of the SDA molecule in proximity of the framework charged site, and this may influence the distribution of the heteroatom in the framework, which can be tailored by altering the charge distribution of the SDA [119]. This implies that, in a given zeolite with MFI topology (orthorhombic), the heteroatoms are not randomly distributed over the 12 crystallographically independent T sites, but are preferentially located in the sites better stabilized by the electrostatic interactions with the charged SDA molecule.

3.5 Preferential Location of Ti in TS-1 Framework

Several research groups have examined the possible existence of preferential sites for Ti incorporation into the MFI framework either experimentally or by theoretical calculations.

Jentys and Catlow studied the geometry of Ti sites using defect energy minimization techniques and quantum mechanical cluster calculations [102]. Differently from the other authors, they used the monoclinic $P2_{1/n}$ MFI structure with 24 crystallographically independent T sites [120] instead of the orthorhombic P*nma* model with 12 T sites, typical of TS-1 samples with high Ti loading [17, 31]. Lattice energy calculations indicated sites T6 and T19 as energetically the most stable and site T18 as the least stable. However, since most of the different T sites do not differ by more than 10 kJ mol^{-1}, they argued that this energy barrier can be easily overpassed at the crystallization temperature of TS-1 and is too small to result in any preferential substitution site for Ti [102]. Moreover, the average Ti–O tetrahedral bond distance was found 1.77–1.78 Å in fairly good agreement with that derived from XRD [17, 31].

All the other studies were performed by considering the orthorhombic P*nma* structure, which involved the 12 crystallographically independent T sites shown in Fig. 10.

Local density functional (LDF) calculations performed on pentameric $[T(O\text{-}SiO_3H_3)_4]$ (T = Si, Ti) clusters with the geometry derived from the 12T sites in the orthorhombic MFI structure [121] gave the following results [122]:

- No clear evidence for the existence of preferential sites for Ti incorporation was achieved (energy difference between the most and the least stable sites 16 kJ mol^{-1}), slight preference for sites T12, T10, and T4.
- Low-energy Ti–O bond distance in the cluster of 1.80 Å, in agreement with the XRD analysis [17, 31].

Oumi et al. performed molecular dynamic (MD) calculations (using a simple two-body interatomic potential) to predict the anisotropic lattice expansion and

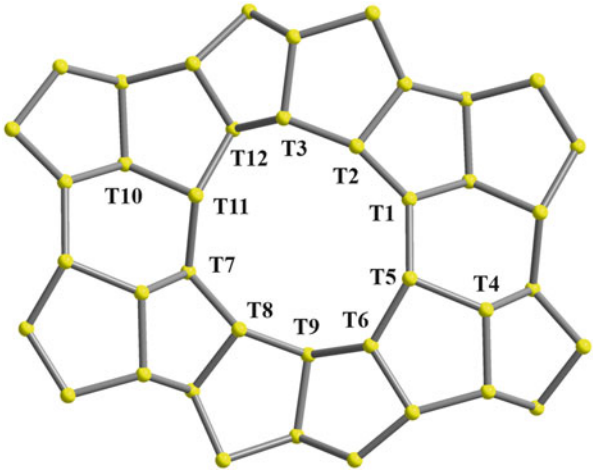

Fig. 10 Orthorhombic MFI unit cell showing the 12 independent T sites

compare it with experimental observations [123]. The equilibrium Ti–O bond distance of 1.85 Å was slightly larger than that determined experimentally or previously predicted theoretically, while comparing the effect of Ti substitution over the 12T sites, the authors concluded that T8 is the most favored site for Ti incorporation.

Njo et al. explored the location of Ti by using a combined Metropolis Monte Carlo and MD approach [124]. The structural model consisted in two MFI unit cells composed of 5 Ti and 187 Si atoms to mimic the highest Ti loading (2.5 Ti/u.c.). The initial location of the Ti atoms was randomly chosen, and after energy and geometry optimization of the model, new Ti atom distributions were generated and energy minimized. The energetically most favorable sites for Ti incorporation were T2 and T12 while T8 resulted the less populated. Moreover, the authors also reported that the location site of Ti influence the lattice symmetry: when T12 site is populated, the energy-minimized model was orthorhombic, while incorporation of Ti in T2 stabilizes the monoclinic symmetry [124].

Hybrid quantum mechanics/molecular mechanics (QM/MM) methods were successively employed [125]. Open pentameric [Ti(O-Si)$_4$] clusters representing the Ti incorporation in the 12T sites were relaxed with the ONIOM method, while the surrounding MFI framework was treated as an inorganic matrix and kept fixed during the calculations. Single point energy of each T site was calculated, and the relative stability of the different T sites was compared, leading to the following conclusions:

- The Ti–O bond length was in the range 1.7–1.78 Å, comparable with the experimental value.
- T9 and T10 were the thermodynamically most stable sites for Ti incorporation.

Gale studied the Ti substitution in orthorhombic MFI structure by periodic density functional theory (DFT) evidencing that, at high Ti loading, T8 and T10

are the most preferred sites, while at low Ti content, T4 and T11 sites may be populated. On the other hand, the optimized Ti–O bond distance was in fairly agreement with the experimental value [126].

More recently, Pirc and Stare performed accurate periodic Hartree-Fock calculations on two models: the orthorhombic P*nma* and the monoclinic $P1.1.2_{1/a}$ [127]. The symmetry imposed the composition of the two models, with 8 and 4 Ti/u.c., respectively. These values are significantly higher than the experimental one (2.5 Ti/u.c.), and the monoclinic model avoided situation with vicinal Ti–O–Ti bonds. These authors considered the monoclinic model more reliable than the orthorhombic one and observed that sites T4, T5, T3, T12, T11, and T8 lie in a low-energy range of 1.37 kcal per mol of Ti; the other sites are characterized by significantly higher-energy gaps.

Yuan et al. performed ab initio DFT calculations to predict the stabilities of different local structures: the tetrahedral Ti site [$Ti(OSi)_4$], the defective Ti site characterized by three Ti–O–Si and Ti–OH bonds and denoted as [$Ti(OSi)_3OH$], and silicon vacancies [128]. They showed that T10, T4, T8, and T11 are energetically the most favorable locations of regular [$Ti(OSi)_4$] site, while Si vacancies are predicted to be at T6, T12, T4, and T8 sites. When defective [$Ti(OSi)_3OH$] were considered, the silicon vacancies at T6 with a Ti in the neighboring T9 and T5 sites (Fig. 10) are predicted to be the most favorable locations.

The situation emerging from the theoretical studies is complex, and there is no consensus among the different authors concerning the preferential sites in which Ti is located. Before drawing some general considerations, it is however useful to examine the results of the experimental studies performed on this topic.

A number of papers appeared during the years 1999–2001 reporting the results of the analysis of synchrotron (SXPD) or neutron powder diffraction (NPD) data. Due to the very low Ti content in TS-1, the location of Ti by structural analysis is very challenging and is further complicated by the unavailability of specimens suitable for single crystal X-ray analysis. The determination of the location of Ti starting from laboratory X-ray powder diffraction (XRD) data is beyond the actual potentialities of even the most advanced instrumentation, particularly when considering the high complexity of the XRD pattern of MFI-type zeolites. Lamberti et al. were the first to face the problem by Rietveld refinement of SXPD data [80]. Refinements of SXPD data collected on TS-1 samples with different Ti contents evidenced that only sites T4, T5, T11, and T12 could be slightly preferred over the others, at least for the sample with 1.93 Ti/u.c. The data collected on other samples, however, did not confirm the preferred population of Ti in these sites, leading to the conclusion that Ti is homogeneously distributed on the MFI framework or may be slightly partitioned on different sites on different samples [80]. Later on, the same group carried out an interesting study on the orthorhombic-monoclinic phase transition on a TS-1 sample with 2.60 wt% TiO_2 by means of low-temperature high-resolution SXPD [129]. The orthorhombic-monoclinic transition was observed at 160 K, and this gave the possibility to refine the structures of both forms at 170 K and 80 K, respectively. It should be underlined that the collection of low-temperature data reduces the thermal contribution to the atomic

displacement parameters increasing the possibility to detect any possible site partitioning of Ti. Indeed, with respect to the data collected at room temperature [80], in this case, it was possible to have weak evidence that ~50% of overall Ti content is located in T10 and T11, the remaining being probably spread among the T1–T3 and T5–T9 sites. On the contrary, Ti does not occupy sites T4 and T12 [129].

The uncertainties in determining the preferential location of Ti by X-ray diffraction are due to the low Ti content and the existence of 12 sites where it can be incorporated. Under these conditions, the higher scattering power of Ti with respect to Si is strongly diluted making it difficult to unambiguously ascertain the possible existence of preferential sites for Ti incorporation. On the other side, neutron powder diffraction technique seems more promising, due to the strong differences in the scattering lengths between Si (4.1491 fm) and Ti (−3.438 fm). Hijar et al. combined NDP with theoretical calculations for examining the location of Ti in a TS-1 sample with 2.47 Ti/u.c [130]. Rietveld refinement of the NPD pattern evidenced the nonrandom siting of Ti, which preferentially occupies sites T3, T7, T8, T10, and T12. They performed semiempirical electronic structure calculations to rationalize these results, but all failed to predict the experimental observations. Notably, the authors examined the interactions between the tetra-alkylammonium cation and the Ti site consisting of a penta-coordinated Ti atom surrounded by four Si–O bonds and a –OH ligand, i.e., the same model later proposed on the basis of NMR evidence [116]. Even in this case, the calculations failed to predict the preferential Ti siting experimentally determined. However, tetramethylammonium (TMA^+) ion was assumed as an SDA, and this is probably an incorrect choice because this small ion is free to occupy all the MFI pores. On the contrary, for steric reasons, the experimentally used TPA^+ cation is constrained to lie at the intersection between the straight and the sinusoidal channels, with a significantly lower degree of freedom with respect to TMA^+. Based on these results, the authors argued that the disagreement between experimental and computational results could be an indication that the kinetics of framework formation rather than the thermodynamics governs the incorporation of Ti in the MFI framework [130].

Rietveld refinement of NPD patterns collected on TS-1 samples prepared according to the original recipes and dehydrated at 120 and 550°C evidenced sites T6, T7, T11, and, in lesser extent, T10 as the most populated, while Ti location in sites T1, T2, T4, T5, T9, and T12 was excluded [110]. These results were achieved after a detailed analysis of the NPD data performed by adopting five different refinement strategies to avoid any bias during the structural analysis. Since defective silicalite-1 exhibits the same preferential sites (T6, T7, T11, and T10) for Si vacancies in orthorhombic silicalite-1 [131], the authors speculated that the incorporation mechanism of Ti in the MFI framework may occur via the insertion of the heteroatom in defective sites [110].

Finally, Henry et al. refined the NPD patterns collected on TS-1 samples prepared with ^{46}Ti- and ^{48}Ti-enriched Ti sources as well as with a natural mixture of these isotopes, in order to exploit the large contrast in neutron scattering lengths of the different Ti isotopes: Ti = −3.438 fm, ^{46}Ti = 4.93 fm, and ^{48}Ti = −6.08 fm.

The comparative analysis of the different datasets indicated that Ti is mainly located on sites T8 and T10 with weak evidence for a small amount of Ti substitution in T3. On the other side, Si vacancies mainly occur on sites T1 and T5 [132].

To give an exhaustive picture of the evidence emerging from theoretical and experimental studies, it is useful to compare the results by evidencing the preferential locations of Ti in the 12T sites predicted/observed by the different authors. As clearly evidenced in Table 4, the situation is quite confusing, without a substantial agreement among the different data. It is true that site T10 is proposed by 67% of the authors, followed by T8 and T11 (50%) and T12 (42%), but the relative population is predicted to be different from one method to the other. How reliable are these predictions/observations? Let's consider first the theoretical calculations. The different authors employed models of different complexity (from the pentameric $[T(O\text{-}SiO_3H_3)_4]$ isolated cluster to the periodic structural model) and computational methods with different levels of approximation, and these introduce severe uncertainties on the reliability of the results. However, most important is the fact that these approaches were mainly used for evaluating the thermodynamic

Table 4 Preferred sites for incorporation of Ti in TS-1

Method[a]	T site												Reference
	1	2	3	4	5	6	7	8	9	10	11	12	
Theoretical calculations													
LDF cluster				X						X		X	[122]
MD, lattice expansion								X					[123]
Metropolis Monte Carlo, MD		X										X	[124]
QM/MM ONIOM									X	X			[125]
DFT periodic				X[b]				X		X	X[b]		[126]
HF periodic			X	X	X			X			X	X	[127]
DFT ab initio[c]				X				X		X	X		[128]
Refinement of powder diffraction pattern													
Rietveld refinement SXPD[d]				X	X						X	X	[80]
Rietveld refinement SXPD										X[e]	X[e]		[129]
Rietveld refinement NPD			X				X	X		X		X	[130]
Rietveld refinement NPD						X	X			X	X		[110]
Rietveld refinement NPD[f]			X					X		X			[132]

[a]For abbreviations, see text
[b]Populated at low Ti content
[c]Si vacancies on sites T5, T6, and T9
[d]Ti homogeneously distributed over the 12 sites with slight preference for T4, T5, T11, and T12
[e]Sites T10 and T11 populated by ~50% of the overall Ti content
[f]Si vacancies on sites T1 and T5

stability of the different substitution sites in the zeolite model corresponding to the calcined form, i.e., without the SDA molecules in the pores. Ti is correctly assumed to be in tetrahedral coordination, and in most cases the optimization of the geometry of the [TiO_4] tetrahedron converges to Ti–O bond lengths close to the experimental one (~1.80 Å). However, given that in as-synthesized phase Ti is negatively charged [116], the incorporation of the heteroatoms would be favored on those sites that maximize the strong coulombic interactions with the TPA^+ ions. Hijar et al. realized that, but they used TMA^+ as model SDA instead of TPA^+, and, as explained above, this was probably one of the causes of the incorrect prediction of the most favored Ti-substitution sites [130].

These considerations may render at least questionable the prediction of the preferential sites for Ti incorporation by theoretical methods, unless reliable structural models are adopted and sufficiently accurate computational methods are employed.

On the other hand, advanced experimental approaches based on the use of diffraction data collected with nonconventional instrumentations as those available at the synchrotron facilities or at the neutron sources may provide the solution of this problem. Indeed, accurate works were carried out through the refinement of SXPD and NPD data, but even in these cases, the different authors obtained contradictory results (Table 4). In spite of the favorable scattering power of Ti with respect to Si, the heteroatom is present in low concentration and could be spread over some (if not all) of the 12 independent T sites of orthorhombic MFI structure. Moreover, the diffraction data were collected on polycrystalline samples, and structural refinements were performed by the Rietveld method. With this approach, serial correlations among some parameters (e.g., the isotropic thermal parameters and the occupation factors of the single sites) exist. If not properly treated, these may lead to physically meaningless results or, at least, to overestimate (or underestimate) the single parameter. Moreover, the samples used were synthesized with even slightly different procedures, and this may influence the pathway of formation of the crystalline phase and, ultimately, the mechanism of Ti incorporation.

In conclusion, although it is now accepted that the distribution of Ti is nonrandom, the preferential sites for the incorporation of Ti in the MFI framework are still undefined. This information is not of secondary importance because the knowledge of the location of Ti may help to better understand the catalytic performances of TS-1 and, in perspective, to design more active and selective catalysts.

4 Synthesis of TS-1: The Morphological Issue

In the previous section, we have briefly examined the methods of preparation of TS-1. With the aim of improving the characteristics of TS-1 obtained with the original recipe, several studies were started up with the aim of increasing the

framework Ti and reducing the catalyst production costs related to the use of high-purity reagents. Approaches based on the use of cheaper reagents, different mineralizing agents, and synthesis conditions have been proposed. Before examining in details the extent of the heteroatom effectively incorporated in the zeolite framework, it is useful to focus the attention on the morphological characteristic of the TS-1 samples obtained by the different synthesis methods. This is an important feature because, as TS-1 is mainly used as a heterogeneous catalyst in oxidation reactions involving H_2O_2, the dimensions of the crystals/primary aggregates may have a strong influence on the overall catalytic performances. In fact, in crystalline microporous solids, the catalytic performances can be enhanced by increasing the accessibility of the active sites located inside the crystals, reducing the diffusion limitations imposed by the narrow pore sizes of medium pore zeolites as TS-1. In general, when relatively large zeolite crystals (and by large we mean on the μm level) are used, the diffusional transport may limit the rate of conversion because the active sites located in the interior of the crystal are hardly accessible to the reactants. This implies a low utilization of the catalyst with the necessity to increase the reactor volume. The diffusional constraints, on the other hand, may influence the selectivity and the life of the catalysts because the probability that the products undergo consecutive reactions increases. A way for eliminating these drawbacks is to use zeolite catalysts with larger pores, but in this case, the peril is to lose the advantages given by the shape selectivity properties of the zeolite catalyst. If we want to maintain such properties, it is necessary to shorten the length of the diffusion path, for instance, by decreasing the dimensions of the crystals [133].

In the case of TS-1, the habitus and the average dimensions of the crystals/primary aggregates depend on the synthesis method adopted [134]. In general, small crystals are obtained by using OH^- as mineralizing agent, the smallest ones being the berrylike aggregates (0.1–0.3 μm) of small crystals reported by Clerici et al. using the original recipe [18]. In the other cases, the average dimensions of the crystals (with coffin-like morphology typical of the MFI zeolites) span from 0.5 to 5–8 μm. On the other hand, when the mineralizing agent is different from OH^-, very large crystals (up to ~80 μm with F^- as mineralizing agent) are usually obtained [134].

Only a few attempts of reducing the size of the TS-1 crystals have been reported. Apart from the works of Cundy et al., who employed MW heating on gels with different aging times [74, 75], the preparation of colloidal suspensions of discrete TS-1 crystals with $<$100 nm average sizes by treating clear homogeneous solutions at low temperature (100°C) is worth citing. These conditions, however, did not favor the incorporation of Ti (0.84 mol%, i.e., ~0.8 Ti/u.c.). Higher amounts of Ti can be incorporated by increasing the crystallization temperature, but larger crystals are formed [135].

In general, the preparation of colloidal suspensions of very small crystals has the drawback of the difficult and costly separation of the solid from the aqueous phase by, e.g., high-speed centrifugation. Alternative methods for improving the diffusional properties of large zeolite crystals are therefore highly desirable, and this can be achieved by generating hierarchical porous structures through the formation of

mesoporosity within the large zeolite crystals or aggregates [136–138], also defined as *mesoporous zeolites* [139]. The mesoporous system is generated in different ways: by using additional components to the reaction mixture in the form of hard (e.g., carbon black pearls, multiple wall carbon nanotubes) or soft mesotemplates (e.g., surfactant micelles, polymers), by recrystallization of preformed amorphous silica-titania xerogels, by zeolitization of the amorphous walls of mesostructured materials, by assembly of seeds or nanocrystals, etc. The concept of hierarchical porous structure was originally developed for the aluminosilicate systems and extended soon to the titanium-zeolites, in particular to the TS-1. Only the most representative synthesis routes will be cited here because, in our opinion, it is more fruitful to highlight the advantages and drawbacks of these approaches rather than to report a mere list of the huge amount of papers published on this topic in the last 20 years.

4.1 Synthesis of Mesoporous TS-1 with Hard and Soft Mesotemplates

The first synthesis of mesoporous TS-1 was reported by Schmidt et al., who impregnated carbon black (CB) pearls with 20% excess relative to incipient wetness with the reactant gel containing TEOS, TEOT, and TPAOH. The hydrothermal treatment at 170°C for 72 h followed by calcination under carefully controlled conditions gave TS-1 crystals containing mesopores with 20 nm average dimension [140]. CB pearls were successively used for preparing mesoporous TS-1 crystals under microwave irradiation [141] and to synthesize hierarchical TS-1 possessing large open voids by using a dissolution/recrystallization process [142]. Recently, multiple wall carbon nanotubes (MWCNT) modified with polyvinyl alcohol (PVA) were used as hard templates, since they provide the possibility to generate mesoporous channels opened to the exterior of the TS-1 crystals [143].

An interesting, though complex, route for the preparation of mesoporous TS-1 is the nanocasting with CMK-3 carbon [144, 145]. CMK-3 is prepared by carbonization of sucrose polymerized within the pores of SBA-15, followed by dissolution of the silica walls with HF; the mesoporous carbon phase is then impregnated to incipient wetness with the reactant gel and the mixture heated at 170°C for 48–72 h. The solid is finally calcined for removing CMK-3 and the SDA molecules giving mesoporous TS-1 formed by hexagonal-shaped nanocrystals (dimensions 20–30 nm) randomly packed to form meso−/macropores [144] or relatively large crystals (dimensions 0.2–0.3 μm) with internal mesoporosity [145]. In order to simplify this route, sucrose was added to the reaction mixture and carbonized directly in the resulting gel before the crystallization [146] or used without the carbonization step [147]. Both synthesis routes led to the crystallization of TS-1 in the form of μm-sized rectangular crystals, containing meso−/macropores.

More recently, chitosan, a cheap and nontoxic polysaccharide derived from the deacetylation of chitin, was used as a soft mesotemplate. Adedigba et al. examined two slightly different recipes: the so-called FD route involved the preparation of a dry SiO_2-TiO_2 gel containing TPA and chitosan, while in the PD route, the gel was only partially dehydrated. In both synthesis routes, the desired amount of aqueous TPAOH was added to the gels, and the resulting mixtures were heated at 170°C for 48 h, recovering samples composed of zeolite particles with average dimensions decreasing upon increasing the chitosan content [148]. In another paper, Gao et al. used ammonium-modified chitosan in a one-step synthesis that produced mesoporous TS-1 in the form of small aggregates of 200–300 nm, with rough surface and with randomly arranged internal mesopores [149]. In both cases, the catalytic performances of mesoporous TS-1 proved to be lower than those of the conventional catalyst in the epoxidation reactions involving small substrates and H_2O_2 as an oxidant but significantly higher in the oxidation reactions of bulky substrates [148, 149].

4.2 Assembly of Seeds

In another research line, the synthesis of mesoporous TS-1 was addressed trying to exploit the porous characteristics of mesostructured materials. After the announcement by researchers at Mobil of the preparation of the family of materials with ordered mesoporosity called M41S [150], the synthesis of mesostructured titanosilicates (e.g., Ti-MCM-41, Ti-MCM-48, Ti-HMS, Ti-SBA-15) was seen as an opportunity for expanding the use of these materials in oxidation reactions involving bulky substrates [151–156]. Unfortunately, however, the great expectations of the researchers have been disregarded as these materials showed lower catalytic activity and hydrothermal stability compared to the crystalline porous titanosilicates, such as TS-1. This was attributed to the amorphous nature of the mesoporous walls, which, in turn, determines different coordination environments of the Ti sites with respect to the crystalline structures. In analogy with the aluminosilicate systems, the improvement of the stability and catalytic activity of mesostructured titanosilicates was attempted through the crystallization (at least partial) of the amorphous walls. Apart from the crystallization of preformed ordered mesoporous phases that lead to the preparation of mesoporous TS-1 samples with medium-high crystallinity depending on the synthesis conditions adopted (e.g., UL-TS-1 [157]), the approaches based on the assembly of preformed titanosilicate seeds are the most extensively studied. Usually, these two-step approaches involve first the preparation of the seeds through the hydrothermal treatment of the reaction gel containing the silica and titania sources and TPA hydroxide or bromide at a temperature well below that are necessary for the crystallization of TS-1. In the second step, a surfactant is added to the solution of seeds and the mixture is heated at 100°C for assembling them in the mesostructured phase. Different surfactants

and conditions were employed in order to increase the stability of the mesostructured phase.

The P123 triblock copolymer was used for preparing MTS-9, characterized by an ordered hexagonal array of mesopores and by remarkable catalytic activity in the hydroxylation of phenol and in the oxidation of bulky substrates (e.g., trimethylphenol) [158–160]. The catalytic performance of MTS-9, however, significantly decreased upon calcination, probably because of the change in the coordination of the Ti atoms. The thermal stability of this phase was successively improved by assembling the seeds in the presence of NH_4Cl (MTS-9A, [161]) or by increasing the temperature in the second step to 160–180°C (MTS-9x, [162]). Yang et al. reported the thermally stable Ti-JLU-20 phase, prepared by heating at 180°C for 40 h the gel containing the TS-1 seeds and a mixture of fluorinated FC-4 and triblock P123 copolymers [163].

The cationic cetyltrimethylammonium ($CTMA^+$) surfactant, typically employed for the preparation of MCM-41 and MCM-48 phases and their compositional variants, was also used. Lin et al. assembled the TS-1 seeds in the presence of CTMABr producing MTS-5 and MTS-8, in strong basic and acidic conditions, respectively. Both samples were treated several times with hot HCl-ethanol mixture and water for removing most of the surfactants, showing remarkable catalytic activity in the hydroxylation of phenol and 2,3,6-trimethylphenol. Upon calcination, only MTS-5 proved to be stable, with a slight decrease of the catalytic activity. In contrast, MTS-8 displayed poor thermal stability since its catalytic activity was significantly lower with respect to the uncalcined form [164]. This behavior was not confirmed by Wang et al. since, after calcination, the phases JQW-3 and JQW-4 (prepared in strong basic and acidic conditions, respectively) displayed the same decrease of catalytic activity with respect to the uncalcined forms [165]. This approach was successively examined in much detail by other authors, who modified the synthesis procedure by assembly of the TS-1 seeds at room temperature [166] or by subjecting the mesoporous phase to a further hydrothermal treatment at 140°C in distilled water [167, 168].

In general, the materials obtained by these synthesis routes maintain the characteristics of the mesostructured phases, i.e., ordered and regular mesoporosity and XRD amorphous pattern. The existence of the zeolite nanodomains, clusters, or secondary building units (SBUs) within the mesoporous walls is assessed by spectroscopic (FT-IR, MAS NMR) as well as by textural analyses, while the tetrahedral coordination of Ti is confirmed by FTIR and by UV-Vis evidences. The catalytic activity of these materials is usually evaluated, providing interesting information about their possible practical use. In general, the catalytic activity of the as-synthesized materials proved to be higher than that of the Ti-containing mesostructured materials prepared by the direct routes (e.g., Ti-MCM-41) and comparable to that of conventional TS-1. However, their thermal stability is still an issue, since after only one calcination, a strong reduction of the catalytic activity is observed. This means that the presence of zeolite seeds or clusters is insufficient to stabilize Ti in tetrahedral coordination, as in crystalline phases. Consequently, the assumptions behind this synthesis approach have been disregarded by the experimental results, and it is difficult to predict a practical use for these materials.

4.3 Seed Silanization

The group of D. P. Serrano recently proposed another interesting route to the preparation of mesoporous TS-1 samples, based on the silanization of zeolite seeds. This route, previously applied to the preparation of mesoporous ZSM-5, ZSM-11, and beta zeolites, involves the addition of phenylaminopropyltrimethoxysilane (PHAPTMS) for functionalizing the TS-1 seeds prepared during the pre-crystallization step; the mixture is then crystallized by microwave heating. After calcination, the product consists of large irregular berrylike aggregates of TS-1 nanocrystals (20–30 nm average dimensions), containing irregular voids forming the secondary porosity [169, 170]. The influence of the PHAPTMS concentration and length of the pre-crystallization step [171] and of the type of alcohol [172] on the crystallization process and on the characteristics of TS-1 were successively examined. The mesoporous TS-1 was also subjected to a post-synthesis reorganization by surfactant-assisted alkali treatment using $H_{2n+1}C_nN(CH_3)_3Br$ ($n = 10, 12, 16, 18$) surfactants [173]. The dissolution-recrystallization process led to the formation of well-crystallized TS-1 phase containing uniform mesoporosity of ca. 40 Å diameter. The effectiveness of this route was demonstrated by the increased catalytic activity with respect to the conventional TS-1 in the epoxidation of 1-octene and cyclohexene with *tert*-butyl-hydroperoxide (TBHP) as well as in the oxidative desulfurization of hydrocarbon fractions with H_2O_2 or TBHP as oxidants [174]. This concept was extended to the preparation of mesoporous TS-1 from SiO_2-TiO_2 xerogels [170, 175]. This quite complex synthesis route involves four different steps: (1) preparation of the SiO_2-TiO_2 xerogels, (2) impregnation with aqueous TPAOH and pre-crystallization at 120°C under microwave heating, (3) silanization with PHAPTMS or isobutyltriethoxysilane (IBTES), and (4) crystallization at 170°C for 8 h under microwave heating. It is interesting to note that, when compared to conventional TS-1, the mesoporous samples prepared by this synthesis route display lower catalytic activity by using H_2O_2 but significantly higher when TBHP was employed as an oxidant [175].

Mesoporous TS-1 was prepared also by adding an organosilane surfactant to the reaction mixture. Cheneviere et al. used [3-(trimethoxysilyl)propyl]octadecyldimethylammonium chloride (TPOAC) as an amphiphilic organosilane (5 mol% with respect to the conventional silica source, TEOS) and obtained well-crystallized mesoporous TS-1 upon heating at 145°C for 6 days [176]. TPOAC creates additional porosity (pore diameter in the range 3.5–4 nm) within the spherical aggregates of TS-1 nanocrystals. The mesoporous TS-1 prepared by this route were characterized by poor catalytic activity in the hydroxylation of phenol with H_2O_2, because of the pronounced hydrophilicity of the external surface. On the other hand, the same samples displayed much higher catalytic activity with respect to conventional TS-1 in the epoxidation of cyclohexene performed in anhydrous environment with TBHP as an oxidant [176]. The use of hexadecyltrimethoxysilane (C16TMS) gave similar results in terms of characteristics of the mesoporous TS-1. The tests performed in the oxidative desulfurization of different substrates

evidenced the superior catalytic performances of mesoporous TS-1 compared to the conventional material [177].

Among the other different approaches, it is worth to report the preparation of thin ZSM-5 nanosheets developed by the group of Ryoo in 2009 [178] and subsequently extended to the TS-1 analogue [179]. TS-1 nanosheets of ca. 2 nm thickness (i.e., single MFI unit cell) were prepared by using $C_{16}H_{33}$–$N^+(CH_3)_2$–C_6H_{12}–$N^+(CH_3)_2$–C_6H_{13} as an SDA. Upon calcination, the arrangement of the nanosheets generates large intersheet mesoporosity and high external surface. These materials possess remarkable catalytic activity in the epoxidation of bulky substrates using H_2O_2 or TBHP as oxidants. The post-synthesis treatment with NH_4F reduced the hydrophilicity of the surface, improving the catalytic performances of the catalyst in reactions involving aqueous H_2O_2 [179]. Wang et al. subsequently confirmed these evidences, working on materials prepared with a slightly different diquaternary SDA ($C_{22}H_{45}$–$N^+(CH_3)_2$–C_6H_{12}–$N^+(CH_3)_2$–C_6H_{13}, [180]).

4.4 General Considerations on Mesoporous TS-1

This section summarizes the most relevant routes to the preparation of mesoporous TS-1. The large number of reports concerning the preparation of these materials testifies the importance of this topic and highlights the advantages and drawbacks associated with the different synthesis routes.

First of all, it is evident that the synthesis of samples consisting of discrete crystalline domains (e.g., nanocrystal size or mesoporous μm-sized crystals) allows a better control of the peculiar characteristics of TS-1, i.e., the stabilization of Ti in tetrahedral coordination and the high thermal/hydrothermal stability of the materials. In fact, experimental evidences show that mesoporous phases resulting from the assembly of preformed zeolitic seeds undergo profound changes during the thermal treatments, with significant decrease of the catalytic activity. This is because the local organization of the structure is not sufficient to stabilize the entire system, as in the case of crystalline materials.

Based on the available evidence, it is therefore difficult to foresee practical applications for these materials, while the crystalline mesoporous materials are certainly more promising, even if they still have some important drawbacks. The first concerns the synthesis methods, which are more complex than that of the industrial TS-1 catalyst and require the use of additional components, necessary for generating the mesoporosity. Obviously, all this affects the cost of production, which can greatly increase and that can be tolerated only if the new materials provide a significant improvement of the performances compared to the commercial TS-1 catalyst. The question is based on the data reported in the literature: is it possible to identify the effective advantages offered by the mesoporous TS-1 materials? Let's examine the most critical points that, in our opinion, are worth to be brought to the attention of the reader.

1. *The choice of the reference TS-1 sample*. The catalytic activity of the mesoporous TS-1 samples is properly compared with that of a conventional catalyst, which in none of the cases examined has the characteristics of the commercial one. Therefore, the conclusion reached by the different authors should be referred exclusively to the system under investigation without pretending to have an absolute value. This concept can be better explained by examining the data reported by Schmidt et al. on the mesoporous TS-1 sample prepared with CB pearls [140]. The catalytic activity of mesoporous TS-1, formed by small (0.3–1.2 μm) irregularly shaped aggregates of crystallites, containing mesopores of ∼20 nm dimension (Fig. 11a), was compared with that of a conventional sample, formed by large, well-shaped crystals of ∼1–2 μm dimension (Fig. 11b). The two samples were tested in the epoxidation of 1-octene and cyclohexene with H_2O_2, and the results were reported in terms of product concentration (epoxide + secondary products) ratio obtained with the two catalysts. Within the contact time examined, in the case of the linear substrate, this ratio was constantly close to 1, while the epoxidation of cyclohexene exhibited a ratio exceeding the value of 10 (Fig. 11c). These results

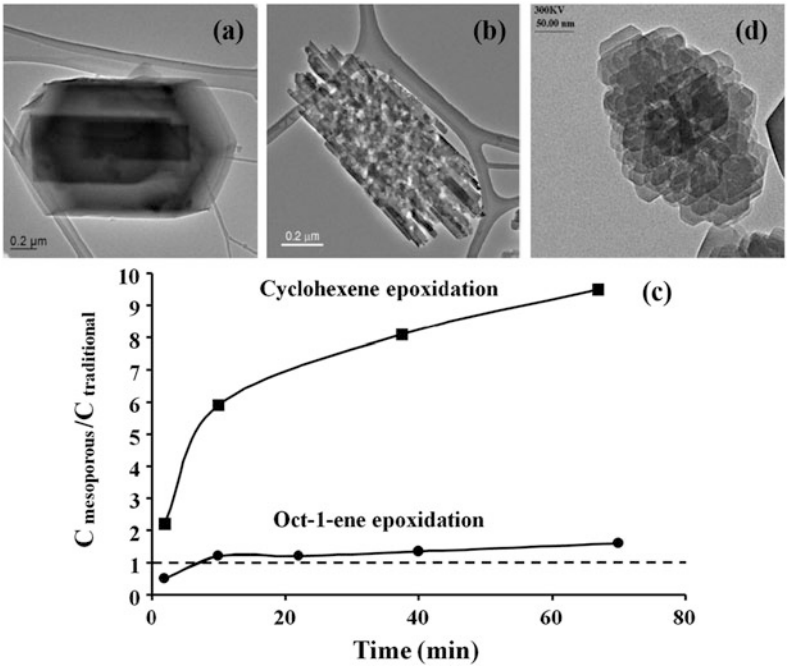

Fig. 11 Transmission electron micrographs (TEM) of (**a**) conventional and (**b**) mesoporous TS-1 samples, with (**c**) their relative product concentrations as a function of time in the epoxidation of cyclohexene and oct-1-ene. The dashed line represents the product concentration expected in the absence of any influence of the hierarchical porous structure on the reaction. The TEM micrograph of TS-1 prepared according to the original recipe is reported in (**d**) for comparison (Adapted from Schmidt et al. [140] with permission of the Royal Society of Chemistry)

confirmed the expectations, i.e., the enhanced catalytic activity of mesoporous TS-1 due to its improved diffusional properties as compared to the μm-sized TS-1 catalyst. Though the experimental data are correctly interpreted, what is at least questionable is to consider the conventional TS-1 sample as a reference. In fact, its morphology is completely different with respect to the actual industrial TS-1 catalyst, constituted by submicronic aggregates of nanocrystals packed in such a way to generate an irregular intercrystalline mesoporosity and, hence, a hierarchical porous system (Fig. 11d). This catalyst is obtained without the use of mesotemplates and is the result of the optimization of the conventional synthesis route. Thus, the work made by Schmidt et al. (and by several other authors on TS-1 samples prepared by different synthesis routes) can be considered as a proof of concept, being certainly useful to assess the benefits resulting from generating an intracrystalline mesoporous system. However, the characteristics of the TS-1 sample taken as a reference are far from those of the industrial catalyst, and the data reported are not sufficient to verify whether the adoption of complex and expensive synthesis routes entails real advantages in terms of catalytic performances of the mesoporous zeolites. For the sake of completeness of information, the attempt made by four European laboratories in the early 1990s to evaluate the catalytic performance of a standard TS-1 sample (called EUROTS-1) is worth mentioning [181], prepared following example 1 of the original patent [4]. The hydroxylation of phenol into catechol and hydroquinone using aqueous H_2O_2 was selected as a standard reaction. The phenol conversion, product selectivity, and H_2O_2 product yield were found to be determined by the calcination conditions of EUROTS-1, the use of internal standard, and the nature and amount of solvent added to the reaction mixture [181]. The initiative would be very important because the availability of a standard TS-1 sample with features close to those of the commercial catalyst would allow a better evaluation of the catalytic properties of the newly prepared materials. However, after the initial work of definition of the standard reaction conditions, EUROTS-1 was abandoned.

2. The mesoporous TS-1 samples constituted by an assembly of nanocrystals are catalytically less active than the conventional catalyst in reactions involving H_2O_2 as an oxidant. On the contrary, they have better catalytic performances when the reaction is performed in nonaqueous solvents and using organic peroxides (e.g., TBHP) as oxidants. There is a consensus among different authors that with the reduction of the size of the crystals, there is the consequent increase of the external surface, rich in silanol groups. This entails an increase in the hydrophilicity of the material with reduced capability to adsorb the reactant molecules within the micropores. On the contrary, when the reaction is performed in organic solvents with an organic oxidant (e.g., TBHP), the mesoporous TS-1 usually proved to be more active than the conventional catalyst. This is certainly not positive as the recognized advantages of TS-1 are to be active with H_2O_2 under mild conditions and to give H_2O as a by-product.

3. The mesoporous TS-1 are catalytically more active than the conventional catalyst in oxidation reactions involving bulky substrates, such as 2,3,6-trimethylphenol, α-pinene, dibenzothiophene, substituted dibenzothiophenes, etc. Since these substrates can hardly be absorbed in the pores of the TS-1, most likely the reactions occur on the outer surface of the crystals or at the pore mouth, with low or no influence of the structure on the reaction and on the nature of the products. In other words, mesoporous TS-1 can be used in the oxidation of bulky substrates, if no shape-selective effects are expected.

Based on these considerations, it is possible to conclude that mesoporous TS-1 should be further optimized in order to render them a valid alternative to the conventional catalyst. Though the generation of a secondary mesoporous system can be considered as a viable method for reducing the mass transport limitations imposed by the micropores, the alternative is to incorporate Ti into the framework of other zeolites possessing different pore architectures and sizes.

5 Other Ti-Containing Zeolites

Table 5 lists the Ti-containing zeolites different from TS-1 reported so far, with some details on the synthesis conditions. Only a few of them (i.e., TS-2, Ti-beta, Ti-ZSM-48, and Ti-MWW) have been thoroughly investigated, while for the remaining, only few data have been reported, without any special insights on their synthesis and characteristics. Because of the limited space allotted, it is not possible to examine each of these systems in detail. In the following, only the most studied systems are treated, while the interested reader can refer to Table 5 for some information on the synthesis of all the other Ti-containing zeolites.

Titanium-Silicalite-2 (TS-2) Incorporation of Ti in the framework of silicalite-2 (the pure silica intergrowth of MFI- and MEL-type structures) was the first to receive attention, due to the close similarities with TS-1. In 1989, Bellussi et al. claimed the synthesis of TS-2 using TBAOH as an SDA and of a family of titanosilicates called TS-3 structurally related to TS-2, but with different degrees of stacking faults [182]. Later on, Reddy et al. extended the method developed by Thangaraj et al. [28–30] to the preparation of TS-2 [183, 184]. The syntheses, performed in the absence of alkali metal ions to avoid the formation of extra-framework Ti species, led to the crystallization of TS-2 in a wide range of SiO_2/TiO_2 molar ratios (17–∞) and with up to ~4 Ti/unit cell [184]. TS-2 was synthesized also with tetrabutylphosphonium (TBP) hydroxide, but compared to TBA, this SDA causes a significant reduction of the crystallization kinetics, the possibility to incorporate up to ~1 Ti/unit cell, and the use of a higher calcination temperature for removing it from the pores [185].

A detailed investigation of the experimental conditions (synthesis procedure, crystallization temperature, and SiO_2/TiO_2 molar ratio) on the preparation of TS-2 by the "dissolved titanium" method (Fig. 1) led to the conclusion that the optimum

Table 5 Synthesis of Ti-containing zeolites

Material	Framework type	Si source[a]	Ti source[b]	SDA[c]	Cryst., temp., time	Other information	Reference
TS-2	MFI/MEL	TEOS	TEOT	**I**	170°C, 3 days	Hydrothermal synthesis	[182]
TS-2	MFI/MEL	TEOS	TBOT	**I**	170°C, 2–8 days	Hydrothermal synthesis, static conditions	[183, 184]
TS-2	MFI/MEL	TEOS	TBOT	**II**	170°C, 4 days	Hydrothermal synthesis, static or stirring conditions; *tetrabutylphosphonium	[185]
TS-2	MFI/MEL	TEOS	TBOT	**I**	165–220°C, 60–100 h	Hydrothermal synthesis; "dissolved titanium" method and variants	[186]
TS-2	MFI/MEL	TEOS	TBOT	**I**	170°C, 0.5–15 h	Hydrothermal synthesis; microwave heating	[187]
Ti-beta	Beta	AEROSIL 200	TEOT	**III**	135°C, time not reported	Hydrothermal synthesis; Al added to favor the crystallization	[188–190]
Ti-beta	Beta	TEOS	TEOT	**III**	140°C, 4 days	Hydrothermal synthesis; addition of highly dealuminated zeolite beta seeds	[191]
Ti-beta	Beta	TEOS	TBOT	**III**	135°C, 7.6–8.6 days	Wetness impregnation of SiO_2-TiO_2 cogel with TEAOH solution containing small amounts of Al	[192]
Ti-beta	Beta	TEOS	TEOT	**III**	140°C	Hydrothermal synthesis in fluoride (HF) or in basic (OH^-) media, eventually seeded with dealuminated zeolite beta	[193, 194]
Ti-beta	Beta	TEOS	TiF_4	**III**	140°C, 12 days	Aging-drying method of gels prepared in fluoride (HF) media; diisopropyl- or diisobutylamine eventually added	[195]
Ti-beta	Beta	AEROSIL 200	TEOT	**IV**	140°C, 14 days	Hydrothermal synthesis, zeolite Si-beta seeds; non-seeded synthesis requires 8 weeks for full crystalline product	[196, 197]
Ti-beta	Beta	TEOS	TBOT	**V**	135°C, 9 days	(a) Two-step synthesis: (1) preparation of SiO_2-TiO_2 cogel; (2) impregnation with aq. SDA and hydrothermal synthesis. (b) Direct hydrothermal synthesis	[198, 199]

(continued)

Table 5 (continued)

Material	Framework type	Si source[a]	Ti source[b]	SDA[c]	Cryst., temp., time	Other information	Reference
Ti-beta	Beta	TEOS	TBOT	**VI, VII, VIII**	170°C, 12–13 days	Hydrothermal synthesis in fluoride (HF) medium, using different SDAs	[200, 201]
Ti-beta	Beta	NH_4-beta	$TiCl_4$	–	500°C, 0.5 h	Chemical vapor deposition (CVD) on dealuminated beta	[202]
Ti-beta	Beta	Al-beta	$(NH_4)_2TiO(C_2O_4)_2$	–	25°C, 1 days	Treatment of Na- or K-exchanged form with an aqueous solution of Ti	[203]
Ti-beta	Beta	H-beta	Cp_2TiCl_2	–	550°C, 12 h	Two-step post-synthesis procedure: (1) dealumination of zeolite beta and (2) high-temperature treatment of a mechanical mixture with Cp_2TiCl_2	[204]
Ti-ZSM-12	MTW	TEOS	TBOT	**IX**	180°C, 6–10 days	Hydrothermal synthesis; alkali-free gel	[205]
Ti-ZSM-48	*MRE	Fumed silica	TBOT	**X**	175°C, 10 days	Hydrothermal synthesis; H_2O_2 added to dissolve the hydrous titanium oxide phase formed from the hydrolysis of TBOT	[206]
Ti-ZSM-48	*MRE	Fumed silica	TBOT	**X**	200°C, 10 days	Hydrothermal synthesis; H_2O_2 added to dissolve the hydrous titanium oxide phase formed from the hydrolysis of TBOT	[207]
Ti-ZSM-48	*MRE	TEOS	TBOT	**XI**	200°C, 7 days	Hydrothermal synthesis; alkali-free gel	[208]
Ti-ZSM-48	*MRE	TEOS	TBOT	**XII**	180°C, 3 days	Hydrothermal synthesis; alkali-free gel	[209]
Ti-UTD-1	DON	Fumed silica	TEOT	**XIII**	175°C, 6 days	Hydrothermal synthesis; NaOH-containing gel	[210, 211]
Ti-UTD-8	–	Fumed silica	TEOT	**XIII**	175°C, 6 days	Hydrothermal synthesis; NaOH-containing gel	[210]
TS-NU-1	RUT	TEOS	TBOT	**XIV**	180°C, 3–8 days	Hydrothermal syntheses with Al-NU-1 seeds; small amounts of Al and $PO_4^{=}$ added to the reaction mixture	[212]
Ti-NU-1	RUT	AEROSIL 200	TBOT	**XIV**	170°C, 5–6 days	Dry gel conversion (DGC) of a TiO_2-SiO_2-TMAOH cogel	[213]
Ti-MWW	MWW	Fumed silica	TBOT	**XV or XVI**	175°C, 3–7 days	Hydrothermal synthesis in the presence of H_3BO_3; the lamellar precursor is treated with strong acids for removing B and extraframework TiO_2	[214, 215]

Ti-MWW	MWW	B-MWW	TBOT	–	175°C, 7 days	Hydrothermal treatment of deboronated MWW with TBOT solution containing a **XV**, **XVI**, or other amines	[216]
Ti-YNU-1	MWW	B-MWW	TBOT	**XV**	170°C, 5 days	Hydrothermal treatment of deboronated MWW with TBOT solution; the solid is refluxed with 2 M HNO_3 and calcined	[217]
IEZ-Ti-MWW	MWW	Ti-MWW	–	–	100°C, 20 h	The layered Ti-MWW precursor is refluxed with a silylating agent (e.g., diethoxydimethylsilane) to expand the interlamellar 10R pore to 12R	[218]
Ti-MWW	MWW	Colloidal or fumed silica	TBOT	**XV or XVI**	170°C, 7–14 days	Dry gel conversion (DGC) of a SiO_2-TiO_2-B_2O_3 gel	[219]
Ti-ferrierite	FER	AEROSIL 200	TEOT	**XVII**	135°C, 10 days	Hydrothermal syntheses in fluoride (HF/NH_4F) media; Ti-FER obtained by calcination of the layered Ti-PREFER precursor	[220]
Ti-ITQ-7	ISV	TEOS	TEOT	**XVIII**	150°C, 12 days	Hydrothermal synthesis in fluoride (HF) medium with ITQ-7 seeds	[221]
Ti-ITQ-7	ISV	TEOS	TEOT	**XVIII**	150°C, 12 h	Hydrothermal synthesis in fluoride (HF) medium; in the presence of GeO_2 crystallization in 12 h, without GeO_2 and with ITQ-7 seeds in 12 days	[222]
Ti-MOR	MOR	Silica sol	TBOT	**XIX**	160°C, 90–100 h	Hydrothermal synthesis in the presence of Al; ternary Ti-Al-Si phases	[223]
Ti-UTM-1	MTF	TEOS	TBOT	**XVI**	140°C, 14 days	Hydrothermal synthesis	[224]
Ti-SSZ-33	CON	B-SSZ-33	$TiCl_4$	–	300°C	Post-synthesis treatment with $TiCl_4$	[225]
Ti-MCM-68	MSE	Al-MCM-68	$TiCl_4$	–	600°C	Post-synthesis treatment with $TiCl_4$	[226]
Ti-YNU-2	MSE	YNU-2	$TiCl_4$	–	500°C	Post-synthesis treatment with $TiCl_4$	[227]
Ti-ITQ-17	BEC	LUDOX AS-40	TEOT	**XX**	175°C, 14 days	Hydrothermal synthesis in fluoride (NH_4F) medium; seeding with ITQ-17 crystals	[228]
Ti-BEC	BEC	TEOS	$(NH_4)_2TiF_6$	**II**	140°C, 8d	Hydrothermal synthesis in fluoride (HF) medium, with GeO_2; other sources of Ti employed but not suitable	[229]
Ti-CHA	CHA	TEOS	TEOT	**XXI**	155°C, 40 h	Hydrothermal synthesis in fluoride (HF) medium	[230]

(continued)

Table 5 (continued)

Material	Framework type	Si source[a]	Ti source[b]	SDA[c]	Cryst., temp., time	Other information	Reference
Ti-STT	STT	TEOS	TEOT	**XXI**	155°C, 10 days	Hydrothermal synthesis in fluoride (HF) medium	[231]
Ti-ITQ-39	*-ITN	TEOS	TIPOT	**XXII**	135°C, 30 days	Hydrothermal synthesis in fluoride (HF) medium	[232]
Ti-CIF-5	CFI	Fumed silica	TBOT	**XXIII**	155–170°C, 6–17 days	Hydrothermal; LiOH added to accelerate the crystallization of the CFI phase	[233]
Ti-UTL	UTL	Fumed silica	TBOT	**XXIV**	175°C, 7 days	Hydrothermal; Ti-IPC-2 and Ti-IPC-4 prepared by the ADOR approach	[234]

[a]*TEOS* tetraethylorthosilicate
[b]*TEOT* tetraethylorthotitanate, *TIPOT* tetra-isopropyl-orthotitanate, *TBOT* tetrabutylorthotitanate
[c]See Fig. 12

crystallization temperature of TS-2 is 176°C from a gel containing precipitated silica, peroxotitanate species, and TBAOH. The increase of the temperature favors the formation of TS-1 impurities, while Ti can be incorporated up to a maximum of four atoms/unit cell without formation of extraframework Ti species [186].

Serrano et al. investigated the use of microwave heating for the crystallization of TS-2 from clear liquid gels. They found that the crystallization was significantly shortened with respect to the conventional heating (15 vs. 48 h, respectively), without affecting the extent of Ti incorporation and the formation of extra-framework Ti species [187].

Ti-Beta The incorporation of Ti into the framework of zeolite beta received much attention since, if successful, it would represent the first large-pore Ti-containing zeolite. Indeed, the first attempts to synthesize Ti-beta by using TEAOH as an SDA failed, since the crystallization requires the presence of aluminum so that the products are ternary Si/Al/Ti phases [188–190]. The amount of Ti incorporated in the framework increases upon lowering the concentration of Al; the upper limit corresponds to 2.4 Ti atoms/unit cell ($x = 0.038$) with the lowest Al content of 0.74 atoms/unit cell ($x = 0.011$) [189]. As in the case of TS-1, the use of alkali metal ions should be avoided; otherwise amorphous titanosilicate species precipitate, hampering the incorporation of Ti [189, 190]. Ti-beta can be prepared by using highly dealuminated zeolite beta seeds (4 g per 100 g of total SiO_2 in the reaction mixture). Only trace amounts of Al (Si/Al > 5,000) were found in the crystalline product. The use of non-dealuminated zeolite beta (Si/Al = 25) led to a Ti-beta sample with Si/Al = 820, without any significant changes on the rate of crystallization [191]. Syntheses were attempted also by applying the wetness impregnation method of preformed SiO_2-TiO_2 cogel proposed for the preparation of TS-1 [61]: in the case of Ti-beta, the addition of small amount of Al to the gel was required for achieving the crystallization [192].

Syntheses were performed also in fluoride media at nearly neutral pH [193, 194]. In this case, seeding with dealuminated zeolite beta was not necessary, unless for reducing the crystal size from 1–5 μm to less than 1 μm. Ti is incorporated to an upper limit of 2.3 atoms/unit cell, beyond which anatase starts to form. The Ti concentration in the framework increases by performing the synthesis in basic medium. More recently, a rather complex aging-drying method based on the hydrothermal treatment of a dry gel resuspended in an organic solvent (diisobutyl- or diisopropylamine) was proposed [195]. The examples reported above demonstrate that TEAOH, the SDA mostly used for the synthesis of the aluminosilicate phase, is not suitable for preparing Ti-beta without the addition of zeolite beta seeds (either as it is or in highly dealuminated form) and/or fluoride ions. These imply that the resulting materials contain trace amounts of Al, deriving from the seeds, and/or fluoride ions strongly bonded to Ti. In order to avoid these drawbacks, the use of SDAs different from TEAOH was evaluated. van der Waal et al. reported the preparation of Al-free Ti-beta by using di-(cyclohexylmethyl)-dimethylammonium (DCDMDA, **IV**) using all-silica beta seeds [196, 197]. Well-crystallized Ti-beta samples were obtained after 14 days at 140°C; at $T \leq 135$°C, the crystallization rate

was very low, while no crystallization occurred at $T \geq 150°C$. The maximum Ti incorporation was ([Ti]/[Ti] + [Si]) ~ 0.02, as demonstrated by the linear expansion of the *a* axis of the tetragonal unit cell. Al-free Ti-beta can be obtained also by using the diquaternary ammonium salt 4,4′-trimethylene-bis-(benzyl-methyl-piperidinium) (**V**) [198, 199].

More recently, a systematic investigation on the crystallization of Ti-beta by using a variety of diquaternary ammonium derivatives of dibromoalkanes and amines such as triethylamine, 1,4-diazabicyclo[2,2,2]octane (DABCO), and quinuclidine as SDAs was carried out by Sasidharan and Bhaumik [200]. Hydrothermal syntheses were performed by heating at 170°C during 11–13 days gels containing the peroxo-titanium species and HF as mineralizing agent. It was found that the size of hydrophobic bridging alkyl-chain length of the template $[R_3N^+–(CH_2)_x–N^+R^3](OH^-)_2$ directs the final crystalline product, Ti-beta, Ti-ZSM-12, Ti-nonasil, or Ti-ZSM-5, as x gradually changes from 6 to 1. The dense phase Ti-nonasil crystallized as the size of hydrophobic bridging alkyl-chain length decreases, but it contains only trace amounts of Ti (Si/Ti = 293.1–345.6 after acid treatment to remove extraframework octahedral Ti species). In the case of Ti-beta samples, prepared in the presence of SDAs **VI–VIII**, the Si/Ti molar ratio was in the range 64.9–91.5 after acid treatment, well above the molar ratio of 50 of the synthesis gels [200].

In general, the incorporation of Ti in the framework of zeolite beta seems to be more difficult than in the case of TS-1. With the exception of the synthesis performed with SDA **V** (indeed, not fully explored but reported only in the patent literature [198, 199]), the crystallization of Ti-beta often requires the use of seeds and/or fluoride ions. Moreover, Ti-beta is less stable than TS-1. In fact, the XRD pattern of a Ti-beta sample synthesized according to Saxton [198, 199] dramatically changed upon calcination at 450°C, with a significant broadening of the reflections and a contraction of the unit cell parameters with respect to the as-synthesized form. Furthermore, the treatment with H_2O_2 causes the extraction of Ti from the zeolite framework and its segregation in extraframework TiO_2 species. Such a behavior, not observed for TS-1, accounts well for the worst catalytic performances of Ti-beta with respect to TS-1 [201].

Alternative routes to the preparation of Ti-beta were proposed, involving the treatment of preformed dealuminated beta samples with $TiCl_4$ at high temperature [202] or with ammonium titanyl oxalate in solution [203] and the calcination of mechanical mixture of dealuminated beta and bis-cyclopentadienyl-titanium dichloride [206]. In general, these post-synthesis treatments actually led to the incorporation of Ti in the sites previously occupied by Al, but octahedral Ti species were observed even in the samples free of TiO_2 anatase.

Ti-ZSM-48 Serrano et al. were the first to report the synthesis of this titanosilicate from a gel containing 1,8-diamino-octane (**X**) as an SDA and fumed silica and peroxotitanate as silica and titania source, respectively [206]. Up to 1.8 Ti/u.c. ($x = 0.037$) were incorporated in the framework, without any evidence of formation of extraframework Ti species. These data were successively confuted, and the

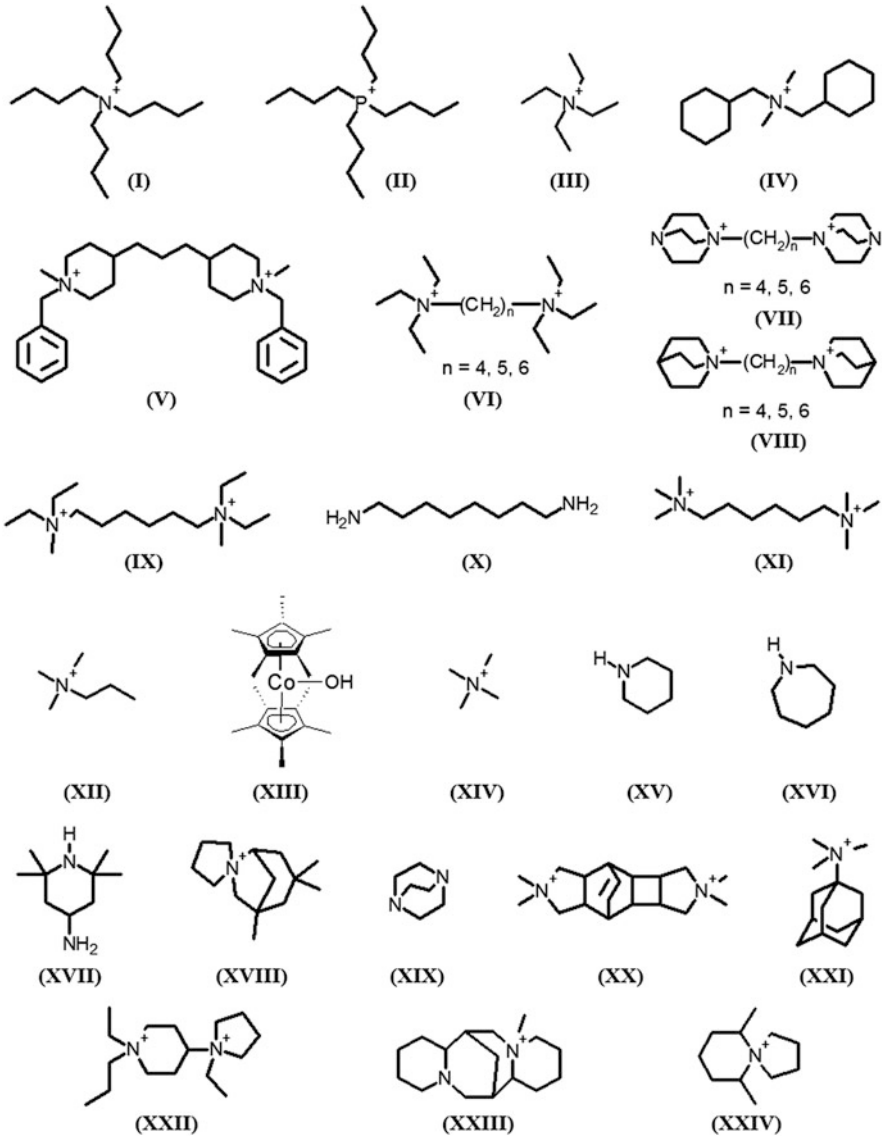

Fig. 12 Structure-directing agents (SDAs) employed in the syntheses of Ti-containing zeolites (see Table 5)

upper limit of 0.7 Ti/u.c. ($x = 0.015$) was tentatively attributed to the inefficient reaction between fumed silica and peroxotitanate, since the latter undergoes hydrolysis upon addition of the SDA [207]. Ti-ZSM-48 was obtained also with hexamethonium hydroxide (**XI**), but the incorporation of Ti proved to be difficult since extraframework TiO_2 was detected in the sample with $x = 0.007$ [208]. More

interesting results were reported by Tuel and Ben Taârit, who succeeded in synthesized Ti-ZSM-48 with up to 1.5 Ti/u.c. ($x = 0.031$) by using trimethylpropylammonium (**XII**) as SDA [211].

Ti-MWW The interest on this system arises from the peculiar pathway of formation of this zeolite, which involves a layered precursor formed by the regular stacking of randomly oriented zeolite sheets [235]. These layers, 2.5 nm thick, corresponding to one unit cell along the *c* direction, can be considered as 2D periodic building blocks for the construction of different materials [236]. Upon calcination, they form the ordered 3D MWW framework through the condensation of the silanol groups present on the surface. On the other hand, the precursor can be fully delaminated to form materials constituted by single layers randomly arranged. Besides, the layers can be permanently expanded by adding pillars constituted by silica and/or alumina oligomers or organosilanes. Finally, the so-called interlayer-expanded zeolites (IEZ) can be synthesized through the treatment of the layered precursor with specific monomeric species (e.g., silylating agents), which react with the surface silanol groups of adjacent layers, expanding the interlayer spacing and generating a 3D structure with pore system larger than that of the conventional MWW structure (i.e., from 10R to 12R).

The first attempt of preparing Ti-containing MWW involved the grafting of titanocene ($TiCp_2Cl_2$) on ITQ-2 (i.e., delaminated pure silica MWW layers) followed by calcination [237]. The authors argued that isolated tetrahedrally coordinated [O_3Ti–OH] and [$O_2Ti(OH)_2$] sites are present on the surface of the layers. This hypothesis, however, is not consistent because the distance between the oxygens of the silanol groups is too long ($O\cdots O = 8.3$ Å) for admitting the formation of such kinds of sites. In spite of that, the materials obtained were very active in the epoxidation of cyclohexene with TBHP, particularly when the weak acid sites present in the samples were deactivated by silylation with $(CH_3)_3SiCl$ [237].

Wu et al. were the first to examine the direct hydrothermal synthesis of Ti-MWW: only amorphous products were obtained by replacing the Al source with TBOT following the recipe of MCM-22 [214, 215]. To foster the crystallization, large amounts of H_3BO_3 (Si/B = 0.75) were added to the reaction mixture, and adopting a rather complex synthesis procedure, ternary Ti-B-MWW samples were obtained by using piperidine (**XV**) or hexamethyleneimine (**XVI**) as SDAs. To remove B from the framework, the as-synthesized and the calcined samples were treated with strong acids (HNO_3 or H_2SO_4). The accurate analysis of the acid-treated samples revealed that calcination produces the formation of anatase, which cannot be removed by the acid. On the other hand, the octahedral extraframework Ti species were easily removed together with B from the precursors, whose calcination led to the formation of Ti-MWW samples with trace amounts of B in the framework [215]. Subsequently, this recipe was modified by performing the synthesis of B-MWW precursor, which was successively calcined and repeatedly treated with 6 M HNO_3. Finally the deeply deboronated sample (Si/B > 1,000) was suspended in an aqueous solution of TBOT hydrolyzed with an amine and the

mixture heated at 175°C for 7 days. To obtain Ti-MWW free of extraframework Ti species, the sample was acid-treated before calcination [216]. An unexpected behavior of this system was later reported with the synthesis of Ti-YNU-1 [217]. The as-synthesized layered precursor obtained by heating at 170°C for 5 days a mixture composed of highly deboronated B-MWW, piperidine (**XV**), and TBOT was refluxed with 2 M HNO_3 for 10 h. The resulting solid, after calcination at 550°C, unexpectedly retained the layered structure, as confirmed by the expansion of the *c* parameter from 24.98 Å of the 3D MWW structure to 27.47 Å. The authors did not explain this unusual behavior; however, the 2.5 Å expansion of the *c* parameter is consistent with the formation of an interlayer-expanded zeolite (IEZ) generated by the insertion of $[(SiO)_2Si(OH)_2]$ tetrahedra interconnecting the silanol groups of adjacent layers during the acid treatment. As a matter of fact, a resonance at 88.6 ppm assigned to Q^2 $[(SiO)_2Si(OH)_2]$ sites was observed in the ^{29}Si MAS NMR spectra. This hypothesis was later on confirmed in a detailed study of Ruan et al. [238]. The expansion from 10 to 12R of the openings of the pores increases the accessibility of the internal large supercages, giving rise to the enhanced catalytic activity in the epoxidation of cyclohexene with H_2O_2 with respect to other Ti-containing zeolites [217]. The possibility to prepare IEZ-Ti-MWW was after confirmed: the Ti-MWW layered precursor was treated with a silylating agent (e.g., diethoxydimethylsilane, $(CH_3)_2Si(OCH_2CH_3)_2$) and calcined producing a 3D MWW structure with a 2.5 Å expansion of the *c* parameter with respect to the conventional MWW phase [218].

Ti-MWW was synthesized also by the dry gel conversion (DGC) method, using colloidal or fumed silica and TBOT, with the assistance of boric acid and piperidine (**XV**) or hexamethyleneimine (**XVI**) as SDA. After extraction of octahedrally coordinated Ti species, the resulting materials showed lower catalytic activity than conventional Ti-MWW in 1-hexene epoxidation, probably because of the larger crystal size [219].

6 Concluding Remarks

The discovery of TS-1, nearly 40 years ago, can be reasonably considered as one of the most important milestones in the history of zeolite science and technology. In fact, this has demonstrated the versatility of the microporous crystalline solids, whose framework may incorporate elements capable of conferring new catalytic properties. The first industrial application of TS-1 (hydroxylation of phenol at the EniChem plant in Ravenna) took place a few years after its discovery, and this attracted the interest of the international scientific community, an interest that continues today. A huge number of studies have been carried out for clarifying the different aspects related to the synthesis, characterization, and catalytic activity of TS-1. In this chapter, we reported the most significant of them, retracing the path that led to the current knowledge on this catalyst. Thanks to the availability of increasingly sophisticated physicochemical techniques, many aspects related to the

synthesis and to the characteristics of TS-1 are well understood now. However, the relatively small dimension of the 10R openings of the MFI pores limits somewhat the extensive application of TS-1, particularly in reactions involving bulky molecules. A possible solution as the insertion of Ti in zeolite frameworks possessing large (12R openings) or extra-large (14R+ openings) pores has been demonstrated by several research groups. However, these systems have shown several drawbacks that, ultimately, prevent them from developing at an industrial level. It is therefore clear that efforts should be directed toward deepening the most promising zeolite systems, exploiting also the enormous knowledge accumulated in the study of TS-1.

Another way for improving the characteristics of TS-1 and for extending its application to reactions involving bulky substrates is the preparation of materials with hierarchical micro-mesoporous systems. Indeed, this goal is pursued by extending to Ti-containing zeolites the approaches developed to generate hierarchical porous systems in the aluminosilicate zeolites, but to date, the results (quite interesting from a scientific point of view) do not provide for application benefits.

References

1. Goldsmith JR (1952) Min Mag 29:952–954
2. Barrer RM, Baynham JW, Bultitude FW, Meier WM (1959) J Chem Soc 195–208
3. Millini R, Perego G, Bellussi G (1999) Top Catal 9:13–34
4. Taramasso M, Perego G, Notari B (1983) US Patent 4 410 501
5. Taramasso M, Manara G, Fattore V, Notari B (1987) US Patent 4 666 692
6. Argauer RJ, Landolt GR (1972) US Patent 3 702 886
7. Gose RW, Flanigen EM (1977) US Patent 4 061 724
8. Flanigen EM, Bennet JM, Grose RW, Cohen JP, Patton RL, Kirchner RM, Smith JV (1978) Nature 271:512–516
9. Taramasso M, Manara G, Fattore V, Notari B (1979) BE Patent 877 205
10. Esposito A, Taramasso M, Neri C (1983) US Patent 4 396 783
11. Buonomo F, Bellussi G, Notari B (1986) US Patent 4 578 161
12. Bellussi G, Buonomo F, Esposito A, Clerici M, Romano U, Notari B (1987) US Patent 4 701 428
13. Bellussi G, Rigutto M (1994) Stud Surf Sci Catal 85:177–213
14. SRI-Consulting, hydroquinone from phenol using Ti-Si catalyst, PEP review 2000-03
15. Roffia P, Padovan M, Moretti E, De Alberti G (1988) US Patent 4 745 221
16. Bassler P, Weidenbach M, Göbbel H (2010) Chem Eng Trans 21:571–576
17. Perego G, Bellussi G, Corno C, Taramasso M, Buonomo F, Esposito A (1987) Proceedings of the seventh international conference on zeolites, Tokyo, pp 129–136
18. Clerici MG, Bellussi G, Romano U (1991) J Catal 129:159–167
19. Notari B (1987) Stud Surf Sci Catal 37:413–425
20. El Hage Al Asswad J, Nagy JB, Gabelica Z, Derouane EG (1989) In: Jansen JC, Moscou L (eds) Proceedings of the 8th international zeolite conference, Amsterdam, 10–14 July 1989, Recent Research Reports, p 475
21. Bellussi G, Carati A, Clerici MG, Esposito A (1990) In: Proceedings of the 5th international symposium on "scientific bases for the preparation of heterogeneous catalysts", Louvain-la-Neuve, 3–6 Sept 1990, Preprints, p 201
22. Huybrechts DRC, Vaese I, Li HX, Jacobs PA (1991) Catal Lett 8:237–244
23. Khouw CB, Li HX, Dartt CB, Davis ME (1992) In: Oyama ST, Hightower JW (eds) Catalytic selective oxidations, ACS Sym Ser, vol 523, pp 273–280

24. Khouw CB, Davis ME (1995) J Catal 151:77–86
25. Bellussi G, Fattore V (1991) Stud Surf Sci Catal 69:79–92
26. van der Pol AJHP, van Hooff JHC (1992) Appl Catal A Gen 92:93–111
27. Kraushaar-Czarnetzki B (1989) Characterization and modification of zeolites and related materials. PhD thesis. Technische Universiteit Eindhoven, Eindhoven
28. Thangaraj A, Kumar R, Mirajkar SP, Ratnasamy P (1991) J Catal 130:1–8
29. Thangaraj A, Eapen MJ, Sivasanker S, Ratnasamy P (1992) Zeolites 12:943–950
30. Thangaraj A, Sivasanker S (1992) J Chem Soc Chem Commun 123–124
31. Millini R, Previde Massara E, Perego G, Bellussi G (1992) J Catal 137:497–503
32. Schuchardt U, Pastore HO, Spinace EV (1994) Stud Surf Sci Catal 84:1877–1882
33. Tuel A, Ben Taârit Y (1994) Appl Catal A Gen 110:137–151
34. Gao X, Suo J, Li S (1995) J Chem Soc Chem Commun 835–836
35. Shibata M, Gérard J, Gabelica Z (1997) Stud Surf Sci Catal 105:245–252
36. Xia QX, Gao Z (1997) Mater Chem Phys 47:225–230
37. Tuel A (1997) Stud Surf Sci Catal 105:261–268
38. Tuel A, Ben Taârit Y (1994) Zeolites 14:594–599
39. Tuel A, Ben Taârit Y, Naccache C (1993) Zeolites 13:454–461
40. Tuel A, Ben Taârit Y (1994) Zeolites 14:272–281
41. Guth JL, Kessler H, Higel JM, Lamblin JM, Patarin J, Seive A, Chezeou JM, Wey R (1989) ACS Symp Ser 398:176–195
42. Popa JM, Guth JL, Kessler H (1988) Eur Patent Appl 292:363
43. Qiu S, Pang W, Yao S (1989) Stud Surf Sci Catal 49:133–142
44. Kooyman PJ, Jansen JC, van Bekkum H (1992) In: Proceedings of the ninth international conference on zeolites, Montreal, pp 505–512
45. Lopez A, Tuilier HM, Guth JL, Delmotte L, Popa JM (1993) J Solid State Chem 102:480–491
46. Carati A, Flego C, Berti D, Millini R, Stocchi B, Perego C (1999) Stud Surf Sci Catal 125: 45–52
47. Grieneisen JL, Kessler H, Fache E, Le Govic AM (2000) Microporous Mesoporous Mater 37: 379–386
48. Fan W, Duan R-G, Yokoi T, Wu P, Kubota Y, Tatsumi T (2008) J Am Chem Soc 130: 10150–10164
49. Fan W, Fan B, Shen X, Li J, Wu P, Kubota Y, Tatsumi T (2009) Microporous Mesoporous Mater 122:301–308
50. Zhu G, Ni L, Qi W, Ding S, Li X, Wang R, Qiu S (2014) Inorg Chem Commun 40:129–132
51. Xue Y, Xie Y, Wei H, Wen Y, Wang X, Li B (2014) New J Chem 38:4229–4234
52. Shibata M, Gérard J, Gabelica Z (1997) Microporous Mater 12:141–148
53. Jorda E, Tuel A, Teissier R, Kervennal J (1997) Zeolites 19:238–245
54. Sulinowski B, Klinowski J (1992) Appl Catal A Gen 84:141–153
55. Tuel A (1996) Zeolites 16:108–117
56. Gontier S, Tuel A (1996) Zeolites 16:184–195
57. Müller U, Steck W (1994) Stud Surf Sci Catal 84:203–210
58. Sabde DP, Hedge SG, Dongare MK (2000) J Mater Chem 10:1365–1370
59. Padovan M, Leofanti G, Roffia P (1989) Eur Patent Appl 311:983
60. Padovan M, Genoni F, Leofanti G, Petrini G, Trezza G, Zecchina A (1991) Stud Surf Sci Catal 63:431–438
61. Uguina MA, Ovejero G, van Grieken R, Serrano DP, Camacho M (1994) J Chem Soc Chem Commun 27–28
62. Uguina MA, Serrano DP, Ovejero G, van Grieken R, Camacho M (1995) Appl Catal A Gen 124:391–408
63. Serrano DP, Uguina MA, Ovejero G, van Grieken R, Camacho M (1995) Microporous Mater 4:273–282
64. Serrano DP, Uguina MA, Ovejero G, van Grieken R, Camacho M (1996) Microporous Mater 7:309–321

65. Uguina MA, Serrano DP, Ovejero G, van Grieken R, Camacho M (1997) Zeolites 18: 368–378
66. Ovejero G, van Grieken R, Uguina MA, Serrano DP, Melero JA (1998) J Mater Chem 8: 2269–2276
67. Melero JA, van Grieken R, Serrano DP, Espada JJ (2001) J Mater Chem 11:1519–1525
68. Serrano DP, Uguina MA, Ovejero G, van Grieken R, Camacho M, Melero JA (1999) J Mater Chem 9:2899–2905
69. Yamamoto K, Borjas Garcia SE, Saito F, Muramatsu A (2006) Chem Lett 35:570–571
70. Yamamoto K, Borjas Garcia SE, Muramatsu A (2007) Microporous Mesoporous Mater 101: 90–96
71. Iwasaki T, Isaka M, Nakamura H, Yasuda M, Watano S (2012) Microporous Mesoporous Mater 150:1–6
72. Uguina MA, Serano DP, Sanz R, Castillo E (1998) In: Proceedings of the 12th international zeolite conference, vol 3, p 1971
73. Ramakrishna Prasad M, Kamalakar G, Kulkarni SJ, Raghavan KV, Narasimha Rao K, Sai Prasad PS, Madhavendra SS (2002) Catal Commun 3:399–404
74. Cundy CS, Forrest JO, Plaisted RJ (2003) Microporous Mesoporous Mater 66:143–156
75. Cundy CS, Forrest JO (2004) Microporous Mesoporous Mater 72:67–80
76. Ahn WS, Kang KK, Kim KY (2001) Catal Lett 72:229–232
77. Kim KY, Ahn WS, Park DW, Oh JH, Lee CM, Tai WP (2004) Bull Kor Chem Soc 25: 634–638
78. Wu EL, Lawton SL, Olson DH, Rohrman Jr AC, Kokotailo GT (1979) J Phys Chem 83: 2777–2781
79. Taramasso M, Perego G, Notari B (1980) In: Proceeding of the fifth international conference on zeolites, Naples, p 40
80. Lamberti C, Bordiga S, Zecchina A, Carati A, Fitch AN, Artioli G, Petrini G, Salvalaggio M, Marra GL (1999) J Catal 183:222–231
81. Millini R, Perego G, Berti D, Parker Jr WO, Carati A, Bellussi G (2000) Microporous Mesoporous Mater 35–36:387–403
82. Boccuti MR, Rao KM, Zecchina A, Leofanti G, Petrini G (1989) Stud Surf Sci Catal 48: 133–144
83. Huybrechts DRC, Buskens PL, Jacobs PA (1992) J Mol Catal 71:129–147
84. Trong On D, Bonneviot L, Bittar A, Sayari A, Kaliaguine S (1992) J Mol Catal 74:233–246
85. Bellussi G, Carati A, Clerici MG, Maddinelli G, Millini R (1993) J Catal 133:220–230
86. Zecchina A, Spoto G, Bordiga S, Ferrero A, Petrini G, Leofanti G, Padovan M (1991) Stud Surf Sci Catal 69:251–258
87. Scarano D, Zecchina A, Bordiga S, Geobaldo F, Spoto G, Petrini G, Leofanti G, Padovan M, Tozzola G (1993) J Chem Soc Faraday Trans 89:4123–4130
88. Dartt CB, Khouw CB, Li H-X, Davis ME (1994) Microporous Mater 2:425–437
89. Duprey E, Beaunier P, Springuel-Huet M-A, Bozon-Verduraz F, Fraissard J, Manoli J-M, Brégeault J-M (1997) J Catal 165:22–32
90. Li C, Xiong G, Xin Q, Liu J-K, Ying P-L, Feng Z-C, Li J, Yang W-B, Wang Y-Z, Wang G-R, Liu X-Y, Lin M, Wang X-Q, Min E-Z (1999) Angew Chem Int Ed 38:2220–2222
91. Bordiga S, Damin A, Bonino F, Ricchiardi G, Zecchina A, Tagliapietra R, Lamberti C (2003) Phys Chem Chem Phys 5:4390–4393
92. Ricchiardi G, Damin A, Bordiga S, Lamberti C, Spanò G, Rivetti F, Zecchina A (2001) J Am Chem Soc 123:11409–11419
93. Damin A, Bonino F, Ricchiardi G, Bordiga S, Zecchina A, Lamberti C (2002) J Phys Chem B 106:7524–7526
94. Bordiga S, Damin A, Bonino F, Zecchina A, Spanò G, Rivetti F, Bolis V, Lamberti C (2002) J Phys Chem B 106:9892–9905
95. Geobaldo F, Bordiga S, Zecchina A, Giamello E, Leofanti G, Petrini G (1992) Catal Lett 16:109–115

96. Liu Z, Davis RJ (1994) J Phys Chem 98:1253–1261
97. Boccuzzi F, Coluccia S, Ghiotti G, Morterra C, Zecchina A (1978) J Phys Chem 82: 1298–1303
98. Behrens P, Felsche J, Vetter S, Schulz-Ekloff G, Jaeger N, Newmann W (1991) J Chem Soc Chem Commun 678–679
99. Behrens P, Felsche J, Newmann W (1991) Catal Today 8:479–490
100. Schultz E, Ferrini C, Prins R (1992) Catal Lett 14:221–231
101. Trong On D, Bittar A, Sayari A, Kaliaguine S, Bonneviot L (1992) Catal Lett 16:85–95
102. Jentys A, Catlow CRA (1993) Catal Lett 22:251–257
103. Pei S, Zajac GW, Kaduk JA, Faber J, Boyanov BI, Duck D, Fazzini D, Morrison TI, Yang DS (1993) Catal Lett 21:333–344
104. Bordiga S, Boscherini F, Coluccia S, Genoni F, Lamberti C, Leofanti G, Marchese L, Petrini G, Vlaic G, Zecchina A (1994) Catal Lett 26:195–208
105. Bordiga S, Coluccia S, Lamberti C, Marchese L, Zecchina A, Boscherini F, Buffa F, Genoni F, Leofanti G, Petrini G, Vlaic G (1994) J Phys Chem 98:4125–4132
106. Lamberti C, Bordiga S, Arduino D, Zecchina A, Geobaldo F, Spanò G, Genoni F, Petrini G, Carati A, Villain F, Vlaic G (1998) J Phys Chem B 102:6382–6390
107. Zecchina A, Bordiga S, Lamberti C, Ricchiardi G, Scarano D, Petrini G, Leofanti G, Mantegazza M (1996) Catal Today 32:97–106
108. Bolis V, Bordiga S, Lamberti C, Zecchina A, Carati A, Rivetti F, Spanò G, Petrini G (1999) Microporous Mesoporous Mater 30:67–76
109. Bolis V, Bordiga S, Lamberti C, Zecchina A, Carati A, Rivetti F, Spanò G, Petrini G (1999) Langmuir 15:5753–5764
110. Lamberti C, Bordiga S, Zecchina A, Artioli G, Marra GL, Spanó G (2001) J Am Chem Soc 123:2204–2212
111. Gallo E, Bonino F, Swarbrick JC, Petrenko T, Piovano A, Bordiga S, Gianolio D, Groppo E, Neese F, Lamberti C, Glatzel P (2013) ChemPhysChem 14:79–83
112. Clerici MG, Ingallina P, Millini R (1993) In: Proceedings of the ninth international conference on zeolites, Montreal, p 445
113. Tozzola G, Mantegazza MA, Ranghino G, Petrini G, Bordiga S, Ricchiardi G, Lamberti C, Zulian R, Zecchina A (1998) J Catal 179:64–71
114. Bordiga S, Damin A, Bonino F, Ricchiardi G, Lamberti C, Zecchina A (2002) Angew Chem Int Ed 41:4734–4737
115. Liu Q-X, Zhou Z-H (2012) Polyhedron 35:1–6
116. Parker Jr WO, Millini R (2006) J Am Chem Soc 128:1450–1451
117. Koller H, Lobo RF, Burkett SL, Davis ME (1995) J Phys Chem 99:12588–12596
118. Shantz DF, Schmedt auf der Gunne J, Koller H, Lobo RF (2000) J Am Chem Soc 122: 6659–6663
119. Shantz DF, Lobo RF (1999) Top Catal 9:1–11
120. van Koningsveld H, Jansen JC, van Bekkum H (1990) Zeolites 10:235–242
121. van Koningsveld H, van Bekkum H, Jansen JC (1987) Acta Crystallogr B43:127
122. Millini R, Perego G, Seiti K (1994) Stud Surf Sci Catal 84:2123–2129
123. Oumi Y, Matsuba K, Kubo M, Inui T, Miyamoto A (1995) Microporous Mater 4:53–57
124. Njo SL, van Koningsveld H, van de Graaf B (1997) J Phys Chem B 101:10065–10068
125. Atoguchi T, Yao S (2003) J Mol Catal A Chem 191:281–288
126. Gale JD (2006) Solid State Sci 8:234–240
127. Pirc G, Stare J (2008) Acta Chim Slov 55:951–959
128. Yuan S, Si H, Fu A, Chu T, Tian F, Duan Y-B, Wang J (2011) J Phys Chem A 115:940–947
129. Marra GL, Artioli G, Fitch AN, Milanesio M, Lamberti C (2000) Microporous Mesoporous Mater 40:85–94
130. Hijar CA, Jacubinas RM, Eckert J, Henson NJ, Hay PJ, Ott KC (2000) J Phys Chem B 104: 12157–12164
131. Artioli G, Lamberti C, Marra GL (2000) Acta Crystallogr B 56:2–10

132. Henry PF, Weller MT, Wilson CC (2001) J Phys Chem B 105:7452–7458
133. Tosheva L, Valtchev VP (2005) Chem Mater 17:2494–2513
134. Perego C, Carati A, Ingallina P, Mantegazza MA, Bellussi G (2001) Appl Catal A Gen 221: 63–72
135. Zhang G, Sterte J, Schoeman BJ (1997) Chem Mater 9:210–217
136. Pérez-Ramírez J, Christensen CH, Egeblad K, Christensend CH, Groenef JC (2008) Chem Soc Rev 37:2530–2542
137. Chal R, Gérardin C, Bulut M, van Donk S (2011) ChemCatChem 3:67–81
138. Bellussi G, Carati A, Rizzo C, Millini R (2013) Cat Sci Technol 3:833–857
139. García-Martínez J, Li K (eds) (2015) Mesoporous zeolites. Wiley-VCH, Weinheim
140. Schmidt I, Krogh A, Wienberg K, Carlsson A, Brorson M, Jacobsen CJH (2000) Chem Commun 2157–2158
141. Ok D-Y, Jiang N, Prasetyanto EA, Jin H, Park S-E (2011) Microporous Mesoporous Mater 141:2–7
142. Lin J, Xin F, Yang F, Zhuang Z (2014) Catal Commun 45:104–108
143. Du Q, Guo Y, Duan H, Li H, Chen Y, Rehman HU, Liu H (2017) J Alloys Compd 699: 386–391
144. Fang Y, Hu H (2007) Catal Commun 8:817–820
145. Park C-W, Kim T-K, Ahn W-S (2009) Bull Kor Chem Soc 30:1778–1782
146. Wang X, Li G, Wang W, Jin C, Chen Y (2011) Microporous Mesoporous Mater 142:494–502
147. Wang W, Li G, Liu L, Chen Y (2013) Microporous Mesoporous Mater 179:165–171
148. Adedigba A-L, Sankar G, Catlow CRA, Du Y, Xi S, Borgna A (2017) Microporous Mesoporous Mater 244:83–92
149. Gao X, An J, Gu J, Li L, Li Y (2017) Microporous Mesoporous Mater 239:381–389
150. Kresge CT, Leonowicz ME, Roth WJ, Vartuli JC, Beck JS (1992) Nature 359:710–712
151. Corma A, Navarro MT, Perez Pariente J (1994) J Chem Soc Chem Commun 147–148
152. Blasco T, Corma A, Navarro MT, Perez-Pariente J (1995) J Catal 156:65–74
153. Koyano KA, Tatsumi T (1996) Chem Commun 145–146
154. Tanev PT, Chibwe M, Pinnavaia TJ (1994) Nature 368:321–323
155. Wu P, Tatsumi T, Komatsu T, Yashima T (2002) Chem Mater 14:1657–1664
156. Newalkar BL, Olanrewaju J, Komarneni S (2001) Chem Mater 13:552–557
157. Trong On D, Lutic D, Kaliaguine S (2001) Microporous Mesoporous Mater 44–45:435–444
158. Han Y, Xiao F-S, Wu S, Sun Y, Meng X, Li D, Lin S (2001) J Phys Chem B 105:7963–7966
159. Xiao F-S, Han Y, Yu Y, Meng X, Yang M, Wu S (2002) J Am Chem Soc 124:888–889
160. Hua D, Zhou Z, Wua Y, Chen Y, Ji L, Xie Q, Yang M (2013) Microporous Mesoporous Mater 171:179–184
161. Meng X, Fan W, Kubota Y, Tatsumi T (2006) J Catal 244:192–198
162. Zou Y, Wang R, Zhang Z, Li G, Qiu S (2013) Microporous Mesoporous Mater 182:178–184
163. Yang X, Han Y, Lin K, Tian G, Feng Y, Meng X, Di Y, Du Y, Zhang Y, Xiao F-S (2004) Chem Commun 2612–2613
164. Lin K, Sun Z, Lin S, Jiang D, Xiao F-S (2004) Microporous Mesoporous Mater 72:193–201
165. Wang R, Hu L, Chu B, Zhao L, Zhu G, Qiu S (2005) Catal Commun 6:485–490
166. Eimer GA, Díaz I, Sastre E, Casuscelli SG, Crivello ME, Herrero ER, Perez-Pariente J (2008) Appl Catal A Gen 343:77–86
167. Reichinger M, Schmidt W, van den Berg MWE, Aerts A, Martens JA, Kirschhock CEA, Gies H, Grünert W (2010) J Catal 269:367–375
168. Reichinger M, Schmidt W, Narkhede VV, Zhang W, Gies H, Grünert W (2012) Microporous Mesoporous Mater 164:21–31
169. Serrano D, Sanz R, Pizarro P, Moreno I (2009) Chem Commun 1407–1409
170. Serrano DP, Sanz R, Pizarro P, Moreno I (2010) Top Catal 53:1319–1329
171. Serrano DP, Sanz R, Pizarro P, Moreno I (2012) Appl Catal A Gen 435–436:32–42
172. Serrano DP, Sanz R, Pizarro P, Peral A, Moreno I (2013) Microporous Mesoporous Mater 166:59–66

173. Serrano DP, Sanz R, Pizarro P, Moreno I, Shami S (2014) Microporous Mesoporous Mater 189:71–82
174. Serrano DP, Sanz R, Pizarro P, Moreno I, Medina S (2013) Appl Catal B Environ 146:35–42
175. Sanz R, Serrano DP, Pizarro P, Moreno I (2011) Chem Eng J 171:1428–1438
176. Cheneviere Y, Chieux F, Caps V, Tuel A (2010) J Catal 269:161–168
177. Lv Q, Li G, Sun H (2014) Fuel 130:70–75
178. Choi M, Na K, Kim J, Sakamoto Y, Terasaki O, Ryoo R (2009) Nature 461:246–249
179. Na K, Jo C, Kim J, Ahn W-S, Ryoo R (2011) ACS Catal 1:901–907
180. Wang J, Xu L, Zhang K, Peng H, Wu H, Jiang J, Liu Y, Wu P (2012) J Catal 288:16–23
181. Martens JA, Buskens P, Jacobs PA, van der Pol A, van Hooff JHC, Ferrini C, Kouwenhoven HW, Kooyman PJ, van Bekkum H (1993) Appl Catal A Gen 99:71–84
182. Bellussi G, Carati A, Clerici MG, Esposito A, Millini R, Buonomo F (1989) Belgian Patent 1 001 038
183. Reddy JS, Kumar R, Ratnasamy P (1990) Appl Catal 58:L1–L4
184. Reddy JS, Kumar R (1992) Zeolites 12:95–100
185. Tuel A, Ben Taârit Y (1993) Zeolites 13:357–364
186. de Lucas A, Rodríguez L, Sánchez P (1999) Appl Catal A Gen 180:375–383
187. Serrano DP, Uguina MA, Sanz R, Castillo E, Rodríguez A, Sánchez P (2004) Microporous Mesoporous Mater 69:197–208
188. Camblor MA, Corma A, Martinez A, Pérez-Pariente J (1992) J Chem Soc Chem Commun 589–590
189. Camblor MA, Corma A, Pérez-Pariente J (1993) Zeolites 13:82–87
190. Blasco T, Camblor MA, Corma A, Pérez-Pariente J (1993) J Am Chem Soc 115:11806–11813
191. Camblor MA, Constantini M, Corma A, Gilbert L, Esteve P, Martinez A, Valencia S (1996) Chem Commun 1339–1340
192. Camblor MA, Constantini M, Corma A, Esteve P, Gilbert L, Martinez A, Valencia S (1995) Appl Catal A Gen 133:L185–L189
193. Blasco T, Camblor MA, Corma A, Esteve P, Martínez A, Prieto C, Valencia S (1996) Chem Commun 2367–2368
194. Blasco T, Camblor MA, Corma A, Esteve P, Guil JM, Martínez A, Perdigón-Melón JA, Valencia S (1998) J Phys Chem B 102:75–88
195. Taborda F, Wang Z, Willhammar T, Montes C, Zou X (2012) Microporous Mesoporous Mater 150:38–46
196. van der Waal JC, Rigutto MS, Lin P, van Bekkum H (1994) Stud Surf Sci Catal 105: 1093–1100
197. van der Waal JC, Kooyman PJ, Jansen JC, van Bekkum H (1998) Microporous Mesoporous Mater 25:43–57
198. Saxton JR (1999) Top Catal 9:43–57
199. Saxton JR (1994) United States Patent 5 453 511
200. Sasidharan M, Bhaumik A (2011) Phys Chem Chem Phys 13:16282–16294
201. Carati A, Flego C, Previde Massara E, Millini R, Carluccio L, Parker Jr WO, Bellussi G (1999) Microporous Mesoporous Mater 30:137–144
202. Krijnen S, Sánchez P, Jakobs BTF, van Hooff JHC (1999) Microporous Mesoporous Mater 31:163–173
203. Reddy JS, Sayari A (1995) J Chem Soc Chem Commun 23–24
204. Tang B, Dai W, Sun X, Guan N, Li L, Hunger M (2014) Green Chem 16:2281–2291
205. Tuel A (1995) Zeolites 15:236–242
206. Serrano DP, Li H-X, Davis ME (1992) J Chem Soc Chem Commun 745–746
207. Reddy KM, Kaliaguine S, Sayari A, Ramaswamy AV, Reddy VS, Bonneviot L (1994) Catal Lett 23:175–187
208. Reddy KM, Kaliaguine S, Sayari A (1994) Catal Lett 23:169–173
209. Tuel A, Ben Taârit Y (1995) Zeolites 15:164–170
210. Balkus Jr KJ, Gabrielov AG, Zones SI (1995) Stud Surf Sci Catal 97:519–525

211. Balkus Jr KJ, Khanmamedova A, Gabrielov AG, Zones SI (1996) Stud Surf Sci Catal 101: 1341–1348
212. Ahedi RK, Shevade SS, Kotasthane AN (1998) Stud Surf Sci Catal 113:201–209
213. Bhaumik A, Tatsumi T (2000) Microporous Mesoporous Mater 34:1–7
214. Wu P, Tatsumi T, Komatsu T, Yashima T (2000) Chem Lett 29:774–775
215. Wu P, Tatsumi T, Komatsu T, Yashima T (2001) J Phys Chem B 105:2897–2905
216. Wu P, Tatsumi T (2002) Chem Commun 1026–1027
217. Fan W, Wu P, Namba S, Tatsumi T (2004) Angew Chem Int Ed 43:236–240
218. Wang L, Wang Y, Liu Y, Wu H, Li X, He M, Wu P (2009) J Mater Chem 19:8594–8602
219. Wu P, Miyaji T, Liu Y, He M, Tatsumi T (2005) Catal Today 99:233–240
220. Corma A, Diaz U, Domine ME, Fornés V (2000) Chem Commun 137–138
221. Díaz-Cabañas M-J, Villaescusa LA, Camblor MA (2000) Chem Commun 761–762
222. Corma A, Díaz-Cabañas M-J, Domine ME, Rey F (2000) Chem Commun 1725–1726
223. Belhekar AA, Das TK, Chaudhari K, Hegde SG, Chandwadkar AJ (1998) Stud Surf Sci Catal 113:195–200
224. Yamamoto K, Plévert J, Uneme M, Tatsumi T (2002) Microporous Mesoporous Mater 55: 81–91
225. Dartt C, Davis ME (1996) Appl Catal A Gen 143:53–73
226. Kubota Y, Koyama Y, Yamada T, Inagaki S, Tatsumi T (2008) Chem Commun 6224–6226
227. Sasaki M, Sato Y, Tsuboi Y, Inagaki D, Kubota Y (2014) ACS Catal 4:2653–2657
228. Moliner M, Serna P, Cantin A, Sastre G, Diaz-Cabañas MJ, Corma A (2008) J Phys Chem C 112:19547–19554
229. Lee FY, Lv L, Su F, Liu T, Liu Y, Sow CH, Zhao XS (2009) Microporous Mesoporous Mater 124:36–41
230. Eilertsen ES, Bordiga S, Lamberti C, Damin A, Bonino F, Arstad B, Svelle S, Olsbye U, Lillerud KP (2011) ChemCatChem 3:1869–1871
231. Eilertsen ES, Giordanino F, Lamberti C, Bordiga S, Damin A, Bonino F, Olsbye U, Lillerud KP (2011) Chem Commun 47:11867–11869
232. Moliner M, Corma A (2012) Microporous Mesoporous Mater 164:44–48
233. Přech J, Kubů M, Čejka J (2014) Catal Today 227:80–86
234. Přech J, Čejka J (2016) Catal Today 277:2–8
235. Millini R, Perego G, Parker Jr WO, Bellussi G, Carluccio L (1995) Microporous Mater 4: 221–230
236. Roth WJ, Nachtigall P, Morris RE, Čejka J (2014) Chem Rev 114:4807–4837
237. Corma A, Díaz U, Fornés V, Jordá JL, Domine M, Rey F (1999) Chem Commun 779–780
238. Ruan J, Wu P, Slater B, Terasaki O (2005) Angew Chem Int Ed 44:6719–6723

Struct Bond (2018) 178: 53–90
DOI: 10.1007/430_2017_21

Published online: 8 February 2018

General Aspects on Structure and Reactivity of Framework and Extra-framework Metals in Zeolite Materials

Manuel Moliner and Avelino Corma

Abstract In the present manuscript, the general aspects involving the synthesis and the most significant catalytic applications of metal-containing zeolites will be addressed and discussed. From the different metal-containing zeolites, metal species present in extra-framework or framework positions will be considered. On the one hand, the section highlighting the extra-framework metallic species will comprise metals with different natures, including single metal cations in exchangeable positions and metal clusters or nanoparticles entrapped within the pores and cavities of the zeolite frameworks. Depending on the nature of the metal, the acid/base and redox properties of these metal-containing zeolites can be tuned, allowing their efficient application as shape-selective heterogeneous catalysts in different industrially relevant chemical processes, including petrochemistry, refining, and fine chemistry, or environmental applications. On the other hand, the isomorphic substitution of isolated transition metals in tetrahedral coordination allows introducing controlled Lewis and/or Brønsted acidities, together with redox properties to zeolites, offering new opportunities for their implementation as selective catalysts for fine chemistry and biomass-derived processes.

Keywords Acid/base catalysts · Alkali cations · Heterogeneous catalysis · Transition metals · Zeolites

Contents

M. Moliner (✉) and A. Corma (✉)
Instituto de Tecnología Química, Universitat Politècnica de València-Consejo Superior de Investigaciones Científicas, Valencia, Spain
e-mail: mmoliner@itq.upv.es; acorma@itq.upv.es

1 Introduction

Zeolites are three-dimensional crystalline frameworks formed by tetrahedral T atoms connected by common O atoms. For years, zeolites have been exclusively prepared in their aluminosilicate form, which means that these tetrahedral T atoms were Si or Al [1]. The presence of Al^{3+} species in tetrahedral coordination within the framework positions creates $(AlO_2)^-$ units that can be compensated by cations through electrostatic forces. Since the former syntheses were performed using alkali or alkaline-earth cations in the synthesis media, the resultant aluminosilicate zeolites show low Si/Al ratios, mostly below 3, because many tetrahedrally connected Al atoms were required to properly balance the large amount of positive charges introduced by these small inorganic cations. At this point, the use of the Al-rich zeolites was limited to adsorption or cation exchange processes [2, 3], and only after dealumination and stabilization they could be used in catalysis.

However, the introduction of some bulky organic molecules in the synthesis media as organic structure-directing agents (OSDAs) allowed decreasing the overall number of entrapped positive charges and, consequently, increasing the Si/Al molar ratios [4–6]. This fact resulted in the improvement of the acid properties and hydrothermal stability of aluminosilicate zeolites, opening the application of high-silica zeolites as very efficient heterogeneous catalysts [7]. On the one hand, these high-silica zeolite catalysts can be employed in their protonic form, which means that the negative charges introduced by tetrahedral Al species are balanced by H^+, resulting in excellent materials for Brønsted acid-catalyzed reactions, such as fluid catalytic cracking, aromatic alkylation, oligomerization, or methanol-to-olefin processes, among others [7–10]. On the other hand, the framework negative charges can be balanced by the presence of metal cations in extra-framework positions, modifying the localized electrostatic field of these cations and then resulting in heterogeneous catalysts with unusual acid/base or enhanced redox properties [11, 12]. Some of the most studied metal cations in extra-framework positions are copper, iron, or nickel, among others, presenting excellent catalytic capabilities, for example, in the selective catalytic reduction of NOx or in the selective oxidation of methane to methanol [13, 14]. Besides the cationic isolated metal species in extra-framework positions, it has been also described the ability of zeolites to stabilize extra-framework metal clusters or small metal nanoparticles within their pores, increasing their confinement and stability against metal aggregation and offering unique opportunities as very active and highly resistant redox catalysts [15–17]. The stabilization of different clusters or small nanoparticles of some noble metals, including Pt, Pd, or Au, has been described for particular catalytic applications, such as CO oxidation,

direct dehydrogenation of propane, or H_2 generation by decomposition of formic acid (FA), among others [15, 18, 19].

In addition to the extra-framework metal species, the insertion of isolated metal species in framework tetrahedral positions, particularly Ti, Sn, Nb, Ta, or Hf, within high-silica or pure-silica zeolites offers unique Lewis acid character to these metals, allowing, for instance, the selective oxidation of many hydrocarbons using H_2O_2 as oxidizing agent [20, 21]. In general, the use of large OSDAs and/or the presence of fluoride anions in the synthesis media has been determinant to prepare diverse zeolitic structures in their high-silica or pure-silica form [22, 23], resulting in very hydrophobic crystals where the incorporated metals maintain their Lewis acid nature, even in presence of polar solvents, as water [24, 25].

In the present manuscript, the synthesis strategies followed to prepare some of the most significant metal-containing zeolites, including metal species in extra-framework or framework positions, will be presented together with their application as selective heterogeneous catalysts in some industrially relevant chemical processes.

2 Zeolites with Extra-framework Metal Species

In general, the design of metal-containing zeolites with the metal species in extra-framework positions, particularly when isolated metal species are required, employs aluminosilicate zeolitic frameworks as macroligand supports, where the localized negative charges generated by the presence of tetrahedrally connected aluminum atoms offer the adequate environment to anchor and stabilize the extra-framework cationic metal species [12]. Interestingly, if the aluminosilicate supports were appropriately designed, in terms of Si/Al molar ratio or crystal size, it would provide high level of metal dispersion along the zeolite crystals, together with high hydrothermal stability for different catalytic applications [11, 13, 26, 27]. However, it has also been described the use of Al-free zeolite supports as host for different metal species, for instance, pure-silica zeolite frameworks, particularly when small metal clusters or nanoparticles are encapsulated within their pores and/or cavities [15, 18]. Interestingly, different rationalized synthesis approaches to obtain these extra-framework metal-containing zeolites have been proposed, including either one-pot or post-synthetic methods [28]. These aspects will be discussed later.

2.1 Alkali Metal Cations in Extra-framework Positions as Basic Zeolite-Type Catalysts

Although acid aluminosilicate zeolites have been extensively applied as industrial catalysts in many relevant chemical processes [7, 9], the potential application of

zeolite-type basic catalysts has not received the same attention in the literature [11]. The substitution of homogeneous by heterogeneous base catalysts has advantages, such as their separation from the reaction media, regenerability, and reusability. However, as far as we know, there are very few basic zeolites in commercial application. Nevertheless, it can be said that for Pt-zeolite reforming catalysts, the zeolite is deeply exchanged with alkalines (K).

The basicity in cation-exchanged zeolites is directly related to the framework negative charges and nature of the cations. Then, stronger basicities are achieved by introducing large alkali metals (i.e., Cs^+) in Al-rich zeolites to enhance the electron density of the framework oxygen atoms (Fig. 1a) [29]. From the different zeolite frameworks, Al-rich FAU zeolites (X and Y, presenting Si/Al ratios of 1.3 and 2.6, respectively) are the preferred zeolite supports for designing basic catalysts, since these materials combine very open frameworks ($12 \times 12 \times 12$-rings), large cavities, and high-aluminum content, favoring the accessibility of reactants and the presence of large amount of framework negative charges, respectively [30]. The basicity strength of FAU-related zeolites exchanged with different alkali metal cations has been evaluated by the blue shift in the UV-Vis adsorption spectrum of adsorbed iodine [31]. As seen in Fig. 1b, Cs- and K-exchanged X zeolites show higher basicity than the other metal-containing FAU zeolites. This fact can be ascribed to the higher Al content of the X zeolite compared to Y zeolite, thus presenting a larger number of framework negative charges. However, if the intrinsic basic strength per metal site is analyzed for CsX and KX, it can be noticed that CsX is considerably higher, since only a fraction of the total positions can be exchanged with Cs^+, whereas almost all these positions can be exchanged by K^+ [31].

Regarding the catalytic properties of this type of basic catalysts, the use of alkali metal-exchanged FAU materials has been studied for the production of different fine chemicals. Indeed, alkali metal-exchanged FAU-related zeolites have been described as very efficient basic heterogeneous catalysts in condensation reactions, as the Knoevenagel reaction of benzaldehyde with derivatives of malonic esters (Fig. 2) [32]. Corma et al. showed that the most active catalyst for these reactions was CsX, demonstrating that there is a direct relationship between the increase of the

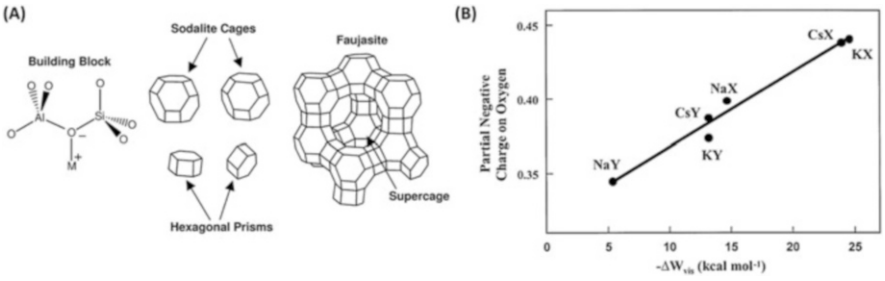

Fig. 1 (**a**) Scheme of the FAU-type framework, presenting the building block where a cationic metal cation (M^+) is balancing the negative charge of the framework, and (**b**) basicity strength of different M-based FAU zeolites measured from adsorbed iodine. Reprinted from [11], with permission from Elsevier

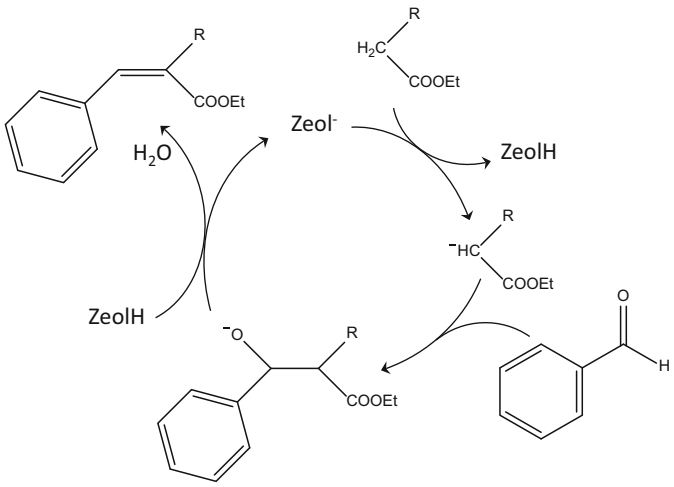

Fig. 2 Scheme for the Knoevenagel condensation of benzaldehyde with derivatives of malonic esters

catalytic activity with the decrease of the Si/Al molar ratio and the increase of the radius of the countercation [32]. These results clearly agree with the basic strength shown in Fig. 1b. The authors studied the mechanism reaction of the Knoevenagel condensation using the alkali-exchanged basic zeolites (Fig. 2), concluding that the controlling step is not the proton abstraction by the basic site of the zeolite from the methylenic compounds to form the carbanion, but the attack of the carbonyl group by the carbanion (Fig. 2). Following a similar mechanistic reaction, Corma et al. have extended the use of basic zeolites to the preparation of prepolymers by condensation of ketones and malononitrile [33]. Since some of the most desired precursors to prepare polymers are alkenes withdrawing nitrile, ester, or amide groups, these researchers have studied the catalytic behavior of basic zeolites for the condensation of ketones (i.e., cyclohexanone, benzophenone, or 4-aminoacetophenone) with malononitrile. CsX zeolite performs as a very active catalyst in these condensation reactions, and as occurred previously with the Knoevenagel reaction, the addition of the carbanion of the malononitrile to the carbonyl groups of the ketone is the controlling step and not the proton abstraction by the basic zeolite.

Davis et al. have also studied the ion-exchanged FAU zeolites as basic catalysts for the side-chain alkylation of toluene with methanol to form styrene and/or ethylbenzene [34, 35]. In this case, the CsX catalyst also showed the highest catalytic activity and selectivity toward styrene compared not only to the other metal-based FAU materials but also to other basic catalysts, such as Cs-doped alumina, which was not active for this reaction [35]. By “in situ” infrared spectroscopy, Palomares et al. concluded that Cs-exchanged FAU zeolite performs well for the side-chain alkylation of toluene with methanol because it presents the adequate basicity strength to dehydrogenate methanol into formaldehyde, stabilizes the sorbed toluene, and polarizes its methyl group [36].

Basic zeolites have been also described as active catalysts for biomass transformation processes [37–39]. Moreau et al. described the use of cation-exchanged zeolites, particularly NaX and KX zeolites, for the isomerization of glucose into fructose using water as solvent, obtaining glucose conversions (~30%) and fructose selectivities (~70–80%) comparable to commercial enzymatic catalysts. Interestingly, the use of inorganic catalysts would allow performing the catalyst reactions at higher temperatures and using higher glucose concentration. Unfortunately, these alkali-exchanged FAU zeolites suffer metal leaching to the aqueous reaction media. The use of basic zeolites as catalysts for transesterification reactions of triglycerides has also been studied by Leclerq et al. [38] and Climent et al. [39]. Although Cs-exchanged X zeolites are active for these transesterification reactions, their catalytic activity is remarkably lower than that of other basic catalysts, i.e., MgO, probably because of the diffusion limitations of the bulky reactants within the pores of the FAU zeolites.

2.2 Isolated Extra-framework Metal Cations: Redox Properties

Many transition metal ions have been introduced in the literature as extra-framework cations in several zeolites in order to generate new catalytic functionalities, taking advantage of the negative charges created by the presence of tetrahedral aluminum atoms [12]. The present paper is not intended to fully revise all the different cases but, instead, will focus on some relevant aspects dealing on the design and use of this type of transition metal-containing zeolites. A subdivision between non-noble and noble metals will be presented, highlighting some of the most significant achievements.

2.2.1 Zeolites Containing Non-noble Metal Cations

Copper-Zeolites

From the non-noble transition metal cations, copper is probably the most studied one in zeolite chemistry [13]. Traditionally, the copper Cu^{2+} cations are introduced by post-synthetic cation exchange within the corresponding zeolite pores using an aqueous solution of the copper salt. In an ideal cation exchange procedure using Cu^{2+} as metal source, the maximum cation exchange capacity would be Cu/Al ~0.5, suggesting that higher values would indicate a precipitation of Cu^{2+} species as copper oxide. To avoid this point, it is very important to control the pH of the exchange solution at values of ~6 [40]. As alternative methodologies, solid-state ion exchange or direct zeolite synthesis using organometallic complexes has also been described to prevent the undesired metal precipitation (Fig. 3) [27, 41, 42]. For

Fig. 3 (**a**) Solid-state ion exchange and (**b**) one-pot synthesis methods to obtain Cu-containing zeolites. Reprinted with permission from [41, 42], copyright 2015 American Chemical Society and The Royal Society of Chemistry, respectively

solid-state ion exchange, a dry powder composed of a mixture of the zeolite and the metal salt is heated at high temperature (~700–800°C), favoring the diffusion of metal cations within the zeolite pores [43, 44]. However, these high temperatures could produce some structural damage into the final metal-zeolite. Vennestrøm et al. have recently described a novel method to perform the copper solid-state ion exchange at lower temperatures (below 250°C) using NH_3 and/or NO as mobilizing metal agents, favoring the metal exchange along the zeolite crystals [41]. For the case of the one-pot synthesis method, different research groups have reported in the last years the use of organometallic complexes of copper with linear or cyclic polyamine molecules as organic ligands, resulting in the crystallization of different Cu-containing zeolites, such as Cu-SSZ-13 [27, 45], Cu-SAPO-34 [46–48], Cu-STA-7 [49], Cu-SAPO-18 [50], or Cu-SSZ-39 [51].

The coordination of the copper cations with the zeolitic framework will be influenced not only by the distribution of the negative framework charges that must balance the cation charges but also by its location in different crystallographic sites and large cavities that will favor their stabilization and confinement. Indeed, the coordination of the divalent transition metal ions and their geometry optimization will have direct implications in their mobility and/or their redox capabilities, affecting not only the catalytic activity but also catalyst deactivation. Many descriptions in the literature deal with the Cu^{2+} coordination chemistry on different zeolite frameworks, as it has been reviewed by Delabie et al. [52]. As an example, it can be

highlighted the study performed by Groothaert et al. for the Cu-MFI zeolite (Fig. 4) [53]. This study combines theoretical and some experimental characterization to evaluate the different optimized local Cu^{2+} coordination within the different α-, β-, and γ-cages present in MFI (Fig. 4a), where, in addition, each of these cages can even present different Al pair distributions, resulting in very broad metal stabilization possibilities (Fig. 4b). From these studies, it can be extracted that the rational and homogeneous construction of specific metal-zeolite sites is a very difficult and challenging task for designing more efficient active heterogeneous catalysts.

Different catalytic reactions have been described in the literature revealing the importance of the Cu coordination within zeolites [13]. Here, we will highlight two reactions that are currently being extensively studied: the selective catalytic reduction (SCR) of NOx and the direct conversion of methane to methanol [26, 54]. In the case of the SCR of NOx, the former description of Iwamoto et al. in the 1980s, using Cu-ZSM-5 as a very active catalyst for this particular reaction [55], has encouraged researchers to study the synthesis of very different Cu-containing zeolites and their evaluation as SCR catalysts [26, 56]. In spite of the excellent SCR catalytic activity shown by Cu-ZSM-5 zeolites, they suffer from permanent deactivation when aged under severe conditions, such as the presence of steam and high temperatures (above 700°C), conditions that have been well-established to evaluate the long-term stability of Cu-based zeolite catalysts under operative conditions in the automotive industry [57, 58]. In contrast, in the last years, the incorporation of Cu^{2+} species within the cavities of different small-pore zeolites, especially CHA, has allowed not only achieving very active but also extremely stable SCR catalysts when aged under harsh conditions (steam and 700°C) [57, 59–61]. Different authors have described that the particular confinement effect achieved within a restricted large cavity that is only accessible by small windows of 3.8 Å, combined with the exceptional coordination of the Cu^{2+} species with three oxygen atoms of the 6-rings present in most of the large cavities of the small-pore zeolites (Fig. 5), allows increasing their hydrothermal stability compared to other Cu-based zeolites presenting larger pores [58, 62].

Although Cu^{2+} species are initially present in the Cu-CHA catalysts, the formation of Cu^{2+}/Cu^{+} redox pairs during the reaction mechanism for the SCR of NOx with ammonia is well-established (Fig. 6) [63]. The full reaction mechanism is still under debate, but one proposal is that the standard SCR mechanism requires the formation of a nitrosoamide-like complex in the reducing half-cycle, whereas an ammonium nitrite-like complex is required in the oxidizing half-cycle (Fig. 6). However, up to now, the SCR reaction mechanism studies were based on the fact that fully isolated cationic copper species were the catalytic active sites (Fig. 6). Nevertheless, very recently, Gounder et al. have demonstrated for the first time that, under reaction conditions, mobilized Cu ions can travel through the small-pore windows, forming transient ion pairs, which are required within the low-temperature SCR mechanism for the oxidation of Cu^{+} to Cu^{2+} in the presence of O_2 [64]. The control of the metal site mobility could open new opportunities in catalyst design for relevant chemical processes.

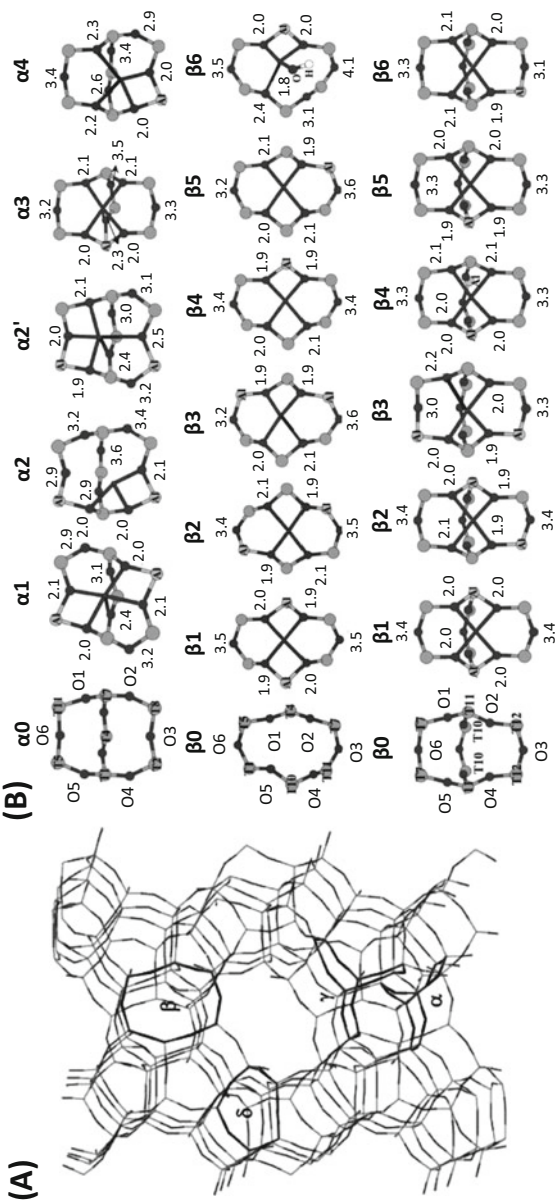

Fig. 4 (**a**) MFI structure presenting the α-, β-, and γ-cages and (**b**) optimized Cu^{2+} coordination within the α-, β-, and γ-cages with different Al distributions. Reproduced from [53] with permission of The Royal Society of Chemistry

Fig. 5 Refined local structure of Cu^{2+} species (black sphere) in CHA zeolite. Reproduced from [58] with permission of The Royal Society of Chemistry

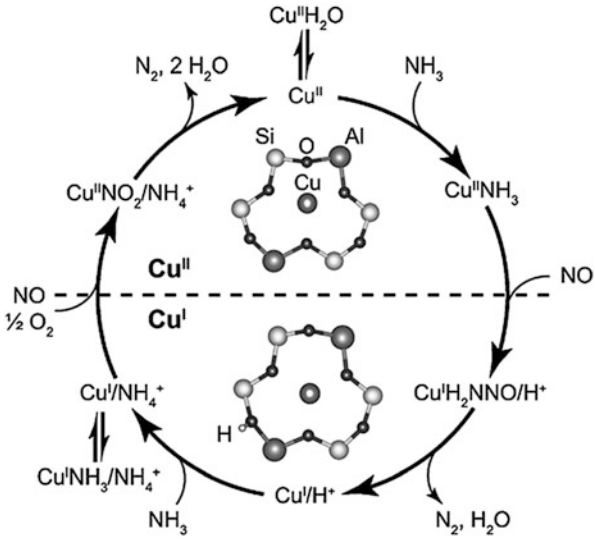

Fig. 6 Proposed SCR cycle of NO over Cu-SSZ-13 catalyst. Reproduced from [63] with permission of Wiley

The direct partial oxidation of methane to methanol is a very challenging reaction, since methane is an abundant feedstock, and its direct transformation into methanol would permit its potential use as simple and less costly energy carrier [65, 66]. From the different catalysts described in the literature, several Cu-containing zeolites have been described as some of the most promising catalysts, even though the achieved CH_4 conversions are, in general, very low when O_2 is used as an oxidant (below 3%), and a three-step reaction procedure is required (Fig. 7a) [54]. Different metal species have been proposed in the literature, including single metal, dicopper, or trinuclear oxo-copper species, as the potential active sites able to undergo the selective oxidation of methane to methanol (Fig. 7b) [67–70]. These results reveal again the high complexity to determine the real metal active sites under reaction conditions, as described previously for the SCR of NOx using also Cu-containing zeolites as catalysts.

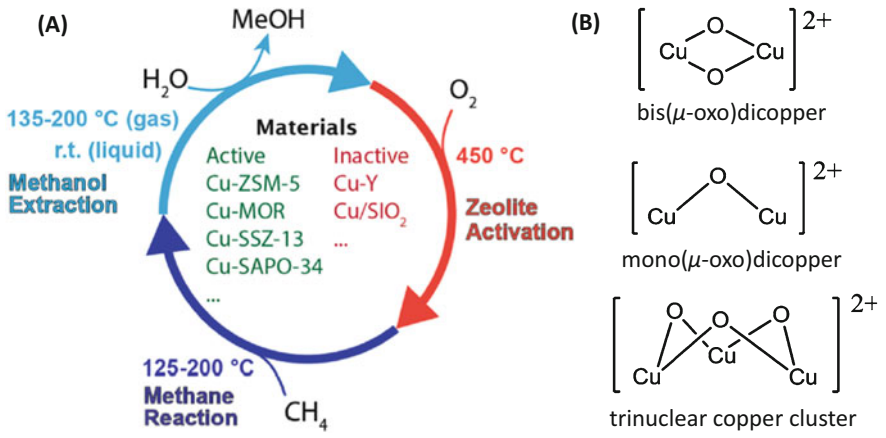

Fig. 7 (**a**) Proposed three-step conversion and (**b**) proposed active sites for the selective oxidation of methane to methanol using different Cu-zeolites. Reprinted with permission from [54]. Copyright 2017 American Chemical Society

Iron-Zeolites

Iron-containing zeolites are another class of relevant metal-containing heterogeneous catalysts. Traditionally, iron metal sites are preferentially introduced within high-silica zeolites by post-synthetic cation aqueous exchange using iron salts [i.e., iron(III) nitrate] [71–73], but there are also other preparation methodologies to introduce the iron species within the zeolite crystals, including chemical vapor deposition (CVD) or direct hydrothermal syntheses [74–76]. The most studied Fe-zeolites are, in general, iron-exchanged medium- and large-pore zeolites (i.e., Fe-ZSM-5, Fe-Beta, or Fe-USY), and the identification of the nature of the different extra-framework iron species has been preferentially characterized by UV-Vis, Mossbauer, and magnetization measurements [71, 72, 75, 77]. These characterization techniques mostly reveal that the Fe-exchanged medium- and large-pore zeolites present mixtures of isolated cationic Fe^{3+} species in extra-framework positions combined with dimeric iron species [71, 72, 78]. In fact, Pidko et al. have demonstrated by theoretical calculations that the extra-framework oxygenated iron cations tend to self-organize into binuclear structures in high-silica open zeolites [78]. However, when these medium- and large-pore Fe-containing zeolites are aged in the presence of steam, there is a large migration of the active iron ions from the exchange sites, resulting in the formation of large Fe_xO_y oligomers, mainly associated with the dealumination of the zeolite frameworks [77].

Very recently, Gao et al. [73, 79] and Martin et al. [76, 80] have also shown the preferential presence of extra-framework Fe(III) species, including $[Fe(OH)_2]^+$ (monomeric) and $[HO\text{-}Fe\text{-}O\text{-}Fe\text{-}OH]^{2+}$ (dimeric) (Fig. 8), within the small-pore CHA and AEI zeolites. Interestingly, these iron-containing small-pore zeolites present a much higher stability against aging treatments compared to Fe-containing large- and

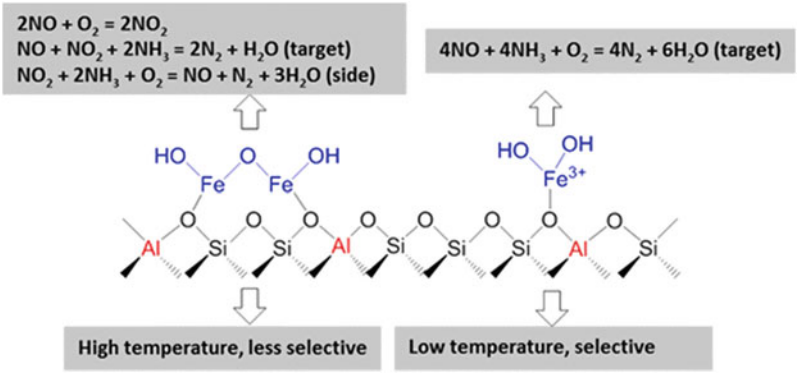

Fig. 8 Iron(III) species present within iron-containing small-pore CHA zeolites and their corresponding catalytic properties for the different SCR of NOx reactions. Reprinted with permission from [73]. Copyright 2016 American Chemical Society

medium-pore zeolites, a fact that could be attributed to the remarkably higher confinement of these extra-framework species within the large cavities of the CHA and AEI structures. Peden et al. have shown that the Si/Al molar ratio or the iron content within the CHA zeolite undoubtedly influences the percentage of the different extra-framework Fe species [73].

The synthesis methodology employed to prepare the iron-containing zeolites can also affect the iron coordination in the final zeolitic material. In fact, the direct synthesis of the iron-containing aluminosilicate zeolites has not been vastly explored in the literature, but the introduction of the iron species in the synthesis gels mainly results in the crystallization of Fe-zeolites where the iron species are preferentially placed in tetrahedral coordination in framework positions [75, 76, 81]. This point can be easily characterized by UV-Vis spectroscopy, since the iron species in tetrahedral coordination show very clear bands centered at 215 and 240 nm, as it can be seen for the as-prepared Fe-ZSM-5 and Fe-Beta materials (Fig. 9a, c, respectively). After calcining in air at 580°C, the resultant calcined Fe-aluminosilicate materials show the preferential extraction of most of the initial tetrahedrally coordinated iron species to isolated extra-framework positions, as demonstrated by the appearance of the signal centered at 275 nm in the UV-Vis spectra (Fig. 9b, d) [75, 76]. However, the Fe-containing Al-free Beta zeolite maintains most of the iron atoms in tetrahedral coordination in the zeolitic framework (see bands at 215 and 240 nm for the sample synthesized with a Si/Al=∞ in Fig. 9d). This result clearly indicates that the extra-framework iron species require the presence of framework Al atoms to be efficiently dislodged from lattice positions.

Iron-containing zeolites have been intensively studied as catalysts in the SCR reaction of NOx [26, 76, 77, 79, 82–84]. One of the most important features of the Fe-based zeolite SCR catalysts is that they perform better than Cu-based zeolite catalysts when high reaction temperatures are tested, particularly above 450°C (Fig. 10). This catalytic behavior is of interest for treating exhaust gases generated in stationary sources, such as power plants or gas turbines. However, the undesired

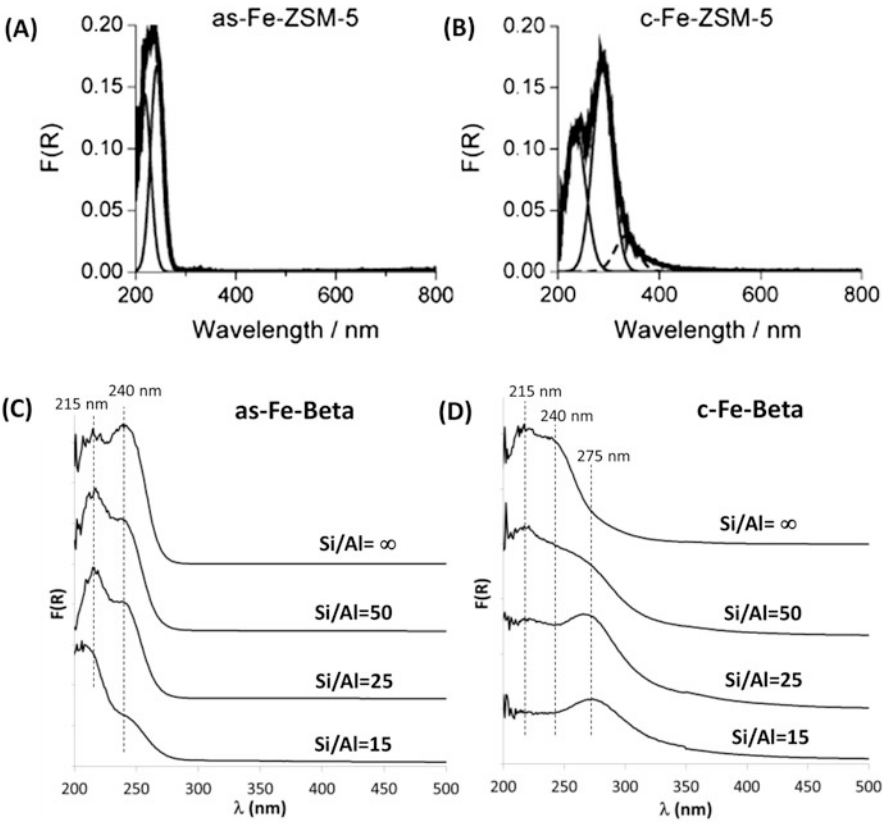

Fig. 9 UV-Vis spectra of the as-prepared Fe-Al-ZSM-5 (**a**), calcined Fe-Al-ZSM-5 (**b**), as-prepared Fe-Beta zeolites with different Si/Al molar ratios (**c**), and calcined Fe-Beta zeolites with different Si/Al molar ratios. Reprinted from [75, 76], with permission from Elsevier and Wiley, respectively

iron oligomerization observed for the initial well-dispersed cationic iron species after different aging treatments, particularly in the presence of steam, has mostly precluded the industrial application of Fe-containing medium- and large-pore zeolites, i.e., Fe-ZSM-5 or Fe-Beta. Nevertheless, Peden et al. have recently described that Fe-exchanged CHA zeolites not only show excellent catalytic activities for the SCR of NOx reaction, but also these catalysts present an outstanding hydrothermal stability after being aged with steam at temperatures above 600°C [73, 79]. These authors have also unraveled that the isolated Fe^{3+} species are the active sites for the low-temperature standard SCR, whereas the dimeric species are the active sites at higher temperatures (Fig. 8) [73]. Corma et al. have also described the excellent catalytic activity and hydrothermal stability of different Fe-containing small-pore zeolites, as Fe-CHA and Fe-SSZ-39, for the SCR of NOx [76, 80]. These authors have shown that the one-pot synthesis of these catalysts allows increasing their catalytic performance, probably by inducing a better metal dispersion within the zeolite crystals.

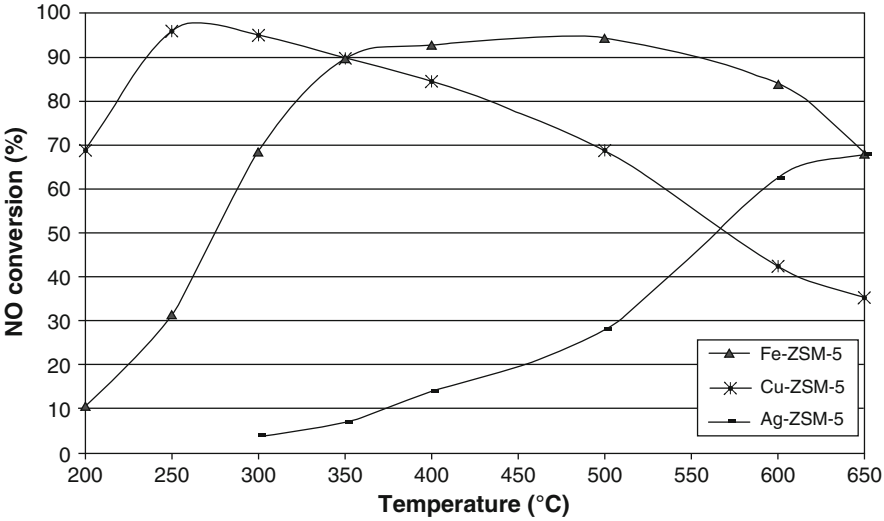

Fig. 10 SCR activity of Cu-, Fe-, and Ag-ZSM-5 zeolites. Reproduced from [26], with permission from Taylor & Francis

Iron-containing zeolites, in particular Fe-based ZSM-5, have also been employed as heterogeneous catalysts to carry out the oxidative dehydrogenation (ODH) of propane assisted by N_2O to obtain propylene [74, 85–87]. In general, different active sites have been proposed for the N_2O-mediated oxidative dehydrogenation of propane, including the presence of extra-framework Fe-oxo complexes [88], oligonuclear iron species [86], or well-isolated iron species [74]. Optimized Fe-ZSM-5 materials with well-defined extra-framework species, which have been prepared via organometallic chemistry grafting of ferrocene, are able to achieve propylene yields of ~30% for the ODH of propene assisted with N_2O (Fig. 11) [85].

Nickel-Zeolites

Traditionally, nickel(II) species can be readily introduced into the desired aluminosilicate structure by simple ion exchange procedures using nickel salt solutions [89]. Interestingly, the intermediate paramagnetic nickel(I) can also be stabilized in extra-framework positions by properly controlling the thermal treatment and the reaction atmosphere, but metallic nickel species can appear depending on the reduction conditions [90]. In addition to classical post-synthetic treatments, Garcia et al. [91–93] and Cui et al. [94] have described one-pot synthesis methods using simple Ni complexes (i.e., Ni^{2+}-diethylenetriamine) for the direct synthesis of Ni-containing small-pore zeolites. These one-pot syntheses would permit better metal dispersions along the zeolite crystals, particularly for small-pore zeolites, and maybe different aluminum distribution in lattice positions, which can offer better stabilization to the extra-framework metals.

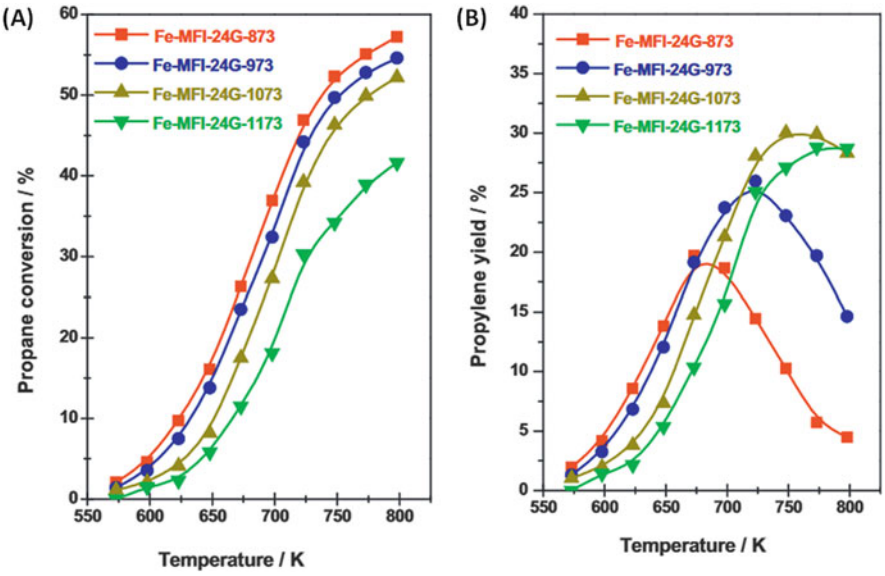

Fig. 11 Propane conversion (**a**) and propylene yield (**b**) for the N_2O-mediated oxidative dehydrogenation of propane using different treated Fe-MFI zeolites as catalysts. Reprinted from [85]. Copyright 2013, with permission from Elsevier

From the very diverse catalytic applications where Ni-containing zeolites have been applied, we would like to highlight the oligomerization of light olefins into distillate-range products [95–97]. This reaction is important because it can be combined with the oxidative coupling of methane to ethylene, resulting in a very interesting gas-to-liquid route for the valorization of unconventional natural gas reserves (i.e., shale gas) [98]. Moreover, the nature of the cationic nickel sites that are active for this reaction is still under debate [96, 97]. It seems well-assumed that isolated nickel cations in exchangeable positions are the preferred active sites for the Ni-catalyzed oligomerization regardless of the acid support, whereas bulk NiO particles are inactive [95, 97]. However, there is more controversy regarding the oxidation state of the active site. Many authors have suggested that monovalent Ni^+ is the active site based on the results observed by in situ FTIR spectroscopy of adsorbed CO and EPR measurements [99–102]. But more recently, other authors have suggested that Ni^{2+} would also be important active sites for the olefin oligomerization reaction. On the one hand, Lallemand et al. proposed both Ni^+ and dehydrated Ni^{2+} ions as cooperative active sites based on FTIR spectroscopy of adsorbed CO [103]. On the other hand, Martinez et al. have proposed that Ni^{2+} are the real active sites, since the formation of Ni^+ would occur by reduction of the Ni^{2+} species with CO during the FTIR-CO characterization, concluding that the Ni^+ species are mere spectators in the olefin oligomerization reaction [104].

2.2.2 Zeolites Containing Noble Metal Cations

Noble metals supported on zeolites are often heterogeneous catalysts in industrial processes, for instance, refinery catalysts, since they do not only allow activating C-H, H-H, and C=C bonds, but also they mainly prevent the catalyst deactivation by coke using hydrogen to maintain the catalyst surface clean of heavy hydrocarbons [105]. These metal species are mostly aggregated in the form of large particles, and their catalytic properties are determined by their exposed faces, including corner and edge sites and metal-support interfaces [106]. However, if these metals were atomically dispersed along the zeolite crystals, they would be present as cationic species, and consequently, their catalytic properties could be substantially different [107]. These precious metal single-site catalysts are receiving significant attention in the last years, and some of the recent descriptions comprise either organometallic complexes or "ligand-free" single atoms [106]. In the present review, we will focus on the recent reports dealing on the stabilization of "ligand-free" precious metal single atoms, referring the reader to specific reviews for additional information [106–108].

Most of the zeolite-supporting noble metals as single atoms described in the literature have been prepared by post-synthetic cation exchange procedures, where the corresponding metal salt has been exchanged in a medium- or large-pore zeolite, preferentially ZSM-5, Beta, or USY [109–112]. In order to obtain good metal dispersion and single-site metal stability, the metal content and the Si/Al molar ratio of the zeolite support are two of the most important parameters. In general, low metal contents, mostly below 0.2%wt, and intermediate Si/Al molar ratios (~10–15) are the preferred chemical compositions. Among the different precious metals, Pd, Pt, and Au are some of the most important ones, since their adequate dispersion as single atoms would offer excellent catalytic properties in very diverse catalytic applications.

The use of late transition metals as homogeneous catalytic systems is broadly described in the literature for many organic syntheses. For instance, different metal chlorides (i.e., $PtCl_2$, $PdCl_2$, or $AuCl_3$) perform as very active homogeneous catalysts for different hydroaddition reactions to alkenes and alkynes. Taking this into account, Corma et al. have recently designed atomically dispersed Pt(II) catalyst using a USY zeolite as support, obtaining an efficient heterogeneous catalyst for a variety of hydroaddition reactions to alkynes and alkenes (Fig. 12) [110].

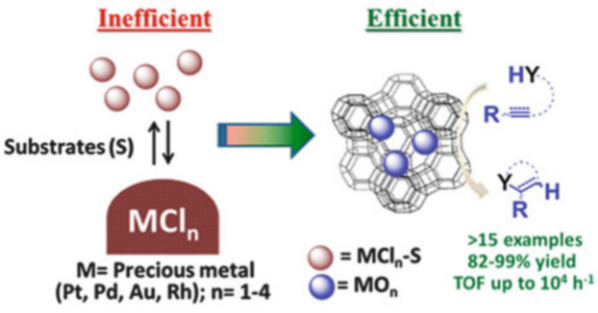

Fig. 12 Atomically dispersed late transition metals within FAU zeolites for their use as efficient heterogeneous catalysts for different hydroaddition reactions of alkynes and alkenes. Reprinted with permission from [110]. Copyright 2015 American Chemical Society

Interestingly, this ligand-free Pt(II)-containing solid catalyst is, at least, two orders of magnitude more active than previously described homogeneous noble metal-based catalysts and can be reused more than ten times without loss of activity. Those are very important advances in the design of noble metal catalysts for organic synthesis approaches considering the high price of precious metals.

The recent description of Pd-containing ZSM-5 zeolite as heterogeneous catalyst for the low-temperature direct transformation of methane to methanol is another example revealing the importance of stabilizing single-site late transition metals [113]. Tao et al. have shown that the presence of Pd_1O_4 single sites anchored to ZSM-5 crystals exhibits higher intrinsic catalytic activity for methane transformation, as demonstrated by the similar catalytic activities observed when comparing Pd-ZSM-5 materials with different Pd contents (0.01% front 2%wt Pd, Fig. 13) [113]. This fact demonstrates that the presence of large PdO particles within the Pd-ZSM-5 zeolite with high Pd loadings does not play any role in the methane activation. Interestingly, the combination of Pd_1O_4 single sites with CuO allows methanol selectivities above 90% at 90°C [113].

Other recent examples highlighting the benefits of single-site transition metals involve the transformation of CO to CO_2 through direct oxidation with air or via "water-gas shift" [109, 111, 112]. Gates et al. have demonstrated the presence of site-isolated platinum LTL-based catalyst with well-defined locations of the Pt atoms (HRTEM images in Fig. 14) [111]. This atomically dispersed metal catalyst shows

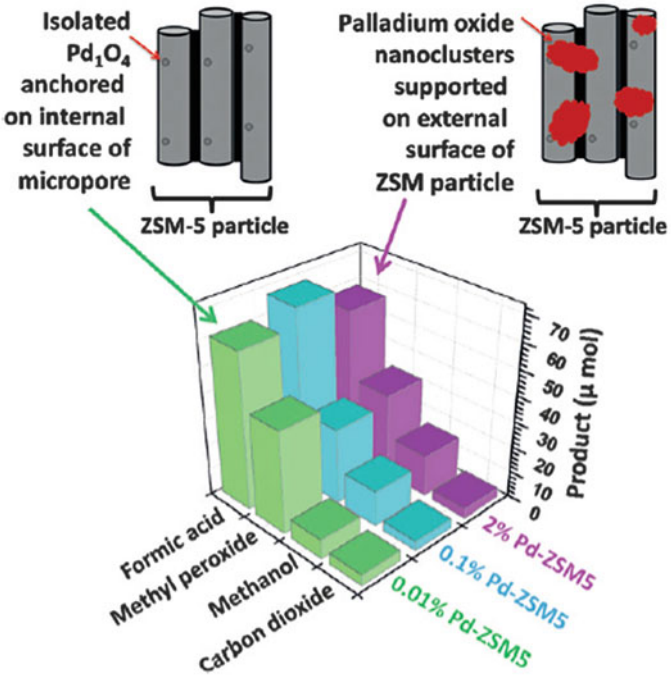

Fig. 13 Product yields for the low-temperature methane oxidation using different Pd-ZSM-5 as catalysts (0.01, 0.1, and 2% of Pd). Reprinted from [113], with permission from Wiley

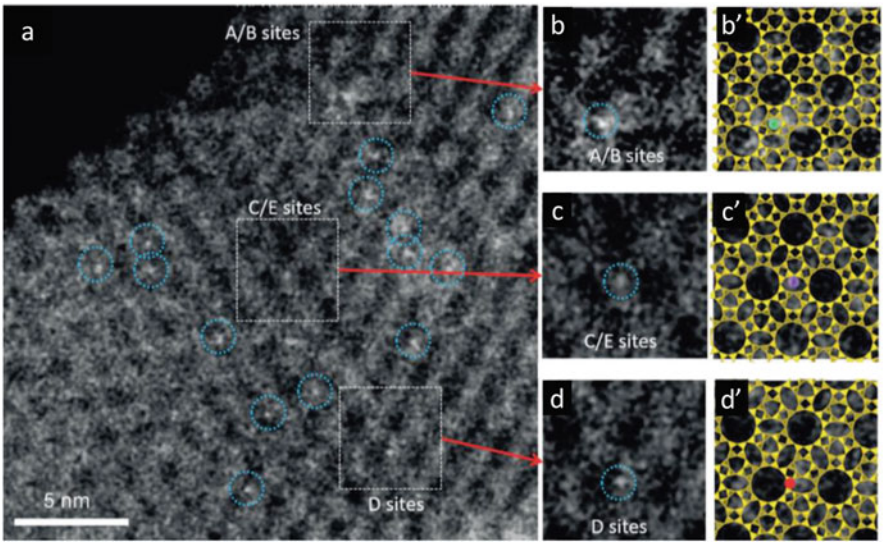

Fig. 14 HRTEM images showing the presence of single-site metal atoms in different crystallographic positions of the LTL zeolite. Reprinted from [111], with permission from Wiley

the highest turnover frequency (TOF) for the CO oxidation reaction at 50°C compared to other metal-based catalysts reported in the literature [111]. In a similar way, Flytzani-Stephanopoulos et al. have described the presence of single-site M-O(OH)x, where M can be Pt or Au, stabilized by sodium cations within the LTL zeolite as very active catalysts for the CO oxidation via "water-gas shift" reaction [109, 112]. The authors propose that the high stability of the single metal atoms is achieved, thanks to the particular binding to sodium ions through −O ligands [109].

One of the main problems of the above described single-site late transition metals is their stability under real reaction conditions, since they used to suffer from metal aggregation when, for instance, high temperatures are required. Recently, we have described a reversible metal transformation from single metal sites to small metal nanoparticles within the cavities of the small-pore high-silica CHA zeolite, depending if the reaction atmosphere is oxidative or reductive, respectively (Fig. 15) [17]. We have shown that the Pt species within the designed Pt-containing CHA zeolite remain as single atoms even after being treated at high reaction temperatures (above 650°C) in the presence of air. These preliminary results open new attractive opportunities to design highly stable single-site catalysts and evaluate the catalytic benefits of the single-site active sites from metal clusters or nanoparticles.

2.3 *Entrapped Clusters or Nanoparticles Within Zeolite Frameworks*

Zeolites could be excellent supports for the encapsulation of small metal clusters or nanoparticles due to their well-defined framework structures, containing pores and

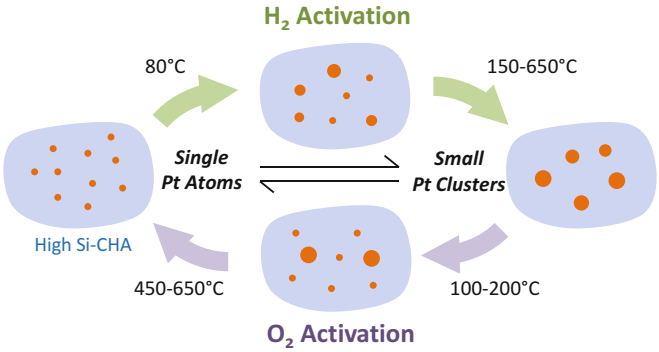

Fig. 15 Reversible metal transformation from single metal sites to small metal nanoparticles within the cavities of the high-silica CHA zeolite. Reprinted with permission from [17]. Copyright 2016 American Chemical Society

cavities in the range of 0.3–2 nm. The crystalline nature of zeolites could mostly preclude the metal agglomeration under reaction conditions or during catalyst regeneration, allowing the increase not only of the catalyst activity but also the catalyst lifetime. In general, the metal nanoparticles are created within the zeolite pores following diverse post-synthetic treatments, where previously the metal species are introduced by cation exchange or wetness impregnation, followed by thermal treatments under reductive atmospheres [114–116]. Unfortunately, these procedures result in poor metal dispersions and heterogeneous nanoparticle sizes, both facts clearly affecting the catalytic activity of these metal-based zeolites [117].

2.3.1 Entrapped Metal Clusters or Nanoparticles Within Medium-Pore Zeolites

In the last years, different one-pot synthesis procedures have been reported in order to improve the confinement of the metal nanoparticles within different medium-pore zeolite pores. On the one hand, Yu et al. have described the direct synthesis of the Pd-containing medium-pore MFI zeolite with well-dispersed ultrasmall rodlike-shaped Pd nanoparticles of ~1.5 nm, which are located in the channel intersection of the MFI structure [18]. For this purpose, the authors have developed a very simple one-pot hydrothermal synthesis using an in situ formed organometallic complex, i.e., $[Pd(NH_2CH_2CH_2NH_2)_2]^{2+}$, as Pd precursor (Fig. 16a). The excellent metal encapsulation within the MFI matrix has been demonstrated by high-resolution scanning transmission electron microscopy (HR-STEM) studies. Interestingly, this Pd-containing MFI catalyst performs as an efficient catalyst for H_2 generation through formic acid decomposition under mild conditions, with excellent recyclability and high thermal stability [18]. It is noticeable that the same authors have recently reported the design of subnanometric bimetallic nanoparticles of

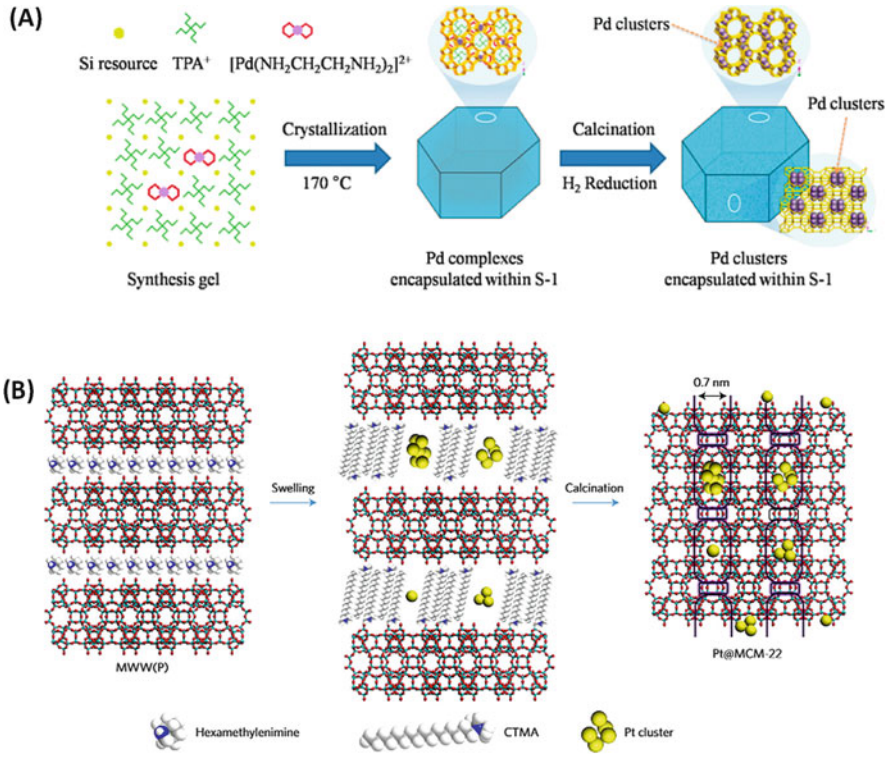

Fig. 16 Synthesis procedures for the Pd-containing MFI zeolite (**a**) and Pt-containing MWW (**b**). Reprinted with permission from [15, 18], copyright 2016 American Chemical Society and Nature Publishing Group, respectively

Pd-$M(OH)_2$ (M=Ni, Co) using similar direct synthesis methods, performing as superior catalysts for the dehydrogenation of formic acid [118].

On the other hand, Corma et al. have developed a different direct synthesis methodology for the encapsulation of Pt clusters and small Pt nanoparticles within the medium-pore MWW zeolite (Fig. 16b) [15]. In this work, the authors have previously generated Pt clusters, which are then introduced in the synthesis media during the swelling process together with the surfactant molecules, being all of them located in the interlayer region (Fig. 16b). Finally, the organic moieties are removed by calcination in air at 540°C, leading to the metal encapsulation within the MWW supercages of the tridimensional MWW zeolite (Fig. 16b). This Pt-containing MWW zeolite shows high thermal stability against different severe redox treatments and performs as an excellent catalyst for the dehydrogenation of propane to propylene [15].

2.3.2 Entrapped Metal Clusters or Nanoparticles Within Small-Pore Zeolites

The post-synthetic cation exchange within small-pore zeolites can be diffusion-limited when the ionic radii of the metal species are relatively large. To prevent this limitation, Iglesia et al. first described a direct synthesis methodology using thiol-based organometallic complexes in the presence of sodium to encapsulate a series of small metal nanoparticles within Al-rich LTA zeolites [16]. Following this strategy, the authors were able to properly encapsulate not only 1–2 nm monometallic nanoparticles of Pt, Pd, or Rh [16] but also entrapped alloys of AuPd, AuPt, and PdPt nanoparticles [119]. Interestingly, the chemical composition of the bimetallic structures is uniform, as it has been determined by X-ray absorption spectroscopy. These materials show excellent catalytic activity for the ethanol oxidative dehydrogenation, even when bulky poisons are present in the reaction media, i.e., dibenzothiophene, highlighting the unique shape selectivity and protecting roles of entrapping metal nanoparticles within small-pore zeolites.

In spite of the excellent performance of the encapsulated metals within Al-rich small-pore zeolites proposed by Iglesia et al., their very low Si/Al molar ratios (below 3) induce limited hydrothermal stability when treated at high temperatures and/or in the presence of steam. In order to overcome these problems, Corma et al. have recently described the combined use of thiol-based organometallic complexes of Pt together with specific OSDA molecules to direct the crystallization of the Pt-containing high-silica CHA zeolite [17]. The as-prepared Pt-CHA zeolite contains remarkably higher Si/Al molar ratios than those achieved previously by Iglesia et al. (Si/Al above 9), resulting in highly stable materials even when treated at high temperatures and/or in the presence of steam [17]. The thermal treatment of the initially calcined material in the presence of H_2 allows the formation of controlled Pt nanoparticles with average sizes of 1–1.5 nm, which are exclusively confined within the cavities present in the CHA crystals (Fig. 15). The exclusive shape selectivity properties of the Pt-containing high-silica CHA zeolite have been proved for the hydrogenation of light olefins, where Pt-CHA is able to selectively hydrogenate ethylene but not propylene in a mixture of the two gases, owing to differences in pore diffusion.

3 Isolated Metals in the Zeolitic Lattice as Exceptional Lewis Acid Active Sites

The introduction of metallic heteroatoms other than aluminum in tetrahedral coordination in the crystalline frameworks of zeolites permits inducing different physicochemical properties to the zeolite-based materials, clearly influencing their catalytic properties and opening new opportunities for their catalytic implementation in novel chemical processes. Among different heteroatoms, titanium is undoubtedly

one of the most interesting tetrahedrally substituted metals, as it can be asserted by the extremely high number of titanosilicates and their catalytic applications reported in the literature [21, 120, 121]. The introduction of isolated Ti(IV) in tetrahedral coordination provides an unprecedented Lewis acidity to zeolite-based titanosilicates, allowing their implementation as very active and selective catalyst for oxidizing many hydrocarbons with H_2O_2 or organic peroxides [122–124]. The excellent results obtained by the isomorphic substitution of Ti in the crystalline silicate zeolites paved the way to attempt the incorporation of other transition metals in framework positions, including Sn, Zr, Nb, Ta, or Hf, among others [125–128]. In particular, Sn- and Zr-containing zeolites have received a significant attention in the last years, since these materials have been broadly applied as efficient heterogeneous catalysts in many fine chemistry and biomass-derived processes [129–132].

3.1 Titanium-Containing Zeolites

The very first description dealing on titanosilicates was the synthesis of the TS-1 zeolite reported by researchers at EniChem [20]. This material has the framework structure MFI (presenting a bidirectional medium-pore system), and interestingly, it can be prepared under very broad synthesis conditions, permitting the control of its physicochemical properties, i.e., titanium content, crystal size, and hydrophobicity character, among others [123]. This large versatility in its preparation has allowed its implementation as oxidant catalyst in diverse processes (Fig. 17a), as hydroxylation of aromatic compounds [133–135], epoxidation of alkenes [136, 137], oxygenation of alkanes and alcohols [138, 139], and ammoximation of ketones [140, 141]. The isolated tetrahedrally coordinated Ti active sites can activate the H_2O_2 molecules, with the corresponding formation of Ti-OOH species, which are then able to catalyze the selective oxidation reactions enumerated above (Fig. 17b) [122, 142].

However, TS-1 has limited pore openings (~5.5 Å), mostly precluding the applicability of this titanosilicate when bulky molecules are present in the chemical process. Taking that in mind, Corma et al. first described the direct synthesis of Ti-containing large-pore Beta zeolite [143, 144]. This Ti-Beta material, initially also containing Al species, was more active than TS-1 for the selective epoxidation of bulky olefins, as cyclohexene or cyclododecene [144]. Although the increase of the catalytic activity was observed when using Ti-Beta for the epoxidation of cyclic olefins, the Brønsted acidity associated with the presence of Al species in tetrahedral coordination favors the opening of the epoxide rings of the desired products, lowering the overall selectivity by producing undesired glycol-derived by-products. To overcome this problem, Corma et al. proposed two different synthesis routes to attempt the Al-free synthesis of Ti-Beta [124, 145, 146]. On the one hand, the authors were able to obtain the Al-free Ti-Beta in alkaline conditions by introducing a small amount of Al-free seeds of nanocrystalline Beta in the synthesis media [145]. These resultant Al-free Ti-Beta zeolites were also more active than TS-1 for the

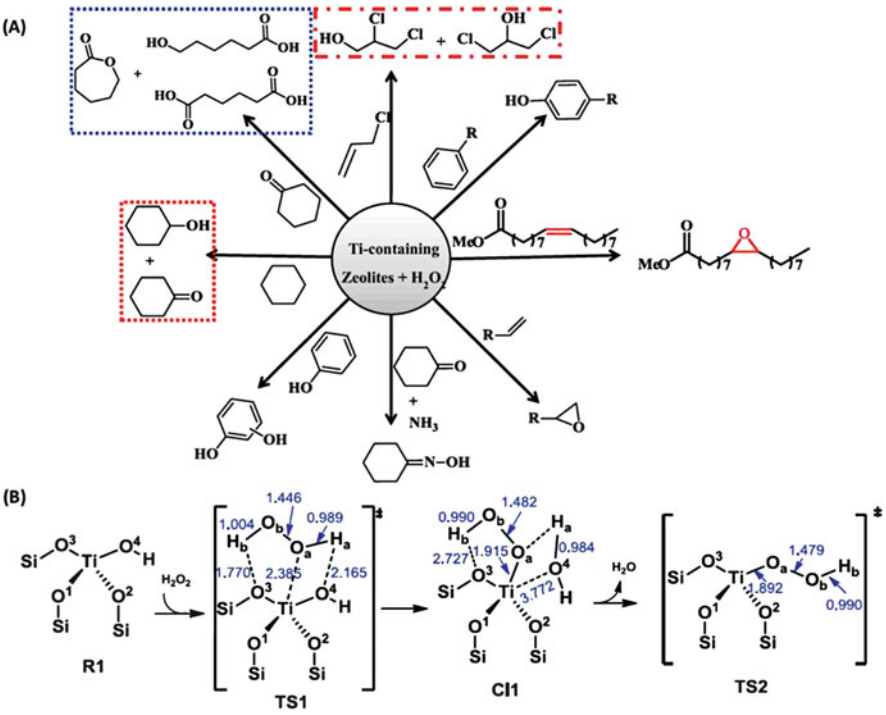

Fig. 17 (**a**) Different organic oxidation reactions catalyzed by Ti-containing zeolites and (**b**) activation of H_2O_2 by tetrahedrally coordinated Ti species in zeolite frameworks. Reproduced from [142], with permission from Intech

selective oxidation of bulky hydrocarbons, but the undesired formation of by-products was still observed (i.e., glycol products during the selective epoxidation reactions of olefins) [145]. The authors suggested that the internal silanol groups created by performing the synthesis in OH media were the responsible functional groups for the undesired reactions, such as the opening of the epoxide rings. To avoid that, Corma et al. performed the direct synthesis of the Al-free Ti-Beta in fluoride media [124, 146]. Following this synthesis route, the resultant Al-free Ti-Beta zeolite does not contain internal defects, creating very hydrophobic zeolite crystals and considerably increasing the overall selectivities toward the desired products [124, 147]. A representative example of the catalytic benefits of using the hydrophobic Ti-Beta zeolite is the selective oxidation of unsaturated fatty oils, i.e., methyl oleate, where the hydrophobic Ti-Beta gives higher conversion (X) and epoxide selectivity (S) than hydrophilic Ti-Beta (X = 81% and S = 95% and X = 28% and S = 80%, respectively) [147].

In addition to Ti-Beta, other Ti-containing large-pore silicates, with pore topologies ranging from one-dimensional to three-dimensional pore systems, have been described in the last 15 years, such as Ti-ZSM-12 [148], Ti-ITQ-7 [149], Ti-ITQ-17

[150], or Ti-YNU-1 [151], among others. From these examples, the rationalized preparation of the Ti-ITQ-17 and Ti-YNU-1, combined with their excellent catalytic activity for the selective epoxidation of bulky olefins, deserves to be highlighted. The ITQ-17 zeolite corresponds to the polymorph C of Beta zeolite, which presents a three-dimensional large-pore system with straight channels, resulting in a very open pore topology that would allow better diffusion pathways to bulky molecules compared to conventional Beta zeolite (note that conventional Beta zeolite is an intergrowth of two different polymorphs, A and B, presenting at least one zigzag pore). The Ti-ITQ-17 has been achieved, thanks to an "ab initio" study by molecular modeling of the most adequate OSDA molecules for directing the crystallization of the polymorph C of Beta zeolite (ITQ-17), observing extraordinary directing roles when using the SDA9 organic molecule toward the target ITQ-17 zeolite (Fig. 18a) [150]. Interestingly, the Ti-ITQ-17 shows remarkably higher activities and selectivities to epoxide compared to Ti-Beta zeolite when bulky cycloolefins are oxidized with H_2O_2 (Fig. 18b). The Ti-YNU-1 zeolite is another interesting material since it has been obtained by pillaring the lamellar MWW precursor by acid treatments, resulting in a new zeolitic structure containing large pores (Fig. 19a) [152]. The expanded MWW-type material shows enhanced catalytic activity for the oxidation of different cycloalkenes, compared to TS-1, Ti-MWW, or Ti-Beta (Fig. 19b) [151].

3.2 Tin-Containing Zeolites

As described above, the Ti-containing zeolites are able to increase the nucleophilicity of H_2O_2, but the resultant Ti-OOH species can react with very different functional groups. This could be a limitation if one would like to perform chemoselective oxidations. The Baeyer-Villiger (BV) oxidation of ketones to form the corresponding lactones, when other functional groups are present, can be a perfect example highlighting this fact. In order to overcome this challenging issue, Corma et al. proposed the synthesis of the Al-free hydrophobic Sn-Beta zeolite as the adequate candidate to undergo the proposed BV chemoselective reactions [125]. The authors hypothesized that isolated tin atoms in tetrahedral coordination would present higher electronegativity, and consequently, their Lewis acidity would be higher than that observed for tetrahedrally coordinated isolated Ti species. If this is so, it could be expected a remarkably higher affinity of isolated Sn sites for activating some polarized functional groups, such as the carbonyl dipole (C=O). To prove this hypothesis, Corma et al. studied the oxidation of dihydrocarvone (Fig. 20), a molecule containing a carbonyl group together with a double bond, both being susceptible to react with the oxidizing agent (i.e., H_2O_2). From the different tested catalysts, Sn-Beta is the only material that was able to selectively oxidize the carbonyl group toward the desired lactone without oxidizing the double bond (Fig. 20) [125]. This unique selectivity observed for the BV reaction has been extended by the authors to other interesting organic reactions involving the

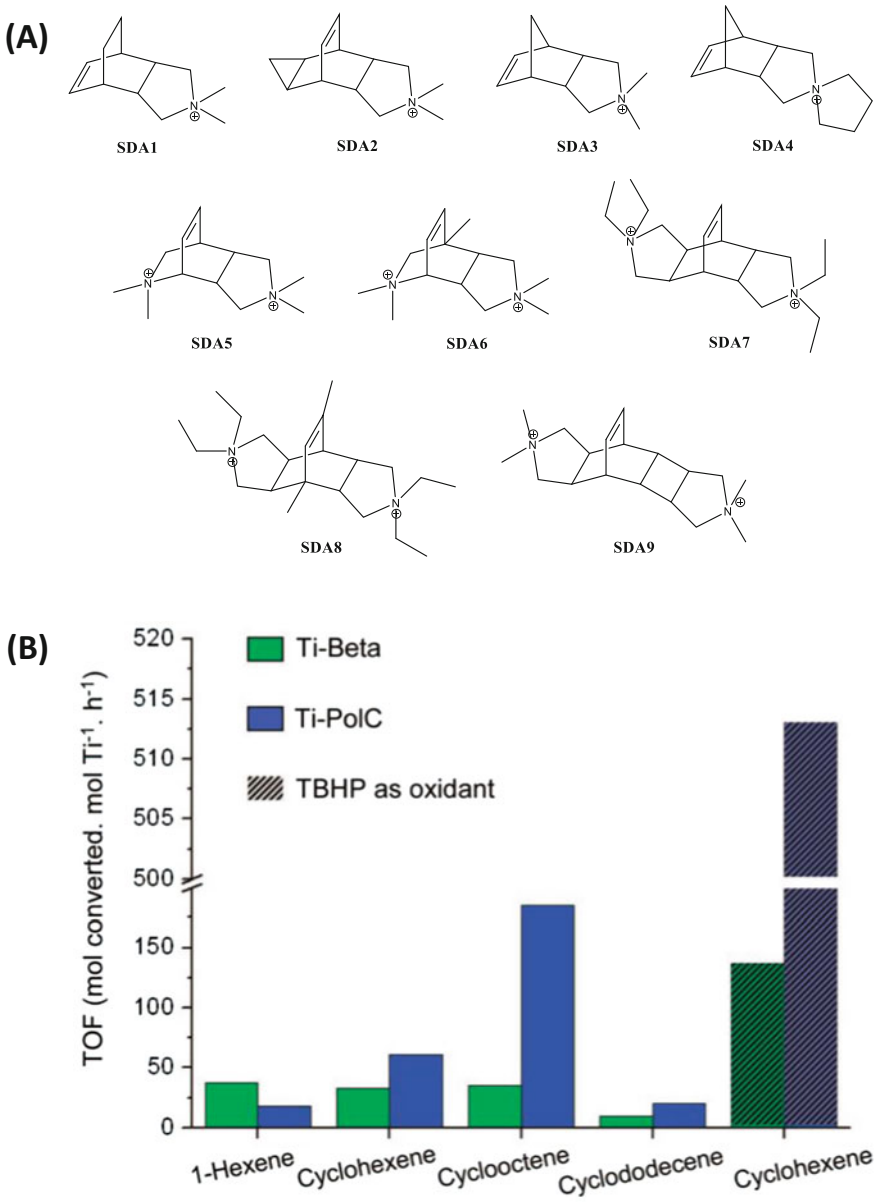

Fig. 18 (**a**) Different OSDA molecules proposed for the synthesis of the Ti-ITQ-17 catalyst and (**b**) intrinsic activity of Ti-Beta and Ti-ITQ-17 for the epoxidation of different olefins. Reprinted with permission from [150]. Copyright 2008 American Chemical Society

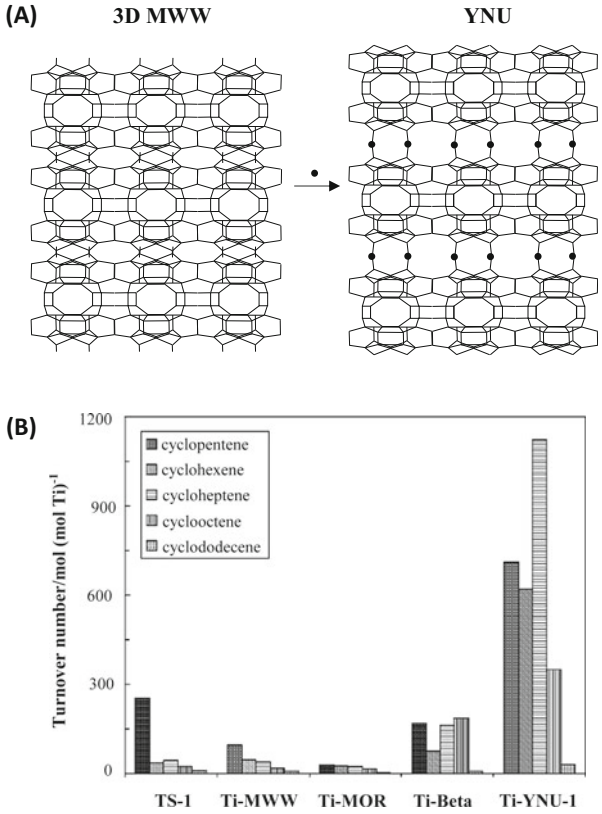

Fig. 19 (**a**) Structures of the MWW and YNU zeolites and (**b**) intrinsic activity of different titanosilicates for the epoxidation of different olefins. Reprinted from [151, 152], with permission from Wiley and Elsevier, respectively

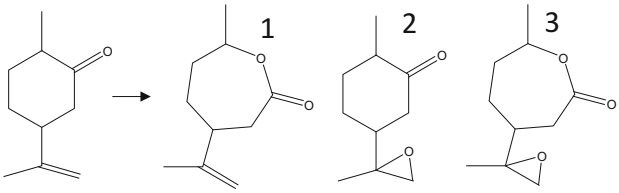

Catalyst/oxidant	X (%)	S1 (%)	S2 (%)	S3 (%)
mCPBA	85	11	71	18
Ti-Beta/H_2O_2	48	0	79	0
Sn-Beta/H_2O_2	68	100	0	0

Fig. 20 Catalytic results for the Baeyer-Villiger oxidation of dihydrocarvone (mCPA refers to *m*-chloroperbenzoic acid)

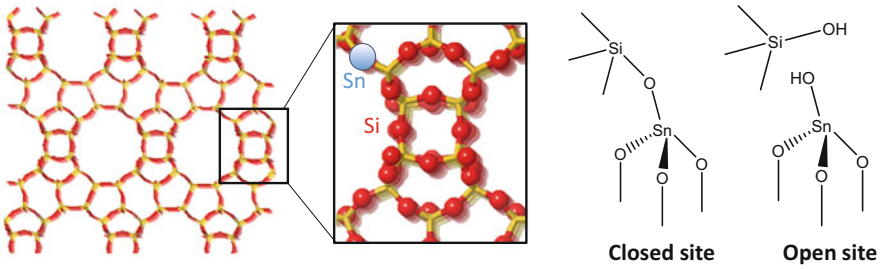

Fig. 21 Structure of Sn-Beta zeolite and the different open and closed Sn sites present in the solid

transformation of carbonyl groups, as the Meerwein-Ponndorf-Verley (MPV) reaction for the selective reduction of aldehydes and ketones to alcohols [24, 153].

The activity of the isolated tin sites within the Sn-Beta catalyst can be particularly explained by the unique bifunctional nature of the metal active site. Although it has been proved, both theoretically and experimentally, the presence of two different tin sites in the framework of the Sn-Beta, such as the partially hydrolyzed $(\text{-Si-O-})_3\text{Sn-OH}$ open sites or the fully coordinated $(\text{-Si-O-})_4\text{Sn}$ closed sites (Fig. 21), the partially hydrolyzed open centers are the most active sites for the BV and MPV reactions [154]. In fact, this partially open Sn center performs as a bifunctional site, since the Lewis acid Sn metal allows activating the carbonyl group, and the oxygen atom of the Sn-OH defect interacts with the H_2O_2 by hydrogen bonding, both favoring the oxidation and molecule rearrangement (Fig. 22) [155, 156].

All this fundamental knowledge acquired for the Sn-Beta, including its synthesis and its catalytic behavior for the BV and MPV reactions, has allowed the design of new Sn-containing materials and their application in other chemical processes. From the point of view of the Sn-containing materials, new synthesis routes have been described for the rapid synthesis of the Sn-Beta zeolite, including direct or post-synthetic methodologies [157–160], and for the synthesis of other Sn-containing zeolites, such as MWW, MFI, or MOR, among others [161, 162]. In addition, the catalytic applications of the tin-containing zeolitic materials have been extended not only to other fine chemistry processes but also to novel biomass transformation processes [131]. Among the different fine chemistry processes where the use of Sn-Beta as catalyst has been described, it can be highlighted the syntheses of the δ-decalactone and melonal fragrances [163, 164], the synthesis of the aromatizer (−)-menthol [165], and the selective oxidation of different aldehydes containing alkoxy substituents to form target phenolic products [166]. Moreover, in the last years, the use of Sn-based zeolites has been intensively extended to very diverse biomass-derived processes, based on the fact that many biomass molecules also contain carbonyl functionalities. Some of the recently reported tin-catalyzed biomass-derived reactions are sugar isomerization reactions [25, 167, 168], sugar epimerization reactions [169–171], sugars to lactic acid derivatives [172, 173], one-pot synthesis of furfural-derived products [174, 175], or production of optically pure γ-lactones [176].

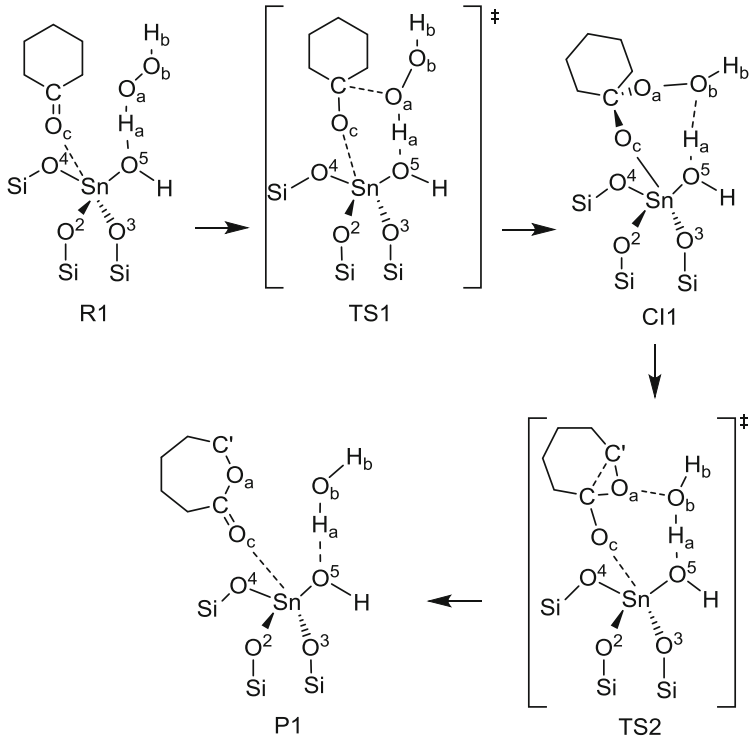

Fig. 22 Mechanism for the Baeyer-Villiger reaction using Sn-Beta zeolite as catalyst. Reprinted from [155], with permission from Wiley

3.3 Other Metal-Containing Zeolites

After the successful insertion of Ti and Sn within the crystalline frameworks of different zeolites, the isomorphic substitution of other tetrahedrally coordinated isolated transition metals has also been described, such as Zr, Ta, Nb, or Hf, particularly within the Beta structure [126–128]. The introduction of these metals is not an easy task, since their large ionic radius can hinder their incorporation in the relatively rigid crystalline zeolitic frameworks. Moreover, high pH values in the synthesis media can favor the precipitation of the former metal precursor into metal oxides, and for this reason, their preferred synthesis conditions involve fluoride media, where the pH values are closer to neutrality.

The presence of all these metals in the final solids offers different Lewis acidity strength depending on the nature of the metal. Indeed, different research groups have theoretically studied the Lewis acid strength order of different metals in zeolite frameworks, predicting that the theoretical order should be Si < Ti < Pb ≤ Sn ≤ Zr [177, 178]. Recently, Roman-Leshkov et al. have attempted to quantify the associated Lewis acidity for each tetrahedrally coordinated transition metal within

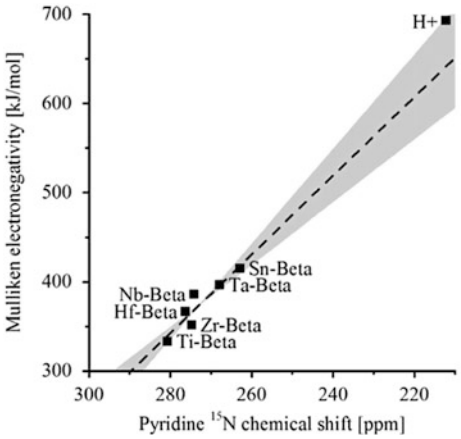

Fig. 23 Experimentally measured electronegativity of the different metal-containing Beta zeolites. Reprinted with permission from [179]. Copyright 2016 American Chemical Society

the Beta zeolite by using magic angle spinning nuclear magnetic resonance (MAS-NMR) of ^{15}N pyridine adsorbed on M-Beta zeolites [132, 179]. The authors found that there is a direct correlation between the experimentally observed ^{15}N chemical shift and Mulliken electronegativities (Fig. 23), providing an experimental scale for calculating the Lewis acid strength for the different metal-containing zeolites.

Regarding their application as catalysts, Zr- and Hf-containing zeolites have been recently described as efficient catalysts to undergo reactions involving intramolecular shifts, etherifications, or aldol condensations [127, 128, 180–182]. For instance, Zr-Beta and Hf-Beta show higher catalytic activity for the MPV than Sn-Beta, particularly when benzaldehyde was selected as reactant [181]. Similar enhanced catalytic behaviors have been observed for the combined MPV reduction and etherification of 5-(hydroxymethyl)furfural [182] and for the cross-aldol condensation of aromatic aldehydes and acetone [128], in both cases when using Hf- or Zr-Beta zeolites.

4 Conclusions and Perspectives

Along the present report, it has been highlighted the unique catalytic properties that the rational preparation of metal-containing zeolites offers for many industrially relevant chemical processes. It has been demonstrated how the fine-tuning control of the metal active sites, both in framework or extra-framework lattice positions, allows notoriously improving their catalytic behavior and their hydrothermal resistance against permanent deactivation of the resultant metal-containing zeolites.

The metal-based zeolites containing cationic metal species in exchangeable positions are receiving high attention in the last years, particularly those containing Cu and Fe. As it has been described, these materials perform as very efficient

heterogeneous catalysts for environmental applications, especially for the selective catalytic reduction of NOx, where Cu-CHA is being commercialized. Many research groups are now developing new synthesis approaches, where one of the most challenging issues is undoubtedly related to controlling the location of the lattice negative charges along the zeolite frameworks, with the aim to increase the confinement and stability of the single-site cationic species. Along this line, new zeolite synthesis methodologies using mimics of the transition state of a given reaction as OSDAs can produce zeolites more adequate to a particular reaction, while influencing the active site location within the structure [183].

The recent descriptions dealing on the efficient metal encapsulation of different clusters or small nanoparticles within the pores of high-silica zeolites, including the formation of homogeneously distributed bimetallic alloys, also give extraordinary opportunities for their use as shape-selective redox catalysts. Interestingly, these protected metal clusters or nanoparticles could present improved resistance against undesired metal aggregation when tested under severe reaction conditions or could favor the metal re-dispersion of the metal particles into single atoms or small clusters at milder conditions than those currently required.

Finally, the incorporation of isolated transition metals in lattice positions has allowed broadening the applicability of metal-based zeolites to new chemical processes, thanks to the exceptional Lewis acidity character offered by these tetrahedrally coordinated metals. The unprecedented ability to maintain the Lewis acidity even when polar solvents are used, i.e., water, permits envisioning that these metal-based zeolites could be employed as active and stable catalysts in new chemical processes, i.e., biomass transformations, for producing target chemicals.

All the knowledge acquired along the years in the design of metal-containing zeolites for their application as heterogeneous catalysts must now be employed to develop the next generation of disruptive catalysts for the new chemical and energy scenarios, where society must be committed to reach increasing new renewable source targets [184].

Acknowledgments This work has been supported by the Spanish Government (MINECO) through "Severo Ochoa" (SEV-2016-0683) and MAT2015-71261-R and by the Fundación Ramón Areces through a research contract of the "Life and Materials Science" program.

References

1. Barrer RM (1982) Hydrothermal chemistry of zeolites. Academic Press, London
2. Barrer RM (1948) Synthesis of a zeolitic mineral with chabazite like sorptive properties. J Chem Soc 2:127–132
3. Barrer RM, Riley DW (1948) Sorptive and molecular-sieve properties of a new zeolitic mineral. J Chem Soc:133–143
4. Barrer RM, Denny PJ (1961) Hydrothermal chemistry of the silicates. IX. Nitrogenous aluminosilicates. J Chem Soc:971–982
5. Lobo RF, Zones SI, Davis ME (1995) Structure-direction in zeolite synthesis. J Incl Phenom Mol Recognit Chem 21:47–78

6. Moliner M, Rey F, Corma A (2013) Towards the rational design of efficient organic structure-directing agents for zeolite synthesis. Angew Chem Int Ed 52:13880–13889
7. Martínez C, Corma A (2011) Inorganic molecular sieves: preparation, modification and industrial application in catalytic processes. Coord Chem Rev 255:1558–1580
8. Yilmaz B, Müller U (2009) Catalytic applications of zeolites in chemical industry. Top Catal 52:888–895
9. Cejka J, Centi G, Perez-Pariente J, Roth WJ (2012) Zeolite-based materials for novel catalytic applications: opportunities, perspectives and open problems. Catal Today 179:2–15
10. Moliner M, Martinez C, Corma A (2015) Multipore zeolites: synthesis and catalytic applications. Angew Chem Int Ed 54:3560–3579
11. Davis RJ (2003) New perspectives on basic zeolites as catalysts and catalysts supports. J Catal 216:396–405
12. Armor JN (1998) Metal-exchanged zeolites as catalysts. Microporous Mesoporous Mater 22:451–456
13. Vanelderen P, Vancauwenbergh J, Sels BF, Schoonheydt RA (2013) Coordination chemistry and reactivity of copper in zeolites. Coord Chem Rev 257:483–494
14. Moliner M, Martinez C, Corma A (2014) Synthesis strategies for preparing useful small pore zeolites and zeotypes for gas separations and catalysis. Chem Mater 26:246–258
15. Liu L et al (2017) Generation of subnanometric platinum with high stability during transformation of a 2D zeolite into 3D. Nat Mater 16:132–138
16. Choi M, Wu Z, Iglesia E (2010) Mercaptosilane-assisted synthesis of metal clusters within zeolites and catalytic consequences of encapsulation. J Am Chem Soc 132:9129–9137
17. Moliner M et al (2016) Reversible transformation of Pt nanoparticles into single atoms inside high-silica chabazite zeolite. J Am Chem Soc 138:15743–15750
18. Wang N et al (2016) In situ confinement of ultrasmall Pd clusters within nanosized silicalite-1 zeolite for highly efficient catalysis of hydrogen generation. J Am Chem Soc 138:7484–7487
19. Kim SJ et al (2016) One-step synthesis of zeolite membranes containing catalytic metal nanoclusters. ACS Appl Mater Interfaces 8:24671–24681
20. Taramasso M, Perego G, Notari B (1983) Preparation of porous crystalline synthetic material comprised of silicon and titanium oxides. U.S. Patent 4410501
21. Moliner M, Corma A (2014) Advances in the synthesis of titanosilicates: from the medium pore TS-1 zeolite to highly-accessible ordered materials. Microporous Mesoporous Mater 189:31–40
22. Flanigen E, Patton RL (1978) Silica polymorph and process for preparing same. U.S. Patent 4073865
23. Camblor MA, Corma A, Valencia S (1996) Spontaneous nucleation and growth of pure silica zeolite-β free of connectivity defects. Chem Commun:2365–2366
24. Corma A, Domine ME, Valencia S (2003) Water-resistant solid Lewis acid catalysts: Meerwein–Ponndorf–Verley and Oppenauer reactions catalyzed by tin-beta zeolite. J Catal 215:294–304
25. Moliner M, Román-Leshkov Y, Davis ME (2010) Tin-containing zeolites are highly active catalysts for the isomerization of glucose in water. Proc Natl Acad Sci U S A 107:6164–6168
26. Brandenberger S, Kröcher O, Tissler A, Althoff R (2008) The state of the art in selective catalytic reduction of NOx by ammonia using metal-exchanged zeolite catalysts. Catal Rev 50:493–531
27. Martínez-Franco R, Moliner M, Thogersen JR, Corma A (2013) Efficient one-pot preparation of Cu-SSZ-13 materials using cooperative OSDAs for their catalytic application in the SCR of NOx. ChemCatChem 5:3316–3323
28. Moliner M (2012) Direct synthesis of functional zeolitic materials. ISRN Mat Sci 1–24. https://doi.org/10.5402/2012/789525
29. Barthomeuf D (1996) Basic zeolites: characterization and uses in adsorption and catalysis. Catal Rev 38:521–612

30. Keller TC et al (2016) Understanding the structure of cationic sites in alkali metal-grafted USY zeolites. J Phys Chem C 120:4954–4960
31. Doskocil EJ, Bordawekar SV, Kaye BG, Davis RJ (1999) UV−Vis spectroscopy of iodine adsorbed on alkali-metal-modified zeolite catalysts for addition of carbon dioxide to ethylene oxide. J Phys Chem B 103:6277–6282
32. Corma A, Fornes V, Martin-Aranda RM, García H, Primo J (1990) Zeolites as base catalysts: condensation of aldehydes with derivatives of malonic esters. Appl Catal 59:237–248
33. Corma A, Martín-Aranda RM (1993) Application of solid base catalysts in the preparation of prepolymers by condensation of ketones and malononitrile. Appl Catal A 105:271–279
34. Wieland WS, Davis RJ, Garces JM (1996) Solid base catalysts for side-chain alkylation of toluene with methanol. Catal Today 28:443–450
35. Wieland WS, Davis RJ, Garces JM (1998) Side-chain alkylation of toluene with methanol over alkali-exchanged zeolites X, Y, L, and β. J Catal 173:490–500
36. Palomares AE, Eder-Mirth G, Rep M, Lercher JA (1998) Alkylation of toluene over basic catalysts-key requirements for side chain alkylation. J Catal 180:56–65
37. Moreau C, Durand R, Roux A, Tichit D (2000) Isomerization of glucose into fructose in the presence of cation-exchanged zeolites and hydrotalcites. Appl Catal A 193:257–264
38. Leclerq E, Finiels A, Moreau C (2001) Transesterification of rapeseed oil in the presence of basic zeolites and related solid catalysts. J Am Oil Chem Soc 78:1161–1165
39. Climent MJ, Corma A, Hamid SBA, Iborra S, Mifsud M (2006) Chemicals from biomass derived products: synthesis of polyoxyethyleneglycol esters from fatty acid methyl esters with solid basic catalysts. Green Chem 8:524–532
40. Charlot G (1957) L'analyse quantitative et les reactions en solution. Masson et Cie, Paris
41. Shwan S et al (2015) Solid-state ion-exchange of copper into zeolites facilitated by ammonia at low temperature. ACS Catal 5:16–19
42. Ren L et al (2011) Designed copper-amine complex as an efficient template for one-pot synthesis of Cu-SSZ-13 zeolite with excellent activity for selective catalytic reduction of NOx by NH_3. Chem Commun 47:9789–9791
43. Zamadics M, Chen X, Kevan L (1992) Solid-state ion exchange in H-SAPO-34: electron spin resonance and electron spin echo modulation studies of copper(II) location and adsorbate interaction. J Phys Chem 96:5488–5491
44. Kanazirev VI, Price GL (1995) Propane conversion on Cu-MFI zeolites. J Mol Catal A 96:145–154
45. Ren L et al (2012) Organotemplate-free and one-pot fabrication of nano-rod assembled plate-like micro-sized mordenite crystals. J Mater Chem 22:6564–6567
46. Martinez-Franco R, Moliner M, Franch C, Kustov A, Corma A (2012) Rational direct synthesis methodology of very active and hydrothermally stable Cu-SAPO-34 molecular sieves for the SCR of NOx. Appl Catal B 127:273–280
47. Deka U et al (2013) Changing active sites in Cu-CHA catalysts: deNOx selectivity as a function of the preparation method. Microporous Mesoporous Mater 166:144–152
48. Martinez-Franco R, Moliner M, Concepción P, Thogersen JR, Corma A (2014) Synthesis, characterization and reactivity of high hydrothermally stable Cu-SAPO-34 materials prepared by "one-pot" processes. J Catal 314:73–82
49. Picone AL et al (2011) A co-templating route to the synthesis of Cu SAPO STA-7, giving an active catalyst for the selective catalytic reduction of NO. Microporous Mesoporous Mater 146:36–47
50. Martínez-Franco R, Moliner M, Corma A (2014) Direct synthesis design of Cu-SAPO-18, a very efficient catalyst for the SCR of NOx. J Catal 319:36–43
51. Martin N, Boruntea CR, Moliner M, Corma A (2015) Efficient synthesis of the Cu-SSZ-39 catalyst for DeNOx applications. Chem Commun 51:11030–11033
52. Delabie A, Pierloot K, Groothaert MH, Schiinheydt RA, Vanquickenborne LG (2002) The coordination of CuII in zeolites − structure and spectroscopic properties. Eur J Inorg Chem:515–530

53. Groothaert MH, Pierloot K, Delabie A, Schoonheydt RA (2003) Identification of Cu(II) coordination structures in Cu-ZSM-5, based on a DFT/ab initio assignment of the EPR spectra. Phys Chem Chem Phys 5:2135–2144
54. Tomkins P, Ranocchiari M, van Bokhoven JA (2017) Direct conversion of methane to methanol under mild conditions over Cu-zeolites and beyond. Acc Chem Res 50:418–425
55. Iwamoto M et al (1986) Copper(II) ion-exchanged ZSM-5 zeolites as highly active catalysts for direct and continuous decomposition of nitrogen monoxide. J Chem Soc Chem Commun 16:1272–1273
56. Beale AM, Gao F, Lezcano-Gonzalez I, Peden CHF, Szanyi J (2015) Recent advances in automotive catalysis for NOx emission control by small-pore microporous materials. Chem Soc Rev 44:7371–7405
57. Kwak JH, Tonkyn RG, Kim DH, Szanyi J, Peden CHF (2010) Excellent activity and selectivity of Cu-SSZ-13 in the selective catalytic reduction of NOx with NH3. J Catal 275:187–190
58. Korhonen ST, Fickel DW, Lobo RF, Weckhuysen BM, Beale AM (2011) Isolated Cu2+ ions: active sites for selective catalytic reduction of NO. Chem Commun 47:800–802
59. Bull I et al (2008) Copper CHA zeolite catalysts. U.S. Patent 0226545
60. Moliner M, Franch C, Palomares E, Grill M, Corma A (2012) Cu-SSZ-39, an active and hydrothermally stable catalyst for the selective catalytic reduction of NOx. Chem Commun 48:8264–8266
61. Ryu T et al (2017) Fully copper-exchanged high-silica LTA zeolites as unrivaled hydrothermally stable NH3 SCR catalysts. Angew Chem Int Ed 56:3256–3260
62. Deka U et al (2012) Confirmation of isolated Cu2+ ions in SSZ-13 zeolite as active sites in NH3-selective catalytic reduction. J Phys Chem C 116:4809–4818
63. Paolucci C et al (2014) Isolation of the copper redox steps in the standard selective catalytic reduction on Cu-SSZ-13. Angew Chem Int Ed 53:11828–11833
64. Paolucci C et al (2017) Dynamic multinuclear sites formed by mobilized copper ions in NOx selective catalytic reduction. Science 357(6354):898–903.
65. Mueller K, Fabisch F, Arlt W (2014) Energy transport and storage using methanol as a carrier. Green 4:19–25
66. Schüth F (2011) Chemical compounds for energy storage. Chem Ing Tech 83:1984–1993
67. Groothaert MH, Smeets PJ, Sels BF, Jacobs PA, Schoonheydt RA (2005) Selective oxidation of methane by the Bis(μ-oxo)dicopper core stabilized on ZSM-5 and mordenite zeolites. J Am Chem Soc 127:1394–1395
68. Woertink JS et al (2009) A [Cu2O]2+ core in Cu-ZSM-5, the active site in the oxidation of methane to methanol. Proc Natl Acad Sci U S A 106:18908–18913
69. Grundner S et al (2015) Single-site trinuclear copper oxygen clusters in mordenite for selective conversion of methane to methanol. Nat Commun 6:7546
70. Palagin D, Knorpp A, Pinar AB, Ranocchiari M, van Bokhoven J (2017) Assessing relative stability of copper oxide clusters as active sites of CuMOR zeolite for methane to methanol conversion: size matters? Nanoscale 9:1144–1153
71. Maeda Y, Kato N, Kawasaki S, Takashima Y (1990) Characterization of iron species in Y-type zeolite and modified form of the zeolite. Zeolites 10:21–27
72. Pirngruber GD, Roy PK, Prins R (2006) On determining the nuclearity of iron sites in Fe-ZSM-5, a critical evaluation. Phys Chem Chem Phys 8:3939–3950
73. Gao F et al (2016) Iron loading effects in Fe/SSZ-13 NH3-SCR catalysts: nature of the Fe ions and structure-function relationships. ACS Catal 6:2939–2954
74. Perez-Ramirez J, Gallardo-Llamas A (2005) Impact of the preparation method and iron impurities in Fe-ZSM-5 zeolites for propylene production via oxidative dehydrogenation of propane with N_2O. Appl Catal A 279:117–123
75. Perez-Ramirez J et al (2005) Evolution of isomorphously substituted iron zeolites during activation: comparison of Fe-beta and Fe-ZSM-5. J Catal 232:318–334

76. Martin N, Vennestrom PNR, Thogersen JR, Moliner M, Corma A (2017) Fe-containing zeolites for NH_3-SCR of NOx: effect of structure, synthesis procedure, and chemical composition on catalytic performance and stability. Chem Eur J 23:13404–13414
77. Krocher O, Brandenberger S (2012) Active sites, deactivation and stabilization of Fe-ZSM-5 for the selective catalytic reduction (SCR) of NO with NH3. Chimia 66:687–693
78. Pidko EA, Hensen EJM, van Saten RA (2012) Self-organization of extra-framework cations in zeolites. Proc R Soc A 468:2070–2086
79. Gao F et al (2015) Fe/SSZ-13 as an NH3-SCR catalyst: a reaction kinetics and FTIR/Mössbauer spectroscopic study. Appl Catal B 164:407–419
80. Martin N, Vennestrom PNR, Thogersen JR, Moliner M, Corma A (2017) Iron-containing SSZ-39 (AEI) zeolite: an active and stable high-temperature NH3-SCR catalyst. ChemCatChem 9:1754–1757
81. Martín N et al (2017) Cage-based small-pore catalysts for NH3-SCR prepared by combining bulky organic structure directing agents with modified zeolites as reagents. Appl Catal B 217:125–136
82. Nedyalkova R, Shwan S, Skoglundh M, Olsson L (2013) Improved low-temperature SCR activity for Fe-BEA catalysts by H2-pretreatment. Appl Catal B 138–139:373–380
83. Long RQ, Yang RT (2001) Fe-ZSM-5 for selective catalytic reduction of NO with NH3: a comparative study of different preparation techniques. Catal Lett 74:201–205
84. Ma AZ, Grüner W (1999) Selective catalytic reduction of NO by ammonia over Fe-ZSM-5 catalysts. Chem Commun:71–72
85. Wu G et al (2013) Oxidative dehydrogenation of propane with nitrous oxide over Fe-ZSM-5 prepared by grafting: characterization and performance. Appl Catal A 468:230–239
86. Kondratenko EV, Perez-Ramirez J (2004) Oxidative functionalization of propane over FeMFI zeolites: effect of reaction variables and catalyst constitution on the mechanism and performance. Appl Catal A 267:181–189
87. Sánchez-Galofré O, Segura Y, Perez-Ramirez J (2007) Deactivation and regeneration of iron-containing MFI zeolites in propane oxidative dehydrogenation by N_2O. J Catal 249:123–133
88. Panov GI, Uriarte AK, Rodkin MA, Sobolev VI (1998) Generation of active oxygen species on solid surfaces. Opportunity for novel oxidation technologies over zeolites. Catal Today 41:365–385
89. Kevan L (1987) Catalitically important metal ion intermediates on zeolites and silica surfaces. Rev Chem Intermed 8:53–85
90. Michalik J, Narayana M, Kevan L (1984) Formation of monovalent nickel in NiCa-X zeolite and its interaction with various inorganic and organic adsorbates. Electron spin resonance studies. J Phys Chem 88:5236–5240
91. Garcia R, Coombs TD, Shannon IJ, Wright PA, Cox PA (2003) Nickel amine complexes as structure-directing agents for aluminophophate molecular sieves: a new route to supported nickel catalysts. Top Catal 24:115–124
92. Garcia R, Philp EF, Slawin AMZ, Wright PA, Cox PA (2001) Nickel complexed within an azamacrocycle as structure directing agent in the crystallization of the framework metalloaluminophosphates STA-6 and STA-7. J Mater Chem 11:1421–1427
93. Garcia R et al (2003) Synthesis, structure and thermal transformations of aluminophosphates containing the nickel complex $[Ni(diethylenetriamine)_2]^{2+}$ as a structure directing agent. Microporous Mesoporous Mater 58:91–104
94. Cui Y et al (2017) One-pot synthesis of Ni-SSZ-13 zeolite using a nickel-amine complex as an efficient organic template. J Mater Sci 52:10156–10162
95. Lacarriere A et al (2012) Distillate-range products from non-oil-based sources by catalytic cascade reactions. ChemSusChem 5:1787–1792
96. Moussa S, Arribas MA, Concepción P, Martínez A (2016) Heterogeneous oligomerization of ethylene to liquids on bifunctional Ni-based catalysts: the influence of support properties on nickel speciation and catalytic performance. Catal Today 277:78–88

97. Lallemand M, Finiels A, Fajula F, Hulea V (2006) Catalytic oligomerization of ethylene over Ni-containing dealuminated Y zeolites. Appl Catal A 301:196–201
98. EU Project OCMOL (Oxidative Coupling of Methane followed by Oligomerization to Liquids), 7th Framework Programme (GA no 228953). http://www.ocmol.eu
99. Sohn JR, Park WC, Park SE (2002) Characterization of nickel sulfate supported on SiO2–Al2O3 for ethylene dimerization and its relationship to acidic properties. Catal Lett 81:259–264
100. Cai T, Cao D, Song Z, Li L (1993) Catalytic behavior of NiS04/γ-Al2O3 for ethene dimerization. Appl Catal A 95:L1–L7
101. Cai T (1999) Studies of a new alkene oligomerization catalyst derived from nickel sulfate. Catal Today 51:153–160
102. Davydov AA, Kantcheva M, Chepotko ML (2002) FTIR spectroscopic study on nickel(II)-exchanged sulfated alumina: nature of the active sites in the catalytic oligomerization of ethene. Catal Lett 83:97–108
103. Lallemand M, Finiels A, Fajula F, Hulea V (2009) Nature of the active sites in ethylene oligomerization catalyzed by Ni-containing molecular sieves: chemical and IR spectral investigation. J Phys Chem C 113:20360–20364
104. Martínez A, Arribas MA, Concepción P, Moussa S (2013) New bifunctional Ni–H-Beta catalysts for the heterogeneous oligomerization of ethylene. Appl Catal A 467:509–518
105. Degnan Jr TF (2000) Applications of zeolites in petroleum refining. Top Catal 13:349–356
106. Gates BC, Flytzani-Stephanopoulos M, Dixon DA, Katz A (2017) Atomically dispersed supported metal catalysts: perspectives and suggestions for future research. Cat Sci Technol 7:4259–4275
107. Liu J (2017) Catalysis by supported single metal atoms. ACS Catal 7:34–59
108. Flytzani-Stephanopoulos M, Gates BC (2012) Atomically dispersed supported metal catalysts. Ann Rev Chem Biomol Eng 3:545–574
109. Yang M et al (2015) A common single-site Pt(II)−O(OH)x− species stabilized by sodium on "Active" and "Inert" supports catalyzes the water-gas shift reaction. J Am Chem Soc 137:3470–3473
110. Rubio-Marqués P, Rivero-Crespo MA, Leyva-Pérez A, Corma A (2015) Well-defined noble metal single sites in zeolites as an alternative to catalysis by insoluble metal salts. J Am Chem Soc 137:11832–11837
111. Kistler JD et al (2014) A single-site platinum CO oxidation catalyst in zeolite KLTL: microscopic and spectroscopic determination of the locations of the platinum atoms. Angew Chem Int Ed 53:8904–8907
112. Yang M et al (2014) Catalytically active Au-O(OH)x species stabilized by alkali ions on zeolites and mesoporous oxides. Science 346:1498–1501
113. Huang W et al (2016) Low-temperature transformation of methane to methanol on Pd1O4 single sites anchored on the internal surface of microporous silicate. Angew Chem Int Ed 55:13441–13445
114. Guczi L, Kiricsi I (1999) Zeolite supported mono- and bimetallic systems: structure and performance as CO hydrogenation catalysts. Appl Catal A 186:375–394
115. Li X, Iglesia E (2008) Pt/[Fe]ZSM-5 modified by Na and Cs cations: an active and selective catalyst for dehydrogenation of n-alkanes to n-alkenes. Chem Commun 5:594–596
116. Guzman J, Gates BC (2003) Supported molecular catalysts: metal complexes and clusters on oxides and zeolites. Dalton Trans 17:3303–3318
117. Gallezot P (2002) Post-synthesis modification I, vol 3. Springer, Berlin, pp 257–305
118. Sun Q et al (2017) Subnanometric hybrid Pd-M(OH)2, M = Ni, Co, clusters in zeolites as highly efficient nanocatalysts for hydrogen generation. Chem 3:477–493
119. Otto T et al (2016) Synthesis of stable monodisperse AuPd, AuPt, and PdPt bimetallic clusters encapsulated within LTA-zeolites. J Catal 342:125–137
120. Ratnasamy P, Srinivas D, Knözinger H (2004) Active sites and reactive intermediates in titanium silicate molecular sieves. Adv Catal 48:1–169

121. Xu H, Wu P (2017) Recent progresses in titanosilicates. Chin J Chem 35:836–844
122. Perego C et al (1986) Titanium-silicalite: a novel derivative in the pentasil family. Stud Surf Sci Catal 28:129–136
123. Perego C, Carati A, Ingallina P, Mantegazza MA, Bellussi G (2001) Production of titanium containing molecular sieves and their application in catalysis. Appl Catal A 221:63–71
124. Blasco T et al (1996) Unseeded synthesis of Al-free Ti-β zeolite in fluoride medium: a hydrophobic selective oxidation catalyst. Chem Commun 20:2367–2368
125. Corma A, Nemeth LT, Renz M, Valencia S (2001) Sn-zeolite beta as a heterogeneous chemoselective catalyst for Baeyer–Villiger oxidations. Nature 412:423–425
126. Corma A, Llabres F, Xamena I, Prestipino C, Renz M, Valencia S (2009) Water resistant, catalytically active Nb and Ta isolated Lewis acid sites, homogeneously distributed by direct synthesis in a beta zeolite. J Phys Chem C 113:11306–11315
127. Zhu Y, Chuah G, Jaenicke S (2004) Chemo- and regioselective Meerwein–Ponndorf–Verley and Oppenauer reactions catalyzed by Al-free Zr-zeolite beta. J Catal 227:1–10
128. Lewis JD, Van de Vyver S, Román-Leshkov Y (2015) Acid-base pairs in Lewis acidic zeolites promote direct aldol reactions by soft enolization. Angew Chem Int Ed 54:9835–9838
129. Corma A, Iborra S, Velty A (2007) Chemical routes for the transformation of biomass into chemicals. Chem Rev 107:2411–2502
130. Roman-Leshkov Y, Davis ME (2011) Activation of carbonyl-containing molecules with solid Lewis acids in aqueous media. ACS Catal 1:1566–1580
131. Moliner M (2014) State of the art of Lewis acid-containing zeolites: lessons from fine chemistry to new biomass transformation processes. Dalton Trans 43:4197–4208
132. Luo HY, Lewis JD, Román-Leshkov Y (2016) Lewis acid zeolites for biomass conversion: perspectives and challenges on reactivity, synthesis, and stability. Ann Rev Chem Biomol Eng 7:663–692
133. Romano U, Esposito A, Maspero F, Neri C, Clerici MG (1990) Selective oxidation with titanium silicalite. Chim Ind 72:610–616
134. Tuel A, Ben Taarit Y (1993) Comparison between TS-1 and TS-2 in the hydroxylation of phenol with hydrogen peroxide. Appl Catal A 102:69–77
135. Bhaumik A, Mukherjiee P, Kumar R (1998) Triphase catalysis over titanium–silicate molecular sieves under solvent-free conditions: I. Direct hydroxylation of benzene. J Catal 178:101–107
136. Clerini MG, Ingallina P (1993) Epoxidation of lower olefins with hydrogen peroxide and titanium silicalite. J Catal 140:71–83
137. Clerici MG, Ingallina P (1998) Oxidation reactions with in situ generated oxidants. Catal Today 41:351–364
138. Huybrechts DRC, De Bruycker L, Jacobs PA (1990) Oxyfunctionalization of alkanes with hydrogen peroxide on titanium silicalite. Nature 345:240–242
139. Esposito A, Taramasso M, Neri C, Buonomo F (1984) Process for oxidizing alcohols to aldehydes and/or ketones. U.S. Patent 4480135
140. Mantegazza MA, Cesana A, Pastori M (1996) Ammoximation of ketones on titanium silicalite. A study of the reaction byproducts. Top Catal 3:327–335
141. Cesana A, Mantegazza MA, Pastori M (1997) A study of the organic by-products in the cyclohexanone ammoximation. J Mol Catal A 117:367–373
142. Xia C et al (2017) Environmental-friendly catalytic oxidation processes based on hierarchical titanium silicate zeolites at SINOPEC. In: Karamé I (ed) Green chemical processing and synthesis. InTech, Rijeka
143. Camblor MA, Corma A, Martínez A, Perez-Pariente J (1992) Synthesis of a titanium-silicoaluminate isomorphous to zeolite Beta and its application as a catalyst for the selective oxidation of large organic molecules. Chem Commun 8:589–590
144. Corma A, Camblor MA, Esteve P, Martinez A, Perez-Pariente J (1994) Activity of Ti-Beta catalyst for the selective oxidation of alkenes and alkanes. J Catal 145:151–158
145. Camblor MA et al (1996) Synthesis and catalytic activity of aluminium-free zeolite Ti-B oxidation catalysts. Chem Commun 11:1339–1340

146. Blasco T et al (1998) Direct synthesis and characterization of hydrophobic aluminum-free Ti-Beta zeolite. J Phys Chem B 102:75–88
147. Camblor MA, Corma A, Esteve P, Martinez A, Valencia S (1997) Epoxidation of unsaturated fatty esters over large-pore Ti-containing molecular sieves as catalysts: important role of the hydrophobic-hydrophilic properties of the molecular sieve. Chem Commun 8:795–796
148. Tuel A (1995) Synthesis, characterization, and catalytic properties of the new TiZSM-12 zeolite. Zeolites 15:236–242
149. Corma A, Diaz-Cabañas MJ, Domine ME, Rey F (2000) Ultra fast and efficient synthesis of Ti-ITQ-7 and positive catalytic implications. Chem Commun 18:1725–1726
150. Moliner M et al (2008) Synthesis of the Ti-silicate form of BEC polymorph of β-zeolite assisted by molecular modeling. J Phys Chem C 112:19547–19554
151. Fan W, Wu P, Namba S, Tatsumi T (2006) Synthesis and catalytic properties of a new titanosilicate molecular sieve with the structure analogous to MWW-type lamellar precursor. J Catal 243:183–191
152. Ruan J, Wu P, Slater B, Terasaki O (2005) Structure elucidation of the highly active titanosilicate catalyst Ti-YNU-1. Angew Chem Int Ed 44:6719–6723
153. Corma A, Domine ME, Nemeth L, Valencia S (2002) Al-free Sn-Beta zeolite as a catalyst for the selective reduction of carbonyl compounds (Meerwein-Ponndorf-Verley reaction). J Am Chem Soc 124:3194–3195
154. Boronat M, Concepción P, Corma A, Renz M, Valencia S (2005) Determination of the catalytically active oxidation Lewis acid sites in Sn-beta zeolites, and their optimisation by the combination of theoretical and experimental studies. J Catal 234:111–118
155. Boronat M, Corma A, Renz M, Sastre G, Viruela PM, Multisite Molecular A (2005) Mechanism for Baeyer–Villiger oxidations on solid catalysts using environmentally friendly H2O2 as oxidant. Chem Eur J 11:6905–6915
156. Boronat M, Corma A, Renz M (2006) Mechanism of the Meerwein−Ponndorf−Verley−Oppenauer (MPVO) redox equilibrium on Sn− and Zr−beta zeolite catalysts. J Phys Chem B 110:21168–21174
157. Li P et al (2011) Postsynthesis and selective oxidation properties of nanosized Sn-beta zeolite. J Phys Chem C 115:3663–3670
158. Kessler H, Patarin J, Schott-Darie C (1994) The opportunities of the fluoride route in the synthesis of microporous materials. Stud Surf Sci Catal 85:75–113
159. Chang CC, Wang Z, Dornath P, Cho HJ, Fan W (2012) Rapid synthesis of Sn-Beta for the isomerization of cellulosic sugars. RSC Adv 2:10475–10477
160. Dijkmans J et al (2013) Productive sugar isomerization with highly active Sn in dealuminated β zeolites. Green Chem 15:2777–2785
161. van der Graaff WNP, Tempelman CHL, Pidko EA, Hensen EJM (2017) Influence of pore topology on synthesis and reactivity of Sn-modified zeolite catalysts for carbohydrate conversions. Cat Sci Technol 7:3151–3162
162. Luo HY, Bui L, Gunther WR, Min E, Roman-Leshkov Y (2012) Synthesis and catalytic activity of Sn-MFI nanosheets for the Baeyer–Villiger oxidation of cyclic ketones. ACS Catal 2:2695–2699
163. Corma A, Iborra S, Mifsud M, Renz M, Susarte M (2004) A new environmentally benign catalytic process for the asymmetric synthesis of lactones: synthesis of the flavouring δ-decalactone molecule. Adv Synth Catal 346:257–262
164. Corma A, Iborra S, Mifsud M, Renz M (2005) A new, alternative, halogen-free synthesis for the fragrance compound Melonal using zeolites and mesoporous materials as oxidation catalysts. J Catal 234:96–100
165. Corma A, Renz M (2004) Sn-beta zeolite as diastereoselective water-resistant heterogeneous Lewis-acid catalyst for carbon–carbon bond formation in the intramolecular carbonyl–ene reaction. Chem Commun:550–551
166. Corma A, Fornes V, Iborra S, Mifsud M, Renz M (2004) One-pot synthesis of phenols from aromatic aldehydes by Baeyer–Villiger oxidation with H2O2 using water-tolerant Lewis acids in molecular sieves. J Catal 221:67–76

167. Román-Leshkov Y, Moliner M, Labinger JA, Davis ME (2010) Mechanism of glucose isomerization using a solid lewis acid catalyst in water. Angew Chem Int Ed 49:8954–8957
168. Bermejo-Deval R et al (2012) Metalloenzyme-like catalyzed isomerizations of sugars by Lewis acid zeolites. Proc Natl Acad Sci U S A 109:9727–9732
169. Gunther WR, Wang Y, Michaelis VK, Hunt ST, Griffin RG (2012) Sn-Beta zeolites with borate salts catalyse the epimerization of carbohydrates via an intramolecular carbon shift. Nat Commun 3:1109
170. Gunther WR, Duong Q, Román-Leshkov Y (2013) Catalytic consequences of borate complexation and pH on the epimerization of l-arabinose to l-ribose in water catalyzed by Sn-Beta zeolite with borate salts. J Mol Catal A 379:294–302
171. Bermejo-Deval R, Gounder R, Davis ME (2012) Framework and extraframework tin sites in zeolite beta react glucose differently. ACS Catal 2:2705–2713
172. Taarning E et al (2009) Zeolite-catalyzed isomerization of triose sugars. ChemSusChem 2:625–627
173. Holm MS, Saravanamurugan S, Taarning E (2010) Conversion of sugars to lactic acid derivatives using heterogeneous zeotype catalysts. Science 328:602–605
174. Nikolla E, Roman-Leshkov Y, Moliner M, Davis ME (2011) "One-pot" synthesis of 5-(Hydroxymethyl)furfural from carbohydrates using tin-beta zeolite. ACS Catal 1:408–410
175. Lew CM, Rajabbeigi N, Tsapatsis M (2012) One-pot synthesis of 5-(Ethoxymethyl)furfural from glucose using Sn-BEA and amberlyst catalysts. Ind Eng Chem Res 51:5364–5366
176. Paris C, Moliner M, Corma A (2013) Metal-containing zeolites as efficient catalysts for the transformation of highly valuable chiral biomass-derived products. Green Chem 15:2101–2109
177. Yang G, Zhou L, Han X (2012) Lewis and Bronsted acidic sites in $M4^{+}$-doped zeolites (M=Ti, Zr, Ge, Sn, Pb) as well as interactions with probe molecules: a DFT study. J Mol Catal A 363:371–379
178. Li H et al (2015) Structural stability and Lewis acidity of tetravalent Ti, Sn, or Zr-linked interlayer-expanded zeolite COE-4: a DFT study. Microporous Mesoporous Mater 218:160–166
179. Gunther WR, Michaelis VK, Griffin RG, Roman-Leshkov Y (2016) Interrogating the Lewis acidity of metal sites in beta zeolites with 15N pyridine adsorption coupled with MAS NMR spectroscopy. J Phys Chem C 120:28533–28544
180. Boronat M, Corma A, Renz M, Viruela PM (2006) Predicting the activity of single isolated Lewis acid sites in solid catalysts. Chem Eur J 12:7067–7077
181. Luo HY, Consoli DF, Gunther WR, Román-Leshkov Y (2014) Investigation of the reaction kinetics of isolated Lewis acid sites in beta zeolites for the Meerwein-Ponndorf-Verley reduction of methyl levulinate to γ-valerolactone. J Catal 320:198–207
182. Lewis JD et al (2014) A continuous flow strategy for the coupled transfer hydrogenation and etherification of 5-(hydroxymethyl) furfural using Lewis acid zeolites. ChemSusChem 7:2255–2265
183. Gallego EM et al (2017) "Ab initio" synthesis of zeolites for preestablished catalytic reactions. Science 355:1051–1055
184. Abate S, Barbera K, Centi G, Lanzafame P, Perathoner S (2016) Disruptive catalysis by zeolites. Cat Sci Technol 6:2485–2501

Struct Bond (2018) 178: 91–154
DOI: 10.1007/430_2018_24

Published online: 25 March 2018

Characterization of Metal Centers in Zeolites for Partial Oxidation Reactions

G. Berlier, V. Crocellà, M. Signorile, E. Borfecchia, F. Bonino, and S. Bordiga

Abstract This chapter addresses the power and possibilities provided by an appropriate combination of advanced characterization techniques in understanding the environment of metal ions in different metal-zeolites, as well as in the role played by them in different catalytic reactions. Three different classes of materials are considered as case studies: (1) Cu-zeolites, where Cu^{I} and Cu^{II} ions are mainly present as counterions; (2) Fe-zeolites, often containing a wide variety of isolated, oligonuclear, and aggregated (oxide/hydroxide) Fe^{II}/Fe^{III} species; and (3) TS-1, which is the closest to a "single-site" catalyst, mainly containing framework Ti^{IV} sites. TS-1 is studied in relation to its activity in the propene epoxidation reaction in the presence of aqueous H_2O_2, while Cu- and Fe-zeolites are here considered in relation to the direct conversion of methane to methanol (MTM) (a so-called dream reaction) with O_2, N_2O, or H_2O_2 as oxidizing agents. Main focus is into the nature of the active site precursors (i.e., mono or di-/trinuclear ions, oxidation state, and local environment) and into the electronic and geometric structure of the oxo species formed upon interaction with the oxidizing agents. Moreover, examples about in situ or operando experiments following changes during the reaction are reviewed. The main considered techniques are X-ray absorption spectroscopy (XAS) and resonance Raman (rR) and diffuse reflectance UV-Vis spectroscopies, often coupled to density functional theory (DFT) modeling. Depending on the studied system, results obtained with infrared, Mössbauer, X-ray emission (XES) and electron paramagnetic resonance (EPR) spectroscopies are also described. The discussion includes the open debates, the main drawbacks and potentialities of the techniques, and the related characterization challenges.

G. Berlier, V. Crocellà, M. Signorile, E. Borfecchia, F. Bonino, and S. Bordiga (✉)
Department of Chemistry, INSTM Reference Center, and NIS Inter-Departmental Centre, University of Turin, Turin, Italy
e-mail: silvia.bordiga@unito.it

Keywords Benzene to phenol · Cu-zeolites · Diffuse reflectance UV-Vis spectroscopy · Fe-zeolites · Hydrogen peroxide · In situ spectroscopy · Infrared spectroscopy · Methane to methanol · Operando techniques · Propylene to propylene oxide · Resonance Raman spectroscopy · Selective oxidation · Ti-silicalite-1 · X-ray absorption spectroscopy

Contents

1 Introduction

1.1 Transition Metal Ions in Zeolites

Metal centers in zeolites for partial oxidation reactions are usually transition metal ions (TMIs) with redox activity, which can be introduced as counterions by chemical vapor deposition/impregnation (CVD/CVI) and liquid or solid ion exchange (LIE or SSIE). These procedures are often carried out on H^+- or NH_4^+-zeolites, where the TMIs exchange for Brønsted acid sites (which in NH_4^+-zeolite are generated by thermal treatment with consequent NH_3 release) or on Na^+ (or other alkaline/alkaline earth metal ions) zeolites. Alternatively, TMI can be directly inserted during the synthesis into framework positions, resulting into neutral frameworks in the case of tetravalent ions (as for Ti^{IV} in TS-1) or in negatively charged frameworks usually compensated by protons or other cations in the case of trivalent ions as in the case of Fe^{III} in Fe-zeolites. This TMI incorporation within frameworks is usually found in MeAlPO zeotypes, where redox-active TMIs can be easily and reversibly converted between the +2 and +3 oxidation state (as in the case of CoAlPO, MnAlPO, FeAlPO, etc. [1–4]) depending on the activation treatment. This also implies the generation of

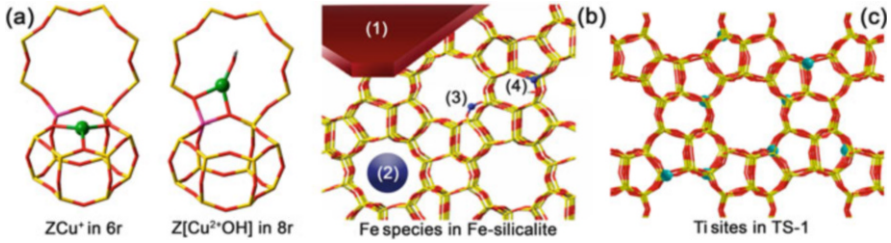

Fig. 1 Examples of possible transition metal ion (TMI) location and structures in different zeolites active in selective oxidation reactions. (**a**) Metals introduced as counterions by ion exchange: density functional theory (DFT)-optimized structures of Cu^{I} and $[CuOH]^{+}$ sites stabilized by one negative framework charge (Z) in the 6r and 8r units of CHA framework (Cu in green, Si in yellow, O in red, Al in pink, H in white). (**b**) Variety of species observed in thermally treated Fe-silicate samples: (1) Fe_2O_3 particles on the zeolite external surface, (2) Fe_xO_y clusters, (3) grafted Fe^{II} dispersed in the pores, and (4) framework Fe^{III} (Fe in blue, O in red, Si in yellow). Reproduced from [10] with permission from the PCCP Owner Societies. (**c**) Representation of the isomorphous substitution of Si atoms of MFI framework by Ti^{IV} in TS-1 (Ti in light blue, O in red, Si in yellow)

Brønsted acid sites when the TMI is reduced to the divalent state. This class of materials is extensively discussed in this book in the chapter by Sankar and will thus not be addressed hereafter. It is only important to mention that the reactivity of TMIs introduced as heteroatoms in zeolites is different with respect to what has been observed in AlPOs. Namely, Ti^{IV} in TS-1 is stable in framework positions and cannot be reduced to Ti^{III} (at variance with what observed in TiAlPO-5 [5–8]), while Fe^{III} is not stable as heteroatom and moves to extraframework positions generating a variety of Fe^{II}/Fe^{III} species during thermal treatments, as extensively discussed in Sect. 3 [9, 10].

In this contribution, we will thus mainly deal with Cu-exchanged zeolites, which are being deeply investigated in recent years for the direct conversion of methane to methanol (MTM) using O_2 as oxidizing agent, and with Fe-zeolites (both prepared by direct synthesis and ion exchange) which are instead active in the same reaction using N_2O or H_2O_2. Moreover, a section will be devoted to TS-1, which is active in selective partial oxidation reactions (e.g., in the epoxidation of propylene) using H_2O_2 as oxidizing agent. Examples of possible location and structures of TMI ions in the three different case studies are shown in Fig. 1.

1.2 Main Characterization Techniques

Usually, the routine characterization of this class of zeolite-based catalysts includes textural and structural properties (specific surface area, porosity, and crystallinity). Moreover, X-ray diffraction (XRD) can be also employed to assess the positions of counterions into the zeolite channels and pores or reticular positions. However, in this chapter, we will mainly focus on the characterization results concerning the structure and properties of the redox-active centers, which are usually studied by

spectroscopic techniques. Namely, these are diffuse reflectance UV-Vis (for information on the TMI oxidation state and ligand symmetry); X-ray absorption and emission (oxidation state and geometry, detailed information on the shells of ligands surrounding the metal center); Raman, also in resonance mode (nature of oxo moieties); and infrared (mainly indirect information on oxidation, coordination, and nuclearity by using probe molecules).

To give a realistic description of the active sites during the reaction, these techniques are often used in operando or in situ conditions. These approaches represent the current frontier for the application of spectroscopic techniques, since their goal is the characterization of the catalytic system while chemical reaction/transformations are occurring (i.e., calling for a significant time resolution). Furthermore, the complexity of the reaction environment (potentially aggressive chemicals are present; high temperature and/or pressure is requested) leads to the development of specific spectroscopic setups able to deal with it. Despite such difficulties, in situ and operando approaches open to valuable information, poorly accessible through conventional methods: some relevant examples will be given along this chapter. Information on the metal ions' redox properties and activity obtained by different techniques, such as electron paramagnetic resonance (EPR) and Mössbauer spectroscopies, will be also mentioned, where relevant.

For more details about the concepts, experimental setups, and issues related to the use of spectroscopies in operando or in situ conditions, readers are referred to [11–14] (DR UV-Vis), [11, 13–17] (Raman), [11, 14, 18] (XAS), and [17, 19, 20] (infrared).

2 Transition Metal Ion-Exchanged Zeolites for Direct Conversion of Methane to Methanol

The direct conversion of MTM represents an important challenge among partial oxidation reactions. This can be considered as a "dream reaction," in relation to the higher chemical inertness of the reactant with respect to the product [21]. Indeed, methane is a symmetric molecule, without low-energy empty orbitals and high-energy filled ones, and is characterized by the highest C-H bond energy among hydrocarbons (413 kJ mol^{-1}). On the contrary, methanol is characterized by a significant dipole moment, and it interacts more easily with available active sites on the catalysts. Thus, kinetic protection or selective separation of the product is necessary to avoid over-oxidation [22]. Moreover, if molecular oxygen is selected as the oxidant, several fundamental issues are encountered: (1) O_2 is a four-electron oxidant that needs to be used as a two-electron one; (2) the reaction has an unbalanced stoichiometry – there is one extra oxygen atom for each molecule of methanol produced; (3) since CH_4 and CH_3OH possess singlet ground states, the reaction is spin forbidden when O_2 is used as terminal oxidant, the so-called spin dilemma [23].

The current industrial process for methane conversion is based on steam reforming to form syngas (a CO/H_2 mixture), which is then converted to methanol.

This two-step process is demanding in terms of energy supply, materials, and technology, due to the high temperature and pressure required. A more direct and less energy-intensive conversion of MTM is thus desirable, particularly to exploit methane where it is naturally abundant. Based on recent estimations, 140 billion cubic meters of methane (approximately 1/3 of the annual methane consumption of Europe) per year are flared or vented into our planet atmosphere [24]. This is not only a waste, but has also a tremendous effect on climate change, considering that methane has a global warming potential 20 times higher than CO_2. Its direct conversion on-site into liquid methanol, an important feedstock for the chemical industry (more than 48 million tonnes produced yearly [25]), would also solve the safety and cost issues related to storage and transport.

In this context, in 2005 medium and large pore Cu-exchanged zeolites (MFI and MOR) were first shown to be able to form methanol upon methane adsorption on samples pretreated in O_2 by Groothaert et al. [26]. Many other reports followed about Cu-zeolite materials, which will be reviewed hereafter. However, it is worth to mention that other TMI containing zeolites were proposed for the same reaction. Namely, Fe-containing zeolites were shown to catalyze the MTM conversion when using N_2O as oxidizing agent, since the pioneering work by Panov and coworkers [27–29]. However, in this case, the interest moved to the application of the same materials in the N_2O-mediated benzene to phenol conversion, due to the difficulties related to methanol extraction from the catalysts' surface [30, 31]. More recently, the same materials were shown to be able to partially oxygenate methane at low temperature with H_2O_2 [32]. In this case, Cu^{II} ions were added to Fe-MFI systems to avoid over-oxidation and obtain 90% selectivity to methanol. Other examples of TMI-containing zeolites for the methane oxidation with O_2 include Co-ZSM-5 [33, 34] and Ni-ZSM-5 [35]. In the following paragraphs, the main results discussed in the literature about the characterization of active sites or active site precursors in Cu-zeolites will be discussed.

2.1 *Cu-Zeolites with O_2 as Oxidizing Agent: The Starting Point*

The first report about the potentiality of Cu-exchanged zeolites in the selective oxidation of methane appeared in 2005 [26]. In their short communication, Groothaert et al. studied the reactivity of methane on an O_2-activated Cu-ZSM-5 sample (MFI framework, Cu/Al = 0.6, Si/Al = 12). Low-temperature (125°C) CH_4 dosage resulted in the formation of methanol, which was extracted from the catalysts' surface in a solvent mixture. The intensity of the UV-Vis band at 22,700 cm^{-1}, which is peculiar of the O_2-activated Cu-ZSM-5 samples [36, 37], was shown to decrease upon methane exposure (Fig. 2a), and a correlation between the intensity of this band in samples with different Cu content and their methanol productivity was also reported. Moreover, Cu-MOR (Si/Al = 9, Cu/Al = 0.43) which is characterized

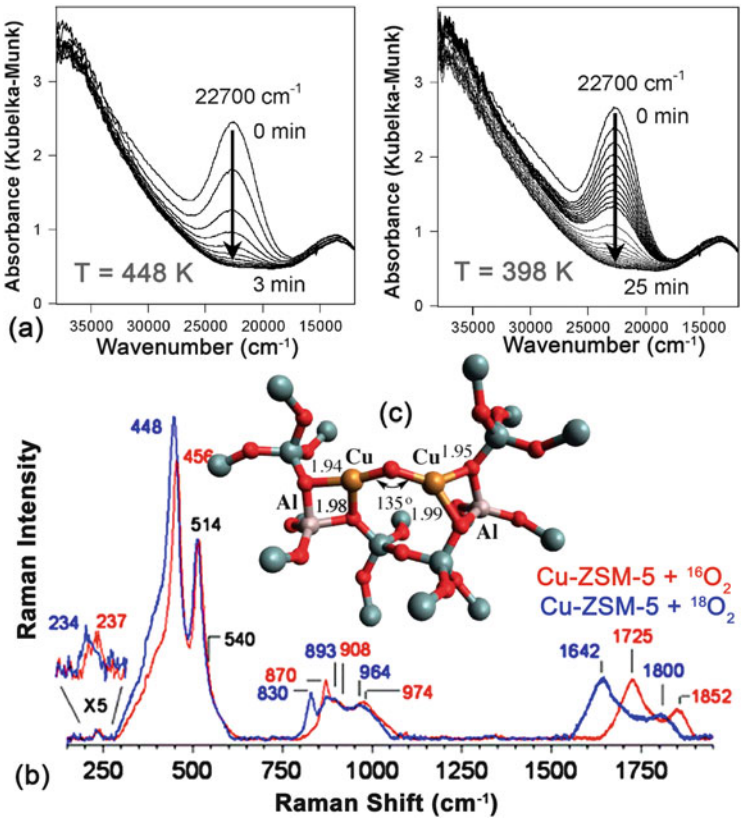

Fig. 2 Spectroscopic fingerprints and proposed structure of copper cores in O_2-activated Cu-ZSM-5: (**a**) UV-Vis fingerprint at 22,700 cm^{-1}, evolving during CH_4 contact at different temperatures. Adapted with permission from [26]. Copyright 2015 American Chemical Society. (**b**) rR spectra in the presence of $^{16}O_2$ (red) and $^{18}O_2$ (blue). Adapted from the Journal of Catalysis, vol 284, P. Vanelderen et al., Cu-ZSM-5: A biomimetic inorganic model for methane oxidation, 157–164, Copyright 2011, with permission from Elsevier [38]. (**c**) DFT-optimized model for the mono(μ-oxo)dicopper core (Cu atoms in yellow, Si atoms in gray, Al atoms in white, O atoms in red). Reprinted with permission from [39]. Copyright 2014 American Chemical Society

by an intense band at 22,200 cm^{-1} when oxidized resulted in even higher methanol yield with respect to Cu-ZSM-5, at variance with inactive Cu-Y and Cu-silica [26].

On these bases, the UV-Vis feature at 22,700–22,200 cm^{-1} was proposed as a fingerprint of the active Cu-oxo precursors. The structural assignment of the spectroscopic feature was based on the comparison with thoroughly characterized Cu cores in enzyme and synthetic models, with the support of EPR and XAS results [40]. More in detail, a Cu-Cu second shell distance ~2.86 Å was measured by EXAFS in a series of Cu-ZSM-5 samples with a Cu/Al ≅ 0.6 (Si/Al = 12 and 31). This was compared with the same parameter in bis(μ-oxo)dicopper $[Cu_2(\mu\text{-}O)_2]^{2+}$

cores in synthetic model complexes [41, 42] and with the (μ-η^2:η^2-peroxo)dicopper $[Cu_2(\mu\text{-}\eta^2\text{:}\eta^2\text{-}O_2)]^{2+}$ active sites in proteins (hemocyanin, tyrosinase, and catechol oxidase) [43] and in synthetic models [44]. The Cu-Cu distance in both planar and bent (μ-η^2:η^2-peroxo)-dicopper complexes was found to be higher with respect to that measured in Cu-ZSM-5 (3.2–3.8 vs 2.79–2.92 Å), pointing to the presence of the bis(μ-oxo)dicopper core (2.73–2.91 Å) in the zeolite. This was found to be in agreement with the spectroscopic features of the synthetic complexes (particularly a relatively intense band in the 22,300–25,000 cm^{-1} range) and with a negative correlation with the EPR signal intensity. The latter was explained on the basis of ab initio calculations indicating a singlet ground state for the bis(μ-oxo)dicopper (structure **A** in Scheme 1) [42].

Notwithstanding the similarities of spectroscopic features and structural parameters described above, the presence of bis(μ-oxo)dicopper cores in Cu-ZSM-5 still presented some weaknesses/inconsistencies. First, the oxidation state indicated by XANES data was found to be lower than the formal Cu^{III} expected for the bis(μ-oxo) dicopper cores (four electrons would need to be transferred from the O_2 ligand to Cu^{I} ions during the oxidation treatment), and this was explained by the twofold coordination of framework oxygen ligands, carrying a negative charge. Moreover, the authors clearly stated that the resulting XAS data were averaging a mixture of both dicopper and monomeric Cu sites, so that the measured Cu-O coordination number of 4.5 was explained with a mixture of fourfold-coordinated Cu ions in the bis (μ-oxo)dicopper cores (two O ligands from O_2 and two from the framework) and fivefold-coordinated monomeric Cu^{II} ions [40]. Even if there are examples in the literature about metal ions coordinated by several of the O atoms forming the zeolite rings, this explanation is somewhat doubtful for Cu^{II} ions in ZSM-5. Indeed, these were shown to be able to accommodate up to three CO ligands, suggesting a highly unsaturated coordination sphere [37]. Also, even if the authors addressed this aspect by invoking the probability of having short-distance Al-Al pairs ($r < 5.5$ Å) in ZSM-5 even at high Si/Al ratio, this seems highly unlikely in a sample with

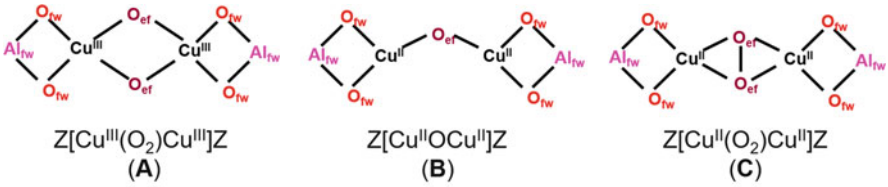

Scheme 1 Binuclear structures proposed as active sites in Cu-ZSM-5. Al_{fw} and O_{fw} represent Al and O framework atoms, respectively, generating a negative charge which stabilizes the positively charged Cu counterions. O_{ef} indicates extraframework oxygen atoms, resulting from the interaction with O_2. (**A**), bis(μ-oxo)dicopper core proposed in [26]; (**B**), mono(μ-oxo)dicopper core proposed in [45]; (**C**), μ-(μ^2:μ^2)peroxodicopper core [46]. The displayed charge of the Cu counterions has been calculated assuming an overall neutral structure, considering −2 as formal charge for μ-oxo ligands and −1 for the peroxo one (see Sect. 2.2 for comments about the alleged Cu^{III} ions in structure **A**).

Si/Al = 31, which showed the same (or similar) UV-Vis and XAS features as described above [47].

One of the main problems in establishing the nature of active sites in catalysis is related to the "single-site" issue, in that most catalysts are often characterized by a variety of sites with different coordination number, ligand geometry, and nuclearity. This implies the intrinsic difficulty in discriminating active sites from "spectators." This also holds for metal-exchanged zeolites, even if they can be often considered as model systems, due to the fact that TMIs are easily stabilized as counterions and many structural information can be found in the literature about their location in the zeolite channels and cavities (see, for instance, [48, 49]). In this case, the distribution of TMIs is affected by the zeolite topology and chemical composition, that is, Me/Al and Si/Al ratios. The influence of chemical composition on the distribution (and redox behavior) of Cu ions in the CHA framework has been recently addressed by Paolucci et al. in the field of the selective catalytic reduction (SCR) of NO_x [50]. The same authors demonstrated that, under reaction conditions in Cu-CHA, multinuclear sites are reversibly formed from mobilized single atoms. This implies that in SCR reaction, the Cu-zeolite cannot be considered as a "single-site catalyst." Moreover, the authors pointed out that the dynamic of Cu ions "falls outside the conventional boundaries of a heterogeneous or homogeneous catalyst" [51]. Even if these works focus on a different reaction, they clearly indicate the difficulty in pinpointing the "true" active sites in complex systems, so that a multi-technique approach, often coupled to modeling, is fundamental to get a realistic picture of the studied system.

This problem is also evident while studying Cu-zeolites in the MTM reaction. Indeed, the reaction should be in principle ideal for characterization studies since it is not a real catalytic process but a multiple step one, including (1) pretreatment of the catalyst in O_2, (2) methane dosage, and (3) subsequent methanol extraction. However, the reaction yield is quite low, in that the methanol productivity normalized to Cu content is often below 0.1 mol_{CH3OH}/mol_{Cu} [26, 52], with the highest values reported up to now of 0.20 [53] and 0.35 mol_{CH3OH}/mol_{Cu} [54, 55] on Cu-ZSM-5 and Cu-MOR, respectively. This would imply that, assuming that one copper atom is needed to produce one methanol molecule, only a small fraction of Cu (varying from 10 to 30%, depending on the zeolite topology, pretreatment, and reaction conditions) is active in the title reaction. On the contrary, the 0.35 mol_{CH3OH}/mol_{Cu} productivity measured in MOR was interpreted by Grundner et al. as a proof of the presence of single-site trinuclear copper oxygen clusters [54, 55]. The lively debate about the different structures proposed as active Cu-oxo sites in the title reaction, following the first hypothesis of a bis(μ-oxo)dicopper core mentioned above, will be thus reviewed in the following section, trying to focus on weak and strong points of each hypothesis and of the corresponding characterization techniques.

2.2 *Nature of Cu-Oxo Species in Medium and Large Pore Zeolites: Cu-ZSM-5 and Cu-MOR*

As mentioned above, the first structure proposed as active site for the MTM reaction in Cu-zeolites is the bis(μ-oxo)dicopper core (structure **A** in Scheme 1). This structure however poses a problem about the charge of the involved Cu ions. Structure **A** can indeed be labeled as $ZCu^{III}(O_2)Cu^{III}Z$, where Z stands for a negative charge on the framework oxygen atoms (O_{fw}), generated by the presence of one Al^{III} heteroatom (A_{fw}). Since the formal charge of oxygen in the μ-oxo ligands is −2, a total −6 charge should be compensated by the two trivalent Cu ions, without any evidence for this unusual oxidation state in zeolites. This assignment was thus successively called into question by the same authors who firstly proposed it, thanks to the use of resonance Raman (rR), in collaboration with Solomon's group [45]. Namely, the rR spectra of an O_2-activated Cu-ZSM-5 were found to be well correlated with the intensity of the UV-Vis band at 22,700 cm^{-1} (Fig. 2a), which in turn was confirmed to be related to the active sites in the methanol formation on the basis of kinetic isotope effect (KIE) analysis as a function of reaction temperature.

The authors pointed out that EXAFS alone cannot provide structural information on the structure of the active Cu core, since this accounts for only a small fraction of the total Cu content (~5% in the studied Cu-ZSM-5, based on the methanol productivity). Being an average technique, EXAFS cannot distinguish the contribution of a minority of active sites from that of abundantly present spectator ones. The main rR bands at 456, 870, and 1,725 cm^{-1} could be safely assigned to a bent mono(μ-oxo) dicopper core (structure **B** in Scheme 1), based on the spectral changes observed when using a mixed isotope $^{16}O_2/^{18}O_2$, which clearly pointed to exclude the presence of μ-1,2-peroxo or hydroperoxo dicopper sites (Fig. 2b). Moreover, normal coordinate analysis (NCA) and density functional theory (DFT) calculations pointed to a Cu-O-Cu bending angle around 140°, which could only be compatible with a mono(μ-oxo) compound (Fig. 2c). Indeed, a Cu-O-Cu angle of 100° was found to be responsible for the Raman band around 600 cm^{-1} typical of bis(μ-oxo)dicopper cores, where the insertion of a second oxo ligand causes the tightening of the bending angles. A μ-(μ^2:μ^2)peroxodicopper core (structure **C** in Scheme 1) was also observed on a pre-reduced Cu-ZSM-5, after O_2 treatment at room temperature (RT). This is characterized by a broad UV-Vis absorption centered at 29,000 cm^{-1} and by rR bands at 736 and 269 cm^{-1}, and it was proposed as a precursor of the mono(μ-oxo)dicopper active sites [46]. For a more comprehensive review of the spectroscopic fingerprints and Cu··Cu distances of mono and dinuclear Cu/O_2 complexes, readers are referred to the following [37, 38, 56, 57].

The mono(μ-oxo)dicopper core (structure **B**) was also proposed as active site in Cu-MOR, which is characterized by larger pores with respect to ZSM-5 and by a higher density of actives sites [58, 59], resulting in the highest reported values of normalized methanol productivity (mol_{CH3OH}/mol_{Cu}) [54, 55]. Indeed, Cu-MOR is characterized by spectroscopic features very similar to Cu-ZSM-5: a UV-Vis band centered at 22,200 cm^{-1} and isotope sensitive rR bands at 450, 850, 1,700, and

1,850 cm^{-1} [60]. Based on the differences between spectra measured in O_2 at different temperatures, it was proposed that the UV-Vis feature in MOR is composed of two components, one centered at 21,900 cm^{-1}, unstable above 330°C, and a persistent one with maximum at 23,000 cm^{-1}. Moreover, kinetic measurements showed that the two copper sites responsible for these bands have different activation enthalpies for methane oxidation. The proposed bent mono(μ-oxo)dicopper core (structure **B**) was found to be very similar to those present in ZSM-5, regarding geometry (Cu-O-Cu bending angle) and electronic structures, so that the different kinetic behavior was explained invoking second-sphere effects related to the zeolite topology [60].

The $[Cu_2O]^{2+}$ core (**B**) in ZSM-5 is proposed to be located at the intersection of straight and sinusoidal ten-membered rings (10r) (Fig. 2c) [39, 45]. Namely, the Cu··Cu distance in the binuclear Cu^I precursor is 4.17 Å, which is reported to be in agreement with the location of Cu^I sites determined by crystal structure analysis [61]. In this structure, Cu ions have a twofold coordination to O_{fw}, with a $O_{fw(Si)}$-Cu-$O_{fw(Al)}$ bite angle ~149° and a Cu-O-Cu bend angle in the $[Cu_2O]^{2+}$ core of 135°. This structure was found to be more stable with respect to other possible structures in the MFI framework, indicating that it is stabilized by a particular framework structural entity.

A similar conformation of O_{fw} was searched for in the MOR framework, notwithstanding the differences in pore size (10r in ZSM-5 vs 12r in MOR) and pore connectivity (3D pore system consisting of straight 10r channels connected by sinusoidal ones vs straight 12r channels with 8r side pockets). Two possible structural motifs were identified at the intersection of the side pocket with the 12r and 8r channels, with adjacent Al framework atoms (Al-Si-Si-Al units with Al··Al distances around 7.55 Å, similarly to what was calculated for ZSM-5) located at the T3 or T4 tetrahedral sites. Thus, the proposed mono(μ-oxo)dicopper core (structure **B**) would be formed at specific framework structural motifs, identified in both ZSM-5 and MOR, with a very precise structural and electronic configuration. The observed differences in activity could be then ascribed to second-sphere effects, meaning that the zeolite lattice could play a role analogous to the active pocket of a metalloenzyme (directing methane approach to the active site, stabilizing transition states, etc.) [60]. The same $[Cu_2O]^{2+}$ core (**B**) in ZSM-5 was also shown to be formed upon N_2O decomposition [39].

2.3 Studying the Modification of Cu Structure During Reaction: Operando X-Ray Absorption Spectroscopy in Cu-MOR

The characterization studies reviewed in the previous paragraph mainly focused on the structure of the Cu-oxo complexes formed during the catalysts' pretreatments in O_2, and the correlation with the catalytic activity was mainly based on kinetic

measurements concerning the evolution of the UV-Vis band around 22,000–23,000 cm^{-1} during reaction with methane [45]. A different and complementary approach to get further insights into the nature of the active sites was proposed by the group of van Bokhoven, mainly focusing on a high-loading Cu-MOR (Si/Al = 11, 4.3 Cu wt%, Cu/Al = 0.38) studied by XAS spectroscopy with the support of DFT calculations [59, 62–64]. A breakthrough communication from this group appeared in 2012, proposing methanol extraction from the surface of the catalyst by a wet stream of He [62]. This approach is alternative to the previous studies based on methanol extraction with solvents. With the goal to move from an intriguing academic playground to a process with potential industrial applications, the same group then showed the possibility to carry out reaction under isothermal conditions at 200°C [65] and very recently made a step forward by carrying out the reaction in anaerobic conditions, using water as selective oxidant [66].

Coming back to the characterization approach, the work by van Bokhoven and coworkers is mainly based on the use of XAS spectroscopy, measured in operando-like conditions, that is, while heating the sample in the presence of gas flows, monitoring the product gas with a mass spectrometer. With this setup, the authors followed the evolution of Cu oxidation state and local environment in Cu-MOR during O_2 treatment, CH_4 interaction, and steam-assisted methanol desorption. Based on the XANES spectra measured under steady-state conditions, the authors showed the reduction of a large fraction of the Cu^{II} sites formed during O_2 activation to Cu^{I}, as a consequence of CH_4 interaction at 200°C [62].

In a more detailed characterization work, the fraction of Cu^{II} reduced to Cu^{I} by CH_4 was quantified as >60%, by applying a linear combination fit (LCF) procedure to high-energy resolution fluorescence-detected (HERFD) XANES spectra [59]. The authors suggested that these could be the active sites, which modify their electronic structure during the reaction with methane, forming adsorbed product intermediates. The large discrepancy between the amount of reduced Cu^{II} sites in their Cu-MOR sample (>60%) and the fraction of active sites estimated in Cu-ZSM-5 on the basis of methanol productivity (~4%, calculated assuming two Cu sites per methanol produced [26]) was explained invoking a different cationic distribution in Cu-MOR, which is usually characterized by lower Si/Al ratios.

The reoxidation of a small fraction of Cu^{I} to Cu^{II} was also observed during extraction with water at 200°C, which was attributed to small contamination of O_2 in the wet He flow [59]. This was proposed to have important implications for a real catalytic process, since it would imply that the oxidation with O_2 at high temperature (400–500°C) is not mandatory for the catalyst reactivation in a continuous cycle, as subsequently shown in [66]. The fact that most of the XANES features remained unchanged after water interaction was explained with the difficulty (kinetic limitation) in desorbing the stable adsorbed intermediates. In the same publication, the authors also used conventional EXAFS to follow the different reaction steps in Cu-MOR [59]. As a general comment, the first shell coordination number (CN) of Cu activated in O_2 at higher temperature was between 4.5 and 5 and only slightly decreased after CH_4 interaction (3.9 ± 0.3). Even if the authors mentioned that the Cu^{II} state observed after O_2 activation is in agreement with the dicopper **B** core

proposed by the groups of Schoonheydt and Solomon on the basis of rR spectra [45, 46], it is important to point out that the measured CN of 4.5 ± 0.4 does not fit with the local environment expected for Cu^{II} in the mono(μ-oxo)dicopper core. As mentioned above, in this structure, Cu has a threefold coordination, with two O_{fw} and one O_{ef} from the oxo ligand. Moreover, the authors clearly stated that second shell contributions were barely observable and could not be unambiguously fitted [59].

A further step to follow the electronic and geometric structural changes of Cu sites in Cu-MOR during the reaction steps consisted in the use of quick XAS (time resolution of about 5 s) [63]. In the related paper, the discussion was mainly based on the XANES features, focusing on desorption of the methane conversion intermediate as methanol in the wet stream. EXAFS data were only mentioned in relation to the small changes observed in the intensity of the first and second shell of Cu sites (at 1.4 and 2.6 Å), implying no changes in the first two coordination spheres during methanol desorption, but clear information about the Cu coordination number was not given. Some representative XANES spectra measured during some of the reaction steps are reported in Fig. 3a, with labels indicating the Cu^{II} and Cu^{I} XANES fingerprints.

In the used experimental conditions, XANES LCF assessed the presence of 41% Cu^{I} after methane interaction at 200°C, with the remaining copper present as "Cu^{II}-

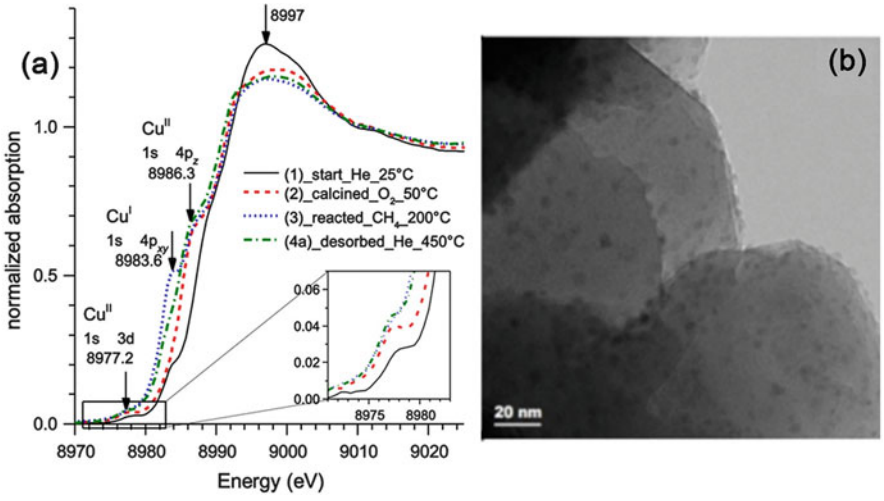

Fig. 3 (**a**) XANES spectra of Cu-MOR measured at different steps of the MTM reaction: (1) starting material at RT, (2) calcined in O_2, (3) reacted with methane, and (4) after product desorption in dry He. Arrows indicate the typical Cu^{II} and Cu^{I} XANES fingerprints with the corresponding involved core levels. Reprinted with permission from [63]. Copyright 2014 American Chemical Society. (**b**) TEM of high-loaded Cu-MOR (Si/Al = 11, Cu/Al = 0.38) after O_2 treatment at 450°C, showing the presence of small (≤3 nm) copper oxide nanoparticles. Adapted from [64] with permission of the PCCP Owner Societies. Similar results were obtained on a Cu-MOR with similar Cu loading (4.7 wt% Cu, Si/Al = 6) after activation at 200°C [65]

O-like" sites and a significant fraction (20%) of hydrated Cu^{II}. The authors observed a noticeable desorption of methanol during the first 5 min of treatment with a He flow saturated with water, which was virtually finished after 20 min [63]. At this point, the amount of Cu^{I} was found to be almost halved, indicating a reoxidation of the sites involved in the intermediate formation and methanol formation. Interestingly, together with a major amount of hydrated Cu^{II} sites (62%), a fraction of "Cu^{II}-O-like" sites was still present. Moreover, analysis of the Cu^{I} and Cu^{II}-O evolution during methanol desorption under both wet (water saturated) and dry He flows suggested that some of the latter were formed by oxidation of the former. This aspect was stressed by the authors, since the mono(μ-oxo)dicopper cores proposed by the group of Schoonheydt are supposed to be water-unstable. It was thus proposed that "Cu^{II}-O-like" sites, whose structure could not be determined, are present in Cu-MOR together with the mono(μ-oxo)dicopper **B** ones and that they are also active for methanol formation [63].

Notwithstanding these evidences, the main XANES results were interpreted in terms of the mono(μ-oxo)dicopper **B** core, with the support of DFT calculations [63]. Namely, the reduction of half of Cu^{II} to Cu^{I} during methane flow was explained with the formation of a mixed-valent dicopper [Cu^{I}-OCH_3-Cu^{II}] stable methoxy intermediate, with the abstracted H atom stabilized as [Cu^{I}-OH-Cu^{II}] on vicinal Cu··Cu pairs. This would imply that, apart from a minor fraction of the "Cu^{II}-O-like" sites resistant to hydration, most of copper ions in the zeolite are involved in the reaction. This hypothesis cannot completely explain the generally low methanol productivity of Cu-zeolites (up to 0.20 and 0.35 mol_{CH3OH}/mol_{Cu} for MFI and MOR, respectively [53–55]). A different interpretation of operando XAS data during the reaction was very recently proposed by Pappas et al. on small-pore zeolite Cu-CHA, as will be discussed below [57].

A similar approach (in situ time-resolved XAS measurements coupled to DFT calculations) was successively used by the same authors to shed new light into the generation of the Cu-oxo active sites prior to methane activation [64]. The work was mainly inspired by the study from Smeets et al., who followed by diffuse reflectance (DR) UV-Vis and rR the formation of the mono(μ-oxo)dicopper **B** core, passing through the evolution of the μ-(μ^2:μ^2)peroxodicopper **C** precursor, by dosing O_2 on a pre-reduced Cu-ZSM-5 [46]. The possible mechanisms for Cu^{II} self-reduction during dehydration (disproportionation and condensation) were briefly discussed, starting from a $[CuOH]^+$ site, similarly to what was well established in Cu-CHA [50, 67]. The authors followed and compared Cu-MOR activation in He and O_2, with the aim to determine the minimum temperature for self-reduction and active site formation (estimated in 200°C). Moreover, LCF was again applied to XANES spectra to quantify the amount of Cu^{I} sites formed by self-reduction in He stream at this temperature, which are supposed to be able to activate O_2 forming the active Cu-oxo sites. The obtained amount (43%) was in good agreement with the fraction of copper sites (>40%) reduced upon methane interaction, supporting the hypothesis that these are the active site precursors [64].

Concerning EXAFS data, the authors included in the fitting model up to four shells in the coordination sphere of Cu when heated in O_2, including two shells of Cu atomic neighbors, which were taken as an indication of the presence of Cu··Cu

dimers. The presence of an O_{ef} scattering path (at longer distance with respect to O_{fw}) was related to a bridging oxo ligand, even though the technique could not discriminate between the bis and mono(μ-oxo)dicopper cores (**A** and **B**) previously proposed in the literature. This aspect was thus dealt with by DFT calculations, which showed how the mono(μ-oxo)dicopper **B** core is favored in zeolites, at variance with homogeneous complexes where the most stable structure is the bis (μ-oxo) one [64].

The XAS features described above for a high Cu-loaded Cu-MOR, namely, a high average coordination number for the oxygen shell (ca 3.2) and small changes in the local geometric coordination sphere of Cu while heating or during the reaction, were successively found to be in agreement with the presence of significant fraction of copper oxide clusters and particles [65]. TEM analysis measured on Cu-MOR after activation at 200°C clearly showed the presence of finely dispersed nanoparticles, too small to be detected by XRD ($\leq$3 nm, with a fraction smaller than 1 nm, Fig. 3b). The authors thus proposed that the observed copper oxide clusters/nanoparticles were active after activation in O_2 at 200°C, in the presence of high methane pressure (36–50 bar).

The DR UV-Vis spectra of Cu-MOR after activation at 200°C mainly consisted in a broad band centered around 13,000 cm^{-1}, which was assigned to Cu^{II} sites stabilized by one and two negative charges on the framework (i.e., in correspondence of one or two Al_{fw} atoms) [65]. Due to the absence of the fingerprint around 22,200 cm^{-1}, it was proposed that the mono(μ-oxo)dicopper cores, which are active at low methane pressure, are only formed after high temperature activation (450°C) [64]. On the contrary, the small copper oxide particles observed after activation at 200°C become active only in the presence of high reactant pressure. These results are in agreement with that previously reported by Beznis et al. on Cu-ZSM-5, who proposed that copper oxide clusters dispersed on the zeolite outer surface (observed by TEM) were not involved in the selective oxidation of methane at ambient pressure [36].

Other interesting and new characterization results were reported by Sushkevich et al., showing the possibility to carry out MTM conversion with water in anaerobic conditions [66]. The authors followed by XANES the redox changes undergone by copper during reaction with methane and successive interaction with water vapor, confirming the $Cu^{II}/Cu^{I}/Cu^{II}$ redox cycle during O_2 activation/CH_4 interaction/wet stream desorption. Importantly, thanks to in situ FTIR spectroscopy it was possible to follow the formation of molecular methanol and methoxy groups adsorbed on the catalyst surface during methane interaction. The growth of the bands related to reaction products was accompanied by a parallel increase of the typical OH stretching (νOH) of Si(OH)Al Brønsted sites. This indicates that the C-H cleavage corresponds to the formation of methoxy groups stabilized by copper sites and Brønsted sites formation, giving important information about the reaction mechanism. The authors also used CO and NO probe molecules to follow the changes of copper oxidation state during the reaction, to give further support to the changes observed by XANES [66]. For details about the typical spectral features and information which could be obtained with these techniques, readers are referred to the work by Giordanino et al. and references therein [37].

2.4 *Nuclearity of Cu-Oxo Active Sites: Size Matters?*

The characterization results described in the previous paragraphs were mainly based on the hypothesis of dinuclear Cu-oxo cores as active sites (Scheme 1), focusing on the electronic and geometric structure of the selective oxo ligand(s). This hypothesis was not called into question even when the authors observed different Cu sites, such as the copper oxide clusters reported by van Bokhoven and coworkers [65]. Indeed, the works from van Bokhoven's group are mainly based on XAS spectroscopy, which being an average technique cannot by itself discriminate between active and spectators sites, especially if the former are a minor fraction.

A different hypothesis about the structure of active Cu-oxo sites in large pore MOR and medium pore ZSM-5 zeolites was put forth in the group led by Lercher [54, 55, 68, 69]. In their very important contribution in Nature Communications, Grundner et al. based their discussion on the correlation between methanol yield and Cu concentration, in Cu-MOR with different Si/Al ratios [55]. This resulted in a linear correlation, with a slope around 0.33, which was taken as an indication that three atoms of Cu are needed to form one methanol molecule (Fig. 4b). Importantly, the reported methanol productivity is the highest so far reported in the literature (0.35 mol_{CH3OH}/mol_{Cu}, corresponding to 160 μmol/g), which was explained on the basis of the peculiar MOR topology motif and the controlled exchange procedure, minimizing copper hydrolysis and precipitation and the competition from alkaline cations. More in detail, the authors used infrared spectroscopy to quantify the amount of framework Al atoms (Al_{fw}) stabilizing Cu ions, by measuring the amount of Brønsted acid sites before and after Cu exchange on a sample with Si/Al = 11 and different Cu/Al ratios (Fig. 4a). Moreover, the use of different probes (pyridine and n-hexane) allowed the authors to conclude that Cu ions are preferentially exchanging

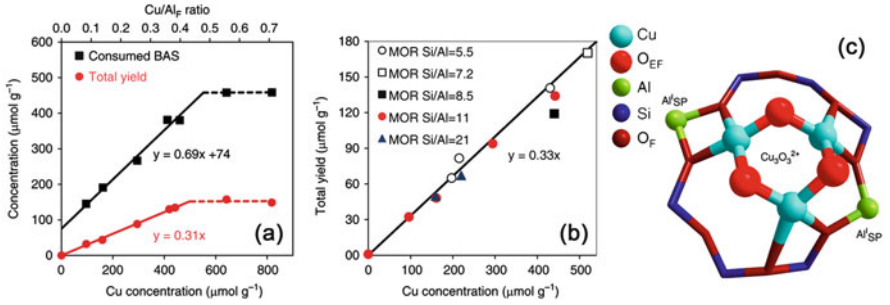

Fig. 4 (**a**) Estimation of the number of residual Brønsted acid sites measured by pyridine adsorption on a sample with Si/Al = 11 and different Cu/Al ratio (square symbols). The slope of 0.69 indicates that 2 H^+ are exchanged by three Cu ions; methanol yield on the same samples (circles). (**b**) Methanol yield as a function of Cu concentration on samples with different Si/Al ratios. The slope of 0.33 suggests that three Cu atoms are needed to obtain one methanol molecule. (**c**) DFT-optimized structure of the tris(μ-oxo)tricopper core (**D**) stabilized by two Al_{fw} at the 8r entrance of MOR side pocket (SP). The three active O_{ef} ligands point to the main 12r channel. From Grundner et al. [55], licensed under CC BY 4.0 (http://creativecommons.org/licenses/by/4.0/)

Brønsted sites located near the 8r pore mouth of the MOR side pockets. They also proposed that the exchange selectivity is related to the relatively high concentration of Al_{fw} in the side pockets (65% of the total, giving the Brønsted νOH band at 3,590 cm^{-1}). These considerations were supported by the observation that the νOH band related to the Brønsted sites in the main 12r channels (3,612 cm^{-1}) was not affected by Cu ion exchange. The quantitative data obtained from the abovementioned studies pointed to the conclusion that two Brønsted sites stabilize three Cu ions, which act as trinuclear single sites in the MTM reaction (core **D** in Scheme 2). This hypothesis was further supported by the observation that a majority of Al_{fw} atoms in samples with Si/Al 11 and 21 are separated by only one or two Si framework atoms.

These interesting findings were rationalized in terms of tris(μ-oxo)tricopper $[Cu_3(\mu\text{-}O)_3]^{2+}$ complexes, on the basis of DFT calculations (structure **D**, Fig. 4c). The structure obtained by DFT, characterized by a low symmetry (i.e., the Cu atoms in the clusters are not equivalent), was found to fit well with the EXAFS data measured on an O_2-activated Cu-MOR. More in detail, different Cu-O distances were fitted in the first shell, in agreement with the presence of O_{fw} and O_{ef} ligands. This was fitted assuming both Cu-Cu and Cu-O scattering path in a low symmetry core, that is, with a nuclearity higher than 2. Importantly, the authors acknowledged the intrinsic limitation of XAS spectroscopy, which gives an average information on all present Cu sites. However, the clear correlation between Cu loading and productivity allowed them to conclude that the analyzed data were related to a trinuclear single site [55].

Interestingly, the authors observed in in situ XAS studies that a second shell in the coordination sphere of Cu is starting to develop at 200°C, indicating that the Cu^{II} ions are moving to form stable oxo clusters in O_2 from this temperature [55]. In the same conditions, the band at 22,700 cm^{-1} assigned to the mono(μ-oxo)dicopper core (structure **B**) was not observed, in agreement with that found by Tomkins et al. [65]. Instead, a broad component was found at 31,000 cm^{-1}, slowly decreasing upon methane interaction. No significant changes were observed in the EXAFS spectra during the same treatment, suggesting that the local structure of copper is not affected by the formation of oxidized adsorbed intermediates.

In another interesting contribution from the same research group, EXAFS was used to assess the presence of tris(μ-oxo)tricopper complexes also in Cu-ZSM-5. In

Scheme 2 The tris(μ-oxo) tricopper core (**D**) proposed by Lercher and coworkers in Cu-MOR [55]

this sample, the trinuclear cores were proposed to coexist with mono and dinuclear clusters, or with copper oxide nanoparticles, depending on Cu loading. Moreover, 50% of the $[Cu_3(\mu\text{-}O)_3]^{2+}$ cores were found to be inactive, suggesting that the reactivity is not only related to the cluster structure, but it is strongly influenced by the ability of the zeolite framework to stabilize them [69].

The intriguing debate about the nuclearity of active copper sites was then addressed by modeling, considering Cu location, structure, and reactivity on different zeolite topology such as MFI [68], MOR [70], and on a series of zeolites with different pore sizes and shapes (MOR, MFI, CHA, AFI, and TON) [71]. A detailed computational study about the structure and reactivity of the mono(μ-oxo)dicopper and tris(μ-oxo)tricopper complexes (structures **B** and **D**, respectively) in Cu-ZSM-5 was carried out by Li et al. [68]. The γ-site, with two Al sites at T7 and T2 lattice positions of the sinusoidal channel of MFI framework, was proposed as representative location for the di- and trinuclear oxo complexes. These were supposed to be formed via self-organization of extraframework mononuclear Cu sites during high temperature activation in O_2. Based on thermodynamic analysis, $[Cu_3(\mu\text{-}O)_3]^{2+}$ structures were found to be more stable at high O_2 pressure, while relatively low chemical potential of O_2 would favor the formation of $[Cu(\mu\text{-}O)Cu]^{2+}$ clusters.

Interestingly, computed Bader atomic charges showed for both complexes a formal charge different from that expected from stoichiometry (two Cu^{II} in the **B** binuclear core, two Cu^{III} and one Cu^{II} in the **D** trimer). Indeed a Bader charge around $-0.7/-0.77$ *e* was calculated for the oxo ligands (di- and trinuclear, respectively), which is lower in comparison to the value of -1.09 *e* for CuO. This points to a radical character of the bridging O_{ef}, necessary to promote homolytic C-H activation and cleavage. This would result in Cu^{II}/Cu^{I} formal charge in the dimer and of a mixture of Cu^{II}/Cu^{I} in the trinuclear. Both structures were however found to be stabilized by charge delocalization, making the Cu sites indistinguishable. Finally, the activation barrier for C-H cleavage was found to be sensibly lower (and close to the experimental value of 64–68 kJ/mol) for the tris(μ-oxo)tricopper **D** complexes with respect to the mono(μ-oxo)dicopper **B** ones. The formation of methanol was proposed to involve the direct radical rebound mechanism for the former and the formation of strongly adsorbed methoxy groups on the latter [68].

In answer to this interesting report, a DFT-based geometry optimization was successively reported by Palagin et al. for Cu-MOR [70]. The authors observed a general trend in the relative stability of copper oxide clusters, with tetra- and pentamers in the 8r channel of MOR being more stable than dimers. This would suggest that, by carefully tuning Al_{fw} content and distribution, one could design catalysts embedding large clusters, stabilized by multiple Cu-O linkages, and allowing for the stabilization of the OH and CH_3 fragments during methane activation, resulting in higher activity.

2.5 Cu-Oxo Moieties in Small-Pore Zeolites: Cu-CHA

Further insights about the properties of Cu-oxo complexes stabilized in zeolites came from the report by Lobo's group about the catalytic activity in the MTM reaction of small-pore zeolites and zeotypes, namely, Cu-SSZ-13 and Cu-SAPO-34 (CHA), Cu-SSZ-16 (AFX), and Cu-SSZ-39 (AEI), all characterized by 8r pore opening [72]. More in detail, the authors measured a relatively high methanol productivity on the three small-pore zeolites, ranging from 28 to 39 μmol of methanol per gram of zeolite, corresponding to 0.03–0.09 mol_{CH3OH}/mol_{Cu}. These values are considerably lower in comparison with the results by Lercher and coworkers on high-loaded Cu-MOR (Si/Al = 11 and 21, Cu/Al = 0.4 and 0.6) [55]. However, they were among the highest conversions reported at the time of publication and point to the fact that the reaction can be obtained also on small-pore zeolites, such as Cu-SSZ-13, where the presence of monomeric extraframework Cu sites had been well established by parallel studies focused on NO_x SCR [37, 50, 67, 73–78].

The DR UV-Vis spectra measured by Wulfers et al. on the tested samples after activation in O_2 are reported in Fig. 5 [72]. It is evident that the feature assigned to the mono(μ-oxo)dicopper cores at 22,700 cm^{-1} is only present in Cu-ZSM-5, which

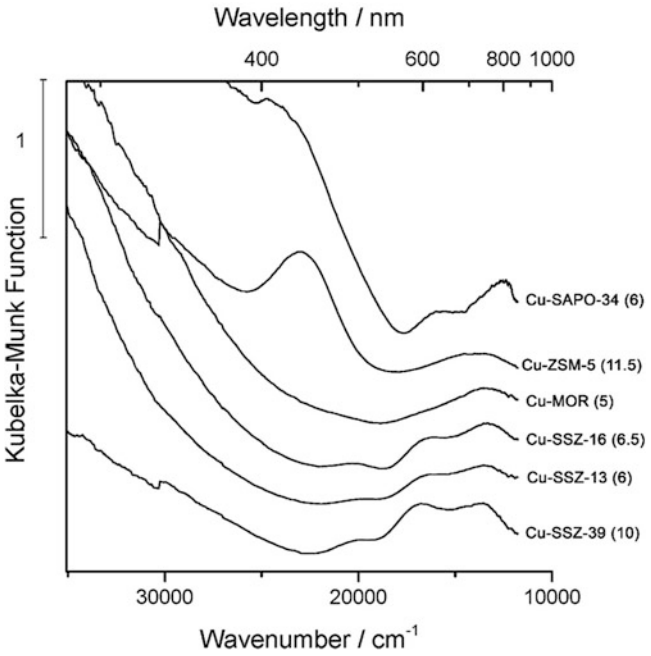

Fig. 5 DR UV-Vis spectra measured at RT on different Cu-exchanged zeolites and zeotypes after activation in O_2 at 450°C. Numbers in brackets refer to the Si/Al ratio (Al + P/Si ratio for SAPO-34). Reproduced from [72] with permission of the Royal Society of Chemistry

showed a lower or comparable productivity with respect to the small-pore zeolites tested in similar conditions (16 μmol/g, corresponding to 0.03 mol_{CH3OH}/mol_{Cu}). Moreover, the DR UV-Vis spectra of the three 8r pore zeolites are characterized by a very similar shape of the low-frequency bands, assigned to ligand field *d-d* transitions, with bands centered around 11,000, 13,600, 16,500, and 19,700 cm^{-1} (the so-called quadruplet) [37]. This would point to a similar geometry of monomeric Cu sites stabilized by the negatively charged framework. The structure of these sites will be discussed in more detail in the following section. However, it is important to underline the fact that this milestone work by Lobo's group extended the discussion about the nuclearity of Cu-oxo active sites in MTM to the lower limit, i.e., to monomeric Cu counterions. Interestingly, Cu-SSZ-13 was also shown to be active in MTM while using N_2O as oxidizing agent (methanol productivity up to 35 μmol/g) [79].

The structure of the Cu-oxo species possibly forming in Cu-SSZ-13 was analyzed by Vilella et al. by DFT calculations [71]. The authors calculated the relative Gibbs energies, geometry (Cu-Cu and O-O bond lengths), spin densities (expressed as Cu/O magnetization), and vibrational frequencies of different monomeric and dimeric Cu-oxo complexes, proposed in the literature as active sites in Cu-zeolites and experimentally characterized. The side-on $[Cu(\eta^2\text{-}O_2)]^+$ monomeric core was found to be more stable than the end-on $[Cu(\eta^1\text{-}O_2)]^+$ one (**F** and **E**, respectively, in Scheme 3). The structure of the mono(μ-oxo)dicopper cores (**B**) was also calculated, and the relative stability of $Cu_2\text{-}O_2$ complexes (which have been characterized in homogeneous complexes or enzymes but discarded as active sites in zeolites by the previously reviewed studies) compared. Moreover, the effect of the zeolite topology on the stability (and presumed reactivity) of the complexes was studied. The side-on $[Cu(\eta^2\text{-}O_2)]^+$ core (**F**) was found to be strongly bonded in correspondence of one

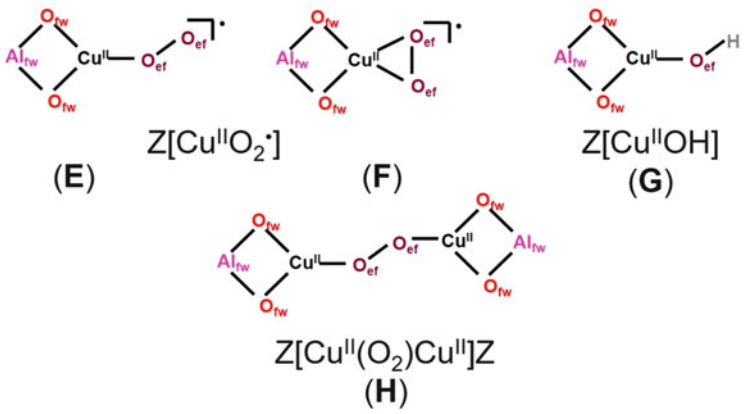

Scheme 3 Mononuclear and dinuclear Cu-oxo structures discussed in relation to small-pore zeolites, particularly CHA: **E**, side-on $[Cu(\eta^2\text{-}O_2)]^+$; **F**, end-on $[Cu(\eta^1\text{-}O_2)]^+$; **G**, $[Cu(OH)]^+$; **H**, *trans*-(μ-1,2-peroxo)dicopper cores [56, 57, 71]. Al_{fw} and O_{fw} represent Al and O framework atoms, respectively, generating a negative charge which stabilizes the Cu^{II} counterions. O_{ef} indicates extraframework oxygen atoms, resulting from the interaction with O_2

Al_{fw} atom in all the considered structures, with a higher adsorption Gibbs energy (−1.56 eV) in the 8r of CHA. On the contrary, the adsorption energy of O_2 was similar (−1.3 eV) in most of the studied structures (apart from MOR, with a value of −1.03 eV), suggesting that the framework is not affecting the introduction of the O_2 ligand on the Cu sites. Moreover, the adsorption energy of O_{ef} in the mono (μ-oxo)dicopper cores **B** was found to be lower in CHA and MOR with respect to the other considered frameworks. In small-pore CHA, the higher stability of the dinuclear core was calculated when the two Al_{fw} atoms necessary for charge compensation were spaced by three Si_{fw} atoms [71]. Further DFT calculations from the same group proposed the $[Cu(OH)]^+$ site (species **G**) as responsible for the MTM activity in Cu-CHA zeolites [80].

The stability of different Cu-oxo structures in CHA was also addressed with DFT calculations by Ipek et al., who carried out a detailed characterization work based on XRD, DR UV-Vis, and Raman spectroscopies on Cu-SSZ-13 samples with Si/Al = 12 and Si/Al = 5 [56]. The authors reported the higher stability of the $[Cu(OH)]^+$ **G** site in CHA, with respect to the mono(μ-oxo)dicopper core **B** and two slightly different *trans*-(μ-1,2-peroxo)dicopper complexes (**H** in Scheme 3), which were however proposed to be also likely present on Cu-CHA after activation in O_2 at 450°C.

The Raman feature at 617 cm^{-1} was assigned to structure **B**, while bands at 476, 510, and 580 cm^{-1} were related to complexes **H** (Fig. 6a). Moreover, the authors assigned the UV-Vis features observed on the different O_2-activated Cu-SSZ-13 catalysts at 34,700, 30,000, 19,700, 16,500, and 13,600 cm^{-1}. Based

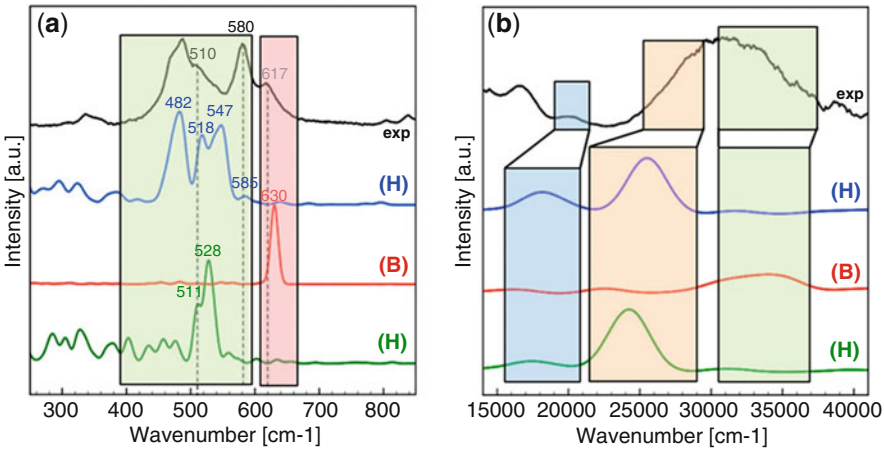

Fig. 6 Comparison of experimental and calculated Raman (**a**) and UV-Vis spectra (**b**) measured on O_2-activated Cu-SSZ-13 samples. Calculations were based on the optimized structures of the mono (μ-oxo)dicopper core **B** and two slightly different *trans*-(μ-1,2-peroxo)dicopper complexes (**H**). The experimental Raman spectrum was measured on a Cu-SSZ-13 sample with Si/Al = 12 and Cu/Al = 0.4; the plotted experimental UV-Vis is the difference spectrum between a sample with Si/Al = 12 and Cu/Al = 0.4 and one with same Al content and Cu/Al = 0.18. Adapted with permission from [56]. Copyright 2017 American Chemical Society

on the difference spectrum between two samples with the same Si/Al ratio and different Cu content, the broad absorption between 22,200 and 37,000 cm^{-1} (Fig. 6b) was assigned to the contribution of the two *trans*-(μ-1,2-peroxo)dicopper complexes **H**, which were proposed to be involved in methane activation based on their disappearance upon methane contact, and to the mono(μ-oxo)dicopper core **B**. The $[Cu(OH)]^+$ site was instead related to the *d-d* band at 13,600 cm^{-1}, not consumed during the interaction with methane [56].

Structure-activity relationships on Cu-CHA were recently addressed by Pappas et al., who combined XAS spectroscopy with a systematic work about the effect of the different experimental parameters (O_2 and methane activation temperature, partial pressure and activation/contact time, water-assisted extraction temperature) to a set of Cu-SSZ-13 catalysts with different Si/Al and Cu/Al ratios (from 5 to 29 and from 0.14 to 0.5, respectively) [57]. Infrared and rR spectroscopies were also used as complementary techniques. By optimizing the experimental conditions, the highest methanol productivity measured on Cu-SSZ-13 catalysts was obtained: 0.2 mol_{CH3OH}/mol_{Cu}, corresponding to 125 μmol/g. Similarly to what was previously done by Ayalon et al. on Cu-MOR [63], the authors followed by XANES and EXAFS the changes in the oxidation and coordination sphere of copper during O_2 activation, He flush, subsequent methane dosage, and water-mediated extraction. XANES LCF allowed estimating the relative fractions of framework-interacting Cu^{II}, hydrated Cu^{II}, and Cu^{I} sites during the different steps to be quantified, evidencing a linear correlation between the catalysts' reducibility and their methanol productivity [57].

However, at variance with the results reported for Cu-MOR, the EXAFS data obtained on Cu-SSZ-13 could be mainly explained in terms of monomeric extraframework Cu sites (Fig. 1a). More in detail, previous characterization studies clearly showed that activation in O_2 at 400°C causes the formation of a monomeric $Z[Cu(OH)]^+$ **G** sites (Fig. 7a and Scheme 3), with a lower fraction of $ZCu^{II}Z$ sites (where Z stands for a negative charge on the framework oxygen atoms generated by the presence of one Al_{fw}) [67], whose relative concentration depends on the Si/Al and Cu/Al ratios [50, 76]. Monomeric ZCu^{I} sites located at both 6r and 8r units were instead formed by self-reduction of $[Cu(OH)]^+$ sites during activation in inert flow (Fig. 1a, left) [50, 67, 74, 76]. These findings were corroborated by using DFT-optimized structures as input for the fit of the EXAFS data. Namely, the second shell of Cu could be satisfactorily described with one Al_{fw} atom, with distances around 2.7–2.8 Å, ruling out a major contribution from Cu-Cu scattering paths in the second shell region (Fig. 7a–c).

Starting from these evidences, in the work related to the activity of Cu-SSZ-13 in MTM, Pappas et al. focused their attention on the formation of Cu-oxo sites as a function of the activation conditions, also decoupling Cu^{II} dehydration/self-reduction and subsequent O_2 interaction [57]. Very similar XAS features and methanol productivity were observed on the catalyst (Si/Al = 12, Cu/Al = 0.5) directly activated in O_2 at 500°C and contacted with O_2 at the same temperature after activation in He flow (Fig. 7d, e). These consisted in the typical pre-edge features of Cu^{II} (red and burgundy XANES spectra, Fig. 7d), with a residual amount of Cu^{I}

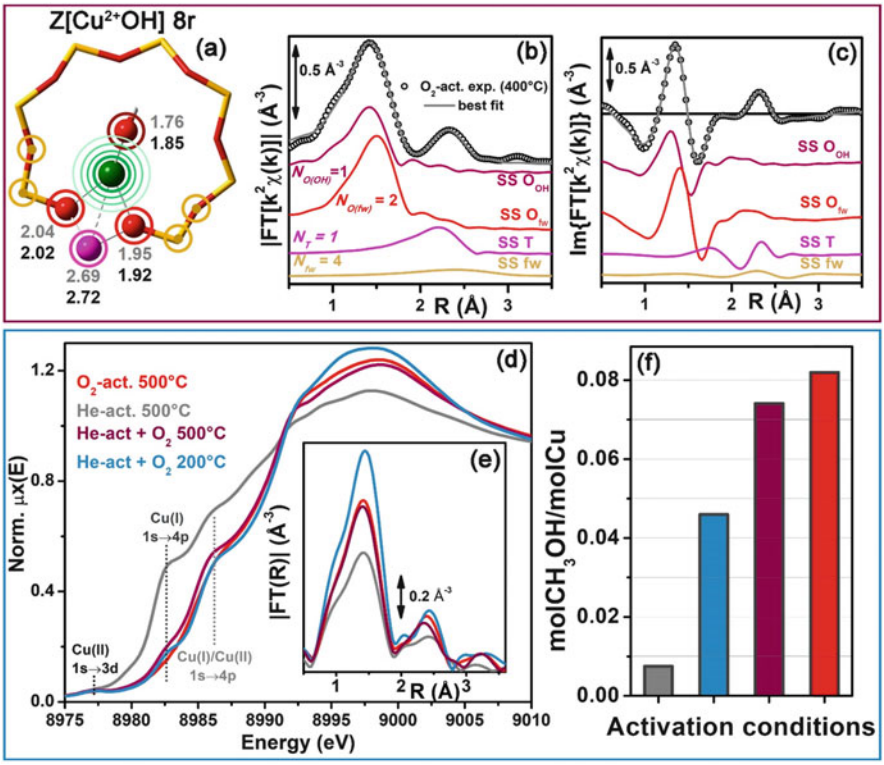

Fig. 7 (**a**) DFT-optimized structure of the most stable Z[Cu(OH)]$^+$ **G** sites in Cu-CHA (Cu, green; O, red; Al, pink; Si, yellow); colored circles highlight the different shells of neighboring atoms, with DFT-optimized distances, (**b**) and (**c**) report the experimental FT-EXAFS spectra (modulus and imaginary parts, black circles) of an O_2-activated Cu-SSZ-13 catalyst (Si/Al = 12, Cu/Al = 0.44), with the best fit (gray curve) corresponding to the DFT model. Single scattering paths for each coordination shells are reported, with the same color code as in part (**a**) [67]. (**d**) XANES and (**e**) FT-EXAFS spectra of a Cu-SSZ-13 with similar composition, after activation in He at 500°C, in O_2 at 500°C, and decoupled dehydration/oxidation steps: activation in He followed by O_2 dosage at 200 and 500°C; (**f**) corresponding methanol productivity [57]

around 10%. A similar Cu^{II}/Cu^{I} ratio was observed on the sample oxidized at 200°C after He treatment, but in this case, the spectrum was characterized by a higher white line intensity (blue curve).

Accordingly, fits of the EXAFS spectra after activation at 500°C resulted in Cu^{II} sites with CN ≅ 3, while reoxidation at 200°C caused an increase to ~4, indicating a different coordination of oxo ligands to the Cu^{II} sites, testified by the higher intensity of the first shell FT-peak (Fig. 7e). While the second shell peak could be assigned to Al_{fw} atoms, as discussed above, the high quality of the spectra allowed the authors to assess the presence of a third FT-EXAFS peak, which was best-fitted including Cu-Cu scattering paths at around 3.4 Å. This suggested the presence of a fraction (estimated around 30%) of Cu_xO_y moieties [57].

The different coordination of oxygen on the monomeric Cu^{II} sites was explained in terms of end-on $[Cu(\eta^1\text{-}O_2)]^+$ **E** and side-on $[Cu(\eta^2\text{-}O_2)]^+$ **F** structures, whose presence was confirmed by rR spectroscopy ($\nu_{O\text{-}O}$ broad bands with maxima at 1,100 and 1,155 cm^{-1}). More in detail, the authors proposed that the former (**E**) is formed by insertion of O_2 on pre-reduced Cu^I sites or by internal pathways involving the $[Cu(OH)]^+$ **G** sites, while the latter is only stable at lower temperature and is thus formed by reaction of Cu^I with O_2 at 200°C or by cooling down the sample in O_2 atmosphere. Due to the higher activity measured on the catalysts activated at 500°C, the tridentate end-on **E** complex was proposed as the most favorable site geometry for methane conversion.

As far as the Cu_xO_y moieties are concerned (accounting for 30% of copper and characterized by Cu-Cu distances around 3.4 Å), different mono(μ-oxo)dicopper (**B**), *trans*-(μ-1,2-peroxo)dicopper (**H**), and μ-(μ^2:μ^2)peroxodicopper (**C**) complexes were considered in the reaction mechanism. In agreement with Ipek et al. [79], rR measurements confirmed the presence of the first two, with bands at 830 cm^{-1} ($\nu_{O\text{-}O}$), 507 and 580 cm^{-1} ($\nu_{Cu\text{-}O}$) for the *trans*-(μ-1,2-peroxo)dicopper core, and the $\nu_{Cu\text{-}O}$ at 618 cm^{-1} for the mono(μ-oxo)dicopper ones. Structure **C**, not experimentally observed by the authors, was proposed to evolve into the more stable mono (μ-oxo)dicopper (**B**), by release of one O_{ef} atom [57].

3 Fe-Zeolites for Selective Oxidations of Methane and Benzene

3.1 N_2O as Oxidizing Agent

The catalytic activity of Fe-containing zeolites in the MTM reaction was firstly reported by the group of Panov at the beginning of the 1990s [28, 29, 31]. Methanol was extracted (with water or water solution of acetonitrile) from the surface of a Fe-exchanged H-ZSM-5. Similarly to what was carried out on Cu-zeolites in more recent years, the product was formed by interaction of methane (at RT) with a sample previously oxidized. The reactivity of Fe-zeolites (mainly MFI, but also BEA and FER [81–88]) was related to the formation of the so-called α-oxygen, an active and selective oxo species adsorbed on Fe sites upon N_2O interaction at relatively low temperature (200–250°C). N_2O was selected as oxidizing agent in relation to the observed activity and selectivity and for the potential application in the cleanup of tail gases of nitric acid plants [89, 90].

Due to the issues related to the methanol extraction from the catalyst surface, the research interest moved to the benzene to phenol reaction, an important process traditionally carried out by within a three-stage cumene technology. However, the active sites responsible for the selective hydroxylation reactions, through formation of α-oxygen, were supposed to be the same for both methane and benzene [91]. The focus of the abundant literature on the subject was mainly on the nature of α-oxygen,

formed upon N_2O interaction/decomposition, and on the electronic and geometric structure of the so-called Fe-based α-sites.

As pointed out in the short review by Zecchina et al., the determination of α-sites structure needs to be guided by well-established facts about the catalytic activity in N_2O decomposition [10]. Namely, (1) Fe-ZSM-5 (containing Al_{fw} and the related Brønsted sites) are always more active than Al-free Fe-silicalite with the same iron loading; (2) active sites are formed during the treatment under inert (particularly at high temperature), resulting in the formation of Fe^{II} α-sites (implying a self-reduction of Fe^{III}, as occurred for copper); (3) when contacted with N_2O at low temperature, Fe^{II} α-sites form α-oxygen species on Fe^{III} sites; (4) α-oxygen able to give selective hydroxylation reactions is not formed when using O_2; and (5) activity normalized to Fe content increases with dilution, pointing to exclude the catalytic activity of clustered/aggregated Fe_xO_y/Fe_2O_3 species: instead, it is believed that they catalyze nonselective over-oxidation reactions.

Even if the reversible redox Fe^{II}/Fe^{III} cycle and related activity in selective oxidation reactions show many resemblance with the Cu^{I}/Cu^{II} one, the chemistry of iron is much more complex. Indeed, Fe^{II} ions are easily oxidized to Fe^{III} in aqueous solution. The latter cannot be easily stabilized as counterion, since three negative charges on the zeolite framework would be required. Moreover, it shows a high tendency to agglomerate in aqueous medium, forming hydroxide suspensions easily evolving into iron oxide/hydroxide clusters or aggregates, dispersed within the zeolite porosity or deposited on the particle external surface (Fig. 1b). Thus, many different exchange procedures were proposed to obtain highly dispersed species, such as sublimation/chemical vapor deposition (CVD) of volatile precursors such as $FeCl_3$ [92–94], aqueous exchange of ferrous salts in inert atmosphere to avoid oxidation from Fe^{II} to Fe^{III} [88, 95], and use of oxalate or similar salts to contrast agglomeration, thanks to the chelating ligand [96, 97].

Then, careful thermal treatments of low-loaded Fe-zeolites (less than 0.6 wt%) initially containing only framework Fe^{III} atoms introduced during the synthesis (Fe_{fw}, Fig. 1b) were found to be one of the most effective ways to obtain highly dispersed and selective α-sites [87]. When iron is inserted as Fe_{fw}, Fe(OH)Si Brønsted sites are generated, with lower acid strength and thermal stability with respect to Al(OH)Si ones [98]. These sites do not show catalytic activity in partial oxidation reactions, being coordinatively saturated [91], but they are transformed into extraframework species (Fe_{ef}) during calcination and successive thermal treatments [10, 91, 98, 99].

A particularly lively debate focused on the nuclearity of α-sites, similarly to that discussed above for Cu-zeolites [10, 87, 88, 100]. Indeed, since the first reports about the possibility to carry out the selective hydroxylation of hydrocarbons with Fe-zeolites, the similarity with the reactivity of monooxygenase (MO) enzymes was pointed out [91]. Methane monooxygenase (MMO), containing two iron atoms, is able to generate oxygen species of outstanding reactivity, capable to selectively form methanol by RT oxidation of methane. Thus, different research groups proposed evidences of the presence of dinuclear Fe moieties stabilized by the zeolite frameworks, mimicking the structure and oxygen activation ability of metal cores in MMO

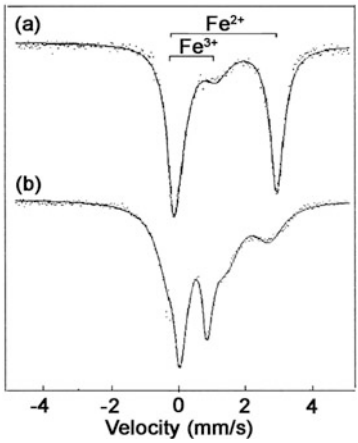

Fig. 8 Mössbauer spectra of ^{57}Fe-ZSM-5 before (**a**) and after (**b**) α-oxygen loading. Reprinted from, Catalysis Today, 41, G. I. Panov et al., Generation of active oxygen species on solid surfaces. Opportunity for novel oxidation technologies over zeolites, 365–385, Copyright 1998, with permission from Elsevier [91]

[91, 101–105]. For instance, Panov reported Mössbauer spectra of ^{57}Fe-ZSM-5 samples before and after loading with α-oxygen (Fig. 8) [91]. Transformation from a broad doublet assigned to Fe^{II} to a narrow one typical of Fe^{III} was observed upon N_2O interaction. Spectra of the supposedly formed α-oxygen complexes could be interpreted either involving two states of Fe^{III} or assuming the nonequivalence of the ligand environment of two Fe^{III} ions of the same complex. Moreover, the good agreement between the spectral parameters of both reduced and oxidized states of iron in ^{57}Fe-ZSM-5 and those of diiron MMO complexes was pointed out [91].

Concerning the α-oxygen properties, the main experimental studies involved KIE measurements and microkinetic analysis with the temporal analysis of products (TAP) approach [91, 106–109]. On the contrary, different spectroscopic techniques were used by different research groups around the world to get insights about the geometric and electronic structure of the Fe α-sites, able to decompose N_2O at low temperature to form the adsorbed and active α-oxygen. The extremely abundant literature which appeared in almost three decades on the subject cannot be reviewed in this contribution. The very recent publication in Nature Communication by Schoonheydt and Solomon groups testifies alone for the still intriguing and controversial scientific debate on the nature of α-sites [88]. Thus, only some examples concerning the most representative techniques used for the characterization of iron sites active in selective hydroxylation reactions with N_2O are here discussed, without trying to give a definite answer to the mono/dinuclear debate about α-sites structure. Generally speaking, the main characterization techniques are the same discussed in relation to Cu-zeolites: DR UV-Vis [81, 82, 84, 86, 100, 110–113], XAS [9, 86, 92, 94, 100, 113–115], infrared [9, 82, 84, 86, 87, 94, 110, 113, 116–123], and Raman [124–127], together with EPR [104, 110, 111, 117], Mössbauer [91, 94, 103–105, 128], voltammetry [82, 128], magnetic circular dichroism (MCD) [88], and resonant inelastic X-ray scattering (RIXS) [129] spectroscopies, often supported by DFT modeling [84, 88, 130–134].

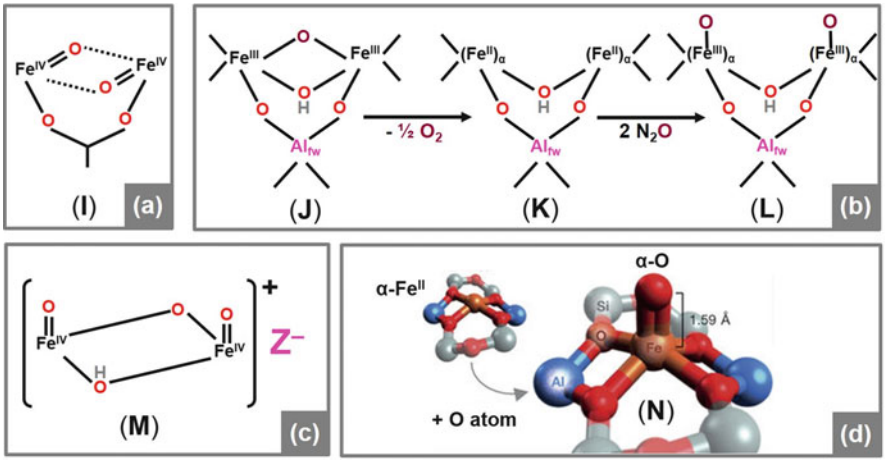

Scheme 4 (**a**) Fe^{IV} $Fe_2(\mu\text{-}O)_2$ core proposed as intermediate Q in MMO (**I**) [102]. (**b**) Ferric mono(μ-oxo)mono(μ-hydroxo)diiron (**J**) evolving into ferrous mono(μ-hydroxo)diiron (**K**) by self-reduction and into complex (**L**) by successive N_2O adsorption [92, 105]. (**c**) Dinuclear "ferryl-like" $[Fe_2O_2H^+]$ cluster (**M**) proposed by Kiwi-Minker et al. [135]; (**d**) DTF-optimized structure of a mononuclear "ferryl-like" α-Fe^{IV}=O site in the BEA 6r window (**N**). Adapted by permission from Macmillan Publishers Ltd.: Nature [88], Copyright 2016

Clearly, the proposed structures of α-oxygen were related to the assumed nuclearity of the involved α-sites. It is not possible to fully review in this contribution the lively debate on the subject. We only mention some of the dinuclear oxo α-sites inspired by what was observed in MMO enzymes [101, 102] and proposed on the basis of experimental results such as XAS and Mössbauer spectroscopy. Scheme 4 reports the high-valent (Fe^{IV}) $Fe_2(\mu\text{-}O)_2$ diamond core proposed as key intermediate Q in MMO [102] (core **I**). On the basis of Mössbauer measurements, a ferric mono(μ-oxo)mono(μ-hydroxo)diiron complex (core **J**, similar to that proposed by Marturano et al. on the basis of XAS [92]) was suggested to evolve into a reduced form during activation (core **K**) and then into core (**L**) after N_2O interaction (Scheme 4) [105]. Indeed, quantitative evaluations about the amount of α-oxygen pointed to the fact that each Fe atom in the complex was capable of generating one α-oxygen (structure **L**). This would mean that α-sites are monatomic entities in a paired arrangement registered by Mössbauer spectroscopy as dinuclear complexes [105].

The presence of coupled "ferryl-like" Fe^{IV}=O structures was instead proposed by Kiwi-Minsker et al. (core **M** in Scheme 4) [135], and successively questioned by Pirngruber et al. on the basis of RIXS measurements, favoring the presence of Fe^{III}-O^- radicals [129]. On the contrary, Zecchina et al. proposed a "ferryl-like" structure, formed upon N_2O reaction on monomeric grafted Fe^{II} sites [10]. A similar monomeric α-site was very recently proposed by Snyder et al., assuming a Fe^{II}

ion stabilized by two negative charges in a 6r window of BEA (structure **N** in Scheme 4; see later for a more detailed discussion) [88].

At the basis of the lively debate about the structure of α-sites, apart from the interesting activity that could possibly mimic that of MMO enzymes, a key issue is that Fe-zeolites are very far from what is generally considered as a "single-site" catalysts. In fact, as resumed in the pictorial representation by Zecchina et al. (Fig. 1b), a variety of Fe_{ef} species are generated by ion exchange or during the thermal treatments causing the breaking of framework bonds and the migration of Fe_{fw}, including grafted/anchored Fe^{II} sites, small $Fe_xO_y(OH)_z$ clusters, and larger Fe_2O_3 particles [10]. This means that averaged techniques, such as XAS, are likely to give a misleading description of the active sites, since the studied material is often characterized by a heterogeneous distribution of Fe species, including isolated/dispersed sites and clusters/agglomerates of different size. Indeed, Zecchina et al. analyzed a large number of literature XAS data on Fe-zeolites, showing a large scattering of the reported Fe-O, Fe-Fe, and Fe-Al distances, indicating a high heterogeneity of Fe speciation [10], as successively confirmed by rR measurements [125].

The problem of Fe species heterogeneity is also encountered using DR UV-Vis spectroscopy. Indeed, UV-Vis spectra of Fe-zeolites are often characterized by complex and broad absorptions, depending on the preparation method, iron content, and activation conditions. This was rationalized by Kumar et al., who carried out spectra deconvolution to assign distinct sub-bands to the variety of isolated/clustered/aggregated iron sites formed in zeolites. Namely, bands between 200 and 250 nm (50,000–40,000 cm^{-1}) were assigned to isolated Fe^{III} sites (Fe_{fw}) and absorptions between 250 and 350 nm (40,000–29,000 cm^{-1}) to small oligonuclear and larger (350–450 nm, i.e., 29,000–22,000 cm^{-1}) Fe_xO_y moieties inside the micropores, while bands above 450 nm (<22,000 cm^{-1}) can be related to extended Fe_2O_3-like agglomerates on the external particles' surface (Fig. 9a) [111, 136]. However, as pointed out in [10], the information that can be extracted from UV-Vis spectra of active Fe-zeolites is intrinsically limited. Indeed, the ligand field *d-d* transitions of Fe^{III} ions (d5 configuration) are very weak, being both Laporte and spin forbidden (inset of Fig. 9b; see also [98] for a more detailed discussion about the expected transitions for Fe^{III} ions and related issues). The corresponding ligand to metal charge transfer (LMCT) bands for isolated Fe^{III} ions (such as those observed in as-prepared Fe-zeolites with Fe_{fw} as unique species, Fig. 9b) are centered at 46,500 and 41,500 cm^{-1}, overlapping to the spectroscopic fingerprints of clustered/agglomerated sites (compare parts a and b of Fig. 9).

On the basis of the smaller ligand field and lower oxidation state of Fe^{II} with respect to Fe^{III}, the corresponding *d-d* transitions are expected at lower frequency (NIR region), and LMCT at higher ones, making them difficult to be detected [10]. Indeed, a clear evidence for Fe^{II} α-sites was only recently reported by Snyder et al., who measured DR UV-Vis spectra on a Fe-BEA zeolite with low Fe content (0.3 wt%, Si/Al = 12) [88]. The sample (activated in He at 900°C and subsequently reduced with H_2 at 700°C) showed three weak ligand-field bands at 15,900, 9,000, and <5,000 cm^{-1}. The band at 15,900 cm^{-1} (observed also on Fe-ZSM-5 and on

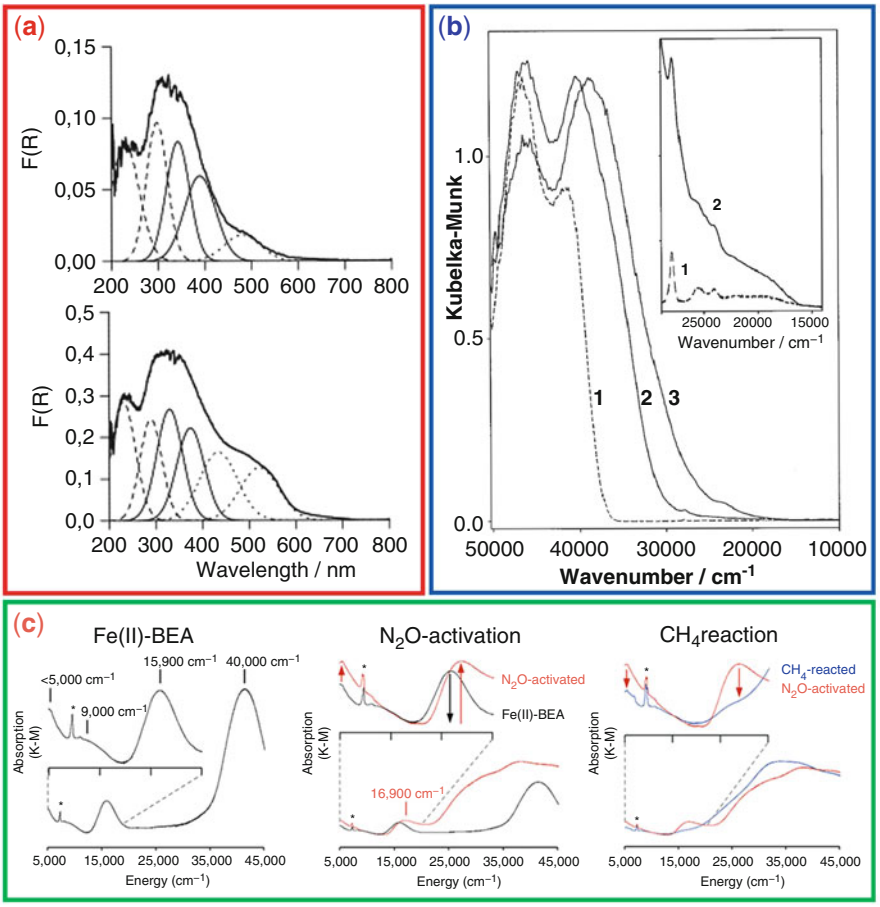

Fig. 9 Examples of DR UV-Vis spectra of Fe-zeolites. (**a**) Spectra of hydrated as-prepared Fe-ZSM-5 samples, prepared by CVD or SSIE (top and down, respectively). Thick solid lines are the experimental spectra, while thin ones are deconvoluted components assigned to: - - - isolated Fe^{III}, — small oligonuclear Fe_xO_y moieties, · · · extended Fe_2O_3-like clusters. Adapted from the Journal of Catalysis, 227, S. M. Kumar et al., On the nature of different iron sites and their catalytic role in Fe-ZSM-5 deNO_x catalysts: new insights by a combined EPR and UV/VIS spectroscopic approach, 384–397, Copyright 2004, with permission from Elsevier [111]. (**b**) Spectra measured in controlled atmosphere on a Fe-silicalite sample as prepared (1) and after calcination at 500 (2) and 700°C (3). The inset reports a magnification of the weak Fe^{III} *d-d* ligand field bands, related to Fe_{fw} sites which are transformed during calcination into clustered/aggregated Fe_xO_y/Fe_2O_3 (responsible for the shift to lower energy of the LMCT absorption passing from 1 to 3) and into silent Fe^{II} sites. Reprinted from the Journal of Catalysis, 158, S. Bordiga et al., Structure and reactivity of framework and extraframework iron in Fe-silicalite as investigated by spectroscopic and physico-chemical methods, 486–501. Copyright 1996, with permission from Elsevier [98]. (**c**) Spectra of (left) reduced Fe-BEA; (middle) activation with N_2O at 250°C; (right) effect of methane interaction at RT. * = OH overtone. Adapted by permission from Macmillan Publishers Ltd.: Nature [88], Copyright 2016

Fe-FER, though with lower intensity) was shifted at 16,900 cm^{-1} upon N_2O activation at 250°C and disappeared by methane interaction at RT (Fig. 9c), supporting its assignment to α-sites.

On the basis of variable-temperature variable-field magnetic circular dichroism (VTVH-MCD), Mössbauer and DTF calculations, the authors assigned these features to a high-spin mononuclear, square planar Fe^{II} sites stabilized in a 6r BEA window [88]. The square planar configuration of the ferrous ion was proposed to be responsible for the unusual high energy of the observed ligand field band at 15,900 cm^{-1}. Moreover, DFT calculations were also in agreement with the formation of a highly covalent square-pyramidal "ferryl-like" Fe^{IV}=O unit (Fe-O bond length 1.59 Å). This structure, unstable in the absence of the framework constraint due to the vacant *trans* axial position, would explain the high reactivity toward H-atom abstraction from methane, in agreement with the RT activity. This rigid framework constraint has been proposed to be similar to that found in some enzymes, known as the "entatic" state [88]. These breakthrough results, in favor of the mononuclear/ferryl hypothesis (structure **N** in Scheme 4), were obtained on a sample prepared by diffusion impregnation of a H-BEA zeolite with highly diluted $Fe(acac)_3$ (acac = acetylacetonate) toluene solutions, to minimize oxide/hydroxide formation. Liquid extraction of methanol resulted in 30–35 μmol of methanol per gram of zeolite (70–80% methanol yield), which is a value similar to that initially measured on Cu-CHA [72].

Finally, it is worth mentioning the use of FTIR spectroscopy coupled to NO as a probe molecule as representative technique to study the coordination environment of iron in Fe-zeolites. This experimental approach was systematically used in the group of Zecchina, to study the nature of Fe_{ef} species formed upon migration of Fe_{fw} as a consequence of calcination [9, 10, 137–139] and the effect of Al_{fw} on the Fe_{ef} sites formed in MFI [138]. Moreover, the differences between the results obtained in static and flow conditions were discussed in a joint paper with Mul [118, 120, 140].

Some representative results are reported in Fig. 10a, showing the infrared spectra in the nitrosyl region obtained during the step-wise reduction of NO equilibrium pressure (p_{NO}) on a Fe-ZSM-5 sample (prepared by ion exchange with ferric oxalate) activated in vacuum [97]. The spectra can be explained with the formation of $Fe^{II}(NO)_3$ complexes at high P_{NO} (bands at 1,846 and 1,767 cm^{-1}), evolving into $Fe^{II}(NO)_2$ (1,918 and 1,807 cm^{-1}) and $Fe^{II}NO$ ones (1,840 cm^{-1}) as a function of p_{NO} decrease. This assignment was confirmed by comparison with the nitrosyl frequencies formed in homogeneous systems (including mononuclear "heme" enzymes) or supported oxides (top panel of Fig. 10a) and by experiments with a $^{14}NO/^{15}NO$ 1:1 isotopic mixture [141]. The band around 1,880 cm^{-1} was instead assigned to Fe^{III} NO adducts formed on the surface of small Fe_2O_3 aggregates, as confirmed by comparison with the spectra obtained on bulk iron oxide (see vertically translated spectrum in left-hand panel of Fig. 10b).

Figure 10b shows a comparison of the nitrosyl region of the FTIR spectra obtained on samples with different Fe loading: by increasing Fe dilution, the relative intensity of the bands related to di-/trinitrosyl adducts on Fe^{II} increases with respect to the $Fe^{III}NO$ fingerprint of oxide aggregates (band around 1,880 cm^{-1}). This series

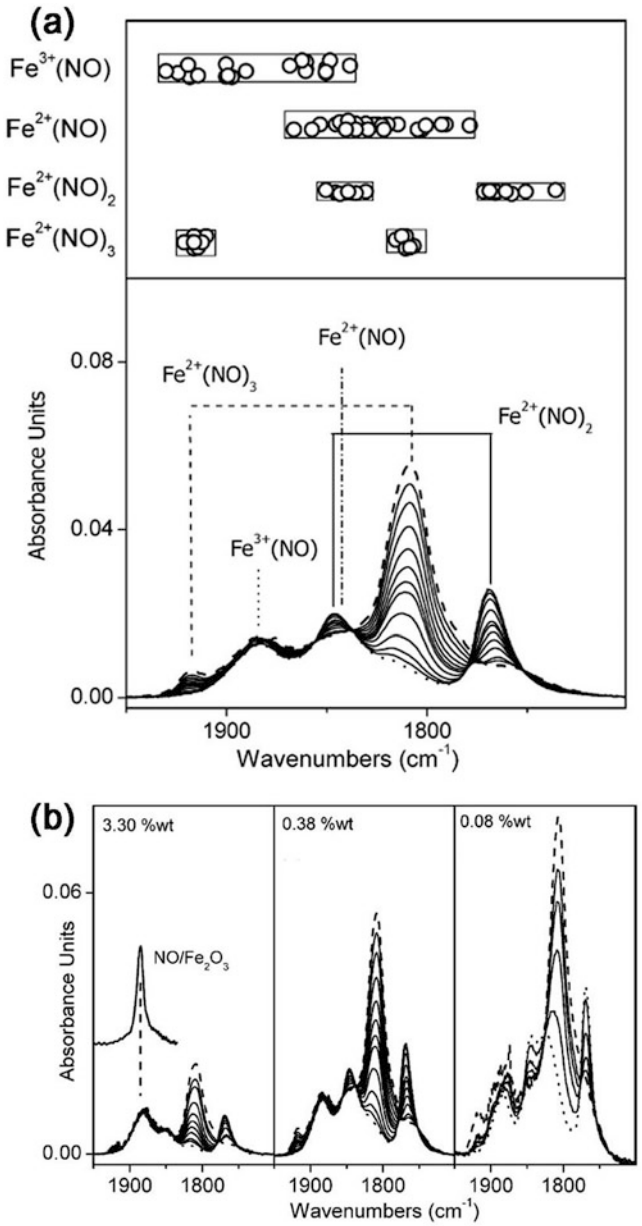

Fig. 10 (**a**) Bottom: FTIR spectra obtained upon NO adsorption at RT under static conditions (varying p_{NO} from 15 Torr, dashed line, to 10^{-3} Torr, dotted line spectrum) on a Fe-ZSM-5 sample prepared by ferric oxalate exchange and activated in vacuum; top: frequencies of Fe nitrosyl complexes in mononuclear homogeneous complexes and supported oxides (see [97]). (**b**) Series of nitrosyl spectra (same conditions and description as in part **a**) obtained on Fe-ZSM-5 samples with different Fe content (see [97] for details). The vertically translated spectrum in left-hand panel

of spectra exemplifies the potential of the technique in selectively pinpointing the presence of highly dispersed Fe^{II} sites. Indeed, the formation of trinitrosyl complexes was interpreted in terms of highly coordinatively unsaturated Fe^{II} sites grafted on the internal zeolite surface. This assignment was also confirmed by comparison with what was observed on amorphous Fe-silica [142], also using rR spectroscopy [125]. Thus, as it is seen by means of the use of NO as a probe molecule, Fe^{II} sites behave as isolated sites. This was also observed by DR-UV-Vis, resulting in relatively intense bands similar to what was observed for the mononuclear $[Fe^{II}(H_2O)_5NO]$ complexes [10]. As a final remark, one cannot in principle exclude that these monomeric sites (each able to form one α-oxygen) have other isolated Fe sites at relatively short distances, resulting in spectroscopic fingerprints compatible with the presence of dinuclear cores, as proposed by Dubkov et al. on the basis of Mössbauer and α-oxygen titration experiments (see above) [105].

3.2 H_2O_2 as Oxidizing Agent

A different reactivity of iron sites in zeolites was reported in more recent years by Hutchings' group, who carried out methane oxidation under mild conditions (50°C, 30 bar CH_4) in aqueous medium with H_2O_2 as oxidizing agent, reaching a 10% conversion with 93% selectivity to methanol [32]. The authors studied a large series of MFI zeolites, both ZSM-5 and silicalite, where Fe and Cu were inserted by different methods, particularly SSIE and hydrothermal synthesis (e.g., Fe insertion in framework positions during the synthesis). The work focused on a Fe-silicalite sample (0.5 Fe wt%), where calcination caused Fe_{fw} migration and formation of Fe_{ef} sites, as discussed above [9, 98]. On this sample, an increase in catalytic activity was observed in relation to the formation of octahedral Fe_{ef} sites, as monitored by XANES spectroscopy [32]. Based on EXAFS measurements (Fe-Fe CN = 1.6), the authors proposed a bis(μ-hydroxo)diiron complex, containing antiferromagnetically coupled high-spin octahedral Fe^{III} centers, in such a way that each Fe atom is coordinated to one additional hydroxo and water ligands, with formula $[Fe_2(\mu_2\text{-}OH)_2(OH)_2(H_2O)_2]^{II}$, thus stabilized by two negative charges on the framework.

A reaction pathway consistent with experimental data was proposed on the basis of DFT calculations, which however did not consider the framework interaction with the dinuclear core. The mechanism involved H_2O_2 coordination to one Fe^{III} atom by a water ligand displacement, evolving by H abstraction and solvent rearrangement into a formally Fe^{IV}/Fe^{II} dimer with a hydroperoxy ligand adsorbed on the Fe^{IV}

Fig. 10 (continued) was obtained on an oxidized bulk Fe_2O_3 (ex-goethite), to confirm the assignment of the band around 1,880 cm^{-1} to $Fe^{III}NO$ adducts on aggregates. Reprinted from Catalysis Letters, vol 103, M.-T. Nechita et al., New precursor for the post-synthesis preparation of Fe-ZSM-5 zeolites with low iron content, pp 33–41. Copyright 2005, with permission from Elsevier [97]

atom. Interaction of a second H_2O_2 molecule with the Fe^{II} site was proposed to result in a ferryl Fe^{IV}=O (in analogy to the Fe^{II} reactivity with H_2O_2 in Fenton's chemistry), due to the absence of an adjacent ligand for H abstraction. Thus, the active site responsible for methane reaction should be a dimer with a ferryl Fe^{IV}=O adjacent to the hydroperoxo Fe-OOH. The reaction was proposed to go through formation of methyl hydroperoxide, formed by immediate reaction of the hydroperoxy ligand with the methyl radical formed by ferryl-mediated H-abstraction, as confirmed by the absence of the EPR signals expected for the methyl radicals. On the contrary, the presence of $^{\bullet}OH$ radicals was correlated to over-oxidation reactions, which were suppressed by insertion of Cu^{II} ions [32].

Further characterization studies were carried out to better understand the nature of the Fe_{ef} sites active in the presence of H_2O_2, mainly by XANES and DR UV-Vis spectroscopy [143]. XANES was used to study the effect of thermal treatments on Fe-ZSM-5 and Al_{fw} free Fe-silicalite samples. The main presence of Fe^{III} sites on active samples was taken as an indication of the different reactivity of the H_2O_2-based catalysis with respect to the N_2O-related one, where Fe^{II} α-sites are instead formed by self-reduction during high temperature treatments under inert atmosphere. The effect of the heat treatments was then followed by UV-Vis, based on the sub-bands obtained by spectral deconvolution, as proposed by Kumar and Perez-Ramirez [111, 136]. Indeed, even if the molar extinction coefficients of each UV-Vis component is unknown, these were supposed to be of the same order of magnitude [136], thus allowing for a semiquantitative evaluation of Fe speciation. Thus, the catalytic activity was found to correlate well with the amount of Fe_{ef} dispersed in the zeolite micropores (absorptions between 250 and 350 nm), with a maximum corresponding to a calcination temperature of 750°C. Accordingly, higher calcination temperature, resulting in the formation of larger clusters and iron oxide aggregates (350–450 nm and ≥450 nm, respectively), caused a decrease in the amount of oxygenated products (Fig. 11a) [136].

Deconvolution of UV-Vis spectra into sub-bands for semiquantitative Fe speciation was also used to assess the effect of isomorphous framework substitution of trivalent non-catalytically active atoms (Al^{III} and Ga^{III}) in MFI. The higher activity of Fe-ZSM-5 with respect to Fe-silicalite was related to the role of Al_{fw} (and similarly to Ga_{fw}) in increasing the migration of Fe_{fw} to Fe_{ef} during calcination (in samples prepared by hydrothermal synthesis) and in maximizing the fraction of Fe_{ef} dispersed inside the micropores (bands in the 250–350 nm range) at the expenses of larger aggregates [145]. This can be explained by an inhibition effect toward clustering from the negatively charged framework, favoring the anchoring and the stabilization of dispersed sites. The authors acknowledged the fact that UV-Vis cannot discriminate alone between all the possible Fe_{ef} dispersed inside the zeolite pores (isolated Fe^{III}, dimers, trimers, and small oligomers). However, these spectroscopic features could be compatible with the $[Fe_2(\mu_2\text{-}OH)_2(OH)_2(H_2O)_2]^{II}$ core proposed on the basis of the match between XANES parameters and DFT calculations [32, 145].

Further efforts were devoted to improve the catalytic performances of Fe-zeolites in the selective oxidation of alkanes (methane and ethane) with H_2O_2 and to

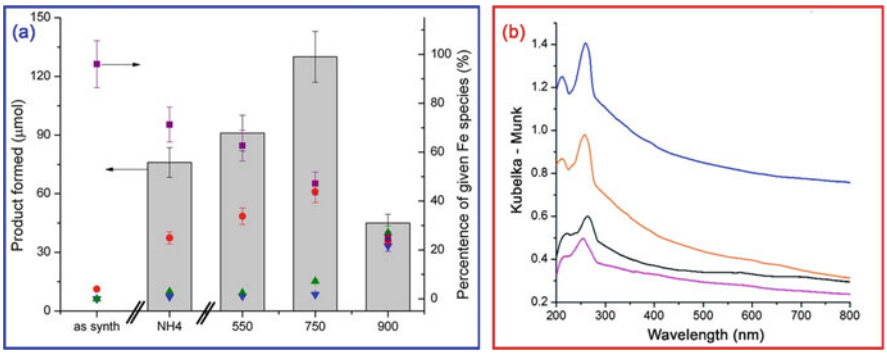

Fig. 11 (**a**) Amount of oxygenated products obtained in H_2O_2 aqueous solution (for details, see [143]) on Fe-silicalite as prepared and after thermal treatments at increasing temperature. The NH_4-form precursor is also shown for comparison. The scatter points refer to Fe speciation calculated from deconvoluted UV-Vis spectra. Key: squares, isolated, tetrahedral framework Fe; circles, extraframework Fe within the micropores; up triangles, larger Fe clusters; down triangles, bulk Fe oxides. Reprinted with permission from [143]. Copyright 2013 American Chemical Society. (**b**) DR UV-Vis spectra of Fe-ZSM-5 samples prepared by CVI from $Fe(acac)_3$ (orange, blue, black, nominal Fe loading 1.1, 2.5, and 0.4 wt%, respectively) and $Fe(acac)_2$ (pink, nominal Fe loading 0.4 wt%), heat treated at 550°C in 5% H_2/Ar for 3 h [144]. Published by the Royal Society of Chemistry, licensed under a Creative Commons Attribution 3.0 Unported License

highlight the nature of active Fe_{ef} sites. Forde et al. carried out a systematic study on a large set of Fe-ZSM-5 samples prepared by CVI with ferric and ferrous acetylacetonate precursors [144]. Interestingly, the samples were heated under hydrogen atmosphere before calcination, in order to reduce the amount of available oxygen in the micropores and thus to limit agglomeration. The samples were shown to be characterized by peculiar DR UV-Vis spectra, with well-defined bands (maxima at 215/235 and 260 nm) in the typical region for LMCT of isolated Fe^{III} sites [98], with less resolved components above 300 nm with respect to the typical Fe-zeolite samples (Fig. 11b). The authors acknowledged the fact, already discussed by Bordiga et al., that these low wavelength bands cannot be used to discriminate between Td and Oh Fe^{III} coordination, which are characterized by similar energy level diagrams [98]. In agreement with previous reports and XANES evidences, they assigned the UV-Vis bands to extraframework Fe^{III} sites in octahedral coordination, both isolated or in small clusters.

Some considerations about these characterization results are the following. First, the discussion of the peak centered at 215–235 nm is doubtful due to the low sensitivity of DR detectors in the high-energy limit, which could cause artifacts, also in relation to luminescence phenomena. Thus, it should be more prudent to consider DR UV-Vis spectra only below 250 nm, for precise band maxima description. Secondly, all the UV-Vis spectra obtained on pre-reduced catalysts appear vertically offset, i.e., although no defined bands are observed above 300 nm, spectra are characterized by an unresolved tail with absorbance never reaching zero, which

could be indicative of the presence of additional, highly heterogeneous species, not detected either by TEM or XAS spectroscopy (Fig. 11b).

Notwithstanding these limitations, comparison of the spectroscopic features and catalytic performances (including ethane oxidation) of a large series of samples allowed the authors to pinpoint the novelty of the proposed preparation method, in particular in relation to the reduction treatment. Thus, the role of the previously proposed diiron-oxo-hydroxo species was partially discarded, pointing to the importance of isolated octahedral extraframework iron-oxo clusters and/or Fe^{II} sites (whose structure could not be precisely described) in directing high selectivity to alcohols, also in the absence of Cu^{II} as $^{\bullet}OH$ radical scavengers [144].

Finally, rR spectroscopy was used to study the Fe-silicalite and Fe-ZSM-5 samples previously characterized by DR UV-Vis and XAS spectroscopy [32, 145]. Hammond et al. observed three Fe-specific modes at 521, 1,120, and 1,160 cm^{-1} upon irradiation with $\lambda_{exc} = 325$ nm, that is, in correspondence to the UV-Vis electronic transitions assigned to the dispersed mono-, di-, and/or oligonuclear Fe_{ef} sites correlated to the catalytic activity [146]. In particular, the intensity of the band at 521 cm^{-1} was shown to increase with calcination temperature, reaching a maximum after treatment at 750°C, with a trend similar to that of oxygenated product formation (Fig. 11a). The authors thus questioned the previous assignment of this band by Bonino et al. and Li and coworkers to framework Fe^{III} sites [125, 147] and proposed its assignment to the extraframework $[Fe_2(\mu_2\text{-}OH)_2(OH)_2(H_2O)_2]^{II}$ core established by DFT/XAS [32]. Active Fe-silicalite was also studied in the presence of H_2O_2, showing a new band at 631 cm^{-1} resonant by irradiation in the visible range ($\lambda_{exc} = 514$ nm), which was assigned to the ν(Fe-O) stretch of a Fe^{III}-OOH complex. The 521 cm^{-1} rR band was instead shown to disappear upon H_2O_2 interaction, being regenerated upon laser irradiation or heating at 110°C. This would thus indicate a reversible shift between the di-μ-hydroxo-bridged complexes and two transient mononuclear a Fe^{III}-OOH sites, operating in a cooperative manner in the remaining catalytic cycle [146]. The flexibility of the mono and dinuclear structures would thus be in agreement with the proposed self-organization of cations in zeolites or molecular complexes [148, 149].

4 Characterization of TS-1 Zeolites

Titanium silicalite-1 (TS-1), along its 30-year history, has been widely characterized by numerous experimental techniques. In the first pioneering stages, the researchers from EniChem demonstrated the introduction of the titanium atoms in the siliceous MFI framework of silicalite-1 on the basis of three simple observations: (1) all the synthesized material, independently from their Ti loading, on the basis of diffraction experiments were isostructural with the purely siliceous silicalite-1; (2) the cell volume derived from diffraction was increasing linearly as the Ti loading increased; and (3) a characteristic infrared band, with maximum at 960 cm^{-1}, was observed in Ti-substituted materials, with an intensity linearly increasing with the Ti loading.

These findings, together with the exceptional activity and selectivity in partial oxidation reaction toward numerous organic substrates in the presence of aqueous hydrogen peroxide, brought in the 1983 to patent the synthesis of TS-1 [150].

Since these first discoveries, TS-1 was the object of several characterization studies which progressively enriched the knowledge on this material. Diffraction techniques gave time by time higher-quality results, improving both the instrumental potentialities and the ability in the sample handling [151–153]. The highest point achieved by diffraction techniques has been the attainment of the Ti distribution among the 12 possible sites of the MFI framework: these results were obtained by neutron diffraction, exploiting its superior contrast among Ti and Si atoms with respect to standard X-ray diffractometers [154, 155]. Simultaneously, even larger developments arose from spectroscopic approaches: FTIR [156–158], Raman [159–163], optical [158, 164, 165], X-ray adsorption [164, 166, 167], and emission [168, 169] spectroscopies were diffusely applied, giving rise to a constant enrichment in the understanding of TS-1 and its catalytic sites. It is important to underline that most of these studies actually exploited the complementarity among the different spectroscopic techniques, allowing a better understanding of the system as observed from different points of view.

4.1 Characterization of Ti Sites

UV-Vis spectroscopy is one of the most important experimental tools, together with vibrational (IR and Raman) and X-ray-based (XAS and XES) spectroscopies, employed in the study of the structure of Ti^{IV} active centers in TS-1, both in the absence or in the presence of adsorbates [158, 164, 170–174] and for the evaluation of the existence of both framework and extraframework Ti species [170].

The DR UV-Vis spectrum of a vacuum-activated TS-1 (black curve in the upper part of Fig. 12) is the unequivocal proof of the presence of Ti^{IV} sites in tetrahedral coordination inside the zeolite framework (see structure (I) in Fig. 12). The black spectrum (dehydrated TS-1) exhibits as unique feature a $Ti^{IV}O^{2-} \rightarrow Ti^{III}O^{-}$ ligand to metal charge transfer (LMCT) around 200 nm ascribable to the charge transfer transition from the oxygen ligand to an unoccupied orbital of a Ti^{IV} ion tetrahedrally coordinated in isolated [TiO_4] sites [160, 164, 170, 171, 174, 175], i.e., perfectly tetrahedral Ti_{fw} centers. The existence of a single band around 200 nm in the UV-Vis spectrum of a vacuum-activated sample can be considered as characteristic of a well-manufactured TS-1, without the presence of extraframework sixfold-coordinated Ti species (Ti_{ef}), which give absorptions at higher wavelengths [170, 176, 177].

The peculiar tetrahedral coordination of framework Ti^{IV} sites in TS-1 is somewhat unusual, and for this reason, these framework Ti species can easily expand their coordination sphere upon interaction with adsorbates. In fact, it is well known that the pure tetrahedral coordination can be observed only when the TS-1 is activated under vacuum at high temperature, i.e., when all adsorbed water, acting as additional ligand, is totally removed from the material (see black spectrum of Fig. 12). When

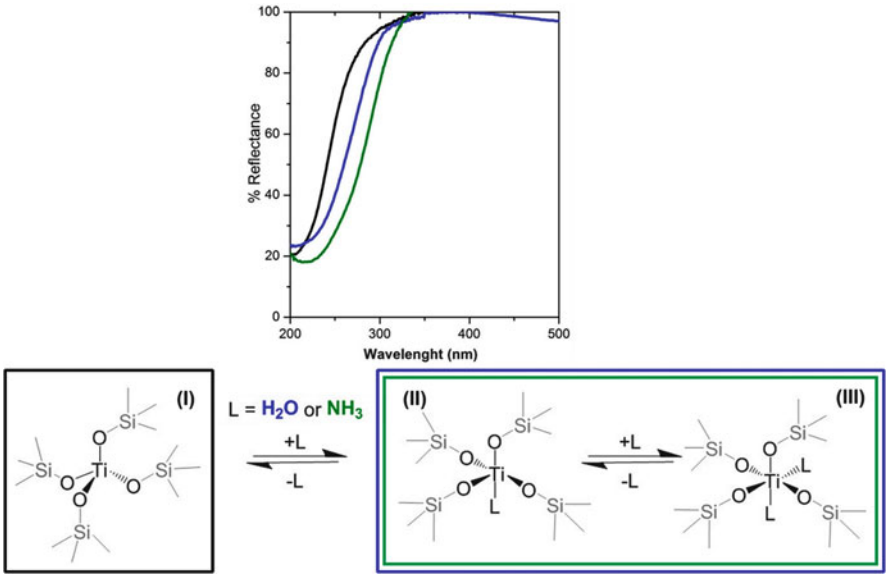

Fig. 12 Top: DR UV-Vis spectra of the TS-1 catalyst vacuum activated at 500°C (black curve) and upon interaction with H_2O (blue curve) and NH_3 (green curve) dosed from the gas phase. Bottom: ability of the Ti^{IV} site to modify its local environment from a tetrahedral-like (structure I) to an octahedral-like (structure III) geometry after interaction with strong ligands (L = H_2O or NH_3), eventually involving intermediate coordination geometries (structure II)

strong ligands, such as water or ammonia, interact with the dehydrated TS-1, they are able to affect the electronic transitions of Ti sites, and therefore, the UV-Vis spectral profile undergoes evident modifications as reported in Fig. 12. The interaction with H_2O molecules from the gas phase (blue spectrum) causes a red shift of the edge, due to the increase of the coordination sphere around the Ti^{IV} centers [158]. At the same time, the interaction with NH_3 from the gas phase (green spectrum) is also responsible of an evident perturbation of the TS-1 UV-Vis spectrum [164]; however, the red shift of the edge is clearly more pronounced in this case. All these spectral variations are generated by the direct interaction of the extra ligands (adsorbates) with the Ti^{IV} atoms, due to the ability of these sites to modify their local environment in a reversible (or nearly reversible) manner from a tetrahedral coordination (structure I in Fig. 12) to an octahedral-like geometry (structure III in Fig. 12) passing through a trigonal bipyramidal coordination (structure II in Fig. 12). The progressive expansion of the Ti coordination sphere is witnessed by the gradual modification of the spectroscopic features toward those of octahedral Ti^{IV} species [156, 159, 164, 170, 174, 178, 179]. In fact, when Ti exhibits six oxygen atoms in its first coordination shell, as in the case of TiO_2 polymorphs, the $Ti^{IV}O^{2-} \rightarrow Ti^{III}O^{-}$ LMCT occurs at around 330 nm [180, 181], i.e., at higher wavelength with respect to the peculiar spectral feature of the perfect tetrahedral Ti^{IV} centers in an activated TS-1 (*ca* 200 nm).

Under the adopted experimental conditions, the interaction with H_2O or NH_3 from the gas phase does not lead to sixfold-coordinated Ti^{IV} species (structure III in Fig. 12). The maximum number of ligands can be obtained just on highly hydrated samples [173] (contacted with water from the liquid phase), in the presence of higher NH_3 pressure or by using aqueous NH_4OH solutions [164, 174].

In conclusion, it is evident that the UV-Vis spectroscopy is a very useful tool as it gives direct information on the chemical events occurring in the first coordination sphere of Ti^{IV}. In fact, by the analysis of the UV-Vis spectra, it has been possible to prove that the Ti^{IV} coordination sphere expands upon adsorption of extra ligands (adsorbates) from the surrounding atmosphere [164]. This statement will be confirmed also in the following sections by the results obtained with other different characterization techniques.

Moving to vibrational spectroscopies, Fig. 13 reports TS-1 infrared and Raman active vibrational modes in the full mid-IR 3,800–700 cm^{-1} range, in comparison with a Ti-free silicalite-1. In part (a) a typical infrared spectrum (in transmission

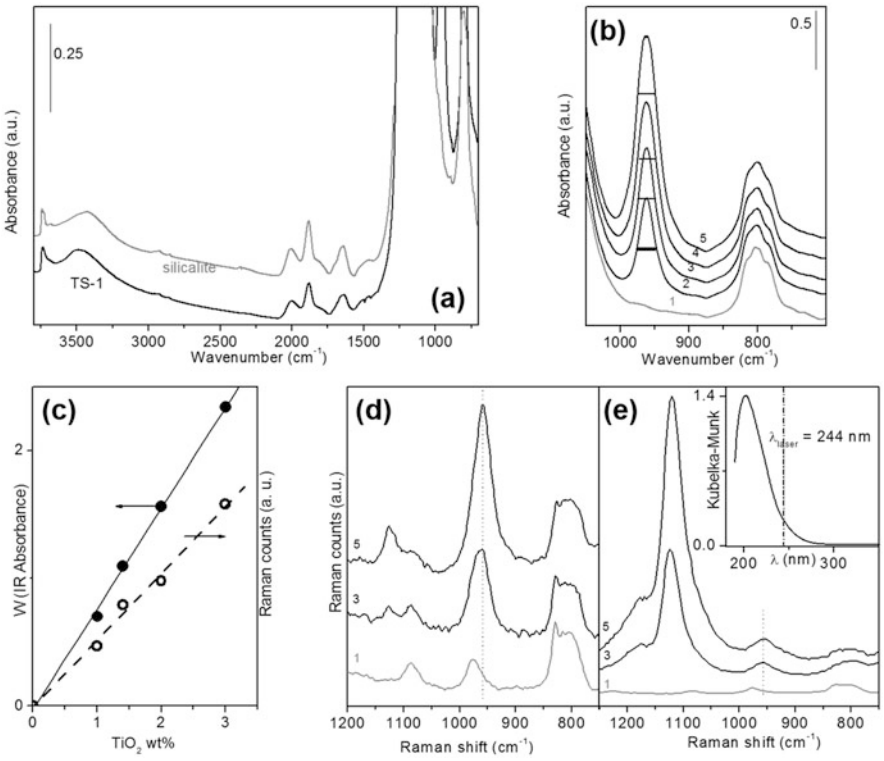

Fig. 13 Infrared (parts **a** and **b**) and Raman (part **d** $\lambda = 1{,}064$ nm and part **e** $\lambda = 244$ nm) spectra of TS-1 samples with different Ti content (black curves) and, for comparison, a silicalite sample (gray curve). Part **c** reports the infrared (full circle) and Raman (empty circle) linear correlation of 960 cm^{-1} fingerprint intensity with Ti content. Parts **b–e**: Adapted with permission from [157]. Copyright (2001) American Chemical Society

mode) of TS-1 activated in vacuum (black curve) is compared to the reference silicalite-1 one (gray curve). In the reported range, both spectra are dominated by hydroxyl groups and skeletal Si-O vibrational modes. As previously discussed in [182, 183], absorption bands can be roughly divided into different groups and assigned as it follows: (1) 3,800–3,650 cm^{-1} range to stretching modes of hydroxyl groups not involved in hydrogen bonding (isolated and terminal, either external and internal, OH), (2) 3,650–3,200 cm^{-1} range to stretching modes of hydrogen-bonded OH groups, (3) 2,100–1,300 cm^{-1} to overtones and combination framework modes, and (4) 1,300–700 cm^{-1} to out of scale fundamental framework modes and in particular to asymmetric (broad band centered at 1,150 cm^{-1}) and symmetric (band at 800 cm^{-1}) vibrational modes of [SiO_4] units. In this last range, exactly between the two previously described absorptions, a clear difference between TS-1 and silicalite-1 can be identified: the famous fingerprint at 960 cm^{-1}, again reported as an out of scale feature.

The main interest is of course the clear distinction of clear vibrational fingerprint ascribable to the presence of Ti inserted in the framework. To this aim, it is necessary to focus the attention on two different operative aspects: (1) to decrease the thickness of the samples studied in transmission or to adopt ATR modality and (2) to activate properly the samples as intensity and frequency can result distorted. A quantitative correlation between the Ti content and its infrared intensity was reported by Ricchiardi et al. [157]. Figure 13b reports the infrared spectra of four TS-1 samples containing increasing Ti content (x) (curves 2–5) in comparison with pure silicalite-1 (curve 1). In order to be quantitative, a normalization to the pure siliceous framework bands in the 1,500–2,000 cm^{-1} range (not reported in this series of spectra) has to be necessarily applied. It is worth noticing that the accuracy of the normalization procedure is testified by the perfect superimposition of the band centered at 800 cm^{-1}, again not affected by the Ti presence.

Full-width at half-maximum (FWHM) of the 960 cm^{-1} band was measured for the lowest Ti content sample (27 cm^{-1}), by assuming the band completely far from saturation, and then for all the samples, the absorbance (W), at the height where the width of the band corresponds to the fixed value, was considered (see Fig. 13c, full circles), and a linear correlation ($r = 0.9998$) was found.

The existence of the 960 cm^{-1} fingerprint and its linearity with Ti content (see Fig. 13c, empty circles) is further confirmed by Raman spectroscopy, where, in addition, saturation problems are absent. Figure 13d, e report Raman spectra of two TS-1 samples (3 and 5, already measured by means of IR spectroscopy) in comparison with a silicalite-1 sample highly defective (large amount of hydroxyl groups), collected with two different laser lines at 1,064 and 244 nm, respectively. Inset of Fig. 13e shows clearly that, by adopting the mid-UV laser line, resonance occurs as it falls in the $Ti^{IV}O^{2-} \rightarrow Ti^{III}O^{-}$ LMCT. It is worth noticing that the Raman spectrum of the silicalite-1 is very similar with both 1,064 nm and 244 nm laser lines as of course no resonance occurs. The features at 1,085 cm^{-1} and the broad band centered at 820 cm^{-1} are ascribable to asymmetric and symmetric vibrational modes of [SiO_4] units, already found in the IR spectra (see Fig. 13a). In silicalite-1 sample, the well-distinguishable band at 975 cm^{-1} must not be confused with the 960 cm^{-1}

fingerprint (see vertical lines) as it is assigned to ν_{asym}(T-O-T*), where T* is a T site where an hydroxyl group is connected. [156].

However, the most eye-catching evidence is the presence of a new band at 1,125 cm^{-1}, visible by adopting the two different laser lines and strongly enhanced by rR effect (see Fig. 13d, e). In addition to this, the constant value of the I(1,125)/I (960) ratio (0.25 in the case of 1,064 nm, 11 in the case of 244 nm laser lines) indicates that the two vibrational features are both related to the isomorphous insertion of Ti in the MFI framework. This observation finds good agreement with the work of Li et al. [160, 184], where Ti-related vibrational fingerprints are found to increase during TS-1 crystallization process.

Besides the laboratory techniques previously commented, synchrotron-based X-ray spectroscopies represent a fundamental tool in the characterization of the dispersed Ti centers in Ti-zeolites and related materials, taking advantage from their superior atomic selectivity. These have been exploited in the investigation of various aspects of TS-1 structure and chemistry, e.g., local structure of the Ti sites, their location in the MFI framework, or interaction of Ti with probe molecules of reactants.

XAS is probably the most used technique, because of the structural information it brings. Indeed, the XANES part of the spectrum is sensitive to both the oxidation state and the coordination environment of the emitting atom, whereas the EXAFS portion allows average structural parameters (e.g., bond distances, coordination numbers) to be obtained through fitting procedures.

The first XAS studies concerning Ti-zeolites was reported in 1991 by Behrens and coworkers [185]: they performed Ti K-edge measurements on TS-1 samples synthesized according to the patent recipe [151–153]. Since the quality of the EXAFS data was not sufficient for fitting, the authors focused on the qualitative analysis of the XANES data through an exhaustive comparison with various mineral references (see Fig. 14).

This strategy accounts on the comparative analysis of the pre-edge features of the XANES spectra (associated to $1s \rightarrow 3d$ electronic transitions), which are strongly indicative of the coordination sphere of Ti. When Ti sits in a tetrahedral ligands sphere, a sharp and intense peak is observed. Conversely, if Ti belongs to an octahedral environment (thus possessing an inversion center), the associated transitions will give weak contributions, since these are Laporte forbidden. Other coordination geometries (such as fivefold Ti or high distortions of octahedral/tetrahedral ligand spheres) give intermediate phenomena, with the intensity of the pre-edge peaks strongly influenced by the degree of centrosymmetry of the system. Upon linear combination of the spectra of ramsayite (containing distorted octahedral Ti), fresnoite (with Ti sitting in a square-pyramidal environment), and barium titanate (representative of Ti in tetrahedral coordination), the pre-edge peak of TS-1 was reconstructed. On the basis of this analysis, the authors claimed that Ti is inserted in TS-1 with various coordination geometries, preferentially octahedral for both the samples they considered in the study. The presence of extended Ti oxide phases was however excluded. Another relevant point was the role of hydration of the samples: indeed, a reduction of the content of octahedral species was recognized upon

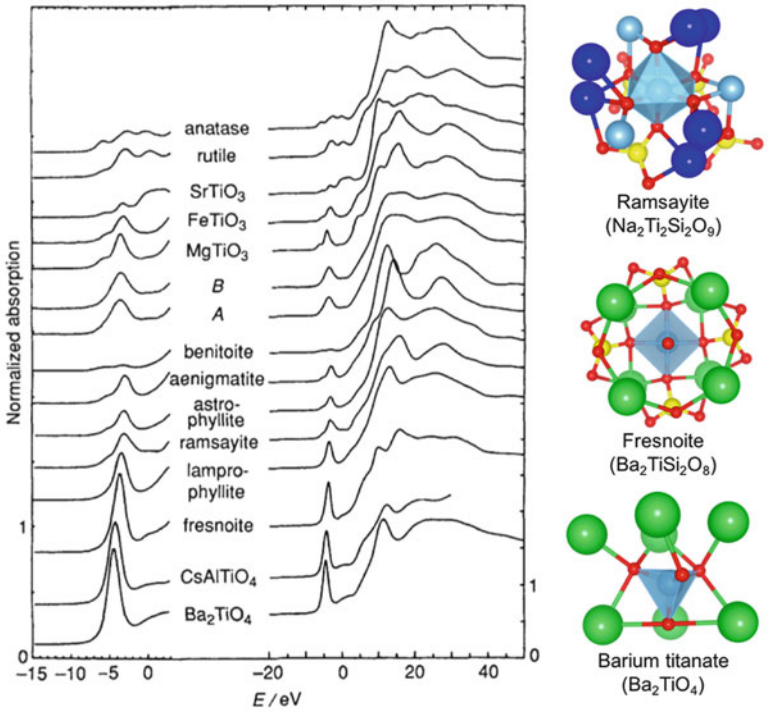

Fig. 14 Ti K-edge XANES spectra of the TS-1 sample as-synthesized (A) and calcined (B) together with those of reference compounds. Spectra are normalized to unity. The zero-point of the energy (*E*) scale was fixed at the first inflection of the K-edge of metallic Ti. Reproduced from [185] with permission of the Royal Society of Chemistry. The Ti local environment for some relevant phases is graphically outlined (Ti in cyan, Si in yellow, Na in blue, Ba in green, O in red)

dehydration, suggesting the coordination sphere of Ti can also contain ancillary ligand (e.g., adsorbed H_2O or neighbor silanol groups) which are desorbed upon appropriate treatment. Similar results were reported by Schultz et al. [186], whereas Pei and coworkers [187] for the first time pointed out that Ti is preferentially inserted as a tetrahedral substituent of Si. The latter inferred that the conclusions from previous reports where biased by the use of a poor-quality sample (i.e., with unexpectedly abundant Ti_{ef} content). With respect to previous reports, they carried out fitting of the EXAFS data, since the pre-edge XANES features alone were not sufficient to unambiguously determine the Ti coordination. The EXAFS analysis revealed a coordination number of 4.1 ± 0.5 for Ti in the first coordination shell, suggesting it preferentially occupies tetrahedral positions. However, due to the large error affecting the result, a five-ligand first coordination sphere cannot be excluded a priori. The final confirmation on the fourfold, almost perfectly tetrahedral first coordination sphere of Ti arose from the works from Lamberti and coworkers [18, 164, 166, 167, 188, 189]: a key step was represented by the careful dehydration procedure (i.e., outgassing at high temperature) they performed on well-

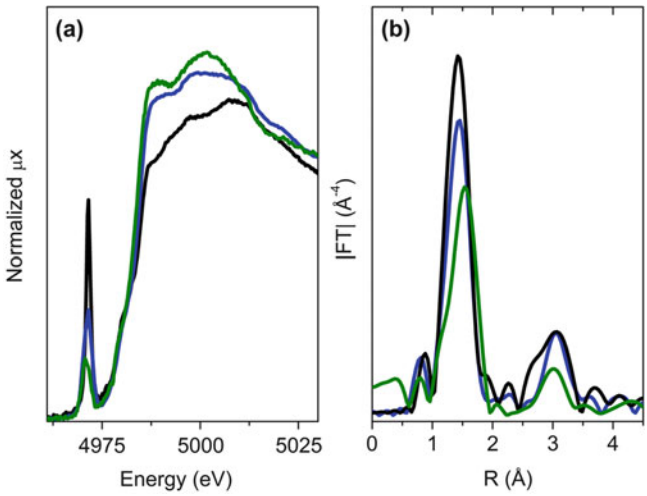

Fig. 15 (**a**) XANES spectra and (**b**) k^3-weighted module Fourier transform of the EXAFS signal for dehydrated TS-1 (black lines), dehydrated TS-1 contacted with H_2O (blue lines), and dehydrated TS-1 contacted with NH_3 (green lines). Unpublished figures reporting data previously published in [167]

manufactured TS-1 samples, thus excluding the influence of the ligands on the local environment of Ti, as well as avoiding the presence of misleading extraframework species. As a cross-check, basic molecules (e.g., H_2O, NH_3) were dosed from the gas phase over the activated materials in order to restore a "hydrated-like" state of the sample. A summary of the main results is given in Fig. 15.

Upon dehydration, the intensity of the *1s* → *3d* peak rises up to an intensity comparable to the white line one, consistently with the establishment of an almost perfect tetrahedral environment for the Ti sites. Upon dosage of H_2O (and even more evidently with NH_3), the intensity of the pre-edge feature decreases by a large extent, testifying the increase of the coordination of Ti toward a more centrosymmetric ligands field. The fit of the EXAFS data further allowed obtaining the Ti-O distances and the number first neighbors of the emitting center: in the case of the bare tetrahedral site, the Ti-O distance was found to be 1.79 ± 0.01 Å, and the coordination number in the first shell resulted to be 4.3 ± 0.3. This latter result definitely demonstrates the preferential tetrahedral coordination of Ti in well-manufactured TS-1, without excluding that a fraction of higher coordination/defective site could however be present. Upon adsorption, the Ti-O distance consistently increases to 1.82 ± 0.02 and 1.88 ± 0.02 Å for H_2O and NH_3, respectively. For the latter molecule, the coordination number relative to N atoms linked to Ti was computed (assuming the number of surrounding O atoms fixed to 4): a value of 1.9 ± 0.3 was found, suggesting that Ti assumes an octahedral coordination at high NH_3 coverages. This last point also confirms the relevance of the activation procedure, since the presence of ancillary ligands adsorbed at the Ti sites has a major effect in determining their XAS features.

Beside the structural information provided by XAS, more recently new insights arose from emission-based techniques, such as X-ray emission spectroscopy (XES). XES allows deeply investigating the electronic features of the sample through a second-order optical process, where (1) an electron is removed from a core level of the emitting atom by the interaction with X-rays and (2) another electron from a higher energy shell fills the vacancy left from the previous, leading to the emission of a photon with characteristic energy. When the filling electron comes from a valence level, the technique is referred as valence-to-core XES (vtc-XES): this has been successfully applied to the characterization of TS-1. The main contributions belong to Gallo et al., who focused on the properties of the bare TS-1 [169], also in interaction with H_2O/NH_3 [168]. The former work elucidated the feasibility of the interpretation of vtc-XES data through a DFT approach, underlining the importance of the structural model and level of theory in the simulation of the emission spectra. On the basis of these results, the latter work exploited the electronic information to derive a more structural insight, i.e., the type of coordination assumed by Ti centers in the presence of basic ligands. This study exploited a further advanced tool, i.e., resonant vtc-XES (rvtc-XES, also referred as resonant inelastic X-ray scattering, RIXS). With respect to regular vtc-XES, rvtc-XES is performed recording the emission profile as a function of the energy of the incident beam, usually in the energy range surrounding a pre-edge feature of the XANES spectrum (in the case of TS-1, the intense *1s* → *3d* peak). In Fig. 16, the case of NH_3 adsorption is reported as an example.

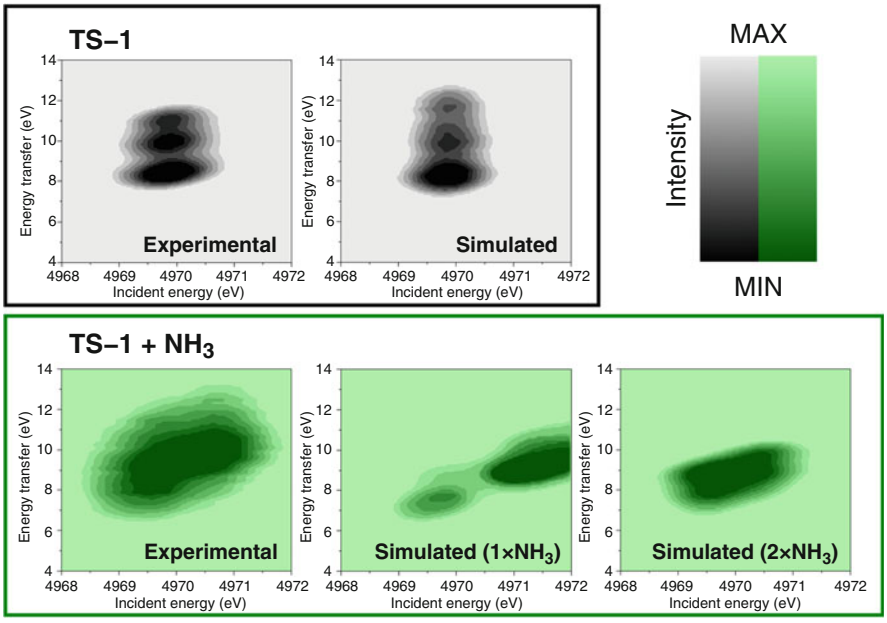

Fig. 16 Experimental rvtc-XES maps of TS-1 (bare and contacted with NH_3) compared with simulations. In the case of NH_3, both single and double NH_3 adsorption at the Ti site have been considered. Unpublished figures reporting data previously published in [168]

Comparison of the experimental rvtc-XES maps with the simulated ones demonstrates (in the case of the bare TS-1) a good agreement of the model with the real system. With respect to NH_3 adsorption, this allowed inferring that the coordination of Ti is most probably fivefold (i.e., allowing the adsorption of a single ligand). Even if this could seem a barely fundamental detail, it could represent a significant datum concerning the catalytic properties of TS-1: indeed, the formation of (hydro)peroxo species upon interaction with H_2O_2/H_2O is most probably affected by the adsorption capability of each Ti site. Furthermore, this outcome sets a discrepancy with respect to previous findings, since a double adsorption was always reported by other techniques [158, 164, 166, 188]. However, it is worth noticing that vtc-XES (and even more rvtc-XES) measurements require a prolonged exposure to the X-rays beam, approximately one order of magnitude longer than in a XAS measurement. Thus, the potential beam damage (or even a simple local heating of the sample) should be taken into account considering this type of data, since it could alter the measured system (and thus the spectroscopic outcome).

4.2 Characterization of Ti-H_2O_2 Adducts

TS-1 is an important selective catalyst in low temperature partial oxidation reactions, with aqueous H_2O_2 as the oxidant agent. For this reason, the systematic investigation of the different active species formed in TS-1 upon interaction with hydrogen peroxide is a high priority target. One of the main experimental problems observed in the study of these active species is due to the use of H_2O_2 solutions. The presence of H_2O does not allow the extended use of IR spectroscopy; therefore, DR UV-Vis spectroscopy (not affected by the presence of H_2O) becomes one of the most important experimental techniques in this type of study, due to the possibility to obtain reliable spectra also in the presence of samples fully immersed in water solutions [158, 173, 174].

As previously explained, Ti^{IV} sites exhibit a high propensity to expand their coordination sphere under the action of reactants. The interaction with hydrogen peroxide can also modify the coordination of Ti atoms, leading to the formation of Ti-peroxo species, without the extraction of Ti from the zeolite framework [173, 190]. It is clear that the identification of these active species, formed in the presence of the TS-1/H_2O/H_2O_2 system, and the understanding of how they are affected by the presence of water molecules become key factors when TS-1 works as catalyst in the presence of aqueous H_2O_2. In particular, the study of the effect of H_2O on the nature, the equilibrium, and the stability of the Ti-peroxo species formed on TS-1 assumes great importance.

In this context, the evaluation of TS-1 behavior in the presence of H_2O from the liquid phase becomes essential. Figure 17a reports the DR UV-Vis spectra of TS-1 without activation (as such in air – black curve) and after interaction with water from the liquid phase (blue curve). The spectrum of the nonactivated TS-1 is characterized by a $Ti^{IV}O^{2-} \rightarrow Ti^{III}O^{-}$ LMCT slightly red shifted (220 nm) with respect to that

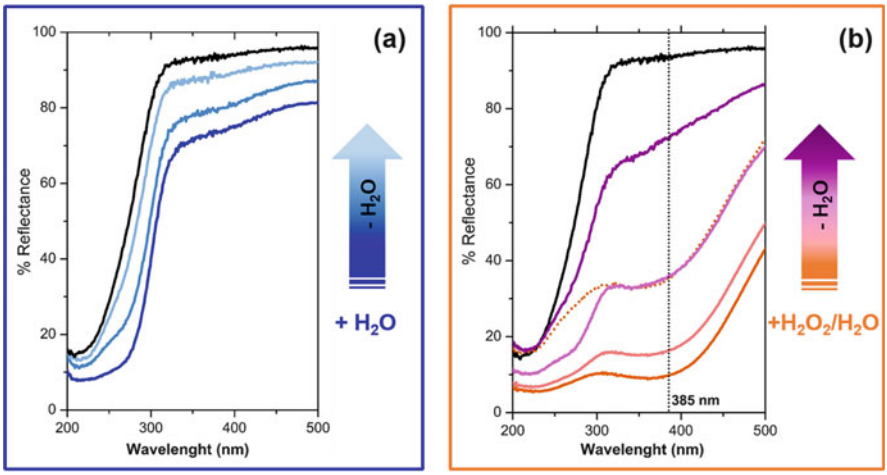

Fig. 17 Section (**a**): DR UV-Vis spectra of the TS-1 catalyst as such in air (black curve), after having been contacted with H_2O drops (blue curve) and after H_2O desorption upon time-lapse in air of 24 h and 7 days (light blue curves). Section (**b**): DR UV-Vis spectra of the TS-1 catalyst as such in air (black curve) and after contact with H_2O_2/H_2O (30 wt%) solution (orange curve). Light orange, pink, and purple curves report the effect of time-lapse in air after 10 h, 24 h, and 15 days, respectively. The orange dotted spectrum refers to the spectrum collected after the longer time elapsed in air (15 days – purple spectrum) upon dosage with H_2O in liquid phase. Unpublished figures reporting data previously published in [173]

measured on the activated material (*ca* 200 nm) because it still contains a fraction of water adsorbed from the atmosphere [173]. After the contact with H_2O drops, a further red shift of the $Ti^{IV}O^{2-} \rightarrow Ti^{III}O^{-}$ LMCT (now at around 280 nm) is observed, due to the increase of the coordination number of Ti^{IV} centers up to six [164]. These spectral modifications are combined with a consistent reduction of the reflectance signal in the whole 300–550 nm range due to the presence of liquid water in the space between adjacent zeolite crystals that causes a reduction of the scattering power of the sample. The following time evolution (light blue curves) of the UV-Vis spectra of TS-1 after interaction with water from the liquid phase shows the progressive evaporation of water molecules. It is evident that these spectra (light blue curves) progressively move toward the spectrum of the nonactivated material (black). The complexity of the spectra collected upon time-lapse in air reflects the heterogeneity of the atoms present in the first coordination sphere of Ti^{IV}, i.e., both chemically bonded framework oxygen atoms and weakly interacting oxygen atoms of physically adsorbed H_2O [158, 191].

Figure 17b reports the DR UV-Vis spectra obtained upon contact of some drops of a 30 wt% H_2O_2/H_2O solution (orange curve) on a nonactivated TS-1 (black curve). A dramatic modification of the spectral features is evident due to the appearance of a new component at around 385 nm. This band can be ascribed to the LMCT of a "side-on" peroxo ligand to the Ti center of the catalyst which confers

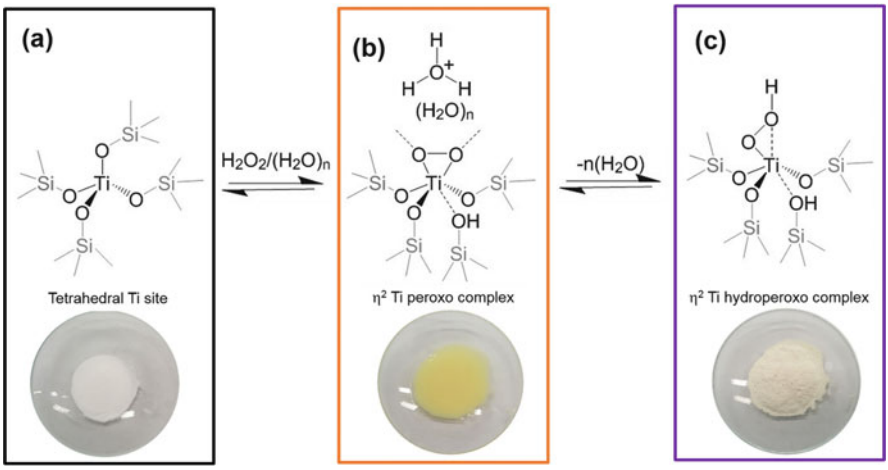

Fig. 18 Schematic representation of the equilibria between tetrahedral Ti^{IV} framework species and "side-on" η^2 Ti-peroxo complexes inside the TS-1 channels upon contact with a H_2O_2/H_2O solution (pictures (**a**) and (**b**)) and between "side-on" η^2 Ti-peroxo and "end-on" Ti-hydroperoxo complexes upon dehydration (pictures (**b**) and (**c**)). The images in the bottom refer to the typical color observed for the TS-1 powder when different complexes with H_2O_2 are formed

to the catalyst a typical yellow color [161, 162, 165, 167, 173, 190], as reported in Fig. 18b.

Clear spectral modifications are evident due to the effect of the progressive water desorption deriving from times elapsed in air of 10 h, 24 h, and 15 days (see Fig. 17b: light orange, pink, and purple spectra, respectively). In fact, upon dehydration, a gradual loss of the yellow color is accompanied by the decrease of the band at 385 nm testifying the progressive consumption of the yellow Ti-peroxo complexes ("side-on" η^2 Ti-peroxo complexes) characterized by a very low stability in the absence of a water excess. The purple spectrum in Fig. 17b reports the effect of a long dehydration time (15 days elapsed in air). In this case, the UV-Vis spectral profile is very similar to that of the material in air without activation (black spectrum); however, some absorption is still present in the 285–485 nm range. The present manifestation reflects the existence of peculiar species, only reversible upon calcination at high temperature. This resistant fraction corresponds to the stable "end-on" η^2 Ti-hydroperoxo complexes, prevailing at low water content and conferring a cream color to the TS-1 powder (Fig. 18c) [161, 162, 167, 173, 190]. Bonino et al. reported that these residual stable species are poorly reactive toward organic substrates [173].

Interestingly, dosing H_2O in the liquid phase on the sample previously contacted with H_2O_2 and then aged for long time in air, it is possible to observe that the component at 385 nm is partially restored, together with the typical yellow color. It means that the yellow "side-on" Ti-peroxo complex is stable only in the presence of an excess of water and, moreover, that the process exhibits a clear reversibility, so

proving that the presence of water plays an important role in determining the ratio between the hydroperoxo and the peroxo Ti species on the working catalyst (see equilibria depicted in Fig. 18b, c) [161, 162, 167, 173, 190].

Bonino et al. [173] also proved that the interaction with hydrogen peroxide is not responsible for an extensive damage of the framework tetrahedral Ti^{IV} sites of the TS-1, as in contrast it usually occurs in the presence of Ti^{IV} grafted species (as in the case of Ti-MCM-41 silica) [192]. In fact, after a preliminary contact with H_2O_2 and a long dehydration in air, the "side-on" Ti-peroxo complexes are formed again upon further addition of a H_2O_2 solution. Bonino and coworkers reported that only a small fraction (about 10%) of Ti^{IV} is involved in the formation of very stable species (the cream colored Ti-hydroperoxo species of Fig. 18c) which, in any case, can be removed upon activation at 400°C [173].

Further insights on active Ti-(hydro)peroxo specie arose from vibrational techniques. However, the detection of infrared fingerprints of Ti-peroxo species (formed upon interaction with H_2O_2/H_2O solution) is a very hard task, as, in standard conditions, the infrared highly active modes of the great amount of water overshadow all the other infrared vibrational modes.

Tozzola et al. [159] focused their attention only on peroxo species infrared active modes (see Fig. 19a). Neutral solution of H_2O_2 (curve 2, left part of Fig. 19a) was dosed at −40°C on activated TS-1 (curve 1, left part of Fig. 19a) and a band centered at 880 cm^{-1} grew up. Since a band at 876 cm^{-1} also appears on Ti-free, on silicalite-1, and being ν(O-O) of liquid H_2O_2 at 875 cm^{-1}, this feature is obviously assigned to physisorbed H_2O_2, mainly present in TS-1 channels.

Upon interaction at −160°C with basic aqueous solutions of H_2O_2 (NH_3/H_2O_2 or $NaOH/H_2O_2$), a new infrared band at 864 cm^{-1} can be appreciated in both cases (dotted curves). The subsequent heating of the sample at about −40°C with a parallel continuous decrease of the equilibrium pressure (Fig. 19a, curve 3) leads to the appearance of another band at 836 cm^{-1}, present, this time, only in TS-1 sample. If the temperature is further increased, the band completely disappears, probably because of thermal lability of the formed species. This feature was considered to be a real fingerprint of Ti-peroxo active species stabilized in basic conditions. It is fundamental to notice that the band can be detected only in a small range of temperatures and in the presence of a small amount of water. Hence the adoption of a particular experimental procedure is fundamental in the spectroscopic identification of labile complexes, as expected for an active species in catalysis.

The existence of Ti-peroxo species was further proved by Lin et al. [193] by means of $H_2{}^{18}O_2$ and photolysis of the complex (see Fig. 19b). In this case, a band not present in silicalite-1 (at 837 or 793 cm^{-1} in the case of $H_2{}^{18}O_2$) is observed when the sample, previously contacted with hydrogen peroxide, is evacuated for 12 h (upper part of Fig. 19b). Another proof for the existence of the complex is given by irradiating at 355 nm the formed Ti-peroxo complex and by observing the erosion of the 837 and 793 cm^{-1} bands (lower part of Fig. 19b), the formation of titanol groups (spectral range not shown for sake of brevity), and the consequent formation of oxygen gas.

Bordiga et al. [161] reported a very exhaustive study of Ti-peroxo species in TS-1 by exploiting rR spectroscopy potentialities. Since Ti-peroxo complexes are colored species (see Fig. 18b), a laser source in the corresponding spectral range should be used to enhance the Raman vibrational modes associated to the active species and fulfilling the selection rules.

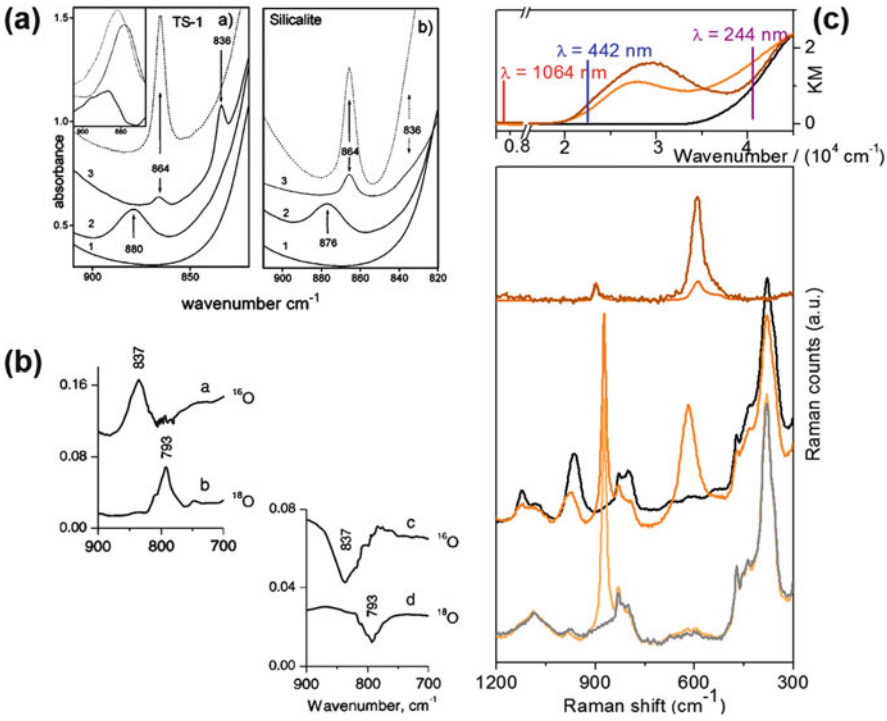

Fig. 19 Infrared (parts **a** and **b**) and Raman spectra (part **c**) of TS-1 interacting with H_2O_2/H_2O. Part **a** shows a comparison between TS-1 and silicalite-1, reporting: dehydrated samples (curves 1), after interaction with H_2O_2/H_2O at −40°C (curves 2), after contact with a solution of NH_3/H_2O_2 at −160°C (dotted curves), and after subsequent heating of the sample at −40°C with parallel outgassing (curves 3). Reprinted from the Journal of Catalysis, vol 179, Tozzola et al., On the structure of the active site of Ti-silicalite in reactions with hydrogen peroxide: A vibrational and computational study, pp 64–71, Copyright 1998, with permission from Elsevier. Part (**b**): TS-1 interacting with aqueous $H_2{}^{16}O_2$ (curve a) and $H_2{}^{18}O_2$ (curve b) and outgassed for 12 h (top); difference spectra recorded after 20 min irradiation of samples a and b at 355 nm (45 mWcm^{-2}) (bottom). Adapted with permission from [193]. Copyright 2002 American Chemical Society. Part (**c**): DR-UV-Vis spectra of a TS-1 sample in vacuo (black curve), in contact with a H_2O_2/H_2O solution (orange curve), and of $[NH_4^+]_3[TiF_5O_2]^{3-}$ (brown curve) (upper part); Raman spectra of $[NH_4^+]_3[TiF_5O_2]^{3-}$ (λ = 1,064 nm dark orange curve and λ = 442 nm brown curve), pure TS-1 (black curve) and interacting with H_2O_2/H_2O (orange curve), pure silicalite-1 (gray curve) and interacting with H_2O_2/H_2O (light orange curve) (lower part). Adapted from [161] Wiley VCH, under the Creative Commons Attribution License (CC-BY). © 2002 WILEY-VCH Verlag GmbH & Co. KGaA, Weinheim

In this respect, these authors [161] adopted the 442 nm laser line, and they observed for the first time a new band at 618 cm^{-1} (see the central orange curve in Fig. 19c), together with some features already found when a laser line at 1,064 nm was adopted [159]: (1) the decrease and blue shift of the 960 cm^{-1} band, (2) the quenching of 1,125 cm^{-1} fingerprint because of the loss of the tetrahedral symmetry, and (3) the appearance of an intense feature at 875 cm^{-1} due to ν(O-O) of physisorbed H_2O_2 solution in the channels.

To properly assign the new feature at 618 cm^{-1}, rR spectra were measured: (1) silicalite-1 in contact with H_2O_2/H_2O solution (see light orange spectrum in the bottom of Fig. 19c), which gave the band at 875 cm^{-1}, already found in the reported infrared spectra, ascribable to ν(O-O) of hydrogen peroxide physisorbed in the channels, and (2) the $[NH_4^+]_3[TiF_5O_2]^{3-}$ model compound, which showed a very intense band at 595 cm^{-1} undergoing a distinct enhancement when the 442 nm excitation source is used (see brown curve in comparison with dark orange in the upper part of Fig. 19c). The last detected feature was unambiguously assigned to the symmetric breathing mode of the $Ti(O)_2$ cycle present in the crystalline structure of $[NH_4^+]_3[TiF_5O_2]^{3-}$ consisting of TiF_5O_2 units intercalated with NH^{4+} counterions. The similarity between rR and UV-Vis spectra of the model compound and Ti-peroxo species formed in TS-1 contacted with H_2O_2 aqueous solution brings to the conclusion that the species giving an electronic absorption band at 385 nm and a rR mode at 618 cm^{-1} have a side-on geometry as in the $[NH_4^+]_3[TiF_5O_2]^{3-}$ model salt.

As in the case of the bare Ti sites, the use of X-ray spectroscopies in the characterization of active sites in TS-1 (i.e., Ti adducts with H_2O_2) gave a further relevant piece of information toward the understanding of their structure and properties. Indeed, (a) IR studies were carried out in model conditions, fairly reproducing the real reaction environment of TS-1, and (b) rR gave direct access only to the highly symmetric Ti-peroxo species, whereas no information about the peculiar features of the Ti-hydroperoxo moieties can be obtained. Even if XAS represents an optimal tool in the study of Ti-(hydro)peroxo, particular care has to be put in the preservation of the samples, since the already commented lability of these active species could result in their modification under the intense X-rays beam (i.e., they could suffer beam damage). A strategy allowing this undesired side effect to be avoided is represented by cryogenic measurement of the active moieties [173]: the stability of Ti-(hydro)peroxo is logically much higher at liquid N_2 temperature (−196°C), thus allowing the XAS data acquisition to be performed without altering the material. A key point of such procedure is the correct evacuation of the cryostat from air, in order to avoid the desorption of H_2O_2/H_2O before these are stabilized at low temperature. The best strategy has been found in a first cooling stage down to moderate temperature (about 0°C) in air, followed by evacuation and finally by the principal cooling phase toward −196°C. Following this methodology, Prestipino et al. reported an in-depth study of the Ti-peroxo/Ti-hydroperoxo equilibrium as a function of hydration (see Fig. 18b, c) [190]. A further advance achieved in this work was the dosage of nearby anhydrous H_2O_2 vapors, generated through the decomposition of its complex with monobasic potassium phosphate (KH_2PO_4), prepared according to patent literature [194]. When TS-1 is contacted with an aqueous solution of H_2O_2 (Path A in Fig. 20), the XANES spectrum is deeply altered in

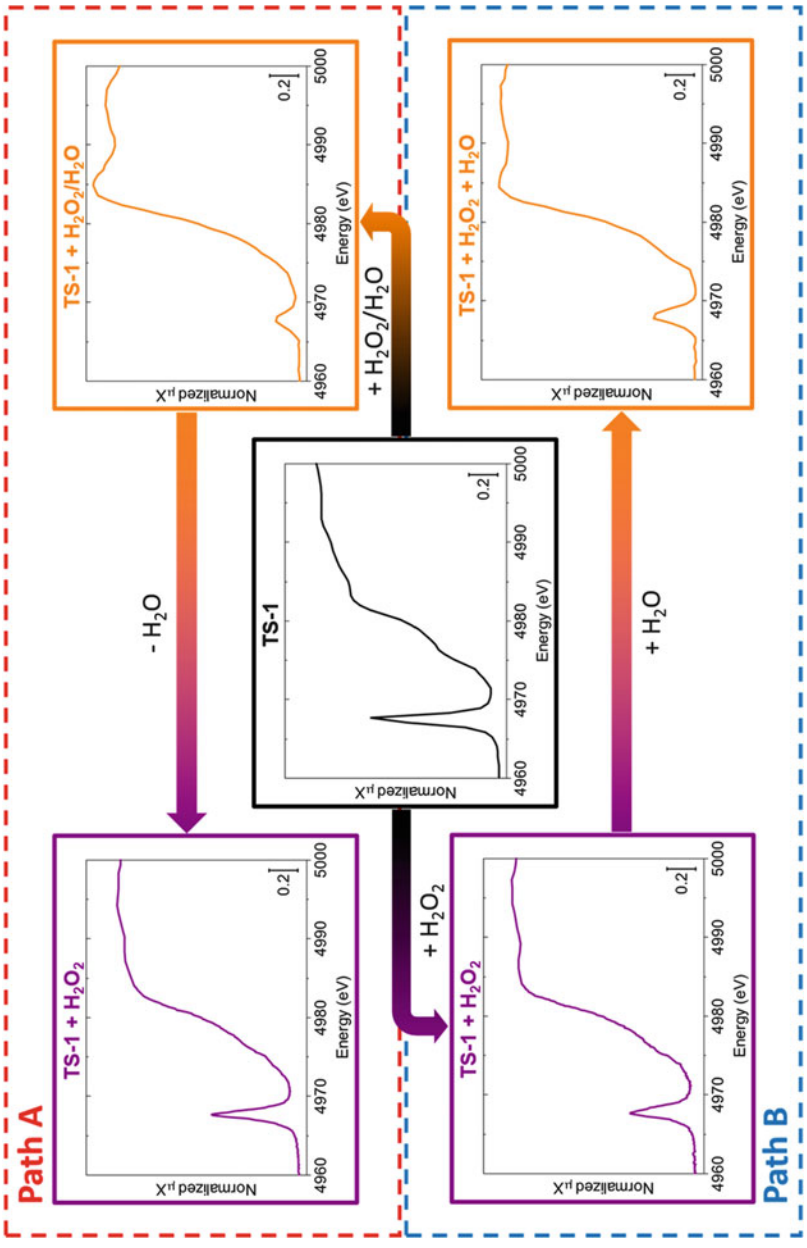

Fig. 20 XANES study of the Ti-peroxo/Ti-hydroperoxo equilibrium as a function of hydration, performed through two different strategies. Path A: from "liquid phase," forming the Ti-peroxo species from a H_2O_2/H_2O solution and thus dehydrating by H_2O sublimation at − 196°C. Path B: from "gas phase," dosing H_2O_2 from decomposition of its adduct with KH_2PO_4 [194] and then hydrating the sample with H_2O vapor. Unpublished figures reporting data previously published in [190]

comparison with the one of the activated material. The most evident modification in the spectrum is the drop of the pre-edge feature intensity down to ~25% of the original one, with a simultaneous increase of FWHM. Such spectral evolution is a strong evidence of the change in the coordination of Ti, definitely altered from the original tetrahedral environment of the bare TS-1. Furthermore, in the edge region, two prominent maxima appear, ascribed to the formation of the side-on Ti-peroxo species [173].

Upon dehydration (achieved through vacuum sublimation of H_2O at cryogenic temperatures), the pre-edge peak is partially recovered, and the edge maxima decrease toward a flat, unresolved spectrum. Such equilibrium is perfectly reversible, since a dosage of H_2O from gas phase fully restores the previous situation. This insight suggests that the spectrum achieved upon dehydration does not generate from the decomposition of the Ti-peroxo adduct, whereas it most probably accounts for its transformation toward a different structure, possibly a Ti-hydroperoxo. This assumption was checked comparing the spectrum of the supposed Ti-hydroperoxo on TS-1 with the one obtained contacting Ti-MSA (an amorphous, mesoporous Ti silicate) [195, 196] with *tert*-butyl hydroperoxide dissolved in an anhydrous solvent, where a nice overlap was observed. The choice of Ti-MSA was due to the need of a wide porosity system (indeed, the micropores of a regular TS-1 do not allow the diffusion of the *tert*-butyl hydroperoxide to reach the Ti sites) having Ti sites mimicking TS-1 ones. As a further cross-check, the activated TS-1 was contacted with anhydrous H_2O_2 vapor (Path B of Fig. 20), with the aim to verify if the same species previously observed are generated. This was actually the finding, since the spectrum closely resembles the one obtained upon dehydration along Path A. Finally, the dosage of H_2O vapor allowed to produce again Ti-peroxo species, testifying the reliability of the proposed Ti-peroxo/Ti-hydroperoxo equilibrium.

4.3 Characterization of Amorphous Ti Species

Besides the characterization of the perfect tetrahedral framework Ti^{IV} sites and their adducts with hydrogen peroxide, the study of the "non-perfect" Ti species (the so-called "amorphous" species) is assuming increasing attention, in order to explain their possible role in catalysis. The nature of these amorphous species can be investigated by means of DR UV-Vis spectroscopy [163, 177, 197].

Su et al. reported the DR UV-Vis spectra of various TS-1 samples characterized by the presence of different Ti species (Fig. 21a) [176]. Three clear absorptions are evident at 200–220, 260–280, and 310–330 nm. The first one is assigned to framework tetrahedral Ti species, whereas the last one can be ascribed to a polymorph of bulk TiO_2. The band in the 260–280 nm spectral range, instead, is derived from the presence of a fraction of peculiar amorphous Ti species that the authors termed non-framework (NFW) Ti species, i.e., Ti oligomers containing hexacoordinated Ti-O-Ti structure.

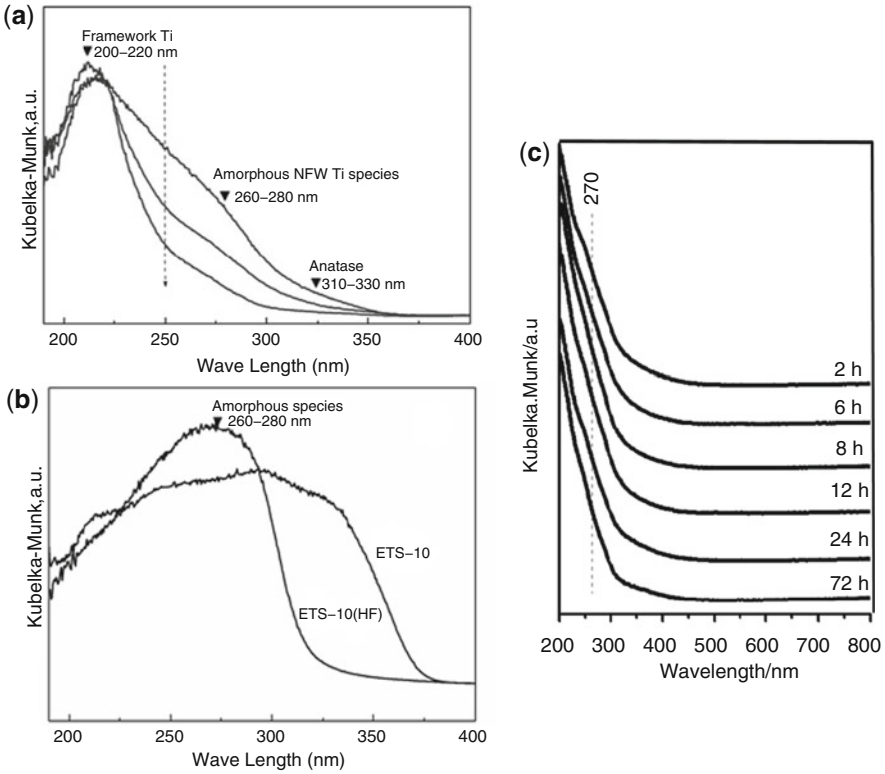

Fig. 21 Section (**a**): DR UV-Vis spectra of different TS-1 catalysts collected without activation. Section (**b**): DR UV-Vis spectra of an ETS-10 sample and of an ETS-10 corroded with a 7 wt.% HF solution. Reprinted from the Journal of Catalysis, vol 288, Su et al., Amorphous Ti species in titanium silicalite-1: Structural features, chemical properties, and inactivation with sulfosalt, pp 1–7, Copyright 2012 with permission from Elsevier [176]. Section (**c**): DR UV-Vis spectra of a TS-1 zeolite (Si/Ti = 50) for different crystallization stages at various times of synthesis. Reprinted with permission from [163]. Copyright 2013 American Chemical Society

In order to confirm their statements, Su and coworkers tried to imitate the structure of these amorphous species by corroding the framework of an ETS-10 titanosilicate with HF solutions. The framework of this titanosilicate is constituted by linear chains of corner-shared TiO_6 octahedra linked by corner-shared SiO_4 tetrahedra [198]. By corroding the ETS-10 framework with a 7 wt.% HF solution, the hexacoordinated Ti-O-Ti chains can be broken up into smaller ones, reproducing in some way the hexacoordinated amorphous NFW Ti-O-Ti species. The DR UV-Vis spectra of an ETS-10 powder before and after the corrosion process with HF are reported in Fig. 21b. It is evident that the amorphous Ti species obtained from the degradation of the ETS-10 are responsible for the appearance of a band centered at around 280 nm.

The intensity of the absorption band generated by NFW amorphous Ti species at around 280 nm obviously increases by decreasing the Si/Ti ratio in the TS-1 [177].

The evolution of different titanium species during the crystallization process of the TS-1 zeolite has been monitored by Guo and coworkers. Figure 21c reports the DR UV-Vis spectra of a TS-1 (Si/Ti = 50) for different crystallization stages at various times of the hydrothermal treatment [163]. All the spectra collected at different time intervals exhibit a similar spectral profile: a strong signal at 210 nm generated by the framework tetrahedral Ti^{IV} sites and a shoulder at 270 nm due to the NFW octahedral amorphous Ti species [197]. This weak shoulder seems to gradually decrease by increasing the crystallization time. Guo et al. tried to explain this phenomenon affirming that a small fraction of tetrahedral Ti species can be "extruded" in the form of isolated amorphous Ti species in octahedral coordination during the framework formation. This species are attached to the solid phase and dissolved into the liquid phase when the coordination environment of the framework Ti centers becomes gradually more rigid [163].

rR spectroscopy was adopted by Guo et al. [197] to characterize the active species formed in two different TS-1 samples: TS-1A and TS-1B (derived from TS-1A upon treatment with NH_4HF_2 and H_2O_2). From the DR UV-Vis spectra of the two samples, it is evident that TS-1B sample shows clearly a new component at 270 nm besides the well-known feature at around 200 nm expected for LMCT of tetrahedral framework Ti. As 244 nm laser line gives rise to resonance for tetrahedral Ti, 266 nm laser line should enhance Raman active vibrational modes of the new detected species, identified as NFW amorphous Ti species [163, 176]. In the case of TS-1B sample, a new intense band appears at 695 cm^{-1} in its rR spectrum. This new signal, not present in a sample showing all the Ti inserted in the framework (e.g. TS-1A), is ascribed to Raman active vibrational modes of the amorphous species giving rise to the electron transition at 270 nm.

To study in depth the structure of the active species and their behavior in the olefin epoxidation reaction, the two samples were also investigated in contact with H_2O_2/H_2O solution to form the active species and then with propylene as a probe reactant, by using UV Raman ($\lambda = 325$ nm) spectroscopy. The active species formed in TS-1A sample shows the same Raman features.

Subsequent interaction with propylene at 60°C gives rise to new Raman bands at 725, 820, 890, 945, 1,021, 1,095, 1,168, and 1,265 cm^{-1}, ascribable to the formation of propylene oxide, whereas the bands at 615 and 875 cm^{-1} disappear and the fingerprint at 1,125 cm^{-1} is restored. This result clearly testifies the formation of active species, upon interaction with H_2O_2/H_2O solution, able to partially oxidize propylene to form propylene oxide.

The same experiment was performed on TS-1B. Upon interaction with H_2O_2/H_2O solution, the already discussed Raman bands at 615 and 875 cm^{-1} appear and the 695 and 1,125 cm^{-1} bands decrease in intensity, suggesting that active species are formed both on tetrahedral and amorphous non-framework Ti. Propylene interaction at 60°C gives rise to new Raman bands at 517, 805, 840, 917, and 983 cm^{-1}, ascribable to the 1,2-propanediol, one of the by-products in the reaction. This assignment is confirmed by the presence of its typical C-H stretching mode around

3,000 cm^{-1} (not discussed for sake of brevity). In this case, the 1,125 cm^{-1} Ti fingerprint seems to be restored after product formation. Guo et al. [197] support their conclusion also with catalytic data, which showed that TS-1A and TS-1B samples have a similar H_2O_2 conversion, but the latter exhibits a lower selectivity toward propylene oxide.

Concerning X-ray spectroscopies, few studies dealt with non-perfect TS-1 materials. Among these, a relevant example is represented by the work by Zuo et al., exploiting the Ti L-edges transition rather than the more conventional K-edge [199]. Considering all the possible L transitions, of particular interest are the so-called L_2 and L_3 edges, generating from the $2p \rightarrow 3d$ transitions from the $2p_{1/2}$ and $2p_{3/2}$, respectively. Each of them is further split in several components, according to the separation of the *d* levels as a consequence of the crystal fields experienced by Ti. Thus, it is clear that this technique has a very high structural sensitivity [200]. The main drawback is due to the energy range where these transitions falls, roughly among 450 and 480 eV (i.e., in the soft X-rays). This implies that experiments should be carried out under ultrahigh vacuum (UHV), imposing constrains which hampers the possibility to run measurements in conditions relevant for catalysis (e.g., in the presence of reactants). Very few studies are available concerning TS-1 and Ti-based materials, but recently Zuo et al. successfully exploited this technique to confirm the presence of a new type of pentahedral Ti site in their TS-1 samples, which they correlated to their higher catalytic activity in propene epoxidation [199]. Recent developments in the soft X-ray experimental tools are progressively opening the application of these measurements at ambient conditions [127], thus making them more accessible and useful to the catalysis community in the near future.

5 Conclusions

The main aim of this chapter was to show the goodness and the potential of combining different advanced characterization techniques in elucidating the metal active sites in metal-zeolites, as well as how the rational design of in situ/operando experiments can provide new catalytic insights. Notwithstanding decades of research efforts, the results described and discussed in this contribution show how the field of metal-exchanged zeolites is still intriguing and open to further findings. This is particularly true in relation to their activity in selective oxidation reactions and the renewed interest in developing closed catalytic cycles for the MTM "dream reaction." Three different kinds of zeolites were considered, with a focus on the geometric and electronic structure of the redox-active TMIs stabilized in the zeolite framework, on the related characterization potentiality and limits, and on the open characterization challenges.

Namely, TS-1 can be considered as an example of "single-site" catalyst, since – when well manufactured – all Ti^{IV} atoms are found in framework positions in a tetrahedral environment. This allowed to precisely define the characteristic

spectroscopic fingerprints, to carry out in-depth studies about interaction with ligands of framework Ti^{IV} and its reactivity toward aqueous solution of H_2O_2. However, the reported survey shows how often a multi-technique approach is important to obtain reliable and significant information about the active site properties. Moreover, the study of the reactivity in aqueous medium with H_2O_2 represented a challenge for the involved researchers, who needed to optimize characterization setups and protocols to discriminate between the effect on the spectroscopic features of the H_2O (ligand) and the H_2O_2 (reactant) and their synergic role. Further degrees of complexity derive from the necessity to carry out the experiments on samples activated under controlled atmosphere (vacuum) and from the lability of the active Ti-peroxo/Ti-hydroperoxo complexes. rR still represents one of the main techniques to study these materials, particularly coupled to optimized setups to carry out in situ experiments, with particular care to avoid spectral modifications due to laser irradiation. In this case, averaged techniques such as DR UV-Vis and XAS/XES showed their potentiality in monitoring changes in the "single-site" Ti^{IV} local environment, even if the lability of the Ti-peroxo/Ti-hydroperoxo complexes suggests caution when working with X-rays, especially from an undulator source, in relation to the possibility of beam damage.

In principle, Cu-exchanged zeolites could be considered as model systems, since the Cu^{I}/Cu^{II} ions are stabilized as counterions and many structural information can be found in the literature about their location in the zeolite channels and cavities, also in relation to Al_{fw} content and distribution. However, the lively debate reviewed in this chapter in relation to the activity in the MTM reaction shows how this system is far from being a "single-site" catalyst. DR UV-Vis spectroscopy was particularly relevant in the study of Cu-ZSM-5 (and Cu-MOR), in relation to the peculiar band around 22,700 cm^{-1}, decreasing its intensity when contacted with methane. However, also in this case, more detailed insights into the structure of the Cu-oxo sites responsible for these spectroscopic fingerprints (and likely involved in methane oxidation) could be obtained only by coupling different techniques, such as rR and NCA or DFT calculations. Moreover, there is still a lot of interest in giving a precise assignment of the spectral features of other Cu-zeolites, such as small-pore Cu-CHA (characterized by a very peculiar and intense "quadruplet" in the *d-d* region), particularly by using operando techniques allowing to work under flow and at high temperatures. This is crucial in relation to the stability and possible interplays among different Cu-oxo species.

An important contribution in the field of Cu-zeolites was given by XAS experiments, concerning the "starting point" (pre-activated catalyst), the formation of active Cu-oxo species, their interaction with methane, and subsequent steam-mediated methanol desorption. Also in this respect, it is important to underline the importance of DFT calculations, which should guide data fitting in order to give reliable and consistent information on the local structure of the involved metal centers. Moreover, being an averaged technique applied to materials to which the concept of "single site" is questioned by many authors, XAS analysis output (especially XANES) should be considered with great care.

The third class of catalysts considered in this contribution, Fe-zeolites, represents a further increase in complexity, due to the difficulties in obtaining materials with a homogenous site distribution. In addition to the difficulties discussed for Cu-zeolites, in this case grafted Fe ions were proposed, together with a variety of di-, tri-, and olinuclear oxo/hydroxo clusters dispersed inside the zeolites channels and large iron oxide aggregates formed on the zeolite particles' external surface. This implies that the main averaged techniques discussed above, i.e., XAS and DR-UV-Vis, have intrinsic limitations, notwithstanding the reported efforts of rationalization of UV-Vis deconvoluted sub-bands. rR still represents one of the most powerful techniques for the characterization of oxo species (as in the case of TS-1 and Cu-zeolites), but the optimization of setups and protocols to study partial oxidation reactions is challenging, so that there is still room for new findings. Moreover, very recent developments about Fe-zeolites for the MTM reaction involved the optimization of exchange procedures (or thermal treatments), aimed to improve Fe insertion and ideally obtain "single-site" catalysts with Fe^{II} stabilized as counterion. Clearly, these approaches could open the way to further spectroscopic insights into the nature of active sites in partial oxidation reactions.

As a final remark, it is important to recall the recently proposed concepts about self-organization of extraframework cations in zeolites and about the role of ion mobility during catalysis [51, 149]. These notions could help in the interpretation of many apparently contradictory results reported in literature. Even if adding up to the complexity of the spectroscopic challenge, they testify about a scientific field still active and intriguing, particularly in relation to the possibility to follow the catalyst in operando conditions with a multi-technique approach.

References

1. Sankar G, Raja R, Thomas JM (1998) Redox solid catalysts for the selective oxidation of cyclohexane in air. Catal Lett 55:15–23
2. Thomas JM (2001) On the nature of isolated active sites in open-structure catalysts for the aerial oxidation of alkanes. Top Catal 15:85–91
3. Raja R, Thomas JM, Greenhill-Hooper M et al (2007) A high-performance selective oxidation system for the facile production of fine chemicals. Chem Commun:1924–1926
4. Raja R, Thomas JM, Xu MC et al (2006) Highly efficient one-step conversion of cyclohexane to adipic acid using single-site heterogeneous catalysts. Chem Commun:448–450
5. Maurelli S, Vishnuvarthan M, Berlier G et al (2012) NH_3 and O_2 interaction with tetrahedral Ti^{3+} ions isomorphously substituted in the framework of TiAlPO-5. A combined pulse EPR, pulse ENDOR, UV-Vis and FT-IR study. Phys Chem Chem Phys 14:987–995
6. Maurelli S, Vishnuvarthan M, Chiesa M et al (2011) Elucidating the nature and reactivity of Ti ions incorporated in the framework of AlPO-5 molecular sieves. New evidence from ^{31}P HYSCORE spectroscopy. J Am Chem Soc 133:7340–7343
7. Morra E, Cuko A, Maurelli S et al (2015) Electronic structure of Ti^{3+}-ethylene complexes in microporous aluminophosphate materials. A combined EPR and DFT study elucidating the role of SOMO orbitals in metal-olefin π·complexes. J Phys Chem C 119:26046–26055

8. Novara C, Alfayate A, Berlier G et al (2013) The interaction of H_2O_2 with TiAlPO-5 molecular sieves: probing the catalytic potential of framework substituted Ti ions. Phys Chem Chem Phys 15:11099–11105
9. Berlier G, Spoto G, Bordiga S et al (2002) Evolution of extraframework iron species in Fe silicalite 1. Effect of Fe content, activation temperature, and interaction with redox agents. J Catal 208:64–82
10. Zecchina A, Rivallan M, Berlier G et al (2007) Structure and nuclearity of active sites in Fe-zeolites: comparison with iron sites in enzymes and homogeneous catalysts. Phys Chem Chem Phys 9:3483–3499
11. Beale AM, van der Eerden AMJ, Kervinen K et al (2005) Adding a third dimension to operando spectroscopy: a combined UV-Vis, Raman and XAFS setup to study heterogeneous catalysts under working conditions. Chem Commun:3015–3017
12. Jentoft FC (2009) Ultraviolet-visible-near infrared spectroscopy in catalysis: theory, experiment, analysis, and application under reaction conditions. Adv Catal 52:129–211
13. Tinnemans SJ, Kox MHF, Sletering MW et al (2006) Dealing with a local heating effect when measuring catalytic solids in a reactor with Raman spectroscopy. Phys Chem Chem Phys 8:2413–2420
14. Tinnemans SJ, Mesu JG, Kervinen K et al (2006) Combining operando techniques in one spectroscopic-reaction cell: new opportunities for elucidating the active site and related reaction mechanism in catalysis. Catal Today 113:3–15
15. Beato P, Schachtl E, Barbera K et al (2013) Operando Raman spectroscopy applying novel fluidized bed micro-reactor technology. Catal Today 205:128–133
16. Rasmussen SB, Lopez-Medina R, Portela R et al (2015) Shaping up operando spectroscopy: Raman characterization of a working honeycomb monolith. Cat Sci Technol 5:4942–4945
17. Bordiga S, Lamberti C, Bonino F et al (2015) Probing zeolites by vibrational spectroscopies. Chem Soc Rev 44:7262–7341
18. Bordiga S, Groppo E, Agostini G et al (2013) Reactivity of surface species in heterogeneous catalysts probed by *in situ* X-ray absorption techniques. Chem Rev 113:1736–1850
19. Lamberti C, Groppo E, Spoto G et al (2007) Infrared spectroscopy of transient surface species. Adv Catal 51:1–74
20. Lamberti C, Zecchina A, Groppo E et al (2010) Probing the surfaces of heterogeneous catalysts by *in situ* IR spectroscopy. Chem Soc Rev 39:4951–5001
21. Tang P, Zhu Q, Wu Z et al (2014) Methane activation: the past and future. Energ Environ Sci 7:2580–2591
22. Park D, Lee J (2013) Biological conversion of methane to methanol. Korean J Chem Eng 30:977–987
23. Schwarz H (2011) Chemistry with methane: concepts rather than recipes. Angew Chem Int Ed 50:10096–10115
24. Smeets PJ, Groothaert MH, van Teeffelen RM et al (2007) Direct and NO-assisted N_2O decomposition over Cu-zeolites. In: Xu R, Gao Z, Chen J, Yan W (eds) From zeolites to porous MOF materials: the 40th Anniversary of International Zeolite Conference, Proceedings of the 15th International Zeolite Conference, pp 1080–1087
25. Olah GA, Prakash GKS, Goeppert A (2011) Anthropogenic chemical carbon cycle for a sustainable future. J Am Chem Soc 133:12881–12898
26. Groothaert MH, Smeets PJ, Sels BF et al (2005) Selective oxidation of methane by the bis(mu-oxo)dicopper core stabilized on ZSM-5 and mordenite zeolites. J Am Chem Soc 127:1394–1395
27. Panov GI, Sobolev VI, Kharitonov AS (1990) The role of iron in N_2O decomposition on ZSM-5 zeolite and reactivity of the surface oxygen formed. J Mol Catal 61:85–97
28. Dubkov KA, Sobolev VI, Panov GI (1998) Low-temperature oxidation of methane to methanol on FeZSM-5 zeolite. Kinet Catal 39:72–79
29. Sobolev VI, Dubkov KA, Panna OV et al (1995) Selective oxidation of methane to methanol on a FeZSM-5 surface. Catal Today 24:251–252

30. Kharitonov AS, Sheveleva GA, Panov GI et al (1993) Ferrisilicate analogs of ZSM-5 zeolite as catalysts for one-step oxidation of benzene to phenol. Appl Catal A Gen 98:33–43
31. Panov GI, Kharitonov AS, Sobolev VI (1993) Oxidative hydroxylation using dinitrogen monoxide – a possible route for organic-synthesis over zeolites. Appl Catal A Gen 98:1–20
32. Hammond C, Forde MM, Ab Rahim MH et al (2012) Direct catalytic conversion of methane to methanol in an aqueous medium by using copper-promoted Fe-ZSM-5. Angew Chem Int Ed 51:5129–5133
33. Beznis NV, van Laak ANC, Weckhuysen BM et al (2011) Oxidation of methane to methanol and formaldehyde over Co-ZSM-5 molecular sieves: tuning the reactivity and selectivity by alkaline and acid treatments of the zeolite ZSM-5 agglomerates. Microporous Mesoporous Mater 138:176–183
34. Kung MC, Lin SSY, Kung HH (2012) In situ infrared spectroscopic study of CH_4 oxidation over Co-ZSM-5. Top Catal 55:108–115
35. Shan JJ, Huang WX, Nguyen L et al (2014) Conversion of methane to methanol with a bent mono(μ-oxo)dinickel anchored on the internal surfaces of micropores. Langmuir 30:8558–8569
36. Beznis NV, Weckhuysen BM, Bitter JH (2010) Cu-ZSM-5 zeolites for the formation of methanol from methane and oxygen: probing the active sites and spectator species. Catal Lett 138:14–22
37. Giordanino F, Vennestrom PNR, Lundegaard LF et al (2013) Characterization of Cu-exchanged SSZ-13: a comparative FTIR, UV-Vis, and EPR study with Cu-ZSM-5 and Cu-β with similar Si/Al and Cu/Al ratios. Dalton Trans 42:12741–12761
38. Vanelderen P, Hadt RG, Smeets PJ et al (2011) Cu-ZSM-5: a biomimetic inorganic model for methane oxidation. J Catal 284:157–164
39. Tsai M-L, Hadt RG, Vanelderen P et al (2014) $[Cu_2O]^{2+}$ active site formation in Cu-ZSM-5: geometric and electronic structure requirements for N_2O activation. J Am Chem Soc 136:3522–3529
40. Groothaert MH, van Bokhoven JA, Battiston AA et al (2003) Bis(μ-oxo)dicopper in Cu-ZSM-5 and its role in the decomposition of NO: a combined in situ XAFS, UV-Vis-near-IR, and kinetic study. J Am Chem Soc 125:7629–7640
41. Halfen JA, Mahapatra S, Wilkinson EC et al (1996) Reversible cleavage and formation of the dioxygen O-O band within a dicopper complex. Science 271:1397–1400
42. Que L, Tolman WB (2002) Bis(μ-oxo)dimetal "diamond" cores in copper and iron complexes relevant to biocatalysis. Angew Chem Int Ed 41:1114–1137
43. Solomon EI, Sundaram UM, Machonkin TE (1996) Multicopper oxidases and oxygenases. Chem Rev 96:2563–2605
44. Holland PL, Tolman WB (1999) Dioxygen activation by copper sites: relative stability and reactivity of (μ-η^2:η^2-peroxo)- and bis(μ-oxo)dicopper cores. Coord Chem Rev 190:855–869
45. Woertink JS, Smeets PJ, Groothaert MH et al (2009) A $[Cu_2O]^{2+}$ core in Cu-ZSM-5, the active site in the oxidation of methane to methanol. Proc Natl Acad Sci U S A 106:18908–18913
46. Smeets PJ, Hadt RG, Woertink JS et al (2010) Oxygen precursor to the reactive intermediate in methanol synthesis by Cu-ZSM-5. J Am Chem Soc 132:14736–14738
47. Smeets PJ, Groothaert MH, Schoonheydt RA (2005) Cu based zeolites: a UV-Vis study of the active site in the selective methane oxidation at low temperatures. Catal Today 110:303–309
48. Smeets PJ, Woertink JS, Sels BF et al (2010) Transition-metal ions in zeolites: coordination and activation of oxygen. Inorg Chem 49:3573–3583
49. Vanelderen P, Vancauwenbergh J, Sels BF et al (2013) Coordination chemistry and reactivity of copper in zeolites. Coord Chem Rev 257:483–494
50. Paolucci C, Parekh AA, Khurana I et al (2016) Catalysis in a cage: condition-dependent speciation and dynamics of exchanged Cu cations in SSZ-13 zeolites. J Am Chem Soc 138:6028–6048
51. Paolucci C, Khurana I, Parekh AA et al (2017) Dynamic multinuclear sites formed by mobilized copper ions in NO_x selective catalytic reduction. Science 357:898–903

52. Sheppard T, Daly H, Goguet A et al (2016) Improved efficiency for partial oxidation of methane by controlled copper deposition on surface-modified ZSM-5. ChemCatChem 8:562–570
53. Narsimhan K, Iyoki K, Dinh K et al (2016) Catalytic oxidation of methane into methanol over copper-exchanged zeolites with oxygen at low temperature. ACS Central Sci 2:424–429
54. Grundner S, Luo W, Sanchez-Sanchez M et al (2016) Synthesis of single-site copper catalysts for methane partial oxidation. Chem Commun 52:2553–2556
55. Grundner S, Markovits MAC, Li G et al (2015) Single-site trinuclear copper oxygen clusters in mordenite for selective conversion of methane to methanol. Nat Commun 6:2553–2556
56. Ipek B, Wulfers MJ, Kim H et al (2017) Formation of $[Cu_2O_2]^{2+}$ and $[Cu_2O]^{2+}$ toward C-H bond activation in Cu-SSZ-13 and Cu-SSZ-39. ACS Catal 7:4291–4303
57. Pappas DK, Borfecchia E, Dyballa M et al (2017) Methane to methanol: structure–activity relationships for Cu-CHA. J Am Chem Soc 139:14961–14975
58. Vanelderen P, Vancauwenbergh J, Tsai ML et al (2014) Spectroscopy and redox chemistry of copper in mordenite. ChemPhysChem 15:91–99
59. Alayon EMC, Nachtegaal M, Kleymenov E et al (2013) Determination of the electronic and geometric structure of Cu sites during methane conversion over Cu-MOR with X-ray absorption spectroscopy. Microporous Mesoporous Mater 166:131–136
60. Vanelderen P, Snyder BER, Tsai M-L et al (2015) Spectroscopic definition of the copper active sites in mordenite: selective methane oxidation. J Am Chem Soc 137:6383−6392
61. Mentzen BF, Bergeret G (2007) Crystallographic determination of the positions of the copper cations in zeolite MFI. J Phys Chem C 111:12512–12516
62. Alayon EM, Nachtegaal M, Ranocchiari M et al (2012) Catalytic conversion of methane to methanol over Cu-mordenite. Chem Commun 48:404–406
63. Alayon EMC, Nachtegaal M, Bodi A et al (2014) Reaction conditions of methane-to-methanol conversion affect the structure of active copper sites. ACS Catal 4:16–22
64. Alayon EMC, Nachtegaal M, Bodi A et al (2015) Bis(μ-oxo) versus mono(μ-oxo)dicopper cores in a zeolite for converting methane to methanol: an *in situ* XAS and DFT investigation. Phys Chem Chem Phys 17:7681–7693
65. Tomkins P, Mansouri A, Bozbag SE et al (2016) Isothermal cyclic conversion of methane into methanol over copper-exchanged zeolite at low temperature. Angew Chem Int Ed 55:5467–5471
66. Sushkevich VL, Palagin D, Ranocchiari M et al (2017) Selective anaerobic oxidation of methane enables direct synthesis of methanol. Science 356:523–527
67. Borfecchia E, Lomachenko KA, Giordanino F et al (2015) Revisiting the nature of Cu sites in the activated Cu-SSZ-13 catalyst for SCR reaction. Chem Sci 6:548–563
68. Li GN, Vassilev P, Sanchez-Sanchez M et al (2016) Stability and reactivity of copper oxo-clusters in ZSM-5 zeolite for selective methane oxidation to methanol. J Catal 338:305–312
69. Markovits MAC, Jentys A, Tromp M et al (2016) Effect of location and distribution of Al sites in ZSM-5 on the formation of Cu-oxo clusters active for direct conversion of methane to methanol. Top Catal 59:1554–1563
70. Palagin D, Knorpp AJ, Pinar AB et al (2017) Assessing the relative stability of copper oxide clusters as active sites of a CuMOR zeolite for methane to methanol conversion: size matters? Nanoscale 9:1144–1153
71. Vilella L, Studt F (2016) The stability of copper oxo species in zeolite frameworks. Eur J Inorg Chem 2016:1514–1520
72. Wulfers MJ, Teketel S, Ipek B et al (2015) Conversion of methane to methanol on copper-containing small-pore zeolites and zeotypes. Chem Commun 51:4447–4450
73. Janssens TVW, Falsig H, Lundegaard LF et al (2015) A consistent reaction scheme for the selective catalytic reduction of nitrogen oxides with ammonia. ACS Catal 5:2832–2845

74. Andersen CW, Borfecchia E, Bremholm M et al (2017) Redox-driven migration of copper ions in the Cu-CHA zeolite as shown by the in situ PXRD/XANES technique. Angew Chem Int Ed 56:10367–10372
75. Lomachenko KA, Borfecchia E, Negri C et al (2016) The Cu-CHA deNO(x) catalyst in action: temperature-dependent NH_3-assisted selective catalytic reduction monitored by operando XAS and XES. J Am Chem Soc 138:12025–12028
76. Martini A, Borfecchia E, Lomachenko KA et al (2017) Composition-driven Cu-speciation and reducibility in Cu-CHA zeolite catalysts: a multivariate XAS/FTIR approach to complexity. Chem Sci 8:6836–6851
77. Beale AM, Gao F, Lezcano-Gonzalez I et al (2015) Recent advances in automotive catalysis for NO_x emission control by small-pore microporous materials. Chem Soc Rev 44:7371–7405
78. Deka U, Juhin A, Eilertsen EA et al (2012) Confirmation of isolated Cu^{2+} ions in SSZ-13 zeolite as active sites in NH_3-selective catalytic reduction. J Phys Chem C 116:4809–4818
79. Ipek B, Lobo RF (2016) Catalytic conversion of methane to methanol on Cu-SSZ-13 using N_2O as oxidant. Chem Commun 52:13401–13404
80. Kulkarni AR, Zhao ZJ, Siahrostami S et al (2016) Monocopper active site for partial methane oxidation in Cu-exchanged 8MR zeolites. ACS Catal 6:6531–6536
81. Perez-Ramirez J, Groen JC, Bruckner A et al (2005) Evolution of isomorphously substituted iron zeolites during activation: comparison of Fe-beta and Fe-ZSM-5. J Catal 232:318–334
82. Capek L, Kreibich V, Dedecek J et al (2005) Analysis of Fe species in zeolites by UV-VIS-NIR, IR spectra and voltammetry. Effect of preparation, Fe loading and zeolite type. Microporous Mesoporous Mater 80:279–289
83. Jisa K, Novakova J, Schwarze M et al (2009) Role of the Fe-zeolite structure and iron state in the N_2O decomposition: comparison of Fe-FER, Fe-BEA, and Fe-MFI catalysts. J Catal 262:27–34
84. Sklenak S, Andrikopoulos PC, Boekfa B et al (2010) N_2O decomposition over Fe-zeolites: structure of the active sites and the origin of the distinct reactivity of Fe-ferrierite, Fe-ZSM-5, and Fe-beta. A combined periodic DFT and multispectral study. J Catal 272:262–274
85. Sobalik Z, Tabor E, Novakova J et al (2012) Role of active oxygen and NO_x species in N_2O decomposition over Fe-ferrierite. J Catal 289:164–170
86. Pieterse JAZ, Pirngruber GD, van Bokhoven JA et al (2007) Hydrothermal stability of Fe-ZSM-5 and Fe-BEA prepared by wet ion-exchange for N_2O decomposition. Appl Catal B Environ 71:16–22
87. Yuranov I, Bulushev DA, Renken A et al (2004) Benzene hydroxylation over FeZSM-5 catalysts: which Fe sites are active? J Catal 227:138–147
88. Snyder BER, Vanelderen P, Bols ML et al (2016) The active site of low-temperature methane hydroxylation in iron-containing zeolites. Nature 536:317–323
89. Perez-Ramirez J, Kapteijn F, Mul G et al (2001) Superior performance of ex-framework FeZSM-5 in direct N_2O decomposition in tail-gases from nitric acid plants. Chem Commun:693–694
90. Perez-Ramirez J, Kapteijn F, Schoffel K et al (2003) Formation and control of N_2O in nitric acid production – where do we stand today? Appl Catal B Environ 44:117–151
91. Panov GI, Uriarte AK, Rodkin MA et al (1998) Generation of active oxygen species on solid surfaces. Opportunity for novel oxidation technologies over zeolites. Catal Today 41:365–385
92. Marturano P, Drozdova L, Kogelbauer A et al (2000) Fe/ZSM-5 prepared by sublimation of $FeCl_3$: the structure of the Fe species as determined by IR, Al-27 MAS NMR, and EXAFS spectroscopy. J Catal 192:236–247
93. Marturano P, Drozdova L, Pirngruber GD et al (2001) The mechanism of formation of the Fe species in Fe/ZSM-5 prepared by CVD. Phys Chem Chem Phys 3:5585–5595
94. Battiston AA, Bitter JH, de Groot FMF et al (2003) Evolution of Fe species during the synthesis of over-exchanged Fe/ZSM5 obtained by chemical vapor deposition of $FeCl_3$. J Catal 213:251–271

95. Feng XB, Hall WK (1997) FeZSM-5: a durable SCR catalyst for NO_x removal from combustion streams. J Catal 166:368–376
96. Marturano P, Kogelbauer A, Prins R (2000) Preparation of overexchanged Fe-ZSM-5 zeolites using the ferrous oxalate method: why does it fail? J Catal 190:460–468
97. Nechita MT, Berlier G, Ricchiardi G et al (2005) New precursor for the post-synthesis preparation of Fe-ZSM-5 zeolites with low iron content. Catal Lett 103:33–41
98. Bordiga S, Buzzoni R, Geobaldo F et al (1996) Structure and reactivity of framework and extraframework iron in Fe-silicalite as investigated by spectroscopic and physicochemical methods. J Catal 158:486–501
99. Perez-Ramirez J, Kapteijn F, Mul G et al (2002) Direct N_2O decomposition over ex-framework FeMFI catalysts. Role of extra-framework species. Catal Commun 3:19–23
100. Pirngruber GD, Roy PK, Prins R (2006) On determining the nuclearity of iron sites in Fe-ZSM-5 – a critical evaluation. Phys Chem Chem Phys 8:3939–3950
101. Shu LJ, Liu Y, Lipscomb JD et al (1996) X-ray absorption spectroscopic studies of the methane monooxygenase hydroxylase component from Methylosinus trichosporium OB3b. J Biol Inorg Chem 1:297–304
102. Shu LJ, Nesheim JC, Kauffmann K et al (1997) An (Fe_2O_2)-O-IV diamond core structure for the key intermediate Q of methane monooxygenase. Science 275:515–518
103. Taboada JB, Overweg AR, Kooyman PJ et al (2005) Following the evolution of iron from framework to extra-framework positions in isomorphously substituted Fe, Al MFI with ^{57}Fe Mossbauer spectroscopy. J Catal 231:56–66
104. Fejes P, Lazar K, Marsi I et al (2003) Isomorphously substituted Fe-ZSM-5 zeolites as catalysts causes of catalyst ageing as revealed by X-band EPR, Mossbauer and ^{29}Si MAS NMR spectra. Appl Catal A Gen 252:75–90
105. Dubkov KA, Ovanesyan NS, Shteinman AA et al (2002) Evolution of iron states and formation of alpha-sites upon activation of FeZSM-5 zeolites. J Catal 207:341–352
106. Kondratenko EV, Kondratenko VA, Santiago M et al (2008) Mechanistic origin of the different activity of Rh-ZSM-5 and Fe-ZSM-5 in N_2O decomposition. J Catal 256:248–258
107. Kondratenko EV, Perez-Ramirez J (2006) Mechanism and kinetics of direct N_2O decomposition over Fe-MFI zeolites with different iron speciation from temporal analysis of products. J Phys Chem B 110:22586–22595
108. Kondratenko EV, Perez-Ramirez J (2007) Micro-kinetic analysis of direct N_2O decomposition over steam-activated Fe-silicalite from transient experiments in the TAP reactor. Catal Today 121:197–203
109. Kondratenko EV, Perez-Ramirez J (2007) Mechanistic peculiarities of the N_2O reduction by CH_4 over Fe-silicalite. Catal Today 119:243–246
110. Ribera A, Arends I, de Vries S et al (2000) Preparation, characterization, and performance of FeZSM-5 for the selective oxidation of benzene to phenol with N_2O. J Catal 195:287–297
111. Kumar MS, Schwidder M, Grunert W et al (2004) On the nature of different iron sites and their catalytic role in Fe-ZSM-5 $DeNO_x$ catalysts: new insights by a combined EPR and UV/VIS spectroscopic approach. J Catal 227:384–397
112. Hensen EJM, Zhu Q, Janssen RAJ et al (2005) Selective oxidation of benzene to phenol with nitrous oxide over MFI zeolites. 1. On the role of iron and aluminum. J Catal 233:123–135
113. Pirngruber GD, Luechinger M, Roy PK et al (2004) N_2O decomposition over iron-containing zeolites prepared by different methods: a comparison of the reaction mechanism. J Catal 224:429–440
114. Jia JF, Sun Q, Wen B et al (2002) Identification of highly active iron sites in N_2O-activated Fe/MFI. Catal Lett 82:7–11
115. Wood BR, Reimer JA, Bell AT et al (2004) Nitrous oxide decomposition and surface oxygen formation on Fe-ZSM-5. J Catal 224:148–155
116. Wood BR, Reimer JA, Bell AG (2002) Studies of N_2O adsorption and decomposition on Fe-ZSM-5. J Catal 209:151–158

117. El-Malki EM, van Santen RA, Sachtler WMH (2000) Active sites in Fe/MFI catalysts for NO_x reduction and oscillating N_2O decomposition. J Catal 196:212–223
118. Mul G, Perez-Ramirez J, Kapteijn F et al (2002) NO adsorption on ex-framework Fe, X MFI catalysts: novel IR bands and evaluation of assignments. Catal Lett 80:129–138
119. Bulushev DA, Renken A, Kiwi-Minsker L (2006) Formation of the surface NO during N_2O interaction at low temperature with iron-containing ZSM-5. J Phys Chem B 110:305–312
120. Berlier G, Lamberti C, Rivallan M et al (2010) Characterization of Fe sites in Fe-zeolites by FTIR spectroscopy of adsorbed NO: are the spectra obtained in static vacuum and dynamic flow set-ups comparable? Phys Chem Chem Phys 12:358–364
121. Roy PK, Prins R, Pirngruber GD (2008) The effect of pretreatment on the reactivity of Fe-ZSM-5 catalysts for N_2O decomposition: dehydroxylation vs. steaming. Appl Catal B Environ 80:226–236
122. Pirngruber GD, Pieterse JAZ (2006) The positive effect of NO on the N_2O decomposition activity of Fe-ZSM-5: a combined kinetic and in situ IR spectroscopic study. J Catal 237:237–247
123. Wood BR, Reimer JA, Bell AT et al (2004) Methanol formation on Fe/Al-MFI via the oxidation of methane by nitrous oxide. J Catal 225:300–306
124. Li C (2003) Identifying the isolated transition metal ions/oxides in molecular sieves and on oxide supports by UV resonance Raman spectroscopy. J Catal 216:203–212
125. Bonino F, Damin A, Piovano A et al (2011) Direct evidence of highly dispersed iron in Fe-silicalite: a Raman spectroscopic study. ChemCatChem 3:139–142
126. Wang JY, Li GN, Ju XH et al (2013) Identification of $Fe_2(\mu\text{-}O)$ and $Fe_2(\mu\text{-}O)_2$ sites in Fe/ZSM-35 by *in situ* resonance Raman spectroscopy. J Catal 301:77–82
127. Knop-Gericke A, Hävecker M, Schedel-Niedrig T et al (2000) High-pressure low-energy XAS: a new tool for probing reacting surfaces of heterogeneous catalysts. Top Catal 10:187–198
128. Perez-Ramirez J, Mul G, Kapteijn F et al (2002) Physicochemical characterization of isomorphously substituted FeZSM-5 during activation. J Catal 207:113–126
129. Pirngruber GD, Grunwaldt JD, Roy PK et al (2007) The nature of the active site in the Fe-ZSM-5/N_2O system studied by (resonant) inelastic X-ray scattering. Catal Today 126:127–134
130. Andrikopoulos PC, Sobalik Z, Novakova J et al (2013) Mechanism of framework oxygen exchange in Fe-zeolites: a combined DFT and mass spectrometry study. ChemPhysChem 14:520–531
131. Hansen N, Heyden A, Bell AT et al (2007) Microkinetic modeling of nitrous oxide decomposition on dinuclear oxygen bridged iron sites in Fe-ZSM-5. J Catal 248:213–225
132. Hansen N, Heyden A, Bell AT et al (2007) A reaction mechanism for the nitrous oxide decomposition on binuclear oxygen bridged iron sites in Fe-ZSM-5. J Phys Chem C 111:2092–2101
133. Heyden A, Hansen N, Bell AT et al (2006) Nitrous oxide decomposition over Fe-ZSM-5 in the presence of nitric oxide: a comprehensive DFT study. J Phys Chem B 110:17096–17114
134. Heyden A, Peters B, Bell AT et al (2005) Comprehensive DFT study of nitrous oxide decomposition over Fe-ZSM-5. J Phys Chem B 109:1857–1873
135. Kiwi-Minsker L, Bulushev DA, Renken A (2003) Active sites in HZSM-5 with low Fe content for the formation of surface oxygen by decomposing N_2O: is every deposited oxygen active? J Catal 219:273–285
136. Perez-Ramirez J, Kumar MS, Bruckner A (2004) Reduction of N_2O with CO over FeMFI zeolites: influence of the preparation method on the iron species and catalytic behavior. J Catal 223:13–27
137. Berlier G, Spoto G, Ricchiardi G et al (2002) IR spectroscopy of adsorbed NO as a useful tool for the characterisation of low concentrated Fe-silicalite catalysts. J Mol Catal A Chem 182:359–366

138. Berlier G, Zecchina A, Spoto G et al (2003) The role of Al in the structure and reactivity of iron centers in Fe-ZSM-5-based catalysts: a statistically based infrared study. J Catal 215:264–270
139. Rivallan M, Berlier G, Ricchiardi G et al (2008) Characterisation and catalytic activity in de-NO_x reactions of Fe-ZSM-5 zeolites prepared via ferric oxalate precursor. Appl Catal B Environ 84:204–213
140. Mul G, Zandbergen MW, Kapteijn F et al (2004) N_2O decomposition over liquid ion-exchanged Fe-BEA catalysts: correlation between activity and the IR intensity of adsorbed NO at 1874 cm^{-1}. Catal Lett 93:113–120
141. Spoto G, Zecchina A, Berlier G et al (2000) FTIR and UV-Vis characterization of Fe-silicalite. J Mol Catal A Chem 158:107–114
142. Berlier G, Bonino F, Zecchina A et al (2003) Anchoring Fe ions to amorphous and crystalline oxides: a means to tune the degree of Fe coordination. ChemPhysChem 4:1073–1078
143. Hammond C, Dimitratos N, Jenkins RL et al (2013) Elucidation and evolution of the active component within Cu/Fe/ZSM-5 for catalytic methane oxidation: from synthesis to catalysis. ACS Catal 3:689–699
144. Forde MM, Armstrong RD, McVicker R et al (2014) Light alkane oxidation using catalysts prepared by chemical vapour impregnation: tuning alcohol selectivity through catalyst pre-treatment. Chem Sci 5:3603–3616
145. Hammond C, Dimitratos N, Lopez-Sanchez JA et al (2013) Aqueous-phase methane oxidation over Fe-MFI zeolites; promotion through isomorphous framework substitution. ACS Catal 3:1835–1844
146. Hammond C, Hermans I, Dimitratos N (2015) Biomimetic oxidation with Fe-ZSM-5 and H_2O_2? Identification of an active, extra-framework binuclear core and an Fe^{III}-OOH intermediate with resonance-enhanced Raman spectroscopy. ChemCatChem 7:434–440
147. Sun KJ, Fan FT, Xia HA et al (2008) Framework Fe ions in Fe-ZSM-5 zeolite studied by UV resonance Raman spectroscopy and density functional theory calculations. J Phys Chem C 112:16036–16041
148. Pidko EA, Degirmenci V, van Santen RA et al (2010) Glucose activation by transient Cr^{2+} dimers. Angew Chem Int Ed 49:2530–2534
149. Pidko EA, Hensen EJM, van Santen RA (2012) Self-organization of extraframework cations in zeolites. Proc R Soc London Ser A Math Phys Eng Sci 468:2070–2086
150. Taramasso M, Perego G, Notari B (1983) Preparation of porous crystalline synthetic material comprised of silicon and titanium oxides. US Patent 4410501A, 18 Oct 1983
151. Lamberti C, Bordiga S, Zecchina A et al (1999) Structural characterization of Ti-silicalite-1: a synchrotron radiation X-ray powder diffraction study. J Catal 183:222–231
152. Millini R, Massara EP, Perego G et al (1992) Framework composition of titanium silicalite-1. J Catal 137:497–503
153. Millini R, Perego G, Berti D et al (2000) Structural characterization of as-synthesized B- and Ti-containing MFI-type molecular sieves. Microporous Mesoporous Mater 35-6:387–403
154. Hijar CA, Jacubinas RM, Eckert J et al (2000) The siting of Ti in TS-1 is non-random. Powder neutron diffraction studies and theoretical calculations of TS-1 and FeS-1. J Phys Chem B 104:12157–12164
155. Lamberti C, Bordiga S, Zecchina A et al (2001) Ti location in the MFI framework of Ti-silicalite-1: a neutron powder diffraction study. J Am Chem Soc 123:2204–2212
156. Scarano D, Zecchina A, Bordiga S et al (1993) Fourier-transform infrared and Raman-spectra of pure and Al-substituted, B-substituted, Ti-substituted and Fe-substituted silicalites – stretching-mode region. J Chem Soc Faraday Trans 89:4123–4130
157. Ricchiardi G, Damin A, Bordiga S et al (2001) Vibrational structure of titanium silicate catalysts. A spectroscopic and theoretical study. J Am Chem Soc 123:11409–11419
158. Bordiga S, Damin A, Bonino F et al (2002) Effect of interaction with H_2O and NH_3 on the vibrational, electronic, and energetic peculiarities of Ti^{IV} centers in TS-1 catalysts: a spectroscopic and computational study. J Phys Chem B 106:9892–9905
159. Tozzola G, Mantegazza MA, Ranghino G et al (1998) On the structure of the active site of Ti-silicalite in reactions with hydrogen peroxide: a vibrational and computational study. J Catal 179:64–71

160. Li C, Xiong G, Xin Q et al (1999) UV resonance Raman spectroscopic identification of titanium atoms in the framework of TS-1 zeolite. Angew Chem Int Ed 38:2220–2222
161. Bordiga S, Damin A, Bonino F et al (2002) The structure of the peroxo species in the TS-1 catalyst as investigated by resonant Raman spectroscopy. Angew Chem Int Ed 41:4734–4737
162. Bordiga S, Damin A, Bonino F et al (2003) Resonance Raman effects in TS-1: the structure of Ti(IV) species and reactivity towards H_2O, NH_3 and H_2O_2: an in situ study. Phys Chem Chem Phys 5:4390–4393
163. Guo Q, Feng ZC, Li GN et al (2013) Finding the "missing components" during the synthesis of TS-1 zeolite by UV resonance Raman spectroscopy. J Phys Chem C 117:2844–2848
164. Bordiga S, Coluccia S, Lamberti C et al (1994) XAFS study of Ti-silicalite – structure of framework Ti(IV) in the presence and absence of reactive molecules (H_2O, NH_3) and comparison with ultraviolet-visible and IR results. J Phys Chem 98:4125–4132
165. Geobaldo F, Bordiga S, Zecchina A et al (1992) DRS UV-Vis and EPR spectroscopy of hydroperoxo and superoxo complexes in titanium silicalite. Catal Lett 16:109–115
166. Bolis V, Bordiga S, Lamberti C et al (1999) A calorimetric, IR, XANES and EXAFS study of the adsorption of NH_3 on Ti-silicalite as a function of the sample pre-treatment. Microporous Mesoporous Mater 30:67–76
167. Bordiga S, Bonino F, Damin A et al (2007) Reactivity of Ti(IV) species hosted in TS-1 towards H_2O_2-H_2O solutions investigated by ab initio cluster and periodic approaches combined with experimental XANES and EXAFS data: a review and new highlights. Phys Chem Chem Phys 9:4854–4878
168. Gallo E, Bonino F, Swarbrick JC et al (2013) Preference towards five-coordination in Ti silicalite-1 upon molecular adsorption. ChemPhysChem 14:79–83
169. Gallo E, Lamberti C, Glatzel P (2011) Investigation of the valence electronic states of Ti(IV) in Ti silicalite-1 coupling X-ray emission spectroscopy and density functional calculations. Phys Chem Chem Phys 13:19409–19419
170. Zecchina A, Spoto G, Bordiga S et al (1991) Framework and extraframework Ti in titanium-silicalite – investigation by means of physical methods. In: Jacobs PA, Jaeger NI, Kubelkova L, Wichterlova B (eds) Zeolite chemistry and catalysis. Elsevier, Amsterdam, pp 251–258
171. On DT, LeNoc L, Bonneviot L (1996) Electron transfer bands of titanium sites in dehydrated silicalites and in TiO_2-SiO_2 gel. Chem Commun:299–300
172. Astorino E, Peri JB, Willey RJ et al (1995) Spectroscopic characterization of silicalite-1 and titanium silicalite-1. J Catal 157:482–500
173. Bonino F, Damin A, Ricchiardi G et al (2004) Ti-peroxo species in the TS-1/H_2O_2/H_2O system. J Phys Chem B 108:3573–3583
174. Zecchina A, Bordiga S, Lamberti C et al (1996) Structural characterization of Ti centres in Ti-silicalite and reaction mechanisms in cyclohexanone ammoximation. Catal Today 32:97–106
175. Blasco T, Camblor MA, Corma A et al (1993) The state of Ti in titanoaluminosilicates isomorphous with zeolite-beta. J Am Chem Soc 115:11806–11813
176. Su J, Xiong G, Zhou JC et al (2012) Amorphous Ti species in titanium silicalite-1: structural features, chemical properties, and inactivation with sulfosalt. J Catal 288:1–7
177. Xiong G, Cao YY, Guo ZD et al (2016) The roles of different titanium species in TS-1 zeolite in propylene epoxidation studied by in situ UV Raman spectroscopy. Phys Chem Chem Phys 18:190–196
178. Zecchina A, Spoto G, Bordiga S et al (1991) IR-spectra of CO adsorbed at low-temperature (77 K) on titanium-silicalite, H-ZSM5 and silicalite. In: Ohlmann G, Pfeifer H, Fricke R (eds) Catalysis and adsorption by zeolites. Elsevier, Amsterdam, pp 671–680
179. Munakata H, Oumi Y, Miyamoto A (2001) A DFT study on peroxo-complex in titanosilicate catalyst: hydrogen peroxide activation on titanosilicalite-1 catalyst and reaction mechanisms for catalytic olefin epoxidation and for hydroxylamine formation from ammonia. J Phys Chem B 105:3493–3501

180. Amtout A, Leonelli R (1995) Optical-properties of rutile near its fundamental-band gap. Phys Rev B 51:6842–6851
181. Tang H, Levy F, Berger H et al (1995) Urbach tail of anatase TiO_2. Phys Rev B 52:7771–7774
182. Zecchina A, Bordiga S, Spoto G et al (1992) Silicalite characterization. 2. IR spectroscopy of the interaction of CO with internal and external hydroxyl-groups. J Phys Chem 96:4991–4997
183. Zecchina A, Bordiga S, Spoto G et al (1992) Low-temperature Fourier-transform infrared investigation of the interaction of CO with nanosized ZSM5 and silicalite. J Chem Soc Faraday Trans 88:2959–2969
184. Li C, Xiong G, Liu JK et al (2001) Identifying framework titanium in TS-1 zeolite by UV resonance Raman spectroscopy. J Phys Chem B 105:2993–2997
185. Behrens P, Felsche J, Vetter S et al (1991) A XANES and EXAFS investigation of titanium silicalite. J Chem Soc Chem Commun:678–680
186. Schultz E, Ferrini C, Prins R (1992) X-ray absorption investigations on Ti-containing zeolites. Catal Lett 14:221–231
187. Pei S, Zajac GW, Kaduk JA et al (1993) Reinvestigation of titanium silicalite by X-ray-absorption spectroscopy – are the novel titanium sites real. Catal Lett 21:333–344
188. Bolis V, Bordiga S, Lamberti C et al (1999) Heterogeneity of framework Ti(IV) in Ti-silicalite as revealed by the adsorption of NH_3. Combined calorimetric and spectroscopic study. Langmuir 15:5753–5764
189. Lamberti C, Bordiga S, Arduino D et al (1998) Evidence of the presence of two different framework Ti(IV) species in Ti-silicalite-1 in vacuo conditions: an EXAFS and a photoluminescence study. J Phys Chem B 102:6382–6390
190. Prestipino C, Bonino F, Usseglio S et al (2004) Equilibria between peroxo and hydroperoxo species in the titanosilicates: an in situ high-resolution XANES investigation. ChemPhysChem 5:1799–1804
191. Ricchiardi G, de Man A, Sauer J (2000) The effect of hydration on structure and location of Ti-sites in Ti-silicalite catalysts. A computational study. Phys Chem Chem Phys 2:2195–2204
192. Tabacchi G, Gianotti E, Fois E et al (2007) Understanding the vibrational and electronic features of Ti(IV) sites in mesoporous silicas by integrated ab initio and spectroscopic investigations. J Phys Chem C 111:4946–4955
193. Lin WY, Frei H (2002) Photochemical and FT-IR probing of the active site of hydrogen peroxide in Ti silicalite sieve. J Am Chem Soc 124:9292–9298
194. Jacobs PT, Lin SM, Chen X (1998) US Patent 5785934A
195. Bellussi G, Perego C, Carati A et al (1994) Amorphous mesoporous silica-alumina with controlled pore size as acid catalysts. Stud Surf Sci Catal 84:85–92
196. Carati A, Ferraris G, Guidotti M et al (2003) Preparation and characterisation of mesoporous silica-alumina and silica-titania with a narrow pore size distribution. Catal Today 77:315–323
197. Guo Q, Sun KJ, Feng ZC et al (2012) A thorough investigation of the active titanium species in TS-1 zeolite by in situ UV resonance Raman spectroscopy. Chem Eur J 18:13854–13860
198. Pavel CC, Park SH, Dreier A et al (2006) Structural defects induced in ETS-10 by postsynthesis treatment with H_2O_2 solution. Chem Mater 18:3813–3820
199. Zuo Y, Liu M, Zhang T et al (2015) Role of pentahedrally coordinated titanium in titanium silicalite-1 in propene epoxidation. RSC Adv 5:17897–17904
200. Henderson GS, Liu X, Fleet ME (2002) A Ti L-edge X-ray absorption study of Ti-silicate glasses. Phys Chem Miner 29:32–42

Struct Bond (2018) 178: 155–178
DOI: 10.1007/430_2018_23

Published online: 27 February 2018

On the Mechanism of Ammonia SCR over Cu- and Fe-Containing Zeolite Catalysts

Ting Jiang and Raul F. Lobo

Abstract New insights from recent reports are integrated to generate an improved depiction of the reaction mechanisms for the selective catalytic reduction (SCR) of NO_x with ammonia over Cu-containing zeolites (mainly chabazite) and Fe-containing zeolite catalysts. The reaction network over Cu-containing zeolites is consistent with the mixed oxidation state of copper cations as determined by operando X-ray spectroscopy, with a "solvated state" form of Cu(II) and Cu(I) at low-temperature (<225°C) reaction conditions; oxidation of Cu-bounded nitrite into nitrate and the subsequent formation and decomposition of ammonium nitrate explains the formation of N_2O as a by-product. A reaction network for NO reduction over Fe-containing zeolites is proposed based on a synthesis from various reported mechanisms. This proposed mechanism is consistent with *operando* EPR and Mossbauer spectroscopy and predicts a limited production of N_2O as compared to Cu-containing zeolites.

Keywords Ammonia SCR mechanism · Cu-zeolite · Fe-zeolite · Selective catalytic reduction (SCR)

Contents

T. Jiang and R. F. Lobo (✉)
Center for Catalytic Science and Technology, Department of Chemical and Biomolecular Engineering, University of Delaware, Newark, DE, USA
e-mail: lobo@udel.edu

1 Introduction

Nitrogen oxides (NO_x) are harmful pollutants generated in internal combustion engines across the world increasing smog production, ground-level ozone concentration and leading to adverse respiratory effects on exposed populations. The use of copper-containing zeolites, especially small-pore zeolites with the chabazite (CHA) structure, has arisen as an effective catalysis technology for the abatement of NO_x in diesel engines and much effort has been devoted to understand and improve the properties of these materials. Recent experimental and theoretical breakthroughs in the understanding of zeolite-based ammonia selective catalytic reduction (SCR) of NO_x catalysts have changed and clarified important aspects of the reaction mechanism and operation of these materials [1–5]. This report illustrates the progress recently achieved, identifies gaps in our understanding, and highlights the areas where further research is needed. Iron-containing zeolites have also been shown to catalyze this reaction (albeit at slower rates) and a number of recent investigations along with a review of the literature are used to propose an updated mechanism consistent with both operando EPR and Mossbauer spectroscopy investigations.

It was recognized since the 1970s that zeolites containing copper ions in extra-framework positions are effective catalysts for the SCR of nitrogen oxides with ammonia [2]. But only since last decade, it has been appreciated that multidimensional small-pore (containing 8-membered ring pore openings) zeolites [6], with pore openings of ~3.8 Å such as chabazite (CHA) and AEI-type materials, are in fact superior to medium-pore (10-ring, 5–6 Å, such as ZSM-5-MFI) [7] and large-pore (12-ring, 7–8 Å such as beta-*BEA [8] or mordenite-MOR) zeolites in various ways. Small-pore zeolites show:

- Higher reaction rates
- Higher hydrothermal stability
- Better tolerance to hydrocarbons
- Higher selectivity to N_2 vs. N_2O

Although experimental evidence for superior performance of small-pore zeolites as practical catalysts became clear early on [6, 9], molecular understanding of the reaction mechanism has been a big challenge that only recently has started to yield to a combination of spectroscopic, kinetic, and computational approaches [10, 11]. This perspective starts with background on the SCR of NO_x reaction and the structure of the zeolite chabazite (the most investigated catalyst for this reaction). It continues describing progress achieved in bringing molecular detail to the reaction mechanism (mostly since 2013) and finally outlines some areas where gaps in our understanding remain and where there is need for further research. For more

information, the reader is directed to two useful reviews of the extensive recent literature on the subject: Gao et al. have reviewed the research up to 2013 [12] and Beale et al. [13] recently reported an in-depth review of the field.

Because of its significance and potential for industrial applications, the reaction mechanism over iron-containing zeolites is also reviewed. Although there is yet no consensus in the literature about some of the key features of this catalytic cycle, here we summarize key experimental evidence that points towards a mechanism with a number of well-understood reaction steps. To close the cycle, a few elementary steps – based on well-known NO^+ and nitrite iron chemistry – are suggested. The elementary steps that are yet to be confirmed are a rich area for future investigations.

2 Selective Catalytic Reduction of NO_x

The so-called *standard SCR reaction* is a 12-electron redox process that converts the undesirable NO into dinitrogen using ammonia as the reducing agent as indicated by Eq. (1).

$$4\,NH_3 + 4\,NO + O_2 \rightarrow 4\,N_2 + 6\,H_2O \tag{1}$$

Here, the nitrogen atom in NO, in a +2 formal oxidation state, is reduced to 0, and the nitrogen in ammonia, in a −3 oxidation state, is oxidized to a 0 oxidation state. Molecular oxygen is needed to rebalance the difference in oxidation states. In addition, there is a "fast SCR reaction" where both NO and NO_2 are present in equimolar amounts.

$$2\,NH_3 + NO + NO_2 \rightarrow 2\,N_2 + 3\,H_2O \tag{2}$$

Reaction (2) is called "fast SCR" reaction because it proceeds at a faster rate than the standard reaction in many catalysts. In this case, the reducing potential of ammonia is balanced by NO and NO_2, where nitrogen is in +2 and +4 oxidation states, respectively. As we shall see, the fast SCR reaction – a 6-electron process – is also essential to understand the catalytic cycle of the standard SCR reaction.

There are two undesired reactions to be minimized by the catalysts: ammonia oxidation and nitrous oxide formation.

$$4\,NH_3 + 3\,O_2 \rightarrow 2\,N_2 + 6\,H_2O \tag{3}$$

$$NH_4NO_3 \rightarrow N_2O + 2\,H_2O \tag{4}$$

Evidently, ammonia oxidation to nitrogen is undesired because it consumes a valuable reactant without decreasing the concentration of NO_x in the gas, but generally this is not kinetically important at temperatures below 300°C in Cu-containing zeolites [14]. Nitrous oxide automobile emissions are not currently regulated but in the future they will be as this is a very stable gas – 114 years half-life in the atmosphere – and has a strong greenhouse gas effect: 298 CO_2 global warming

equivalents in 100 years [15]. It is assumed in reaction (4) that nitrous oxide is produced by ammonium nitrate decomposition, but there may be other mechanisms of N_2O formation.

The gas that contacts the SCR reactor contains predominantly nitrogen (80%), oxygen (~5–10%), carbon dioxide (5–10%), and water (5–10%) [5]. The stream also contains a few hundred ppm of NO_x ($NO + NO_2$) and a similar – usually larger – amount of ammonia added as a urea solution prior to contacting the SCR reactor. Carbon dioxide is inert under practical reaction conditions. The temperature of operation of the reactor ranges from 175°C to over 650°C, a maximum achieved when the exhaust stream of the engine is heated to reactivate the particulate filter that is placed before the SCR reactor to remove sooth. Under usual conditions, the operating temperature range is between 200 and 600°C. Good SCR activity is desired below 150°C, to minimize NO_x emissions during cold start, but at this time, other than Cu-SAPO-34 [16], catalytic rates on Cu-zeolites are slow below this temperature.

3 Selective Catalytic Reduction Mechanism on Cu-Containing Zeolites

3.1 Key Structural Features of Chabazite Selective Catalytic Reduction Catalysts

Chabazite [17, 18] is the most investigated small-pore zeolite for this reaction and is currently the commercial catalyst of choice. Chabazite (Fig. 1), also known by its industrial name as SSZ-13 [19], is formed of layers of 6-rings stacked in an AABBCC ... sequence forming two double-6-rings at the top and bottom of the chabazite cage (see Fig. 1). The CHA framework is composed only of 4-, 6-, and 8-ring building units; its chemical composition can range from completely siliceous to samples containing Si/Al ~1, the maximum allowable by Lowenstein's Al neighbors avoidance rule. The industrial catalysts typically have Si/Al ratios between 12 and 15, an optimum range that balances catalytic activity and catalyst stability. The chabazite cage is formed by 36 T-atoms (T = tetrahedral) and has an accessible internal diameter of ~8 Å (the void space circumscribed by a 12-ring). The rhombohedral unit cell of CHA has one cage per cell and contains only 12 T-atoms – not 36 as often stated in the literature – because the T-atoms forming the chabazite cage are shared between three cages. Each chabazite cage has six 8-ring windows that directly connect it to adjacent cages (see Fig. 1). Chabazite is considered a "simple" zeolite structure because it has only one T-atom in the asymmetric unit, and as such can be thought of as a model system. At the same time, this point of view may be deceivingly simple because there are multiple sites where Cu^{2+} (and other) ions can coordinate to the framework: 6-rings, 8-rings, and the face of the 4-rings among others [18, 20, 21]. Furthermore, of the four surfaces of this

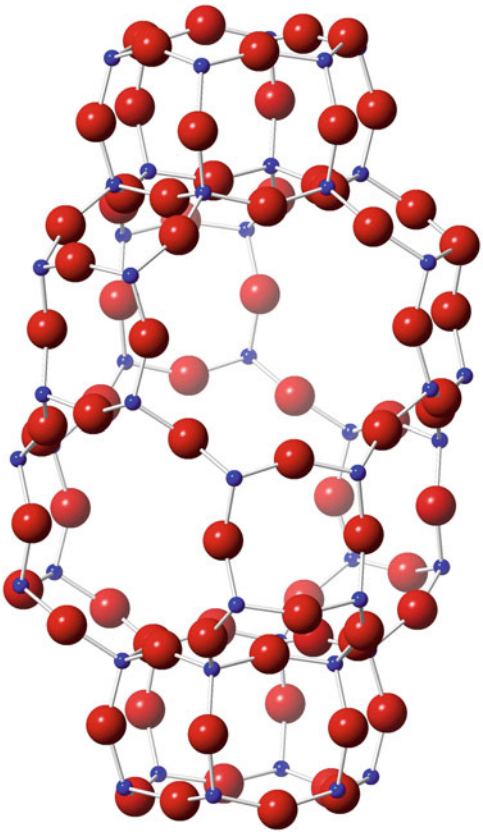

Fig. 1 Illustration of the chabazite cage of Cu-chabazite selective catalytic reduction (SCR) catalysts. Red = oxygen, blue = silicon/aluminum

crystallographically unique T-site, one faces the double 6-ring, a second faces the chabazite cage above the 6-ring, and the other two point towards neighboring chabazite cages. From electrostatic considerations alone then, copper cations could migrate between different cages with little energetic costs. For a typical catalyst composition (Si/Al ratio ~12), there will be on average three framework aluminum atoms per cage since each cage has 36 T-atoms. For typical Cu/Al ratios of ~0.4, there is on average less than one copper atom per cage (~0.4 in fact), but statistically, some cages can have two Cu atoms per cage. This is, however, the largest expected number of Cu atoms per cage because the Al T-atoms are shared between three cages. In practice, most Cu cations will be isolated from other Cu cations in the chabazite cages under most circumstances. There is a small fraction of 6-rings with two Al atoms in the ring at this composition [2].

There are a few important differences between the CHA framework structure, and the structure of the more common zeolite frameworks ZSM-5 (MFI) and beta (*BEA), also previously investigated as potential Cu-based SCR catalysts [22]. First, chabazite is formed only of even-membered rings (4-, 6-, and 8-rings), while ZSM-5 and beta contain large numbers of 5-rings. As a consequence, the Cu-coordination

environment in CHA versus the other zeolites can be quite different. Second, CHA has higher microporosity (0.3 cm^3/g) than MFI (0.15 cm^3/g) and *BEA (0.24 cm^3/g) and thus for similar silicon/aluminum and copper/aluminum ratios, the effective concentration of Cu ions in the pores is substantially higher in MFI and *BEA than in CHA. This may be a relevant consideration if the formation of metal oxide clusters is important for the catalytic reaction.

3.2 Minimal Redox Cycle

A simplified catalytic cycle for NO reduction is illustrated in Fig. 2 [10]. Here, it is assumed that the charge of the Cu(II) cation is balanced by only one $[AlO_2]^-$ unit, and thus the copper is depicted as $[CuOH]^+$. Most of the Al atoms in framework compositions of interest (Si/Al = 12–15) will be isolated. This diagram emphasizes the fact that Cu cations flip between +2 and +1 oxidation states through the catalytic cycle. It also emphasizes that both NO and ammonia are needed to reduce the Cu(II) to Cu(I). But, this simple model is lacking in several respects: first, the standard SCR reaction is a 12-electron process and this cycle is only a 6-electron process. Second, the co-oxidant in the standard SCR reaction (1) is O_2, and O_2 does not appear in this simplified reaction cycle (Fig. 2).

There is ample evidence indicating that both NO and ammonia are needed to complete the reduction half-cycle of $[CuOH]^+$ depicted in Fig. 2 [1, 10, 23]. The formation of Cu(I) starting with a pre-oxidized sample of Cu-CHA in the presence of NO and NH_3 (no dioxygen) has been verified by X-ray absorption spectroscopy (XAS), EPR spectroscopy, and IR spectroscopy [1]. Computational investigations also show that ammonia coordinated to $[CuOH]^+$ is activated towards electrophilic attack by gas-phase NO. In a concerted reaction, a proton transfers to the copper-coordinated hydroxide group producing water and adsorbed H_2N-NO (nitrosamine) [2]. The adsorbed nitrosamine rapidly isomerizes and decomposes to form N_2 and water. This reaction is analogous to the reductive nitrosilation of ligands in Cu(II)–amine complexes by NO [24–26], as has been observed, for example, in

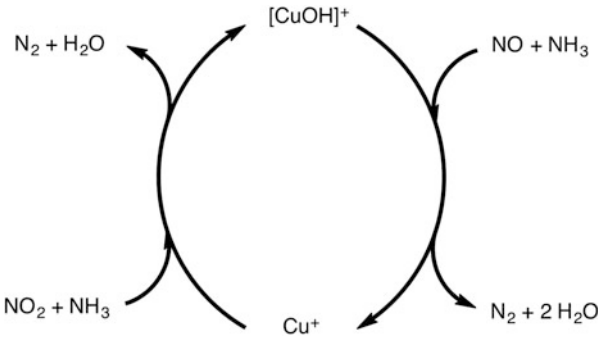

Fig. 2 Simplified diagram illustrating the redox cycle of the (fast) ammonia SCR reaction

the nitrosilation of tetraazacyclotetradecane Cu(II) complexes that yield the corresponding N-nitrosylated ligand and Cu(I) [27].

It has also been proposed that NO binds first to $[CuOH]^+$ forming NO^+ that then reacts with ammonia to form N_2 and water [1], but recent phase diagrams and binding energies computed on periodic models of Cu-CHA indicate that ammonia binds $[CuOH]^+$ much more strongly than NO and that at reaction conditions ammonia is the preferred ligand. In addition, XAS investigations show that in the presence of only NO in the gas phase there is little, if any, reduction of the copper. Formation of NO^+ upon coordination of NO to $[CuOH]^+$ is thus not favored. The details of the oxidation half-cycle in Fig. 2 have been harder to pin down since the only nitrogen oxide species observed after oxidation of the Cu(I) moiety with NO_2 is nitrate, not nitrite [1, 21]. In part, this is because the IR absorption modes of nitrite (NO_2^-) overlap with the strongly absorbing IR bands of the zeolite framework. It was only recently shown, using transient response methods and trapping techniques, that nitrite was confirmed as intermediate during ammonia SCR of Cu-containing zeolites [28, 29]. Still, nitrate is the dominant nitrogen oxide species observed under operando conditions on Cu-chabazite catalysts.

3.3 Solvation of Copper Ions by Ammonia

An important aspect of the SCR-copper chemistry is the recognition that the Cu ions are solvated by gas-phase molecules, ammonia in particular. Extra-framework cations are usually depicted as strongly coordinated to zeolite framework oxygen atoms and associated to $[AlO_{4/2}]^-$ tetrahedral by electrostatic forces [17, 18]. Nonetheless, recent investigations characterizing the state of Cu in zeolite SCR catalysts show that both Cu(I) and Cu(II) are present as ammonia complexes under reaction conditions (200°C in the presence of ammonia and NO). Cu(I) forms linear $(Cu(NH_3)_2)^+$ complexes [1, 2, 30, 31], and Cu(II) forms square-planar $(Cu(NH_3)_4)^{2+}$ or $(Cu(NH_3)_3X)^+$, X = OH^-, NO_3^-, or NO_2^-, or alternatively, square pyramidal complexes $(Cu(NH_3)_4X)^+$, X = OH^-, NO_3^-, or NO_2^- [32–34]. These anions coordinate via oxygen atoms to the Cu cation. The linear and square-planar coordination environments – under reaction conditions – are supported by first-principles thermodynamic analysis using simulated reaction conditions. These studies predict not only strong Cu–NH_3 bonds (see Table 1) [2] but also that ammonia-solvated

Table 1 Computed sequential absorption energies of ammonia on Cu(I) and Cu(II) in zeolites [2]

	Adsorption energy (kJ/mol)[a]			
	1	2	3	4
$ZCu^{II}OH$	−117	−119	−116	−47
ZCu^{I}	−137	−151	−75	−41

[a]For a given number of ammonia molecules coordinated to the complex

complexes are the dominant species under reaction conditions. Ammonia forms the strongest copper–ligand bond of all the ligands investigated [1].

XAS and IR spectroscopy studies [4] also find little difference between the spectra of the proposed tetra- and di-ammine species and the spectra of aqueous solutions of ammonia–Cu(II) and ammonia–Cu(I) complexes, respectively. Tetra-ammine Cu(II) complexes are formally 17-electron complexes and do not form strong bonds to ligands in axial positions. This is evidenced by the long Cu–OH bond observed in aqueous Cu(II)OH tetra-ammine complexes [34]. At reaction conditions (200°C and above), it is reasonable to expect that the axial ligand will not be present since the bond strength of this ligand is weak. $[Cu(I)(NH_3)_2]^+$ are 14-electron complexes and are expected to be linear based on classical ligand-field theory. Histidine and other Cu(I) complexes in peptides and peptide analogues show a preponderance of linear two-coordinate geometry and in addition show resistance to O_2 oxidation [35–37].

The solvated state of copper in the zeolite implies that copper ions are not directly bonded to the framework; they are instead displaced away from the zeolite walls towards the middle of the chabazite cage [2]. This solvated environment increases the mobility of the copper ions [11] and in the case of linear $[Cu(I)(NH_3)_2]^+$ species, increases the probability of inter-cage motion and perhaps the potential for di-copper complexes formation [2]. Tetra-ammine Cu(II) complexes are far too bulky to pass through an 8-ring window without drastic changes in coordination environment. An example of the zeolite acting as a solid solvent for guest species in this catalytic system is the stabilization of such Cu–ammonia complexes in the zeolite pores under reaction conditions [38]. The solvation of the copper cations by ammonia near 200°C is a very important effect that must be considered when analyzing reaction mechanisms. Investigations under experimental conditions that do not include ammonia or the use of molecular models that do not contain ammonia as a ligand may yield incorrect conclusions about reaction mechanisms and the relative stability of reaction intermediates. In what follows, it is assumed that in all cases the copper atoms are coordinated to ammonia, although this is not indicated for brevity.

3.4 Oxidation Half-Cycle

To explain the fact that the standard SCR reaction is a 12-electron process while the cycle depicted in Fig. 2 is a 6-electron process, Janssens et al. [1] have suggested that the catalytic cycle must run twice. The first time the cycle runs it follows path **1** (Fig. 3). Here, the first step of the half-cycle – the rate determining step – is the reaction of NO and O_2 on Cu(I) to form nitrate. In this reaction, nitrogen is oxidized by 3 units to +5 and Cu(I) is oxidized by one unit to Cu(II). This reaction forms what appears to be a stable intermediate $(CuNO_3)^+$ that still, in the presence of NO, continues to react forming nitrite $(CuNO_2)^+$ and nitrogen dioxide (gas) [28]. The nitrite rapidly reacts with ammonia to produce N_2 and water and reform $[CuOH]^+$ to start the reduction half-cycle (top of Fig. 2). Note that the equilibrium

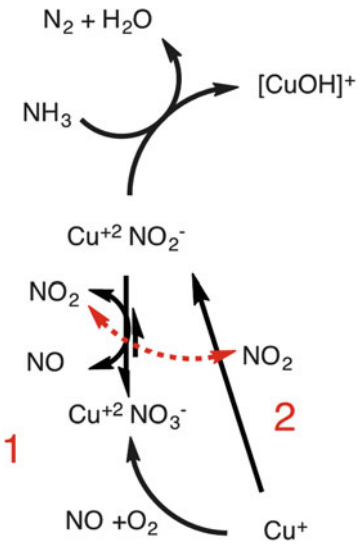

Fig. 3 Illustration of the two oxidation half-cycles for the ammonia SCR reaction on Cu-zeolites proposed by Janssens et al. [1]

constant of the reduction of $Cu^{2+}NO_3^-$ complex to $Cu^{2+}NO_2^-$ by NO is very small [1] and that the nitrate will be present at much higher concentrations than nitrite in the zeolite pores under reaction conditions. In fact, in situ IR spectroscopy studies clearly reveal the presence of nitrate on the zeolite after Cu(I) oxidation with NO and O_2 and do not reveal the presence of any nitrite [1]. No nitrite is observed neither if Cu(I) is oxidized with NO_2 possibly because under reaction conditions it is present only at low concentrations [1, 28].

In Fig. 3, path **1** accounts for six electrons transferred between reactants and catalyst; the second group of six electrons are accounted for by path **2**, which is the path followed in the second oxidation half-cycle and where the NO_2 produced in path **1** is used to oxidize Cu(I) producing nitrite (and Cu(II)). As stated above, starting from a sample reduced to Cu(I) and reacting with nitrogen dioxide, only nitrate is observed using IR spectroscopy. This is because the equilibrium constant for the nitrate reduction with NO is very small and this reaction step proceeds in reverse generating nitrate from nitrite and NO_2.

The predicted activation energy [2] for the reaction of O_2 and NO to form nitrate over Cu(I) is larger than the experimentally determined activation energy of the ammonia SCR reaction on Cu-chabazites (96 kJ/mol vs. ~70 kJ/mol) [1], and as has been indicated, alternative reaction mechanisms may be preferable. Although this is a valid argument, activation energy determinations on Cu-chabazite have been conducted at the low-temperature end of the operating temperature range of the system (from 170 to 220°C) [1] and at these conditions other physical processes may also affect reaction rates. For example, Cu-chabazites adsorb ammonia at low temperature (below 150°C) and release the weakly adsorbed ammonia in the 150–300°C temperature range [39]. Water, as well, adsorbs strongly in the zeolite pores and on copper cations and it is desorbed within the 170–250°C temperature

range [3]. At low temperatures then, there is limited or no space for the gas-phase reactants to reach the copper sites in the zeolite pores, leading to an experimentally measured activation energy that is affected by these (lower energy) adsorption/desorption processes. The measured apparent activation energies then may not be directly comparable to the DFT-determined activation energy of the oxidation of Cu^+ with NO and O_2. The DFT-determined activation energies were conducted on bare Cu^+ bonded to the framework, not linear di-ammine complexes, and this could have affected the calculated activation energies.

A valuable feature of the reaction network depicted in Fig. 3 is that it predicts the presence of some Cu(II) under reaction conditions, stabilized as $(CuNO_3)^+$. Several XAS investigations have shown that under operando conditions copper is in both +1 and +2 oxidation states in the catalyst [1, 40, 41]. If the oxidation of Cu(I) is the rate determining step of the catalytic cycle (Fig. 3, path **1**), it follows that most of the copper in the catalyst will be in a +1 oxidation state. The model in Fig. 3 predicts, in contrast, that a fraction of the extra-framework copper must be present in the catalyst as Cu(II) since the equilibrium constant of the copper nitrate reduction with NO is very small ($\Delta G_{rxn}{}^0(200°C) = 40–50$ kJ/mol, K ~10^{-6}).

Furthermore, this model can be easily modified to include reactions that explain the formation of N_2O [5]. Copper nitrate, for instance, can react with ammonia and water to produce adsorbed ammonium nitrate and $[CuOH]^+$, as indicated by reaction (5).

$$[Cu \cdot NO_3]^+ + NH_3 + H_2O \rightleftharpoons [Cu \cdot OH]^+ + NH_4NO_3 \tag{5}$$

Thermal decomposition of ammonium nitrate formed in the zeolite can thus be the path for the production of N_2O in this system [5]. In this respect, the zeolite still plays a stabilizing effect on the ammonium nitrate because bulk ammonium nitrate starts to decompose into N_2O at temperatures as low as 175°C. Chen et al. have investigated the effect of $NO_2/(NO + NO_2)$ ratios on the SCR reaction on Cu-chabazite and Cu-beta zeolites [5]. At ratios of ~0.8, there is a striking difference between the two zeolites. Cu-chabazite produces ammonium nitrate to the point that the pore space is consumed by this salt leading to pore blockage and to complete loss of catalytic activity (at 200°C). This is not observed on Cu-beta where instead there is an increase in the formation rate of N_2O from ammonium nitrate decomposition. Based on this and other observations, the authors conclude that Cu-chabazite has the ability to stabilize ammonium nitrate much more effectively than other zeolites and that this leads to higher SCR selectivity to N_2. At higher temperatures, the nitrate can react with NO to form NO_2, reenter the catalytic cycle, and form N_2 by reaction with ammonia.

The observation that higher $NO_2/(NO + NO_2)$ (>0.7) ratios lead to accumulation of ammonium nitrate in Cu-chabazite catalysts is also consistent with the oxidation half-cycles depicted in Fig. 3. This reaction network shows that in the presence of higher NO_2 concentrations, path **2** will be dominant over path **1**, and in that case, the accumulation of ammonium nitrate can be explained by the rapid oxidation of Cu(II) nitrite by NO_2 forming Cu(II) nitrate; that is, this reaction proceeds in the reverse direction than is expected during NO oxidation following path **1**.

3.5 *Reaction Network of Ammonia Selective Catalytic Reduction on Cu-Chabazite*

These new insights, taken together, are the basis for the reaction network illustrated in Fig. 4. Here, the Cu(II) complexes are depicted solvated, as square-planar complexes with ammonia as the main equatorial ligand, as observed in aqueous solution and in many crystalline forms of copper tetra-ammine complexes [32, 33, 42]. The crystal structures of both copper tetra-ammine nitrate [43, 44] and nitrite [45] show short (i.e., strong) Cu–NH_3 bonds (~2.02 Å for the nitrate and 1.99 Å for the nitrite), and longer bonds to the axial ligands. The key difference between these two ligands is that the coordination is via the oxygen in the nitrate (d(Cu-O) = 2.5 Å) but is via the nitrogen (d(Cu-N) = 2.65 Å) in the nitrite. The long bonds indicate that these nitrate anions are only weakly bonded to the metal center.

The steps that lead to the formation of these complexes are not elementary and require further research for clarification. Path **1** is a four-electron process and possibly proceeds as two-electron two-step reactions. Janssens et al. [1] have suggested that the nitrate forms a bidentate complex with Cu(II) adopting a square-

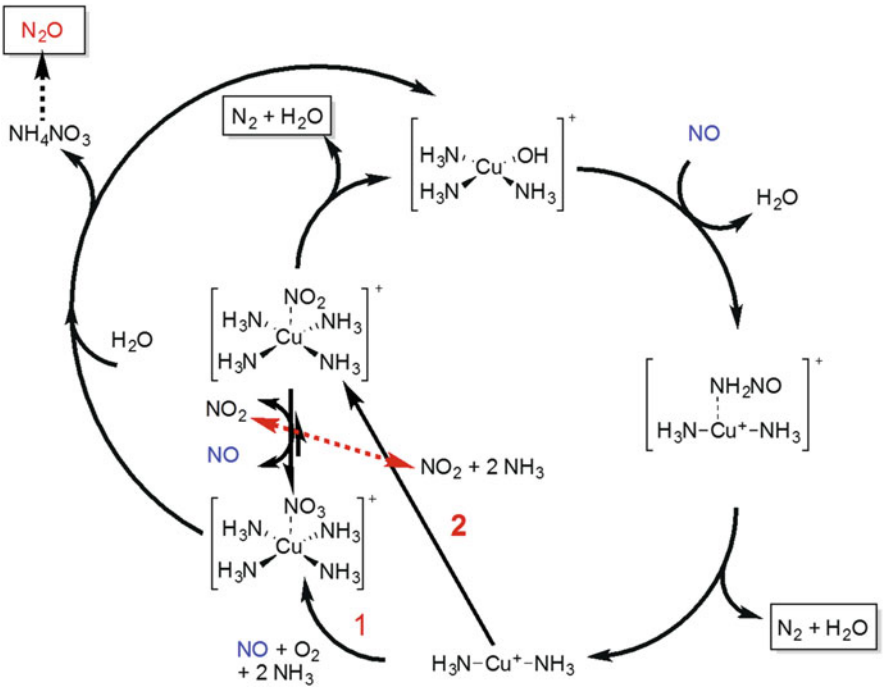

Fig. 4 Reaction network for the selective catalytic reduction of NO_x with ammonia on Cu-containing zeolite catalysts. The diagram illustrates the points where N_2 (in black rectangular boxes) and the by-product N_2O (in red) are generated. The red arrow shows that the NO_2 produced during the first oxidation half-cycle is used as a reactant by the second oxidation half-cycle

planar geometry. This intermediate can further bind to two ammonia molecules to form a tetra-ammine species as indicated in reaction (6). The nitrate anion changes its coordination to monodentate upon the strong coordination of two ammonia molecules.

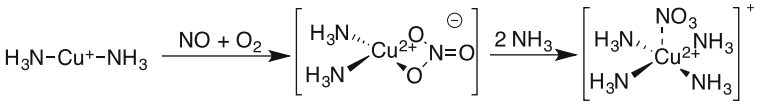

(6)

But, the thermodynamic stability of this square-planar $[Cu(NH_3)_2NO_3]^+$ moiety has yet to be calculated and the assignment of the structure of this complex in the working catalyst is only tentative. Gas-phase oxygen is essential to form the nitrate anion as depicted in Fig. 4. In the case of path **2**, the reaction (as depicted in Fig. 4) is a two-electron process that requires not only the bonding of NO_2 to copper but also the coordination of two ammonia molecules. The order of addition of these species is important and has yet to be determined.

In Fig. 4, Cu(I) species are depicted as di-ammine linear copper complexes, as have been observed in ferrierite and in aqueous systems [30, 31]. The reaction network of Fig. 4 is likely to be valid at the low-temperature range of Cu-chabazite operation (below 300°C). At higher temperatures, the copper cations will start to desolvate and the copper will bind more strongly to the zeolite framework. The relative rates of the NO reaction also change and there is a rapid increase in direct ammonia combustion and in NO_2 production [14]. These changes in coordination environment – and possibly reaction mechanism – are likely the reasons behind the so-called seagull curve shape of conversion versus temperature in the reactivity of Cu-chabazite for ammonia SCR (see Fig. 5) [15].

One of the interesting characteristics of the reaction scheme illustrated in Fig. 4 is the absence of the zeolite in any of the reactions. If the zeolite is not important for this chemistry, then reaction rates should be independent of the zeolite structure. In fact, this was recently confirmed by Paolucci et al. [2], who measured turn-over-frequencies per Cu atom for Cu-chabazite, Cu-ZSM-5, and Cu-beta. In the three cases, the TOF are nearly the same, confirming that the zeolite framework plays a supporting role in the chemistry. Selectivity to the SCR of NO_x vs. N_2O can, in contrast, be very different depending on the zeolite structure [5], an observation that shows that the details of the zeolite structure can have a large effect on the stabilization of ammonium nitrate formed as a by-product during the SCR of NO_x.

4 Selective Catalytic Reduction Mechanism on Fe-Containing Zeolites

Iron-containing zeolites have also shown to be effective NO_x SCR catalysts, but the chemistry of iron is different from the chemistry of copper in a number of important ways. First, Fe forms strong complexes with NO and forms only weak complexes

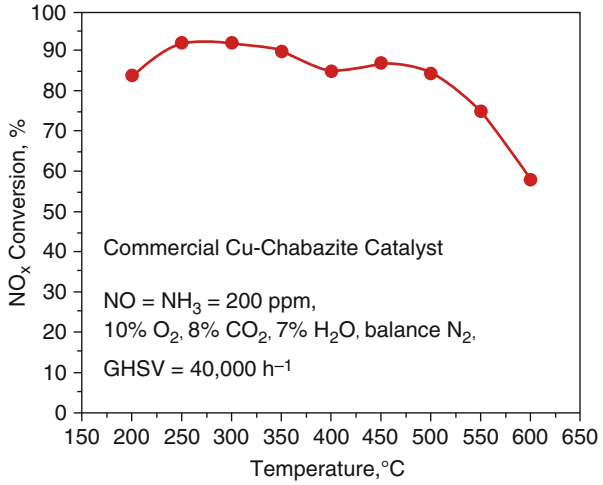

Fig. 5 Steady-state NO_x conversion on a commercial Cu-chabazite catalyst. This figure illustrates the bimodal structure of this catalyst system. The high-temperature mode possibly occurs upon decomposition of the Cu–ammonia complexes discussed here. Reprinted from Journal of Catalysis, Vol 319, Feng Gao, Eric D. Walter, Marton Kollar, Yilin Wang, János Szanyi, and Charles H. F. Peden, Understanding ammonia selective catalytic reduction kinetics over Cu/SSZ-13 from motion of the Cu ions, Page No. 1–14, Copyright (2014), with permission from Elsevier

with ammonia; Cu-coordination strength is the opposite. Second, Fe is coordinated with framework oxygen atoms in Fe-containing zeolites, while Cu is solvated by adsorbed NH_3 in Cu-containing zeolites. Third, since iron is oxophilic and binds to the zeolite framework strongly, the zeolite structure and composition can change the ability of Fe sites to coordinate with additional ligands like OH^- and/or NO and alter the rate of reaction of NO_x SCR. Lastly, Fe strong oxophilicity makes it prone to hydrolysis when exposed to water. These characters have aroused interest in exploring Fe-containing zeolites in NO_x SCR and several advantages that outweigh Cu-containing zeolites have been identified so far.

Fe-containing zeolites, such as Fe-ZSM-5, Fe-beta, and Fe-chabazite, are effective catalysts for NO_x SCR [46–53]. Fe-ZSM-5 has demonstrated high NO conversion over a broad temperature window (300–550°C) and reached close to 100% NO conversion at 350–550°C (GHSV ~200,000 h^{-1}) [54]. Fe-containing zeolites display faster catalytic rates than Cu-containing zeolites at temperatures above 450°C although low-temperature reaction rates (<250°C) are slower [55]. The low-temperature activity of Fe-containing zeolites (MFI) can be improved by better dispersion of Fe species during catalyst preparation; this has led to up to 70% NO conversion below 300°C [56]. After hydrothermal aging at 600°C for 13 h, the Fe-containing AEI-type catalyst, for example, still maintains 90% NO conversion at 350–550°C [57]. These results show that Fe-containing zeolites are promising, stable, and competitive ammonia SCR catalysts. Their main disadvantage is their low reactivity at low temperatures. Research on Fe-containing zeolites during the

last decade has focused on exploring Fe incorporating methods during catalyst preparation, improving catalyst reaction rates and hydrothermal stability, and also in understanding the reaction mechanism of the Fe-catalyzed SCR.

Understanding NH_3-SCR mechanism on Fe-containing zeolite is imperative to improve the properties of these materials through catalyst design; a number of recent reports have provided new insights using both ex situ and in situ characterization techniques. Herein, we summarize these results and attempt to identify gaps and uncertainties in the current understanding of the NO_x SCR mechanism on Fe-containing zeolites.

The active sites in Fe-zeolite catalyzed NO_x SCR could be: (1) isolated Fe ions, (2) dimeric iron species, (3) oligomeric species, (4) ion-exchanged oxo-Fe^{3+}, (5) Fe_xO_y, and (6) aggregated Fe_2O_3 [58–60]. Based on the characteristic signals of dinuclear Fe^{3+} complexes in an ex situ Mossbauer spectroscopy investigation, Gao et al. [54, 61] have suggested that extra-framework monomeric $[Fe(OH)_2]^+$ and dimeric $[HO\text{-}Fe\text{-}O\text{-}Fe\text{-}OH]^{2+}$ are the major active Fe species in chabazite zeolites. The presence of monomeric Fe species is consistent with several previous reports [62–64]. The identification of dimeric Fe species in zeolites is also reasonable because assembly of FeO^+ into $Fe_2O_2^{2+}$ inside the zeolite (MFI) pores is a highly exothermic process, as was shown based on DFT calculations by Pidko et al. [65]. Besides major contributions from monomeric and dimeric Fe species, it is also possible that other species, such as oligomeric iron oxides and iron oxyhydroxides, also contribute to SCR reaction, depending on temperature [58].

The positions of active Fe ion in the ZSM-5 zeolite pores have been explored by Velez et al. [62] using UV-Vis spectroscopy and *operando* EPR. They found that the so-called α sites (monomeric Fe sites in 10-member rings) remained trivalent in both standard and fast SCR conditions while β sites (monomeric Fe sites in 6-member rings) and γ sites (monomeric Fe sites in 5-member rings) were permanently reduced to Fe(II) (claimed to be inactive) under standard SCR conditions but remained trivalent and active in the fast SCR reaction. During fast SCR, NO_2 is suggested to quickly reoxidize β and γ sites, keeping them in a redox-active state; this is advantageous because distortion of β and γ sites, caused by different steric constraints in different positions of the pore, should lead to a faster redox rate than α sites. Combining the results from kinetic measurements of standard and fast SCR, and *operando* EPR spectroscopy, they concluded that the α sites, which stay trivalent in both standard and fast SCR, contribute significantly to the standard SCR and also contribute to the "slow" reactions (that is, the shared reaction steps of standard and fast SCR cycles) of fast SCR, whereas the β and γ sites, which stay trivalent only in fast SCR, mostly participate in the "fast" part (NO_2 involved reactions) of fast SCR. This is consistent with the expectation that trivalent Fe sites are the only active sites in SCR reaction.

The coordination environment of Fe cations in zeolites has been widely investigated and the consensus is that the coordination number of Fe is four in fresh Fe-containing catalysts [59, 66]. The coordination number increases to between four and five under SCR conditions and after adsorption of NO [67]. The increase of coordination number means that, besides bonding with the zeolite, Fe directly

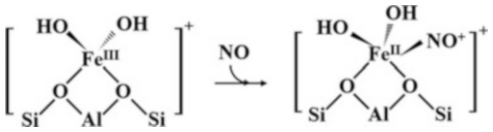

Fig. 6 The change of coordination number of Fe in Fe-containing zeolite due to bonded NO species

bonds with one reactant during the SCR reaction (Fig. 6). Boubnov et al. [67] studied the species absorbed on Fe sites under standard SCR condition, trying to determine which ligands are coordinated with Fe in Fe-ZSM-5. Based on DFT calculation of the valence-to-core X-ray emission spectra – although signal to noise ratio of the spectra was low – they ascertain that ligands with nitrogen lone pairs are coordinated with the Fe center. That is, they suggested that NH_3, having a lone pair, directly coordinated with Fe. As the other four bonds of Fe are occupied by oxygen or hydroxyl group in the original sample, the only possibility for NO adsorption on Fe is via an $O^{\delta+}$ atom from a hydroxyl group, e.g., as $Fe^{2+} - O^{\delta+}H - N = O$. However, they did not consider π backbonding between Fe and NO. Since NO is a π-acceptor ligand, besides the σ bond formed by electron transfer from NO into empty 3d orbital of Fe, there is also π backbonding by electron transfer from the 3d orbital of Fe into the empty π* orbital of NO. Consequently, when NO directly coordinated with Fe, the nitrogen in NO also has lone pairs because of the presence of this π backbonding. This means that it is NO, and not NH_3, what is directly coordinated with Fe under standard SCR conditions. From the perspective of coordination chemistry, Fe(II) and Fe(III) species have six and five electrons in their *d* orbitals, respectively, which can have either a high-spin or low-spin electronic configuration. Compared with NH_3 ligand, nitrosyl ligands can give rise to a larger energy difference between *d* orbitals (Δ), thus forming more stable low-spin complexes with Fe coordination centers. Note too that iron–amine complexes are not common and not very stable (in contrast to Cu–amine complexes) [68–70]. Considering that many stable iron nitrosyl complexes have been described in the past, such as nitroprusside, $[Fe(CN)_5NO]^-$ [71], the evidence points to the direct NO coordination to the Fe species during the SCR reactions.

The transformation of active sites in Fe-containing zeolites has been observed after high-temperature hydrothermal aging of the samples [72]. The decay of SCR reaction rate after hydrothermal aging is mainly attributed to the loss of Fe single sites. The hydrothermal stability of Fe-containing zeolite has been improved by modifying the catalyst preparation process, such as using one-step method, or removal of alkali cations and Al, or synthesizing the catalyst in fluoride media. Traditionally, ion exchange has been used to introduce Fe into the zeolite: Fe^{2+} should be used for ion exchange and the low oxidation state is maintained by keeping the pH low and by using an inert atmosphere during the ion-exchange process. Preservation of Fe(II) oxidation state prevents the formation of hydrated Fe^{3+} in the solution, an ion with larger diameter than the pore size of small-pore zeolites. This enables incorporation of Fe^{2+} into zeolite pores, forming isolated Fe^{3+} sites in zeolites instead of small oligomeric Fe_xO_y clusters or Fe_xO_y nanoparticles [73]. Attempts have been recently made to introduce Fe into the zeolite by a one-pot synthesis method [57, 74,

75]. Compared to ion exchange, the one-step method appears to form catalysts with better hydrothermal stability in NO_x SCR due to a better dispersion of Fe within the zeolite crystals [57, 76]. Fe-containing zeolites (AFX, ERI, and CHA) with low or no alkali cations showed better hydrothermal stability in NO_x SCR compared to those with alkali cations [74, 77]. The origin of the negative effects of alkali cations on NO_x conversion and on the hydrothermal aging process has not been explained clearly. These effects could be due to competitive charge balance between extra-framework alkali and Fe species or hydrophilic and electrophilic characteristics of alkali cations [77]. Fe-containing zeolite beta (BEA) without Al showed better hydrothermal stability and long-time durability than the one with Al (Si/Al ratio = 14.2) [78]. This implies that the loss of Fe single sites after hydrothermal aging might be promoted by Brönsted acid sites or species similar to hydroxyl group (such as the hydroxyl groups on iron oxides surface). However, the Brönsted sites generated by framework Al increase the low-temperature (<250°C) activity of Fe-zeolite [78]. The Brönsted acid sites might promote one of the SCR reaction steps at low temperature. For example, the decomposition of nitrosamide (NH_2NO) has been shown to have very low activation energy barrier (14.5 kcal/mol) if it occurs on Brönsted acid sites [79], compared to activation energy barrier (30–40 kcal/mol) of the corresponding gas-phase reaction [80, 81]. Zeolites prepared in fluoride media have fewer structural defects (internal silanols) leading to higher thermal stability and a more hydrophobic character. The improvement of hydrothermal stability by using fluoride media in the synthesis of chabazite was found, on the other hand, to have a limited effect [74]. This suggests that silanol groups in the zeolite interior may not be involved in the agglomeration of iron sites during the hydrothermal aging process.

A reaction mechanism of SCR on Fe-containing zeolite catalysts is proposed (Fig. 7) based on the following consensus aspects of the literature. First, standard SCR and fast SCR reactions share elementary reactions, reactants, intermediates, products, and catalyst sites. The mechanisms of these two reactions, then, probably go through similar reaction steps as it was shown above for Cu-containing zeolites. Secondly, in the initial Fe-containing zeolite catalysts, most of Fe species are trivalent and tetrahedrally coordinated. During the reaction, a fraction of the Fe species become divalent and form distorted octahedral or distorted tetrahedral coordination complexes. Fe(II) species is then possibly one of the active centers of the SCR reactions. Thirdly, the presence of NO_2 accelerates the SCR reaction, especially at the low-to-mid temperature range (250–450°C). NO_2 could possibly alter the reaction paths by coordinating with Fe active center at low-mid temperature, thus changing the relative concentration of intermediates and the relative rates of several SCR reaction steps.

In the proposed mechanism, mononuclear Fe(III) species ($[Fe(OH)_2]^+$ or $[FeO]^+$) are used as the starting point of the catalytic cycle: $[FeO]^+$ represents the active forms of single-site Fe(III). Firstly, $[FeO]^+$ goes through a redox activation process with NO, generating Fe(II) and the nitrosyl cation (NO^+), and changing the coordination number of Fe to 5 (reaction ①, in Fig. 7). Then, $[FeO(NO^+)]^+$ intermediate undergoes a nucleophilic addition [71], where the electron-rich NH_3 molecule reacts with the triple bond of nitrosyl group (reaction ②). The complex [FeO(N(OH)-

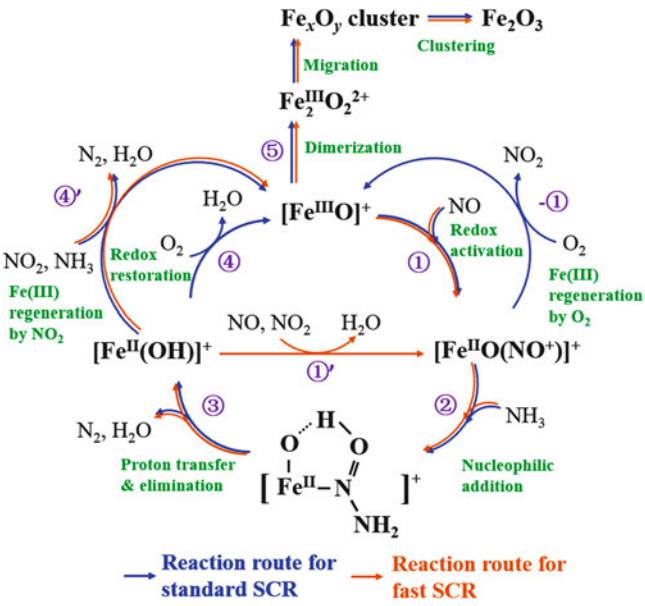

Fig. 7 Scheme of the proposed reaction mechanism of SCR on Fe-containing zeolites. Reactions ①, ②, ③, ④′, and ⑤ are part of both the standard and fast SCR catalytic cycles. Reaction ①: $[FeO(NO^+)]^+$ is formed by the redox reaction between $[FeO]^+$ and NO; reaction ②: $[FeO(NO^+)]^+$ reacts with NH_3 (the nucleophile) to form $[FeO(N(OH)\text{-}NH_2)]^+$; reaction ③: NH_2NO is eliminated from $[FeO(N(OH)\text{-}NH_2)]^+$ complex to generate $[Fe(OH)]^+$, and NH_2NO decomposes to N_2 and H_2O; reaction ④′: NO_2 regenerates $[FeO]^+$ from $[Fe(OH)]^+$ in the presence of NH_3; reaction ⑤: $[FeO]^+$ single site aggregates to form Fe_2O_3 by dimerization, migration, and clustering via a hydrothermal process. Reactions −① and ④ are part of the standard SCR catalytic cycle. Reaction −①: $[FeO(NO^+)]^+$ is oxidized by O_2 on dimeric Fe sites, generating $[FeO]^+$ and NO_2; reaction ④: $[Fe(OH)]^+$ is oxidized by O_2. Reaction ①′ is proposed to be part of the fast SCR catalytic cycle. Reaction ①′: NO and NO_2 together bond to $[Fe(OH)]^+$ to form $[FeO(NO^+)]^+$

$NH_2)]^+$ generated by nucleophilic addition is likely to form an intramolecular hydrogen bond [82, 83]. Afterwards, the proton (H^+) attached to oxygen of the nitrosyl group transfers to the oxygen bonded to Fe to form $[Fe(OH)]^+$, and NH_2NO (nitrosamide) is eliminated from the complex (reaction ③). The NH_2NO finally decomposes into N_2 and H_2O on Brönsted sites or thermally.

Depending on the gas composition and temperature of the SCR reaction, the regeneration of the $[FeO]^+$ active center or the $[FeO(NO^+)]^+$ intermediate might proceed through several pathways. In the standard SCR reaction, at low temperatures (<250°C), $[FeO]^+$ may be regenerated by oxidizing $[FeO\text{-}NO]^+$ with O_2 through a nitrosyl bridged dimeric Fe complexes, in which two nitrosyl groups bridge two Fe centers (reaction −①): this is suggested because it is common to form bridged dimeric complexes with iron [84–89], and because the process is formally a 4-electron redox reaction that is unlikely to occur just on one iron center. Note that during reaction −①, O_2 reacts with the dimeric complex to form an intermediate peroxynitrite ($N(O)O_2^-$, FeO-N(O)O_2) (Fig. 8). Then, the intermediate reacts with

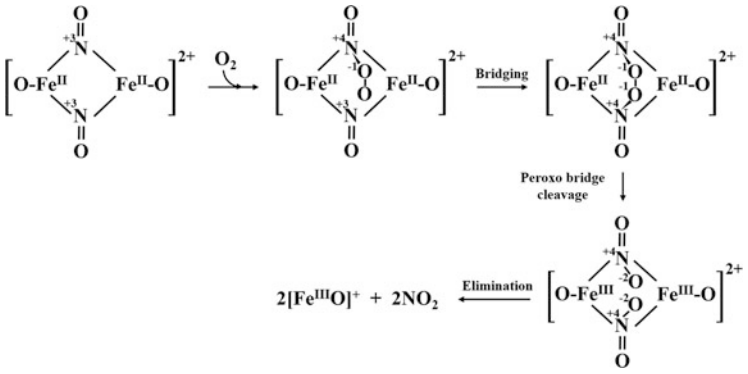

Fig. 8 Proposed elementary steps of reaction −① in the proposed mechanism of Fig. 7, where O_2 oxidizes dimeric $[Fe_2O_2(NO^+)_2]^{2+}$ to $2[FeO]^+$ and releases $2NO_2$. The atoms involved in the redox reaction are labeled with oxidation state

another nitrosyl group to form a dimer with an unstable peroxo N–O–O–N linkage [90]. In this process, two electrons on the nitrogen atoms are transferred to peroxo oxygens, changing the nitrogens in nitrosyl groups and the nitrogen into a +4 oxidation state. Then O–O bond cleaves and two Fe(II) centers are oxidized to Fe(III), where two electrons in Fe centers are transferred to oxygen atoms via nitrogen atoms in nitrosyl groups. After that, two NO_2 molecules are eliminated from the complex. Detailed steps of reaction −① are shown in Fig. 8. It has been already shown that iron zeolites can catalyze NO oxidation to NO_2 in the presence of O_2 [54]. In the presence of NO_2 (that is, under fast SCR conditions or by reaction with $[Fe(III)O(NO^+)]^+$), $[Fe(II)OH]^+$ can react through reaction ①′ to form $[FeO(NO^+)]^+$ intermediate or go through reaction ④′ to regenerate $[FeO]^+$ species (see below). Since reaction ② is competing with reaction −①, the rate of $[FeO]^+$ regeneration by reaction −① can be slowed down. This means, at low temperatures (<250°C), the overall relatively slow reaction rate of standard SCR, compared to that of fast SCR, may be limited by reaction rate of reaction −①. In standard SCR, at high temperatures (>250°C), $[FeO]^+$ is mainly regenerated by oxidation of $[Fe(OH)]^+$ directly with O_2 (reaction ④). This 4-electron reaction takes place easily at high temperatures (>250°C), but not at low temperatures (<250°C).

Overall, in the standard SCR reaction, the regeneration of Fe(III) (reaction −① and reaction ④) is proposed to involve O_2 participation. At low reaction temperatures (<250°C), reaction −①, where O_2 oxidizes dimeric $[Fe(II)O(NO^+)]^+$ to two $[FeO]^+$, dominates Fe(III) regeneration (though reaction rate is low due to the competing reaction ②) while at high reaction temperatures, reaction ④, where O_2 oxidizes $[Fe(OH)]^+$ to $[FeO]^+$, becomes the dominating Fe(III) regeneration channel [91]. This means that the Fe-containing zeolites, which contain dimeric Fe species or favorably form dimeric Fe species, will likely have higher reaction rate at low reaction temperatures. This is consistent with the higher reaction rate of Fe-beta catalyst at low temperatures, i.e., the relative flexibility and the larger pore diameter of the BEA framework can promote diffusional movement of $[FeO]^+$, allowing the formation of dimeric Fe sites [92].

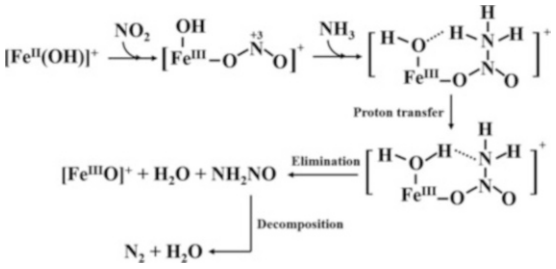

Fig. 9 Proposed elementary steps of reaction ④′ in the proposed mechanism of Fig. 7, where NO_2 regenerates $[Fe(OH)]^+$ to form $[FeO]^+$ in the presence of NH_3. The atoms involved in the redox reaction are labeled with oxidation state

In the fast SCR catalytic cycle, at low temperatures (<250°C), NO and NO_2 are proposed to bond to divalent Fe species ($[Fe^{II}(OH)]^+$) to form $[FeO\text{-}NO]^+$ (reaction ①′) [71]. The origin of Fe(II) can be from reduction of Fe(III) by NH_3 exposure. Then, $[FeO\text{-}NO]^+$ process a nucleophilic addition with NH_3 (reaction ②) and finally generate N_2 and H_2O (reaction ③). This alternate route of generation of $[FeO\text{-}NO]^+$ from $[Fe^{II}(OH)]^+$ reduces the amount of reactions and skips complicated reaction network of regenerating Fe(III) species, reactions ④ and ④′. In the fast SCR catalytic cycle, at high temperatures, $[Fe(OH)]^+$ is proposed to be oxidized by NO_2 in the presence of NH_3 (reaction ④′) [93]. During reaction ④′, NO_2 is first coordinated with $[Fe(OH)]^+$ to form $[Fe(OH)\text{-}NO_2]^+$, where Fe(II) is oxidized to Fe(III) and nitrogen is reduced to the +3 oxidation state. Then, $[Fe(OH)\text{-}NO_2]^+$ is attacked by NH_3 to form an encounter complex, $[Fe(OH)\text{-}NO_2\text{-}NH_3]^+$, which finally becomes $[FeO]^+$, N_2, and H_2O by proton transfer, elimination, and decomposition reactions. Proposed elementary steps of reaction ④′ are shown in Fig. 9. Overall, NO_2 could accelerate the fast SCR reaction by providing an alternative route for $[FeO]^+$ regeneration.

After hydrothermal aging, in both standard and fast SCR, the Fe species have been found to transform into Fe aluminates and disordered Fe_xO_y species [72]. The formation of iron aluminates is understandable because some Al_2O_3 can be dissolved in Fe_2O_3 at high temperature and vice versa [94]. The alumina is believed to be generated by hydrolytic dealumination at high temperatures, followed by atomic rearrangement of the SiO_2 framework. Agglomeration of $[FeO]^+$ species into $Fe_2O_2^{2+}$ species and further into Fe_xO_y and Fe_2O_3 is a potential mechanism for deactivation of Fe zeolite catalysts after hydrothermal aging (reaction ⑤) [65, 95]. Although severe steaming deactivates the catalyst, Pieterse et al. [96] found that applying modest steam on Fe-containing zeolite (MFI) can increase the catalyst activity in the four-electron N_2O decomposition reaction. Without any literature support, we boldly predict that similar phenomena can also be observed in NO oxidation (reaction −①) over Fe-containing zeolite. The increased catalytic activity after modest steaming can possibly be explained from the perspective of Fe-containing zeolite structure and oxophilicity of Fe metal. Since Fe species are divalent or trivalent and directly bonded to lattice oxygens (Fig. 6), there will be local positive charges on Fe sites and negative charges on lattice oxygens in Fe-containing zeolite [67]. The negatively charged lattice oxygens facilitate movement of the hydrolyzed Fe species, formed in the presence of steam due to the

oxophilicity property of Fe, resulting in the formation of Fe dimer, trimer, oligomer, etc., via dehydration reaction. We highly suspect that, among these oligomeric Fe species, the dimer, formation of which is favorable during the modest steam treatment, is the most active species in the two-Fe-center catalyzed four-electron oxidation reaction (reaction −①), because extra Fe centers in trimer or oligomer might compete with the Fe centers in the $[Fe_2O_2(NO^+)_2]^{2+}$ intermediate, distorting the structure of intermediate and further affecting the peroxo bridge formation during oxidation process (Fig. 8). In reality, another reaction $NO + NO_2 + H_2O \leftrightarrows HNO_2$ might also occur when the automobile exhaust passes through the SCR catalyst, which competes with reaction ① [97]. The consumption of NO by water increases the lifetime of $[FeO]^+$, giving $[FeO]^+$ larger chance to agglomerate, thus decreasing hydrothermal stability of Fe-containing zeolite catalyst.

Below, we list the chemical equations of the reactions depicted in the proposed ammonia SCR mechanism on Fe zeolites:

Reaction ①: $[Fe^{III}O]^+ + NO \rightarrow [Fe^{II}O(NO^+)]^+$

Reaction −①: $2[Fe^{II}O(NO^+)]^+ \rightarrow [Fe^{II}O(\mu - NO^+)]_2^{2+}$

$[Fe^{II}O(\mu - NO^+)]_2^{2+} + O_2 \rightarrow [Fe^{II}{}_2O_2(\mu - N_2O_4)(\mu - O_2)]^{2+}$

$[Fe^{II}{}_2O_2(\mu - N_2O_4)_2(\mu - O_2)]^{2+} \rightarrow 2[Fe^{III}O]^+ + 2NO_2$

Reaction ①′: $2[Fe^{II}(OH)]^+ + NO + NO_2 \rightarrow 2[Fe^{II}O(NO^+)]^+ + H_2O$

Reaction ②: $[Fe^{II}O(NO^+)]^+ + NH_3 \rightarrow [Fe^{II}(OH)NONH_2)]^+$

Reaction ③: $[Fe^{II}(OH)NONH_2)]^+ \rightarrow [Fe^{II}(OH)]^+ + NH_2NO$

$NH_2NO \rightarrow N_2 + H_2O$

Reaction ④: $4[Fe^{II}(OH)]^+ + O_2 \rightarrow 4[Fe^{III}O]^+ + 2H_2O$

(Note: This reaction cannot be elementary and it will not really make an iron tetramer.)

Reaction ④′: $[Fe^{II}(OH)]^+ + NO_2 \rightarrow [Fe^{III}(OH)(NO_2)]^+$

$[Fe^{III}(OH)(NO_2)]^+ + NH_3 \rightarrow [Fe^{III}(OH)NO_2NH_3]^+$

$[Fe^{III}(OH)NO_2NH_3]^+ \rightarrow [Fe^{III}(H_2O)(O)(NONH_2)]^+$

$[Fe^{III}(H_2O)(O)(NONH_2)]^+ \rightarrow [Fe^{III}O]^+ + NH_2NO + H_2O$

$NH_2NO \rightarrow N_2 + H_2O$

Reaction ⑤: $2[Fe^{III}O]^+ \rightarrow [Fe_2O_2]^{2+} \rightarrow Fe_xO_y \rightarrow Fe_2O_3$

5 Concluding Remarks

The details of the mechanism of ammonia SCR of NO_x on Cu-containing zeolite catalysts have started to yield to a combination of kinetic, spectroscopic, and thermodynamic investigations of reaction intermediates under various reaction conditions. Perhaps the most important takeaway is that because of the strong Cu–NH_3 bond, copper is present in the zeolite (at least below 300°C) predominantly as Cu(II) square-planar ammine complexes and as Cu(I) di-ammine complexes. This is concluded on the basis of computational and operando X-ray and IR spectroscopy

investigations. Conceptually, this changes what has been considered the active site of the reaction; rather than thinking of zeolite-framework bonded Cu ions, the active site is a solvated copper cation, a more mobile and dynamic entity that is located near the center of the zeolite cavities. Incorporation of the effects of solvation is thus essential to understand the low-temperature catalytic properties of Cu-chabazite and possibly all other Cu-zeolites for the SCR of NO_x with ammonia.

At this point, more research is needed to understand the chemistry and properties of occluded Cu–ammonia complexes. Further experimental and theoretical investigations are needed to assess what is the role of the ammonia ligands on activation energies. The oxidation of $[Cu(I)(NH_3)_2]^+$ species by NO and O_2 is a four-electron redox process that needs better understanding because it is not elementary, and because the change in Cu coordination from reactant to product could play a kinetic role and follow non-Arrhenius behavior [98].

More information is also needed about the factors that control the rate of formation of ammonium nitrate in different zeolites and how geometric and composition details affect the thermal stability of ammonium nitrate in the zeolite pores. The production of N_2O by ammonia SCR catalysts will become an increasingly important issue and learning how to minimize N_2O production is critical. A step in this direction has been recently reported by Gao et al., who showed that reduction of the concentration of acid sites in Cu-chabazite by ion exchange with alkali-metal ions is an effective strategy to minimizing the rate of N_2O generation [39]. The alkali-metal ions reduce the relative rate of nitrate decomposition versus the rate of nitrate reduction into nitrite by reaction with NO (Fig. 5).

It is important to recognize how similar is the reaction scheme depicted in Fig. 4 to catalytic reaction mechanisms of classical aqueous inorganic chemistry. The mechanism depicted in Fig. 4 is striking by its lack of striking features: Cu cations cycle through the most stable oxidation states of copper, forming 17 or 14 electron complexes as is common in copper chemistry, and coordinate to stable and well-known ligands such as ammonia, NO_3^-, NO_2^-, OH^-, and nitrosamine. The lack of unusual characteristics in the reaction network suggests that we are, in fact, in the right track.

A reaction network for mechanism of ammonia SCR of NO_x on Fe-containing zeolite has been proposed, integrating information from a variety of sources. It is important to recognize that the mechanisms of ammonia SCR of NO_x on Fe-containing and Cu-containing zeolite must be different due to chemical properties of metal active site. Strong Fe–NO bonds drive Fe ions in zeolite to predominantly coordinate with NO while the strong Cu–NH_3 bond drives Cu in the zeolite to predominantly coordinate with NH_3. In Fe-containing zeolites, Fe is more likely to be coordinated to framework oxygen ions while Cu is “solvated” by ammonia and water. The reaction pathways and intermediates changed accordingly. The nucleophilic attack of NH_3 on $[FeO(NO^+)]^+$ makes sense from the perspective of inorganic chemistry: though evidence of the formed complex is in the literature, this step is still worthy of further investigation via time-resolved operando characterization techniques. Low-temperature and high-temperature reaction channels in standard and fast SCR were proposed based on the literature results and arguments from general

chemistry. It is still not clear what is the role of different gas compositions and temperature, or the importance of dimeric Fe species and NO_2 in regenerating Fe(III) species. It is also still not clear what is the origin of the negative effect of alkali cations and Bronsted acid sites on Fe-containing zeolite during the hydrothermal aging process. This is important to improve hydrothermal stability of the catalyst.

Comparing to the proposed mechanism on Cu-containing zeolite, the nitrate, which produces N_2O in Cu-containing zeolite catalyzed SCR, is absent in the proposed mechanism over Fe-containing zeolite. So, we predict that the accumulation of nitrate in Fe-containing zeolite as well as N_2O production of SCR over Fe-containing zeolite will not be as high as they are observed in Cu-containing zeolite. Moreover, compared to Cu, Fe metal is considered to have strong oxophilicity character, which makes Fe in zeolite prone to hydrolysis. The repeated hydrolysis and condensation can promote the movement of Fe in zeolite, thus inducing agglomeration and clustering of Fe active sites.

Acknowledgements The authors are grateful for critical reviews of earlier versions of the manuscript by S. Mossin (T.U. of Denmark) and Young Jin Kim (U. of Delaware) as well as for constructive comments by an anonymous reviewer and the editors of this issue.

References

1. Janssens TVW, Falsig H, Lundegaard LF, Vennestrom PNR, Rasmussen SB, Moses PG, Giordanino F, Borfecchia E, Lomachenko KA, Lamberti C, Bordiga S, Godiksen A, Mossin S, Beato P (2015) ACS Catal 5:2832–2845
2. Paolucci C, Parekh AA, Khurana I, Di Iorio JR, Li H, Albarracin Caballero JD, Shih AJ, Anggara T, Delgass WN, Miller JT, Ribeiro FH, Gounder R, Schneider WF (2016) J Am Chem Soc 138:6028–6048
3. Borfecchia E, Lomachenko KA, Giordanino F, Falsig H, Beato P, Soldatov AV, Bordiga S, Lamberti C (2015) Chem Sci 6:548–563
4. Giordanino F, Borfecchia E, Lomachenko KA, Lazzarini A, Agostini G, Gallo E, Soldatov AV, Beato P, Bordiga S, Lamberti C (2014) J Phys Chem Lett 5:1552–1559
5. Chen HY, Wei ZH, Kollar M, Gao F, Wang YL, Szanyi J, Peden CHF (2015) J Catal 329:490–498
6. Kwak JH, Tonkyn RG, Kim DH, Szanyi J, Peden CHF (2010) J Catal 275:187–190
7. Shpiro ES, Joyner RW, Grunert W, Hayes NW, Siddiqui MRH, Baeva GN (1994) Stud Surf Sci Catal 84:1483–1492
8. Corma A, Fornes V, Palomares E (1997) Appl Catal B Environ 11:233–242
9. Fickel DW, D'Addio E, Lauterbach JA, Lobo RF (2011) Appl Catal B Environ 102:441–448
10. Gunter T, Carvalho HWP, Doronkin DE, Sheppard T, Glatzel P, Atkins AJ, Rudolph J, Jacob CR, Casapu M, Grunwaldt JD (2015) Chem Commun 51:9227–9230
11. Gao F, Walter ED, Kollar M, Wang YL, Szanyi J, Peden CHF (2014) J Catal 319:1–14
12. Gao F, Kwak JH, Szanyi J, Peden CHF (2013) Top Catal 56:1441–1459
13. Beale AM, Gao F, Lezcano-Gonzalez I, Peden CHF, Szanyi J (2015) Chem Soc Rev 44:7371–7405
14. Joshi SY, Kumar A, Luo J, Kamasamudram K, Currier NW, Yezerets A (2015) Appl Catal B Environ 165:27–35
15. Kamasamudram K, Currier N, Szailer T, Yezerets A (2010) SAE Int J Fuels Lubr 3:664–672

16. Leistner K, Mihai O, Wijayanti K, Kumar A, Kamasamudram K, Currier NW, Yezerets A, Olsson L (2015) Catal Today 258:49–55
17. Fickel DW, Lobo RF (2010) J Phys Chem C 114:1633–1640
18. Andersen CW, Bremholm M, Vennestrom PNR, Blichfeld AB, Lundegaard LF, Iversen BB (2014) Int U Cryst J 1:382–386
19. Zones SI, Vannordstrand RA (1988) Zeolites 8:166–174
20. Kwak JH, Zhu HY, Lee JH, Peden CHF, Szanyi J (2012) Chem Commun 48:4758–4760
21. Godiksen A, Stappen FN, Vennestrom PNR, Giordanino F, Rasmussen SB, Lundegaard LF, Mossin S (2014) J Phys Chem C 118:23126–23138
22. Corma A, Palomares A, Marquez F (1997) J Catal 170:132–139
23. Bates SA, Verma AA, Paolucci C, Parekh AA, Anggara T, Yezerets A, Schneider WF, Miller JT, Delgass WN, Ribeiro FH (2014) J Catal 312:87–97
24. Tsuge K, DeRosa F, Lim MD, Ford PC (2004) J Am Chem Soc 126:6564–6565
25. Ford PC, Fernandez BO, Lim MD (2005) Chem Rev 105:2439–2455
26. Zolfigol MA, Zebarjadian MH, Chehardoli G, Keypour H, Salehzadeh S, Shamsipur M (2001) J Org Chem 66:3619–3620
27. Khin C, Lim MD, Tsuge K, Iretskii A, Wu G, Ford PC (2007) Inorg Chem 46:9323–9331
28. Selleri T, Ruggeri MP, Nova I, Tronconi E (2016) Top Catal 59:678–685
29. Ruggeri MP, Nova I, Tronconi E, Pihl JA, Toops TJ, Partridge WP (2015) Appl Catal B Environ 166:181–192
30. Mathisen K, Stockenhuber M, Nicholson DG (2009) Phys Chem Chem Phys 11:5476–5488
31. Lamble G, Moen A, Nicholson DG (1994) J Chem Soc Faraday Trans 90:2211–2213
32. Hathaway BJ, Tomlinso AAG (1970) Coord Chem Rev 5:1–43
33. Morosin B (1969) Acta Crystallogr Sect B: Struct Sci 25:19–30
34. Yamaguchi T, Ohtaki H (1979) Bull Chem Soc Jpn 52:415–419
35. Himes RA, Park GY, Barry AN, Blackburn NJ, Karlin KD (2007) J Am Chem Soc 129:5352–5353
36. Maurin A, Varatharajan S, Colasson B, Reinaud O (2014) Org Lett 16:5426–5429
37. Peck KL, Clewett HS, Schmitt JC, Shearer J (2013) Chem Commun 49:4797–4799
38. Derouane EG (1998) J Mol Catal A Chem 134:29–45
39. Gao F, Wang YL, Washton NM, Kollar M, Szanyi J, Peden CHF (2015) ACS Catal 5:6780–6791
40. Verma AA, Bates SA, Anggara T, Paolucci C, Parekh AA, Kamasamudram K, Yezerets A, Miller JT, Delgass WN, Schneider WF, Ribeiro FH (2014) J Catal 312:179–190
41. Paolucci C, Verma AA, Bates SA, Kispersky VF, Miller JT, Gounder R, Delgass WN, Ribeiro FH, Schneider WF (2014) Angew Chem Int Ed 53:11828–11833
42. Morosin B, Larson AC (1969) Acta Crystallogr Sect B Struct Sci 25:1417–1419
43. Chukanov NV, Britvin SN, Mohn G, Pekov IV, Zubkova NV, Nestola F, Kasatkin AV, Dini M (2015) Mineral Mag 79:613–623
44. Morosin B (1976) Acta Crystallogr Sect B Struct Sci 32:1237–1240
45. Porai-Koshits MA, Bukovska M (1962) J Struct Chem 3:33–37
46. Grossale A, Nova I, Tronconi E, Chatterjee D, Weibel M (2008) J Catal 256:312–322
47. Grossale A, Nova I, Tronconi E (2008) Catal Today 136:18–27
48. Balle P, Geiger B, Kureti S (2009) Appl Catal B Environ 85:109–119
49. Colombo M, Nova I, Tronconi E (2010) Catal Today 151:223–230
50. Iwasaki M, Shinjoh H (2010) Appl Catal Gen 390:71–77
51. Ruggeri MP, Grossale A, Nova I, Tronconi E, Jirglova H, Sobalik Z (2012) Catal Today 184:107–114
52. Long RQ, Yang RT (1999) J Am Chem Soc 121:5595–5596
53. Ma A-Z, Grunert W (1999) Chem Commun 1:71–72
54. Gao F, Zheng Y, Kukkadapu RK, Wang Y, Walter ED, Schwenzer B, Szanyi J, Peden CHF (2016) ACS Catal 6:2939–2954
55. Li J, Chang H, Ma L, Hao J, Yang RT (2011) Catal Today 175:147–156
56. Qi G, Yang RT (2005) Appl Catal B Environ 60:13–22

57. Martín N, Vennestrøm PNR, Thøgersen JR, Moliner M, Corma A (2017) ChemCatChem 9:1754–1757
58. Brandenberger S, Kröcher O, Tissler A, Althoff R (2010) Appl Catal B Environ 95:348–357
59. Kumar MS, Schwidder M, Grünert W, Brückner A (2004) J Catal 227:384–397
60. Schwidder M, Kumar M, Klementiev K, Pohl M, Bruckner A, Grunert W (2005) J Catal 231:314–330
61. Gao F, Kollár M, Kukkadapu RK, Washton NM, Wang Y, Szanyi J, Peden CHF (2015) Appl Catal B Environ 164:407–419
62. Pérez Vélez R, Ellmers I, Huang H, Bentrup U, Schünemann V, Grünert W, Brückner A (2014) J Catal 316:103–111
63. Høj M, Beier MJ, Grunwaldt J-D, Dahl S (2009) Appl Catal B Environ 93:166–176
64. Ma L, Chang H, Yang S, Chen L, Fu L, Li J (2012) Chem Eng J 209:652–660
65. Pidko EA, Hensen EJM, van Santen RA (2012) Proc Royal Soc A 468:2070–2086
66. Long RQ, Yang RT (2000) J Catal 194:80–90
67. Boubnov A, Carvalho HW, Doronkin DE, Gunter T, Gallo E, Atkins AJ, Jacob CR, Grunwaldt JD (2014) J Am Chem Soc 136:13006–13015
68. Brandt WW, Howsmon WBJ (1954) Notes 76:6319–6320
69. Pflaum RT, Brandt WW (1955) J Am Chem Soc 76:6215–6219
70. Pflaum RT, Brandt WW (1955) Notes 77:2019–2022
71. Macie Jowksa I, Stasicka Z (2002) Bull Pol Acad Sci Chem 50:67–76
72. Kovarik L, Washton NM, Kukkadapu R, Devaraj A, Wang A, Wang Y, Szanyi J, Peden CHF, Gao F (2017) ACS Catal 7:2458–2470
73. Lai S, She Y, Zhan W, Guo Y, Guo Y, Wang L, Lu G (2016) J Mol Catal A Chem 424:232–240
74. Martin N, Vennestrom PNR, Thogersen JR, Moliner M, Corma A (2017) Chem Eur J 23:13404–13414
75. Yuan E, Wu G, Dai W, Guan N, Li L (2017) Cat Sci Technol 7:3036–3044
76. Martínez-Franco R, Moliner M, Concepcion P, Thogersen JR, Corma A (2014) J Catal 314:73–82
77. Martín N, Paris C, Vennestrøm PNR, Thøgersen JR, Moliner M, Corma A (2017) Appl Catal B Environ 217:125–136
78. Song S, Wu G, Dai W, Guan N, Li L (2016) Cat Sci Technol 6:8325–8335
79. Li J, Li S (2007) Phys Chem Chem Phys 9:3304–3311
80. Gilardoni F, Weber J, Baiker A (1997) J Phys Chem A 101:6069–6076
81. Soyer S, Uzun A, Senkan S, Onal I (2006) Catal Today 118:268–278
82. Lacy DC, Mukherjee J, Lucas RL, Day VW, Borovik AS (2013) Polyhedron 52:261–267
83. Reedijk J (2013) Chem Soc Rev 42:1776–1783
84. Jang JH, Lee JG, Lee H, Xie Y, Schaefer HF (1998) J Phys Chem A 102:5298–5304
85. Macchi P (2003) Coord Chem Rev 238–239:383–412
86. Kubat-Martin KA, Barr ME, Spencer B, Dahl LF (1987) Organometallics 6:2570–2579
87. Nagao H, Nagao N, Yukawa Y, Ooyama D, Sato Y, Oosawa T, Kuroda H, Howell FS, Mukaida M (1999) Bull Chem Soc Jpn 72:1273–1284
88. Legzdins P, Martin DT, Nurse CR, Wassink B (1983) Organometallics 2:1238–1244
89. Calderón JL, Fontana S, Frauendorfer E, Day VW, Iske SDA (1974) J Organomet Chem 64: C16–C18
90. Furutachi H, Okawa H (1998) Bull Chem Soc Jpn 71:671–677
91. Kiyama M (1974) Bull Chem Soc Jpn 47:1646–1650
92. Boron P, Chmielarz L, Gurgul J, Latka K, Gil B, Marszałek B, Dzwigaj S (2015) Microporous Mesoporous Mater 203:73–85
93. Li J, Li S (2008) J Phys Chem C 112:16938–16944
94. Bolt PH, Habraken FHPM, Geus JW (1998) J Solid State Chem 135:59–69
95. Krocher O, Brandenberger S (2012) Chimia (Aarau) 66:687–693
96. Pieterse JAZ, Booneveld S, van den Brink RW (2004) Appl Catal B Environ 51:215–228
97. Waldorf DM, Babb AL (1963) J Chem Phys 39:432–435
98. Blumberger J (2008) J Am Chem Soc 130:16065–16068

Struct Bond (2018) 178: 179–250
DOI: 10.1007/430_2017_17

Published online: 28 December 2017

Structure and Reactivity of Zeolites Containing Group Five Elements (V, Nb, Ta)

Maria Ziolek, Izabela Sobczak, Maciej Trejda, and Anna Wojtaszek-Gurdak

Abstract This chapter is devoted to the inclusion of group five metals (vanadium, niobium and tantalum) into different zeolite structures (mainly AFI, AM-11, BEA, FAU, LTA, MEL, MFI, MOR, MWW) in order to achieve zeolites with novel catalytic and photocatalytic properties. The focus is on the achievement in the last two decades in the field of methods of metal incorporation and characterization of structure of species formed by different modification methods and their acid-base and redox properties. Special attention is paid to the reactivity of metal species in zeolites with reagents in selected catalytic processes. Their catalytic activity is considered in oxidation processes (in liquid and gas phases), reduction and acid-catalysed reactions as well as photocatalytic processes. From among liquid-phase oxidation processes, hydroxylation of benzene and oxidation of olefins and sulphides with hydrogen peroxide are considered. As examples of gas-phase redox processes, propane and methanol oxidation and catalytic reduction of nitrogen oxide are presented. The tandem reaction, ethanol to 1,3-butadiene, and transformation of glycerol to acrolein are discussed in details as examples of acid-catalysed reactions. The use of zeolites as supports for group five metals is demonstrated to be a good solution for designing attractive photocatalysts.

Keywords Catalytic activity • Methods of metals' incorporation • Surface properties • Zeolites containing V • Zeolites containing Nb • Zeolites containing Ta

Contents

M. Ziolek (✉), I. Sobczak, M. Trejda, and A. Wojtaszek-Gurdak
Faculty of Chemistry, Adam Mickiewicz University, Poznań, Poland
e-mail: ziolek@amu.edu.pl

1 Introduction

Traditionally, zeolites were defined as crystalline aluminosilicates. The interest in the syntheses of zeolites stemmed from their attractive use in science and technology. One of the milestones activating the progress in zeolite syntheses was the discovery of the possible replacement of silicon or aluminium in zeolite structure by different elements, among others, transition metals exhibiting catalytic properties. Transition metal ions well dispersed in zeolite framework are well known to be active sites of catalytic and photocatalytic processes. Therefore, the incorporation of metal ions into the zeolite framework as isolated mononuclear sites appears to be an important goal.

The first syntheses with introduction of different elements (germanium and gallium) to zeolite structures (thomsonite, zeolite A, faujasite and harmotome) have been made by Goldsmith [1] and Barrer et al. [2]. Following their discoveries and further fascinating achievements of Milton, Breck, Flanigen and others in the Union Carbide laboratories, plenty of zeolites and related materials containing different elements have been synthesized, and novel materials in this class are still discovered. However, the incorporation of transition metals to the zeolite structure was for many years a difficult task, and the development in this issue dates back to the end of the 1970s. Their syntheses performed in 1998 are widely described in the first volume of the series "Molecular Sieves – Science of Technology" edited by Karge and Weitkamp [3]. The ability of a given ion M^{n+} to be incorporated into the zeolite structure depends on many factors, not only on the ionic radii and the tendency of the element to assume tetrahedral coordination in its oxide. Therefore, it is not easy to establish simple criteria for predicting the ability of a given element to be incorporated in the zeolite framework. Generally such incorporation can be performed by two synthetic routes: incorporation of the desired metal (1) through crystallization together with silicon and aluminium species under hydrothermal conditions and (2) through post-synthesis modification of zeolites via different treatments. The choice of the modification route depends on

the kind of zeolite structure, thermal/hydrothermal stability of zeolite, available metal source and many other parameters.

The introduction of transition metals of high oxidation states via conventional ion exchange in aqueous solution of metal salt is usually rather difficult if not impossible for many reasons. The required cations are frequently not available in simple metal salts. Even if such salts are available, the metal cations may exist only in strong acidic solutions which show two disadvantages: (1) competition of extra-framework cations with proton exchange and (2) the destruction of zeolite by acid attack. For the polyvalent transition metals mentioned (group five elements belong to them), the solution to this drawback could be solid-state ion exchange which allows the incorporation of polyvalent cations and their homogeneous distribution [4]. This simple method developed in the mid-1980 in two groups, Slinkin's in Moscow [5] and Karge's in Berlin [6], is a good alternative to the incorporation of polyvalent cations to zeolites.

Last decades have brought different solutions for incorporation of polyvalent metal cations to zeolite structures. They cover both, the incorporation of metals during the synthesis and after the synthesis by special treatments of zeolites before the incorporation of metals. This chapter is devoted to the inclusion of group five metals (vanadium, niobium and tantalum) into different zeolite structures. The focus is on the methods of metal incorporation and characterization of the structure of the chemical species formed by different modification methods and their acid-base and redox properties. Special attention is paid to the reactivity of metal species in zeolites in selected catalytic processes. Their catalytic activity is considered in oxidation processes (in liquid and gas phases), reduction and acid-catalysed reactions as well as photocatalytic processes.

2 Vanadium Species in Zeolites

2.1 Methods of Including Metal to Zeolites, Metal Location, Sample Structure and Stability

Vanadium-containing zeolites are very attractive catalysts because of their acidic and redox properties. A number of reports have been devoted to the preparation, structure characterization and spectroscopic analyses of these materials. Catalytic performance of V zeolites strongly depends on many factors, the most important ones being the nature and local environment of vanadium species. It is very important to know the oxidation state and coordination of V as well as the mechanism of its introduction into the zeolite lattice. This information can be very helpful for better understanding of the catalytic properties of the catalysts and to design new ones. Many authors [7–11] have reported that the oxidation state of vanadium (+4 or +5) strongly depends on the synthesis procedure and on the post-synthesis treatment of the catalysts. When the vanadium +5 ions are in the

zeolite lattice, they can be easily reduced to V^{4+}, whereas extra-framework V^{4+} ions can be oxidized to V^{5+} upon calcination in air. However, it has been proved that extra-framework species are less catalytically active, e.g. in toluene oxidation with H_2O_2 and V^{5+} can be easily eliminated by washing with aqueous ammonium acetate (NH_4OAc) [8, 9].

Generally, zeolites can be modified by vanadium by two sets of methods: direct hydrothermal synthesis and post-synthesis techniques like ion exchange, solid-state reaction, chemical vapour deposition or wet impregnation [12].

2.1.1 Extra-Framework Vanadium Species

One of the most popular post-synthesis methods of zeolite modification is ion exchange. This technique takes advantage of one of the most important features of zeolites, that is, the presence of cations that neutralize the negative charge of the lattice. These cations are not strongly bonded to the zeolite and can be relatively easily exchanged by other ones. However, a disadvantage of the ion exchange method is the difficulty of controlling the pH of the metal salt solution [13]. Vanadium cations have been introduced by ion exchange procedure into both natural and synthetic zeolites. The kind of vanadium species formed after ion exchange procedure, which later determine the activity and selectivity of zeolites obtained, strongly depends on the zeolite structure and vanadium precursor. For instance, the application of $VOCl_3$ as a metal precursor can cause destruction of zeolite structure [14]. An example of the ion exchange as a zeolite modification method with vanadium is given in [15].

A very simple method of Na exchange to vanadyl cation in Y zeolite was used to obtain an active and selective catalyst for the oxidation of cyclohexane to cyclohexanone. For this purpose, $VOSO_4 \cdot 5H_2O$ solution was applied as vanadium precursor. A mixture of NaY zeolite and water solution of vanadium precursor was stirred at 363 K for 24 h. A change in colour from blue to deep green was observed during the ion exchange process. In the next step, the mixture was cooled down and the product was filtered and washed. This procedure was repeated twice. Finally, the zeolite prepared was dried at 373 K and calcined at 773 K for 4 h to obtain VY zeolite yellow in colour. The above-described modification is shown in Fig. 1.

As mentioned above, the cations exchanged replace those originally present in the zeolite before ion exchange procedure. Therefore, they are located in extra-framework positions. For vanadium-exchanged Y zeolites, XRD analysis confirmed well-defined crystal structure of VY zeolite. However, the comparison of the XRD diffractograms of Y zeolite before and after vanadium modification indicated a decrease in peak intensity. The cell parameter (a_0) of NaY (2.4608) and VY (2.4567) did not differ much. Indeed, these results confirmed that metal exchange occurred in the extra-framework position. The chemical environment and oxidation state of vanadium were characterized by XPS method. The binding energies observed for vanadium at 516.51 eV ($2p_{3/2}$) and 523.43 eV ($2p_{1/2}$) are

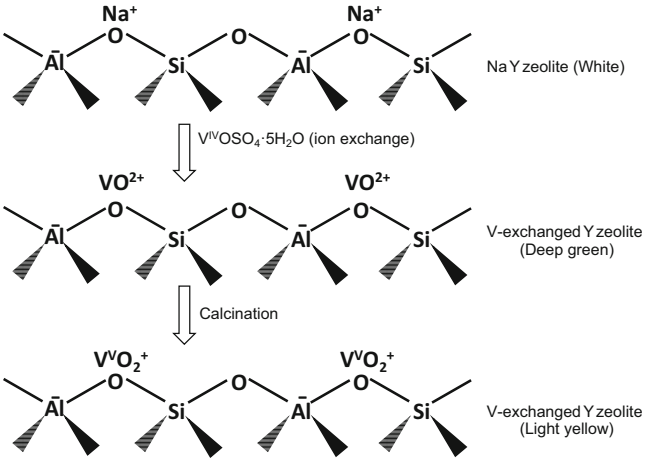

Fig. 1 The mechanism of ion exchange of Na^+ for vanadyl cations in NaY (after [15])

typical of intra-zeolite V^{5+} oxide. This result suggests that V^{4+} of vanadyl sulphate has been oxidized to V^{5+} during the calcination process.

The ion exchange in zeolites usually performed in the aqueous solutions of different metal salts can be replaced by a procedure that does not involve the application of metal salt solutions. For this purpose, a mixture of hydrogen form of zeolite and metal salt or metal oxide are contacted at elevated temperature. Such a modification of the procedure is called solid-state ion exchange and has been also applied for vanadium incorporation into zeolite. For instance, Narayanan and Sultana have prepared a series of different zeolites (HX, HY, HM and HZSM-5) with vanadium using this method [16]. To obtain the final materials, the zeolites containing 5% of vanadium (V_2O_5 was used as metal precursor) were physically mixed in the mortar for 1 h and then heated in nitrogen flow at 673 K for 7 h. The isotherm of N_2 adsorption and desorption indicated that the surface area of zeolites decreased after vanadium addition. This suggested that the zeolite pores were blocked by dispersed vanadium oxides. Nevertheless, a weak V^{4+} ESR signal was detected for these materials. The interpretation was that after heating of V_2O_5-zeolite mixture in nitrogen, the V_2O_5 species were reduced to VO^{2+} ones. The latter migrated into the cationic positions in the zeolite channels.

Impregnation and grafting are the other post-synthesis modification techniques that can be applied for the preparation of vanadium-containing zeolites. However, the application of the above-mentioned methods could be limited if a large number of vanadium species well dispersed on the surface of the support are required. Similarly to the ion exchange techniques, different factors influence the impregnation and grafting procedures. Garcia et al. have examined ultrastable zeolite Y modified by vanadium oxides VO_x. Two post-synthesis methods were applied: grafting procedure with organic $V(AcAc)_3$ and impregnation technique with inorganic NH_4VO_3 at controlled pH of 4 or 7 [17]. The main goal of their work was to

obtain highly dispersed vanadium species and to avoid the formation of crystalline vanadium oxide and the destruction of the zeolite framework. The results of different characterization techniques (XRD, TPR, N_2 adsorption isotherms) indicated that in the sample obtained by impregnation with NH_4VO_3 a high dispersion of vanadium was not achieved. In the acidic conditions applied in the process, a destruction of the zeolite structure was observed, while under pH 7, V_2O_5 crystals were detected. In contrast, the VO_x/USY materials obtained by grafting with V $(AcAc)_3$ showed no destruction of the USY structure. Moreover, highly dispersed VO_x species were formed.

2.1.2 Isomorphous Substitution of Vanadium

One-Pot Methods

Isomorphous substitution of vanadium in zeolites can be achieved by vanadium ion introduction during the hydrothermal synthesis into different zeolite frameworks: ZSM-5 type [18, 19], MEL [20], ZSM-12 [21], ZSM-48 [18, 22] and BEA [23]; see Table 1.

The purpose of application of zeolite hydrothermal synthesis with the source of metal usually is to locate this metal in zeolite framework positions. However, part of vanadium species can take extra-framework positions. In this context, it is very important task to follow the actual location and amount of vanadium in the materials prepared in this way. Firstly, it should be noticed that it is not easy to obtain a high efficiency of vanadium incorporation by this method. For example,

Table 1 The role of synthesis conditions on the vanadium loading and location in zeolites

Zeolite type	Modification method (description)	V source	V loading as assumed (Si/V)	Real V loading (Si/V)	V location	Ref.
BEA	One-pot synthesis (autoclave, 413 K, 20 days)	V_2O_5	Si/V = 30	n.d.	Extra-framework	[23]
BEA	Two-step method (dealumination and impregnation with V)	$VOSO_4$	Si/V = 335 Si/V = 122 Si/V = 63	Si/V = 335 Si/V = 122 Si/V = 63	Framework	[11]
MFI	One-pot synthesis (autoclave, 473 K, 7 days)	$VOSO_4$	Si/V = 80	n.d.	Framework	[8]
MFI	One-pot synthesis, rapid crystallization	$VOSO_4$ VOC_2O_4 VCl_3 $V(C_5H_7O_2)_3$	Si/V = 90	Si/V = 174 Si/V = 246 Si/V = 178 Si/V = 176	Extra-framework	[24]
Silicalite	One-pot synthesis	$VOSO_4$	Si/V = 184 Si/V = 87 Si/V = 57 Si/V = 45 Si/V = 36	Si/V = 461 Si/V = 122 Si/V = 65 Si/V = 49 Si/V = 45	Framework, extra-framework	[25]

Chien et al. have carried out the hydrothermal synthesis of VBEA (Si/Al = 30) zeolite using vanadium(V) oxide as a heteroatom precursor [23]. On the basis of the ICP analysis, they found that only 1.3 wt% of vanadium was included into the zeolite. Nevertheless, the VBEA material showed well-developed crystal structure, typical of BEA zeolite, which was estimated by XRD analysis. The spectroscopic studies indicated that all vanadium was at +4 oxidation state. These vanadium species were atomically dispersed at the cation or vacant acid sites near aluminium cations; thus, they occupy extra-framework position.

Location of vanadium introduced during the zeolite hydrothermal synthesis is determined by different factors. For example, Bellussi and Rigutto have demonstrated that the isomorphous substitution of vanadium into silicalite structure is affected by the chemical composition of the reaction mixture, crystallization conditions, metal precursor and the reaction media [26]. The last factor has been intensively studied by Sen et al. aiming to obtain vanadium-containing zeolites of MFI structure [8]. It was found that the synthesis in alkaline media led to incorporation of vanadium in the lattice as distorted tetrahedral species at defect sites, whereas acidic media led to obtain mostly V^{4+} species in an octahedral environment that later transformed to V^{5+} species on calcination.

The next important factor influencing the location of vanadium in the framework position is the type of metal precursor. Some studies have been made in this regard by Inui et al. [27]. To obtain VMFI zeolite, a new method, the so-called rapid crystallization method, has been designed. This new procedure is based on the gel used in the synthesis, which was precipitated from the solution containing the silica and vanadium sources, the organic template agent and NaCl. The kind of metal precursor has been shown to have a significant effect on the crystallized product, its morphology and catalytic properties. With the use of a common source of vanadium, i.e. NH_4VO_3, it was found to be impossible to introduce vanadium to MFI structure by the rapid crystallization method. The main reason may be the weak interaction between vanadate ions and silica gel. However, starting from $V(AcAc)_5$, V-MFI zeolite with high crystallinity, the uniform crystal size and high BET surface were obtained [24].

The incorporation of vanadium species via hydrothermal synthesis into a given zeolite and the location at the position demanded (framework or extra-framework) is the first condition to obtain a material with unique properties. Another important factor that should be taken into account is the stability of the metal species obtained. It is especially important for the incorporation of vanadium in extra-framework positions. These kinds of species are usually less stable due to a weaker interaction with the support. This feature has been extensively studied by Guo et al. for silicalite-1 modified with vanadium [25]. In their work a series of VS-1 zeolites with different vanadium content (0.5, 1.0, 1.5, 2.0 and 2.5 wt%) was prepared by hydrothermal synthesis. As a result, both framework and extra-framework vanadium species were obtained. For all samples the stability of V species was tested by washing the materials prepared with aqueous ammonium acetate (NH_4OAc), acetic acid, hydrogen peroxide (H_2O_2 30 wt%) or a mixture of acetic acid and hydrogen peroxide ($HOAc:H_2O_2$ = 10:1, v/v). All catalysts prepared showed well-defined

crystalline structure with MFI topology. The results of elemental analysis showed that the vanadium content was lower than the nominal values for all catalysts prepared. The highest content of vanadium was 1.9 wt% (2.5 wt% nominal). During the washing of the catalyst with different solutions, partial vanadium leaching was observed. However, in the majority of the samples tested, the vanadium content was still about 1 wt% after washing. According to literature [8, 9], the extra-framework vanadium species weakly bonded to the zeolite walls are easily removed on washing. After the washing procedure, it was shown that all vanadium species present in the samples were in the framework positions. The authors of the above-mentioned paper compared the influence of different solutions indicated above on the vanadium leaching. The smallest amount of V was lost in the sample washed with acetic acid solution (0.2 wt%) and then 0.6 wt% vanadium leached after H_2O_2 washing. The experiments showed that vanadium species are not stable on washing with a mixture of acidic and oxidant solution (0.8 wt% V leached).

Another very important factor in determining the catalytic properties of zeolites modified with vanadium is the form in which the metal is introduced, i.e. its oxidation state and coordination. For instance, it has been observed that vanadium introduced via hydrothermal synthesis into MFI structure can occur at various oxidation states and, what is more important, it can very easily change its oxidation state [28]. On the basis of XPS and DR UV-Vis studies, the same conclusion has been drawn by Guo et al. [25] for vanadium-containing silicalite-1 material prepared also by hydrothermal synthesis. It was observed that vanadium in the framework position is present at different oxidation states and in different coordination (mononuclear octahedral V^{5+}, tetrahedral V^{5+} and V^{4+}). As mentioned above, these framework species were stable on washing with acetic acid and/or hydrogen peroxide solution, indicating a strong interaction with the zeolite lattice. In contrast, unstable vanadium species present in extra-framework positions were mainly detected as octahedral V^{5+} oligomers.

To sum up, the main problem with the incorporation of vanadium during the hydrothermal synthesis is related to the minor fraction of vanadium ions that are incorporated into the zeolite framework. Most of the vanadium species were located in the extra-framework sites. They were unstable and very easily removed by the washing with ammonium acetate solution [8, 9]. Because of these difficulties, a lot of work has been devoted to design new and more effective methods for vanadium incorporation into zeolite structures.

The influence of synthesis conditions on the vanadium loading and its location in zeolites is summarized in Table 1.

Post-synthesis Methods

As presented so far, the post-synthesis methods applied for vanadium incorporation into the zeolite gave extra-framework metal species that were more or less dispersed. However, also post-synthesis procedures can lead to location of vanadium in the framework position. For this purpose a different methodology was developed.

For instance, Niederer et al. have prepared VBEA zeolite by isomorphous substitution of vanadium by post-synthesis gas-phase modification of boron-containing zeolite BEA with $VOCl_3$ followed by methanolysis for the removal of boron [29]. The catalysts prepared showed crystal structure typical of BEA zeolite, and no phase of impurities was detected. However, zeolites suffered some loss of crystallinity when compared to the starting material. The catalysts prepared were characterized by ^{29}Si MAS NMR. If boron was completely isomorphously substituted by vanadium, there should be no SiOH groups left in the zeolite. In the NMR spectra of vanadium-containing zeolites, the Q^3-signal at −103 ppm assigned to $Si(OSi)_3OH$ was visible. This suggested that vanadium did not completely substitute boron. This resulted in formation of silanol nests consisting of four silanol groups associated with vacancies left after the removal of boron from the framework. The ESR spectrum of the vanadium-containing material did not show any signal, which indicated that vanadium was mainly present as the ESR inactive vanadium(V).

A different methodology for vanadium substitution into the framework position of zeolites using post-synthesis modification procedure has been applied by Kim et al. [30]. The substitution process proposed by these authors took place in two steps. The first one consisted of dealuminating of mordenite. In the next step, the material was treated with an aqueous solution of ammonium metavanadate (NH_4VO_3) that was used as a vanadium precursor. Characterization of the material obtained confirmed the introduction of vanadium into the structure of mordenite. However, the orange colour of the sample indicated the presence of vanadium in the form of polymer. This post-synthesis methodology in relation to BEA zeolites has been further developed by Dzwigaj et al. [12, 31]. In the first step, vacant T sites were created by dealumination of BEA zeolite with nitric acid. The next step was impregnation of SiBEA zeolite with an aqueous solution of ammonium metavanadate (NH_4VO_3) used as V^{5+} precursor. The FTIR, DR UV-visible and ^{51}V MAS NMR studies have shown that vanadium was successfully incorporated into BEA lattice and was present as V^{5+} in tetrahedral coordination. The chemical analysis indicated that vanadium was not eliminated by the washing with NH_4OAc solution [12]. The same methodology was applied to introduce vanadium at +4 oxidation state into dealuminated BEA zeolite; however an aqueous solution of vanadyl sulphate ($VOSO_4$) was used as vanadium +4 precursor [11]. The results have documented that vanadium can be present in SiBEA at +4 and +5 oxidation states. The metal oxidation state depends on the way the solid is recovered after impregnation as well as on the temperature of drying. It was found that in the solids recovered by centrifugation, washed with distilled water, and then dried at 298 K in argon, vanadium was present as V^{4+} in octahedral coordination in the extra-framework position. Different behaviour was observed for the solids not washed but directly dried overnight at 353 K in air or argon. In such a treatment, vanadium was introduced as lattice tetrahedral V^{5+} ions. Diffuse reflectance UV-visible, ^{51}V MAS NMR and also photoluminescence measurements indicated that these ions were incorporated into vacant T sites associated with SiOH, SiO^-, oxygen vacancies (OVs) or nonbridging oxygen (NBO) defects. This result was related to the

oxidation of V^{4+} into V^{5+} upon electron transfer probably from V^{4+} to trigonal $\equiv Si^{+}$ defect, and then the reaction of V^{5+} thus formed with different types of defect sites. The results of chemical analysis showed that lattice tetrahedral V^{5+} ions were more stable in the structure of zeolite than octahedral V^{5+} ions. They were very resistant to washing with aqueous NH_4OAc solution. The octahedral V^{5+} ions were easily eliminated upon washing, which showed that they were loosely bound to the zeolite.

The possibility of vanadium introduction into the faujasite structure [32, 33] and into BEA zeolite has been also investigated by theoretical calculation [32, 34, 35]. The calculation was performed on sodalite model (SOD). Different site models were used to study substitution of T site by vanadium. All results obtained were compared with the experimental ones published for BEA in [36, 37] and FAU in [38, 39]. The studies performed showed that substitution of Si by vanadium is energetically not favoured. The calculated most energetically stable vanadium +5 species is the vanadium ion with one double bond with an oxygen atom and linked by three V-OSi groups. The less stable are V^{5+} species in V-OH group. These results were also confirmed by photoluminescence and UV-Vis and IR spectroscopies. In the calculations performed for faujasite structure, the sodalite model was modified by exchanging one silicon atom by aluminium. The negative charge of the framework was compensated by sodium cations. In thus modified sodalite model, 11 different positions of vanadium relative to aluminium were considered. The final results showed that the most stable species of vanadium is V=O close to aluminium.

2.2 Surface Properties

Vanadium-containing zeolites are usually applied as catalysts for different oxidation processes, as presented in Sect. 3. In this context, it is important to discuss first some surface properties that obviously influence the above-mentioned processes. Among them the acidic properties of vanadium zeolites are very important. They determine the adsorption ability as well as the hydrophilic/hydrophobic properties of the catalyst surface. The latter properties are responsible for co-adsorption of water or other catalytic reaction products. Another very important factor that should be taken into account is the oxidation state and reducibility of vanadium species on the material surface. The reducibility depends on the type of vanadium species and their interaction with the support. For instance, it is known from literature that monomeric VO_x species are the most reducible ones, followed by polymeric vanadium species and amorphous and crystalline V_2O_5 species when they are deposited on TiO_2 [40, 41]. The possible types of vanadium species on material surface are schematically presented in Fig. 2 according to Wachs [42]. Fig. 2 is related to metal oxide supports, however, it could be helpful later for discussion related also to zeolites.

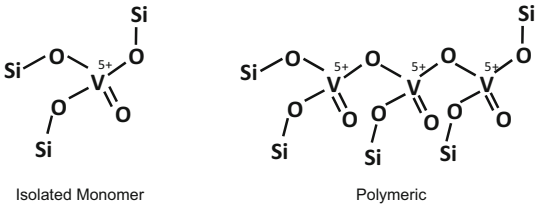

Fig. 2 The possible types of vanadium species on silica support (after [42])

The acidity of vanadium-containing zeolites can originate from the incorporated vanadium species as well as from the active centres present in zeolite structure before its modification. In this context to examine the properties of vanadium-containing zeolites, it is important to characterize the surface of the support. To show the significance of this problem, two commercial BEA zeolites were first dealuminated and next modified with ammonium metavanadate by the similar methodology [43, 44]. The first was dealuminated SiBEA zeolite prepared in [43] which did not show the presence of Brønsted acid centres as estimated by the pyridine adsorption followed by FTIR measurements. Only low-intense bands at 1,597 and 1,445 cm^{-1} were observed after adsorption of pyridine. The authors related these bands to the interaction of pyridine with weak Lewis acid sites. In contrast, the SiBEA material reported in [44] showed the presence of both Lewis and Brønsted acid sites estimated by the same method. Independently of the initial acidity of the support, for both zeolites after vanadium incorporation, the number of Lewis acid sites much increased. Nevertheless, there was a difference in the way the Brønsted acid sites evolved in both samples. When there were no Brønsted acid sites in the support before its modification, the number of these centres increased with increasing vanadium amount in the sample. For SiBEA-containing Brønsted acid sites with a small amount of vanadium introduced to the support, the number of Brønsted acid sites initially decreased and then increased with increasing vanadium loading in the sample. The mentioned decrease in Brønsted acidity is in agreement with another report on HBEA zeolites, showing that upon incorporation of vanadium to zeolite BEA, Lewis acidity was enhanced, whereas Brønsted acidity was weakened slightly [23]. The Brønsted acid sites present in hydrogen forms of zeolites are related to the proton linked with bridged oxygen in Si-O-Al groupings. As far as vanadium substituted in the zeolite framework is concerned, it is generally claimed that vanadium is tetrahedrally coordinated and exists as +5 oxidation state. For this reason vanadyl V=O bond is formed and three other bonds are created with oxygens from the zeolite lattice, similarly as presented for isolated monomer species of vanadium in Fig. 2. On the basis of the experiments related to the incorporation of vanadium species in different kinds of oxides, it was suggested that Brønsted hydroxyls in vanadium-containing materials may be located as bridging V-OH-support sites [45]. The same origin of Brønsted hydroxyls was proposed for vanadium-containing zeolites [43, 44]. It was concluded that Brønsted acid centres in VSiBEA zeolite are related to the acidic proton of OH group of framework hydroxylated $(SiO)_2(HO)V{=}O$ species presented in Fig. 3. On the basis of computational studies, it was also found that only a small part of all

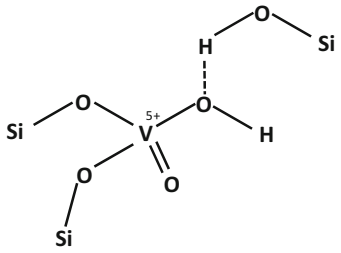

Fig. 3 Framework hydroxylated $(SiO)_2(HO)$ V=O species (after [44])

tetrahedral V^{5+} species appeared as such species [35]. It is in line with literature, in which it has been pointed out that incorporation of vanadium into zeolite increases mainly Lewis acidity of the sample obtained.

The acidity of vanadium-containing BEA zeolites has been also tested using NH_3 and CO as probe molecules followed by FTIR measurements [43]. In the case of some space limitation in the material examined, the former probe molecule being smaller than pyridine allows the access to a higher number of acid centres. For vanadium-containing BEA zeolites, the same number of Brønsted acid sites was determined using both probe molecules, i.e. pyridine and NH_3. However, the number of Lewis acid centres calculated for these zeolites was higher when using ammonia. This is one of the reasons why the NH_3 molecules are commonly applied to determine the number and strength of acidic sites in zeolites using thermo-programmed desorption technique (NH_3-TPD). The properties of vanadium-containing zeolites measured by the above-mentioned method will be described later in this section.

As described above, the introduction of vanadium into zeolite can result in the formation of different metal species, namely, monomeric tetrahedral lattice species, extra-framework monomeric species and polynuclear species containing V-O-V groupings. Thanks to the diversity of chemical surroundings, each of these species should exhibit different strength of Lewis acidity, which can be distinguished by the application of CO as probe molecules adsorbed and monitored by FTIR measurements. Incorporation of small amounts of vanadium into SiBEA zeolite resulted in the formation of both Brønsted and Lewis acid sites as proved by pyridine adsorption [43]. The creation of former sites was also manifested by the appearance of the FTIR band at 2,157 cm^{-1} after adsorption of CO. The position of this band was only slightly shifted (3 cm^{-1}) with respect to that coming from silanol groups present in SiBEA material. This observation indicates relatively low strength of V-OH hydroxyls. This is also in line with the decrease in Brønsted acid strength observed when vanadium is incorporated into BEA zeolites having acidic hydroxyl groups due to the presence of Si-OH-Al groupings prior to the modification with vanadium [23, 44]. The adsorption of CO on SiBEA zeolite containing a small amount of vanadium led also to the appearance of another FTIR band at 2,173 cm^{-1}, which was assigned to the interaction of carbon monoxide with Lewis acid sites in the form of mononuclear vanadium species. This was the only chemical species observed for the materials having a small amount of vanadium incorporated into

SiBEA zeolite. Further increase in the vanadium content of SiBEA structure resulted in the appearance of two FTIR bands after CO adsorption, namely, at 2,192 and 2,201–2,205 cm^{-1}. They were related to two kinds of Lewis acid sites that vary in strength; the higher the frequency, the stronger the Lewis acid sites. On the basis of another experiment, the above-mentioned adsorption bands were assigned to the interaction of CO with extra-framework mononuclear vanadium and polynuclear vanadium species, respectively.

To sum up the results of spectroscopic characterization of vanadium-containing zeolites with the use of probe molecules, it can be concluded that the incorporation of vanadium species into zeolite framework generates Lewis acidic sites whose strength depends on the type of vanadium species. The relatively weak Brønsted acid sites are related to the hydrogen linked to the Si-O-V groupings in the case of vanadium incorporation into the zeolite lattice.

As mentioned above, the acid centres on the zeolite surface can be alternatively followed up using the NH_3-TPD technique. Although similar information could be obtained using spectroscopic methods, the advantage of NH_3-TPD technique lies in the conditions applied. NH_3-TPD analysis does not need dehydroxylation of the material surface in vacuum before measurement. In this way the characterization of material surface is carried out in more adequate conditions to those of the catalytic processes in which the zeolites are involved.

Adsorption of ammonia followed by desorption upon increasing temperature in the reactor gives the information on the number of acid sites calculated according to the amount of NH_3 that desorbs from the material surface. The latter value is estimated by the integration of the area of desorption peak on the NH_3 desorption profile. The maximum temperature of desorption peak characterizes the strength of acidic sites, and the higher the temperature, the stronger the acidic character of the centres. For vanadium-containing zeolites, two peaks of ammonia desorption on the NH_3-TPD profiles were usually observed with the maximum peak temperature centred at ca 443–493 and 633–693 K [19, 23, 41, 46]. Nevertheless, similarly to the spectroscopic analyses, the impact of the support acidity should be taken into account. For example, silicalite-1 material reported in literature showed no ammonia desorption peak [47] or one centred in the region of low temperatures [19]. On the other hand, zeolites, in particular their hydrogen forms, showed two NH_3 desorption peaks, namely, at a lower temperature due to the presence of Lewis acid sites and at a higher temperature region assigned to the Brønsted acidity [41]. After vanadium incorporation into the zeolite, the appearance of NH_3 desorption peaks can be observed or the modification of peaks characteristic of the support is noticed, depending on the acidity of the support. For example, the addition of vanadium to the hydrogen form of ZSM-5 zeolite by impregnation technique led to an increase in total surface acidity; however, the Lewis acidity increased, whereas the Brønsted acidity decreased [41]. This observation is in agreement with the above-described results of pyridine adsorption [23, 44].

The acidity of vanadium-containing zeolites was also determined by the Si/Al ratio in the support. Putluru et al. have prepared a series of vanadium-containing zeolites by impregnation with vanadium oxalate solution with Si/Al ratio between

15 and 140 [46]. They noticed that an increase in the Si/Al ratio of the V_2O_5/HZSM-5 catalysts resulted in a significant decrease in intensity of the NH_3 desorption peak in both temperature regions (443–493 and 633–693 K), which was due to the lower acidity of the samples obtained. Besides this observation, another interesting feature was noticed. With increasing Si/Al ratio, the temperature at the maximum of the desorption peaks was shifted towards lower temperatures, from 489 to 449 K and from 694 to 638 K for Lewis and Brønsted acid sites, respectively. The shift of this temperature can be considered as a decrease in the acid site strength; however, it can be also explained by the decrease in the acid site density that hamper the re-adsorption of NH_3 on the acid sites in the pores during its desorption [46].

As mentioned at the beginning of this section, other important properties of vanadium species introduced on the surface of the support are the oxidation state and metal reducibility. It is known that in many oxidation processes involving vanadium catalysts the reaction proceeds via Mars-van Krevelen mechanism that assume the participation of oxygen from the surface of the catalyst in the oxidation process and further reoxidation of active sites using molecular oxygen. In this mechanism vanadium is first reduced to V^{4+} and then oxidized to V^{5+}. Thus for vanadium-containing catalysts, the estimation of metal reducibility is quite important.

Changes in the vanadium oxidation state depending on reduction/oxidation atmosphere and hydroxylation/dehydroxylation processes are presented in Fig. 4. The vanadosilicate materials (KVS-5) have a MFI topology and were prepared by modified recipe for ZSM-5 zeolite including the addition of different compounds containing V^{5+} and V^{4+} to the synthesis gel [28].

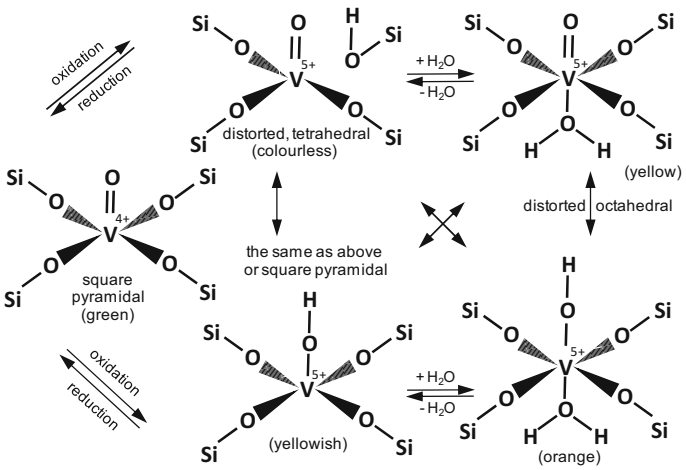

Fig. 4 Model of transformation of the square-pyramidal vanadyl complexes in KVS-5 materials (after [28])

Different colours of KVS-5 zeolites were achieved depending on the conditions of synthesis, calcination and storage of vanadium catalysts. Detailed analysis of this phenomenon is given in [28]. KVS-5 materials obtained using various vanadium precursors differing in vanadium valence structure were studied. In these zeolites vanadium was observed in the form of V^{4+} and V^{5+} ions in various coordinations. After calcination of the material in the air, a complete oxidation of V^{4+} to V^{5+} with tetrahedral and square coordination was observed, but the adsorption of water caused a strong distortion of the octahedral coordination. All changes described were accompanied by a change in the colour of the material (Fig. 4).

H_2-TPR is a very useful characterization technique for determining the metal reducibility. Depending on the method of vanadium incorporation and the amount of this metal loaded, usually one up to three reduction peaks were observed on H_2-TPR profiles [25, 41, 48, 49]. As found by Centi et al. for V silicalite, the temperature of the maximum rate of reduction was related to the strength of the V-O-M bond (e.g. M = Si, Ti, Al) more than to the coordination of vanadium [9]. This observation can explain the appearance of the reduction peak of vanadium species at high temperature (ca 840–950 K) when vanadium was incorporated to the zeolite framework both during hydrothermal synthesis of zeolite [25] and using post-synthesis modification procedure [49]. The strong bonding of vanadium species to zeolite lattice was documented by Guo et al. [25], and the stability of vanadium species to different leaching agents was presented in the previous section. It was demonstrated that leaching procedure allowed the removal of only vanadium species present in the form of extra-framework oligomeric species (maximum rate of reduction at 710 K) or dispersed vanadium species located in zeolite channels (maximum rate of reduction at 750–830 K). As a result of these treatments, only one reduction peak at ca 840–950 K was present on H_2-TPR profile. This peak corresponded to the reduction of V^{5+} to V^{4+}, while the deep reduction of framework V^{5+} to V^{3+} needed much higher temperature and could occur at 1,520 K [25].

As mentioned above, the consumption of hydrogen at temperatures of 750–830 K for vanadium-containing zeolites is usually assigned to well-dispersed extra-framework vanadium species whose reduction is easier that those located in the zeolite framework [25, 48]. However, there is no significant impact of the post-synthesis modification method on the temperature of vanadium species reduction if the procedure applied allows obtaining well-dispersed species. For instance, the same reduction temperature (ca 780 K) was observed for BEA zeolite prepared using ion exchange and impregnation techniques [48].

To sum up, it can be concluded that the surface properties of vanadium-containing zeolites are determined inter alia by the location of vanadium species (framework or extra-framework position) and the kind of these species. Both factors are to a large extent determined by the synthesis technique applied for material preparation. The surface properties obviously influence the catalytic behaviour of vanadium-containing zeolites as it will be presented below.

3 Niobium Species in Zeolites

In catalysis by niobium zeolites, Nb species can act as a promoter or active phase [50]. The role and properties of niobium species depend on the method of its introduction into zeolites, which determines its location and influence the interaction with the support and other metals. Both these factors are responsible for surface and catalytic properties of niobium-containing zeolites.

3.1 Methods of Incorporation of Niobium to Zeolites, Metal Location, Sample Structure and Stability

Like in the case of vanadium, modification of zeolites with niobium can lead to the introduction of this metal into the zeolite framework or as extra-framework species (in the form of cations or niobium oxide phase deposited on the support).

3.1.1 Extra-Framework Niobium Species

The traditional method used for modification of zeolites by cation exchange in aqueous solution cannot be applied because niobia salts are very sensitive to moisture [50]. Among the first reports on introduction of niobium species into zeolites are those by Wierzchowski and Zatorski [51] and Chang et al. [52]. They used the impregnation method with niobium pentachloride methanol solution [51] or aqueous solution of niobium oxalate [52] for the incorporation of niobium to ZSM-5 zeolite. Nb_2O_5 supported on ZSM-5 was obtained by calcination at 773 K. Also a solid-state exchange method between niobia and zeolite was explored. The first efforts for niobium introduction to NaY by solid-state interaction between niobium oxide and sodium upon heating of the sodium form of zeolite with Nb_2O_5 at 975 K were unsuccessful [53]. However, Ziolek et al. [54] have found that, in the same conditions, exchange of cations occurs on ammonium and dealuminated forms of Y zeolites with the maintenance of zeolite structure. Niobium species were localized in zeolites at extra-framework positions, most probably as $NbO^{\delta+}$ cations. Successful introduction of niobium into a zeolite was proved by a decrease in the density of Brønsted acid sites and an increase in the density of Lewis acid sites (indicated by IR spectroscopy following pyridine adsorption described in Sect. 3.2). The possibility to exchange cations in zeolites by solid-state exchange was confirmed by Romotowski et al. [55] who obtained the niobium oxide supported ZSM-5 by calcination of NH_4ZSM-5 with Nb_2O_5 (Nb/Nb+Si = 0.015, 0.03, 0.06) at 953 K. Moreover, it was found that the addition of Nb_2O_5 decreased the amount of aluminium atoms eliminated from the zeolite lattice upon thermal treatment (^{27}Al MAS NMR). The zeolite framework was preserved as a result of the specific role of niobia in the ZSM-5 channels.

Since 2000, the impregnation method has been the most often used for preparation of zeolite catalysts modified with niobium localized at extra-framework positions. Dias et al. [56, 57] have studied Nb_2O_5/ZSM-5 containing different Nb_2O_5 loadings (2, 5, 13, 19 wt%) and calcined at 823 K. The structure of ZSM-5 zeolite was preserved after impregnation with niobium oxalate and calcination, irrespective of the niobium loading (as shown by XRD patterns). Niobium promoted also thermal stabilization of ZSM-5. ^{29}Si NMR results indicated that the modification of ZSM-5 with niobia prevents structural dealumination after calcination (almost identical values of Si/Al ratio were observed before and after thermal treatment of niobium zeolites in contrast to calcined HZSM-5). Moreover, dehydroxylation was found smaller in niobium-containing zeolites (with 2–15 wt% of Nb_2O_5) than in NH_4ZSM-5 sample (DTA-DTG studies). However, a significant decrease in surface area and pore volume was observed for the zeolites modified with more than 13 wt% of Nb_2O_5. At this loading, Nb_2O_5 blocked zeolite channels and cavities, and acted as a modifying agent of the zeolite structure, besides the formation of an Nb_2O_5 monolayer on HZSM-5 (observed for the zeolites with Nb_2O_5 loading lower than 13 wt%, the higher monolayer coverage with higher niobium content).

Brites-Nobrega et al. [58, 59] have modified NaX zeolite with niobium. The loading of Nb_2O_5 introduced by wet impregnation was 5 and 10 wt%. As observed for ZSM-5 zeolite, the crystallinity of Nb_2O_5/X zeolites was maintained after calcination (at 773 K), but a significant decrease in surface area and the total pore volume was found as a result of partial blocking of the pores by small Nb_2O_5 clusters. However, it is important to note that the agglomeration of niobium oxide particles in the zeolite pores did not prevent the homogeneity of the Nb_2O_5 active phase on the zeolite surface as proved by SEM-EDX analysis. Besides the impregnation method, the ion exchange in toluene and ethanol under air atmosphere using niobium chloride has been applied for zeolite modification. Using this method (cation exchange of sodium cations in PdY for Nb^{5+}), NbPdY was prepared [60]. FTIR and XRD studies revealed the stability of the zeolite structure after Nb(V) modification. However, a decrease in the peak intensities and a very small shift of its position was identified in XRD patterns of NbPdY in comparison with those of NaY. It was attributed to exchange of sodium ions by Pd^{2+} and Nb^{5+} metal ions. Again, the surface area and pore volume of NbPdY were drastically reduced suggesting the presence of Pd^{2+} and Nb^{5+} species in the pores (cavities) of Y zeolite (in the form of monomeric niobium oxide as shown by FTIR spectra displaying the band at 660 cm^{-1} assigned to Nb-O frequencies). The thermal stability of niobium composites in the Y matrix was confirmed by TGA analysis.

Recently [61], a new group of zeolites of MWW topology characterized by layered 2D structures has been used as support for niobium. MCM-22 (SiO_2/Al_2O_3 = 54) and delaminated MCM-56 (SiO_2/Al_2O_3 = 23) were impregnated using an aqueous solution of ammonium niobate(V) oxalate (5 wt% of Nb). Niobium modification of layered and delaminated MWW zeolites did not change the zeolites' structure. However, like for 3D zeolites, changes in the textural properties were found. The BET surface areas of Nb/HMCM-22 and Nb/HMCM-

56 decreased in comparison to the zeolites supports, which was caused by a decrease in the external surface area as a consequence of Nb location partially outside the zeolite pores. The UV-Vis spectra of Nb/zeolites were characterized by bands at ca 220 and 250 nm indicating the presence of tetra- and penta-coordinated niobium species located in the zeolite framework, respectively. These species are called isolated niobium species. XPS study indicated binding energies typical of niobium +5, and the binding energy of Nb3d was shifted to higher values in comparison to that of bulk niobium oxide (from 207.1 eV for Nb_2O_5 to 207.6 and 208.6 eV for Nb/HMCM-56 and Nb/HMCM-22, respectively). The results obtained from UV-Vis and XPS studies suggested that Nb introduced by impregnation was partially localized in the framework of zeolites after calcination.

The impregnation method was used also for the modification of TS-1 (titanosilicalite-1, zeolite of MFI structure) with niobium [62]. The XRD pattern of Nb/TS-1 revealed that the MFI structure of the TS-1 support was preserved upon incorporation of niobium (3.4 wt%) and that niobium was well dispersed on the support in the form of amorphous niobia. However, a decrease in the XRD reflections intensity (up to 60%) was observed. Moreover, the FTIR spectra of Nb/TS-1 showed a significant decrease in the number of Si-OH silanol groups on the support after niobium modification. These two factors indicated that there was a strong interaction between Nb and TS-1 support and that niobium was covering the surface of TS-1. Octahedral coordination of niobium in Nb/TS-1 was confirmed by UV-Vis study.

3.1.2 Isomorphous Substitution of Niobium

Modification of zeolites with niobium can be also performed by adding the metal source to the reaction mixture (synthesis gel) from which zeolites are synthesized in order to obtain the isomorphous substitution of metal into the framework of crystalline zeolite. Some of the most relevant results are summarized in Table 2. The first substitution of niobium into ZSM-5 zeolites was performed by Prakash and Kevan in 1998 [63]. Niobium ethoxide as a source of metal (0.05–0.1 mol of NbO in the gel) was added during the synthesis of a zeolite of MFI structure (denoted as NbS-1). The location of niobium was studied by various techniques (e.g. ESR, XRD, UV-Vis, FTIR). XRD pattern of NbS-1 corresponds to MFI structure and did not show any peaks corresponding to the crystalline Nb_2O_5 phase. Moreover, some differences were noted in the intensities of some peaks between the patterns of MFI and NbS-1. In the UV-Vis spectra of the materials studied, a sharp band at 220 nm was identified as due to NbO_4 tetrahedral units. On the other hand, the band at 970 cm^{-1} in the IR spectrum of NbS-1 was assigned to the presence of Si-O-Nb units in the zeolite framework. These methods initially confirmed the incorporation of Nb(V) into the silica framework. However, the strongest evidence for the substitution of Nb into the silicate framework was obtained from ESR studies of NbS-1 sample after γ-irradiation. They indicated two radiation-induced hole centres located at Si-O-Si and Nb-O-Si units of

Table 2 The role of synthesis conditions on the niobium loading and location in zeolites

Zeolite type	Modification method (description)	Nb source	Nb loading as assumed (Si/Nb)	Real Nb loading (Si/Nb or Al/Nb)	Nb location	Ref.
MFI	One-pot synthesis (autoclave, 443 K, 40 h)	Nb $(C_2H_5O)_5$	n.d.	Si/Nb = 28 Si/Nb = 61	Framework	[63]
AlPO-5	One-pot synthesis (autoclave, 423 K, 24 h)	Nb $(C_2H_5O)_5$	n.d.	Al/Nb = 18 Al/Nb = 37	Framework	[64]
SAPO-11	One-pot synthesis (autoclave, 473 K, 24 h)	$KNbO_3$	n.d.	Nb/T = 0.017[a]	Extra-framework	[65]
BEA	Two-step method (dealumination and impregnation with Nb)	Nb $(C_2H_5O)_5$	Si/Nb = 220 Si/Nb = 153 Si/Nb = 102 Si/Nb = 76	Si/Nb = 220 Si/Nb = 153 Si/Nb = 102 Si/Nb = 76	Framework Framework Framework Framework and extra-framework	[66, 67]
BEA	One-pot synthesis (autoclave, 413 K, fluoride media)	Nb $(C_2H_5O)_5$	Si/Nb = 50 Si/Nb = 100	Si/Nb = 53 Si/Nb = 109	Framework	[68]
Y	One-pot synthesis (PP bottle, 373 K, 5 h)	Nb $(C_2H_5O)_5$	Si/Nb = 32 Si/Nb = 64	Si/Nb = 80 Si/Nb = 730	Framework	[38, 39]

[a]T = Si + Al + P

the framework. The latter was identified through a ten-line hyperfine structure from ^{93}Nb (I = 9/2, 100% abundance). Silicalite-1 showed radiation-induced hole centres located only at Si-O-Si units. Moreover, it was found that Nb(IV) ions in NbS-1 are also formed by radiolytic reduction of Nb^{5+} on isolated NbO_4 units. The reaction mechanisms for the formation of radiation-induced hole centres in NbS-1 molecular sieve was proposed (Fig. 5).

As a consequence of the substitution of Nb(V) for Si(IV), an excess of positive charge in the framework of Nb-S1 was generated. It was suggested that the additional positive charge was probably balanced by hydroxyl groups or by non-framework anions.

In the same research group, microporous aluminophosphate NbAPO-5 (Al/Nb = 18 and 37) was synthesized [64]. Using XRD, ESR and UV-Vis techniques, it has been proved that it is possible to prepare niobium-containing aluminophosphates, in which isolated Nb(V) species are connected to the framework defect sites via formation of Nb-O-P or Nb-O-Al bonds. The XRD patterns of NbAPO-5 confirmed the AFI structure irrespective of the Al/Nb ratio, whereas the UV-Vis spectra indicated the presence of niobium in the NbO_4 tetrahedra (the band at 220 nm). Similarly to NbS-1, the signal with the ten-line hyperfine structure was present in the ESR spectrum of NbAPO-5 after γ-irradiation. This signal was

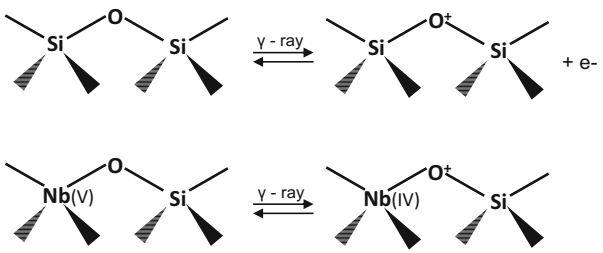

Fig. 5 Radiation-induced hole centres in NbS-1 zeolite (after [63])

assigned to the hole centres located at P-O-Nb or Al-O-Nb units in the framework of NbAPO-5. However, the underlying broad spectrum (characteristic of Nb(IV)) was not observed, indicating that the mechanism of isomorphous substitution of niobium into zeolites and aluminophosphates was clearly different. Using the method of hydrothermal synthesis, Nb was successfully introduced also into FeAPO-5 and FeAPSO-5 structures [69]. NbFeAPO-5 and NbFeAPSO-5 molecular sieves containing 0.39 wt% of Nb and 5 wt% of Fe in the framework were prepared. The introduction of niobium during the synthesis (with $KNbO_3$ as Nb source) was also performed for another AEL structure material – SAPO-11 [65]. XRD patterns indicated that pure AEL phase was obtained for NbSAPO-11 (Nb/T = 0.017), but a decrease in crystallinity was observed (by about 20%) suggesting the presence of structural defects. The increase in Si content in SAPO-11 (Nb/T = 0.015; T=Si, Al, P) led to a further reduction of crystallinity due to amorphization of the material, which was proved by SEM images. Contrary to NbAPO-5, niobium incorporated into SAPO-11 is present in the form of two extra-framework species (based on H_2-TPR studies): isolated Nb^{5+} cations (the peak below 1,000 K) and small niobium oxide particles (the peak above 1,000 K). The Nb^{5+} species compensate partly the negative charges generated by the introduction of Si into the AlPO matrix.

Dzwigaj et al. [66, 67] and Corma et al. [68, 70] have attempted to introduce niobium into BEA zeolite structure. Dzwigaj et al. [66] used the two-step post-synthesis method like in the case of vanadium incorporation (first dealumination process of BEA to obtain vacant T sites associated with silanol groups and next the niobium ions introduction into vacant T sites by impregnation) with $Nb(OC_2H_5)_5$ as a metal precursor, whereas Corma et al. [68] applied the direct introduction of Nb (V) ethoxide during BEA synthesis. Using the first method, NbSiBEA samples were prepared with different niobium loadings (0.7, 1.0, 1.5, 2.0 wt%) [66, 67]. The incorporation of Nb into the SiBEA framework has been evidenced by various complementary techniques (XRD, ^{29}Si MAS NMR, IR, UV-Vis). XRD patterns confirmed a typical BEA structure of niobium zeolites. A significant increase in the d_{302} spacing from 3.92 Å for SiBEA to 3.95 Å for NbSiBEA indicated the expansion of the unit cell as a result of the longer Nb-O bond. The lowest d_{302} value was obtained for the zeolite with the highest niobium loading $Nb_{2.0}$SiBEA suggesting that only a part of niobium was incorporated into the zeolite framework. The ^{29}Si MAS NMR spectra showed a significant decrease in the intensity of

–102.5 ppm signal (assigned to the framework Si atoms in $Si(OH)(OSi)_3$ environment) with increasing Nb content after incorporation of Nb ions into SiBEA. It confirms the reaction between niobium ethoxide and silanol groups and incorporation of almost all niobium as isolated mononuclear Nb(V) into the BEA structure in zeolites with lower niobium contents (up to 1.5 wt% of Nb). However, the absence of further decrease in the peak at −102.2 ppm in the spectra of $Nb_{2.0}$SiBEA (2.0 wt % of Nb) suggests that the major part of niobium is not incorporated in the framework of this material, but occupies extra-framework positions as polynuclear Nb(V). Moreover, three well-distinguished ^{29}Si MAS NMR signals at −111.1, −112.5 and −115.2 ppm in the spectra of the zeolite with higher niobium loading suggest that the incorporation of Nb into the framework of BEA led to some modification of the Si environment. The changes in the environment of Si atoms in NbSiBEA were confirmed by IR studies, which revealed a shift of the IR band characteristic of Si-O stretching vibration from 955 cm^{-1} for SiBEA to 960 cm^{-1} for NbSiBEA. The band at this position comes from vacant T-atom sites associated with silanol groups generated upon dealumination of BEA. The incorporation of Nb at such sites modifies the Si-O stretching vibration. Moreover, the observed decrease in the intensity of the band at 797–802 cm^{-1} (assigned to the Si-O-Si symmetrical stretching modes) was interpreted as a proof of Nb incorporation in the framework. The UV-Vis spectra evidenced the presence of two types of framework mononuclear Nb(V) ions in NbSiBEA zeolite, by the two bands at ca 222–228 and 236 nm (assigned to the oxygen tetrahedral Nb(V) ligand-to-metal charge-transfer transition). The intensity of these bands increased with Nb content. In the UV-Vis spectrum of $Nb_{2.0}$SiBEA, the intensity of the band at 228 nm was the lowest, which revealed lower content of mononuclear Nb(V) in this sample. Moreover, two additional bands at 248 and 370 nm appeared. The authors assigned these bands to the extra-framework polynuclear Nb(V) and niobium oxides, respectively. However, the band at 248 nm should be assigned to penta-coordinated niobium species located in the zeolite framework as was shown above for Nb/HMCM-22 and Nb/HMCM-56 (Sect. 3.1.1). The results described in [66, 67] indicated that the location of niobium in BEA structure depended on the loading of the metal. The high loading of niobium (>1.5 wt%) gave rise to zeolites with a mixture of the framework mononuclear and extra-framework polynuclear Nb(V). Ab initio periodic DFT calculations [32, 71] indicated that niobium(V) was stabilized in the BEA framework in a fivefold coordination with one hydroxyl group. The structure with Nb(V)O-H group and Nb linked by four Nb-OSi bonds to the zeolitic framework appeared as the most favourable. Nb-OH groups pointed into the zeolite channel in BEA structure.

The introduction of niobium into network positions of zeolite BEA by isomorphous substitution is also possible during the direct synthesis in fluoride media (Si/Nb = 53 and 109) [68, 70]. Typical zeolite BEA structure was detected in the XRD patterns of Nb-BEA zeolites, irrespectively of Si/Nb ratio. The incorporation of the metal into the zeolite structure was proven by X-ray absorption spectroscopies (EXAFS and XANES). The results indicated a decrease of two

different Nb-O distances (from 1.72/2.01 to 1.73/1.89 Å for as-synthesized sample/sample after template removal and degassing) and the average coordination number (from 0.78/3.60 to 0.70/3.30), without strong changes in the second coordination shell and therefore confirmed the penta- and tetracoordination of Nb in as-synthesized and calcined samples, respectively. According to the results, the calcined samples contain tetracoordinated Nb^{5+} with three siloxane bridges and one Nb=O bond (to preserve electric neutrality). Upon exposure to ambient moisture, the Nb^{5+} ions are coordinated with water molecule (as in the as-synthesized sample) (Fig. 6).

It has been also shown in other studies [33, 38] that it is possible to incorporate Nb into faujasite (FAU) structure containing aluminium. NbY was prepared in one-pot synthesis with niobium ethoxide as a source of niobium (Si/Nb = 32 and 64, Si/Al = 2.3) and without organic structure-directing agent, and in both cases faujasite structure was obtained. For further investigation of the location of niobium in these materials, UV-Vis and XPS spectroscopies were used [38]. The UV-Vis spectra of NbY-32 showed the only one band at ca 220 nm typical of tetrahedrally coordinated Nb species. The band corresponding to octahedrally coordinated polynuclear niobium species (at 330 nm) was not detected. These observations indicated the tetrahedral coordination of niobium species in NbY and suggested the location of niobium in the zeolite framework. Such a location of Nb was confirmed by XPS study. It was found that the binding energies of Nb^{5+} 3d in niobium-containing Y zeolites were higher than those characteristics of bulk Nb_2O_5. The increase in the binding energy was observed (from 207.1 eV for Nb_2O_5 to 207.9 and 208.1 eV for NbY-32 and NbY-64, respectively) and attributed to different surroundings of niobium species in zeolites and in bulk niobium(V) oxide. Different neighbourhood of niobium in zeolite is created when the Si-O-Nb link is formed as a result of niobium incorporation into the zeolite framework. DFT calculations proved that Nb-OH species were the most stable in NbY structure and that the most preferred position for the Nb-OH group with relation to aluminium atom is that at the nearest neighbour position (Al-O-Si-O-Nb) [33].

The influence of synthesis conditions on the niobium loading and its location in zeolites is summarized in Table 2.

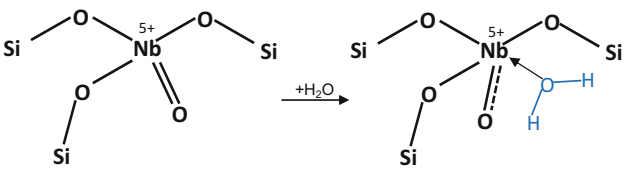

Fig. 6 Tetracoordinated Nb^{5+} in calcined-degassed NbBEA and interaction with water molecule (after [68])

3.2 Surface Properties

The location of niobium in the support (in extra-framework or framework positions) strongly influences the acid-base properties of zeolites. Changes in the type and distribution of active sites as a result of modification of molecular sieves with niobium by various methods were observed and identified mainly using FTIR spectroscopy with the adsorption of probe molecules (pyridine-Py, NO) and test reactions.

The solid-sate interaction between NH_4NaY (Si/Al = 2.56) and DNH_4Y (partially dealuminated Y containing ammonium cations, Si/Al = 4.25) zeolites and niobium oxide led to a decrease in the density of Brønsted acid sites (BAS) and an increase in the number of Lewis acid sites (LAS) when compared with those in the zeolite supports. The FTIR study with Py adsorption indicated a decrease in absorbance ratio A(PyB at 1,545 cm^{-1})/A(PyL at 1,455 cm^{-1}), from 4.99 to 0.06 for NH_4NaY and NH_4NaY/Nb_2O_5 evacuated at 975 K, respectively [54]. It should be stressed that evacuation at 975 K led to a higher reduction of Brønsted acid sites than heating at the same temperature in air (from 4.99 to 0.56 for NH_4NaY and NH_4NaY/Nb_2O_5 heated in air at 975 K, respectively). The changes caused by the modification of zeolites with Nb_2O_5 have impact on the catalytic properties of the samples as shown by test reactions (2-propanol dehydration/dehydrogenation and cumene decomposition) [54]. The reactions of 2-propanol and cumene decomposition showed a decrease in the activity of niobium-containing Y zeolites in comparison to that of NH_4NaY and DNH_4Y, as a result of replacement of protons in the zeolite by niobium cations. However, the decrease in cumene conversion was lower than that observed for 2-propanol conversion. Taking into account that cumene cracking occurs on strong Brønsted acid sites, it was concluded that the modification of NH_4NaY and DNH_4Y with Nb_2O_5 caused mainly a decrease in the number of weak Brønsted acid sites. The changes in the activity in 2-propanol decomposition were accompanied by the selectivity changes. DNH_4Y was active in the dehydration reaction leading to propene as the main product and indicating the presence of acidic sites on its surface. The modification of this zeolite with Nb_2O_5 caused dehydrogenation activity, which was concluded from the appearance of acetone as a reaction product. This indicates that redox or basic centres were generated as a result of the modification of DNH_4Y with niobium oxide. The authors of [54] did not prove the presence of such active centres by the other methods than the test reaction. However, the DFT calculations [33] clearly indicated the enhancement of basicity in aluminosilicate zeolites by the inclusion of niobium into the zeolite framework.

The acidity of Nb_2O_5/ZSM-5 zeolites prepared by impregnation was studied by adsorption and desorption of pyridine and analysed by thermal TG/DTA method and FTIR spectroscopy [56]. DTA curves showed an endothermic peak between 403 and 591 K and an exothermic peak between 693 and 1,008 K, which were assigned to weaker and stronger acidic sites, respectively. The higher number of total acid sites (0.46 mmol g^{-1}) was found for HZSM-5 support activated at

723 K. After the modification with niobium, this number decreased as the Nb_2O_5 content increased (reaching 0.38 mmol g^{-1} for Nb_2O_5/HZSM-5 with 19 wt% of niobia). The increase in the activation temperature up to 823 K led to a considerable loss of acidity due to the dehydroxylation of zeolite surface. The FTIR spectra recorded after pyridine adsorption on Nb_2O_5/ZSM-5 zeolites allowed the identification of Brønsted acid sites (pyridine cations giving a band at 1,543 cm^{-1}) and hydrogen bond sites (1,444 cm^{-1}) on the surface of the modified zeolite. A similar trend was observed for Nb-modified MWW zeolites [61]. The introduction of niobium by impregnation on HMCM-56 and HMCM-22 decreased the acidity of the modified samples. Brønsted and Lewis acid sites were identified, but BAS were predominant and their number was higher for Nb/HMCM-22 than Nb/HNbMCM-56. The decrease in the number of BAS after niobium modification suggested that this metal interacted with hydroxyl groups in the zeolite. The results of dehydration and cyclization of 2,5-hexanedione confirmed the acidic character of Nb-containing zeolites. High conversion of 2,5-hexanedione was obtained, and DMF (2,5-dimethylfuran) was observed as the main product of the reaction (96–98% of selectivity) indicating the presence of Brønsted acid sites.

FTIR spectroscopy with the adsorption of probe molecules (NO and pyridine) has been applied for the identification of active centres on the surface of NbZSM-5 containing niobium located in the framework [72]. Two bands were found in the IR spectra of NbZSM-5 after NO adsorption: at 1,602 and 1,896 cm^{-1}, which were assigned to NO adsorbed on NbO^- skeletal species and to N_2O_3 formed as a result of dinitrosil coordinated with the oxygen from the framework of zeolite, respectively. NbO^- centres are generated after dehydroxylation of zeolite according to the scheme (Fig. 7).

The presence of cationic niobium-Lewis centres in the skeleton of NbZSM-5 was confirmed by the FTIR study with pyridine adsorption. Moreover, it was found that the introduction of niobium instead of aluminium in the framework of ZSM-5 eliminated Brønsted acidic centres from the surface of the zeolite. Only LAS were identified using FTIR spectroscopy with pyridine adsorption in NbBEA zeolites containing niobium in the framework or in the framework and extra-framework

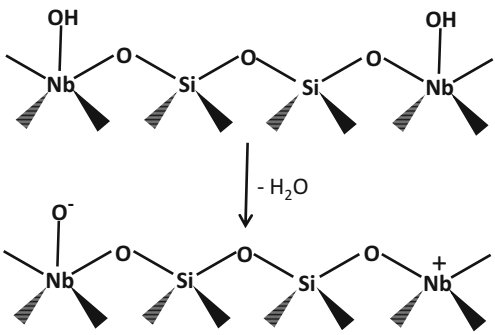

Fig. 7 Active centres formed upon dehydroxylation of NbZSM-5 (after [72])

positions, depending on the niobium loading [67]. It was observed that the intensity of the IR bands (at 1,611, 1,600 and 1,450 cm^{-1}) assigned to pyridine coordinatively bonded to Lewis acidic sites (Nb^{5+} species) was similar for the samples with 0.7 and 2 wt% of niobium. The calculated number of LAS was only slightly different in both samples (8 and 11 mmol g^{-1} after evacuation at 523 K for $Nb_{0.7}$SiBEA and $Nb_{2.0}$SiBEA, respectively). It was concluded that the major number of LAS were formed by niobium introduced in the framework of SiBEA as mononuclear Nb(V). However, it should be stressed that the presence of weak Brønsted acidic sites was identified in both samples on the basis of FTIR studies with 2,6-di-tert-butylpyridine adsorption. Ab initio periodic DFT calculations [71] proved that niobium(V) was stabilized in BEA zeolite framework as a penta-coordinated site bonded to one hydroxyl group, but the Nb-OH groups are not as acidic as V-OH, which follows from the analysis of deprotonation energies calculated for different Nb model sites. However, the Nb-OH groups are a little more acidic than the silanol groups ($\Delta E_{deprot} = 5.95$ and 5.19 eV for SiO-H and NbO-H, respectively). The most acidic site was found on the bridging hydroxyl group Nb-O(H)-Si ($\Delta E_{deprot} = 4.6$ eV), but this structure was the least stable. On the other hand, the calculated protonation energy showed that the most basic site was the bridging oxygen in (Nb-O(H^+)-Si) ($\Delta E_{prot} = 3.66$ eV), if the model without aluminium was considered. The protonated Nb site in zeolite is energetically more favourable than the deprotonated one. Taking it into consideration, the calculations indicated that NbBEA materials have Brønsted basic character. The presence of Lewis acidity and basicity (tetrahedral Nb^{5+} and penta-coordinated NbO^-, respectively) in NbBEA after dehydration was also confirmed. The calculated value of substitution reaction energy ($\Delta E_r = -1.19$ eV) implies that both Lewis sites are stable. Similar experimental and theoretical studies were performed to determine acid-base properties of faujasite structure of Y zeolite containing niobium in the framework described above [33, 38]. The FTIR spectra recorded after the adsorption of pyridine on NbY-32 and NbY-64 showed two main bands at 1,598 and 1,444 cm^{-1} indicating that pyridine was adsorbed via weak hydrogen bond on hydroxyl groups which are weakly or no acidic (e.g. silanol groups and/or Nb-OH). However, the latter band covered also pyridine adsorbed on LAS. Only for NbY-64, the presence of BAS was observed (a small intensity band at 1,550 cm^{-1} assigned to pyridinium cations). Therefore, it was concluded that LAS centres and OH groups dominated on the surface of NbY. The increase in niobium content led to the weakening of niobium Lewis centres due to possible interactions between niobium species. To identify and distinguish acid and basic OH groups as well as LAS in NbY zeolites, several test reactions were carried out. Cumene cracking confirmed the presence of Lewis acid sites in NbY zeolites. High selectivity to α-methyl styrene (formed on electron-transfer centres) was observed, and the selectivity increased with increasing number of Nb atoms in the sample (from 39 to 52% for NbY-64 and Nb-Y-32, respectively). On the other hand, the results of 2,5-hexanedione cyclization showed that with decreasing Si/Nb ratio (from 64 to 32), the conversion (23 and 39% for NbY-64 and NbY-32, respectively) and selectivity to 3-methyl-2-cyclopentenone (MCP) increased (from 67 to 97% for NbY-64 and NbY-32, respectively). It indicated

that the number of basic OH groups (active in MCP formation) increased with the number of Nb atoms in the zeolite. NaY zeolite showed lower activity (16% of conversion) and much lower selectivity to MCP (27%) indicating that even small amounts of Nb (NbY-64) changed the selectivity of the reaction towards this product [33]. This phenomenon supports the presence of $Nb(V)^{+}$-OH^{-} species (Nb in the skeleton), in which OH groups compensate for the local positive charge in NbY framework. Moreover, the FTIR study with NO adsorption on NbY [73] indicated the lack of NbO^{-} and Nb^{+} species on the zeolite surface after activation at 673 K (the IR bands assigned to NO adsorbed on the framework Nb^{+} cations and to nitrate NO_3^{-} species were not observed in IR spectra) suggesting that the dehydroxylation process did not occur. This behaviour is another proof of the presence of Nb-OH (basic) species in the zeolite framework (Fig. 8).

In the presence of NO and oxygen, the formation of NO_2^{-} species on NbY was concluded from the presence of the IR band at 1,404 cm^{-1}. The electron transfer from basic oxygen to NO_2 led to formation of such nitrite ions. Periodic density functional theory calculations [33] implied that the most basic site in the aluminium-containing NbY zeolite is the bridging oxygen (Si-O-Al, oxygen #3 in Fig. 8) ($\Delta E_{prot} = 4.06$ eV). The increase in basicity of Al-O-Si bridged oxygen resulting from Nb incorporation (Al-O-Si-O-Nb) was proved. Moreover, it was shown that the basicity of the oxygen in Nb-OH group (#1 in Fig. 8) in NbY decreases (ΔE_{prot} increases from 4.32 to 5.04 eV), whereas the basicity of oxygen in Si-O-Nb (#2 in Fig. 8) increases (ΔE_{prot} decreases from 4.82 to 4.19 eV) in comparison to the zeolite framework without aluminium.

In contrast to the above-described NbZSM-5, NbBEA and NbY zeolites, for NbSAPO-11 [65], prepared by introduction of niobium during synthesis, but containing only extra-framework niobium species, both Lewis and Brønsted acid sites were found, irrespective of Nb/T ratio. The band at 1,440 cm^{-1} in the FTIR spectrum was assigned to pyridine interacting with Lewis acid sites from Nb_2O_5-like species. The increase in the silica content led to a slight increase in Brønsted acidity. However, the number of BAS and total number of LAS was lower than in SAPO-11 support. Most probably the extra-framework-isolated Nb species neutralize the negative charges from the SAPO-11 framework and hence reduce the number of Brønsted acid sites available to interact with pyridine. Moreover, the Nb_2O_5 particles also could block the access to Brønsted and Lewis sites (present in SAPO matrix).

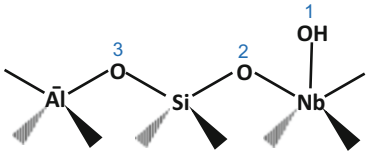

Fig. 8 NbY zeolite framework after calcination (after [73])

3.2.1 Transition Metals in Nb-Containing Zeolites

Niobium species are known to be engaged in moderately strong interactions with transition metals [74–76]. The modification of niobium-containing zeolites with transition metals as well as alkaline, alkaline earth or noble metals leads to formation of catalysts with new surface properties.

It has been proved that the modification of NbZSM-5 with copper significantly changes the ability of copper species to auto-reduction (under vacuum or in an inert gas flow) if compared with ZSM-5 containing aluminium in the molecular sieve framework [72]. It means that the reducibility of copper cations depends on the nature of metal substituted in the MFI framework. Sobczak et al. [72] studied NbZSM-5 and AlZSM-5 zeolites modified with copper cations by cation exchange of protons in an aqueous solution of a copper salt. The results showed that a lower number of Cu^{2+} cations were reduced, under the same conditions, on Cu-NbZSM-5 than on Cu-AlZSM-5. A comparison of the intensity of ESR signals from paramagnetic Cu^{2+} after evacuation of zeolites at 723 K indicated that 90% and 77% of Cu^{2+} ions were reduced on Cu-AlZSM-5 and Cu-NbZSM-5, respectively. Also the transformation of Cu^{2+} from octahedral to square-pyramidal and square-planar structure was more difficult in Nb-containing sieves as evidenced by the ESR study of the samples evacuated at increasing temperatures. This behaviour was a result of the stronger interaction of niobium-containing zeolite with Cu cations than that of aluminosilicate ZSM-5. On the other hand, the reduction of copper cations by hydrogen (H_2-TPR studies) was easier in ZSM-5-type zeolite with niobium in the lattice, indicating that the interaction of copper with the reductant in the NbZSM-5 matrix was stronger than that in AlZSM-5. The reducibility of Cu^{2+} in NbZSM-5 by hydrogen increased with Cu loading. The tendency to the stronger bonding of ligands was the reason for the easier reduction of copper by hydrogen (a stronger interaction of copper with hydrogen), whereas in ESR experiment vacuum treatment is a source of reduction. Moreover, FTIR study with NO adsorption on ZSM-5 zeolites indicated that the reduction of Cu^{2+} was deeper in NbZSM-5 than AlZSM-5. In the FTIR spectra after NO adsorption on Cu-AlZSM-5 and Cu-NbZSM-5, bands at 1,811 and 1,783 cm^{-1} were observed, respectively. The first band was assigned to $Cu^{+}NO$ complex, whereas the second to $Cu^{\delta+}NO$ species ($\delta < 1$). It indicates that copper in Cu-NbZSM-5 is more metallic than Cu^{+}. It was concluded that the negative charge located at $Nb\text{-}O^{-}$ in the framework of NbZSM-5 made the copper reduction deeper than in AlZSM-5 support. The reduced copper was more weakly bonded to oxygen in NbO^{-}, and therefore it had higher metallic character.

A charge transfer from the metal ion (cerium in the form of CeO_2, Ce^{4+} and Ce^{3+} and niobium in the form of isolated mononuclear Nb_2O_5 (Nb^{5+}) in the framework of BEA) towards copper has been found in Cu-BEA-Nb and Cu-BEA-CeNb zeolites prepared by cation exchange method [77]. The shift of the band assigned to $Cu2p_{3/2}$ (Cu^{2+}) to a higher binding energy in the XPS spectra of both zeolites was observed in comparison to Cu-BEA, indicating the modification of electronic properties of

the Cu species due to the strong interaction between niobium and cerium additives with copper and the electron transfer among the Nb_2O_5, CeO_2 and CuO species.

The strong interaction between Nb and another transition metal, titanium, has been indicated in the TS-1 material modified with niobium by impregnation [62]. The H_2-TPR profile of Nb/TS-1 did not show any peak from the reduction of niobium. In contrast, the peak attributed to the reduction of Nb^{5+} to Nb^{4+} in the form of Nb_2O_5 to NbO_2 was observed in H_2-TPR profile of amorphous niobia. It was explained that highly dispersed niobium on the surface of TS-1 is not reduced due to strong interaction between niobium and titanium in TS-1, which makes the reduction of Nb^{5+} more difficult than in niobia.

Niobium also interacts with noble metals as has been indicated for NbPdY zeolite [60]. The shift of UV-Vis band assigned to d-d transition in NbPdY (from 406 for PdY to 420 nm for NbPdY) was observed as result of Nb-O formation in the cavity of zeolite and the interaction between palladium species and niobium.

To sum up, niobium in the zeolite framework enhances Lewis acidity and basicity and exhibits strong interaction with other transition metals included in the zeolites.

4 Tantalum Species in Zeolites

4.1 Methods of Incorporation of Metal to Zeolites, Metal Location, Sample Structure and Stability

The chemistry of tantalum is much poorer known than that of vanadium or niobium which belongs to the same group in the periodic table. There are several publications concerning the introduction of tantalum to various zeolite structures such as LTA [78], MFI [47], BEA [68, 79] and FAU [33, 38, 39].

4.1.1 Extra-Framework Tantalum Species: Attempts to Introduce Ta^{5+}

A very popular method of zeolite modification with metals is the post-synthesis ion exchange from aqueous solution. However, the application of this method for tantalum is problematic. Up to now in literature, no reports on extra-framework Ta^{5+} ions in zeolites have been found. The main reason for this (like in the case of niobium) is the lack of simple soluble salts of Ta^{5+} from which the aqueous solution for ion exchange could be prepared [80]. To overcome the difficulties associated with aqueous ion exchange and to achieve Ta^{5+} exchange into zeolite, the thallous ion exchange method can be used [78]. The above-mentioned method can be applied to all porous materials with ion exchange capacity. In the first step of modification, zeolite or other porous material was fully ion exchanged with Tl^+ from aqueous solution and also fully dehydrated. In the next step, the material was

exposed to the anhydrous vapour of halide MX_n where M^{n+} was the incoming cation [78]. After successful and full cation exchange, TlX, which was a volatile product, was easily removed leaving the pure ion-exchanged zeolites. This method has been used by Lim et. al. [80] to introduce Ta^{5+} and Ta^{2+} into a LTA zeolite in extra-framework positions. These authors used $TaCl_5$ as a metal source expecting that the ion exchange reaction would occur as follows:

$$Tl_{12} - LTA + 2.4TaCl_5(g) \rightarrow Ta_{2.4} - LTA + 12\ TlCl(g)$$

Unfortunately, the reaction did not occur. $TaCl_5(g)$ decomposed to $TaCl_2$ and $Cl_2(g)$ and Cl^- ions in $TaCl_2$ moved to additional $TaCl_5$ molecules to form $TaCl_6^-$. These anions were found in 24.6% of the zeolite large cavities.

4.1.2 Isomorphous Substitution of Tantalum

In 1999, Ko and co-workers [47] synthesized for the first time tantalum silicalite-1 (TaS-1) under hydrothermal conditions (Table 3). These authors used tantalum ethoxide as a metal source. Almost identical diffractograms of TaS-1 were obtained irrespective of the tantalum contents in the range up to 3 mol% in the synthesis gel. The symmetry of the calcined TaS-1 was orthorhombic (single reflections around 2 theta at 24.5° and 29.2°) which can suggest that tantalum ions are present in the framework positions. The substitution of Si^{4+} by larger ions like Ta^{5+} can cause expansion in unit cell parameters and volume. This phenomenon was observed in TaS-1 zeolite. The unit cell volume increased linearly with increasing tantalum content in the reaction mixture up to 3 mol%. The same authors investigated the

Table 3 The role of synthesis conditions on the tantalum loading and location in zeolites

Zeolite type	Modification method (description)	Ta source	Ta loading as assumed (Si/Ta)	Real Ta loading (Si/Ta)	Ta location	Ref.
MFI	One-pot synthesis (autoclave, 448 K)	Ta $(C_2H_5O)_5$	Si/Ta = 16–39	n.d.	Framework	[47]
BEA	Two-step method (dealumination and impregnation with Ta)	Ta $(C_2H_5O)_5$	Si/Ta = 293 Si/Ta = 150	Si/Ta = 293 Si/Ta = 150	Framework	[79]
BEA	One-pot synthesis (autoclave, 413 K, fluoride media)	Ta $(C_2H_5O)_5$	Si/Ta = 50 Si/Ta = 100	Si/Ta = n.d. Si/Ta = 78	Framework	[68]
Y	One-pot synthesis (PP bottle, 373 K, 5 h)	Ta $(C_2H_5O)_5$	Si/Ta = 32 Si/Ta = 64	Si/Ta = 45 Si/Ta = 78	Framework	[38, 39]

influence of tantalum on the crystallization process. To reach the maximum crystallinity of TS-1 (titanosilicalite), the crystallization time needed was 3–4 days; however, for TaS-1 to reach the same crystallinity level, it was necessary to extend this time to 7 days. Such a trend is generally observed in the synthesis of metal-substituted silicate molecular sieves and may be a consequence of the radius of tantalum (145 pm) atoms being larger than, for example, that of titanium (140 pm). It is therefore more difficult for Ta to enter the silicalite framework. The evidence of the successful isomorphous substitution of large heteroatoms into the zeolite framework can be given by IR spectra in the mid-infrared region [81, 82]. The band at around 1,100 cm^{-1} corresponds to the asymmetric vibrations of internal tetrahedra, and the symmetric stretching of T-O was found at around 820–780 cm^{-1} [83]. When tantalum was incorporated into silicalite-1 framework, the IR band at around 1,100 cm^{-1} shifted progressively to lower-frequency region as the amount of Ta increased. Moreover, the IR spectra of TaS-1 showed a characteristic absorption band at 965 cm^{-1} which may be ascribed to the Si-O-Ta stretching vibrations. The UV-Vis diffuse reflectance spectra showed a strong transition band at around 200 nm which was assigned to the presence of Ta^{5+} in the framework positions. Distribution of tantalum in the framework was also confirmed by ^{29}Si MAS NMR spectroscopy. ^{29}Si MAS NMR spectrum of TaS-1 was significantly different from those of pure silicalite-1, and the lines in the spectra of TaS-1 were broadened. This kind of broadness of the line in the spectrum seems to be characteristic of the location of metal in the zeolite framework. According to literature [10], the broadening of ^{29}Si MAS NMR spectrum of vanadium silicalite-1 seems to indicate the statistical distribution of V in the framework. Ko and Ahn [47] have suggested that the same behaviour may be in the case of tantalum-containing zeolites.

Tantalum was also incorporated into the large-pore zeolite BEA by hydrothermal synthesis by Corma et al. [68]. The syntheses of the Ta-containing zeolite BEA were performed in fluoride media (like for niobium incorporation), since the probabilities for metal incorporation should be higher than those in OH^- media. In the basic medium, the precursor is often precipitated as metal oxide that has to be redissolved to be incorporated into the zeolite framework. This behaviour was not observed in the fluoride route. Another advantage of using fluoride medium is the minimization of silanol defect sites in the zeolite. The samples obtained are more hydrophobic which allows the reaction with less polar substrates while minimizing re-adsorption of more polar products. Tantalum(V) ethoxide was used as metal source (Si/Ta in the gels = 50, 100); the synthesis was performed in the presence of HF as reaction medium. The XRD patterns show that introduction of tantalum in the synthesis gel slows down the rate of crystallization of BEA zeolite. TaBEA with Si/Ta = 100 forms well-developed crystals. For lower Si/Ta ratio, the crystallinity of the resultant material reached 50% after much longer time of crystallization. The chemical analysis confirmed that all metal present in the gel was incorporated into the solids (Si/Ta = 78). The incorporation of Ta into the zeolite structure was proven by X-ray absorption spectroscopies (EXAFS and XANES). The Ta-O bonds were detected. In as-synthesized material, the bond length was 1.96 Å and the coordination number 5.54, whereas after calcination and degassing, both

parameters were reduced to 1.90 Å and 4.50, respectively. Thus, the thermal treatment and degassing led to the formation of tetracoordinated Ta species in the zeolite framework. No Ta-O-Ta units were detected, while the most probable structure for the tantalum is isolated tetrahedrally coordinated species. The IR spectra in the framework vibration region of the Ta-containing zeolite show a band at 960 cm^{-1}, which is attributed to Si-O-Ta vibration. This band was not observed in pure silica BEA zeolite neither in Ta/BEA zeolite into which tantalum was incorporated by impregnation. It is generally taken as the evidence of metal incorporation into the zeolite framework.

A completely different method of introducing tantalum into the BEA zeolite was applied by Dzwigaj et al. [79]. They used two-step post-synthesis method described in detail in the previous sections devoted to vanadium and niobium incorporation. Tantalum(V) ethoxide was used as a metal source to restrict the types of Ta to a single type of mononuclear Ta(V) species and obtain Ta(V) single site in SiBEA zeolite. The samples prepared contained 1 and 2 Ta wt% and Si/Ta molar ratio of 293 and 150, respectively [79] (Table 3). The advantage of this method is the incorporation of all assumed amount of tantalum into the zeolite framework. A high amount of tantalum can be also incorporated to BEA zeolite in the one-pot synthesis, but the crystallinity of the zeolite decreases with the increase in tantalum content. Corma et al. [68] showed that Si/Ta ratio in the synthesized zeolite was even lower than in the synthesis gel (Si/Ta = 78 vs 100, respectively – see Table 3), but the crystallinity of the zeolite slightly decreased to 90%. The increase of Ta content in the gel to Si/Ta = 50 resulted in the decrease in crystallinity to 50%.

TaSiBEA zeolites were characterized in detail by XRD, ^{29}Si magic angle spin (MAS) NMR, IR and diffuse reflectance UV-Vis spectroscopy. The XRD patterns of pure BEA zeolite and tantalum-containing samples were very similar, typical of zeolite BEA structure. No evidence of extra-framework crystalline compounds or amorphous phase of zeolite was found. Moreover, a significant increase in d_{302} spacing from 3.920 Å (SiBEA) to 3.946 Å and 3.951 Å for tantalum-containing BEA was observed. Incorporation of Ta into SiBEA produced some expansion of the unit cell due to longer Ta-O bond (1.90 Å) for mononuclear Ta(V) species in zeolites than typical Si-O bond (1.60–1.65 Å) [79]. Successful metal incorporation was proved by NMR analysis. The data show significant changes in the $Si(OSi)_4$ environment after incorporation of Ta into zeolite. The same result has been observed in the case of TaS-1 zeolite. Thus, it seems to be a common phenomenon for tantalum-containing zeolites. In ^{29}Si MAS NMR spectra, three well-distinguished, narrow peaks at ca −111.1, −112.4 and −114.7 ppm appeared. In contrast, the spectrum of SiBEA zeolite showed a broad peak at −110.5 ppm with a shoulder at −114.2. These results were confirmed by IR spectroscopy. In the spectra of TaSiBEA zeolite, a band at 966 cm^{-1} was observed. A similar band was observed in TaBEA zeolite obtained by hydrothermal synthesis [68] and attributed to asymmetric stretching of Si-O-Ta linkages. Moreover, a comparison of the spectra of SiBEA and TaSiBEA showed changes in the intensity of the band at 800–802 cm^{-1} (higher for TaSiBEA), assigned to Si-O-Si symmetrical stretching and in the position of the band at 750–500 cm^{-1} (shifted to the lower values for

TaSiBEA). All these results confirmed that tantalum was incorporated into the zeolite framework. The ^{1}H MAS NMR spectra of TaSiBEA exhibited a main peak at 3.82–3.90 ppm and a less intense one at 1.98 ppm. There were no peaks at 5.38 and 1.36 ppm which were observed in the spectrum of SiBEA. These peaks are assigned to protons of H-bonded SiO-H and to isolated and/or terminal SiO-H at vacant T-atom sites. The disappearance of these peaks in the TaSiBEA spectrum is an evidence of the reaction of tantalum ethoxide with H-bonded and isolated and/or terminal SiO-H groups. The nature and environment of tantalum in TaSiBEA was checked by diffuse reflectance UV-Vis spectroscopy. There was no band characteristic of extra-framework octahedral Ta(V). The spectra of tantalum-containing samples exhibited only one intense band at 216 nm which is characteristic of ligand-to-metal charge transfer. A similar band was observed for mononuclear Ta(V) in TaSBA-15 [84].

Faujasite is another example of large-pore zeolites but having a low Si/Al ratio, to which tantalum was incorporated by one-pot synthesis. Trejda et al. [38, 39] used the modified two-step procedures reported originally by Ginter et al. [85] to incorporate tantalum into Y zeolite. No metal oxide phase was detected, also by UV-Vis spectroscopy. The UV-Vis spectra of both TaY-32 and TaY-64 (Si/Ta = 45 or 78 in the final zeolite, respectively) showed one symmetric band at 221 nm which is typical of tetrahedrally coordinated Ta species. For further investigation of the metal state in the prepared zeolites, the XPS spectroscopy was used. The oxidation state of tantalum in both samples was estimated as +5. Moreover, the binding energies observed for tantalum introduced into Y zeolite (TaY-64, 26.7 eV; TaY-32, 26.3 eV) were higher than those typical of bulk tantalum oxide (26.1 eV). The increase in the binding energy can be attributed to different surroundings of Ta in the zeolite (Si-O-Ta) than in the oxide (Ta-O-Ta). Thus, the XPS results evidenced the location of the metal in the zeolite framework. The efficiency of metal incorporation was estimated from XRF data, and it was found that the assumed metal amount was not reached in the final material. The results from the above study were compared with those of niobium-containing zeolites prepared in the same way. Surprisingly, tantalum was easier to introduce into FAU structure than niobium, although the atomic radius of tantalum was greater than that of niobium. The higher efficiency of Ta incorporation can be explained by the role of metal pentaethoxide as a space-filling agent, which makes the contact of metal source with the forming zeolite crystal cavities much easier. The ^{27}Al NMR spectra evidenced the presence of tetrahedrally coordinated aluminium in the samples prepared, whereas no octahedrally coordinated aluminium was observed. Moreover, the SEM images showed that the particles of the pure Y and TaY zeolites were similar in size and shape. This proved that the introduction of a metal source in the synthesis gel did not have any impact on the crystal morphology.

The possibility of Ta incorporation into faujasite structure based on sodalite (SOD) units as well as into large-pore BEA zeolite has been investigated by theoretical calculations [32, 33]. In both SOD and BEA, the DFT calculations show the preference of Ta to be present as penta-coordinated Ta-OH groups [32, 33]. The position of tantalum in SiAl zeolite framework, modelled by sodalite

framework, was found to be surrounded by Si atoms Al-(O-Si)-O-Ta with the charge compensating that of the Na cation in the neighbourhood of the Si-O-Al linkage [33]. The same trend was also observed in the case of DFT calculations for niobium-containing zeolites.

The influence of synthesis conditions on the tantalum loading and its location in zeolites is summarized in Table 3.

4.2 Surface Properties

Surface properties of tantalum-containing zeolites are determined by different factors, e.g. the location of metal, i.e. at the framework or extra-framework positions, dispersion of metal or nature of zeolite surface before modification with tantalum. It is clear that all above-mentioned factors are strongly dependent on the preparation protocol that is able to vary even for the same type of zeolite. For example, let's consider the effect of the type of medium used in the synthesis. The basic solution leads to the relatively high concentration of silanol defect groups that obviously influences the surface properties of materials obtained increasing hydrophilic character of the surface. On the contrary, the use of fluoride medium, besides significant reduction of silanol defect sites and thus improving the hydrophobic character of the solid, increases the efficiency of metal incorporation into zeolite framework [68].

As described in the previous section, tantalum species were incorporated into various crystalline structures, like BEA [68, 70, 86], MFI [47], FAU [38, 39] or lamellar silicate like ilerite [87]. These solids were prepared using either fluoride or basic media, and tantalum was located both at the framework and in extra-framework positions.

The main purpose of the tantalum incorporation into zeolite structure was the generation of well-defined single isolated sites that are able to serve as Lewis acid centres in different catalytic processes as those previously described and applied, e.g. titanium silicalite-1, known as TS-1 [88]. Like Ti in TS-1, tantalum was incorporated by both hydrothermal synthesis method and impregnation procedure (Ta/Si+Ta molar ratio was 0.01, 0.02 or 0.03) [47]. The acidity of tantalum silicalite-1 materials was characterized by using the thermo-programmed desorption of ammonia (NH_3-TPD). Incorporation of Ta species by hydrothermal synthesis led to ammonia desorption profile with a broad peak between 400 and 700 K in which at least two maxima could be found at ca 460 and 600 K. These desorption peaks were assigned to rather weak acidic sites and were correlated by the authors with the presence of silanol groups located in the neighbourhood of tantalum sites (Ta-(OH)-Si). After impregnation of silicalite-1 with tantalum, only one desorption peak centred at ca 460 K was observed. Despite a similar metal content, much smaller desorption of ammonia was observed. It was concluded that hydroxyl group of the extra-framework Ta_2O_5 are involved in the adsorption of NH_3. These results are in line with the characterization of material structure given in Sect. 4.1.2.

Zeolites prepared in OH media showed a higher number of defect sites leading to form groupings like Si-OH, which can interact with tantalum. This was also supported by the NH_3 adsorption on Ta containing silicalite-1 described, e.g. in Ko and Ahn [47] or by the interaction of silanols with pyridine presented in Kyriienko et al. [86]. In contrast, samples prepared in fluoride media showed much smaller number of defect sites. In fact for these samples, the bands related to pyridine interacting with silanols are not observed [68].

Similar methodology of probing the acid properties of the surface was applied for the tantalum-containing ilerite [87]. In this work, Ta species were incorporated into the support via pillaring process. The NH_3-TPD profile obtained for Ta-ilerite was quite similar to that recorded for Ta-silicalite-1 [47]. A broad desorption peak was observed at temperatures between ca 373 and 676 K with the maximum of ammonia desorbed at 473 K. For comparison, similar studies were conducted for Si-ilerite. No desorption peak of ammonia was found. It was concluded that tantalum incorporated into ilerite was a source of a large number of weak acidic sites.

The generation of Lewis acidity in medium pore size zeolites (diameter of ten-membered ring as Ta-silicalite) via tantalum incorporation limits the application of materials obtained to relatively small reactant molecules that need to reach the active centres. To overcome this problem, some attempts have been made to incorporate tantalum species into 12-membered ring zeolites, in particular into the BEA structure [68, 70, 86]. Corma et al. [68] have used two modification methods, as mentioned above, i.e. direct hydrothermal synthesis and impregnation procedure. Surface properties of the materials obtained were characterized by pyridine and cyclohexanone adsorption followed by FTIR measurements. Pyridine adsorbed on the surface of the material obtained via one-pot synthesis protocol clearly indicated the presence of Lewis acid sites (the band at 1,450 cm^{-1}). It was not the case for the materials prepared by the impregnation procedure. The spectrum of this sample showed a band at 1,450 cm^{-1} of a very low intensity.

The characterization of the surface properties of Ta-silicalite [47] and TaBEA [68, 70] clearly led to the conclusion that the incorporation of tantalum into the zeolite structure is a key point in the generation of materials having Lewis acidity and can be realized by hydrothermal synthesis procedure. The acidity of such synthesized BEA material was also tested by the adsorption of cyclohexanone. The measurement of interaction of carbonyl group from cyclohexanone with Lewis acid centres provided information on their quantity and strength. When tantalum was incorporated into the BEA framework, a shift of the band related to carbonyl group towards lower wavenumber was observed, in comparison to its position after adsorption of cyclohexanone on BEA or BEA impregnated with tantalum. These results confirmed that the generation of well-defined single isolated sites by the incorporation of tantalum into the zeolite structure during the hydrothermal synthesis allows obtaining Lewis acid sites that strongly interact with carbonyl groups. For this reason, these materials can be applied as catalysts in processes involving this kind of acidity.

Tantalum was also incorporated into the BEA zeolite using the two-step post-synthesis procedure described in Sect. 4.1.2 [86]. This method allowed obtaining isolated tantalum sites in the BEA framework. Lewis acid sites were present in the materials and their amount depended on the quantity of tantalum incorporated in the BEA structure. These results are in line with those reported by Corma et al. [68, 70]. However, in the case of TaSiBEA samples described in [86], the interaction of pyridine with hydroxyl groups was also manifested by the bands at ca 1,598 and 1,445 cm^{-1}. Nevertheless, the difference in the surface properties of samples should be rather connected with the methodology of BEA synthesis. Corma et al. have synthesized the materials in fluoride medium, while Kyriienko et al. have done it in basic medium (high pH). It is known that the latter leads to the much higher concentration of hydroxyl groups on the zeolite surface. These hydroxyl groups (silanol Si-OH) present on BEA surface can interact with pyridine giving characteristic bands at ca 1,598 and 1,445 cm^{-1}. However, in the previous papers related to the materials prepared via a similar technique, the above-mentioned bands for SiBEA zeolites were not observed [89] or the intensity of these bands was low [44]. The presence of Lewis acid sites in TaSiBEA samples was also confirmed by pyrrole adsorption. This probe molecule has amphoteric character and can react with both acid and basic sites. Indeed, the bands at 3,480 and 1,490 cm^{-1} appeared in FTIR spectra after pyrrole adsorption on TaSiBEA confirming the interaction of the probe molecule with Lewis acid sites. Nevertheless, a shoulder at ca 3,390 cm^{-1} was also detected, which could suggest the presence of basic sites on the surface of TaSiBEA zeolite. In fact the application of another probe molecule, i.e. $CDCl_3$, confirmed the presence of weak and medium basic sites due to the presence of bands at 2,558 and 2,224 cm^{-1}. However, for TaBEA materials prepared by Corma et al. [68], basicity test was not performed. Nevertheless, on the basis of the above-mentioned spectroscopic investigation, one can draw a general conclusion that incorporation of tantalum into zeolite structure results in the formation of both acid and basic sites, wherein based on Dzwigaj et al. [86], the former ones are more numerous. The basic sites in tantalum-containing zeolites should be rather related to the OH groups attached to penta-coordinated Ta, which is supported by the results of $CDCl_3$ adsorption on TaSiBEA and by the results discussed later (2,5-hexanedione cyclization on TaY zeolites and computational data related to TaBEA materials).

Another method for characterization of surface properties is the performance of catalytic test reactions. This methodology was used to determine the acid/base properties of tantalum-containing zeolites having faujasite structure [38]. The presence of Lewis acid sites was estimated on the basis of the results of cumene cracking. The electron-transfer centres led mainly to the formation of α-methyl styrene, which was the only product observed for TaY-32 (Si/Ta = 32) sample. Nevertheless, some propene for TaY-64 (Si/Ta = 64) sample, having a lower number of tantalum atoms, was also detected, which suggested the presence of some Brønsted acid sites in this material. Indeed, the pyridine adsorption indicated a small number of acid sites of this type. The second reaction applied, i.e. the 2,5-hexanedione cyclization and dehydration, allowed determination of the basic

properties of materials obtained. For both tantalum-containing samples, 3-methyl-2-cyclopentenone (MCP) was a dominant product testifying to the presence of basic sites. For a higher concentration of tantalum species, a higher yield of MCP was observed. It is known that the incorporation of tantalum species at +5 oxidation state generates an excess of local positive charge in the faujasite framework that have to be compensated. It was concluded that it can be realized by the OH groups attached to tantalum and having basic character.

The surface properties and thus the reactivity of tantalum species in zeolites can be also explored by using computational approach, namely, molecular electrostatic potential (MEP) or protonation and deprotonation energies [32, 90–93]. This methodology was applied for characterization of zeolites having tantalum substituted into the framework. On the basis of the minimum MEP values, the stability of different Ta species was investigated, mainly Ta-OH and Ta=O located at the framework positions. It was found that the latter species were less stable [90].

To estimate the Brønsted acidity of active sites, the deprotonation energy can be calculated as the difference between the energy of the conjugated base and the acid. The value of this energy can be taken as an indicator of acidity; the higher the energy, the weaker the acidity of hydroxyl groups. It was found that Ta-OH species show just slightly more acidic character than the silanol groups [92]. On the other hand, the calculation of the protonation energy can estimate the surface basicity. A comparison of both energies for tantalum-substituted zeolites suggested that it was energetically more favourable to protonate than to deprotonate the Ta sites in zeolites. On the basis of the above-mentioned calculations, it was postulated that tantalum-containing zeolites have stronger basic than acidic properties [92]. The basicity calculated for tantalum-containing zeolites is in line with the experimental measurements described in literature for Ta-substituted BEA pointing on basic character of the samples, i.e. adsorption of $CDCl_3$ on TaSiBEA [86] and FAU, i.e. results of 2,5-hexanedione cyclization [38] zeolites.

Besides the alteration of surface properties of the tantalum-containing zeolites in terms of acidity and basicity, the incorporation of tantalum species can generate other features that can be attractive from the aspect of gaining new knowledge and potential application. For instance, the materials having photoluminescence properties are very interesting. The solid samples showing such properties were prepared by the introduction of Ta species into the LTA zeolites using the thallous ion exchange method [80] described in Sect. 4.1.1. The material obtained, in contrast to thallium LTA precursor, showed the UV-induced photoluminescence behaviour. It was found that upon UV excitation with maximum intensity at 270 nm, a broad emission band between 350 and 500 nm (peaking at 410 nm) was observed. This blue emission was explained by a metal-to-ligand radiative transition.

To sum up, it has been shown that tantalum species can be incorporated into different zeolite structures and various methods can be applied to obtain this goal. The materials obtained show interesting surface properties that can be beneficial in different catalytic processes. Some examples will be described in the next chapter.

5 Catalytic Activity of Zeolites Containing Group Five Metals

Group five elements located in zeolite structures can act as active species in oxidation and reduction processes as well as in acid-base-catalysed reactions and photocatalysis. Their activity is determined mainly by the nature of a given element. However, there are many other features affecting catalytic properties of modified zeolites. Among them, location of metal species (framework vs extra-framework positions) plays a crucial role. If group five metals are incorporated into the zeolite framework, their properties strongly depend on their oxidation state and type of the zeolite (mainly Si/Al ratio). As indicated in the previous sections, vanadium can take both oxidation states, +4 and +5, in zeolite structure, whereas niobium and tantalum preferably are in +5 oxidation state in metal-oxygen tetrahedra. If metals have +5 charge and are located in the framework, the metal-oxygen tetrahedra cumulate positive charge can be compensated by hydroxyls (penta-coordinated M-OH) or M=O double bond. The predominance of one of these species is determined by the nature of metal, vanadium being in both forms (with the domination of V=O), whereas niobium and tantalum preferably exist as hydroxylated species (although they partially occur as M=O as well) [32]. Interestingly, V(V)-OH reveals weak acidic properties, whereas hydroxyls in Nb(V)-OH and Ta(V)-OH are not acidic (Ta-OH shows basicity) [34, 71, 91–94]. Vanadium can be reduced to V^{4+} and in this form located in the zeolite framework [35]. The dehydroxylation of M zeolites (M=V, or Nb, or Ta) performed before the catalytic reaction generates Lewis acid sites-metal cations in the framework. One has to consider also that compensation of positive charge in the zeolite framework can occur by negative charge of the aluminium-oxygen tetrahedra. Therefore, the properties of metal-modified zeolites also depend on silica to alumina ratio in zeolites. The higher the number of alumina tetrahedra, the better the compensation of the excess of positive charge is possible. Thus, the presence of group five metals in the zeolite framework also influences the properties related to the presence of AlO_4^- species. DFT calculations supported by experimental data [33] have documented that niobium and tantalum incorporated into zeolites containing aluminium tetrahedra enhance the basicity of zeolites. This effect is more pronounced in niobium-modified zeolites.

Group five elements can be also located at extra-framework positions in zeolites at which they occur in the form of bulk oxides (e.g. Nb_2O_5) or metal-oxo cations (e.g. VO^+ species). Such extra-framework species reveal different properties than those in the framework.

In this chapter, the catalytic activity of zeolites containing group five metals is presented in four sets of catalytic processes: oxidation (liquid and gas phase), reduction, acidic catalysis and photocatalysis is considered.

5.1 Liquid-Phase Oxidation

Many parameters affect the activity and selectivity of oxidation reactions performed in liquid phase [95]. Some of them are (1) the nature of matrix of metal species limiting diffusion effects, (2) isolation of metals, (3) hydrophobicity of catalysts, (4) nature of solvent, (5) reducibility of metal species and (6) leaching of metal from the solid. For the zeolites modified with group five elements, the effect of the two last features should be especially emphasized. Among the group five metals, vanadium is more easily reduced than niobium and tantalum. Leaching of the metal by reagents or solvent, an undesirable phenomenon, is determined by the nature of metal (generally vanadium is easier leached than niobium and tantalum, but it depends also on the kind of metal species), location of metal (easier leaching takes place if metals occupy extra-framework positions in zeolites) and the nature of solvent and oxidant (hydrogen peroxide as oxidant is a potential agent inducing the leaching of active phase). To avoid leaching, special procedures of metal incorporation to zeolites are applied. They allow the generation of metal species hardly leached even by hydrogen peroxide, the most often used green oxidant. It is worth noting that vanadium located in zeolites is generally more stable than vanadium incorporated into amorphous mesoporous molecular sieves [96].

The interaction of hydrogen peroxide with metal species in zeolites is crucial for the activity in liquid-phase oxidation. Such interaction can proceed via three different ways [97]: homolytic pathway and two heterolytic pathways (Fig. 9).

The homolytic pathway proceeds via free radical mechanism in whose first step the metal active species participates in homolytic cleavage of O-O bond of hydrogen peroxide forming $^{\bullet}OH$ radicals. Two active oxidant species, peroxometal and oxometal, can be formed in heterolytic pathways. Heterolytic peroxometal pathway dominates when the metal in its highest oxidation state is both a Lewis acid and a weak oxidant, e.g. early transition metal ions with d^0 configurations such as Nb(V).

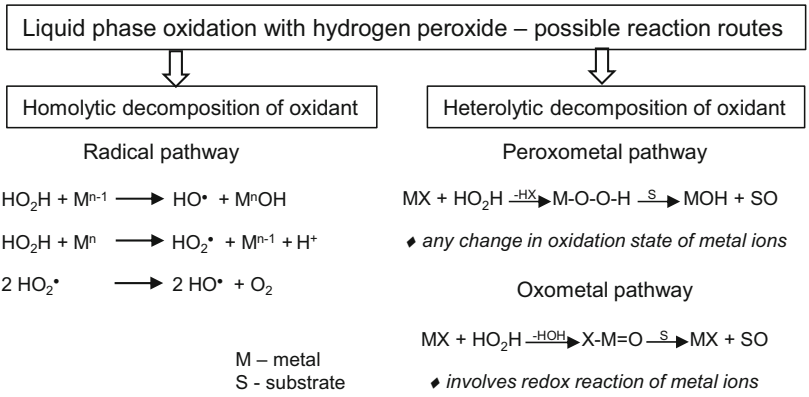

Fig. 9 The possible interactions of hydrogen peroxide with transition metals (loaded on the catalyst surface) and substrates (after [97])

Catalytic process occurs on metal species playing the role of Lewis acid site, and metal oxidation state does not change during the catalytic cycle. Strong (one-electron) oxidants, e.g. late transition metals and/or first-row transition elements, favour oxometal pathways and/or homolytic decomposition of hydrogen peroxide. Vanadium(V) is both a strong Lewis acid and a relatively strong (one-electron) oxidant and, hence, exhibits all three types of activity. The favourable pathway on vanadium zeolites depends on the kind of metal species formed after zeolite modification. Olefin epoxidation, sulphoxidation and oxidation of nitrogen compounds are typical examples of reactions proceeding via the peroxometal pathway. It is worth mentioning that peroxo species are favoured in alkaline pH, whereas in acidic pH superoxo radicals dominate [98].

In this section, we present selected oxidation processes performed with hydrogen peroxide (hydroxylation of benzene, epoxidation of olefins and oxidation of sulphides) and show the advantages and disadvantages of the use of zeolites modified with group five elements as catalysts for these reactions.

5.1.1 Hydroxylation of Benzene

Phenol, an important intermediate in the production of antioxidants, agrochemicals and polymers, is mostly produced by the three-step cumene process known to be charged with many drawbacks. Among them, there are low yield per pass of phenol (~5%), necessary use of high pressure and high temperature and explosive intermediates. Thus, the direct hydroxylation of benzene with high efficiency in phenol production is one of the most challenging tasks and has attracted much attention. Both homogeneous and heterogeneous catalytic hydroxylations of benzene have been studied. Among the different transition metals studied as active species in this reaction, vanadium has been applied in the form of sodium metavanadate [99] or in Keggin structure [100] if used in homogeneous system and located in zeolites [25, 101] if applied in heterogeneous liquid-phase process. It was proved that in homogeneous catalytic process with sodium metavanadate as catalyst and hydrogen peroxide as oxidant, $[VO_2]^+$ was the active species in benzene hydroxylation. This vanadium species interacted with H_2O_2 towards peroxovanadate species such as $HVO(O_2)_2$ or $VO(O_2)^+$, which oxidized benzene to phenol. One can expect that similar vanadium species would be active in heterogeneous reaction, which is more favourable because of the possibility of reuse of heterogeneous catalysts. However, to get this advantage, the solid containing vanadyl cations must be stable, and no leaching of the active phase should occur. $[VO_2]^+$ or VO^{2+} cations can be obtained by modification of zeolites with a proper source of vanadium and proper modification method. Simple liquid-phase cation exchange method does not lead to stable vanadium cations. Therefore, more sophisticated techniques have been proposed.

Vanadium-containing BEA, ZSM-5 [101, 102] and VS-1 [25] zeolites were investigated. The starting material for the preparation of vanadium BEA and ZSM-5 zeolites was boron analogues of these zeolites and their deboronated primary forms [101]. The reductive solid-state ion exchange with V_2O_5 allowed

obtaining $[VO_2]^+$ and/or V^{4+} strongly bonded to the zeolite framework. Vanadium hydroperoxide species formed by the interaction of V^{4+} cations with hydrogen peroxide took part in the hydroxylation of benzene to phenol and hydroquinone (the product of phenol hydroxylation). If the initially deboronated samples were used for vanadium solid-state ion exchange, the activity of such zeolites was higher, which was due to better dispersion of vanadium and better accessibility of active centres. The same catalysts used for phenol hydroxylation were less active than in benzene hydroxylation. The above authors could not precisely determine the leaching of vanadium species because of the low concentration of vanadium in zeolites. They found nearly the same amount of vanadium in the regenerated sample as in the fresh one.

A more complex study of the stability of different vanadium species existing in vanadium silicalite-1 (VS-1) zeolite in the hydroxylation conditions has been performed by Guo et al. [25]. These authors prepared vanadium silicalite-1 with different content of vanadium by a modified hydrothermal synthesis method described in Sect. 2.1.2. The materials contained both extra-framework and framework vanadium species. Hydrogen peroxide and/or acetic acid was found to remove the vanadium oligomers (octahedral V^{+4} and octahedral V^{+5}) located in extra-framework positions of VS-1. These vanadium species were unstable in hydroxylation of benzene, but they were also active. However, they promoted the deep oxidation of phenol (undesired reaction path in hydroxylation of benzene to phenol). Highly dispersed distorted octahedral V^{5+} species located in the pore of zeolite were also unstable in HOAc. The mononuclear octahedral V^{5+}, tetrahedral V^{5+} and V^{4+} species in the framework containing V=O double bond showed good stability in the hydroxylation conditions. The amount of vanadium loading appeared to be crucial in reaching high activity and selectivity in hydroxylation of benzene to phenol because it determines the distribution of framework and extra-framework vanadium species. The lower the vanadium loading, the lower the amount of extra-framework vanadium is. The VS-1 catalyst with 1.0 wt% of vanadium incorporated in the framework showed a stable hydroxylation activity yielding about 11% phenol (TOF = 63.0) with above 90% selectivity.

5.1.2 Oxidation of Olefins

Oxidation of olefins with hydrogen peroxide will be discussed on the example of cyclohexene oxidation. This reaction can proceed via different reaction pathways [103, 104]. Two of them are shown in Fig. 10 [103–106].

Route #1 directing the reaction towards epoxide requires the presence of redox centres on the catalyst surface, whereas diols are formed from epoxide if acidic centres strong enough are present on the catalyst [107]. Diols are also formed if the reaction is performed in the homogeneous system because of the lack of stabilization of epoxide formed in the first stage of the reaction. The oxidation of cyclohexene with hydrogen peroxide has been mostly studied in acetonitrile as the reaction medium. Many studies have been devoted to titanium species used as

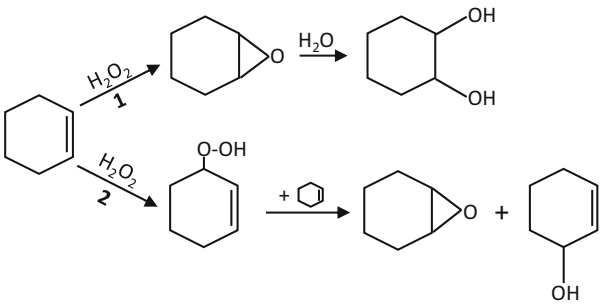

Fig. 10 Cyclohexene oxidation with hydrogen peroxide – examples of the possible routes (1 – non-radical, 2 – radical route) (after [103–106])

active phase for this reaction [103, 104]. Jorda et al. [103] used Ti-silicalite as a catalyst for this reaction and found the importance of radical mechanism of this process leading to the allylic oxidation products like cyclohexenyl hydroperoxide. This intermediate reacted further with cyclohexene to cyclohexene oxide and cyclohexenol (reaction route #2 in Fig. 10). The radical reaction route was initiated by the formation of titanium hydrosuperoxo species (Ti-OH + H_2O_2 → Ti-OOH + H_2O). From these species, hydroxyl radicals were formed which are active oxidants in the reaction route mentioned. Cyclohexene oxide can also be formed via non-radical route if small amounts of hydrogen peroxide are added step by step. Moreover, the presence of Brønsted acid sites results in the formation of cyclohexanediol according to route #1 (Fig. 10). The role of peroxo complexes and their protonated forms in epoxidation of cyclohexene was stressed by Kholdeeva et al. [104] who have studied Ti(IV)-monosubstituted Keggin polyoxometalate as the catalyst. They indicated that the number of protons can control the oxidation mechanism and, therefore, the oxidation products. Titanium peroxo and hydrosuperoxo species were proposed as active in the reaction discussed.

As follows from of the knowledge shortly presented above, in the consideration of the use of zeolites containing group five elements, the strength of metal-oxygen bond has to be taken into account because it determines the possibility of formation of metal-peroxo and superoxo species in the interaction with hydrogen peroxide. Moreover, the acidic-basic properties play an important role. As indicated in Wojtaszek et al. [33] and Hartman et al. [64], among the zeolites with group five metals incorporated into the framework, the highest acidity corresponds to those containing vanadium. The highest basicity of metal-OH groups was assigned to Ta-OH, whereas the zeolites containing aluminium besides niobium presented the highest basicity of bridge oxygen. As a consequence, zeolites containing tantalum have not been discussed in literature in the context of cyclohexene epoxidation, whereas the niobium-containing zeolites were tested in this reaction. Niobium silicalite-1 (NbS-1) appeared to be more active [64] than the counterpart of titania-silicalite-1 (TS-1) [108, 109]. On the other hand, the epoxidation of cyclohexene was observed over VAPO-5 [110] and TAPSO-5 [108], while NbAPO-5 exhibited no activity [64]. The lack of NbAPO-5 activity and the superior activity of NbS-1 were explained by the fact that Nb-O-Si bonds are significantly more reducible and redox

active than the stable Nb-O-Al and Nb-O-P ones. That is why also NbY zeolite was almost inactive in comparison with the activity of mesoporous niobiosilicate NbMCM-41 and NbSBA-15 [107]. However, not only the presence of aluminium and Nb-O-Al sites in the catalyst but also the crystallinity of NbY zeolite was the reason for lower activity. It was proved that the active niobium peroxo or superoxo radical species were not generated in the interaction between crystalline NbY or Nb_2O_5 with hydrogen peroxide, although they were easily generated if niobium was located in the amorphous phase (niobiosilicates or amorphous niobia) [98, 107]. However, it was not the case for niobium located in zeolite BEA previously dealuminated with nitric acid Bregante et al. [111]. Niobium located in the silanol nests of the dealuminated zeolite interacted with hydrogen peroxide. Furthermore, Nb-bound superoxide (Nb^{IV}-$(O_2)^-$) and hydroperoxide/peroxide (Nb^V-OOH and Nb^V-$(O_2)^{2-}$) intermediates were formed by irreversible activation of H_2O_2 at Nb atoms. These observations were in contrast to the mechanisms proposed for olefin epoxidation over similar catalysts (e.g. TS-1 [112], Ta-SBA-15 [84] and Ta-SiO_2 [113, 114]) that assumed reversible (and quasi-equilibrated) H_2O_2 activation. The most important finding from [111] was that in contrast to the widely recognized activity of peroxo species (two-electron oxidant) in olefin oxidation, superoxide Nb^{IV}-$(O_2)^-$ (one-electron oxidant) was identified as the active intermediate in cyclohexene oxidation over NbBEA zeolite. This niobium(IV)-supereroxide species participated directly in the epoxidation of olefins by a biradical, stepwise reaction pathway.

Interesting combination of redox properties of titanosilicalite-1 (TS-1) and the acidity of niobium(V) oxide was utilized by Prasetyoko et al. [62] who prepared Nb_2O_5/TS-1 bifunctional catalyst for the synthesis of diol in 1-octene oxidation to 1,2-octanediol through the formation of 1,2-epoxyoctane. The production of epoxide and diol was correlated with the presence of oxidative and Brønsted acidic sites in the catalyst.

Vanadium-modified zeolites are active in epoxidation of cyclohexene. However, the main problem with commercialization of such zeolites is the leaching of the active phase under the conditions used for this reaction. The stability of vanadium in liquid-phase reactions depends on the nature of the substrate, the solvent and the oxidant [115]. The V-leaching has been reported for a variety of V-doped zeolites in which vanadium was incorporated by impregnation or cation exchange [116]. It appeared also that VAlPO-5 catalysed olefin epoxidation, but the reaction partially occurred in the homogeneous phase and was catalysed by leached vanadium species [117]. Pore size did not affect this undesired property because the leaching of vanadium occurred in micro- and mesoporous materials. Niederer and Hölderich [29] studied vanadium isomorphously substituted zeolite BEA in cyclohexene epoxidation with TBHP (tert-butyl-hydroperoxide). The zeolite contained V=O species which were active in contact with peroxides. Thus, VBEA zeolite was active in this reaction. However, even TBHP caused leaching of vanadium species and the catalyst was not reusable.

To sum up, niobium species are stable under treatment with hydrogen peroxide, but they are not active if present in the neighbourhood of aluminium because of too strong Nb-O-Al bonds to achieve the interaction with oxidant. Only NbS-1 and

Nb-dealuminated BEA zeolites appeared to be applicable for this reaction. NbS-1 was even more active than TS-1, commonly recognized as the catalyst addressed to the epoxidation of cyclohexene. Thus, niobium located in dealuminated zeolites, also with structures other than BEA and MFI, can be considered as attractive catalyst for epoxidation. Vanadium-containing zeolites are active in epoxidation of cyclohexene, but vanadium species are leached to the solution and therefore the catalysts are not reusable.

5.1.3 Oxidation of Sulphides

Sulfoxides which are formed in the liquid-phase oxidation of sulphides are important chemicals exhibiting biological and pharmacodynamic properties. Usually sulfone is also produced besides sulfoxide in this reaction. Among the metal catalysts for asymmetric sulphide oxidation, titanium-based systems are the most prominent ones. Similar properties can be expected for other d^0 metals like V(V). Such metals easily react with hydrogen peroxide and organic hydroperoxides towards the formation of peroxo complexes, which are effective and selective oxidants, usually much stronger than the parent peroxides, as mentioned above. The use of vanadium catalysts for oxidation of sulphides has been reviewed in Bolm [118]. The focus was on chiral metal complexes anchored on zeolites which were active in oxidation of sulphides. Interestingly, high yields and enantioselectivity have been reached with a limited number of substrates. For instance, good enantiomeric excesses have never been achieved with simple sulphides like methyl phenyl sulphide.

Oxo-vanadium complex ([$V(O_n)L(acac)$]; ligand L = (2*S*,4*R*)-*N*-benzyl-4-hydroxy-4-phenyl-2-(1,1-diphenylmethyl)pyrrolidinylmethanol) anchored into USY zeolite (ultrastable Y zeolite) was tested in the oxidation of methyl phenyl sulphide and (2-ethylbutyl) phenyl sulphide with H_2O_2 and TBHP [119] at 273 K. Higher reaction temperatures led to a dramatic decrease in the selectivity to sulfoxide as well as significant loss of asymmetric induction which involves direct interaction of the nucleophile with the chiral ligand. It was confirmed that the sulfoxide was a primary and unstable product, while the corresponding sulfone appeared as a secondary and stable product at high conversion. These results were obtained irrespective of the oxidant agent employed, H_2O_2 or TBHP. The oxidation of (2-ethylbutyl) phenyl sulphide with hydrogen peroxide was carried out at different temperatures showing a significant enhancing enantioselectivity at lower temperatures. It means that the sulphoxidation process is asymmetrically induced. The activity and stability of oxo-vanadium(V) complexes in USY zeolite were compared with those of dioxomolybdenum(IV) one. Although vanadium complexes were more active than the molybdenum analogues, vanadium active species were easily leached, whereas molybdenum ones were much more stable.

Another vanadium complex, [$VO(sal\text{-}oaba)(H_2O)$] (where sal-oaba means Schiff base derived from salicylaldehyde and *o*-aminobenzyl alcohol) was also anchored in Y zeolite and tested in oxidation of methyl phenyl sulphide by H_2O_2 at

room temperature in acetonitrile as the reaction medium [120]. A maximum of 93.2% conversion of methyl phenyl sulphide and 96.9% selectivity to sulfoxide were achieved, if sulphide to oxidant ratio was 1:1. Unfortunately, similarly to Fuerte et al. [119], vanadium complex was leached into the solution. Thus, this catalyst is also not recyclable.

Niobium species in zeolites are more stable than vanadium ones under treatment with hydrogen peroxide, but they do not form easily active niobium-peroxo or superoxo species. However, the application of bifunctional zeolites containing Brønsted acid sites and niobium species allowed avoiding the low activity of niobium in the zeolite. To increase the possibility of formation of active species of niobium in zeolites, MWW layered zeolites were transformed to hydrogen forms and then modified with niobium source. Hydrogen forms of MCM-22 and delaminated MCM-56 zeolites were used for the modification with niobium species [61] described in Sect. 3.1.1. The recently established phenomenon [98] that the interaction of the acidic hydroxyls with hydrogen peroxide gives rise to the formation of hydrosuperoxo species was crucial for achieving high activity of Nb/HMCM-22 and Nb/HMCM-56 in oxidation of dibutyl sulphide to dibutyl sulfoxide. These species interacted with the excess of H_2O_2 towards hydroxyl radicals, which are the most active species in the catalytic oxidations. The role of the niobium centres was to trap superoxo ($O_2^{-\bullet}$) and peroxo (O_2^{2-}) species on the surface. This process enhanced the production of hydroxyl radicals highly active in oxidation processes. The zeolite texture also influenced the effectiveness of sulphide oxidation. Nb/HMCM-56 exhibited higher activity (>90% conversion of dibutyl sulphide) than Nb/HMCM-22 zeolite. Both catalysts were stable and leaching of niobium was not detected.

5.2 Gas-Phase Oxidation

In the catalytic oxidation with oxygen, different reaction mechanisms can be considered: (1) Mars-van Krevelen's mechanism in which oxygen from the catalyst takes part in the formation of oxidation product and oxygen from the gas phase is used for the reoxidation of catalyst; (2) Langmuir-Hinshelwood's mechanism in which oxygen and the oxidized molecule are chemisorbed on the catalyst surface and the reaction occurs between two chemisorbed species; and (3) Eley-Rideal's mechanism in which one substrate is chemisorbed and the other interacts with the species physisorbed or from the gas phase. The first mechanism would seem to be much easier if metal oxides occupy extra-framework positions in zeolites per analogy to vanadium oxide supported on silica or other oxides. However, this reaction path cannot be excluded for metals (M) incorporated into the framework if they form, e.g. M=O species. Below two examples of gas-phase oxidation on zeolites containing vanadium are shown, oxidation and oxidative dehydrogenation of propane and methanol oxidation. Both reactions differ in mechanism.

5.2.1 Oxidation and Oxidative Dehydrogenation of Propane

Oxidation of light alkanes to valuable oxygenates proceeds via oxidative dehydrogenation (ODH) towards olefins further oxidized by oxygen. Especially, ODH of propane to propene is a very active area of research because of the rapid growth of the market for acrolein, acrylic acid and methyl-t-butylether (MTBE – the key ingredient of reformulated gasoline), the products of this reaction [121]. Propane is unreactive. Its dehydrogenation to propene is a highly endothermic process and has to be carried out at temperatures above 873 K [122]. The introduction of a hydrogen acceptor into the reaction medium shifts the thermodynamic equilibrium making the reaction irreversible even at lower temperatures. The challenging fact also is that propane is less reactive than the desired products, and further oxidation to total oxidation products, CO_x, is thermodynamically favoured. Despite this thermodynamic limitation, literature describes several successful ODH of propane mainly on vanadium- or molybdenum-supported catalysts. Niobium species have been often used as additives playing the role of promoters. ODH of propane on metal oxide catalysts proceeds via the Mars-van Krevelen redox mechanism [123, 124]. The following reaction steps were distinguished on VO_x/SiO_2 and VO_x/ZrO_2 systems [124, 125]:

$$C_3H_8 + O^* \leftrightarrow C_3H_8O^*$$
(weak adsorption of propane by interaction with lattice oxygen (O^*))

$$C_3H_8O^* + O^* \rightarrow C_3H_7O^* + OH^*$$
(abstraction of H atom by neighbouring oxygen atom)

$$C_3H_7O^* \rightarrow C_3H_6 + OH^* \text{ (desorption of propene by hydride elimination)}$$

$$OH^* + OH^* \leftrightarrow H_2O + O^* + *$$
(recombination of OH groups to form water and vacancy ($*$))

$$O_2 + * + * \rightarrow O^* + O^*$$
(reoxidation of vacancy centres via dissociative chemisorption of O_2)

where O* is the lattice oxygen in V=O or V-O-V structures, OH* a hydroxyl group in V-O-H, $C_3H_7O^*$ the adsorbed propoxide bonded to V through an O atom and * the surface vacancy associated with either one V^{3+} or two V^{4+} atoms in the VO_x lattice.

For oxidative dehydrogenation of propane, not only mixed oxides containing vanadium and supported vanadium oxides but also vanadium-containing zeolites were studied. Taking into account the Mars-van Krevelen mechanism of propane ODH, it is clear that the nature of vanadium centres determined by the modification method and the location of metal in zeolites (framework vs extra-framework) play a crucial role in this reaction. A detailed study on this matter was performed on VSiBEA zeolites in which vanadium was incorporated to both above-mentioned positions [126]. Vanadium was incorporated to the nests formed by dealumination of BEA zeolite under different pH of impregnating solution. Such a procedure

allowed the location of vanadium preferentially in the framework in the form of pseudo-tetrahedral containing bridged V-O-Si and terminal V=O oxygens or preferentially in the extra-framework positions in the form of VO_x oligomers. It was documented that isolated pseudo-tetrahedral framework vanadium species were active sites of the C_3H_8 ODH catalytic reaction.

Another important feature influencing the selectivity of the reaction (to propene vs total oxidation to CO_2) is the concentration of vanadium species in the zeolite. It was proved that if in VSiBEA the content of vanadium was very low (0.14 V atoms/u.c.), so that isolated VO_4 tetrahedral were observed, the catalyst was active but not selective, the only reaction product being CO_2 [127]. At higher vanadium content, propene appeared in the reaction products. The selectivity grew with the vanadium content in zeolite, i.e. with the increase in the amount of tetrahedral species up to 1.22 V atoms/u.c. With higher vanadium amount, at which octahedral V species appeared, the selectivity to propene decreased. C_3H_8 TPR study showed that ODH of propane to propene may take place with the participation of the catalyst lattice oxygen. This form of oxygen was inactive in total combustion of propane. Interestingly, although the samples with very low vanadium loading (0.14 V atoms/u.c.) contained only tetrahedral vanadium species, they were not selective in ODH of propane to propene. The authors [127] have explained this behaviour by the different reaction mechanism on low-loaded vanadium zeolite, involving the participation of chemisorbed oxygen species instead of lattice ones.

Zeolite membranes were also tested in ODH of propane [128]. Both MFI and VMFI membranes provided an activated transport for both propane and oxygen above 673 K. They produced propene with about 40% selectivity but with higher O_2 and C_3H_8 conversions for the VMFI. The activity and selectivity of propane oxidation over vanadyl ion-exchanged zeolite BEA (VO-H-BEA) with oxygen were compared to those obtained on mixed oxides, $Mo_1V_{0.3}Te_{0.23}Nb_{0.12}O_x$ [129]. The first reaction product on both catalysts was propene obtained from oxidative dehydrogenation of propane. Further oxidation of propene differed over both catalysts. Over VO-H-BEA, acetic acid was a sequential oxidation product of the formed propene possibly through an acetone intermediate. On $Mo_1V_{0.3}Te_{0.23}Nb_{0.12}O_x$, the selectivity was significant to acrylic acid (valuable product) and acetone. For the production of acrylic acid, the allylic oxidation pathway was crucial (Fig. 11a). In this pathway, the reaction must first go through a dehydrogenation prior to terminal oxygenation, but not vice versa. The allylic oxidation capability of VO-H-BEA was poor because of

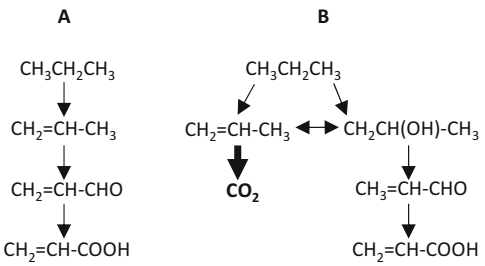

Fig. 11 Main reaction pathways of propane oxidation over (**A**) $Mo_1V_{0.3}Te_{0.23}Nb_{0.12}Ox$ and (**B**) VO-H-BEA (after [129])

the acidity of this zeolite. On this catalyst propene formed in the first step of the reaction is oxidized to propanol which, in intermolecular dehydration on acidic sites of the zeolite, is again transformed to propene (Fig. 11b). A high surface area, and long diffusion time in contact with the catalytic active sites resulting from the microporous structure of zeolites, caused that the total oxidation product, CO_2, was the major one. Thus, for vanadium zeolites, the enhancement of selectivity to acrylic acid requires the reduction in acidity.

Neither niobium nor tantalum zeolites were described in literature as catalysts attractive for ODH of propane, most probably because of the small amount of stable double bond M=O species. In vanadium zeolites, pseudo-tetrahedral vanadium species contain bridged V-O-Si and terminal V=O oxygens. The latter seems to be crucial in the Mars-van Krevelen mechanism of the reaction in which oxygen from V=O lattice species takes part in the reaction.

5.2.2 Oxidation of Methanol

Catalytic methanol oxidation is applied in dual roles, for the production of valuable chemicals and as a useful reaction to test the properties of catalyst surface. The product distribution of methanol oxidation is sensitive to the redox and/or acid-base properties of the surface active species. Generally, redox centres catalyse the selective oxidation of methanol to formaldehyde, acidic sites yield dimethyl ether, and basic species produce CO_2 [130, 131]. However, for multifunctional catalysts containing all of the above-mentioned centres, the methanol oxidation process is more complex.

Busca at al. [132] have proposed the rake mechanism for methanol oxidation (Fig. 12) in which all of the above-mentioned centres take part and the product distribution is determined by the strength of chemisorption of the intermediates and final products as well as the content of the desired active species. An example is vanadium oxide loaded on titania catalyst containing active hydroxyl groups (V-OH). In the first step of the reaction, methanol is dissociatively chemisorbed on acidic hydroxyls, and methoxy species are chemisorbed on the catalyst surface.

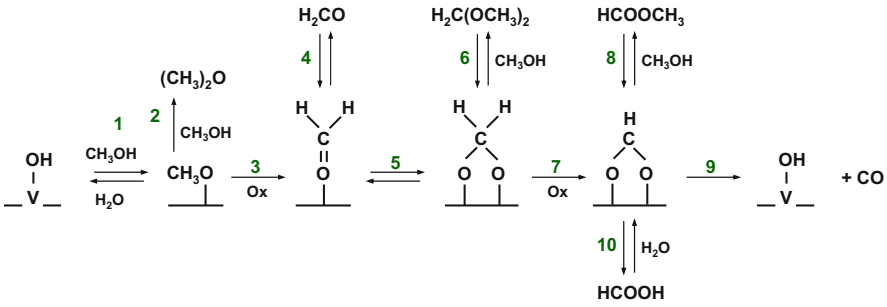

Fig. 12 Methanol oxidation on vanadium-hydroxyl species (after [132])

Dissociative chemisorption of methanol can also occur on pairs of Lewis acid-base sites. Routes #3 and 7 are typical oxidation pathways (oxidative dehydrogenation) requiring redox centres (vanadium species playing this role) on the catalyst surface, whereas #2, 6 and 8 require the presence of acidic sites for the reaction of intermediate with the other methanol molecules. The abstraction of proton from methoxy species is usually the rate-determining step. The subsequent reactions towards dimethoxy methane, methyl formate or total oxidation to CO_2 depend on many factors, among others, the strength of intermediate chemisorption and the concentration of active centres. The catalysts that are active and selective to methyl formate require high surface areas and vanadium loadings in order to favour consecutive reactions. Long contact times are desired too. Moreover, the excess of oxygen favours consecutive processes, whereas an excess of methanol gives rise to formaldehyde production. The reaction temperature also plays an important role because it influences the chemisorption of intermediates and, through this, the possibility of desorption or further reaction with methanol molecules.

Taking into account the above-mentioned pathway of methanol oxidation demonstrating the importance of acidic centres as well as redox sites on the catalyst surface, it can be expected that vanadium-containing zeolites can be attractive catalysts for this reaction. Particularly useful is the possibility of dispersion of vanadium species on high surface area of zeolites and possible achievement of different loadings which determine the selectivity of the reaction. Moreover, the zeolite matrix permits changing vanadium environment to control nucleophilicity of oxygen in the surrounding of active vanadium species. It is known that the high selectivity towards formaldehyde is observed when the nucleophilicity of oxygen present in the neighbourhood of vanadium is moderate [133]. Stronger chemisorption of formaldehyde and more efficient formation of dimethoxymethane, which can be transformed into methyl formate by further reaction with CH_3OH, are observed if the nucleophilicity in the surrounding of vanadium species is higher. Further increase in nucleophilicity causes the total oxidation of methanol.

Different vanadium loadings were obtained in BEA zeolite after dealumination and impregnation with NH_4VO_3 solution [44]. Depending on the vanadium loading, different species were formed as described in the previous sections. For low vanadium content, the V(V) ions were only in pseudo-tetrahedral coordination, either in non-hydroxylated $(SiO)_3V{=}O$ or hydroxylated $(SiO)_2(OH)V{=}O$ species in the framework positions. The amount of the latter species increased with vanadium content and determined the changes in conversion and selectivity in methanol oxidation. The methanol conversion was low for low vanadium loading and increased with increasing content of vanadium in the zeolite. As mentioned above, the rate-determining step in methanol oxidation is the abstraction of protons from methoxy species (step #3 in Fig. 12). This process depends on the nucleophilicity of oxygen in the neighbourhood of chemisorbed methoxy groups. The formation of methoxy

species in the first step of the reaction on both non-hydroxylated $(SiO)_3V{=}O$ or hydroxylated $(SiO)_2(OH)V{=}O$ species can be described as follows:

$$(SiO)_3V = O + CH_3OH \rightarrow (SiO)_3(CH_3O)V - OH$$
$$(SiO)_2(OH)V = O + CH_3OH \rightarrow (SiO)_2(CH_3O)V = O + H_2O$$

Only the hydroxylated vanadium species led to the location of methoxy group adjacent to vanadyl oxygen responsible for the abstraction of proton from methoxy group towards the formation of chemisorbed formaldehyde. The selectivity to formaldehyde grew with the concentration of $(SiO)_2(OH)V{=}O$ species, which was related to the moderate nucleophilicity of vanadyl oxygen (V=O) in this hydroxylated species. The increase in vanadium content increases the amount of partial oxidation products and decreases the dehydration of methanol to dimethyl ether and total oxidation to CO_2. The presence of strong acidic centres and the absence of basic centres in the neighbourhood of methoxy species may cause its interaction with a second CH_3OH molecule to form dimethyl ether.

DFT calculations were performed to get a deeper insight into the mechanism of methanol oxidation on VSiBEA [134]. The activation energy of the transition state (TS) associated with the formation of V-OCH_3 group on different vanadium species was calculated. The value of activation energy (66.4 kJ/mol) of TS formed on hydroxylated $(SiO)_2(OH)V{=}O$ indicated that the formation of formaldehyde or dimethyl ether (the other potential product) is plausible. Interestingly, the activation energy of TS formed on non-hydroxylated $(SiO)_3V{=}O$ species was similar (slightly lower, i.e. 56.9 kJ/mol). It means that the dissociative adsorption of methanol occurred at a similar rate on both vanadium species considered. As mentioned above, the step #3 is rate-determining and the difference in both vanadium species was important. The possibility of product formation (formaldehyde, step #3, and dimethyl ether, step #2, were considered as the reaction products) was discussed in relation to the reaction temperature and type of vanadium species. It was found that at 523 K the formation of products was possible for all vanadium structures considered. At temperatures below 523 K, the reaction ended with the formation of methoxide if hydroxylated $(SiO)_2(OH)V{=}O$ species participated in the chemisorption of methanol. Dimethyl ether or formaldehyde molecules were not obtained at these temperatures.

5.3 Catalytic Reduction of Nitrogen Oxide

Selective catalytic reduction (SCR) of nitrogen oxide with ammonia has been the most comprehensively studied process of NOx removal from waste gases for many decades [135]. It is the most efficient technology for reducing NOx emission from

both mobile and stationary sources proceeding according to the equation shown below.

$$2NO + 2NH_3 + 1/2O_2 \rightarrow 2N_2 + 3H_2O$$

Firstly, SCR-NO was applied for gas purification from stationary sources like power plants. The importance of this technology increased by commercial implementation of urea-based DENOX converters for heavy diesel engines by Siemens [136]. For the last two decades, a revival of the interest in SCR process has been noted. The main types of catalysts involved in the SCR of NO by NH_3 are noble metals, metal oxides and zeolites.

In this section, some examples of SCR-NO by NH_3 performed on vanadium-containing zeolites are shown and discussed. Tantalum and niobium zeolites have not been proposed for this reaction. Niobium in ZSM-5 zeolite has been discovered as a promoter for copper species active in NO decomposition [72] but was not studied in SCR-NH_3 process.

Vanadium-exchanged zeolites are excellent SCR catalysts, but the activity and selectivity of these materials depend crucially on the zeolite structure, the vanadium precursor and the applied modification method [14]. Adams et al. [137] have studied the SCR of NO over vanadium grafted in Y zeolite. They used $VOCl_3$ as vanadium precursor and the chemical vapour deposition method. They observed that the zeolite structure collapsed either during vapour deposition or under the SCR reaction. Among different zeolite structures, ZSM-5 was mainly proposed as the zeolite containing vanadium species active in SCR of NO with ammonia [14, 46, 138–142]. Different protocols of vanadium insertion were applied in the above-mentioned studies, and therefore different properties in selective reduction of NO with ammonia were observed. According to Miyamoto et al. [143], the active vanadium sites are V=O species. At these sites, the reaction between NO and ammonia occurs towards N_2, H_2O and V−OH (see equation below). Then vanadium hydroxyls are reoxidized by gaseous oxygen to rebuild the parent V=O species.

$$V = O + NH_3 + NO \rightarrow V - OH + N_2 + H_2O$$
$$2V - OH + 1/2O_2 \rightarrow 2V = O + H_2O$$

Thus, active vanadium zeolites should contain V=O species. They were formed, for instance, as vanadyl ions in extra-framework positions by the treatment of NaZSM-5 zeolite with aqueous solution of $VOSO_4$ at pH 1.5–2 [141] or by oxidative degradation of vanadyl acetylacetonate loaded on ZSM-5 [139]. In the latter case, it was proved by FTIR spectroscopy that V=O groups (isolated terminal species anchored on the zeolite surface) were reduced by ammonia which was adsorbed as NH_4^+, whereas NO was not adsorbed on the catalyst in the SCR performed over this catalyst. In the formation of ammonium cation, Brønsted acid sites participated. This indicates the necessity of the use of a bifunctional catalyst for this reaction, i.e. the zeolite containing V=O species and BAS. Taking

into account the importance of BAS in SCR-NO reaction, the hydrogen forms of different zeolite structures (ZSM-5, BEA, mordenite, Y) were modified by impregnation with vanadium oxalate solution towards final loading of V_2O_5 in zeolite pores [46]. The SCR activity was correlated directly with Brønsted acidity of the zeolites used.

Interesting results were obtained on BEA zeolite modified with vanadium species (by the two-step method: dealumination of zeolite and V impregnation of dealuminated sample) with different loadings [138]. At low vanadium loading, $V_{1.0}$SiBEA, the zeolite contained isolated pseudo-tetrahedral V(V) species (containing bridged V-O-Si and terminal V=O oxygens) which were active in SCR of NO reaction with a maximum conversion of NO about 60% at 773 K and very low selectivity to undesired N_2O. With higher vanadium loading (especially $V_{7.5}$SiBEA), the zeolites contained mainly extra-framework octahedral V(V) and vanadium oxide species which were less active in SCR-NO at higher temperature and catalysed N_2O formation.

The catalytic performance of vanadium zeolites in SCR of NO with ammonia was studied by adding molybdenum to the vanadium VZSM-5 zeolite [140]. Solid-state ion exchange of H-ZSM-5 zeolite with both vanadium and molybdenum salts resulted in the improvement of catalyst performance in NO-SCR by NH_3, if the amount of molybdenum added remained low. After solid-state ion exchange, ZSM-5 contained different types of vanadium and molybdenum species depending on the amount of Mo loading. Molybdenum can be present in cationic ion exchange position, or can be grafted to the silanol groups, or as molybdenum oxide particles in the channel and/or on the external surface of zeolite. These molybdenum species influenced considerably the catalytic properties of the resulting solids by the electronic interaction with vanadium species. The insight into vanadium-molybdenum HZSM-5 zeolites used in SCR of NO with ammonia is presented in [14]. Acid sites in HZSM-5 zeolite were not affected by the presence of vanadium during the solid-state exchange. It was not the case for molybdenum. Molybdenum cations diffused inside the zeolite channels and consumed different acid sites. The species formed on the zeolite surface was determined by the molybdenum source. The possibility of formation MoO_3 phase, which is undesired species because it catalyses the side reaction towards N_2O, was pointed out. MoO_3 was formed in the reaction:

$$Al_2(MoO_4)_3 + V_2O_5 \rightarrow 2AlVO_4(s) + 3MoO_3$$

Thus, the important issue is to avoid the formation of $Al_2(MoO_4)_3$. The best performance in SCR-NO with ammonia was achieved if both vanadium and molybdenum interacted with BAS towards the formation of active Mo-V-O species. It was achieved if molybdenum chloride was used as Mo precursor.

The important feature of catalysts used in SCR of NO with ammonia is their resistance to poisoning with water and/or sulphur dioxide. The V-ZSM-5 catalyst described in [142] exhibited a stable activity for NO reduction in the presence of H_2O and SO_2, but rapid deactivation was observed in the presence of 10 ppm SO_3.

VO-ZSM-5 catalyst studied in [141] also exhibited resistance to sulphur dioxide admission (200 ppm at 623 K). The poisoning effect of water (up to 4.5 vol.%) was weak at temperatures between 623 and 773 K. However, the deactivation which occurred under dry conditions, by oxidation of vanadyl ions into pentavalent vanadium species, was significantly accelerated in the presence of water.

5.4 *Acidic and Bifunctional Catalysts in Transformation of Alcohols*

In contrast to the above-described gas-phase catalytic processes in which only vanadium zeolites revealed attractive activity, in the reactions activated by acidic sites and bifunctional sites (acid-base and redox), vanadium-, niobium- and tantalum-containing zeolites were involved in different processes. Considerations in Sects. 2.2, 3.2, and 4.2 indicated that both BAS and LAS can be created in zeolites containing group five elements, and the predominance of any of them depends on the metal nature, species formed, structure and composition of zeolites. Thus, both kinds of acidic centres will be taken into account in consideration of acidic catalytic activity. Zeolites containing group five elements exhibit usually different types of active centres, e.g. besides acidic ones also redox and basic active sites. Therefore, they appeared to be attractive also for the so-called tandem reactions which occur via different steps in which different active centres are required. The acidic and bifunctional activity of vanadium-, niobium- and tantalum-containing zeolites will be discussed on the example of the transformations of simple alcohols, methanol [144] and ethanol [67, 86, 145] to different products over niobium and tantalum zeolites as well as glycerol dehydration on vanadium zeolites.

AM-11 zeolite (crystalline niobium silicate consisting of needles ca 10 μm in length containing NbO_6 octahedra; Si/Nb = 4.6, Na/Nb = 0.3) was tested in methanol dehydration. In the synthesis of this microporous niobiosilicate, AM-11, both Brønsted and Lewis acid centres were generated [146]. Lewis acid sites were accommodated predominantly on the external surface of the zeolite. They came from sodium cations and extra-framework niobium species. The Brønsted acidity in the as-synthesized AM-11 was related to the NH_4^+ cations, added to the synthesis gel during preparation, which upon dehydration decomposed to form ammonia and acidic protons. Substantial amount of strong BAS was located on the internal surface of the material. Such distribution of acidic centres was responsible for the catalytic activity and selectivity in the transformation of methanol. If the reaction was performed in flow reactor, methanol was rapidly dehydrated on LAS to produce dimethyl ether which failed to enter the pore system and desorbed as the main product. It was suggested that methanol, which at the beginning of the reaction diffused in the micropores, was dehydrated and further transformed to hydrocarbons (methanol to gasoline, MTG, reaction), but the products were not able to

desorb. Thus, the products blocked the pore system and the reaction occurred only on the external surface towards dimethyl ether. In contrast, if the reaction was performed in batch reactor, methanol diffused into the internal surface area where it was adsorbed and with the participation of BAS was dehydrated and yielded a range of C1-C5 hydrocarbons.

NbSiBEA and TaSiBEA zeolites (both Al-free samples) are typical multifunctional catalysts (redox and acidic-basic centres are present on their surfaces), and they were tested in different tandem reactions [67, 86, 145]. Both were investigated in gas-phase ethanol conversion to 1,3-butadiene (BD) which belongs to the most important conjugated dienes and is used as a monomer in synthetic rubbers and polymers [147].

Catalytic conversion of ethanol to 1,3-butadiene is a multistep process. It involves several consecutive stages (Fig. 13): (1) dehydrogenation, (2) aldol condensation, (3) crotonic condensation, (4) Meerwein-Ponndorf-Verley (MPV) reduction and (5) dehydration. The key steps of the process are (2) and (4) [86]. The first step of the reaction path is the abstraction of a proton from alcohol to form acetaldehyde. This reaction occurs on redox/basic centres. The competitive reaction is the dehydration of alcohol to dimethyl ether and ethylene which proceeds on strong acidic sites. Therefore, the catalysts with weak acidity are welcome to achieve high selectivity in 1,3-butadiene production. Selective synthesis of 1,3-butadiene from ethanol preferably requires a bifunctional catalyst capable of catalysing both hydrogen transfer (redox process) and aldol condensation and dehydration (acidic route).

Niobium introduced into the framework of BEA zeolite as mononuclear Nb (V) framework species play the role of Lewis acid sites with lower ($Nb_{0.7}$SiBEA) and higher ($Nb_{2.0}$SiBEA) niobium loading as discussed in Sect. 3.2. Weak Brønsted acid sites were also identified in both samples. The total number of LAS was slightly higher for $Nb_{2.0}$SiBEA (a part of niobium occupied extra-framework

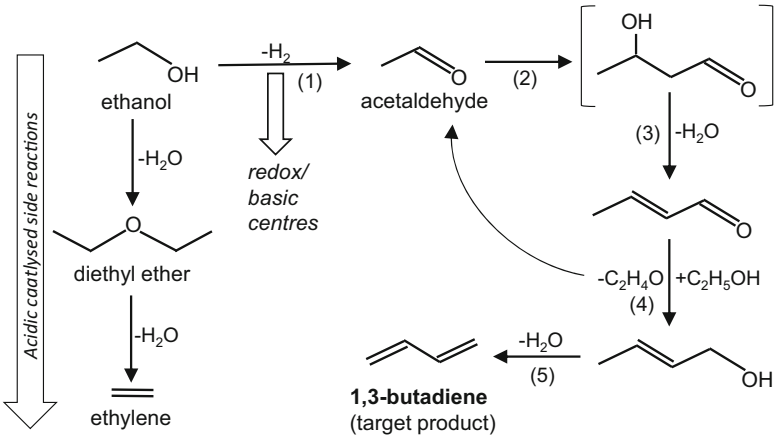

Fig. 13 Ethanol conversion to 1,3-butadiene and side reaction products (after [67])

positions as octahedral niobium(V) oxide), but the amount of stronger mononuclear framework niobium species was higher for $Nb_{0.7}$SiBEA. The amount of BAS was somewhat higher for the latter zeolite. Both NbSiBEA catalysts were tested in transformation of ethanol to 1,3-butadiene [67]. The activity and the selectivity were determined by the distribution of the niobium species in both catalysts. The isolated mononuclear Nb(V) species (acidic sites) more effectively catalysed the aldol condensation of acetaldehyde and the ethanol dehydration to dimethyl ether and ethylene. Therefore TOF (turnover frequency) of $Nb_{0.7}$SiBEA, containing higher amount of mononuclear Nb(V) species, was several times higher than that of $Nb_{2.0}$SiBEA. Moreover, TOF of the dehydrogenation of ethanol to acetaldehyde was almost four times higher for the catalyst with lower niobium loading, indicating the important redox properties of this catalyst. The authors of [67] did not mention the phenomenon of redox centres generation in high silica zeolites containing niobium in the framework positions (described in Sect. 2.2, Fig. 7 [72]), but it is obvious that its high TOF in the dehydrogenation of ethanol is related to the number of redox (oxidative) centres. The formation of NbO^- oxidative centres is accompanied by the generation of LAS-Nb^+ sites. Therefore, the side reaction for BD synthesis, dehydration of ethanol to dimethyl ether and ethylene, also occurred on framework niobium species.

The main products in the reaction were 1,3-butadiene, acetaldehyde, dimethyl ether and ethylene. A small amount of crotonaldehyde was also observed. For the reaction carried out at 623 K, a significantly higher yield of BD was achieved (ca 17%) over $Nb_{0.7}$SiBEA than over $Nb_{2.0}$SiBEA (ca 8%) due to greater ethanol conversion (~75% vs ~42%). It is worth noticing that selectivity to BD did not differ too much on both catalysts under the reaction conditions (~23% vs ~20%). The interesting difference in product distribution was ca twice higher selectivity to acetaldehyde over $Nb_{2.0}$SiBEA (ca 23%) than over $Nb_{0.7}$SiBEA (ca 11%). The number of framework niobium species in the former catalyst was insufficient for effectively further catalysed the reaction of acetaldehyde to crotonaldehyde and 1,3-butadiene. High selectivity to ethylene and dimethyl ether given by $Nb_{0.7}$SiBEA testified its greater quantity of acidic sites, on which the dehydration reaction occurred in parallel with the dehydrogenation to acetaldehyde. The selectivity to both dehydration products can be lowered by a decrease in the reaction temperature to 598 K. For $Nb_{0.7}$SiBEA catalysts, the mentioned selectivity was reduced from ca 65% (dimethyl ether + ethylene) at 623 K to ca 44% at 598 K.

TaSiBEA zeolites containing only Lewis acid-base sites (BAS were not generated in these zeolites) were also applied in the tandem reaction from ethanol to 1,3 butadiene [86]. Table 4 compares the results obtained for niobium and tantalum zeolites with similar metal loadings ($Nb_{0.7}$SiBEA and $Ta_{1.0}$SiBEA). It is clear that tantalum-containing zeolite exhibited much lower ethanol conversion and BD yield than its counterpart containing niobium. It is important to stress the difference between surface properties of NbBEA and TaBEA. Niobium zeolite exhibits more acidic properties than tantalum-containing one. Ta-OH in Ta-zeolites shows basic properties in contrast to non-basic Nb-OH [34, 71, 91–94]. It could be the reason why although the yield and activity over NbSiBEA was higher than that over

Table 4 Catalytic performance of Nb and Ta zeolites in ethanol conversion after 4 h time on stream (after [67, 86])

Temp. (K)	Total EtOH conv. (%)	Selectivity (C_1 mol %)				BD yield (C_1 mol %)
		BD[a]	AA[a]	DEE[a] + ethylene	Others	
$Nb_{0.7}$SiBEA						
598	42.4	27.9	16.8	54.2	1.1	11.9
623	74.6	22.8	11.2	64.9	1.1	17.0
$Ta_{1.0}$SiBEA						
598	13.3	16.4	33.0	51.1	1.5	2.2
623	31.1	28.9	21.1	48.5	1.5	9.0

[a]*BD* 1,3-butadiene, *AA* acetaldehyde, *DEE* diethylether

Table 5 Catalytic performance of Nb and Ta zeolites in ethanol conversion with acetaldehyde after 4 h time on stream (Ethanol/AA = 2.7; WHSV = 0.8 $g_{reagent}\ g_{catalyst}^{-1}$) (after [67, 86])

Temp. (K)	Total EtOH conv. (%)	Selectivity (C_1 mol %)			BD yield (C_1 mol %)
		BD[a]	DEE[a] + ethylene	Others	
$Nb_{0.7}$SiBEA					
598	38.5	54.8	39.2	6.0	21.1
623	42.8	55.1	38.5	6.4	23.6
$Ta_{1.0}$SiBEA					
598	31.2	86.9	9.8	3.3	27.1
623	43.0	79.6	16.4	4.0	34.2

[a]*BD* 1,3-butadiene, *AA* acetaldehyde, *DEE* diethylether

TaSiBEA, the selectivity to ethanol dehydration products (dimethyl ether and ethylene) was higher over NbSiBEA than TaSiBEA.

To avoid the dehydration of ethanol as a reaction parallel to the required dehydrogenation of alcohol to acetaldehyde, the reaction between ethanol and acetaldehyde to BD was performed (Table 5).

Not only NbSiBEA but also TaSiBEA, containing isolated mononuclear metal (V) and possessing Lewis acidic-basic pairs [79, 92], which are required for this process, were used in this reaction [67, 86]. The active sites (their types and strength) appeared to be more attractive for the reaction between ethanol and acetaldehyde to 1,3-butadiene over $Ta_{1.0}$SiBEA than $Nb_{0.7}$SiBEA (Table 5). The selectivity and yield of BD were much higher for the former catalyst with similar alcohol conversion values.

The presented results opened the possibilities of designing zeolites containing group five metals with the proper amount of lattice metal species that would be more effective in the main reaction to BD or the admission of some dopants promoting the direction of the reaction to BD production. Different dopants (catalytic promoters), silver, copper and zinc, were added to TaSiBEA zeolites, and the so-prepared catalysts were tested in the reaction between ethanol and acetaldehyde [145]. The acid-base properties of the catalysts were modified by this way

enhancing their dehydrogenation activity. Ethanol conversion and butadiene selectivity over the catalysts increased in the order: TaSiBEA < ZnTaSiBEA < AgTaSiBEA < CuTaSiBEA. A 73% selectivity to BD was achieved over CuTaSiBEA (at 88% ethanol conversion and $T = 598$ K).

Another example of alcohol transformation with the use of bifunctional transition metal zeolites is the dehydration of glycerol to acrolein and further oxidation to acrylic acid, which occurs according to the scheme presented in Fig. 14 [148, 149].

The production of acrylic acid in one-step catalytic reaction requires the presence of both acidic and redox centres on the catalyst surface. Vanadium-modified zeolites exhibit such properties. Zeolites of different topologies, FAU, FER, MEL, MFI, MOR, MWW and OFF, were synthesized, impregnated with 5% vanadium and tested in gas-phase oxidative dehydration of glycerol [149]. The impregnation with vanadium species was performed on hydrogen forms of zeolites obtained via cation exchange on NH_4^+ and further deamination. Protons in the zeolite supports were the source of acidity (BAS), whereas vanadium oxide in extra-framework position played the role of redox centres (V^{5+}/V^{4+}). Too high acidity decreased the activity of the catalysts by coke formation. Oxygen in the reaction medium was necessary for the regeneration of redox centres which participated in the oxidation of acrolein to acrylic acid. The best results were observed for the catalysts whose acid site density was near to 0.8 mmol g^{-1}. For the zeolites with such a concentration of acidic sites, the structure was found to be important. The order of acidic activity at 593 K was as follows: V/H-ZSM-11(MEL) > V/H-MCM-22 (MWW) > V/H-ZSM-5 (MFI) ~ V/H-ferrierite (FER). As concerns redox centres, one could observe that the catalysts characterized by a molar ratio V^{5+}/V^{4+} of around 0.5 showed higher yields of acrylic acid. Acrylic acid selectivities were related to the ability of a specific zeolite topology to stabilize the redox pair V^{5+}/V^{4+}. The Mars-van Krevelen mechanism was proposed for this reaction in which glycerol interacts via C2-hydroxyl group with BAS in zeolite towards the formation of dehydration product – 3-hydroxypropionaldehyde as an intermediate product dehydrated further to acrolein. Acrolein readsorbs on vanadium species and is oxidized to acrylic acid with reduction of V^{5+} to V^{4+}. In the last step, the reoxidation of V^{4+} to V^{5+} occurs by consuming molecular oxygen. The optimum oxygen/glycerol molar ratio was equal to 4.

To improve the catalytic performance in glycerol oxidation to acrylic acid, the micro-mesoporous zeolites of MFI structure modified with V_2O_5 were applied

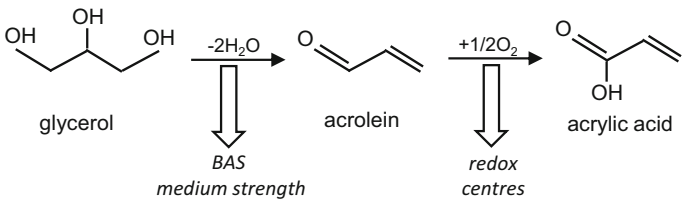

Fig. 14 Glycerol oxidehydration (dehydration combined with oxidation) on bifunctional acid and redox active sites (after [148])

[148]. Mesopores were created in MFI structure by NaOH treatment followed by the removal of extra-framework aluminium species by acid (the most effective for this purpose was oxalic acid which additionally acted as chelating agent). The so-treated zeolite was impregnated with V_2O_5. The conversion values exceeded 65%, even after 6 h of the reaction. The distribution of products strongly reflected the effects of pore formation, acid treatment with oxalic acid and the presence of vanadium oxide. The effects of these modifications resulted in higher selectivity to acrolein and acrylic acid, at a reduced rate of coke accumulation in the zeolite, and a longer catalyst lifetime in comparison with the other catalysts used. The mesopores in the zeolites made the mass transport of reactant and products easier and, in this way, promoted the catalytic activity. Moreover, the formation of the extra porosity allowed the accommodation of much less volatile polymeric coke molecules, hence maintaining access to the micropores and in this way enhanced the activity.

5.5 *Photocatalytic Reactions*

The photocatalytic activity of semiconductors has been successfully applied in advanced oxidation processes for degrading organic pollutants in water or to reduce toxic agents in air. The main steps of a photocatalytic reaction are the light absorption, charge carrier separation and diffusion onto the particle surface, followed by subsequent surface redox reactions with adsorbed molecules/atoms at the active sites of the photocatalyst (Fig. 15) [150, 151].

The energy difference between the valence band and the conductivity band (band gap) in a semiconductor is crucial for initiating the photocatalytic process by absorption of photon with energy equal or higher than the band gap. Upon such absorption, an electron from valence band becomes excited to the conductivity band leaving a hole, h^+, in the valence band. In the following step, the species are generated by light absorption diffuse onto the particle surface. On the particle surface, the positive hole (h^+) can interact with the adsorbed water or hydroxyl groups towards the formation of very active hydroxyl radicals. If oxygen is present

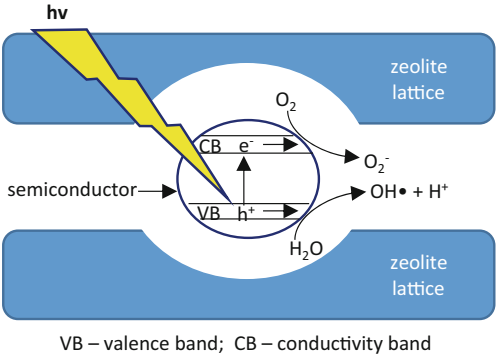

Fig. 15 Overall scheme of photocatalytic activity of semiconductors located in the zeolite lattice

in the medium, the electron induced into the conductivity band can be transferred to oxygen molecule and form a superoxide ion. Formed in this way, very strong oxidants are able to totally oxidize the organic molecules. The formed species can interact with different molecules subjected to photocatalytic reaction. The efficiency of photocatalysis depends on the process by which the electron is removed from the semiconductor surface and the process of recombination of electron-hole pair [152]. Recombination of charge carriers is an undesired process because it leads to decreasing photocatalytic activity. Various factors determine the recombination rates, including the mobility and trapping of charge carriers influenced by crystallinity, size and shape of the photocatalyst particles and their surface area. It also depends on the density of defects in the semiconductor lattice or the presence of an interface with a secondary material which acts as an electron or a hole sink.

Taking into account the above description, one can expect that the use of zeolites (crystalline materials with large surface area) as supports for metal semiconductors is a good solution for designing attractive photocatalysts [153]. The transition metal oxides highly dispersed in a specific structure of the zeolite framework can be excited under UV irradiation to form the corresponding charge-transfer excited state involving an electron transfer from oxygen anion to metal cation. High dispersion of photocatalytic active phase is very important for the effectiveness of this process. Zeolites does not only act as supports which control the dispersion and local structure of the active sites, but they can also induce the condensation effect for reactant gasses or shape selectivity due to their unique pore structure and restricted molecular-scale size.

In this section, the examples of zeolites used as supports for vanadium, niobium and tantalum are considered in the context of their photocatalytic activity.

Anpo with some co-workers and collaborators [153–156] have studied vanadium silicalites as photocatalysts in different reactions. V silicalites exhibited different and/or, in some cases, improved photocatalytic performance as compared with that of the supported vanadium oxide catalysts [154]. Detailed characterization (including the effect of irradiation) of vanadium species in vanadium silicalites (VS-1 and VS-2) and vanadium loaded on silica and mesoporous silica allowed identification of the reasons for the observed differences in photocatalytic properties [155]. The role of the zeolite structure was crucial. It allows obtaining a highly dispersed tetrahedrally coordinated V-oxides, VO_4 unit (within the zeolite framework), having a short V=O bond. The length of V=O bond is important because the charge-transfer excited state of this oxide species is well localized in the shorter V=O bond [156]. This length is one of the fundamental differences between two groups of materials, vanadium silicalites and vanadium loaded on silica. FT-EXAFS study allowed the estimation of the V=O bond length to be 1.68 Å in the zeolite framework and 1.62 Å if vanadium oxide was anchored to Vycor glass or silica. Thanks to the zeolitic rigid framework, the properties of VO_4 units are different, not only in the V=O bond length but also in the vibrational energy, O=V-O(Si, H) bond angle (smaller in the zeolite structure) and lifetime of the excited triplet state from those in a more flexible structure of, e.g. V/SiO_2. V species in the zeolite structure showed the dynamic quenching of the phosphorescence by the addition of

reactants such as NO or propane, which explains the activity of vanadium silicalites in photocatalytic NO decomposition and reduction with propane [153, 156]. The reduction of NO with propane on VS-1 was about five times higher than on the V-oxide photocatalyst deposited on porous Vycor glass or silica [153]. The efficiency of photocatalytic reduction was studied for different hydrocarbons, methane, ethane and propane. The latter was the most effective because of the highest rate of abstraction of H atom from hydrocarbons by the charge-transfer excited state, $(V^{4+}-O^{-})^*$, which plays a significant role in the enhancement of the reaction effectiveness. Interestingly, only small amounts of NO were adsorbed on the catalyst upon UV irradiation, while the adsorption of NO was much enhanced in the coexistence of propane. It was caused by the formation of important intermediate species between NO and hydrocarbon radicals, which was subsequently followed by further reactions with NO to produce N_2, oxygenates and CO_2.

Not only photocatalytic reduction of NO but also other photocatalytic reactions such as the decomposition of NOx (NO, N_2O) into N_2 and O_2, the partial oxidation of various hydrocarbons with O_2 or NO or N_2O and the polymerization of ethylene were successfully performed on vanadium-containing zeolites [156]. The high photocatalytic efficiency and the selectivity given by the single-site vanadium species located in the zeolite in significant reactions, which could not be observed with semiconducting bulk photocatalysts, were found to depend strongly on the unique and isolated local structure of the metal within the restricted framework structure of the zeolites. This local structure can be modified within zeolites lattice and thus can enhance the effectiveness of different photocatalytic reactions. The addition of alkali metal ions (Na^+, K^+, Rb^+) to vanadium silicalite (VS-1) zeolite by impregnation (Na_2O-VS-1, K_2O-VS-1, Rb_2O-VS-1) led to the formation of VO_4 tetrahedral where two V-O bonds interact with an alkali metal ion. Because of this interaction, the photocatalytic activity for the partial oxidation of hydrocarbons upon visible light irradiation ($\lambda > 400$ nm) arises. For example, Rb_2O-VS-1 photocatalytically oxidized propane with conversion of ~67% to CO_x (the selectivity 34%) and propanone (the selectivity 60%) [157].

An interesting photocatalytic activity in polymerization of ethylene upon visible light irradiation was obtained when vanadium was incorporated to ETS-10 zeolite (titanosilicalite) to form ETVS-10 (V/(V + Ti) = 0.43) [158]. The introduction of vanadium resulted in a decrease of the band gap energy from 4.32 for ETS-10 to 3.58 eV for ETVS-10. Thanks to that, the absorption of visible light above 400 nm was possible.

The above-presented examples of the photocatalytic activity of the vanadium-containing zeolites indicate that the incorporation of V species into the zeolite framework makes it possible to control the local structure and electronic state of the vanadium species on a molecular scale, important in photocatalytic processes. Not only vanadium but also niobium and tantalum-containing zeolites have been investigated in various photocatalytic reactions, e.g. [58–60]. In contrast to vanadium zeolites (mainly vanadium silicalite), niobium and tantalum zeolite photocatalysts described so far are based on faujasite-type zeolites, X and Y. FAU composition (Si/Al ratio) and structure was convenient for liquid-phase photocatalytic reactions,

degradation of dyes, to which the prepared Nb and Ta-FAU photocatalysts were addressed.

Wet impregnation of NaX with niobium source (10 wt%) and subsequent thermal treatment at 773 K led to the formation of Nb_2O_5/NaX system which was sunlight-active supported photocatalyst [59]. The synergistic effect between niobia and the zeolite material was found responsible for reduction in the absorption band energy of the zeolite from 4.7 to 4.3 eV. Zeolites exhibit low-wavelength absorption bands in the range $\lambda < 350$ nm, caused by the charge transfer $O^{2-} \rightarrow Al^{3+}$ with the participation of aluminium atoms arranged in specific locations (surface, corners, defects, etc.). Well-dispersed Nb_2O_5 crystallites in NaX cavities showed high-energy photon absorption at 428 nm (in the visible region) which allows its coupling with solar irradiation. The value found for the band gap of the Nb_2O_5/NaX photocatalyst was 2.9 eV, i.e. much lower than that of bulk Nb_2O_5 calcined also at 773 K (3.4 eV) due to the small crystal size of niobia in the zeolite pores. This reduction of band gap of niobia supported on NaX was the reason for effective (40%) dye mineralization if irradiated by visible radiation. Such results could not be achieved if bulk Nb_2O_5 catalyst was used because of a higher band gap of this material. It is another proof that the zeolite structure played an important role in the formation of photocatalysts activated by visible energy. The hydrolytic nature of the zeolite led to the formation of surface hydroxyl radicals, which increased the activity of the photocatalyst. Thus, Nb_2O_5 supported on NaX zeolite are promising for their use in photocatalysis [58]. Photocatalytic experiments were performed using solutions of reactive blue 5G dye. The influence of pH of the reaction medium was evidenced. In acidic pH an increase in discoloration rate occurred. This phenomenon is attributed to the interaction between the solution and the protonated surface of the catalyst.

The photocatalytic effect of niobium and tantalum located in zeolites can be enhanced by the synergism with other metal elements. In Reddy et al. [60], palladium-exchanged zeolite Y (PdY) has been used as the support for niobium and tantalum oxides incorporated by impregnation (NbPdY and TaPdY were obtained). All three materials were used as photocatalysts in the degradation of rhodamine-B (RhB), reactive red-198 (RR), 2-chlorophenol (2CP) and 4-chlorophenol (4CP) upon visible light irradiation. The NbPdY and TaPdY composites show higher photocatalytic efficiency than those of NaY and PdY. The radical-ion mechanism for RhB, RR, 2CP and 4CP degradation is proposed. The photogeneration of pairs (e^- and h^+) is enhanced by the presence of niobium and tantalum species. The photogenerated electron and holes reacted with surface hydroxyl groups, adsorbed water or oxygen and generated oxidative ionic radicals active in dye degradation. The generated peroxo radicals reacted with niobium and tantalum oxides leading to the formation of nascent oxygen which was involved in degradation of dyes. The pentavalent oxidation state of Nb and Ta provides the multiple electrons to vary the electrical conductivity. In the proposed mechanism of photodegradation, the acidity of the photocatalyst is important as it enhances the radical formation. Impregnation of PdY with niobium and tantalum oxides increases the acidity of the photocatalysts.

An important feature of the photocatalysts used in liquid media for dye degradation is their stability. The discussed NbPdY and TaPdY zeolites exhibited very good stability. The recovered and reused catalysts showed activity comparable with that of the fresh ones.

The analysis presented in this section has clearly showed that the use of zeolites as host materials for group five metal species active in various photocatalytic reactions is much promising in both the design and the development of unique photocatalysts characterized by high activity and selectivity.

6 Summary

This chapter has summarized recent progress in the methods for the introduction of group five metals (vanadium, niobium and tantalum) into different zeolite structures (mainly AEL, AM-11, BEA, FAU, LTA, MEL, MFI, MOR, MWW) in order to achieve materials with novel catalytic and photocatalytic properties. The importance of metal inclusion to silicate or aluminosilicate zeolite framework has been accentuated, and the methods which allow successful location of isolated metals in the zeolite skeleton by forming M-O-Si bonds have been presented in detail. Although the techniques allowing the effective metal incorporation into zeolites are similar for all three metals, the metal species obtained are different. Vanadium is easily reduced to V^{4+}, whereas niobium and tantalum prefer +5 oxidation state. The metal-oxygen tetrahedra with metals containing +5 charge cumulate positive charge which can be compensated by hydroxyls (penta-coordinated M-OH) or M=O double bond. Both forms occur in V-, Nb- and Ta-containing zeolites. However, vanadium preferentially forms V=O species, whereas niobium and tantalum preferably exist as hydroxylated species. Hydroxylated metals exhibit different properties depending on the kind of metal: V-OH presents weak acidic properties, whereas Nb-OH and Ta-OH in zeolites are not acidic. These differences imply different properties of metal species in catalytic and photocatalytic reactions.

Among liquid-phase oxidation processes, hydroxylation of benzene and oxidation of olefins and sulphides with hydrogen peroxide were discussed. Vanadium-containing zeolites were active in all these reactions but were not stable because hydrogen peroxide caused leaching of vanadium active species even if located in the zeolite framework. In contrast, niobium-containing zeolites were stable, and even if less active than vanadium ones, they were attractive in liquid-phase oxidation because of the possibility of reusing the catalysts. There is still much work to do in order to improve the activity of niobium zeolites. In this connection, the development of niobium modification of MWW zeolites seems to be one of the most promising ways. Zeolites containing tantalum have not been discussed in literature in the context of liquid-phase epoxidation.

In gas-phase oxidation of propane and methanol as well as selective catalytic reduction of nitrogen oxide, only vanadium-containing zeolites have been widely

studied in literature, but they were less active than other non-zeolite-based vanadium catalysts.

In contrast to the gas-phase catalytic oxidation processes in which only vanadium zeolites revealed attractive activity, in the reactions activated by acidic sites and bifunctional sites (acid-base and redox), vanadium, niobium and tantalum were involved in different processes. Among others, the tandem reaction, ethanol to 1,3-butadiene, and transformation of glycerol to acrolein have been discussed in detail.

The use of zeolites as supports for group five metal semiconductors has been demonstrated to be a good solution for designing attractive photocatalysts. The methods for obtaining high dispersion of photocatalytically active phase have been described. The activity of zeolite-based catalysts in the photocatalytic NO decomposition and reduction with propane, the decomposition of NOx (NO, N_2O) into N_2 and O_2, the partial oxidation of various hydrocarbons with O_2 or NO or N_2O and the polymerization of ethylene have been analysed. The stability of niobium and tantalum zeolites applied as photocatalysts used in liquid media for dye degradation was deeply studied.

New frontiers for further progress in obtaining catalytically and photocatalytically attractive zeolites containing group five elements are set by the modification of zeolites towards bifunctional active centres and photocatalytic properties. Thus layered zeolites with pillars containing group five metals and also other zeolites modified by a combination of group five and noble metals seem to be good direction for further study on the improvement of catalytic and photocatalytic activity.

Acknowledgement National Science Centre in Poland (Grant No. 2014/15/B/ST5/00167) is acknowledged for the financial support.

References

1. Goldsmith JR (1952) Ming Mag 29:952
2. Barrer RM, Baynham JW, Bultitude FW, Meier WM (1959) 36. Hydrothermal chemistry of the silicates. Part VIII. Low-temperature crystal growth of aluminosilicates, and of some gallium and germanium analogues. J Chem Soc (Resumed) 1959:195–208. https://doi.org/10.1039/JR9590000195
3. Karge HG, Weitkamp J (1998) Synthesis. Molecular sieves – science of technology, vol 1. Springer, Berlin. https://doi.org/10.1007/3-540-69615-6
4. Karge HG, Weitkamp J (2002) Structures and structure determination. Molecular sieves – science of technology, vol 2. Springer, Berlin. https://doi.org/10.1007/3-540-69749-7
5. Kucherov AV, Slinkin AA (1986) Introduction of transition metal ions in cationic positions of high-silica zeolites by a solid state reaction. Interaction of copper compounds with H-mordenite or H-ZSM-5. Zeolites 6(3):175–180. https://doi.org/10.1016/0144-2449(86)90044-8
6. Beyer HK, Karge HG, Borbély G (1988) Solid-state ion exchange in zeolites: part I. Alkaline chlorides/ZSM-5. Zeolites 8(1):79–82. https://doi.org/10.1016/S0144-2449(88)80035-6

7. Kornatowski J, Wichterlová B, Rozwadowski M, Baur WH (1994) Simultaneous occurrence of differently coordinated framework heteroatoms in one zeolite: MFI type vanadium silicalite, KVS-5. Stud Surf Sci Catal 84:117–124. https://doi.org/10.1016/S0167-2991(08)64104-X
8. Sen T, Rajamohanan PR, Ganapathy S, Sivasanker S (1996) The nature of vanadium in vanado-silicate (MFI) molecular sieves: influence of synthesis methods. J Catal 163 (2):354–364. https://doi.org/10.1006/jcat.1996.0337
9. Centi G, Perathoner S, Trifiro F, Aboukais A, Aissi CF, Guelton M (1992) Physicochemical characterization of V-silicalite. J Phys Chem 96(6):2617–2629. https://doi.org/10.1021/j100185a042
10. Moudrakovski IL, Sayari A, Ratcliffe CI, Ripmeester JA, Preston KF (1994) Vanadium-modified zeolite with the structure of ZSM-12. EPR and NMR studies. J Phys Chem 98 (42):10895–10900. https://doi.org/10.1021/j100093a035
11. Dzwigaj S, Che M (2005) Oxidation state of vanadium introduced in dealuminated β zeolite by impregnation with VIVOSO4 solution: influence of preparation parameters. J Phys Chem B 109(47):22167–22174. https://doi.org/10.1021/jp0582134
12. Dzwigaj S (2003) Recent advances in the incorporation and identification of vanadium species in microporous materials. Curr Opin Solid State Mater Sci 7(6):461–470. https://doi.org/10.1016/j.cossms.2004.03.011
13. Wark M, Brückner A, Liese T, Grünert W (1998) Selective catalytic reduction of NO by NH3 over vanadium-containing zeolites. J Catal 175(1):48–61. https://doi.org/10.1006/jcat.1998.1974
14. Mejri I, Ayari F, Mhamdi M, Delahay G, Ksibi Z, Ghorbel A (2016) SCR of NO by NH3 catalyzed by Mo- and V-exchanged zeolite: effect of Mo precursor salt. Microporous and Mesoporous Materials 220:239–246. https://doi.org/10.1016/j.micromeso.2015.09.014
15. Pal N, Pramanik M, Bhaumik A, Ali M (2014) Highly selective and direct oxidation of cyclohexane to cyclohexanone over vanadium exchanged NaY at room temperature under solvent-free conditions. J Mol Catal A Chem 392:299–307. https://doi.org/10.1016/j.molcata.2014.05.027
16. Narayanan S, Sultana A (1998) Aniline alkylation with ethanol over zeolites and vanadium modified zeolites prepared by solid state exchange method. Appl Catal Gen 167(1):103–111. https://doi.org/10.1016/S0926-860X(97)00304-9
17. Garcia EM, Sanchez MD, Tonetto G, Volpe MA (2005) Preparation of USY zeolite supported catalysts from V(AcAc)3 and NH4VO3. Catalytic properties for the dehydrogenation of n-butane in oxygen-free atmosphere. J Colloid Interface Sci 292(1):179–185. https://doi.org/10.1016/j.jcis.2005.05.055
18. Habersberger K, Jíru P, Tvaruzková Z, Centi G, Trifirò F (1989) Synthesis of ZSM zeolites modified with vanadium and their application in the catalytic oxidation of butadiene. Reaction Kinetics and Catalysis Letters 39(1):95–100. https://doi.org/10.1007/bf02061861
19. Kornatowski J, Sychev M, Kuzenkov S, Strnadova K, Pilz W, Kassner D, Pieper G, Baur WH (1995) V-Ti and V-Al silicate molecular sieves of MFI topology: synthesis and characteristics. J Chem Soc Faraday Trans 91(14):2217–2227. https://doi.org/10.1039/FT9959102217
20. Ramaswamy AV, Sivasanker S, Ratnasamy P (1994) Selective oxidation reactions over metallosilicate molecular sieves: a comparison of titanium and vanadium silicates with MEL structure. Microporous Materials 2(5):451–458. https://doi.org/10.1016/0927-6513(94)00018-2
21. Reddy KM, Moudrakovski I, Sayari A (1994) VS-12: a novel large-pore vanadium silicate with ZSM-12 structure. J Chem Soc Chem Commun 12:1491–1492. https://doi.org/10.1039/C39940001491
22. Tuel A, Ben Taârit Y (1994) Synthesis and characterization of vanadium silicates with the ZSM-48 structure. Zeolites 14(1):18–24. https://doi.org/10.1016/0144-2449(94)90049-3
23. Chien SH (1997) Hydrothermal synthesis and characterization of the vanadium-containing zeolite beta. Zeolites 18(2–3):182–187. https://doi.org/10.1016/S0144-2449(96)00139-X

24. Miyamoto A, Medhanavyn D, Inui T (1986) Vanadosilicate catalysts prepared from different vanadium sources and their characteristics in methanol to hydrocarbon conversion. Applied Catalysis 28:89–103. https://doi.org/10.1016/S0166-9834(00)82495-1
25. Guo B, Zhu L, Hu X, Zhang Q, Tong D, Li G, Hu C (2011) Nature of vanadium species on vanadium silicalite-1 zeolite and their stability in hydroxylation reaction of benzene to phenol. Cat Sci Technol 1(6):1060–1067. https://doi.org/10.1039/C1CY00105A
26. Bellussi G, Rigutto MS (1994) Metal ions associated to the molecular sieve framework: possible catalytic oxidation sites. Stud Surf Sci Catal 85:177–213. https://doi.org/10.1016/S0167-2991(08)60768-5
27. Inui T, OY, Fukuda K, Itoh A, Tarumoto J, Morinaga N, Hagiwara T, Takegami Y (1984) Paper presented at the eighth international congress on catalysis, Berlin
28. Kornatowski J, Wichterlová B, Jirkovský J, Löfller E, Pilz W (1996) Spectroscopic studies of vanadium-substituted zeolitic silicates of MFI topology. J Chem Soc – Faraday Trans 92 (6):1067–1078. https://doi.org/10.1039/FT9969201067
29. Niederer JPM, Hölderich WF (2002) Oxidation capabilities of BEA isomorphously substituted with molybdenum, vanadium and titanium: an explorative study. Appl Catal Gen 229(1–2):51–64. https://doi.org/10.1016/S0926-860X(02)00015-7
30. Kim G-J, Cho D-S, Kim K-H, Ko W-S, Kim J-H, Shoji H (1995) Incorporation of vanadium into the mordenite structure by direct hydrothermal crystallization and secondary synthesis. Catal Lett 31(1):91–102. https://doi.org/10.1007/bf00817036
31. Dzwigaj S, Peltre MJ, Massiani P, Davidson A, Che M, Sen T, Sivasanker S (1998) Incorporation of vanadium species in a dealuminated β zeolite. Chem Commun 1:87–88. https://doi.org/10.1039/A704556E
32. Wojtaszek A, Ziolek M, Dzwigaj S, Tielens F (2011) Comparison of competition between T = O and T–OH groups in vanadium, niobium, tantalum BEA zeolite and SOD based zeolites. Chemical Physics Letters 514(1–3):70–73. https://doi.org/10.1016/j.cplett.2011.08.005
33. Wojtaszek A, Ziolek M, Tielens F (2012) Probing acid–base properties in group V aluminum containing zeolites. J Phys Chem C 116(3):2462–2468. https://doi.org/10.1021/jp208638k
34. Tielens F, Trejda M, Ziolek M, Dzwigaj S (2008) Nature of vanadium species in V substituted zeolites: a combined experimental and theoretical study. Catalysis Today 139 (3):221–226. https://doi.org/10.1016/j.cattod.2008.04.007
35. Tielens F, Calatayud M, Dzwigaj S, Che M (2009) What do vanadium framework sites look like in redox model silicate zeolites? Microporous and Mesoporous Materials 119 (1–3):137–143. https://doi.org/10.1016/j.micromeso.2008.10.007
36. Dzwigaj S, Matsuoka M, Franck R, Anpo M, Che M (1998) Probing different kinds of vanadium species in the VSiβ zeolite by diffuse reflectance UV−visible and photoluminescence spectroscopies. J Phys Chem B 102(33):6309–6312. https://doi.org/10.1021/jp981454+
37. Dzwigaj S, Matsuoka M, Anpo M, Che M (2000) Evidence of three kinds of tetrahedral vanadium(V) species in VSiβ zeolite by diffuse reflectance UV−visible and photoluminescence spectroscopies. J Phys Chem B 104(25):6012–6020. https://doi.org/10.1021/jp0000331
38. Trejda M, Wojtaszek A, Floch A, Wojcieszak R, Gaigneaux EM, Ziolek M (2010) New Nb and Ta–FAU zeolites – direct synthesis, characterisation and surface properties. Catalysis Today 158(1–2):170–177. https://doi.org/10.1016/j.cattod.2010.06.018
39. Trejda M, Wojtaszek A, Floch A, Wojcieszak R, Gaigneaux EM, Ziolek M (2010) Incorporation of group five elements into the faujasite structure. In: Gaigneaux EM, Devillers M, Hermans S, Jacobs PA, Martens JA, Ruiz P (eds) Scientific bases for the preparation of heterogeneous catalysts: proceedings of the 10th international symposium, vol 175. Studies in surface science and catalysis. Elsevier Science BV, Amsterdam, pp 445–448. https://doi.org/10.1016/s0167-2991(10)75081-3

40. Besselmann S, Freitag C, Hinrichsen O, Muhler M (2001) Temperature-programmed reduction and oxidation experiments with V2O5/TiO2 catalysts. Phys Chem Chem Phys 3 (21):4633–4638. https://doi.org/10.1039/B105466J
41. Gallastegi-Villa M, Aranzabal A, González-Marcos JA, González-Velasco JR (2016) Metal-loaded ZSM5 zeolites for catalytic purification of dioxin/furans and NOx containing exhaust gases from MWI plants: effect of different metal cations. Appl Catal Environ 184:238–245. https://doi.org/10.1016/j.apcatb.2015.11.006
42. Wachs IE (2013) Catalysis science of supported vanadium oxide catalysts. Dalton Trans 42 (33):11762–11769. https://doi.org/10.1039/C3DT50692D
43. Góra-Marek K, Datka J, Dzwigaj S, Che M (2006) Influence of V content on the nature and strength of acidic sites in VSiβ zeolite evidenced by IR spectroscopy. J Phys Chem B 110 (13):6763–6767. https://doi.org/10.1021/jp0582890
44. Trejda M, Ziolek M, Millot Y, Chalupka K, Che M, Dzwigaj S (2011) Methanol oxidation on VSiBEA zeolites: influence of V content on the catalytic properties. J Catal 281(1):169–176. https://doi.org/10.1016/j.jcat.2011.04.013
45. Wachs IE, Weckhuysen BM (1997) Structure and reactivity of surface vanadium oxide species on oxide supports. Appl Catal Gen 157(1):67–90. https://doi.org/10.1016/S0926-860X(97)00021-5
46. Putluru SSR, Riisager A, Fehrmann R (2010) Vanadia supported on zeolites for SCR of NO by ammonia. Appl Catal Environ 97(3–4):333–339. https://doi.org/10.1016/j.apcatb.2010.04.009
47. Ko YS, Ahn WS (1999) Synthesis and characterization of tantalum silicalite molecular sieves with MFI structure. Microporous and Mesoporous Materials 30(2–3):283–291. https://doi.org/10.1016/S1387-1811(99)00039-6
48. Li W, Luo L, Yamashita H, Labinger JA, Davis ME (2000) Synthesis and characterization of zeolite beta containing oxide clusters of antimony and vanadium. Microporous and Mesoporous Materials 37(1–2):57–65. https://doi.org/10.1016/S1387-1811(99)00193-6
49. Baran R, Millot Y, Onfroy T, Averseng F, Krafft J-M, Dzwigaj S (2012) Influence of the preparation procedure on the nature and environment of vanadium in VSiBEA zeolite: XRD, DR UV–vis, NMR, EPR and TPR studies. Microporous and Mesoporous Materials 161:179–186. https://doi.org/10.1016/j.micromeso.2012.05.023
50. Nowak I, Ziolek M (1999) Niobium compounds: preparation, characterization, and application in heterogeneous catalysis. Chem Rev 99(12):3603–3624. https://doi.org/10.1021/cr9800208
51. Wierzchowski PT, Zatorski LW (1991) Aldol condensation in gaseous phase by zeolite catalysts. Catal Lett 9(5):411–414. https://doi.org/10.1007/bf00764833
52. Chang YF, Somorjai GA, Heinemann H (1995) An 18O2 temperature-programmed isotope exchange study of transition-metal-containing ZSM-5 zeolites used for oxydehydrogenation of ethane. J Catal 154(1):24–32. https://doi.org/10.1006/jcat.1995.1142
53. Nowak I, MZ (1995) Paper presented at the 2nd Polish-German Zeolite Colloquium, Toruń
54. Ziolek M, Nowak I, Karge HG (1995) Solid-state interaction between niobium oxide and Y-type zeolites. Studies Surface Science and Catalysis 94:270–277. https://doi.org/10.1016/S0167-2991(06)81232-2
55. Romotowski T, Komorek J, Terskikh VV (1998) A contribution to ZSM-5 zeolite modified with niobia. Polish J Chem 72(12):2564–2572
56. Barros ICL, Braga VS, Pinto DS, de Macedo JL, Filho GNR, Dias JA, Dias SCL (2008) Effects of niobium addition on ZSM-5 studied by thermal and spectroscopy methods. Microporous and Mesoporous Materials 109(1–3):485–493. https://doi.org/10.1016/j.micromeso.2007.05.050
57. Cavalcanti RM, Barros ICL, Dias JA, Dias SCL (2013) Characterization of ZSM-5 modified with niobium pentoxide: the study of thiophene adsorption. J Braz Chem Soc 24:40–50. https://doi.org/10.1590/S0103-50532013000100007
58. de Brites-Nóbrega FF, Polo ANB, Benedetti AM, Leão MMD, Slusarski-Santana V, Fernandes-Machado NRC (2013) Evaluation of photocatalytic activities of supported

catalysts on NaX zeolite or activated charcoal. J Hazard Mater 263(Part 1):61–66. https://doi.org/10.1016/j.jhazmat.2013.07.061
59. Brites-Nóbrega FF, Lacerda IA, Santos SV, Amorim CC, Santana VS, Fernandes-Machado NRC, Ardisson JD, Henriques AB, Leão MMD (2015) Synthesis and characterization of new NaX zeolite-supported Nb, Zn, and Fe photocatalysts activated by visible radiation for application in wastewater treatment. Catalysis Today 240(Part A):168–175. https://doi.org/10.1016/j.cattod.2014.06.036
60. Reddy GR, Balasubramanian S, Chennakesavulu K (2015) Zeolite encapsulated active metal composites and their photocatalytic studies for rhodamine-B, reactive red-198 and chlorophenols. RSC Adv 5(99):81013–81023. https://doi.org/10.1039/C5RA13034D
61. Wojtaszek-Gurdak A, Ziolek M (2015) Nb and Zr modified MWW zeolites – characterisation and catalytic activity. RSC Adv 5(29):22326–22333. https://doi.org/10.1039/C5RA00411J
62. Prasetyoko D, Ramli Z, Endud S, Nur H (2005) Preparation and characterization of bifunctional oxidative and acidic catalysts Nb2O5/TS-1 for synthesis of diols. Mater Chem Phys 93 (2–3):443–449. https://doi.org/10.1016/j.matchemphys.2005.03.030
63. Prakash AM, Kevan L (1998) Synthesis of niobium silicate molecular sieves of the MFI structure: evidence for framework incorporation of the niobium ion. J Am Chem Soc 120 (50):13148–13155. https://doi.org/10.1021/ja982262v
64. Hartmann M, Prakash AM, Kevan L (2003) Characterization and catalytic evaluation of mesoporous and microporous molecular sieves containing niobium. Catalysis Today 78 (1–4):467–475. https://doi.org/10.1016/S0920-5861(02)00334-6
65. Bértolo R, Martins Â, Silva JM, Ribeiro F, Ribeiro FR, Fernandes A (2011) Incorporation of niobium in SAPO-11 materials: synthesis and characterization. Microporous and Mesoporous Materials 143(2–3):284–290. https://doi.org/10.1016/j.micromeso.2011.03.010
66. Dzwigaj S, Millot Y, Méthivier C, Che M (2010) Incorporation of Nb(V) into BEA zeolite investigated by XRD, NMR, IR, DR UV–vis, and XPS. Microporous and Mesoporous Materials 130(1–3):162–166. https://doi.org/10.1016/j.micromeso.2009.10.027
67. Kyriienko PI, Larina OV, Popovych NO, Soloviev SO, Millot Y, Dzwigaj S (2016) Effect of the niobium state on the properties of NbSiBEA as bifunctional catalysts for gas- and liquid-phase tandem processes. J Mol Catal A Chem 424:27–36. https://doi.org/10.1016/j.molcata.2016.06.024
68. Corma A, Llabrés i, Xamena FX, Prestipino C, Renz M, Valencia S (2009) Water resistant, catalytically active Nb and Ta isolated lewis acid sites, homogeneously distributed by direct synthesis in a beta zeolite. J Phys Chem C 113(26):11306–11315. https://doi.org/10.1021/jp902375n
69. Nchare M, Wang L, Anagho S (2016) Synthesis of NbFAPO-5 and NbFAPSO-5 molecular sieve by hydrothermal method and comparison of their XRD patterns and their acidic properties evaluation by infrared. Open J Inorg Chem 6(3):155–162. https://doi.org/10.4236/ojic.2016.63011
70. de la Torre O, Renz M, Corma A (2010) Biomass to chemicals: rearrangement of β-pinene epoxide into myrtanal with well-defined single-site substituted molecular sieves as reusable solid Lewis-acid catalysts. Appl Catal Gen 380(1–2):165–171. https://doi.org/10.1016/j.apcata.2010.03.056
71. Tielens F, Shishido T, Dzwigaj S (2010) What do the niobium framework sites look like in redox zeolites? A combined theoretical and experimental investigation. J Phys Chem C 114 (7):3140–3147. https://doi.org/10.1021/jp910956j
72. Sobczak I, Decyk P, Ziolek M, Daturi M, Lavalley J-C, Kevan L, Prakash AM (2002) Physicochemical properties and catalytic activity of Cu–NbZSM-5 – a comparative study with Cu–AlZSM-5. J Catal 207(1):101–112. https://doi.org/10.1006/jcat.2002.3510
73. Wojtaszek A, Sobczak I, Ziolek M (2012) NO adsorption combined with FTIR spectroscopy as a useful tool for characterization of niobium species in crystalline and amorphous molecular sieves. Catalysis Today 192(1):149–153. https://doi.org/10.1016/j.cattod.2011.11.009

74. Noronha FB, Schmal M, Moraweck B, Delichère P, Brun M, Villain F, Fréty R (2000) Characterization of niobia-supported palladium−cobalt catalysts. J Phys Chem B 104 (23):5478–5485. https://doi.org/10.1021/jp992777o
75. Ahón VR, Lage PLC, de Souza CDD, Mendes FM, Schmal M (2006) Kinetic rates of the fischer tropsch synthesis on a Co/Nb2O5 catalyst. J Nat Gas Chem 15(4):307–312. https://doi.org/10.1016/S1003-9953(07)60011-5
76. Mendes FMT, Uhl A, Starr DE, Guimond S, Schmal M, Kuhlenbeck H, Shaikhutdinov SK, Freund H-J (2006) Strong metal support interaction on Co/niobia model catalysts. Catal Lett 111(1):35–41. https://doi.org/10.1007/s10562-006-0127-6
77. Zhao Y, Choi B, Kim D (2017) Effects of Ce and Nb additives on the de-NOx performance of SCR/CDPF system based on Cu-beta zeolite for diesel vehicles. Chem Eng Sci 164:258–269. https://doi.org/10.1016/j.ces.2017.02.009
78. Seff K (2010) A general method for the ion exchange of zeolites utilizing the volatility of thallous compounds as leaving products. J Phys Chem C 114(31):13295–13299. https://doi.org/10.1021/jp101477k
79. Dzwigaj S, Millot Y, Che M (2010) Ta(V)-single site BEA zeolite by two-step postsynthesis method: preparation and characterization. Catal Lett 135(3):169–174. https://doi.org/10.1007/s10562-010-0284-5
80. Lim HS, Kim JY, Heo NH, Seff K (2016) Preparation, crystal structure, and luminescence properties of zeolite LTA containing extraframework tantalum(V), tantalum(II), thallium(I), and chloride. J Phys Chem C 120(22):12139–12148. https://doi.org/10.1021/acs.jpcc.6b03943
81. Boccuti MR, Rao KM, Zecchina A, Leofanti G, Petrini G (1989) Spectroscopic characterization of silicalite and titanium-silicalite. Stud Surf Sci Catal 48:133–144. https://doi.org/10.1016/S0167-2991(08)60677-1
82. Huybrechts DRC, Vaesen I, Li HX, Jacobs PA (1991) Factors influencing the catalytic activity of titanium silicalites in selective oxidations. Catal Lett 8(2):237–244. https://doi.org/10.1007/bf00764122
83. Breck DW (1974) Zeolite molecular sieves: structure, chemistry and use. Wiley, New York
84. Ruddy DA, Tilley TD (2008) Kinetics and mechanism of olefin epoxidation with aqueous H2O2 and a highly selective surface-modified TaSBA15 heterogeneous catalyst. J Am Chem Soc 130(33):11088–11096. https://doi.org/10.1021/ja8027313
85. Ginter DM, Bell AT, Radke CT (1992) In: Ocelli ML, Robson HE (eds) Synthesis of microporous materials: molecular sieves, vol 1. Van Nostrand Reinhold, New York
86. Kyriienko PI, Larina OV, Soloviev SO, Orlyk SM, Dzwigaj S (2016) High selectivity of TaSiBEA zeolite catalysts in 1,3-butadiene production from ethanol and acetaldehyde mixture. Cat Com 77:123–126. https://doi.org/10.1016/j.catcom.2016.01.023
87. Kim MH, Ko Y, Kim SJ, Uh YS (2001) Vapor phase Beckmann rearrangement of cyclohexanone oxime over metal pillared ilerite. Appl Catal Gen 210(1–2):345–353. https://doi.org/10.1016/S0926-860X(00)00818-8
88. Munakata H, Oumi Y, Miyamoto A (2001) A DFT study on peroxo-complex in titanosilicate catalyst: hydrogen peroxide activation on titanosilicalite-1 catalyst and reaction mechanisms for catalytic olefin epoxidation and for hydroxylamine formation from ammonia. J Phys Chem B 105(17):3493–3501. https://doi.org/10.1021/jp0022196
89. Dzwigaj S, Millot Y, Krafft J-M, Popovych N, Kyriienko P (2013) Incorporation of silver atoms into the vacant T-atom sites of the framework of SiBEA zeolite as mononuclear Ag(I) evidenced by XRD, FTIR, NMR, DR UV–vis, XPS, and TPR. J Phys Chem C 117 (24):12552–12559. https://doi.org/10.1021/jp401849e
90. Tielens F (2009) Exploring the reactivity of intraframework vanadium, niobium and tantalum sites in zeolitic materials using the molecular electrostatic potential. J Mol Struct (THEOCHEM) 903(1–3):23–27. https://doi.org/10.1016/j.theochem.2008.09.045
91. Tielens F (2009) Exploring the reactivity of framework vanadium, niobium, and tantalum sites in zeolitic materials using DFT reactivity descriptors. J Comput Chem 30 (12):1946–1951. https://doi.org/10.1002/jcc.21192

92. Tielens F, Shishido T, Dzwigaj S (2010) What do tantalum framework sites look like in zeolites? A combined theoretical and experimental investigation. J Phys Chem C 114 (21):9923–9930. https://doi.org/10.1021/jp102181m
93. Tielens F, Dzwigaj S (2010) Group V metal substitution in silicate model zeolites: in search for the active site. Chem Phys Lett 501(1–3):59–63. https://doi.org/10.1016/j.cplett.2010.10.038
94. Tielens F, Dzwigaj S (2010) Probing acid-base sites in vanadium redox zeolites by DFT calculation and compared with FTIR results. Catalysis Today 152(1–4):66–69. https://doi.org/10.1016/j.cattod.2009.09.006
95. Ziolek M (2004) Catalytic liquid-phase oxidation in heterogeneous system as green chemistry goal – advantages and disadvantages of MCM-41 used as catalyst. Catalysis Today 90 (1):145–150. https://doi.org/10.1016/j.cattod.2004.04.020
96. Arends IWCE, Sheldon RA (2001) Activities and stabilities of heterogeneous catalysts in selective liquid phase oxidations: recent developments. Appl Catal Gen 212(1–2):175–187. https://doi.org/10.1016/S0926-860X(00)00855-3
97. Sheldon RA, Arends IWCE, Lempers HEB (1998) Liquid phase oxidation at metal ions and complexes in constrained environments. Catalysis Today 41(4):387–407. https://doi.org/10.1016/S0920-5861(98)00027-3
98. Ziolek M, Sobczak I, Decyk P, Sobańska K, Pietrzyk P, Sojka Z (2015) Search for reactive intermediates in catalytic oxidation with hydrogen peroxide over amorphous niobium(V) and tantalum(V) oxides. Appl Catal Environ 164:288–296. https://doi.org/10.1016/j.apcatb.2014.09.024
99. Jian M, Zhu L, Wang J, Zhang J, Li G, Hu C (2006) Sodium metavanadate catalyzed direct hydroxylation of benzene to phenol with hydrogen peroxide in acetonitrile medium. J Mol Catal A Chem 253(1):1–7. https://doi.org/10.1016/j.molcata.2006.02.054
100. Wang J, Hu C, Jian M, Zhang J, Li G (2006) Catalytic oxidation performance of the α-Keggin-type vanadium-substituted heteropolymolybdates: a density functional theory study on [PVnMo12−nO40](3+n)− (n = 0–3). J Catal 240(1):23–30. https://doi.org/10.1016/j.jcat.2006.03.005
101. Dimitrova R, Spassova M (2007) Hydroxylation of benzene and phenol in presence of vanadium grafted Beta and ZSM-5 zeolites. Cat Com 8(4):693–696. https://doi.org/10.1016/j.catcom.2006.03.019
102. Dimitrova R, Neinska Y, Mihályi M, Pal-Borbély G, Spassova M (2004) Reductive solid-state ion exchange as a way to vanadium introduction in BZSM and BBeta zeolites. Appl Catal Gen 266(1):123–127. https://doi.org/10.1016/j.apcata.2004.02.001
103. Jorda E, Tuel A, Teissier R, Kervennal J (1998) Synthesis, characterization, and activity in the epoxidation of cyclohexene with aqueous H2O2 of catalysts prepared by reaction of TiF4with silica. J Catal 175(1):93–107. https://doi.org/10.1006/jcat.1998.1982
104. Kholdeeva OA, Trubitsina TA, Timofeeva MN, Maksimov GM, Maksimovskaya RI, Rogov VA (2005) The role of protons in cyclohexene oxidation with H2O2 catalysed by Ti (IV)-monosubstituted Keggin polyoxometalate. J Mol Catal A Chem 232(1):173–178. https://doi.org/10.1016/j.molcata.2005.01.036
105. Nowak I, Kilos B, Ziolek M, Lewandowska A (2003) Epoxidation of cyclohexene on Nb-containing meso- and macroporous materials. Catalysis Today 78(1):487–498. https://doi.org/10.1016/S0920-5861(02)00332-2
106. Kilos B, Aouine M, Nowak I, Ziolek M, Volta JC (2004) The role of niobium in the gas- and liquid-phase oxidation on metallosilicate MCM-41-type materials. J Catal 224(2):314–325. https://doi.org/10.1016/j.jcat.2004.03.002
107. Ziolek M, Decyk P, Sobczak I, Trejda M, Florek J, Klimas HGW, Wojtaszek A (2011) Catalytic performance of niobium species in crystalline and amorphous solids – gas and liquid phase oxidation. Appl Catal Gen 391(1):194–204. https://doi.org/10.1016/j.apcata.2010.07.022
108. Tuel A (1995) Synthesis, characterization, and catalytic properties of titanium silico-aluminophosphate TAPSO-5. Zeolites 15(3):228–235. https://doi.org/10.1016/0144-2449(94)00036-R

109. Corma A, Camblor MA, Esteve P, Martinez A, Perezpariente J (1994) Activity of Ti-Beta catalyst for the selective oxidation of alkenes and alkanes. J Catal 145(1):151–158. https://doi.org/10.1006/jcat.1994.1017
110. Rigutto MS, van Bekkum H (1993) Vanadium site in VAPO-5: characterization and catalytic properties in liquid-phase alkene epoxidation and benzylic oxidation. Journal of Molecular Catalysis 81(1):77–98. https://doi.org/10.1016/0304-5102(93)80024-O
111. Bregante DT, Priyadarshini P, Flaherty DW (2017) Kinetic and spectroscopic evidence for reaction pathways and intermediates for olefin epoxidation on Nb in *BEA. J Catal 348:75–89. https://doi.org/10.1016/j.jcat.2017.02.008
112. Gao H, Lu G, Suo J, Li S (1996) Epoxidation of allyl chloride with hydrogen peroxide catalyzed by titanium silicalite 1. Appl Catal Gen 138(1):27–38. https://doi.org/10.1016/0926-860X(95)00276-6
113. Morlanes N, Notestein JM (2010) Kinetic study of cyclooctene epoxidation with aqueous hydrogen peroxide over silica-supported calixarene–Ta(V). Appl Catal Gen 387(1):45–54. https://doi.org/10.1016/j.apcata.2010.07.063
114. Morlanés N, Notestein JM (2010) Grafted Ta–calixarenes: tunable, selective catalysts for direct olefin epoxidation with aqueous hydrogen peroxide. J Catal 275(2):191–201. https://doi.org/10.1016/j.jcat.2010.07.010
115. Sudhakar Reddy J, Liu P, Sayari A (1996) Vanadium containing crystalline mesoporous molecular sieves Leaching of vanadium in liquid phase reactions. Appl Catal Gen 148 (1):7–21. https://doi.org/10.1016/S0926-860X(96)00222-0
116. Whittington BI, Anderson JR (1993) Nature and activity of some vanadium catalysts. J Phys Chem 97(5):1032–1041. https://doi.org/10.1021/j100107a010
117. Haanepen MJ, Elemans-Mehring AM, van Hooff JHC (1997) VAPO as catalyst for liquid phase oxidation reactions. Part II: Stability of VAPO-5 during catalytic operation. Appl Catal Gen 152(2):203–219. https://doi.org/10.1016/S0926-860X(96)00349-3
118. Bolm C (2003) Vanadium-catalyzed asymmetric oxidations. Coord Chem Rev 237 (1):245–256. https://doi.org/10.1016/S0010-8545(02)00249-7
119. Fuerte A, Iglesias M, Sánchez F, Corma A (2004) Chiral dioxomolybdenum(VI) and oxovanadium(V) complexes anchored on modified USY-zeolite and mesoporous MCM-41 as solid selective catalysts for oxidation of sulfides to sulfoxides or sulfones. J Mol Catal A Chem 211(1–2):227–235. https://doi.org/10.1016/j.molcata.2003.10.013
120. Maurya MR, Chandrakar AK, Chand S (2007) Zeolite-Y encapsulated metal complexes of oxovanadium(VI), copper(II) and nickel(II) as catalyst for the oxidation of styrene, cyclohexane and methyl phenyl sulfide. J Mol Catal A Chem 274(1–2):192–201. https://doi.org/10.1016/j.molcata.2007.05.018
121. Ziolek M, Sobczak I, Trejda M (2011) The role of niobium in heterogeneous catalysis-selected aspects. Niobium: properties, production and application. Nova Science, New York, pp 1–46
122. Haber J (1997) In: Ertl G, Knözinger H, Weitkamp J (eds) Handbook of heterogeneous catalysis, vol 5. Wiley, Weinheim
123. Cavani F, Ballarini N, Cericola A (2007) Oxidative dehydrogenation of ethane and propane: how far from commercial implementation? Catalysis Today 127(1):113–131. https://doi.org/10.1016/j.cattod.2007.05.009
124. Chen K, Khodakov A, Yang J, Bell AT, Iglesia E (1999) Isotopic tracer and kinetic studies of oxidative dehydrogenation pathways on vanadium oxide catalysts. J Catal 186(2):325–333. https://doi.org/10.1006/jcat.1999.2510
125. Chen K, Bell AT, Iglesia E (2000) Kinetics and mechanism of oxidative dehydrogenation of propane on vanadium, molybdenum, and tungsten oxides. J Phys Chem B 104(6):1292–1299. https://doi.org/10.1021/jp9933875
126. Chalupka K, Thomas C, Millot Y, Averseng F, Dzwigaj S (2013) Mononuclear pseudo-tetrahedral V species of VSiBEA zeolite as the active sites of the selective oxidative dehydrogenation of propane. J Catal 305:46–55. https://doi.org/10.1016/j.jcat.2013.04.020

127. Dźwigaj S, Gressel I, Grzybowska B, Samson K (2006) Oxidative dehydrogenation of propane on VSiβ catalysts. Catalysis Today 114(2–3):237–241. https://doi.org/10.1016/j.cattod.2006.02.022
128. Julbe A, Farrusseng D, Jalibert JC, Mirodatos C, Guizard C (2000) Characteristics and performance in the oxidative dehydrogenation of propane of MFI and V-MFI zeolite membranes. Catalysis Today 56(1–3):199–209. https://doi.org/10.1016/S0920-5861(99)00277-1
129. Luo L, Labinger JA, Davis ME (2001) Comparison of reaction pathways for the partial oxidation of propane over vanadyl ion-exchanged zeolite beta and Mo1V0.3Te0.23Nb0.12Ox. J Catal 200(2):222–231. https://doi.org/10.1006/jcat.2001.3214
130. Tatibouët JM (1997) Methanol oxidation as a catalytic surface probe. Appl Catal Gen 148 (2):213–252. https://doi.org/10.1016/S0926-860X(96)00236-0
131. Briand LE, Jehng J-M, Cornaglia L, Hirt AM, Wachs IE (2003) Quantitative determination of the number of surface active sites and the turnover frequency for methanol oxidation over bulk metal vanadates. Catalysis Today 78(1):257–268. https://doi.org/10.1016/S0920-5861(02)00350-4
132. Busca G, Elmi AS, Forzatti P (1987) Mechanism of selective methanol oxidation over vanadium oxide-titanium oxide catalysts: a FT-IR and flow reactor study. J Phys Chem 91 (20):5263–5269. https://doi.org/10.1021/j100304a026
133. Khaliullin RZ, Bell AT (2002) A density functional theory study of the oxidation of methanol to formaldehyde over vanadia supported on silica, titania, and zirconia. J Phys Chem B 106 (32):7832–7838. https://doi.org/10.1021/jp014695h
134. Tranca DC, Keil FJ, Tranca I, Calatayud M, Dzwigaj S, Trejda M, Tielens F (2015) Methanol oxidation to formaldehyde on VSiBEA zeolite: a combined DFT/vdW/transition path sampling and experimental study. J Phys Chem C 119(24):13619–13631. https://doi.org/10.1021/acs.jpcc.5b01911
135. Nakajima F (1991) Air pollution control with catalysis -past, present and future. Catalysis Today 10(1):1–20. https://doi.org/10.1016/0920-5861(91)80070-P
136. Fränkle G, Held W, Hosp W, Knecht W, Hofmann L, Mathes W, Neufert R, Zürbig J (1997) VDI-Ber, Ser 12:306–365
137. Adams RC, Xu L, Moller K, Bein T, Delgass WN (1997) Zeolite encapsulated vanadium oxo species for the catalytic reduction of NO by NH3. Catalysis Today 33(1):263–278. https://doi.org/10.1016/S0920-5861(96)00154-X
138. Baran R, Onfroy T, Grzybek T, Dzwigaj S (2013) Influence of the nature and environment of vanadium in VSiBEA zeolite on selective catalytic reduction of NO with ammonia. Appl Catal Environ 136–137:186–192. https://doi.org/10.1016/j.apcatb.2013.02.014
139. Lavat A, Quincoces CE, González MG (2005) Preparation and characterization of VO-ZSM5 catalyst for the selective reduction of NO with ammonia. Mater Lett 59(24–25):2986–2989. https://doi.org/10.1016/j.matlet.2005.04.049
140. Mhamdi M, Ghorbel A, Delahay G (2009) Influence of the V + Mo/Al ratio on vanadium and molybdenum speciation and catalytic properties of V–Mo–ZSM-5 prepared by solid-state reaction. Catalysis Today 142(3–4):239–244. https://doi.org/10.1016/j.cattod.2008.07.026
141. Piehl G, Liese T, Grünert W (1999) Activity, selectivity and durability of VO–ZSM-5 catalysts for the selective catalytic reduction of NO by ammonia. Catalysis Today 54 (4):401–406. https://doi.org/10.1016/S0920-5861(99)00203-5
142. Ramachandran B, Herman RG, Choi S, Stenger HG, Lyman CE, Sale JW (2000) Testing zeolite SCR catalysts under protocol conditions for NOx abatement from stationary emission sources. Catalysis Today 55(3):281–290. https://doi.org/10.1016/S0920-5861(99)00252-7
143. Miyamoto A, Yamazaki Y, Hattori T, Inomata M, Murakami Y (1982) Study on the pulse reaction technique. J Catal 74(1):144–155. https://doi.org/10.1016/0021-9517(82)90018-5
144. Philippou A, Brandão P, Ghanbari-Siahkali A, Dwyer J, Rocha J, Anderson MW (2001) Catalytic studies of the novel microporous niobium silicate AM-11. Appl Catal Gen 207 (1–2):229–238. https://doi.org/10.1016/S0926-860X(00)00623-2

145. Kyriienko PI, Larina OV, Soloviev SO, Orlyk SM, Calers C, Dzwigaj S (2017) Ethanol conversion into 1,3-butadiene by the lebedev method over MTaSiBEA zeolites (M = Ag, Cu, Zn). ACS Sustain Chem Eng 5(3):2075–2083. https://doi.org/10.1021/acssuschemeng.6b01728
146. Rocha J, Brandao P, Phillippou A, Anderson MW (1998) Synthesis and characterisation of a novel microporous niobium silicate catalyst. Chem Commun 24:2687–2688. https://doi.org/10.1039/A808264B
147. Makshina EV, Dusselier M, Janssens W, Degreve J, Jacobs PA, Sels BF (2014) Review of old chemistry and new catalytic advances in the on-purpose synthesis of butadiene. Chem Soc Rev 43(22):7917–7953. https://doi.org/10.1039/C4CS00105B
148. Possato LG, Chaves TF, Cassinelli WH, Pulcinelli SH, Santilli CV, Martins L (2017) The multiple benefits of glycerol conversion to acrolein and acrylic acid catalyzed by vanadium oxides supported on micro-mesoporous MFI zeolites. Catalysis Today 289:20–28. https://doi.org/10.1016/j.cattod.2016.08.005
149. Silva TQ, dos Santos MB, Santiago AAC, Santana DO, Cruz FT, Andrade HMC, Mascarenhas AJS (2017) Gas phase glycerol oxidative dehydration over bifunctional V/H-zeolite catalysts with different zeolite topologies. Catalysis Today 289:38–46. https://doi.org/10.1016/j.cattod.2016.08.011
150. Marschall R, Wang L (2014) Non-metal doping of transition metal oxides for visible-light photocatalysis. Catalysis Today 225:111–135. https://doi.org/10.1016/j.cattod.2013.10.088
151. Lam S-M, Sin J-C, Satoshi I, Abdullah AZ, Mohamed AR (2014) Enhanced sunlight photocatalytic performance over Nb2O5/ZnO nanorod composites and the mechanism study. Appl Catal Gen 471:126–135. https://doi.org/10.1016/j.apcata.2013.12.001
152. Brites FF, Santana VS, Fernandes-Machado NRC (2011) Effect of support on the photocatalytic degradation of textile effluents using Nb2O5 and ZnO: photocatalytic degradation of textile dye. Topics in Catalysis 54(1):264–269. https://doi.org/10.1007/s11244-011-9657-2
153. Matsuoka M, Anpo M (2003) Local structures, excited states, and photocatalytic reactivities of highly dispersed catalysts constructed within zeolites. J Photochem Photobiol C Photchem Rev 3(3):225–252. https://doi.org/10.1016/S1389-5567(02)00040-0
154. Higashimoto S, Matsuoka M, Zhang SG, Yamashita H, Kitao O, Hidaka H, Anpo M (2001) Characterization of the VS-1 catalyst using various spectroscopic techniques and its unique photocatalytic reactivity for the decomposition of NO in the absence and presence of C3H8. Microporous and Mesoporous Materials 48(1):329–335. https://doi.org/10.1016/S1387-1811(01)00349-3
155. Anpo M, Higashimoto S, Matsuoka M, Zhanpeisov N, Shioya Y, Dzwigaj S, Che M (2003) The effect of the framework structure on the chemical properties of the vanadium oxide species incorporated within zeolites. Catalysis Today 78(1–4):211–217. https://doi.org/10.1016/S0920-5861(02)00339-5
156. Anpo M, Kim T-H, Matsuoka M (2009) The design of Ti-, V-, Cr-oxide single-site catalysts within zeolite frameworks and their photocatalytic reactivity for the decomposition of undesirable molecules – the role of their excited states and reaction mechanisms. Catalysis Today 142(3–4):114–124. https://doi.org/10.1016/j.cattod.2008.11.006
157. Tanaka T, Takenaka S, Funabiki T, Yoshida S (1994) 4.18 photocatalytic oxidation of ethanol over tantalum oxide supported on silica. Stud Surf Sci Catal 90:485–490. https://doi.org/10.1016/S0167-2991(08)61863-7
158. Nash MJ, Rykov S, Lobo RF, Doren DJ, Wachs I (2007) Photocatalytic activity of vanadium-substituted ETS-10. J Phys Chem C 111(19):7029–7037. https://doi.org/10.1021/jp067259+

Struct Bond (2018) 178: 251–304
DOI: 10.1007/430_2018_25

Published online: 30 June 2018

Metal-Substituted Microporous Aluminophosphates

Gopinathan Sankar and Manuel Sánchez-Sánchez

Abstract This chapter aims to present the zeotypes aluminophosphates (AlPOs) as a complementary alternative to zeolites in the isomorphic incorporation of metal ions within all-inorganic microporous frameworks as well as to discuss didactically the catalytic consequences derived from the distinctive features of both frameworks. It does not intend to be a compilation of either all or the most significant publications involving metal-substituted microporous aluminophosphates. Families of AlPOs and zeolites, which include metal ion-substituted variants, are the dominant microporous materials. Both these systems are widely used as catalysts, in particular through aliovalent metal ions substitution. Here, some general description of the synthesis procedures and characterization techniques of the MeAPOs (metal-contained aluminophosphates) is given along with catalytic properties. Next, some illustrative examples of the catalytic possibilities of MeAPOs as catalysts in the transformation of the organic molecules are given. The oxidation of the hardly activated hydrocarbons has probably been the most successful use of AlPOs doped with the divalent transition metal ions Co^{2+}, Mn^{2+}, and Fe^{2+}, whose incorporation in zeolites is disfavoured. The catalytic role of these MeAPOs is rationalized based on the knowledge acquired from a combination of the most advanced characterization techniques. Finally, the importance of the high specificity of the structure-directing agents employed in the preparation of MeAPOs is discussed taking *N,N*-methyldicyclohexylamine in the synthesis of AFI-structured materials as a driving force. It is shown how such a high specificity could be predicted and how it can open great possibilities in the control of parameters as critical in catalysis as crystal size, inter- and intracrystalline mesoporosity, acidity, redox properties, incorporation of a great variety of heteroatom ions or final environment of the metal site (surrounding it by either P or Al).

G. Sankar (✉)
Department of Chemistry, University College London, London, UK
e-mail: g.sankar@ucl.ac.uk

M. Sánchez-Sánchez (✉)
Instituto de Catálisis y Petroleoquímica (ICP), CSIC, Madrid, Spain
e-mail: manuel.sanchez@icp.csic.es

Keywords Air oxidation of hydrocarbons · Aluminophosphates · Divalent transition metals · Heterogeneous catalysis · Structure-directing agents

Contents

1 Microporous Crystalline AlPOs

Since the discovery of natural zeolites [1], more than two and a half centuries ago, these materials were considered as crystalline aluminium-containing tectosilicates having pores of molecular dimension. The definition continues to exist, even today, with more than 230 different zeolite structures that have been identified [2, 3]. Any of the three mentioned key properties of zeolites, i.e. crystallinity, molecular-size porosity (microporosity) and aluminosilicate composition, has been extensively studied and exceeded. In this context, it is particularly highlighted the alteration in composition, primarily due to the incorporation of numerous heteroatom ions, other than Si^{4+} and/or Al^{3+}, into the zeolitic frameworks. As a consequence of such heteroatom incorporation, Ti-zeolites [4], B-zeolites [5], V-zeolites [6], Zr-zeolites [7], Sn-zeolites [8], Fe-zeolites [9, 10], Ga-zeolites [10], Ge-zeolites [11] and other heteroatom-zeolites [12–14] have been investigated widely. All of them have SiO_4 tetrahedra as the basic and more abundant unit, they do not necessarily contain Al, and the heteroatom ions are part of the zeolite framework occupying tetrahedral sites. The incorporation of these metallic heteroatoms within the zeolitic framework is not limited to an academic exercise but allows these materials to reach new industrial catalytic applications [12]. In this sense, in previous chapters of this issue, countless examples of applications of metal-zeolites, particularly focused on the field of heterogeneous catalysis, which are unable to be reached by their counterpart metal-free zeolites, have been presented.

In metal-zeolites, the metal is almost always a dopant in terms of its loadings against that of the predominant Si. Al^{3+} is the only heteroatom ion able to be quantitatively closer to Si in certain zeolites, including in the natural ones. However, there are other inorganic oxide-based materials, which are also crystalline and possess microporosity, but they are not based on SiO_2 [15, 16]. In addition, some of these materials are closely related to zeolites in critical properties as their microporous crystalline structures or their thermal/hydrothermal stability. All these similarities led to name these materials as zeotypes, denoting the various likenesses with the zeolites family and, at the same time, highlighting that they are not zeolites. Nevertheless, it is quite common to even refer them as zeolites [17–19].

Therefore, zeotypes can be defined as materials that have crystalline and microporous frameworks having similar physical and chemical properties of aluminosilicate zeolites but whose atoms at the tetrahedral sites are not silicon or aluminium, e.g. cobalt phosphate [20] zincophosphate [21], beryllophosphate [21] aluminophosphates [22, 23], nickel phosphates [24], gallium phosphates [25] or beryllium hydroxides [26], among many others. Microporous frameworks based on metal phosphates are particularly abundant [27]. Among these zeotypes, the microporous aluminophosphates, also known as AlPOs ($AlPO_4$ or simply AlPO in singular) have been the most investigated for so many reasons. Firstly, they were the first described zeotypes [22, 23], and indeed the term zeotype was introduced to integrate $AlPO_4$ materials within the 'zeolite world'. Besides, they have thermal stability quite similar to that found in zeolites and much higher than most of other zeotypes. Like pure SiO_2 zeolites, in the absence of heteroatom ions, they are neutral and isoelectronic with zeolites since the sum of the formal charges of an Al^{3+} ion and a P^{5+} ion, which are strictly alternated in an $AlPO_4$ framework, is equal to the charge of two contiguous Si^{4+} ions in a zeolite. Moreover, many of the $AlPO_4$-based materials have common topologies with zeolites [2, 3]. Finally, and maybe the most important reason, AlPOs have contributed the family of microporous materials that expand the structures and the (catalytic) applications of zeolites. The following three cases are excellent examples. (1) Until the relatively recent discovery of ITQ-33 [28] and ITQ-37 [29], the $AlPO_4$ material known as VPI-5 [30] (IZA three-letter code VFI [2, 3]) allowed zeolitic family to 'boast' of pore entrances as large as 12 Å through an 18-R pore (rings having 18 tetrahedral atoms plus 18 oxygens). (2) The implantation of several industrial plants to produce olefins from methanol in the very recent years in China [31, 32] is a first but important starting point to reduce the undesired energetic and chemical dependency of petroleum, and such process is catalysed by the Si-doped small-pore $AlPO_4$-34, the so-called SAPO-34. (3) The possibility of direct incorporation of divalent transition metal ions in the Al positions of a $AlPO_4$ material, which is not obvious in zeolites because it implies a charge balance problem, led to materials such as CoAPOs, MnAPOs, ZnAPOs, etc. [33, 34], some of which resulted active as catalysts in the direct oxidation of the low-reactive hydrocarbons with oxygen [35–37]. Precisely the latter is closely related to both the scope and the focus of this issue in general and this present chapter in particular.

Apart from these selected examples, AlPOs as zeotypes can contribute with singular features, hardly found in zeolites. Table 1 summarizes some of these singularities of AlPOs compared to the corresponding properties of conventional zeolites, thinking in terms of their ability to incorporate heteroatoms and their catalytic applications.

In spite of the significant similarities between AlPOs and zeolites, Table 1 makes clear that both families of microporous materials have very different behaviour in various aspects either directly or indirectly related to the incorporation of transition metal ions within their frameworks. Next, the different properties compiled in Table 1 will be developed more extensively.

1.1 Hydrophilicity/Hydrophobicity

Hydrophilicity/hydrophobicity of solid materials is a key parameter in several industrial applications but becomes even more important if the material is used taking advantage of their porosity. A way to measure this parameter is through water adsorption isotherms (Fig. 1a [38]). $AlPO_4$ frameworks, which provide water isotherms either type I with sorption equilibrium at relatively high relative pressure or type V (Fig. 1b [39]), are much more hydrophilic than SiO_2 frameworks (type VII isotherms). However, the Al-rich zeolites give isotherms type I with equilibrium reached at low pressures and are much more hydrophilic than AlPOs (Fig. 1b [39]). This is because SiO_2 framework is neutral, whereas the notable hydrophilicity of low Si/Al ratio zeolites is due to their negatively charged framework and to the presence of charge-compensating extra-framework cations, whose nature is controllable by its ion exchange capacity [38]. The huge hydrophilicity/hydrophobicity range given by zeolites allows them to find applications in fields as diverse as water adsorption (the hydrophilic zeolites) or certain catalytic oxidation of organic molecules in liquid phase (generally requiring hydrophobic zeolites). The medium hydrophilicity of

Table 1 Comparison of some properties between conventional zeolites and $AlPO_4$ zeotypes

Property	Zeolites	AlPOs
Hydrophilic/hydrophobic character	Hydrophobic (tuned to hydrophilic co-incorporating Al)	Hydrophilic
pH of the synthesis gel	Basic	Acidic-neutral
Predominant SDA nature	Quaternary ammonium	Amines
Phase specificity of SDAs	Medium	Low
Incorporable oxidation state	3+ and 4+	from 2+ to 5+
Framework charge	No (if Al-free)	No
Known topologies	200+	ca. 50
Proportion of 1D topologies[a]	25%	40%

[a]Percentage of 1D topologies with respect to the whole known structures. In the case of AlPOs, only the structures able to be prepared as a non-doped $AlPO_4$ form have been considered

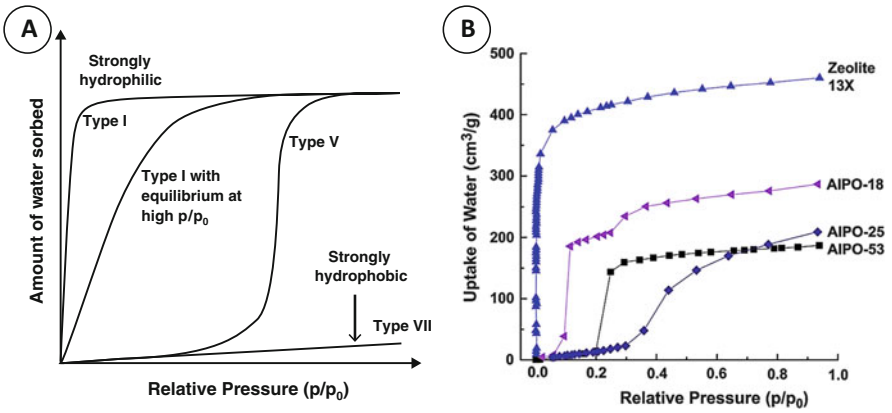

Fig. 1 (**a**) Models of water sorption isotherms of four nanoporous solids with different degrees of hydrophilicity. Adapted from Microporous Mesoporous Mater, 114, E. P. Ng et al., Nanoporous materials with enhanced hydrophilicity and high water sorption capacity, 1–26, Copyright 2007, with permission from Elsevier [38]. (**b**) Experimental water adsorption isotherms of various narrow pore AlPOs at 293 K, compared with the zeolite 13X. Reproduced from Ref. [39] with permission of The Royal Society of Chemistry

AlPOs [38], which is difficult to be tuned, becomes a drawback when compared to zeolites in any of these applications.

Nevertheless, as mentioned previously in this chapter, AlPOs can be doped by certain heteroatom ions, mainly divalent or tetravalent ones, whose introduction into the framework makes these materials negatively charged. Like Al-containing zeolites, these charged AlPOs can be potentially ion exchanged to enhance their hydrophilic character [40]. However, this strategy is far from reaching the hydrophilic character of zeolites due to two important limitations. It is difficult to incorporate high loadings of heteroatoms in AlPOs similar to Al in zeolites, which could reach Si/Al ratio as low as 1; Si is the heteroatom that can be incorporated at highest concentration in AlPOs, but when concentrated, it tends to form SiO_2 islands where only part of the incorporated Si introduces charge in the $AlPO_4$ framework. Indeed, the amount of isolated Si incorporated is theoretically limited to around 12.5% of the tetrahedral (P) sites [41, 42], far from the 50% of Al found in zeolites with a Si/Al ratio of 1. Microporous Co-rich aluminophosphates have also been reported [43]. These materials are cobalt phosphates doped with Al, but, to the best of our knowledge, they are not stable when the organic structure-directing agent is removed and lose its porosity because of their low stability to calcination. As a consequence, the ion exchange in AlPOs has been less investigated and could hardly provide any real contribution to the hydrophilic-related applications of Al-zeolites.

In any case, making the AlPOs hydrophobic, which would be them closer to zeolites for certain catalytic applications of interest in this chapter, is intrinsically avoided by their own aluminophosphate nature. On the contrary, the already-hydrophobic Al-free zeolites can become even more hydrophobic by changing the

conventional synthesis mineralizing agent OH- by a fluoride medium, which allows the preparation of zeolites free of hydrophilic Si-OH defects [44, 45].

1.2 pH of the Synthesis

pH value of the starting gels is undoubtedly one of the most determinant parameters in controlling the kinetics of the zeolite crystallization but also in terms of the nature of the crystallized phase(s), the amount of defects, the Si/Al ratio, etc. [46]. The synthesis of conventional zeolites, which are prepared in OH^- media, is carried out at very alkaline pH, commonly covering the pH range of 10–13. As an alternative to OH^- as the mineralizing agent, F^- can be also used for the preparation of zeolites at lower pHs, between 7 and 12, which result in practically a defect-free form [45].

The synthesis of AlPOs can be carried out starting from gels of pH values in the range 3–10, although the most common pHs are acid, between 3 and 7. From gels with pH below 3, normally dense (i.e. non-porous) phases such as tridymite, cristobalite or $AlPO_4$ hydrated are formed [47]. Thinking in terms of incorporation of metal ions within these two microporous frameworks, it is convenient to be aware of the existence of the different thermodynamically stable metal species in aqueous solution along the all pH range. Figure 2 shows the Pourbaix diagram of cobalt as an example. Pourbaix diagrams map out the possible stable (equilibrium) phases of a metal as a function of pH and electrochemical potential of the solution [48]. In aqueous solution, the stable species are these included between the oblique dashed dotted lines denoted as ‘a’ and ‘b’, which delimits the oxidation and reduction voltage potentials of water. Like most transition metal, cobalt is soluble at low pH. In particular, cobalt is stable as soluble Co^{2+} in the pH range from -2 to around 9. Above pH 9, Co is found in a solid form, either as $Co(OH)_3$ or mainly as $Co(OH)_2$. It implies that, in aqueous solution and in the absence of any other chemical species, the most stable Co species (and in general any transition metal species) are different at the typical pH of the synthesis of zeolites (9–13) and at that of the synthesis of AlPOs (3–7). It is presumably that this fact has a strong influence on the way in which transition metal ions are incorporated in zeolites or in the zeotypes AlPOs, beyond the environmental and/or crystallographic restriction intrinsically imposed by each framework. In our opinion, this aspect has not been addressed with enough clarity in the literature yet.

1.3 Nature and Phase Specificity of Structure-Directing Agents

Generally speaking, the most conventional structure-directing agents of the zeolites are alkaline hydroxides for low Si/Al zeolites and quaternary ammonium hydroxides

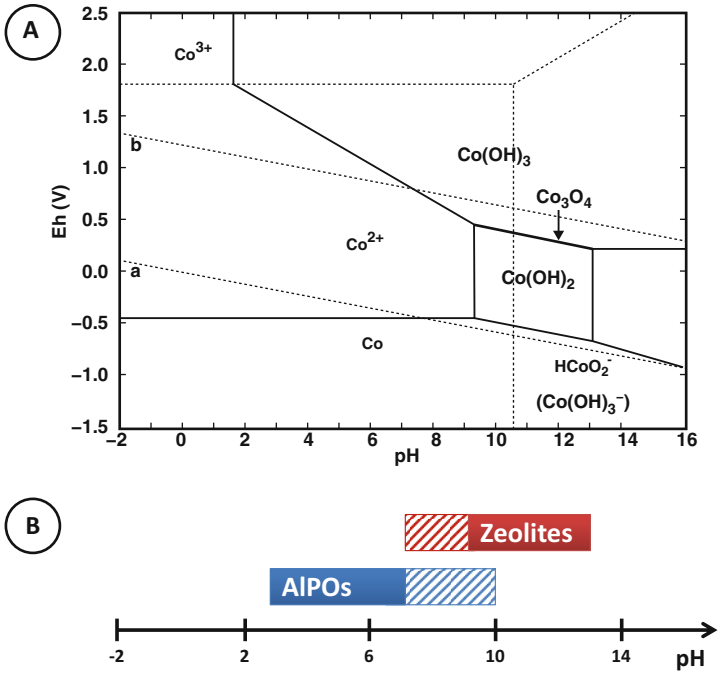

Fig. 2 (**a**) Pourbaix diagram of cobalt. The thermodynamically stable species in aqueous solution are these found between the segment delimiting by dotted lines **a** and **b**. (**b**) Scheme of the pH range at which zeolites (red region) and AlPOs (blue region) are normally prepared. The stripped region represents pHs at which AlPOs (blue) and zeolites (red) can also be prepared beyond conventional pHs

for high Si/Al zeolites [49, 50], whereas amines are the most preferred structure-directing agents (SDAs) for AlPOs [51]. That observation finds so many exceptions in the literature. The most evident one is that AlPOs can be prepared with quaternary ammonium hydroxides [52, 53] and zeolites can be prepared with certain amines [54, 55]. The reason behind the extensive use of either inorganic or organic hydroxides in the synthesis of zeolites and the less basic amines for the synthesis of AlPOs is evidently related to the required pH by the silica- or aluminophosphate-based materials to be crystallized (Fig. 2).

Table 2 compiles the nature of the SDAs most frequently used in the preparation of different AlPOs/MeAPOs. The prevalence of amines as SDA of AlPOs is marked form Table 2. On the other hand, the large number of organic molecules able to direct the crystallization of certain AlPOs, particularly these having AFI and AEL topologies, indicates that in general amines has low phase specificity. As an example, 23 different organic SDA were reported to direct the crystallization of $AlPO_4$-5 in 1983 [56], just 1 year after $AlPO_4$ materials were patented [22]. Similarly, some amines like DPA are able to direct the crystallization of several $AlPO_4$-based materials with different topology [57–59]. The specificity of organic SDA in zeolites

Table 2 $AlPO_4$ materials accepted by IZA and their homologues doped with heteroatom ions

nD[a]	MR[b]	IZA code[c]	$AlPO_{4-n}$[d]	Incorporated Me[e]	SDA[f]
1D	18R	VFI	VPI-5/ $AlPO_4$-54	None, Co, Mg, Mn, Ti, Fe, Cr, V	None, DPA, TBAOH
	14R	AET	$AlPO_4$-8	None, Mn	By heating VPI-5
	12R	AFI	$AlPO_4$-5	None, Co, Zn, Mg, Mn, Ti, Fe, Cr, Ni, V, Cu, Mo, Sn, Zr, Ca, Sr, Ba, Be, Ge, Li, Ce, Cd, Ru	TEA, TEAOH, TPA, TPAOH, MCHA and 50+ more amines
		ATO	$AlPO_4$-31	None, Co, Zn, Mg, Mn, Ti, Cr, V, Cu, Cd	DPA, DBA, DPentA, DHA, HMI
		ATS	$AlPO_4$-36	None, Co, Zn, Mg, Mn, Ti, Fe, V, Be, Ga	TPA, ECHA, DPBA
		SAF	STA-15	None	TPAOH
	10R	AEL	$AlPO_4$-11	None, Co, Zn, Mg, Mn, Ti, Fe, Cr, Ni, V, Cu, Nb, As, Be, Ge, Cd	DPA, DiPA, DiBA and a few more
		AFO	$AlPO_4$-41	None, Co, Mn, Ti, V, Zr	DPA, DiPA, DiPFA, DEA, DBA, DPentA,
		JRY	CoAPO-CJ40	Co, Zn, Mn, Fe	DEA
		AHT	$AlPO_4$-H2	None	None
	8R	ATN	$AlPO_4$-39	None, Co, Zn, Mg	DPA, DiBA
		ATV	$AlPO_4$-25	None, Co	By heating $AlPO_4$-21
		AWW	$AlPO_4$-22	None	HMTA, HMI, MDEA, DDO
2D	12R	AFR[g]	$AlPO_4$-40	None, Co, Zn	TPAOH (+ TMAOH)
		SBE[g]	UCSB-8Co	Co, Zn, Mg, Mn	DAN
		SFO[g]	SSZ-51	None, Co	DMAP
	8R	AEN	$AlPO_4$-EN3/−53	None, Co, Mn, Cu	MA, DMA
		AFV	$AlPO_4$-57	Zn, Mg	DEDMA
		APC	$AlPO_4$-C	None, Co	By heating $AlPO_4$-H3
		APD	$AlPO_4$-D	None	By heating $AlPO_4$-C
		ATT	$AlPO_4$-33	None	TMAOH
		AVL	$AlPO_4$-59	Zn, Mg	ETMA
		AWO	$AlPO_4$-21	None	EA, pyrrolidine, TEA, PA, MDEA, etc.
		LEV	$AlPO_4$-35/ −67	None, Co, Zn, Mg	HEM, TrOH, DABCO, ETMA, DEDMA, MCA
		OWE	ACP-2/ UiO-28	Co, Mg	DET
		ZON	ZnAPO-M1	None, Co, Zn, Mg	TMAOH
3D	12R	AFS[g]	$AlPO_4$-46	Co, Zn, Mg, Mn, Ni	DPA
		AFY[g]	$AlPO_4$-50	Co, Zn, Mg, Mn	DPA
		DFO[g]	DAF-1	Co, Mg, Ni	DMOH
		FAU	$AlPO_4$-37	Co, Zn	TPAOH + TMAOH
		SAO	STA-1	Zn, Mg	BPM, BP
		SBS	UCSB-6	Co, Zn, Mg, Mn	DAH
		SBT	UCSB-10	Co, Zn, Mg	TTD
	8R	AEI	$AlPO_4$-18	None, Co, Zn, Mg, Mn, Ti, Fe, Ni, V, As, Ge, Ga	TEA, TEAOH, DiPE
		AFN	$AlPO_4$-14	None, Co, Zn, Mg, Mn, Cr,	PDA, DABCO, iPA, tBA

(continued)

Table 2 (continued)

nD[a]	MR[b]	IZA code[c]	$AlPO_{4-n}$[d]	Incorporated Me[e]	SDA[f]
		AFT	$AlPO_4$-52	None	TEAOH + DPA
		AFX	$AlPO_4$-56	Co, Mn, Zr	TMHD
		ANA	$AlPO_4$-24	None, Co	Na+, Cs+
		CHA	$AlPO_4$-34	None, Co, Zn, Mg, Mn, Fe, Cr, Ni, Cu, Be, Li	TEAOH, TEA, DPA, DEA, MA and others
		DFT	DAF-2	Co	EDA
		EDI	Edingtonite	Co	1,2-DAP
		ERI	$AlPO_4$-17	None, Co, Mg, Fe	Q, NPA, CA, piperidine
		GIS	$AlPO_4$-43	None, Co, Zn, Mg	DPA
		LTA	$AlPO_4$-42	None, Co, Zn, Mg, Mn, Fe	TMAOH + Na+
		MER	Merlinoite	Co	DMA
		PHI	DAF-8	Co, Zn	DACH
		RHO	Rho	Co, Mg, Mn	DiPPD
		SAT	STA-2	Mg	BQNB
		SAV	Mg-STA-7	Co, Zn, Mg	tmtact, hmhaco
		SIV	SIZ-7	Co	EMIm
		THO	Thomsonite	Co	MEDA

The dimensionality of their pore system, the number of tetrahedral atoms in their largest ring, their common names and the structure-directing agents are also given. Si has been discarded as heteroatom ion as it is out of the scope of this chapter

Organic SDA abbreviations: *DPA* *n*-dipropylamine, *TBAOH* tetrabutylammonium hydroxide, *TEA* trimethylamine, *TEAOH* triethylammonium hydroxide, *TPA* tripropylamine, *TPAOH* tetrapropylammonium hydroxide, *MCHA* *N*-methyldicyclohexylamine, *DBA* *n*-dibutylamine, *DPentA* *n*-dipentylamine, *DHA* *n*-dihexylamine, *HMI* hexamethyleneimine, *ECHA* *N*-ethyldicyclohexylamine, *DPBA* *N,N*-diisopropylisobutylamine, *DiPA* diisopropylamine, *DiPFA* diisopropylformamide, *DEA* diethylamine, *DiBA* diisobutylamine, *HMTA* hexamethylenetetramine, *MDEA* *N*-methyldiethanolamine, *DDO* *N,N′*-dimethyl-1,4-diazabicyclo(2.2,2) octane dihydroxide, *TMAOH* Tetramethylammonium hydroxide, *DAN* 1,9-diaminononane, *DMAP* 2- or 4-dimethylaminopyridine, *MA* methylamine, *DMA* dimethylamine, *DEDMA* diethyldimethylammonium, *ETMA* ethyltrimethylammonium, *EA* ethanolamine, *PA* *n*-propylamine, *MEA* *N*-methylethanolamine, *TrOH* tropine hydroxide, *DABCO* triethylenediamine, *MCA* 2-methylcyclohexylamine, *DET* diethylenetriamine, *DMOH* decamethonium hydroxide, *BMP* (S)-(−)-*N*-benzylpyrrolidine-2-methanol, *BP* benzylpyrrolidine, *DAH* 1,7-diaminoheptane, *TTD* 4,7,10-trioxa-1,13-tridecane diamine, *DiPE* *N,N*-diisopropylethylamine, *PDA* 1,3-propyldiamine, *iPA* isopropylamine, *tBA* tert-butylamine, *TMHD* *N,N,N′,N′*-tetramethyl-hexane-1,6-diamine, *EDA* ethylenediamine, *1,2-DAP* 1,2-diaminopropane, *Q* quinuclidine, *NPA* neopentylamine or 2,2-dimetil-1-propanamina, *CA* cyclohexylamine, *DACH* 1,4-diaminocylcohexane, *DiPPD* *N,N′*-diisopropyl-1,3-propanediamine, *BQNB* 1,4-bis-*N*-quinuclidiniumbutane, *tmtact* 1,4,8,11-tetramethyl-1,4,8,11-tetraaza cyclotetradecane, *hmhaco* 1,4,7,10,13,16-hexamethyl-1,4,7,10,13,16-hexaazacyclooctadecane, *EMIM* 1-methyl-3-ethylimidazolium, *MEDA* *N*-methylethylenediamine

[a]Dimension of the pore system

[b]Number of tetrahedral atoms in their largest ring

[c]Three-letter code given by IZA [2, 3]

[d]Common names. The name following the format '$AlPO_{4-n}$' is preferred

[e]The term 'None' indicates the possibility to prepare the material in the non-doped $AlPO_4$ form

[f]Structure-directing agent or any other strategy used in the preparation of the material. The term 'None' indicates the possibility of preparing the corresponding material in the absence of any SDA

[g]Structure having extra micropore(s) with lesser number of tetrahedral members (10R or 8R). For details, see Refs. [2, 3]

is normally much higher, in spite of their role was reduced from the ambitious concept of 'template' to the simple SDAs some decades ago [49]. The importance of the specificity and the efficiency of a given SDA towards a particular topology is

made clear in a below section of this chapter expressly dedicated to that subject (Sect. 5).

1.4 Heteroatoms Incorporable into $AlPO_4$ Frameworks and Their Structure-Directing Role

In an all-silica zeolite framework, all atoms in the tetrahedral coordination are tetravalent Si^{4+}. That Al-free zeolite is hydrophobic and does not have any overall charge. Practically all applications of zeolites are based on the partial substitution of Si by other heteroatoms, which provide acid/redox centres, basicity, hydrophilicity, ion exchange capacity, etc. The isomorphic substitution of a Si^{4+} by a tetravalent ion such as Ti^{4+}, Zr^{4+} or Sn^{4+} does not alter the neutrality of the framework. However, the incorporation of Al^{3+} ions isomorphically substituting Si^{4+} entails the introduction of a negative charge, which has to be compensated by a cation, commonly a protonated SDA molecule, a proton H^+, alkaline or alkaline earth cations. Similarly, the incorporation of a pentavalent ion, for instance, P^{5+}, would positively charge the framework, and the presence of an extra-framework anion would be required. To the best of our knowledge, the latter substitution (P or any other pentavalent ion by Si^{4+} one) has not been reported in the literature. In this sense, it has been noted that introduction of phosphate ions in the zeolite MFI synthesis gel seems to assist the crystallization process, but no evidence for P incorporation has been seen [60]. The incorporation of divalent atom instead of a Si^{4+} ion has been also attempted, but either two monovalent extra-framework cations or a divalent one must be present to compensate the double charge of the framework associated to the incorporation of a divalent ion. In spite of the incorporation of divalent cations in zeolites that has been described [61–64], this is far from being a widespread strategy, and the heteroatom incorporation in zeolites is reduced, for practical purposes, to tri- and tetravalent ions.

Since the aluminophosphate framework consist of alternating P^{5+} and Al^{3+} ions, the possible oxidation states of the incorporated heteroatoms are significantly expanded. Figure 3 shows various mechanisms (MS) of heteroatom substitutions, as well as the subsequent charge modification of the framework, if any, as a function of the oxidation state, covering from 2+ to 5+ ions. These mechanisms are in principle easy to achieve in an $AlPO_4$ framework, contrasting with the limited oxidation states of metal ions within a SiO_2 framework (3+ or 4+, Table 1). Similar to the divalent heteroatom incorporation in zeolite framework described in some particular cases [61–64], the incorporation of monovalent ions into $AlPO_4$ frameworks has also been claimed [65, 66].

Apart from the evident improvement in terms of versatility of incorporable oxidation states, Fig. 3 makes clear that two further important distinctions are found in AlPOs in comparison with zeolites. Firstly, the incorporation mechanisms of a given heteroatom (and then also its final environment within the $AlPO_4$

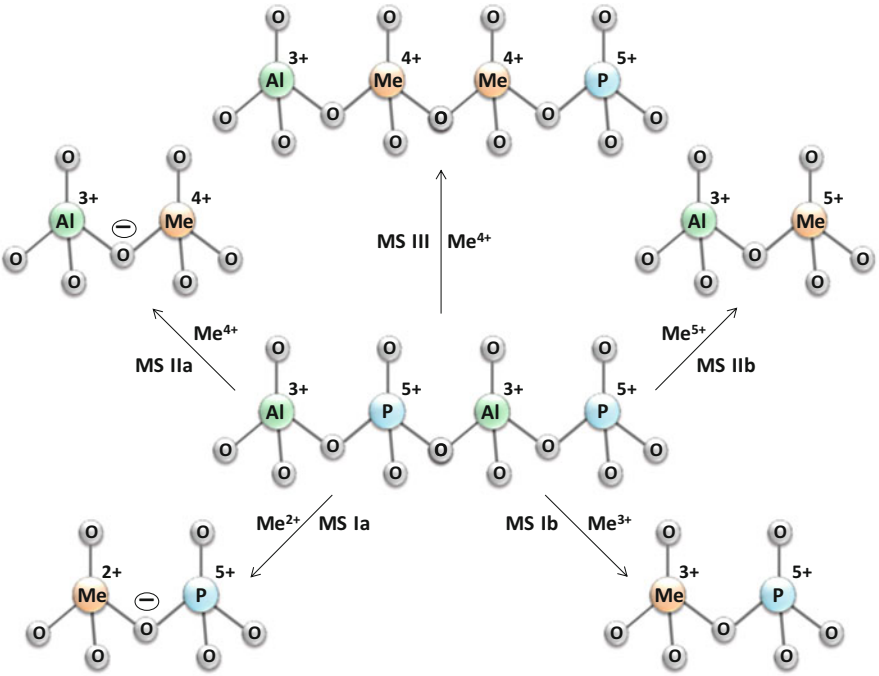

Fig. 3 Mechanisms of substitution of heteroatoms with oxidation states 2+, 3+, 4+ and 5+ into an $AlPO_4$ framework

framework) cannot be always predicted by just knowing their oxidation state. This is particularly true for tetravalent ions, which can provide up to three different incorporation mechanisms (MS IIa, MS III and the substitution of Me^{4+} by Al^{3+} ions, which has not been considered in Fig. 3 because its existence has not been proved in AlPOs) or a combination of them in different degree. Such MS variety for tetravalent ions has been developed by Si^{4+}, giving rise to very different environments including isolated Si (by MS IIa) and a notable variety of SiO_2 islands (by combination of MS III and MS IIa mechanisms) (Fig. 4). The environment of each Si atom shown in Fig. 4 has strong influence on its acidity and then on its catalytic potential. Any incorporated Si surrounded at least by an Al atom in the first tetrahedral coordination sphere gives an acidic site. The acidity of these sites increases in the order: $Si(OSi)_3(OAl) > Si(OSi)_2(OAl)_2 > Si(OSi)(OAl)_3 > Si(OAl)_4$ [67], the latter being formed by the isolated incorporation of a Si^{4+} ion substituting a P^{5+} ion (MS IIa, Fig. 3). So, the whole acidity of the SAPO catalysts (number and strength of their sites) with a given Si content is controlled by the size of the SiO_2 islands [68]. On the contrary, Si^{4+} atoms in $Si(OSi)_4$ environments within zeolite-like SiO_2 islands have no acidic properties at all; therefore, one may consider the incorporation of such Si^{4+} as heteroatom is useless as they do not provide any net catalytic site, although they can catalytically contribute in some other ways such as to increase hydrophobicity of the catalyst [69], to tune the acidity of other acidic Si sites beyond the isolated Si

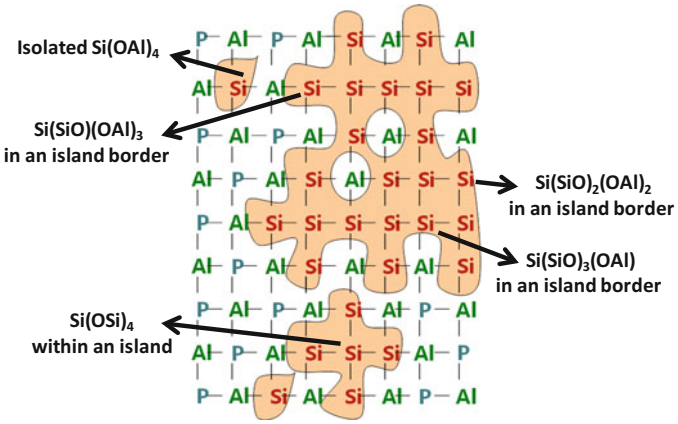

Fig. 4 Different Si environments in an $AlPO_4$ framework formed by diverse combinations of heteroatom incorporation mechanisms MS IIa and MS III (Fig. 3). The orange regions indicate the Si islands. Oxygen atoms, which are present between two consecutives tetrahedral atoms (P, Al or Si), are omitted for clarity

sites $Si(OAl)_4$ [42] or to improve thermal stability of the material [70]. Despite that diversity of environments has been exclusively attributed to the Si^{4+} ion during decades, the recent certification of the existence of Ti-O-Ti in TAPO materials [71] evidenced that such incorporation complexity is extendable to other tetravalent dopants.

Secondly, irrespective of its oxidation state, the incorporation of a given heteroatom ion has different consequences in terms of framework charge of zeolites and $AlPO_4$ zeotypes. For instance, if the incorporation of trivalent heteroatoms is the normal way to introduce charge (and then acidity, hydrophilicity, etc.) in zeolite frameworks, the same heteroatom incorporated into AlPOs does not alter the neutrality of the framework. It implies that the incorporation of a given heteroatom is never strictly comparable in both frameworks, as different breaking and/or preserving of neutrality will be certainly found in both systems.

Whilst previous sections showed the importance of organic structure-directing agent or pH of the starting gel in directing specific structures, it is also reported in literature that certain incorporated heteroatom ions along with the SDA can direct specific microporous structures. This is particularly true for $AlPO_4$-based materials as illustrated in Fig. 5. It has been found that 1,2-diaminocyclohexane produces a highly crystalline layered material in the absence of any divalent cations that substitutes Al^{3+}. However, the introduction of ca. 30% of divalent metal ions in Al^{3+} sites, in particular cobalt or zinc, produces a material with chabazite structure [72]. Likewise, 1,4-diaminocyclohexane, which produces a layered material very similar to that formed from 1,2-diaminocyclohexane in the absence of any dopant, promotes the formation of a three-dimensional microporous materials with PHI structure when a divalent metal ion such as Co^{2+} or Zn^{2+} is introduced in the synthesis gel [72]. It has been also observed that the heteroatom cation concentration

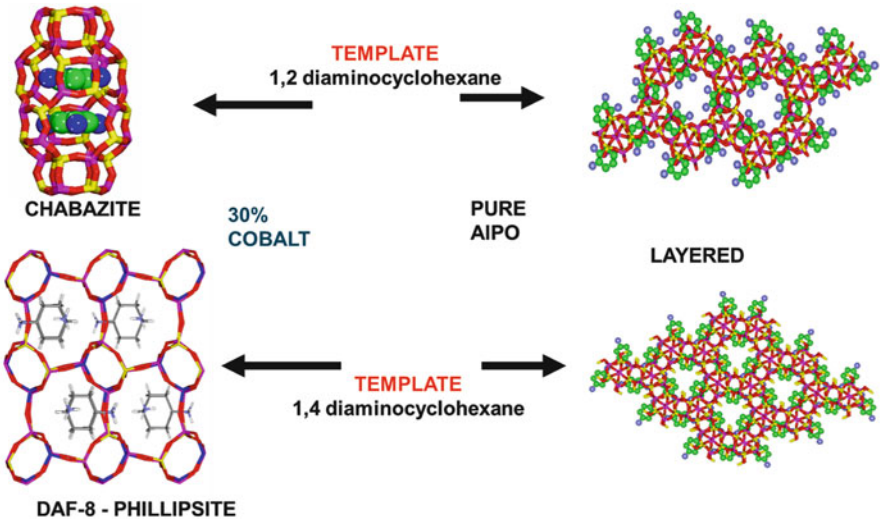

Fig. 5 Effect of the presence of divalent ions Co^{2+} in tilting the structure direction from a layered $AlPO_4$ material to a 3D microporous Co-doped aluminophosphates system

can tilt the formation of CHA over AEI structure (both having highly related topologies [2, 3]) when TEAOH is used in conjunction with Co^{2+} ions in the synthesis gel [73].

Other strong structure-directing role by an ion is found in the system AFI/CHA in the presence/absence of Zn^{2+} ion, whose role has been clarified through molecular interactions [52]. Similar effect has been also observed under ionothermal conditions, in particular by the presence of either V (introduced as V^{3+}, V^{4+} or V^{5+}) or Ti^{4+} ions, which favour the crystallization of CHA-structured materials to the detriment of AEL ones [74].

These examples and many others in the literature make clear the outstanding structure-directing effect given by certain heteroatom ions in the $AlPO_4$ systems, generally characterized by a low phase specificity. Since this section focuses on the distinctness of zeotypes AlPOs versus zeolites, it must be highlighted that some heteroatom ions also possess a notable capacity to direct the formation of zeolites with particular structures. In this aspect, two of the most relevant ions are Ge^{4+} [11] and Zn^{2+} [61–63].

1.5 $AlPO_4$ Topologies: The Abundance of 1D Pore Systems

$AlPO_4$-based microporous materials with around 50 different topologies have been prepared (Table 2). Therefore, the versatility is more than acceptable, considering that they cover all range of (1) microporosity, as there are AlPOs with small pores

(channels of eight-membered rings, 8R), medium pores (10R), large pores (12R) or extra-large pores (>12R); (2) pore dimensionality, with 1D, 2D or 3D pore systems; and (3) the presence of either simple pores or pores plus (super-)cavities [2, 3]. In addition, there are so many topologies able to be prepared as AlPOs and as zeolites, which allows comparison and systematic studies. Even though, the versatility is far from reaching that of zeolites, since more than 230 topologies of the latter have been described and accepted by IZA [2, 3].

On the other hand, the non-doped $AlPO_4$ materials have marked tendency to crystallize as 1D-pore topologies. In particular, among the topologies prepared so far as pure $AlPO_4$ (which are marked as 'None' in the column 'Incorporated Me' in Table 2), 40% of them has unidirectional pore systems. It must be noted that only 25% of the known zeolite frameworks has 1D pore system [2, 3]. Moreover, the most investigated $AlPO_4$-based materials, $AlPO_4$-5 (AFI), $AlPO_4$-11 (AEL) and VPI-5 (VFI), possess such pore arrangement and can be prepared with so many organic SDAs. Then, one can deduce that the phase specificity of these SDAs is quite weak. Indeed, VPI-5 can even be prepared without any organic SDA [75] as water molecules arranged in a triple helix act as the real structure-directing agent [76]. When amines or quaternary ammonia are added to the synthesis media, they would have certain role in the nucleation/crystal growth processes (mainly through pH control), but they are not found within the large (18R) VFI pores, indicating their negligible templating role [30]. The presence of heteroatom ions having certain structure-directing role often favours the formation of 3D-topology MeAPO materials versus 1D-topology ones, as above explained [72–74]. It must be also highlighted the difficulty of preparing zeolitic materials having these topologies: AEL and VFI have not been described, whereas the AFI-structured zeolite SSZ-24 was described after the discovery of $AlPO_4$-5. In the same sense, the preparation of non-doped $AlPO_4$ materials having typical zeolite structure with 3D pore systems is rather hard. The emblematic FAU topology in zeolites has only been prepared as $AlPO_4$-based form when they are doped with Si^{4+} [77], Co^{2+} [78, 79] or Zn^{2+} [79] and using a combination of SDAs, whereas the highly demanded CHA-structured SAPO-34 materials for the use of SAPO-34 in MTO process [32] can only be prepared as pure $AlPO_4$ under very restrictive conditions including the use of HF [17, 80]. Nevertheless, it must be pointed out that these two low-dense cage-contained zeolites FAU and CHA are also difficult to be prepared in the non-doped SiO_2 form [81], suggesting that their preparation is favoured by the negative charge of the framework irrespective of their silica or aluminophosphate forms.

From a catalytic point of view, topologies with 1D pore systems possess inherent drawbacks when compared with the 3D ones, due to both the diffusional problems of chemicals [82] and the quicker deactivation of the catalysts [83] found in the former.

Fortunately, the introduction of heteroatom ions to lead MeAPOs increases the percentage of 2D and 3D topologies to that found for zeolites (Table 2).

2 General Aspects of the Synthesis of AlPOs

Almost all microporous aluminophosphate-based systems are synthesized using an organic structure-directing agent (SDA) (Table 2). In a typical synthesis, appropriate stoichiometric amounts of aluminium source (aluminium hydroxide hydrate and pseudoboehmite are two of the most popular sources, but other aluminium compounds such as aluminium isopropoxide have also been investigated), phosphoric acid, water, metal salts if necessary and the SDA are taken and mixed in a specific order to create a gel; the order of addition needs to be optimized for specific synthesis of a given structure and composition. Similarly, the pH of the gel needs to be adjusted to obtain phase pure of a specific structure. The prepared gel is introduced in a Teflon-lined autoclave and heated to specific temperatures for several hours to days depending on the system. A typical schematic diagram showing the general approach used in microporous aluminophosphates synthesis is shown in Fig. 6. A selection of aluminophosphate-based systems as well as the SDAs used to produce them is listed in Table 2. It has been noted that, although SDA is used for producing specific structured material, in many instances, other structures are favoured depending on the pH of the starting gel, temperature and time of reaction. Even the co-crystallization of more than one $AlPO_4$-based is quite often. Figure 7 shows a representation of such effect based on different systematic studies [84–86].

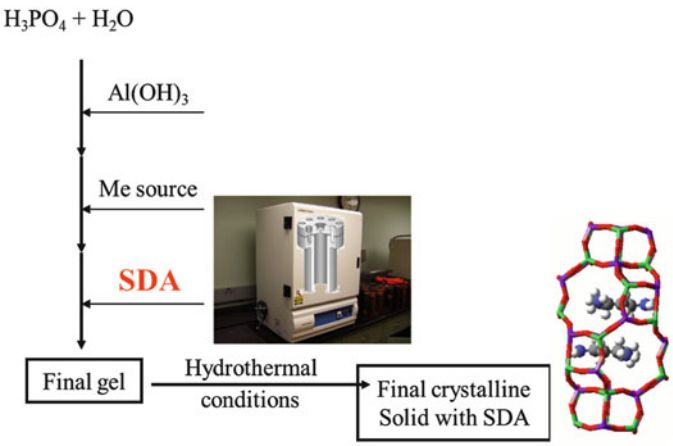

Fig. 6 A schematic diagram of a typical synthesis of (heteroatom-doped) aluminophosphate material. *SDA* structure-directing agent, typically an organic amine or ammonium hydroxide templates. Macrocycle-based metal complexes and multi-templating approaches have also been used in many cases [86, 87]

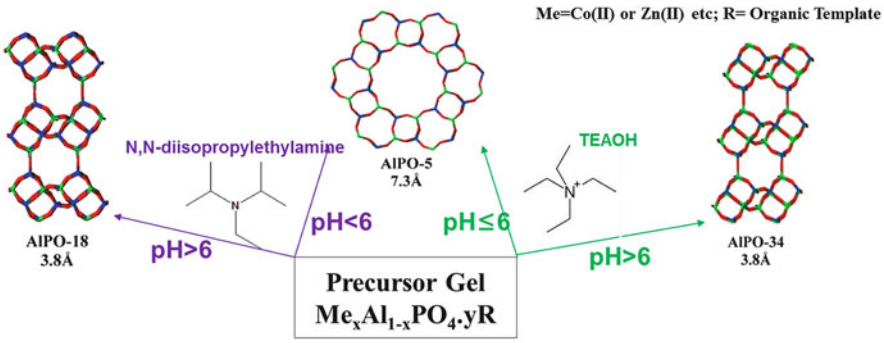

Fig. 7 Scheme of the competitive formation behaviour of two structures that are formed using the same template and temperature. The control of pH of the starting gel is shown to be important to produce specific structure [85, 88]

3 Characterization of the Metal Sites Incorporated Within AlPOs

To characterize aluminophosphates in general and heteroatom-substituted systems in particular, a range of techniques are used. The main reasons of such variety of available characterization methods are as follows: (1) the complete characterization of a solid (catalyst) includes so different aspects as crystalline structure, chemical composition, chemical/thermal stability, porosity, surface area, chemical environment of Al, P and dopants, morphology crystal size, acidity/redox strength, etc.; (2) the $AlPO_4$-based materials possess great variety of topology and composition; (3) the active centres used as dopants are normally found in low loadings; (4) the different characterization techniques give complementary information; and (5) each technique has some limitations.

3.1 Structural Characterization

As these materials are highly crystalline with ordered arrangement of atoms, X-ray diffraction is the primary technique used to determine (a) phase purity of the prepared systems, (b) lattice parameters (by simple Rietveld analysis using a method known as Le Bail method) and (c) complete structure solution using Rietveld analysis by providing an initial structure and refining structural parameters such as atom positions, occupancies, temperature factors, etc. to obtain the best match between experimental and calculated diffraction pattern from the refined structure [89–92]. In some cases, when the initial structure is not available or not well-defined,

many other combinations of methods, in particular molecular modelling methods or electron microscopic methods, were used to provide initial structural information and further refined using powder diffraction data to obtain more accurate structures of the synthesized materials [90, 93–96]. Whilst powder diffraction is used routinely as obtaining well-defined single crystals of certain size is difficult in many aluminophosphates systems, in some instances, single crystals could be obtained, and hence single crystal diffraction methods are used here. With advent of micro-crystal diffraction methods, it is now possible to obtain high-quality data of crystals as small as 10 μm or less in a synchrotron radiation source [97]. At the same time, one grain in a large batch of sample with a crystal used for structure solution may not provide the confidence that entire powder has the same material and structure. It is best to carry out powder diffraction of the same material with multiple crystalline parts and use the structure obtained from single crystal diffraction as the starting structure to ensure the entire powder can be modelled with this structure. Figure 8 shows the structure obtained from combined single crystal and powder diffraction of the same DAF-5 material (CHA structure, synthesized using a computationally determined SDA, 4,4, piperidinopiperidine) proving that entire powder pattern can be modelled with the structure determined from single crystal diffraction [98]. Powder diffraction of the as-synthesized materials alone is not sufficient as it is required to calcine the material to remove the organic template for many applications. Therefore, it is strongly recommended to carry out powder diffraction of calcined material to ensure the structure has not changed in the process of heating the sample. Ideally, one should use in situ methods or to avoid exposing the calcined material to

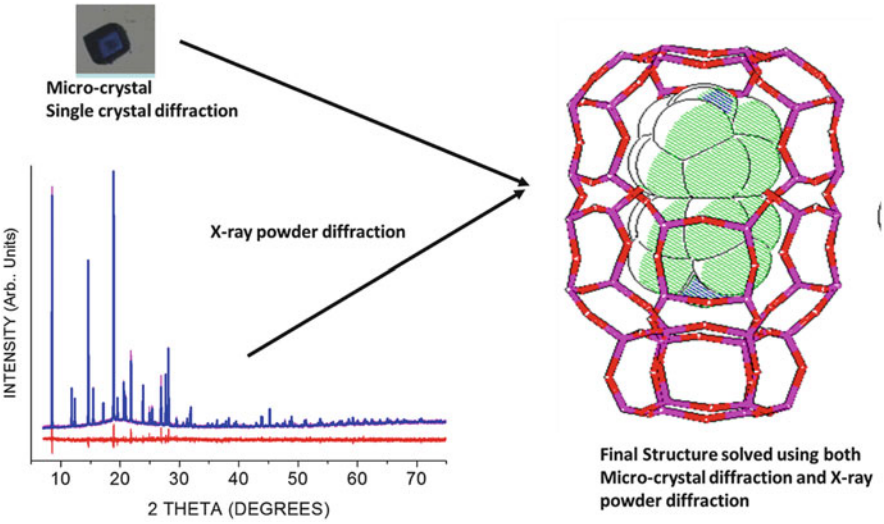

Fig. 8 Scheme structure solved using microcrystal diffraction methods using station 9.8 at Daresbury laboratory and subsequently verified using high-resolution powder diffraction recorded at station 2.3 at Daresbury laboratory of DAF-5, a CoAPO-34 material synthesized using computationally designed organic SDA [98]

atmosphere (dry state) to prevent any post-calcination interactions with atmosphere, especially water molecules, as these materials are hydrophilic and this interaction can distort the structure of calcined material.

Although X-ray diffraction provides unique structural details, in particular atomic architecture, pore distribution, template location and in some cases if the heteroatom is ordered enough their possible site location and occupancies, often the technique fail to produce the location of heteroatoms located in the T-site. Some of the reasons are that they may not be ordered and also that in the majority of the cases, the concentration of the metal ions is too small to show any effect. However, Simmance et al. [99, 100] indeed show that there are specific lattice expansions in certain directions, in cobalt- and zinc-substituted aluminophosphates. Despite this observation, it is difficult to determine the local structure of the substituted metal ions unless a more specific local structural tool is used, specifically adaptable to systems with low concentrations of heteroatoms. NMR is ideal, but accessing such nuclei is difficult. X-ray absorption spectroscopy is another preferred technique as it is a local structural technique and element specific, which is discussed later.

3.2 *Characterization of Heteroatoms Incorporated in $AlPO_4$ Frameworks*

High-resolution solid-state ^{27}Al and ^{31}P NMR have been extensively used to understand the local environment of the framework and extra-framework ions. However, most of the studies are limited to pure $AlPO_4$ materials or those doped with non-paramagnetic heteroatom ions, like Si^{4+}, Mg^{2+} or Zn^{2+}. The presence of paramagnetic dopants does not only avoid the NMR-based study of the heteroatoms themselves, but it also avoids to study the sample itself. In spite of significant effort made by Tuel et al. [101, 102] recording ^{31}P NMR spectra of CoAPO materials over an extended acquisition window, this technique is far from being able to be applied routinely in conventional laboratory-based NMR instruments. They detected different $P(Co_n,Al_{4-n})$ $(0 \geq n \geq 4)$ environments separated by several thousands of ppm. Moreover, among the diamagnetic (non-paramagnetic, able to be studied by NMR) heteroatoms, just a few of them, such as Si^{4+}, Sn^{4+} or Cd^{2+}, possess isotopes with good enough NMR sensitivity or natural abundance to be able to be studied by this spectroscopic technique. However, in most cases, the low loadings of heteroatoms in AlPOs critically limit the acquisition of good signal-to-noise NMR spectra. In practice, just ^{29}Si NMR spectra have been used to directly detect the different heteroatom (Si) environments in Si-substituted AlPOs. Other important diamagnetic heteroatoms, from a catalytic point of view, in particular Mg^{2+}, Zn^{2+} or Ti^{4+} have very poor sensitivity to NMR, but their incorporation mechanisms or their chemical environment into the $AlPO_4$ frameworks can be indirectly studied by solid-state ^{27}Al and especially ^{31}P NMR [103–106].

Some metal ions containing AlPOs, in particular those containing cobalt and manganese, change their colour when the oxidation state of the metal changes. In this sense, UV-vis spectroscopy could be an ideal technique for studying these systems [107–114]. For example, cobalt-substituted system CoAPO-36 was studied using this technique, and the colour change from blue (as synthesized) to green (in the calcined and oxidized form) was used as an evidence for the formation of Co^{3+} upon calcination in air [110]. Weckhuysen et al. reported a 30% conversion of Co (II) to Co(III) [115] which is in line with the findings reported by Barrett et al. [116] using Co K-edge EXAFS technique, discussed later. A representative spectrum is shown in Fig. 9 which shows as-synthesized, calcined and reduced forms of CoAPO-5.

Fourier-transform infrared spectroscopy (FTIR) has been very useful in characterizing a range of heteroatom-substituted system for two reasons: (a) if the metal ions are present in a lower valence state (whether it is 2+ in Al^{3+} site or 4+ in P^{5+} site), a charge-compensating proton should be present resulting in a bridging hydroxyl, which will have a specific OH stretching frequency, similar to the one seen in zeolitic solids and different from terminal hydroxyls associated with parent Al^{3+} or P^{5+} cations. A characteristic band appears around 3,600 cm^{-1} associated with bridging hydroxyls when divalent metal ions are present [117–119] (Fig. 10); terminal hydroxyls appear at a higher wavenumber of ca. 3,680 cm^{-1} and above. This method is routinely used in addition to proton NMR (if non-paramagnetic metal ions are present) in selected heteroatom-substituted aluminophosphates (in completely dehydrated form) to establish the presence of Brönsted acidity in

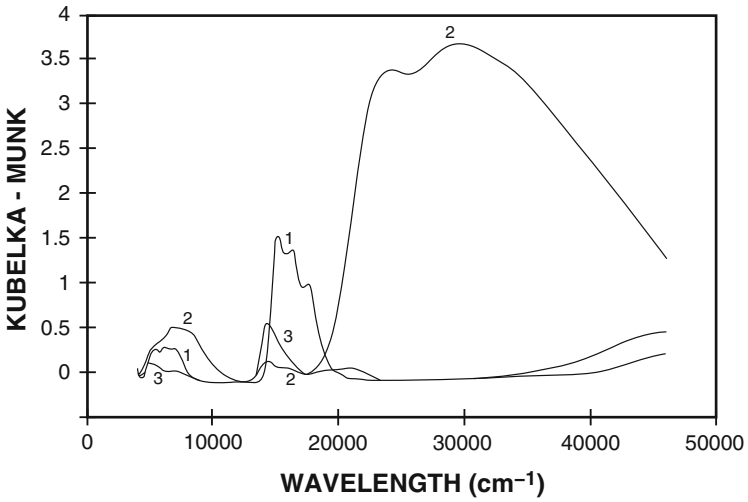

Fig. 9 DRS spectra of CoAPO-5 materials as a function of the pretreatment: (1) in as-synthesized form, (2) after calcination overnight at 773 K and (3) after reduction with H_2 at 623 K. Reprinted from Zeolites, 19, A. A. Verberckmoes et al., Framework and extra-framework Co^{2+} in CoAPO-5 by diffuse reflectance spectroscopy, 180–189, Copyright 1997, with permission from Elsevier [111]

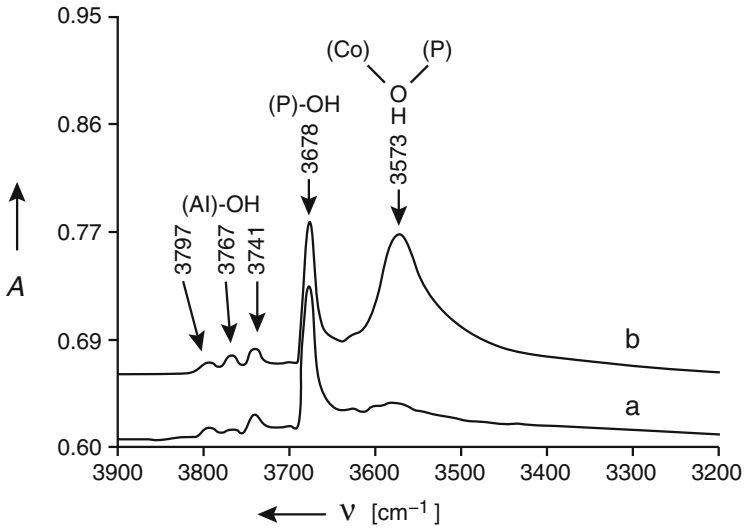

Fig. 10 Typical FTIR spectra showing OH stretching vibration mode of CoAP0-18. (**a**) Calcined in oxygen at 550°C, (**b**) reduced in hydrogen at 400°C. *A* absorption. Thomas JM, Greaves GN, Sankar G, Wright PA, Chen J, Dent AJ, Marchese L: On the nature of the active site in a CoAPO-18 solid acid catalyst. Angew. Chem. Int. Ed. 1994, 33, 1871–1873. Copyright Wiley-VCH Verlag GmbH & Co. KGaA. Reproduced with permission [119]

these systems. However, it is difficult to use this method to establish the extent of conversion of transition metal ions (example Co^{2+} to Co^{3+} upon calcination) as the intensity of the OH band does not clearly reflect the extent of conversion. Furthermore, it is difficult to deduce the presence of Lewis acid sites by FTIR unless a probe molecule is used to this aim.

Extensive studies using ESR technique were conducted on a range of transition metal ion-substituted AlPOs [115, 120–129]. Although it was established by a range of techniques that 2+ ions substitute for Al(III), some of the results were interpreted in such a way that the metal (2+) ions may substitute for P(IV) site instead of Al(III) sites. Although it is possible, in such an event, a large number of protonated sites (almost 3 times as that of the 2+ ions substituted in 3+ sites) are needed for charge compensation. Therefore, as there are no direct proofs that such mechanism existed, one can most probably discount such substitution mechanism due to the nature of charge-compensating species. Beale et al. [130] carried out ESR studies of cobalt- and manganese-containing aluminophosphates. They investigated both as-synthesized and calcined materials (the samples were sealed in vacuum after the calcination treatment in an ESR compatible tube). This study indeed supports the substitution of Mn (II) and Co(II) in the Al(III) sites in the as-synthesized materials and the formation of 3+ ions upon calcination [130].

X-ray absorption spectroscopy (XAS) is a powerful method as it is element specific and provides average oxidation state and coordination environment (qualitatively) from X-ray absorption near edge structure (XANES) and coordination

number and bond distance (local structure) more quantitatively from the analysis of the extended X-ray absorption fine structure (EXAFS). As this technique does not suffer from the lack of concentration of the dopant and irrespective of whether the material is crystalline or amorphous, it can be used for estimating the nature of substitution of the metal ions; when the concentration of the metal ions are low and measured at their absorption edge, one uses fluorescence mode as opposed to transmission to overcome the issues of collecting good-quality XAS data. A range of reports in literature utilized this technique and reported the substitution of 2+ metal ions in the framework and has become a routine method to convincingly establish the metal ions substitution. One of the main reasons that this method is required is that the diffraction analysis fails to show the presence of metal ions in their analysis as the metal ions are not ordered, in addition to their low concentration. Furthermore, the majority of the AlPOs and MeAPOs (where Me is a divalent cation) possess high symmetry space group in diffraction analysis and have only one or two crystallographic sites which prevent the accurate determination of metal ion location. Barrett and Jones [97] used resonant scattering X-ray diffraction method to show that there is an unequal distribution of Co(II) in two Al(III) sites in DAF-8 having Phillipsite structure. A systematic study by Barrett et al. [72] revealed that the extent of oxidation state changes based on the metal-oxygen distance as the ionic radii of the different oxidation states and coordination numbers are different (Table 3).

It emerged that some structures favour a higher degree of redox reaction of Me (II) ions compared to others. For example, AFI structure seems to show the least of Co(II) ions present in its framework that can be converted to Co(III) compared to CoAPO-34 or CoAPO-18 systems, during calcination in air. However, for Mn(II)-substituted system, although the trend appears to be similar to that of cobalt, it is found that higher amounts of Mn(II) are converted to Mn(III) in AFI structure, compared to cobalt-containing AFI material (Table 4) [116, 131], upon calcination.

Table 3 Refined occupancy of Al and Co sites in the four tetrahedral (T) sites wherein Al and Co occupy in DAF-8 material

Crystallographic position T	% Al occupancy	% Co occupancy	Average bond length M–O (Å)
T1	70.5(10)	29.5(10)	1.779
T2	42.2(10)	57.8(10)	1.843
T3	35.1(10)	64.9(10)	1.879
T4	73.9(10)	26.1(10)	1.780

Respective average distances of those sites agree with the percentages estimated in their occupancies. Typical distance of cation-oxygen distances for Al–O is 1.73 Å and for Co–O is 1.94 Å. Reproduced from Barrett PA, Sankar G, Stephenson R, Catlow CRA, Thomas JM, Jones RH, Teat SJ. 'A new addition to the Phillipsite family of molecular sieves: a divalent metal-ion-framework substituted microporous aluminophosphate (DAF-8)' [72]

Table 4 Amount of 3+ ions present in the calcined state, at room temperature, under inert dry conditions, estimated from the average metal ion-oxygen distance estimated from EXAFS at the respective metal (Co or Mn) K-edges

System	Average Me–O distance in the as-synthesized state (Å), R_{2+}	Average Me–O distance in the calcined (oxidized) state (Å), R_{av}	Amount of Me ions 3+ state (percent)[a]-X(%)
CoAPO-5	1.94	1.91	23
MnAPO-5	2.02	1.92	58
CoAPO-36	1.93	1.86	58
MnAPO-36	2.02	1.89	76
CoAPO-18	1.93	1.82	100
MnAPO-18	2.02	1.85	100

[a]The amount was estimated based on the Eq. $X(\%) = (R_{2+} - R_{av})/(R_{2+} - R_{3+})$. R_{3+} was obtained based on the ionic radii displayed in Shannon ionic radii table – $O^{2-} = 1.35$, $Co^{2+} = 0.58$ and $Mn^{2+} = 0.66$. Both Mn^{3+} and Co^{3+} are not listed as it is very difficult to stabilize them in tetrahedral coordination. Therefore, the calcined state in MeAPO-18 was taken as the evidence for Me^{3+}-O distance as the edge shift in respective X-ray absorption data correspond to 3+ containing model compounds. Therefore, Co^{3+}-O distance of 1.82 Å and Mn^{3+}-O distance of 1.85 Å were taken as representative distance for tetrahedrally coordinated Me^{3+}-O distance. The values are reported in Refs. [116, 131]

Based on these studies, a simple picture emerged on the extent of oxidation of, for example, cobalt-substituted aluminophosphates. A schematic model based on the amount of oxidized cobalt present in the system and the nature charge compensation in the case of non-oxidized cobalt ions in the framework is proposed by Barrett et al. [116] and shown in Fig. 11.

In addition, a detailed time-resolved combined XRD/XAS (at the Co K-edge) investigation of CoAPO-18 revealed the pathway in which the template decomposition takes place accompanied by acid site formation prior to the conversion of Co (II) to the oxidized 3+ ions. Figure 12 shows the evolution of the environments and oxidation states of Co incorporated in CoAPO-18 during a cycle of calcination and subsequent reduction, according to in situ Co K-edge XAS and FTIR studies. Furthermore, the in situ XRD/XAS (XAS at the Co K-edge) studies indeed revealed that the overall structure of the material is intact during the calcination and reduction processes and more importantly the conversion of Co^{2+} to Co^{3+} occurs at ca. 500°C whilst the charge-compensating organic cations decomposes much earlier, suggesting that both the events are not related. The results based on the study of CoAPO-18 are shown in Fig. 12.

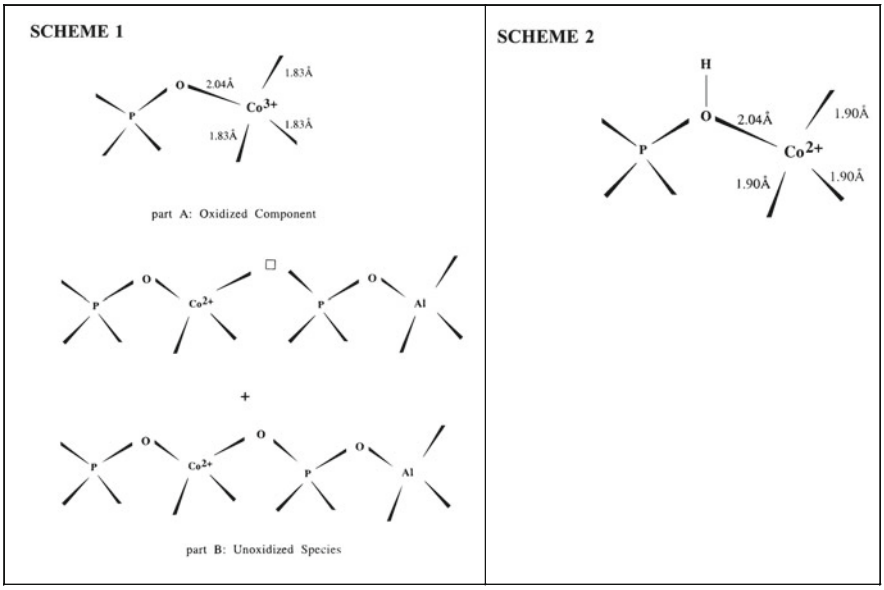

Fig. 11 Schemes proposed based on results from EXAFS study at the cobalt edge of a series of CoAPOs in the calcined state and reduced state, taking into account the oxidized and non-oxidized component (Scheme 1) estimated from EXAFS in the calcined state and reduced component after reduction in hydrogen (Scheme 2). Reprinted with permission from [116]. Copyright 1996 American Chemical Society

4 MeAPOs as Efficient Catalysts

A range of catalytic studies have been undertaken to establish the performance of these metal ion-substituted systems; the field is exhaustive, and only selected reported applications are given here to demonstrate the use of these solids for a range catalytic applications. First and foremost, studies focused on the acid-catalysed reaction of methanol to hydrocarbon. If metal ions are in 2+ state, there will be charge-compensating protons (similar to aluminosilicate zeolites), and these are expected to catalyse the transformation of methanol to olefins. Indeed, several studies showed that the deactivation also appears to be an issue in some of these systems. Although these metal-containing systems show performance for acid-catalysed reactions, SAPO-based systems were found to be superior [117, 122, 132–134].

The more promising area in the field of heterogeneous catalysis for metal ion-substituted aluminophosphates is the selective oxidation of hydrocarbons utilizing the redox reaction associated with the transition metal ions, in particular, cobalt-, manganese-, iron-, vanadium- and titanium-based systems [135–144]. One of the examples in the field of hydrocarbon oxidation was the cyclohexane oxidation to alcohol, ketone and acid using metal-substituted aluminophosphates materials. It

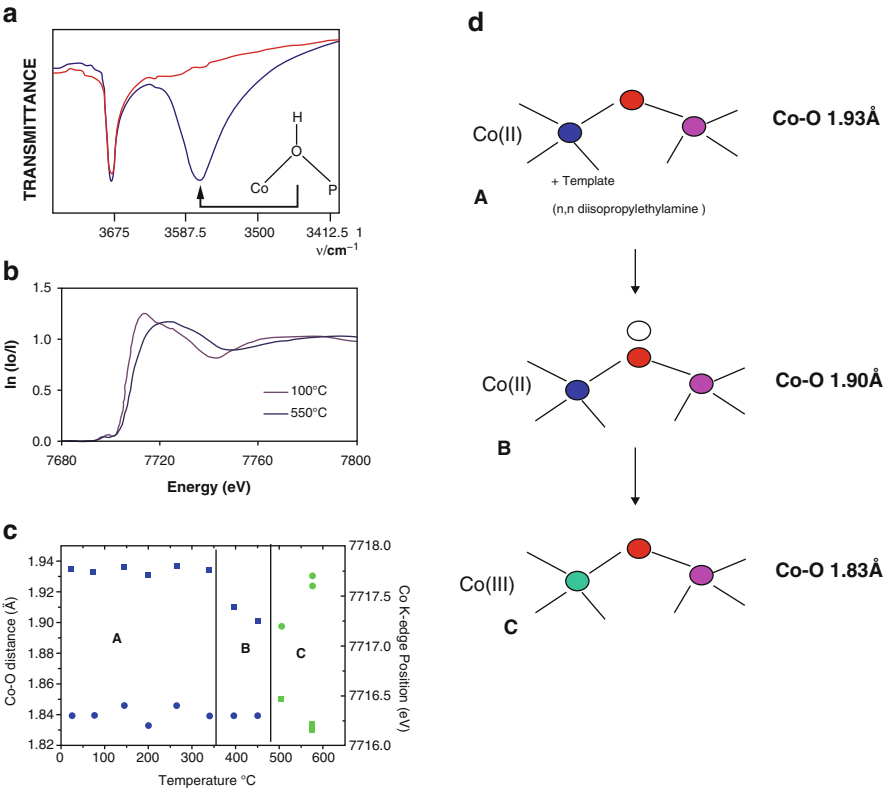

Fig. 12 On the left, summary of the results obtained from a combination of XRD (not shown), FTIR spectra (only the calcined and reduced forms are shown here), Co K-edge XANES spectra and Co–O distance vs. temperature of a CoAPO-18 material. On the right, the different Co environments at different experimental stages deduced from the results of the characterization techniques shown on the left: (**a**) in the starting material, (**b**) an intermediate structure when the SDA decomposes leaving a proton resulting in an acid catalyst, and (**c**) the oxidized cobalt state that appears above ca. 480°C

was first shown that CoAPO-36, which has the appropriate large-pore dimension for the cyclohexane molecule to enter into the structure and in addition fairly good conversion of Co(II) to Co(III) ions (based on EXAFS studies), showed a good conversion from cyclohexane to adipic acid under moderate temperatures of ca. 100°C and pressures of ca. 10 bar of oxygen/air [145]. The use of so environmentally benign oxidants is an extraordinary industrial advantage. Although EXAFS studies indicated that CoAPO-34 and CoAPO-18 8-R materials have almost all the Co(II) sites converted to Co(III) after calcination [116], the activity was very poor, which was explained as due to their small-pore dimensions which prevent the entry of cyclohexane molecule (Fig. 13).

Therefore, further investigations were made on the effect of type of transition metal ions on the large-pore $AlPO_4$-5 structure [36], as it can be prepared using a

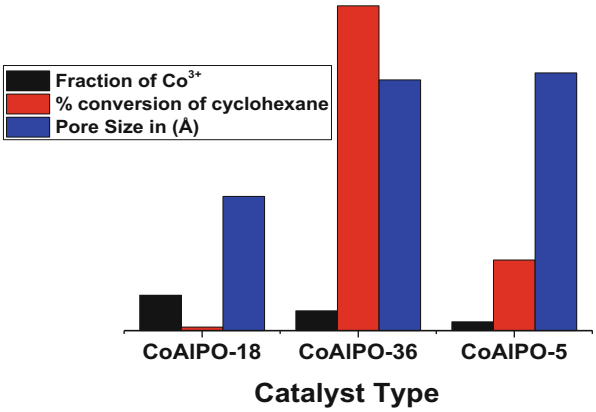

Fig. 13 Comparison of the fraction of Co^{3+} formed upon calcination, as estimated by EXAFS (black column), the conversion of cyclohexane (red column) and the pore size of three CoAPO catalysts

range of organic templates and relatively short time is required to produce these materials compared to $AlPO_4$-36 framework. It has been found that manganese- and iron-containing $AlPO_4$-5 structures, wherein the redox reaction for the conversion of 2+ ions to 3+ is facile compared to cobalt-based systems, showed considerably higher activity for the conversion of cyclohexane (Fig. 14).

The study also showed that introduction of free radical initiator, in particular tert-butyl hydroperoxide, enhanced the activity, whilst the activity decreased considerably in presence of a radical quencher, such as hydroquinone.

Thomas and coworkers [35, 37, 146] showed that CoAPO-18 is an excellent system to oxidize selectively the end carbon of an *n*-hexane molecule as it has restricted entry through only one direction. With CoAPO-18 (and CoAPO-34) having much higher conversion of 2+ to 3+ ions during the catalytic activation, they exhibited a good regioselective oxidation of linear *n*-hexane molecule (Fig. 15). Similarly, the manganese-containing small-pore materials also showed very promising selective oxidation of linear hydrocarbons. Whilst these studies established the ability of these small-pore catalysts to restrict the molecular entry and regioselective oxidation (C1 in this case), there are reports in the literature on the nature of redox reaction and catalytic performance on these systems, which seems to suggest that an alternative redox mechanism can operate and specifically the reported region-selective conversion of primary carbon in *n*-hexane [138, 142]. However, this area of selective oxidation with redox metal ion-substituted system is a promising field to explore in the future. Computational studies by Catlow and coworkers indeed provided a detailed mechanistic insight into the path of the selective oxidation process that takes place in MeAPOs in oxidizing alkane molecules with molecular oxygen. Specifically, these studies revealed that the catalytic efficiency of Mn-APOs in oxidation reactions is intrinsically linked to the Mn redox activity, in particular the

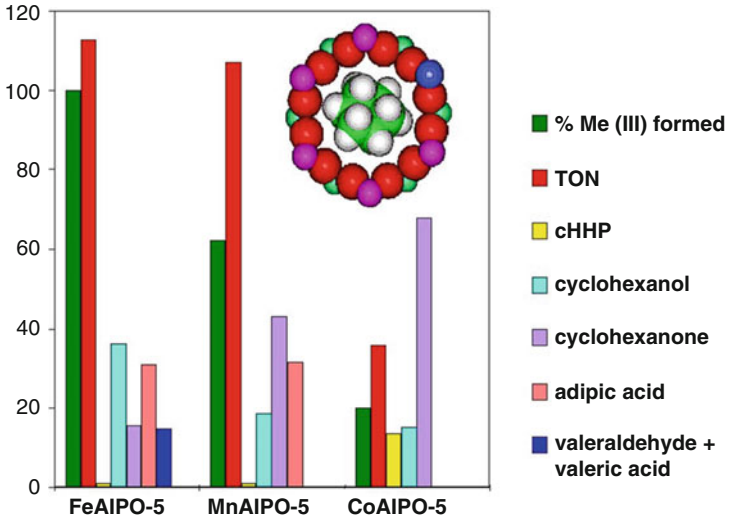

Fig. 14 Conversion of cyclohexane to various products over three different metal ions (identical metal ion concentration of ca. 4%) substituted $AlPO_4$-5. The red and green columns represent percent of M(III) ions present (estimated from EXAFS) in the calcined FeAPO-5, MnAPO-5 and CoAPO-5 and their catalytic activity (TON) for the oxidation of cyclohexane after 24 h at 403 K, respectively. Individual product distributions are also shown. Reprinted with permission from [36]. Copyright 1999 American Chemical Society

interconversion between 2+ and 3+ oxidation states, and the coordinatively unsaturated nature of tetrahedral Mn present in AlPO frameworks. The proposed mechanism demonstrates the crucial role of both Mn-III and Mn-II in the reaction in which the Mn^{3+} sites (in the calcined form) undergo an initial reaction to form alkyl hydroperoxide intermediate, which is transformed into the oxidative products (alcohol, aldehyde and acid) by reduced Mn^{2+} [131, 147–155].

It is also significant that the same kind of MeAPO catalysts, in particular FeAPO-5 and MnAPO-5, was reported to be active in the oxidation of cyclohexene under soft/mild conditions, in liquid phase, at 80°C and under ambient pressure, but using hydrogen peroxide as oxidant agent [156]. That activity was clearly overtook several years ago by the use of multi-transition metal-doped $AlPO_4$-5 or MeAPO-5 (Me = heavy metal) catalysts [157], as it would be explained in detail in the next section. However, as a precaution under peroxide presence, one needs to establish that metal ions are not leaching from the solid, which could be an issue which needs to be addressed in this and many other liquid-phase oxidation reactions.

Iron-containing ZSM-5 was reported to be an efficient catalyst for the conversion of benzene to phenol using N_2O as an oxidation reagent. Whilst several studies were undertaken to understand this process, Shiju et al. [158] explored iron-substituted $AlPO_4$-5 as a catalyst for the same reaction through one-step calcination instead of steaming to extract (typical process used in creating active Fe-ZSM5 catalysts) some of the Fe^{3+} from the ZSM-5 framework. They reported a good activity for the

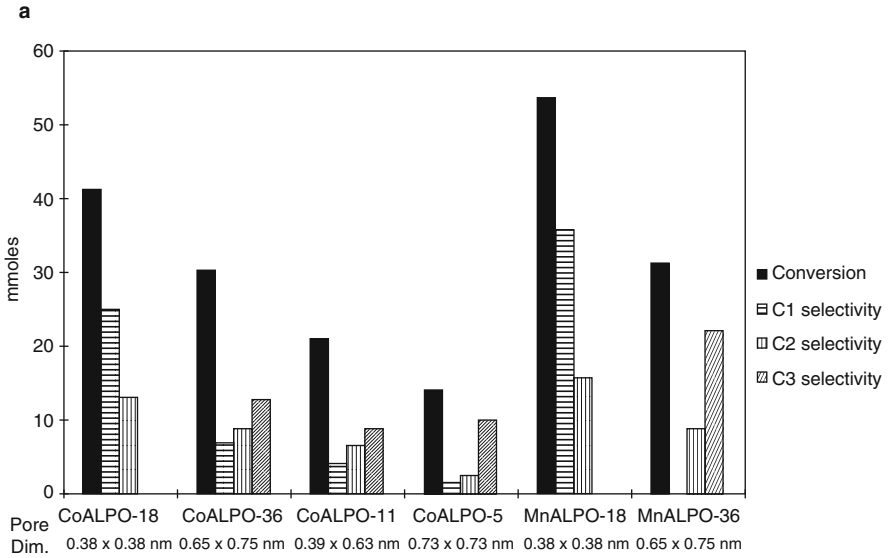

Fig. 15 Comparison of catalytic oxidation of *n*-hexane in presence of molecular oxygen and cobalt- or manganese-substituted aluminophosphate molecular sieves. Selectivity towards the oxidation of C1 part of the *n*-hexane molecule is achieved in small-pore material, primarily due to restrictions in the way the molecule can enter the small pore. In addition, both cobalt- and manganese-containing $AlPO_4$-18 have highest conversion of Me^{2+} to Me^{3+} and therefore show good conversion compared to $AlPO_4$-5 or $AlPO_4$-11 or $AlPO_4$-36 structures. Reproduced by permission from Macmillan Publishers Ltd.: Nature [35], copyright 1999

conversion of benzene to phenol with a good selectivity for phenol comparable to FeZSM-5 catalyst (Fig. 16). They investigated three different concentrations of iron and found that ca. 1% of Fe in Al^{3+} site is sufficient to provide good activity and selectivity. Subsequent detailed study by Wei et al. [159] explained that N_2O did not decompose at the Fe^{3+} sites forming 'alpha' oxygen similar to Fe-ZSM5 catalyst and, instead, possibly undergone reduction from Fe^{3+} to Fe^{2+} by reacting with benzene and subsequently the oxidation takes place.

There are several other examples of a range catalytic studies reported with MeAPOs which include epoxidation of alkenes [160], Baeyer-Villiger oxidation [161], alkylation of benzene with aromatics by benzyl chloride over iron-containing aluminophosphates [162], multifunctional MeAPO-5 catalyst containing a redox and non-redox metal ions for one-step conversion from cyclohexanone to caprolactam [163], liquid-phase oxidation of styrene and synthesis of adipic acid from cyclohexanone using MnAPO-5 in presence of tert-butyl hydroperoxide [164], phenol hydroxylation over iron-containing $AlPO_4$-5 prepared by hydrothermal methods, ion exchange and impregnation methods for phenol hydroxylation and ethane oxydehydrogenation over MnAPO-5 [165].

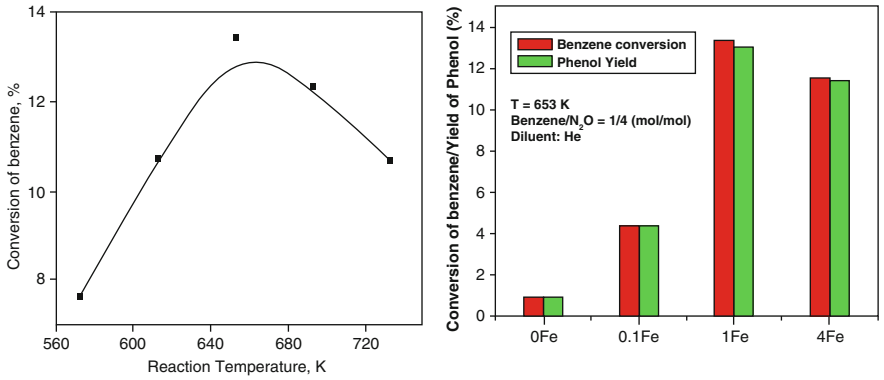

Fig. 16 On the left, catalytic activity of 1 wt.% FeAPO-5 as a function of temperature for the oxidation of benzene to phenol. Benzene:N_2O:He = 1:3.6:5.4, contact time factor = 0.5 s. Reproduced from Ref. [158] with permission of The Royal Society of Chemistry. On the right, activity and phenol yield for various concentrations of iron-substituted $AlPO_4$-5 material

5 Structure-Directing Effect in MeAPOs: The Importance of Phase Specificity in the Design of Improved Catalyst

As it has been mentioned above (Table 1), the phase specificity is one of the main disadvantages of the synthesis of $AlPO_4$-based microporous materials in comparison with the preparation of zeolites. For instance, $AlPO_4$-5 or $AlPO_4$-11 materials can be prepared in the presence of tens of different amines, but they only become pure under very narrow synthesis conditions. Similarly, several topologies with $AlPO_4$ composition can be prepared, for instance, using *n*-dipropylamine (DPA) as SDA by just minimally changing certain parameters such as crystallization temperature, crystallization time, pH of the starting gel, dilution, order of addition of the reactants or the presence/absence of heteroatoms. The fact that a particular $AlPO_4$-based material can be prepared in pure form only under narrow conditions is particularly relevant for the subject of this chapter, so it is addressed more in depth in this section.

Among the $AlPO_4$-based frameworks, it seems that some topologies are easy to be prepared as pure $AlPO_4$ composition, such as AFI ($AlPO_4$-5) or AEL ($AlPO_4$-11), whereas some others such as CHA ($AlPO_4$-34) or ATS ($AlPO_4$-36) are relatively easy to be synthesized in the presence of a heteroatom and extremely hard to be prepared in the Me-free $AlPO_4$ form [80, 166]. Some other scarcely investigated $AlPO_4$-based materials like AFY ($AlPO_4$-50), AFX ($AlPO_4$-56), AFV ($AlPO_4$-57), SAO (STA-1) or AFS ($AlPO_4$-46) have not been reported until today as non-doped AlPOs, but they exist in their SAPO, MeAPO or MeAPSO forms (Table 2) [2, 3]. Indeed, almost half of the reported metal-substituted AlPOs has not been able to be prepared as AlPOs [167] (Table 2). A clear example is seen with AFI and CHA structures, as only AFI-structured materials are obtained from a non-doped aluminophosphate gel, whereas the same gel containing Zn as dopant led to pure CHA phase ZnAPO-34 [52, 168]. Something similar happens in an ionothermal

media with the topologies AEL and CHA [74], where the presence of V or Ti favours the crystallization of the latter to the detriment of the former, which is the only crystallized phase starting from heteroatom-free $AlPO_4$ mixtures. In other words, the structure-directing role in AlPOs is not exclusive of the amines, but the heteroatoms themselves have a key effect on the phase specificity to certain topologies, suggesting the direct involvement of heteroatom ions in the formation of the first crystallization nuclei [52]. The series of Me-rich $AlPO_4$-based materials known as DAF-n [20, 72, 169], described in a previous section and that are not able to be prepared in the absence of Me, could be taken as the link between these $AlPO_4$-based materials preferably prepared in the presence of certain amount of metal ions and the Al-free zeotypes also based on phosphates [21, 27, 43].

Despite that such involvement of heteroatom ions is in principle desired because it somehow guarantees the right incorporation of the metals within the $AlPO_4$ framework, it also entails a significant drawback in the design of systematic studies, for instance, by varying the nature (and/or the loading) of the metal ion for a given structure. Using the same phase-specific organic SDA in this kind of systematic studies does not only guarantee the achievement of the same structure, but it also makes practically equal other features of the resultant materials such as (1) the (limited) number of metal ions to be incorporated as a function of the size and the number of charge of the SDA; (2) the pH of the crystallization process, which influences on the possible hydrolysis of the heteroatom sources and on the subsequent formation of solid metal-rich impurities [47]; (3) the crystal size, which could become the most critical parameter of these MeAPO materials when used as heterogeneous catalysts; and (4) the crystal morphology, particularly important in the 1D topologies, which are abundant in the $AlPO_4$ family, etc.

For that goal, a suitable strategy is to enhance the phase specificity of the organic SDAs. In this sense, theoretical simulations can contribute in the design/prediction of more efficient organic molecules as templates for $AlPO_4$-based structures [170]. Even the following simpler strategy showed to be of great help.

The low structure-directing effect of amines in the synthesis of AlPOs generally dissuades of establishing a rational and direct correlation between the shape/size of the amines acting as SDA and the pores of the $AlPO_4$ topologies directed by them. Nevertheless, $AlPO_4$ family offers a series of quite systematic and simple topologies having 1D pore systems which crystallize in the presence of amines used as SDA [2, 3]. Taking the most common SDA amines NR_3 (where R represents the three substituent groups of N in an amine, and it can be -H, $-CH_3$, $-CH_2CH_3$, etc. depending of the nature of the amine) in their most thermodynamically favourable conformation, an acceptably good matching between the shape of the so-conformed amine and the shape of the $AlPO_4$ pore was found if the bulkiest R groups are positioned along the channel [171]. It suggests that amines have indeed certain templating role in the synthesis of microporous aluminophosphates and they are not only pH modulator or simple pore fillers [172, 173].

As a proof of concept of this empirical model, several other amines scarcely studied by then in the synthesis of AlPOs were tested and led to either very important improvements in the specificity towards a particular topology or to the discovery of

new amine-based SDA molecules for certain 1D pore $AlPO_4$ materials [171]. The following subsections focus on each of these two achievements by this rational-empirical method, specifically on the interest for incorporating heteroatom ions within the $AlPO_4$ frameworks.

5.1 *N-methyldicyclohexylamine (MCHA), the By Far Most Specific SDA to an $AlPO_4$ Material*

5.1.1 MCHA as a Phase-Specific SDA for AFI-Structured Materials

The ease of preparing $AlPO_4$-based materials has strongly conditioned the choice of certain aluminophosphate structures to deepen their physicochemical knowledge and their subsequent applications. It does not seem a coincidence that (1) $AlPO_4$-5 and $AlPO_4$-11 (IZA codes: AFI and AEL, respectively [2, 3]) can be prepared with dozens of SDAs [55] and at the same time (2) they are the widest investigated AlPOs. Even $AlPO_4$-34 (CHA), which is other of the extensively studied aluminophosphates, mainly pushed by the catalytic interest in SAPO-34 in MTO process [32], can be prepared in the presence of different organic SDAs [174]. These three AlPOs practically cover all micropore range: small- (CHA), medium- (AEL) and large-pore (AFI) materials [2, 3].

The most evident example of such relationship between the straightforward synthesis and the selected topologies for being investigated is probably found in the comparison between the large-pore structures AFI ($AlPO_4$-5) and ATS ($AlPO_4$-36). Both have quite similar topologies with 1D pore system and very similar pore 12R apertures, so they have the same potential applications. Even both phases become competitive in the scarce crystallization systems in which ATS can be synthesized [175–177]. Moreover, the metal ion incorporation within the $AlPO_4$ frameworks, which gives them their primary potential applications, is almost compulsory for ATS-structured materials to be formed, but it is expendable and sometimes self-defeating for AFI ones. Moreover, when both materials were tested as catalysts under similar conditions in certain reactions, MeAPO-36 materials often beat MeAPO-5 ones [37, 178, 179]. In spite of that, the latter has received much more attention by scientific community, undoubtedly due to the straightforward and versatile methodologies reported.

Contrasting with such SDA versatility in the $AlPO_4$-5 materials preparation, practically any of the reported amines have very narrow synthesis conditions under which pure AFI-structured materials are crystallized. That low specificity is generally accentuated in the presence of doping metal ions. Therefore, it is a great challenge to find a highly specific SDA for this structure. By applying the above simple method, among the commercial amines, *N*-methyldicyclohexylamine (MCHA) was the one that best fits within the AFI pores (Fig. 17). Confirming that perspective and the validity of the approach, MCHA was indeed shown as an extraordinary structure-directing agent for $AlPO_4$-5 materials and their Me-doped

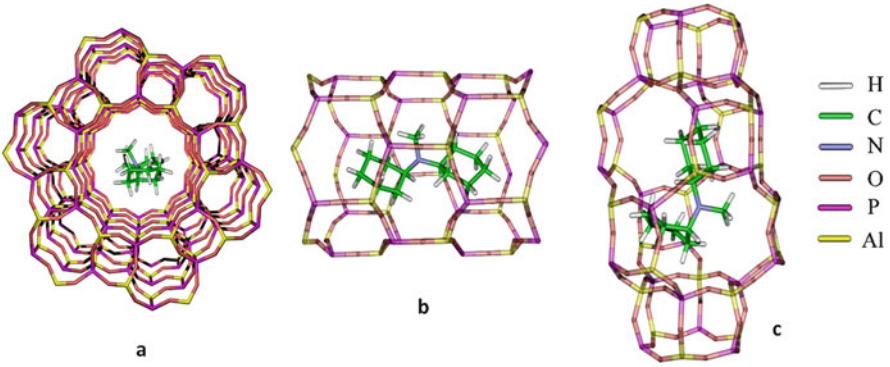

Fig. 17 Energy minimized conformation of *N*-methyldicyclohexylamine within an $AlPO_4$-5 pore (**a** and **b**) and $AlPO_4$-34 cavity (**c**). (**a**) and (**b**) represent two different views of the one-dimensional channel showing the collinear alignment of the organic template molecule with the channel direction. Reprinted by permission from Springer Nature: Springer, Catalysis Letters, 'The Extremely High Specificity of *N*-Methyldicyclohexylamine for the Production of the Large-Pore Microporous AFI Material', M. Sanchez-Sanchez et al., Copyright 2003 [84]

counterparts under a wide range of gel compositions and synthesis conditions, much wider than that given by any other amine reported up to then [84]. The MCHA specificity for the phase AFI was so high that further simulation studies were carried out trying to find extra explanation. These studies found so high specificity was also favoured by the impossibility of fitting MCHA in any of their possible stable conformation within the cavity of $AlPO_4$-34 structure (CHA) (Fig. 17c), which is by far the most common phase co-crystallizing with $AlPO_4$-based AFI materials templated by so many amines or quaternary ammonia. In fact, the microporous $AlPO_4$-based phase that appears as an impurity of $AlPO_4$-5/MeAPO-5 phase in the MCHA system, especially when high loadings of heteroatom ions are present in the gel, is the large-pore $AlPO_4$-36/MeAPO-36, in whose pores MCHA molecules also fit well.

MCHA-templated $AlPO_4$-5 system is probably the system able to produce a pure $AlPO_4$ phase under the widest range of conditions and/or compositions ever reported. The specificity to AFI materials is much higher than triethylamine (TEA), triethylammonium hydroxide (TEAOH) [84] or tripropylamine [180, 181], which are three of the most frequently used SDA for $AlPO_4$-5/MeAPO-5 materials. As an example of the phase specificity over so wide conditions, Co-doped $AlPO_4$-5 materials can be crystallized as pure form in the presence of MCHA under wide range of (1) Me content (Me/(Me+Al) ratios from 0 to 0.15), (2) pH of the starting gel (4 units!, from 5 to 9) or (3) crystallization temperature (from 150 to 200°C). Moreover, these materials can be fully synthesized in short crystallization times (in 3 h), with excellent yields [84], are composed by relatively small crystal size and even contain some intercrystalline mesoporosity [180, 181].

Taking advantage of the exceptional properties of MCHA as a specific structure-directing agent, in the following subsections, this amine is taken as a driven force of

a 'travel' through: (1) the incorporation of very different metal ions (including some heavy metals) in different environments and/or oxidation states; (2) the co-incorporation of different heteroatoms; (3) the diverse strategies to reduce the diffusional problems by either reducing the crystal size or introducing inter- and inter-crystalline mesoporosity; or (4) through the catalytic performance of these microporous materials in different organic reactions.

5.1.2 Catalytic Significance of Structure-Directing Power of MCHA: SAPO-5 Prepared at Different pHs

The catalytic value of such specificity was initially made clear in the Pt-impregnated Si-doped $AlPO_4$-5 (the so-called Pt/SAPO-5) in the isomerization of *n*-heptane [182]. SAPO-5 materials resulted the only crystallized phase irrespective of any of the three Si sources (fumed silica, tetraethyl orthosilicate or stabilized colloidal silica suspension in deionized water), in a large Si content range (Si/(Si + Al) ratio from 0 to 0.4) and, more importantly, in a large interval of pH (from 5 to 9). The samples prepared at pH 9 became much more acid that their counterparts prepared at pH 5, as made clear by pyridine temperature-programmed desorption studies (Fig. 18a). Accordingly, the catalytic performance of the corresponding Pt-impregnated SAPO-5-pH-9 was several times higher than their homologous Pt/SAPO-5-pH-5 (Fig. 18b). To the best of our knowledge, so large difference in catalytic activity of this kind of samples by just changing a synthesis parameter is unique, and it could not have been achieved in any other system than that templated by MCHA.

It must be highlighted that $AlPO_4$-5/SAPO-5 materials have been also prepared under very different pH values of the starting gel (pH from 3 to 10) using

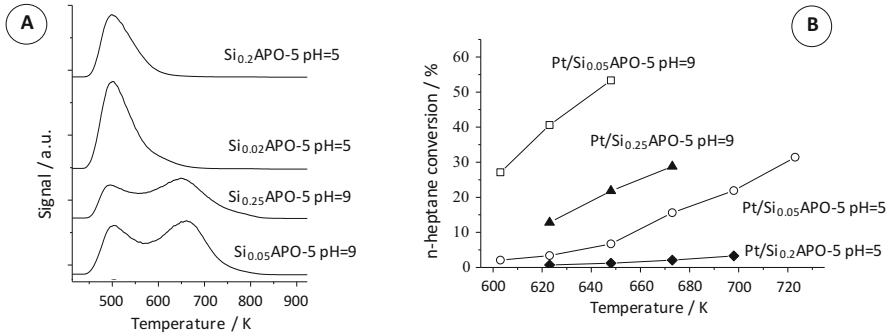

Fig. 18 (**a**) Temperature-programmed desorption curves of pyridine (**a**) of SAPO-5 samples prepared with MCHA as SDA by systematically changed Si content and pH of synthesis gel. (**b**) Conversion of *n*-heptane in the isomerization reaction catalysed by the same SAPO-5 samples after impregnation of Pt. Adapted from Microporous Mesoporous Mater, 99, R. Roldan et al., Influence of pH and Si content on Si incorporation in SAPO-5 and their catalytic activity for isomerization of *n*-heptane over Pt loaded catalysts, 288–298, Copyright 2006, with permission from Elsevier [182]

triethylamine (TEA) as SDA [183]. The strategy was to use fixed and large amount of TEA (TEA/P ratio of 1.75) and controlled the pH by addition of different acids such as sulphuric, hydrochloric, acetic, nitric and hydrofluoric acids, also at high content. The study focused on kinetics of crystallization and on the changes in physicochemical properties of the resultant SAPO-5, particularly on crystal morphology. Unfortunately, all samples were composed by crystals of several micrometres, the different acidities of the samples were not discussed, and no catalytic studies were carried out to prove any possible influence of pH synthesis in the catalytic performance.

5.1.3 Heteroatom Versatility in MeAPO-5 Prepared with MCHA

Although strictly speaking Si should not be among the heteroatom ions addressed in this chapter, the preceding example emphasizes the importance of discovering more specific SDA in the synthesis of AlPOs as well as the power of MeAPO-5/MCHA system for academic and applied catalytic investigations in a systematic way. Obviously, such specificity has been extended to the incorporation of heteroatom ions more related to the subject of this chapter. Pure $AlPO_4$-5 and 11 heteroatom-substituted $AlPO_4$-5 were synthesized under exactly the same synthesis conditions and composition, excepting the nature of Me [180]. Although the metal ion nature played an important role in different physicochemical properties of the achieved samples such as crystal size, morphology arrangement of the crystals, intercrystalline mesoporosity, etc. (see below), MCHA invariably led to pure AFI-structured MeAPO materials [180].

5.1.4 Additional Mesoporogen Role of MCHA

In a catalytic context, the reactants accessibility to the active centres as well as the diffusion of products from the microporous catalysts to the reaction media could become as important as the intrinsic activity of the (metal) sites. In other words, the catalytic potential given by microporosity to the zeolitic materials through both size discriminating and reactant confinement entails at the same time severe diffusion problems of molecules towards/from the pores, lowering both the conversion and the catalyst lifetime by blocking the pores. That is why the avoiding/reducing of diffusion problems is being paid so much attention and different synthesis or post-synthesis strategies have been developed [184]. Among these approaches, the synthesis of nanocrystalline samples and the introduction of either inter- or intracrystalline mesoporosity are the most direct ones, and consequently they have been the most broadly explored. The diffusion of reactants/products is even more limiting for structures with unidirectional pore systems, such as the case of $AlPO_4$-5 and many other microporous crystalline aluminophosphates, which besides used to be formed by very large crystals. In this sense, it can be highlighted that the direct preparation procedure of Me-substituted $AlPO_4$-5 in the presence of MCHA with no

synthesis/post-synthesis effort/modification already gives MeAPO-5 materials of nanocrystals orderly agglomerated/aggregated in micron-sized particles (Fig. 19a). For comparison purposes, crystals of a CoAPO-5 prepared with TPA as SDA is also shown in Fig. 19a. The crystals of CoAPO-5 prepared with MCHA are ca. three order of magnitude smaller! Moreover, the ordered aggregation of the nanocrystals in the particles leads to the existence of intercrystalline mesoporosity, suggested by SEM images (Fig. 19a) and confirmed by N_2 adsorption/desorption isotherms (Fig. 19b). The ability of MCHA to direct AFI-structured $AlPO_4$-based materials with so small crystal size suggests a strong structure-directing effect towards such topology, as the achievement of nanocrystals implies ease, simultaneous and abundant nucleation in very different parts of the synthesis gel. Such idea is also supported by the rapid crystallization of these materials in the presence of MCHA: at crystallization temperature of 175°C, in conventional Teflon-lined autoclaves, a full crystallized CoAPO-5 can be achieved in just 3 h [84]; in a synchrotron cell, where the kinetics of heating is higher, XRD diffraction peaks appeared after crystallization times as short as 66 min [99]; under microwave-assisted heating, CoAPO-5 is full crystallized after 1 h [181].

Interestingly, each heteroatom ion strongly conditioned the morphology and crystal size, and consequently the shape, the consistence or the intercrystalline mesoporosity of the arranged particles of the resultant MeAPO-5 crystallized from the MCHA-containing gel, even for low dopant loadings (Me/P ratio of 0.04) [180]. Figure 20 shows the SEM images and the N_2 isotherms of different as-prepared MeAPO-5/MCHA samples. It must be highlighted that the MeAPO-5 samples are not calcined, so the shown porosity is exclusively due to the intercrystalline mesoporosity. The MeAPO-5 samples doped with Zr, Cr, Si, Fe or the non-doped $AlPO_4$-5 have similar crystal size and arrangements than these shown

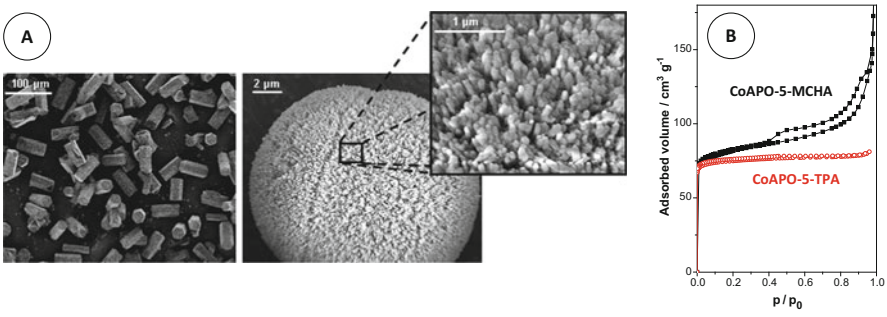

Fig. 19 (**a**) SEM images of the samples CoAPO-5 prepared with TPA (left) and MCHA (right) as SDAs. An insert of a portion of a CoAPO-5-MCHA particle is also shown. Note through the size-scaled bar the very different magnification used for the shown images, what gives an idea of the difference in particle/crystal size. (**b**) N_2 adsorption/desorption isotherms at −196°C of the same samples (CoAPO-5-TPA in red and CoAPO-5-MCHA in black). Adapted from Catalysis Today, 179, A. Manjon-Sanz et al., Towards the control of intercrystalline mesoporosity in inorganic microporous materials: The case of CoAPO-5, 102–114, Copyright 2011, with permission from Elsevier [181]

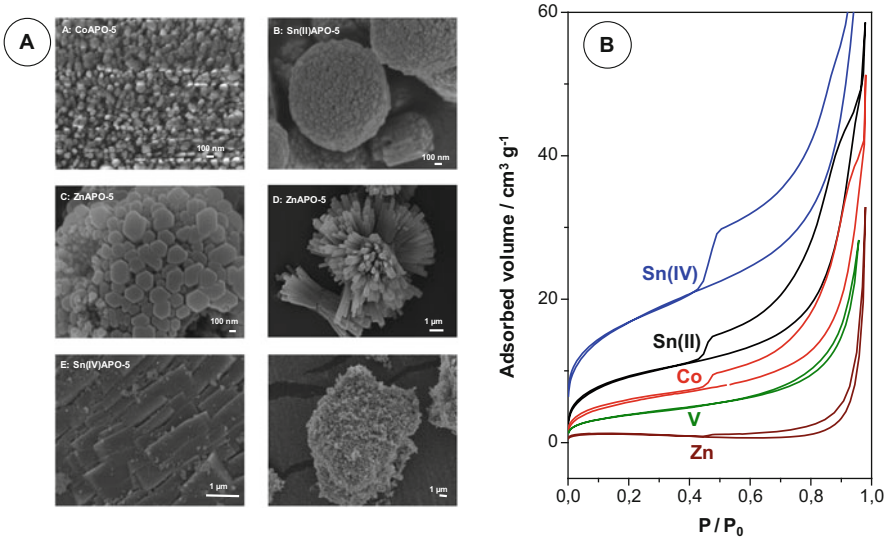

Fig. 20 SEM images (**a**) and N_2 adsorption/desorption isotherms at 77 K (**b**) of as-synthesized Co-, Sn(II)-, Zn-, Sn(IV) and V-doped $AlPO_4$-5 samples prepared with MCHA as SDA. Adapted from Microporous and Mesoporous Materials, 131, A. Manjon-Sanz et al., Non-templated intercrystalline mesoporosity in heteroatom-doped $AlPO_4$-5 using *N*-methyldicyclohexylamine as structure-directing agent, 331–341, Copyright 2010, with permission from Elsevier [180]

for Sn(II)APO-5; the MeAPO-5 samples where Me is either Mg or Mn are morphologically similar to the CoAPO-5 samples, whereas the morphology of any of the samples doped with Zn, V or Sn(IV) are unique in this series.

Although the influence of the heteroatom ion nature seems to be fundamental in both the crystal size and intercrystalline mesoporosity of the MeAPO-5 prepared with MCHA, it must be remembered that so many synthesis parameters can be varied along a considerably large range without changing the nature of the crystallized phase, taking advantage of the high specificity of MCHA towards the AFI materials. Moreover, it precisely offers a unique opportunity of studying the effect of these parameters in the morphologic and textural properties of an $AlPO_4$/MeAPO material. In this sense, a wide and systematic study with CoAPO-5/MCHA system was carried out [181]. The magnitude and the homogeneity of intercrystalline mesoporosity of CoAPO-5 samples were improved at short crystallization times (2 h), at the highest tested crystallization temperature (210°C), at the high Co content (Co/P ratio of 0.08), at low pH of the starting gels (pH 5) and at high dilution (H_2O/P ratio of 25), the two latter being the most influent parameters. However, overcoming any other influence, the microwave-assisted heating led to a decrease and a homogenization of crystal width and generated more ordered mesoporosity of smaller pores (Fig. 21).

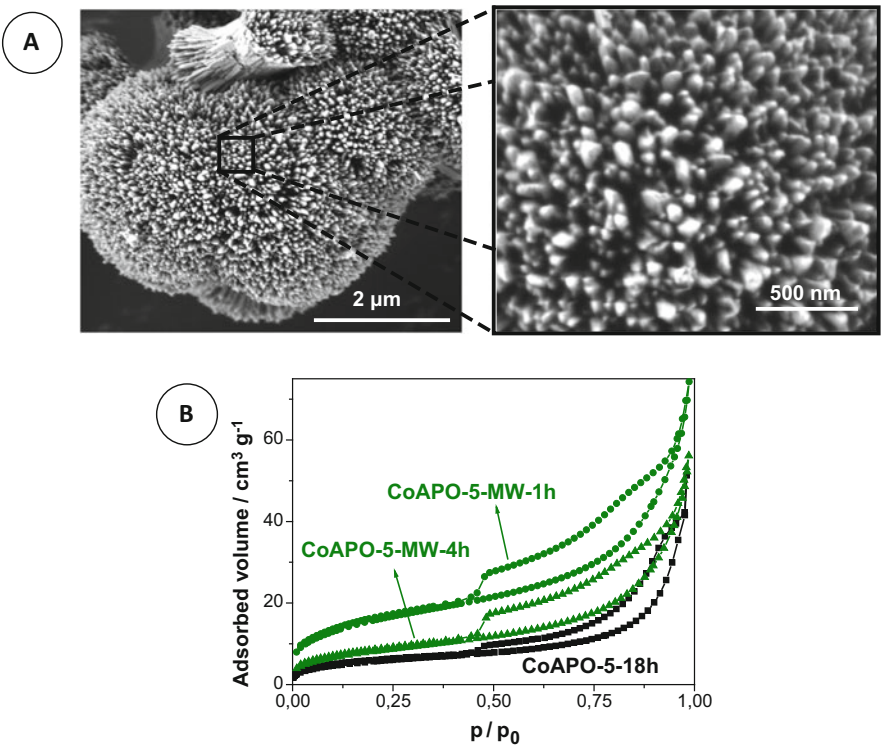

Fig. 21 SEM images (**a**) and N_2 adsorption/desorption isotherms at 77 K (**b**) of microwaved-assisted as-synthesized CoAPO-5 sample prepared with MCHA as SDA for 1 h and 4 h, respectively (green curves). For comparison purposes, the isotherm of CoAPO-5 prepared with the same SDA but under conventional heating for 18 h is also shown (black curve) in (**b**). Adapted from Catalysis Today, 179, A. Manjon-Sanz et al., Towards the control of intercrystalline mesoporosity in inorganic microporous materials: The case of CoAPO-5, 102–114, Copyright 2011, with permission from Elsevier [181]

5.1.5 Generating Intracrystalline Mesoporosity in the MCHA-MeAPO-5 System

The generation of the intercrystalline mesoporosity in certain AlPOs, particularly in these having 1D pore systems, does not always imply a substantial improvement of the diffusional problems, because their crystals used to be of a rod-like morphology in such a way that the intercrystalline mesoporosity between such crystals does not communicate the microporous of different crystals located within the same particle. Two further strategies have been developed to enhance the chemical (reactants and products) diffusion: (1) the introduction of intracrystalline mesoporosity and (2) the change of morphology making that the 1D pores run along the short dimension of the crystals [185, 186]. The former is relatively common in zeolites by either the post-synthesis treatments of the framework by reagents able to partially dissolve silica,

such as NaOH, NH_4OH, HF, etc., or by the inclusion of different macromolecules or nanoparticles during the synthesis processes, which subsequently act as mesoporogens (generators of mesopores) once they are removed by calcination [183]. To the best of our knowledge, the post-synthesis strategy has not been successful in $AlPO_4$-based materials, probably due to the difficulty of finding a chemical treatment able to efficiently generate mesoporosity in the $AlPO_4$ crystals keeping their topology. The second strategy has been applied with relative success to different $AlPO_4$, such as SAPO-34 materials [187, 188], but the afforded mesoporosity is however far from that generated in zeolites.

One of the most celebrated approaches to reduce diffusional problems in zeolites is the crystallization of the framework inside of a mesoporous amorphous commercial carbon matrix, which in this case is not a mesoporogen but provides confinement space allowing the nucleation of the zeolitic crystals but severely limiting the crystal growing further to the available pore dimension of the carbon [189, 190]. In other words, it was a method to reach nanocrystalline zeolites. In spite of the success of this method in the synthesis of nanocrystalline zeolites, it was not applied to AlPOs/MeAPOs systems during the years, probably because the method requires starting from soluble sources, which is not common in synthesis of AlPOs and not easy to be implemented in so phase-unspecific systems. In this context, MCHA is a quite phase-specific system towards $AlPO_4$-5/MeAPO-5 materials, and it easily directs the crystallization of these materials by changing conventional sources of Al, which are almost always insoluble solid, by the highly soluble-in-water source $AlCl_3 \cdot 6H_2O$ [191]. After that previous optimization, the reactants necessary to form CoAPO-5 were incorporated within the carbon matrix one by one through successive witness impregnation. The subsequent hydrothermal treatment generated CoAPO-5/carbon composites (Fig. 22). The size of the pencil-like CoAPO-5 crystals was of several micrometres, indicating that the resultant CoAPO-5 material was not nanocrystalline, as intended. Paradoxically, the peaks of the XRD pattern were quite broad

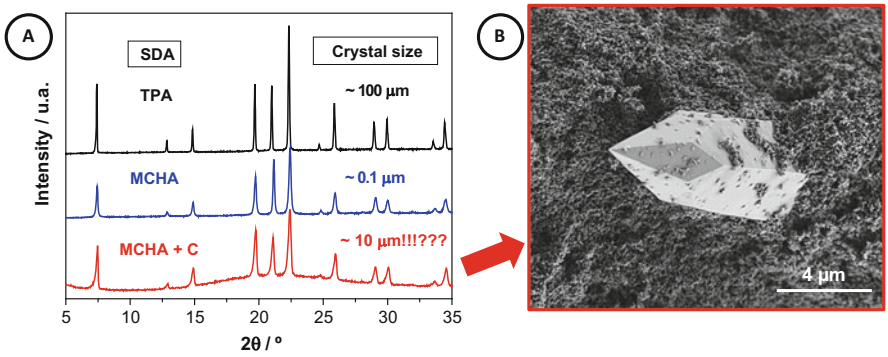

Fig. 22 (**a**) XRD patterns of three as-prepared CoAPO-5 samples prepared with TPA (top, black line), MCHA (middle, blue line) and MCHA within porous carbon BP-2000 (bottom, red line). (**b**) SEM image of the latter showing a pencil-like crystal emerging from the host carbon matrix. Adapted with permission from [191]. Copyright 2017 American Chemical Society

indicating the expected nanocrystalline nature (Fig. 22). This apparent incongruity was solved out through the calcination of the sample (Fig. 23). The apparently solid pencil-like crystals of CoAPO-5 actually contained extensive amount of embedded carbon matrix, which are burned during the calcination, leaving substantial both inter- and, more important, intracrystalline mesoporosity.

5.1.6 Incorporation of Me in Different Oxidation States in MCHA-MeAPO-5 System: Sn and Ti

The high specificity of MCHA towards AFI-structured $AlPO_4$-based materials has been also used in the incorporation of 'uncommon' heteroatom ions. It is particularly interesting the incorporation of a given heteroatom in different oxidation states. In that way, the same heteroatom could potentially reach different environments in the $AlPO_4$ framework. That environment versatility is not possible to be designed in zeolites, as Si^{4+} is the only ion to be substituted by the incorporated heteroatoms.

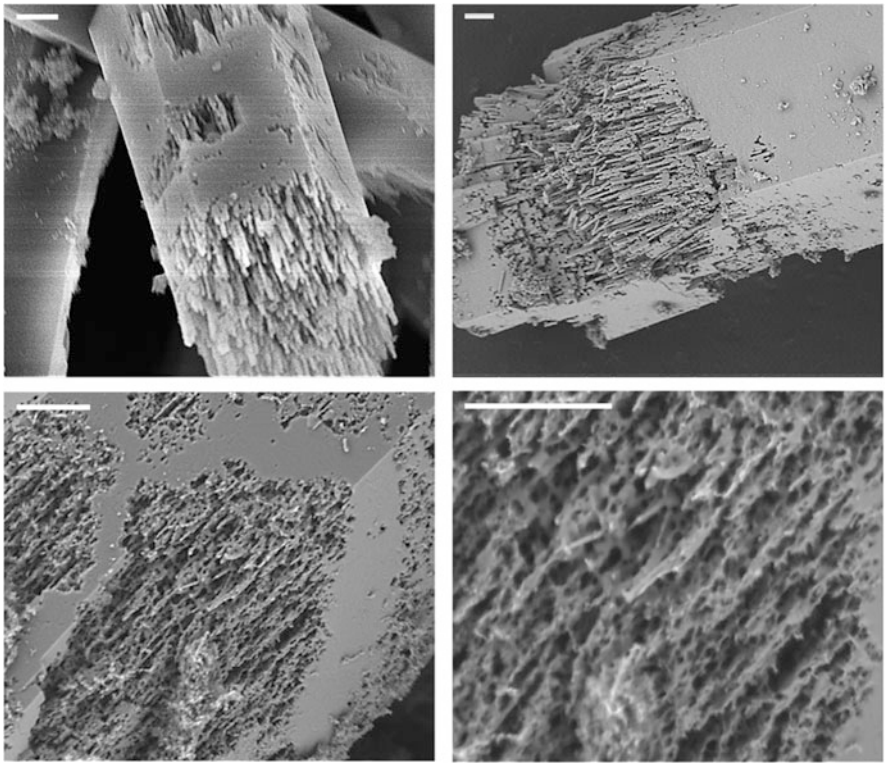

Fig. 23 SEM images of different particles forming the sample CoAPO-5 shown in Fig. 22 after calcination. The scale bar indicates 1 μm in all cases. Adapted with permission from [191]. Copyright 2017 American Chemical Society

The first study in this sense was carried out with the incorporation of tin. As a promising antecedent, Sn-beta was shown to be an excellent Lewis catalyst in different reactions such as Baeyer-Villiger [8, 192] or Meerwein-Ponndorf-Verley [193] ones. Meanwhile, the reported SnAPO materials before the irruption of MCHA had very scarce impact. All these SnAPOs had been prepared from Sn (IV) sources, whose incorporation mechanism is potentially varied and of doubtful effectiveness in terms of acidify if 2 Sn(IV) atoms substitutes a pair Al(III)-P(V). However, it is well-known that tin has two quite stable oxidation states, 4+ and 2+. The incorporation of Sn(II) in an $AlPO_4$-5 framework has necessarily to be in Al positions, and no Sn-O-Sn environments should be formed. Therefore, all Sn (II) centres should be equal, and each incorporated Sn(II), unlike Sn(IV), entails the generation of a Brönsted acid site. Such predictions were indeed confirmed once both materials Sn(IV)APO-5 and Sn(II)APO-5 were successfully prepared taking advantage of the high specificity of MCHA [194]. The characterization by means of X-ray diffraction (through their unit cell parameters), UV-visible spectroscopy, solid-state ^{31}P MAS NMR and temperature-programmed desorption (TPD) of ammonia confirmed that all Sn(II) but just a part of Sn(IV) were rightly incorporated into the $AlPO_4$ framework in different environments and that the acidity of Sn(II)APO-5 was higher than that of Sn(IV)APO-5 (Fig. 24). Confirming this characterization evidence, the catalytic performance of Sn(II)APO-5 in the Friedel-Crafts acylation of

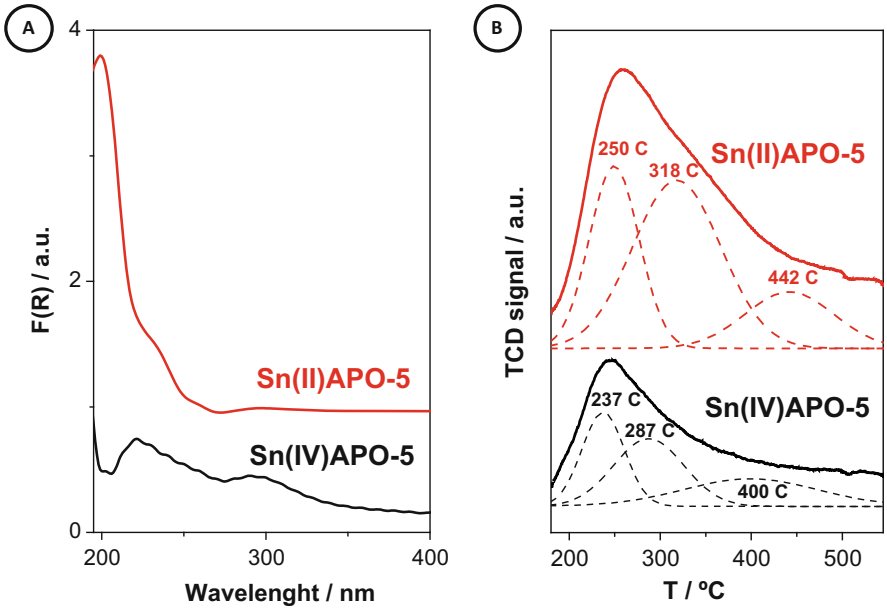

Fig. 24 DR-UV-vis spectra (**a**) and NH_3-TPD profiles (**b**) of Sn(IV)APO-5 (red lines) and Sn(II) APO-5 (black lines) samples. In Fig. 24b, the three components in which each profile has been decomposed are also shown to underline the higher acidity of the Sn(II)APO-5 sample. Reproduced from Ref. [194] with permission of The Royal Society of Chemistry

anisole, which requires the presence of Brönsted acid sites, clearly overcomes that given by Sn(IV)APO-5, SAPO-5 and even by a zeolite H-Al-beta [194].

The incorporation of Ti into zeolite frameworks revolutionized the applications of inorganic microporous materials, as they started being used as catalysts in so many fine chemistry reactions [4, 195]. It was the germ of the metal-zeolites, the subject of this issue. Ti-zeolites have been the most extensively investigated metal-zeolites, not only because of their pioneer condition but also because of their outstanding catalytic performance in different reactions of industrial interest. On the contrary, Ti-containing AlPOs, which are known as TiAPO, TiAPOs or TiAlPOs, have been scarcely studied, undoubtedly due to their much more modest catalytic power compared with their counterpart Ti-zeolites. In principle, there are several reasons behind that substantial difference. Firstly, $AlPO_4$ framework is quite hydrophilic (Table 1) contrasting with the hydrophobic nature of the Al-free zeolites, which severely limits the application of the former in organic reactions. Secondly, the incorporation mechanism of heteroatom ions into microporous materials, which is richer in AlPOs than in zeolites (Table 1), could become somehow unfavourable in aluminophosphates when tetravalent ions are desired to be incorporated. It is due to the following: (1) its isolated incorporation (by either Al or P) necessarily entails a charge deficiency/excess, so their intrinsic activity is seriously modified, particularly by the existence of Brönsted acid sites Ti-OH-Al if the most accepted Ti incorporation in P sites of an $AlPO_4$ framework is assumed; and (2) the incorporation mechanism is not unique, but several mechanisms and even a combination of them can be taken place in a given material, and then several types of active sites could be found. Finally, the intrinsic activity of Ti in an $Ti(OSi)_4$ environments is much more active than in an $Ti(OAl)_4$ environments. These three facts (hydrophilicity, associated Brönsted acidity and intrinsic activity) are indeed responsible of the much lower activity of Ti-Al-zeolites than that of Al-free Ti-zeolites [196, 197], and it is expected that their negative influence is higher in the catalytic activity of TAPOs.

Until recently, all the TAPO materials had been synthesized starting from Ti (IV) sources. However, since 2013, again taking advantage of the high specificity of MCHA towards AFI-structured materials, the synthesis of TAPO-5 using Ti(III) source was proposed and carrying out the gel formation and crystallization under inert conditions, in order to avoid the spontaneous oxidation of Ti(III) to Ti (IV) under an oxidant atmosphere [106, 198–201]. This approach could in principle solve two of the three above-mentioned drawbacks of TAPOs vs. Ti-zeolites: (1) the Ti environment would be $Ti(OP)_4$ instead of $Ti(OAl)_4$ found in conventional TAPOs, and (2) the Brönsted acidity associated to Ti incorporation is avoided. The third drawback, i.e. the hydrophilic nature, is basically unaffected. Once Ti (III)APO-5 material was exposed to the ambient atmosphere, it was transformed to a Ti(IV)APO-5, which however possesses very different physicochemical properties (as evidenced by means of thermogravimetric analysis and UV-visible and multinuclear solid-state NMR spectroscopies) to the conventional TAPO-5 (Fig. 25). These new TAPO-5 materials were catalytically tested in the oxidation of cyclohexene with anhydrous H_2O_2, leading to two important conclusions: (1) they can reach catalytic conversion quite similar to Ti-beta, a large-pore Ti-containing

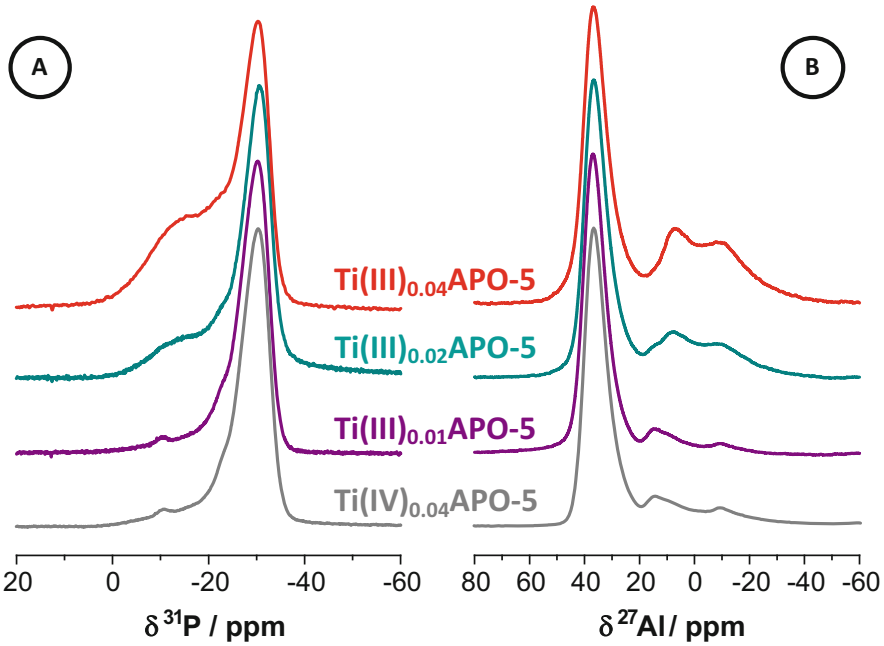

Fig. 25 ^{31}P (**a**) and ^{27}Al (**b**) MAS NMR spectra of a series of Ti(III)APO-5 samples with different Ti content. The spectra of a Ti(IV)APO-5 having the same Ti content than the Ti-richest Ti(III) APO-5 sample are also shown for comparison purposes. Adapted from Microporous Mesoporous Mater, 190, A. Alfayate et al., Incorporation of Ti(III) into the $AlPO_4$-5 framework by direct synthesis, 334–345, Copyright 2007, with permission from Elsevier [106]

zeolite having a 3-D pore system [198], and (2) not least, unlike the epoxidation route followed by the oxidation of cyclohexene by peroxides in the presence of Ti-zeolites, this new TAPO-5 catalysed the allylic oxidation of the olefin under the same conditions [198, 199, 201]. In other words, TAPO-5 materials prepared with Ti(III) sources could become as active as Ti-zeolites under certain experimental conditions and both materials could be catalytically complementary rather than competitors.

To the best of our knowledge, this is the first time that a heteroatom in an unstable oxidation state has been incorporated into an $AlPO_4$ framework. Moreover, this strategy has been rationally designed to change the metal environment within the microporous framework and then their catalytic behaviour.

5.1.7 Multi-metal-Substituted $AlPO_4$-5 Materials: Synergic Catalytic Effect

The simultaneous incorporation of different heteroatom ions in zeolites [202–204] and AlPOs [205–207], each one to generate centres of different nature (the most common being redox and acid centres or Brönsted and Lewis sites), is well known

and has been rationally designed to catalyse successive steps of a given reaction in just one step. However, the synergic catalytic effect of two different metal ions incorporated in microporous materials providing the same catalytic functionality (for instance, two redox catalytic centres), which is relatively common in metal-supported oxide-based catalysts, does not seem easy to be reached in metal-substituted crystalline microporous materials. The conventional synergic effect is based on the modification of the electronic properties (and then the catalytic potential) of an active metal by a second supported/incorporated metal, in such a way that the resultant multi-metallic catalysts become more active/selective than the corresponding monometallic counterparts. In zeolites and zeotypes, the isomorphic incorporation of metal ions generally leads to isolated metal sites surrounded by oxygen atoms and subsequently by the framework tetrahedral atoms (Si in the case of zeolites, P and/or Al in AlPOs) in the second coordination sphere. Therefore, the electronic influence of a second metal ion (incorporated in poor loadings imposed by zeolite/zeotype limitation) over the active metal is quite unlikely.

Nevertheless, simulation studies on the complex mechanism of the oxidation of hydrocarbons by oxygen in Mn- and Fe-substituted AlPOs [147–155] indicate that each transition metal can favour a particular step of the global mechanism. In particular, it was expected that co-doped FeMnAPO samples are more active than their counterpart FeAPO and MnAPO samples for a given metal content [153]. That prediction was indeed experimentally corroborated [208]. Therefore, a synergic catalytic effect is also possible to be reached in multi-metal-substituted $AlPO_4$ materials. However, this synergic effect is conceptually different to that frequently used: the co-incorporation of metal ions does not modify the electronic properties with respect to these of the same metals individually incorporated in the same $AlPO_4$ structure, but any metal could act effectively in different steps of a given reaction, accelerating the global kinetics.

MCHA/$AlPO_4$-5 system was again the option selected by Raja et al. for a systematic study on the multi-metal-substituted $AlPO_4$-based catalysts [157, 209]. Pure AFI materials were crystallized irrespective of the number and/or loading of dopants. Metal ions as heavy as Ru(III) were used, and the simultaneous incorporation up to three different metals (in the sample RuZnSnAPO-5) was achieved [157]. Figure 26 shows the catalytic benefits of using bimetallic MeAPO-5 catalysts against their monometallic counterpart in the oxidation of cyclohexene using acetylperoxyborate as the oxidant. The improvement of the turnover of co-doping $AlPO_4$-5 with both Co and Ti in the oxidation of cyclohexene becomes ca. four times with respect to CoAPO-5 and twice with respect to the monometallic TAPO-5. In the heavy metal-containing RuSnAPO-5 samples, the catalytic enhancement, although evident, is not as high as in the previous example, because the monometallic SnAPO-5 and RuAPO-5 are already quite active.

In a similar way, the bimetallic Ti,V-doped $AlPO_4$-5 was also more active than their monometallic homologues in the same reaction [209]. Its characterization by means of a combination of HYSCORE EPR and in situ FTIR studies indicated that V and Ti centres play distinct roles in a concerted fashion that synergistically boost the overall catalytic performance. Ti centres link the oxidant to activate it through the

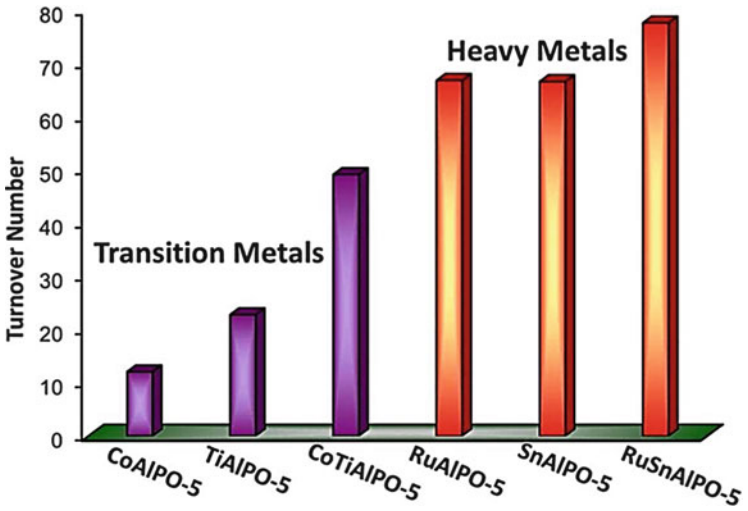

Fig. 26 Turnover number of the differently doped $AlPO_4$-5 materials prepared with MCHA as SDA in the epoxidation of cyclohexene with acetylperoxyborate at 66°C. The turnover of the samples doped with transition metals (Co and/or Ti) is plotted as purple columns, and the samples doped with heavy metals (Ru and/or Sn) are given as orange columns. Reprinted with permission from [157]. Copyright 2012 American Chemical Society. Further permissions related to the material excerpted should be directed to the ACS

formation of peroxo species, whereas V possesses lower barrier than Ti to carry out the oxidation itself once the oxidant is activated [209].

5.2 Designing New SDAs for AlPOs/MeAPOs Able to Be Prepared by Just One SDA

If the low phase specificity is problematic and quite limiting for AlPO materials that can be non-specifically prepared with dozens of known SDAs, it becomes much more serious when only one (low phase specific) SDA has been described for a given $AlPO_4$ structure. Obviously, the knowledge of a unique SDA able to direct the crystallization of a given structure does not imply high specificity. Also in these cases, the above-described strategy to find new amine-based SDA for a particular 1D-pore $AlPO_4$ topology can be an elegant and simple solution. In this section, the application of that approach is described for two additional $AlPO_4$ structures: the large-pore ATS ($AlPO_4$-36) and the small-pore ATN ($AlPO_4$-39) [171]. Before this approach was applied to these systems, the only described SDA able to direct the crystallization of these materials were tripropylamine and dipropylamine (DPA), respectively. The first one can also lead to AFI-structured materials, whereas DPA is probably the less phase-specific amine as it has been used for at least ten different $AlPO_4$-based materials (ATN, AFO, AEL, VFI, ATO, APC, AFS, GIS, AFS or

AFY) [131–133]. In addition, DPA mainly tends to give $AlPO_4$-11, and the experimental conditions to generate $AlPO_4$-39/MAPO-39 are really narrow [57].

Figure 27 shows the fits of the conventional SDAs for $AlPO_4$-5, -36 and -39, as well as the fits of the new proposed SDAs for these structures. Both conventional and proposed SDAs are configured as the model predicts, that is, in its most stable conformation and with the bulkiest R hydrocarbon substituent group in the amine NR_3 running along the $AlPO_4$ channel [171]. Given the high symmetry of both DPA and ATN pore, the fit is relatively good from the shape point of view, but it is quite improvable in terms of size. Diisobutylamine (DiBA) is not as symmetric as DPA, but in that conformation, the general fit within the ATN pore could be better than that given by DPA. The experiments confirmed that DiBA was at least as specific as DPA in the preparation of CoAPO-39 [171]. Like DPA, when some experimental conditions were altered, CoAPO-11 (AEL topology) appeared as impurity, and even it could be purely crystallized with DiBA. At least, an alternative to the unique SDA able to lead ATN topology was found.

In the case of ATS-structured MeAPO materials, the fit of TPA within their pores was rather poor but a bit better than in AFI pore (Fig. 27). Tripropylamine (TPA) has been selected as the SDA for AFI among the dozens of SDAs able to crystallize $AlPO_4$-5 materials [56] precisely to compare its fitting to that found in ATS structure. The slightly better fit in ATS than in AFI pores could be behind the fact that TPA was the only known organic SDA that led to the formation of ATS materials before applying our simple method. The relatively poor fit of TPA within ATS pore suggested the existence of a great room in the search of new SDAs for such topology. In principle, much better fit was achieved by the commercial amines *N*-ethyldicyclohexylamine (ECHA) and diisopropylisobutylamine (DPBA) (Fig. 27)

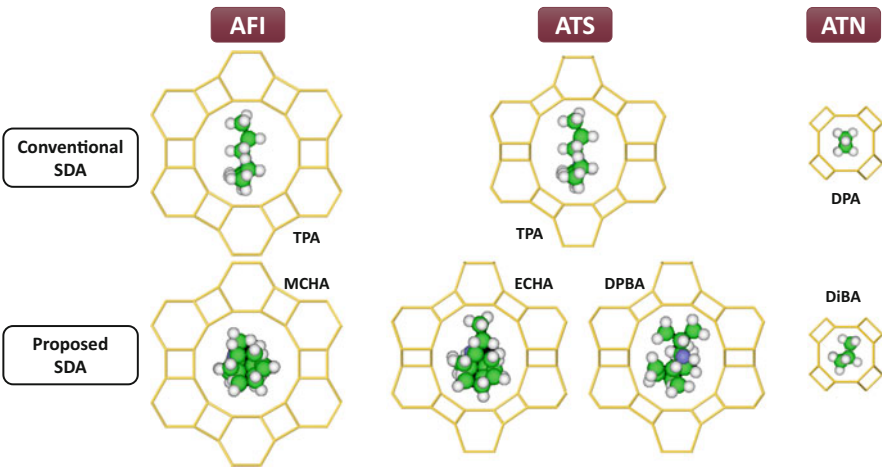

Fig. 27 Schematic representation of some conventional (top) and proposed (bottom) amine-based SDA fitted within the pores of the 1D topologies AFI (left), ATS (middle) and ATN (right)

[171]. Indeed, these two new templates were experimentally able to direct the crystallization of ATS-structured $AlPO_4$-based materials in an efficient way.

An exhaustive study of the crystallization kinetics of CoAPO-36 together with some simulation calculations was also carried with the three amine-based SDAs. It confirmed that the two new proposed SDA needed less activation energy to produce these materials (Fig. 28) [210], which is consistent with the much quicker crystallization experimentally found for DPBA and ECHA. In addition, computational calculations confirmed that the interaction energy (defined as the difference between the total energy of the framework/template system and the energy of an isolated gas-phase template molecule) is much lower for DPBA and ECHA than for TPA. Such comparison could be questioned as kinetically controlled rates of reaction are compared with the thermodynamic products. However, previous studies have shown an unequivocal and strong correlation between energetics of template fit and rates of crystallization for a series of zeolite structures, so that the crystallization is faster for template fits of lower energy [211].

Therefore, the effectiveness in filling the pore, that is, the goodness of the fit SDA pores shown in Fig. 28 can be taken as a reliable indication of the power of an amine as structure-directing agent in AlPOs. In other words, we believe that the structure-directing effect of the amines in the synthesis of $AlPO_4$-based materials indeed includes an important contribution of 'template' effect, although some other contributions to the SDA role, such as pH controller, compensation of the charge framework (if any) or the simple filling of the confined space of the pores, etc., would call into question this fact. Such contribution of the 'template' effect to the general structure-directing role could become an important tool in the rational design of more efficient and more specific organic SDA for $AlPO_4$-based materials.

In summary, along this section, it has been made clear that finding specific and effective SDAs for the preparation of metal-substituted AlPOs could be key in two contexts: (1) in an academic one, allowing to carry out systematic works in which just one parameter (metal nature, synthesis pH, etc.) could be varied keeping practically constant the rest, and (2) in the context of application, improving the (catalytic) properties of a given MeAPO by different strategies such as reducing crystal size, introducing inter- or intracrystalline mesoporosity, controlling the chemical environment of the metal dopants by rational choice of their oxidation state (even if they are unstable under ambient conditions), incorporating very large heteroatom ions including heavy metals or favouring the synergic effect when more than one heteroatom are incorporated.

6 Conclusions

Aluminophosphate microporous materials (AlPOs) are the zeotypes possessing most similar properties to zeolites, especially in their use as catalysts. Thus, like zeolites, AlPOs are crystalline, microporous and thermally stable (depending on the structure and heteroatom content) and can be crystallized in a variety of topologies (some of

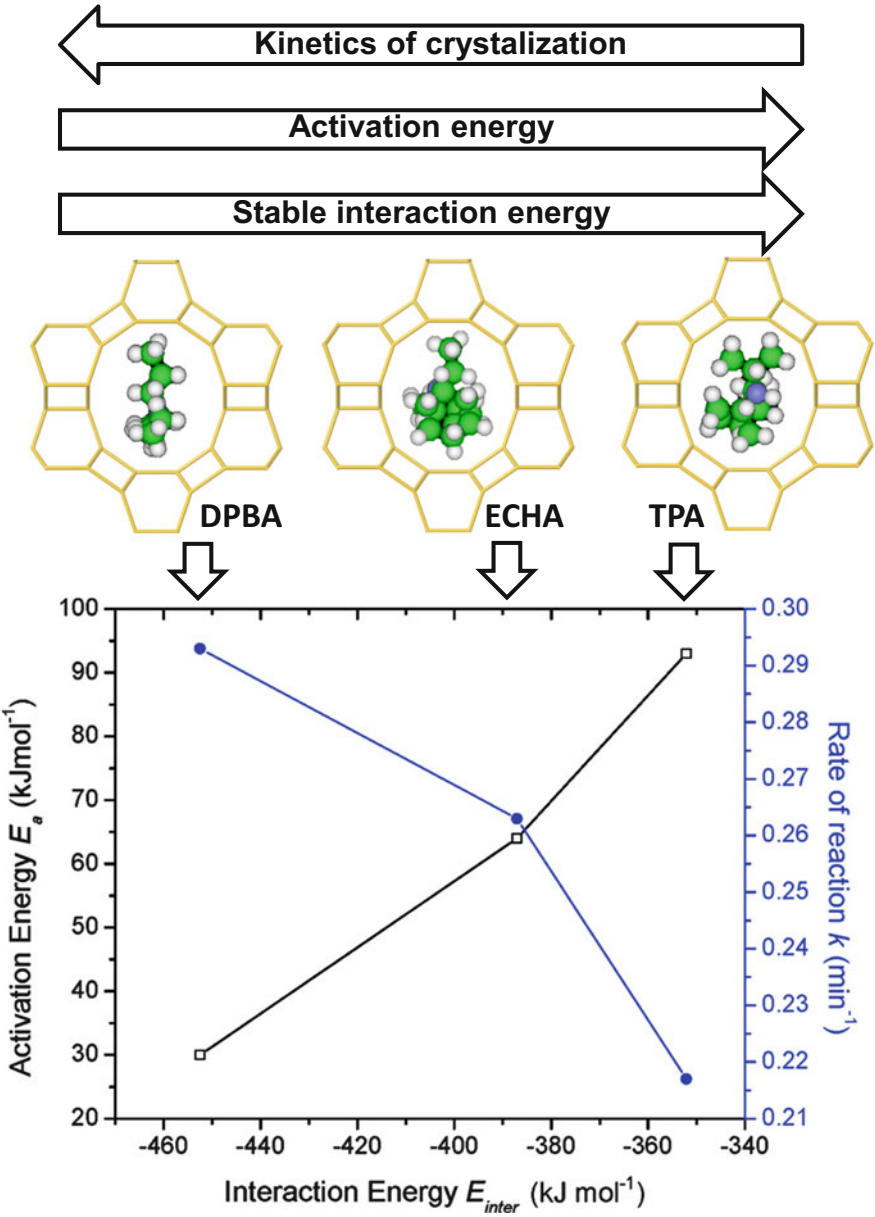

Fig. 28 On the bottom, computational calculated interaction energies of the SDAs TPA (left), ECHA (middle) and DPBA (right) within an CoAPO ATS pore plotted versus both activation energy (black line, left *Y*-axis) and rate of crystallization (blue line, right *Y*-axis). Reprinted with permission from [210]. Copyright 2012 American Chemical Society. In the middle, representation of the fit of the three SDA within the ATS pore. On the top, order of kinetics of crystallization, activation energy and interaction energy for the three SDAs

them can also be prepared as zeolite forms) having small, medium, large and/or very large micropores. Besides, both families of microporous materials have also in common the general use of amines and or quaternary ammonium hydroxides as structure-directing agents.

The general common properties with zeolites make $AlPO_4$-based materials being used in similar applications than zeolites. However, the real potential of $AlPO_4$-based materials is mostly found in the diversity of heteroatom incorporation by isomorphic substitution. Such diversity includes oxidation states, cation sizes, incorporation mechanism, pH of the incorporation or final chemical environment in the framework, which are difficult to achieve by silica-based zeolite frameworks. In addition, some microporous $AlPO_4$ topologies cannot be prepared with a SiO_2-based composition.

It must be noted that a range of divalent cations with catalytic relevance as Co^{2+}, Mn^{2+}, Fe^{2+}, etc. can be easily introduced into the $AlPO_4$ framework (in Al^{3+} sites) of these materials; similarly, tetravalent ions as Ti^{4+} and V^{4+} can be introduced in P^{5+} sites. Besides, the $AlPO_4$ frameworks allow these heteroatoms to change its oxidation state (normally in redox cycles 2+ to 3+) as many times as the reaction requires with no leaching. These catalysts have been successfully used in the highly demanding oxidation of inert alkanes with air or oxygen as oxidants. The catalytic results combined with an adequate selection of advanced characterization techniques and computational calculations led to a deeper understanding of the active sites and the reaction mechanism. And such knowledge allowed the rational design of more active catalysts by careful choice of the metal nature as a function of their Me^{2+}/Me^{3+} ratio in the calcined catalysts. Similarly, the right choice of the Me content and the structure depending of the reactants to be catalysed led to the design of regioselective catalysts.

Some of the apparently intrinsic disadvantages of $AlPO_4$-based materials can be solved out. That is the case of the low phase specificity of amines as structure-directing agents, which limits both the systematic studies and the improvement of the physicochemical properties of the MeAPO catalysts. Starting from a simple method based on the most probable and stable conformation of the amines along the 1D-pore topologies, new SDAs was found for ATS and ATN structures as effective alternatives to the known SDAs for these materials. Moreover, MCHA showed to be most specific SDA for AFI materials. Taking advantage of that, all MeAPO-5 materials can be prepared under the same conditions by just changing the metal (Me) nature. In addition, it allows the control of parameters as metal content, metal ion size, incorporation of metals in different oxidation state, metal environment, crystal size, hierarchical meso-/micro-porosity or easy/direct co-incorporation of different metal ions in a given $AlPO_4$-5 framework promoting synergic catalytic effects.

As a final and more general conclusion, metal-substituted aluminophosphates provide unique features to the exciting catalytic world of heteroatom-containing microporous materials.

Acknowledgements GS thank EPSRC and Royal Society for funding. MSS acknowledges the financing by the Spanish State Research Agency (AEI) and the European Regional Development

Fund (FEDER) through the Project MAT2016-77496-R (AEI/FEDER, UE). Thanks to Dr. A. Alfayate for kindly providing us a figure.

References

1. Cronstedt AF (1756) Kongl Vetenskaps Academiens Handlingar Stockholm 17:120–123
2. http://www.iza-structure.org/databases/
3. Baerlocher CH, McCusker LB, Olson DH (2007) Atlas of zeolite framework types, 6th edn. Elsevier, Amsterdam
4. Taramasso M, Perego G, Notari B (1983) US Patent 4 410 501
5. Barrer RM, Freund E (1974) J Chem Soc Dalton Trans 10:1049–1060
6. Rigutto MS, van Bekkum H (1991) Appl Catal 68:L1–L7
7. Dongare MK, Singh P, Moghe PP, Ratnasamy P (1991) Zeolites 11:690–693
8. Corma A, Nemeth LT, Renz M, Valencia S (2001) Nature 412:423–425
9. Chu CT, Chang CD (1985) J Phys Chem 89:1569–1571
10. Calis G, Frenken P, de Boer E, Swolfs A, Hefni MA (1987) Zeolites 7:319–326
11. Corma A, Diaz-Cabanas MJ, Martinez-Triguero J, Rey F, Rius J (2002) Nature 418:514–517
12. Sulikowski B (1996) Heterog Chem Rev 3:203–268
13. Barrer RM (1982) Hydrothermal chemistry of zeolites. Academic Press, London, p 251
14. van Bokhovena JA, Lamberti C (2014) Coord Chem Rev 277–278:275–290
15. Corma A, Martinez A (1995) Adv Mater 7:137–144
16. Ma Y, Tong W, Zhou H, Suib SL (2000) Microporous Mesoporous Mater 37:243–252
17. Cooper ER, Andrews CD, Wheatley PS, Webb PB, Wormald P, Morris RE (2004) Nature 430:1012–1016
18. Vomscheid R, Briend M, Peltre MJ, Man PP, Barthoumeuf D (1994) J Phys Chem 98:9614–9618
19. Chen G, Sun Q, Yu QJ (2017) Chem Commun 53:13328–13331
20. Chen J, Natarajan S, Thomas JM, Jones RH, Hursthouse MB (1994) Angew Chem Int Ed 33:639–640
21. Gier ET, Stucky GD (1991) Nature 349:508–510
22. Wilson ST, Lok BM, Flanigen EM (1982) US Patent 4 310 440
23. Wilson ST, Lok BM, Messina CA, Cannan TR, Flanigen EM (1982) J Am Chem Soc 104:1146–1147
24. Forster PM, Eckert J, Chang JS, Park SE, Ferey G, Cheetham AK (2003) J Am Chem Soc 125:1309–1312
25. Parise JB (1985) J Chem Soc Chem Commun 606–607
26. Littlefield BTR, Weller MT (2012) Nat Commun 3:1114
27. Murugavel R, Choudhury A, Walawalkar MG, Pothiraja R, Rao CNR (2008) Chem Rev 108:3549–3655
28. Corma A, Diaz-Cabanas M, Jorda JL, Martinez C, Moliner M (2006) Nature 443:842–845
29. Sun J, Bonneau C, Cantin S, Corma A, Diaz-Cabanas MJ, Moliner M, Zhang D, Li M, Zou X (2009) Nature 458:1154–1157
30. Davis ME, Saldarriaga C, Montes C, Garces J, Crowder C (1988) Nature 331:698–699
31. Rouhi AM (2015) Chem Eng News 93:30–31
32. Tian P, Wei YX, Ye M, Liu ZM (2015) ACS Catal 5:1922–1938
33. Messina CA, Lok BM, Flanigen EM (1985) US Patent 4 544 143
34. Wilson ST, Flanigen EM (1986) US Pat 4 567 029
35. Thomas JM, Raja R, Sankar S, Bell RG (1999) Nature 398:227–230
36. Raja R, Sankar G, Thomas JM (1999) J Am Chem Soc 121:11926–11927
37. Thomas JM, Raja R, Sankar G, Bell RG (2001) Acc Chem Res 34:191–200

38. Ng EP, Mintova S (2008) Microporous Mesoporous Mater 114:1–26
39. Cheung O, Hedin N (2014) RSC Adv 4:14480–14494
40. Hartmann M, Kevan L (1996) J Chem Soc Faraday Trans 92:3661–3667
41. de Saldarriaga LS, Saldarriaga C, Davis ME (1987) J Am Chem Soc 109:2686–2691
42. Man PP, Briend M, Peltre MJ, Lamy A, Beaunier P, Barthomeuf D (1991) Zeolites 11:563–572
43. Feng P, Bu X, Stucky GD (1997) Nature 388:735–741
44. Camblor MA, Corma A, Valencia S (1996) Chem Commun 2365–2366
45. Camblor MA, Villaescusa LA, Diaz-Cabanas MJ (1999) Top Catal 9:59–76
46. Lechert H (2004) Microporous Mesoporous Mater 22:519–523
47. Ren X, Komarneni S, Roy DM (1991) Zeolites 11:142–148
48. Pourbaix M (1974) Atlas of electrochemical equilibria in aqueous solutions. National Association of Corrosion Engineers, Houston
49. Davis ME, Lobo RF (1992) Chem Mater 4:756–768
50. Cundy CS, Cox PA (2003) Chem Rev 103:663–702
51. Prasad S, Liu SB (1994) Chem Mater 6:633–635
52. O'Brien MG, Beale AM, Catlow CRA, Weckhuysen BM (2006) J Am Chem Soc 128:11744–11745
53. Beale AM, O'Brien M, Kasunic M, Golobic A, Sanchez Sanchez M, AJW L, Lewis DW, Wragg DS, Nikitenko S, Bras W, Weckhuysen BM (2011) J Phys Chem C 115:6331–6340
54. Valyocsik EW, Rollmann LD (1985) Zeolites 5:123–125
55. Ren L, Zhu L, Yang C, Chen Y, Sun Q, Zhang H, Li C, Nawaz F, Meng X, Xiao FS (2011) Chem Commun 47:9789–9791
56. Wilson ST, Lok BM, Messina CA, Cannan TR, Flanigen EM (1983) In: Stucky GD, Dwyer FG (eds) Intrazeolite chemistry, ACS Symposium Series 218, American Chemical Society, Washington, DC, p 79
57. Ojo AF, McCusker LB (1991) Zeolites 11:460–465
58. Akolekar DB, Kaliaguine S (1993) J Chem Soc Faraday Trans 89:4141–4147
59. Akolekar DB (1995) Zeolites 15:583–590
60. Kumar R, Bhaumik A, Ahedi RK, Ganapathy S (1996) Nature 381:298–300
61. Annen MJ, Davis ME, Higgins JB, Schlenker JL (1991) J Chem Soc Chem Commun 1175–1176
62. Annen MJ, Davis ME (1993) Microporous Mater 1:57–65
63. Takewaki T, Beck LW, Davis ME (1999) J Phys Chem B 103:2674–2679
64. Zhang X, Liu P, Wu Y, Yao Y, Wang J (2010) Catalogue Lett 137:210–215
65. Flanigen EM, Lok BM, Patton RL, Wilson ST (1986) Stud Surf Sci Catal 28:103–112
66. Qiu S, Tian W, Pang W, Sun T, Jiang D (1991) Zeolites 11:371–375
67. Barthomeuf D (1994) Zeolites 14:394–401
68. Blasco T, Chica A, Corma A, Murphy W, Agundez-Rodriguez J, Perez-Pariente J (2006) J Catal 242:153–161
69. Sanchez-Sanchez M, Gomez-Hortiguela L, Sankar G (2008) Microporous Mesoporous Mater 114:485–494
70. Zanjanchi MA, Ghanadzadeh A, Khadem-Nahvi F (2002) J Incl Phenom Macrocycl Chem 42:295–299
71. Maurelli S, Vishnuvarthan M, Berlier G, Chiesa M (2012) Phys Chem Chem Phys 14:987–995
72. Barrett PA, Sankar G, Stephenson R, Catlow CRA, Thomas JM, Jones RH, Teat SJ (2006) Solid State Sci 8:337–341
73. Muncaster G, Davies AT, Sankar G, Catlow CRA, Thomas JM, Colston SL, Barnes P, Waltonc RI, O'Hare D (2000) Phys Chem Chem Phys 2:3523–3527
74. Sanchez-Sanchez M, Romero AA, Pinilla-Herrero I, Sastre E (2017) Catal Today 296:239–246
75. Duncan B, Stocker M, Gwinup D, Szotak R, Vinje V (1993) Bull Soc Chim Fr 129:98–110
76. McCusker LB, Baerlocher C, Jahn E, Bulow M (1991) Zeolites 11:308–313

77. Martens JA, Janssens C, Grobet PJ, Beyer HK, Jacobs PA (1989) Stud Surf Sci Catal 49:215–225
78. Gabelica Z, Louti A, Borges C, Ribeiro MF, Lourenco JP, Murphy DM (2004) Stud Surf Sci Catal 154:1649–1654
79. Sierra L, Patarin J, Guth JL (1997) Microporous Mater 11:19–35
80. Harding MM, Kariuki BM (1994) Acta Cryst C50:852–854
81. Diaz-Cabanas MJ, Barrett PA, Camblor MA (1998) Chem Commun 1881–1882
82. Onyestyak G, Valyon J, LVC R (2001) Solid State Ionics 141–142:93–97
83. Bejblova M, Zones SI, Cejka J (2007) Appl Catal A Gen 327:255–260
84. Sanchez-Sanchez M, Sankar G, Simperler A, Bell RG, Catlow CRA, Thomas JM (2003) Catal Lett 88:163–168
85. Davies AT, Sankar G, Catlow CRA, Clark SM (1997) J Phys Chem 101:10115–10120
86. Zenonos C, Sankar G, Cora F, Lewis DW, Pankhurst AQ, Catlow CRA, Thomas JM (2002) Phys Chem Chem Phys 4:5421–5429
87. Patinec V, Wright PA, Lightfoot P, Aitken RA, Cox PA (1999) J Chem Soc Dalton Trans 3909–3911
88. Garcia R, Philp EP, Slawin AMZ, Wright PA, Cox PA (2001) J Mater Chem 11:1421–1427
89. Grosse-Kunstleve RW, McCusker LB, Baerlocher CH (1997) J Appl Crystallogr 30:985–995
90. Inge AK, Fahlquist H, Willhammar T, Huang Y, McCusker LB, Zou X (2013) J Appl Crystallogr 46:1094–1104
91. McCusker LB (1991) Acta Cryst A47:297–313
92. McCusker LB (1994) Stud Surf Sci Catal 84:341–356
93. Wright PA (2008) 'Microporous framework solids' RSC materials monographs. RSC Publishing, Cambridge, pp 79–147
94. Gramm F, Baerlocher CH, McCusker LB, Warrender SJ, Wright PA, Han B, Hong SB, Liu Z, Ohsuna T, Terasaki O (2006) Nature 444:79–81
95. Sun J, He Z, Hovmoller S, Zou X, Gramm F, Baerlocher CH, McCusker LB (2010) Z Kristallogr Cryst Mater 225:77–85
96. Wright PA, Natarajan S, Thomas JM, Bell RG, Gai-Boyes PL, Jones RH, Chen J (1992) Angew Chem Int Ed 31:1472–1475
97. Barrett PA, Jones RH (2000) Phys Chem Chem Phys 2:407–412
98. Sankar G, Wyles JK, Jones RH, Thomas JM, Catlow CRA, Lewis DW, Clegg W, Coles SJ, Teat SJ (1998) Chem Commun 117–118
99. Simmance K, Sankar G, Bell RG, Prestipino C, van Beek W (2010) Phys Chem Chem Phys 12:559–562
100. Simmance K, van Beek W, Sankar G (2015) Faraday Discuss 177:237–247
101. Canesson L, Tuel A (1997) Chem Commun 241:242
102. Canesson L, Boudeville Y, Tuel A (1997) J Am Chem Soc 119:10754–10762
103. Barrie PJ, Klinowski J (1989) J Phys Chem 93:5972–5974
104. Shea WL, Borade RB, Clearfield A (1993) J Chem Soc Faraday Trans 89(3143):3149
105. Tuel A, Arcon I, Tusar NN, Meden A, Kaucic V (1996) Microporous Mater 7:271–284
106. Alfayate A, Sanchez-Sanchez M, Perez-Pariente J (2014) Microporous Mesoporous Mater 190:334–345
107. Schoonheydt RA, De Vos R, Pelgrims J, Leeman H (1989) Stud Surf Sci Catal 49:559–568
108. Kraushaar-Czarnetzki B, Hoogervorst WGM, Andrea RR, Emeis CA, Stork WHJ (1991) J Chem Soc Faraday Trans 87:891–895
109. Uytterhoeven MG, Schoonheydt RA (1994) Microporous Mater 3:265–279
110. Nakashiro K, Ono Y (1993) Bull Chem Soc Jpn 66:9–17
111. Verberckmoes AA, Uytterhoeven MG, Schoonheydt RA (1997) Zeolites 19:180–189
112. Verberckmoes AA, Uytterhoeven MG, Schoonheydt RA (1998) Microporous Mesoporous Mater 22:165–178
113. Weckhuysen BM, Rao RR, Martens JA, Schoonheydt RA (1999) Eur J Inorg Chem 1999:565–577

114. Tusar NN, Mali G, Arcon I, Kaucic V, Ghanbari-Siahkali A, Dwyer J (2002) Microporous Mesoporous Mater 55:203–216
115. Weckhuysen BM, Verberckmoes AA, Uytterhoeven MG, Mabbs FE, Collison D, de Boer E, Schoonheydt RA (2000) J Phys Chem B 104:37–42
116. Barrett PA, Sankar G, Catlow CRA, Thomas JM (1996) J Phys Chem 100:8977–8985
117. Chen J, Thomas JM (1994) J Chem Soc Chem Commun 603–604
118. Chen J, Thomas JM, Sankar G (1994) J Chem Soc Faraday Trans 90:3455–3459
119. Thomas JM, Greaves GN, Sankar G, Wright PA, Chen J, Dent AJ, Marchese L (1994) Angew Chem Int Ed 33:1871–1873
120. Hartmann M, Elangovan SP (2009) Adv Nanoporous Mater 1:237–312
121. Hartmann M, Kevan L (1999) Chem Rev 99:635–663
122. Hartmann M, Kevan L (2002) Res Chem Intermed 28:625–695
123. Kurshev V, Kevan L, Parillo DJ, Pereira C, Kokotailo GT, Gorte RJ (1994) J Phys Chem 98:10160–10166
124. Nagarajan V, Rings D, Moschkowitz L, Hartmann M, Poppl A (2005) Chem Lett 34:1614–1615
125. Prakash AM, Hartmann M, Zhu Z, Kevan L (2000) J Phys Chem B 104:1610–1616
126. Prakash AM, Kevan L (1999) J Phys Chem 103:2214–2222
127. Zahedi-Niaki MH, Kaliaguine S (1999) J Phys Chem B 103:831–837
128. Prakash AM, Kurshev V, Kevan L (1997) J Phys Chem B 101:9794–9799
129. Zhu Z, Kevan L (1999) Phys Chem Chem Phys 1:199–206
130. Beale AM, Sankar G, Catlow CRA, Anderson PA, Green TL (2005) Phys Chem Chem Phys 7:1856–1860
131. Cora F, Sankar G, Catlow CRA, Thomas JM (2002) Chem Commun 734–735
132. Franklin IL, Beale AM, Sankar G (2003) Catal Today 81:623–629
133. Ono Y (2003) J Catal 216:406–415
134. Zhang HX, Chokkalingam A, Subramaniam PV, Joseph S, Takeuchi S, Wei MD, Al-Enizi AM, Jang HG, Kim JH, Seo G, Komura K, Sugi Y, Vinu A (2016) J Mol Catal A Chem 412:117–124
135. Concepcion P, Lopez Nieto JM, Mifsud A, Perez-Pariente J (1997) Appl Catal A Gen 151:373–392
136. Fan W, Fan B, Song M, Chen T, Li R, Dou T, Tatsumi T, Weckhuysen BM (2006) Microporous Mesoporous Mater 94:348–357
137. Masters AF, Beattie JK, Roa AL (2001) Catal Lett 75:159–162
138. Moden B, Zhan BZ, Dakka J, Santiesteban JG, Iglesia E (2007) J Phys Chem C 111:1402–1411
139. Schuchardt U, Cardoso D, Sercheli R, Pereira R, da Cruz RS, Guerreiro MC, Mandelli D, Spinace EV, Pires EL (2001) Appl Catal A Gen 211:1–17
140. Vanoppen DL, De Vos DE, Genet MJ, Rouxhet PG, Jacobs PA (1995) Angew Chem Int Ed 34:560-563
141. Wang XH, Li J, Wan YJ, Yan JL, Zhang BQ, Liu XF (2010) Chin Sci Bull 55:4112–4115
142. Moden B, Oliviero L, Dakka J, Santiesteban JG, Iglesia E (2004) J Phys Chem B 108:5552–5563
143. Moden B, Zhan BZ, Dakka J, Santiesteban JG, Iglesia E (2006) J Catal 239:390–401
144. Dugal M, Sankar G, Raja R, Thomas JM (2000) Angew Chem Int Ed 39:2310–2313
145. Sankar G, Raja R, Thomas JM (1998) Catal Lett 55:15–23
146. Raja R, Sankar G, Thomas JM (2000) Angew Chem Int Ed 39:2313–2316
147. Cora F, Gomez-Hortiguela L, Catlow CRA (2012) Proc R Soc A 468:2053–2069
148. Gomez-Hortiguela L, Cora F, Catlow CRA (2011) ACS Catal 1:18–28
149. Gomez-Hortiguela L, Cora F, Catlow CRA (2011) ACS Catal 1:945–955
150. Gomez-Hortiguela L, Cora F, Catlow CRA (2011) ACS Catal 1:1487–1497
151. Gomez-Hortiguela L, Cora F, Catlow CRA (2011) ACS Catal 1:1475–1486
152. Gomez-Hortiguela L, Cora F, Catlow CRA (2012) J Phys Chem C 116:6691–6702

153. Gomez-Hortiguela L, Cora F, Catlow CRA (2013) Phys Chem Chem Phys 15:6870–6874
154. Gomez-Hortiguela L, Cora F, Sankar G, Zicovich-Wilson C, Catlow CRA (2010) Chem Eur J 16:13638–13645
155. Gomez-Hortiguela L, Cora F, Catlow CRA (2013) Modelling and simulation in the science of micro- and meso-porous materials. Elsevier, Amsterdam, pp 265–295
156. Raja R, Lee SO, Sanchez-Sanchez M, Sankar G, Harris KDM, Johnson BFG, Thomas JM (2002) Top Catal 20:85–88
157. Potter ME, Paterson AJ, Raja R (2012) ACS Catal 2:2446–2451
158. Shiju NR, Fiddy S, Sonntag O, Stockenhuber M, Sankar G (2006) Chem Commun 4955–4957
159. Wei W, Moulijn JA, Mul G (2008) Microporous Mesoporous Mater 112:193–201
160. Raja R, Thomas JM, Sankar G (1999) Chem Commun 829:830
161. Raja R, Thomas JM, Sankar G (1999) Chem Commun 525–526
162. Hentit H, Bachari K, Ouali MS, Womes M, Benaichouba B, Jumas JC (2007) J Mol Catal A Chem 275:158–166
163. Raja R, Sankar G, Thomas JM (2001) J Am Chem Soc 123:8153–8154
164. Chatterjee S, Bhanja P, Paul L, Bhaumik A (2018) Dalton Trans 47:791–798
165. Wu JY, Chien SH, Wan BZ (2001) Ind Eng Chem Res 40:94–100
166. Zahedi-Niaki MH, Xu GY, Meyer H, Fyfe CA, Kaliaguine S (1999) Microporous Mesoporous Mater 32:241–250
167. Li J, Yu J, Xu R (2012) Proc R Soc A 468:1955–1967
168. Sanchez-Sanchez M, Serrano DP, van Grieken R, Melero JA (2007) Stud Surf Sci Catal 170:499–505
169. Wright PA, Jones RH, Natarajan S, Bell RG, Chen JS, Hursthouse MB, Thomas JM (1993) J Chem Soc Chem Commun 633–635
170. Yu J, Xu R (2010) Acc Chem Res 43:1195–1204
171. Sanchez-Sanchez M, Sankar G (2004) Stud Surf Sci Catal 154:1021–1027
172. Lok BM, Cannan TR, Messina CA (1983) Zeolites 3:282–291
173. Cundy CS, Cox PA (2005) Microporous Mesoporous Mater 82:1–78
174. Alvaro-Munoz T, Marquez-Alvarez C, Sastre E (2012) Catal Today 179:27–34
175. Akolekar DB (1993) J Catal 143:227–238
176. Flanigen EM, Lok BM, Patton RL, Wilson ST (1986) Pure Appl Chem 58:1351–1358
177. Nakashiro K, Ono Y (1991) J Chem Soc Faraday Trans 87:3309–3313
178. Machado MS, Perez-Pariente J, Sastre E, Cardoso D, Giotto MV, Garcia-Fierro JL, Fornes V (2002) J Catal 205:299–308
179. Akolekar DB (1994) Catal Lett 28:249–262
180. Manjon-Sanz A, Sanchez-Sanchez M, Munoz-Gomez P, Garcia R, Sastre E (2010) Microporous Mesoporous Mater 131:331–341
181. Manjon-Sanz A, Sanchez-Sanchez M, Sastre E (2012) Catal Today 179:102–114
182. Roldan R, Sanchez-Sanchez M, Sankar G, Romero-Salguero FJ, Jimenez-Sanchidrian C (2007) Microporous Mesoporous Mater 99:288–298
183. Jhung SH, Hwang YK, Chang JS, Park SE (2004) Microporous Mesoporous Mater 67:151–157
184. Egeblad K, Christensen CH, Kustova M, Christensen CH (2008) Chem Mater 20:946–960
185. Karanikolos GN, Garcia H, Corma A, Tsapatsis M (2008) Microporous Mesoporous Mater 115:11–22
186. Veziri CM, Palomino M, Karanikolos GN, Corma A, Kanellopoulos NK, Tsapatsis M (2010) Chem Mater 22:1492–1502
187. Wu LL, Hensen EJM (2014) Catal Today 235:160–168
188. Bonilla MR, Valiullin R, Karger J, Bhatia SK (2014) J Phys Chem C 118:14355–14370
189. Schmidt I, Madsen C, Jacobsen CJH (2000) Inorg Chem 39:2279–2283
190. Jacobsen CJH, Madsen C, Houzvicka J, Schmidt I, Carlsson A (2000) J Am Chem Soc 122:7116–7117

191. Sanchez-Sanchez M, Manjon-Sanz A, Diaz I, Mayoral A, Sastre S (2013) Cryst Growth Des 13:2476–2485
192. Renz M, Blasco T, Corma A, Fornes V, Jensen R, Nemeth L (2002) Chem Eur J 8:4708–4716
193. Corma A, Domine ME, Nemeth L, Valencia S (2002) J Am Chem Soc 124:3194–3195
194. Sanchez-Sanchez M, van Grieken R, Serrano DP, Melero JA (2009) J Mater Chem 19:6833–6841
195. Notari B (1996) Adv Catal 41:253–334
196. Corma A, Camblor MA, Esteve P, Martinez A, Perez-Pariente J (1994) J Catal 145:151–158
197. Torres JC, Cardoso PR (2010) Microporous Mesoporous Mater 136:97–105
198. Alfayate A, Marquez-Alvarez C, Grande-Casas M, Bernardo-Maestro B, Sanchez-Sanchez M, Perez-Pariente J (2013) Catal Today 213:211–218
199. Alfayate A, Marquez-Alvarez C, Grande-Casas M, Sanchez-Sanchez M, Perez-Pariente J (2014) Catal Today 227:57–64
200. Mayoral A, Sanchez-Sanchez M, Alfayate M, Perez-Pariente J, Diaz I (2015) ChemCatChem 7:3719–3724
201. Alfayate A, Sepulveda R, Sanchez-Sanchez M, Perez-Pariente J (2016) Top Catal 59:326–336
202. Ovejero G, van Grieken R, Uguina MA, Serrano DP, Melero JA (1996) Catal Lett 41:69–78
203. Winoto HP, Ahn BS, Jae JJ (2016) Ind Eng Chem 40:62–71
204. Padovan D, Al-Nayili A, Hammond C (2017) Green Chem 19:2846–2854
205. Tuel A, Taarit YB (1994) J Chem Soc Chem Commun 14:1667–1668
206. Blasco T, Fernandez L, Martinez-Arias A, Sanchez-Sanchez M, Concepcion P, Lopez-Nieto JM (2000) Microporous Mesoporous Mater 39:219–228
207. Gianotti E, Manzoli M, Potter ME, Shetti VN, Sun D, Paterson J, Mezza TM, Levy A, Raja R (2014) Chem Sci 5:1810–1819
208. Zhou LP, Xu J, Chen C, Wang F, Li XQ (2008) J Porous Mater 15:7–12
209. Leithall RM, Shetti VN, Maurelli S, Chiesa M, Gianotti E, Raja R (2013) J Am Chem Soc 135:2915–2918
210. O'Brien MG, Sanchez-Sanchez M, Beale AM, Lewis DW, Sankar G, Catlow CRA (2007) J Phys Chem C 111:16951–16961
211. Harris TV, Zones SI (1994) Stud Surf Sci Catal 84:29–36

Index